Ru-Shi Liu   *Editor*

Phosphors, Up Conversion Nano Particles, Quantum Dots and Their Applications

Volume 2

Phosphors, Up Conversion Nano Particles, Quantum Dots and Their Applications

Ru-Shi Liu

Editor

Phosphors, Up Conversion Nano Particles, Quantum Dots and Their Applications

Volume 2

Springer

Editor
Ru-Shi Liu
Department of Chemistry
National Taiwan University
Taipei
Taiwan

and

Department of Mechanical Engineering
    and Graduate Institute of Manufacturing
    Technology
National Taipei University of Technology
Taipei
Taiwan

Preface

This book is divided into two volumes. In Volume 1, we start with an introduction to the basic properties of luminescent materials (phosphors), before addressing the principle of energy transfer and pressure effect of phosphor. Moreover, we present the theoretical first-principles calculation of luminescent materials. After having established a basic understanding of phosphors, we then discuss a variety of phosphors of oxides, nitrides, (oxy)nitrides, fluorides, etc. In Volume 2, we shift the focus to the applications of phosphors in light-emitting diodes, field emission displays, agriculture, solar spectral convertors and persistent luminescent materials. We then demonstrate through the basic upconversion nanoparticles their applications in biomedical contexts. Lastly, we introduce readers to the basics and applications of quantum dots.

Taken together, the two volumes offer essential insights on the basics and applications of phosphor at the bulk and nanoscale.

Taipei, Taiwan   Ru-Shi Liu

Contents

Chapter 1
Exploration of New Phosphors Using a Mineral-Inspired Approach in Combination with Solution Parallel Synthesis

Masato Kakihana, Hideki Kato, Makoto Kobayashi, Yasushi Sato, Koji Tomita and Tetsufumi Komukai

Abstract We introduce the concept, as well as the methodology, of using a mineral-inspired approach in combination with solution parallel synthesis for the exploration of new phosphors. The key to successful discovery of new phosphors is the construction of a promising composition library. In this chapter, the construction of an artificial composition library inspired by minerals is proposed. By employing this approach, we have discovered various new phosphors including $NaAlSiO_4:Eu^{2+}$, $BaZrSi_3O_9:Eu^{2+}$, $Na_3ScSi_3O_9:Eu^{2+}$, $SrCaSiO_4:Eu^{2+}$, and $Ca_2SiO_4:Eu^{2+}$ that emit green-yellow (553 nm), cyan blue-green (480 nm), green (520 nm), orange-red (615 nm), and deep-red (650 nm) light, respectively, when excited at 365–460 nm. Among these phosphors, the most prominent result was the observation of unusual deep-red emission from $Ca_2SiO_4:Eu^{2+}$, which originated from the phase transition from the normal β-phase to an $\alpha'l$-phase when a sizable number of Ca^{2+} sites were substituted by Eu^{2+} (up to 40 mol%). The reason for the emergence of the deep-red emission of $\alpha'l$-$Ca_2SiO_4:Eu^{2+}$ is discussed in terms of "crystal site

M. Kakihana (✉) · H. Kato · M. Kobayashi
Institute of Multidisciplinary Research for Advanced Materials,
Tohoku University, Sendai 980-8577, Japan
e-mail: kakihana@tagen.tohoku.ac.jp

Y. Sato
Department of Chemistry, Faculty of Science,
Okayama University of Science, Okayama 700-0005, Japan

K. Tomita
Department of Chemistry, School of Science, Tokai University,
Hiratsuka 259-1292, Japan

T. Komukai
Ichikawa Research Center, Sumitomo Metal Mining Co., Ltd.,
Ichikawa, Japan

engineering." In addition to these silicate-based phosphors, exploration of new oxide up-conversion phosphors was carried out using solution parallel synthesis. Among various niobates and tantalates of rare earth elements, $Y_{0.5}Yb_{0.4}Er_{0.1}Ta_7O_{19}$ was discovered as a new oxide up-conversion phosphor with a good internal quantum efficiency (2.05 %) compared with those of previously known up-conversion phosphors, which are typically below 1 %.

1.1 Introduction

One of the characteristic features of inorganic materials is that they include almost all the elements in the periodic table. In other words, the types of existing inorganic substances are enormous, and countless unknown new inorganic substances may also exist. We will focus on silicon, which has the second highest Clarke number and is the second most abundant element on Earth after oxygen. According to the database of inorganic compounds (https://icsd.fiz-karlsruhe.de/), among the inorganic materials that include silicon, as of September 2014, there are 21,386 types of inorganic substances with known crystal structures. Most of these substances are mineral-derived. For example, $(Ba, Sr)_2SiO_4$, which is a well-known host for phosphors, is also a mineral-derived inorganic substance called orthosilicate. Many functional inorganic substances are artificial substances that can also achieve new functions or structures by forming solid solutions. Solid solutions are substituted inorganic substances, such as the new structure created by substituting the barium and strontium of $(Ba, Sr)_2SiO_4$ with magnesium and calcium. By including such solid solutions, the types of inorganic substances increase from 21,386 to 100,000 or 1,000,000, etc., up to astronomical numbers. It is impossible to comprehensively synthesize such an abundance of inorganic substances, and therefore, new materials and new functions are left unexplored in the present situation.

In this chapter, we first briefly introduce the basis of (thin film) combinatorial, melt combinatorial, combinatorial-based computing science, and solution parallel synthesis, which are methods to search for new inorganic substances and inorganic materials (Sect. 1.2). Next, we introduce the details with applied examples of the "solution parallel synthesis method," which the authors' group has developed (Sect. 1.3). In particular, it is noted as a precaution that there are limits to the solution methods that can be used for solution parallel synthesis. In Sect. 1.4, an actual example of a search for new phosphors using the solution parallel synthesis method guided by minerals is introduced as a new approach to new material searches. In particular, the importance of the selection of the lead compound, a key to the search, is referred to in order to indicate that a material search can be reasonably performed by using a mineral as a hint.

The solution parallel synthesis method can be deemed one of the most effective methods of searching for phosphors, and examples of new phosphors discovered using this method are introduced. The application of the solution parallel synthesis

method to search for new dielectrics, battery materials, photocatalysts, etc., indicates that there are still some problems to be overcome, but we believe that it is useful for the researchers concerned with new inorganic material searches to know the solution parallel synthesis method.

1.2 Methods for Exploring New Inorganic Substances and Materials

1.2.1 Combinatorial Approach

Thin film combinatorial is one of the ultrahigh-speed material screening techniques, which was actively studied from the mid-1990s to the early 2000s, and laser molecular beam epitaxy (MBE) and chemical vapor deposition (CVD) are used as methods for forming thin films. In principle, tens of thousands of types of thin films can be manufactured at a time, which is effective for the exploration of new functions in ferroelectric thin films [1, 2]. Figure 1.1 schematically shows the principle of thin film combinatorial using laser MBE.

Within a vacuum chamber, the targeted materials (A, B, C, etc.) are volatilized under high-power UV laser irradiation to form the components of thin films laminated on a substrate. By rotating the target as well as moving a shielding plate (i.e., mask) in the x–y direction, a substance with the desired composition is formed as a film on the substrate. The lower part of the substrate is irradiated with another laser, such as an infrared laser, to produce a temperature gradient, which allows determination of the optimum film production temperature. This method has resulted in brilliant achievements in the creation of new functions by the formation of epitaxial films and artificial superlattices, through the use of single-crystal substrates with ultraclean surfaces [1, 2].

Fig. 1.1 Schematic illustration of the combinatorial synthesis of functional thin films
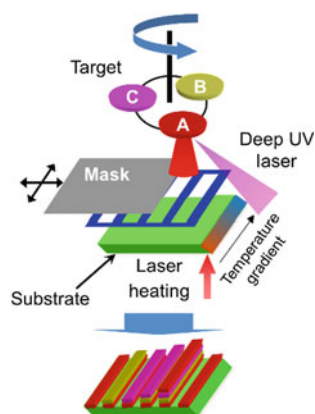
In recent years, this technique has been extensively expanded using combinatorial and high-throughput screening of materials to search for a variety of new materials, including hydrogen storage materials [3], Li-ion battery materials [4], Pd-based metal oxide catalysts [5], and piezoelectric materials [6].

1.2.2 Melt Combinatorial

Melt combinatorial is a method to melt multiple oxide mixed powders using an arc imaging furnace, which enables efficient material searches. However, because melting makes it easy to obtain glass substances and may induce evaporation of some components, there are problems with the versatility of this method. Melt combinatorial was developed as a new phosphor exploration method by Professor Toda's group at Niigata University [7]. As a result of this approach, the group successfully discovered a new red-emitting phosphate phosphor caused by blue photoexcitation by activating Eu^{2+} in $NaMgPO_4$ with an olivine-type structure. $NaMgPO_4$ is a common phosphor that usually has a glaserite-type structure, and the material in which Eu^{2+} was activated has blue emission under ultraviolet photoexcitation [8]. Phosphate is a kind of oxide, and red emission under blue photoexcitation is very rare, except in nitrides. Even when the temperature is elevated to 150 °C, this phosphor, with good temperature quenching characteristics, maintains about 80 % of the emission intensity compared with that at room temperature. The exploration of new phosphors by melt combinatorial will be accelerated in the future [7].

1.2.3 Combinatorial by Computational Science Algorithms

Combinatorial by computational science algorithms is a highly effective method that enables a reasonable prediction of composition optimization and can be applied to a search for materials in conjunction with an experimental combinatorial method. This method, developed by Professor Kee-Sun Sohn's group at Sejong University in South Korea, is especially effective for the exploration of new phosphors. In recent years, the combination of this method with experimental combinatorial methods has been extended to the exploration of new oxynitride phosphors [9–15].

1.2.4 Solution Parallel Synthesis Method

Figure 1.2 schematically shows the solution parallel synthesis method [16–19]. Aqueous solutions are prepared containing various concentrations of metal salts (A, B, C, D, E, etc.). In the example shown in Fig. 1.2, the solution referred to as
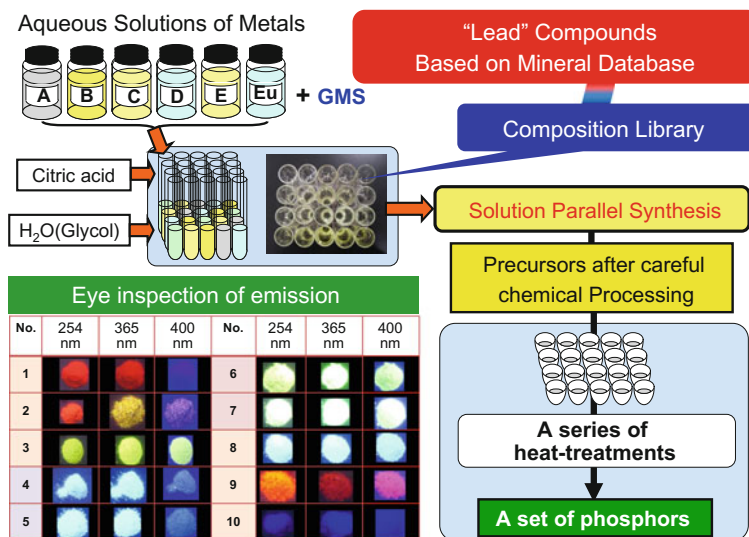
Fig. 1.2 Scheme of solution parallel synthesis for the exploration of new phosphors; GMS (glycol-modified silane) was used as a convenient silicon source; visual observation of emission under UV to near-UV irradiation [16]

Eu is prepared because europium ions are used as an activator. Also, in this example, GMS (glycol-modified silane) [17] is used as a silicon source, as the exploration of a new silicate-based phosphor is simulated. In addition, citric acid is required to stabilize the solution system; when using water as the solvent, the solution method is the amorphous metal complex method, whereas, when using glycol as the solvent, the solution method is the polymerizable complex method [16, 20, 21]. Using the "composition library" described later, a series of solution samples are produced in vitro. The composition library is a set of compositions corresponding to the sample series aimed at synthesis. The solution set of this series is chemically processed at the same time to obtain gelation or polyester resins, and then subjected to a series of heat treatments to perform the phosphor synthesis of interest. Phosphor screening can be performed by irradiating the completed set of phosphors with a portable lamp to observe the emission by visual inspection. The picture in the bottom left of Fig. 1.2 shows the emission of synthesized phosphor samples when irradiated at 254, 365, and 400 nm. For example, sample No. 3 is strongly yellow-green luminescent and sample No. 7 is strongly green-white luminescent. Therefore, a second cycle of solution parallel synthesis was implemented to fine-tune the composition in the vicinity of these samples for the purpose of identifying the composition of phosphors with stronger emission intensities. This repetition leads to the discovery of new phosphors.

Although the solution parallel synthesis method enables the parallel synthesis of dozens of samples at a time, as evident in Fig. 1.2, it requires extra time compared with the thin film combinatorial and melt combinatorial approaches because it

involves multiple processes. However, the use of a highly reliable solution method makes it possible to increase the accuracy of each synthesis process, resulting in improved reliability of the material search. In addition, the high versatility of this method is a significant benefit. The details of the solution parallel synthesis method are described in the next section.

1.3 Details of the Solution Parallel Synthesis Method

1.3.1 Conditions Required for Solution Parallel Synthesis

The solution parallel synthesis method we have developed is applied to the efficient search for new materials, quick determination of the optimum composition in the functional materials, and realization of high functionalization [16, 18, 22, 23]. In order to accomplish this, the following conditions must be met.

1. A solution method with excellent composition control for ceramics should be applied.
2. The parallel synthesis of substances with different compositions should be possible using the same experimental conditions, including reaction time.
3. Substances should be relatively insensitive to moisture in the air.

The solution methods that meet these three conditions are limited, and any one of those solution methods cannot always be applied.

In Fig. 1.3, we select the solution methods available for solution parallel synthesis in light of the above three requirements. Depending on the type of metal ions in the solution, the precipitation method [20] may or may not form a precipitate. In

Method	Condition		
	1	2	3
Precipitation method	×	×	○
Sol-gel alkoxide method	△	×	×
Polymerizable complex method	◎	○	○
Hydrothermal method	△	×	○
Amorphous metal complex method	○	○	○
PVA method	○	△	○

Fig. 1.3 Selection criteria of the solution method to incorporate in the solution parallel synthesis method; ① Excellent composition control to ensure homogeneity, ② Able to perform parallel synthesis under the same condition, ③ Insensitive to humidity and able to perform synthesis in air; ◎: Excellent, ○: Good, △: fair, ×: Poor

addition, even if a precipitate is formed, the solubility varies depending on the type of metal. Therefore, this method does not meet Conditions 1 and 2. Thus, the precipitation method is ineligible as a solution method for the solution parallel synthesis method.

Furthermore, the sol–gel method using an alkoxide [20] does not meet Condition 2 because the hydrolysis rate or polycondensation rate varies depending on the type of metal alkoxide. In addition, many typical metal alkoxides are unstable compounds and are affected by humidity in the atmosphere; therefore, this method does not meet Condition 3. Thus, the sol–gel method using an alkoxide is ineligible as a solution method for the solution parallel synthesis method.

In the hydrothermal method [20, 21], depending on the type of metal ions used, the rate of the chemical reaction in aqueous solution under a given hydrothermal condition varies. Therefore, this method does not meet Condition 2, and the hydrothermal method also cannot be used as a solution method for the solution parallel synthesis method.

On the other hand, because of its principle, the polymerizable complex method [20, 21] has excellent composition control, and without much attention to the type of metal, synthesis is possible under the same conditions. Moreover, because this process can be carried out in air, it is the most appropriate solution method for the solution parallel synthesis method. Methods similar to the polymerizable complex method, including the amorphous metal complex (AMC) method [20] and the polyvinyl alcohol (PVA) method [20, 21], can also be used as solution methods for the solution parallel synthesis method.

1.3.2 Pictures of the Solution Parallel Synthesis Method in Operation

To help understanding the readers, an actual phosphor search using the solution parallel synthesis method with the polymerizable complex method as the solution method is introduced in the photographs shown in Figs. 1.4, 1.5, and 1.6.

First, 20 types of solutions with different metal composition ratios are prepared in test tubes (construction of the composition library), and citric acid and glycol are added to these test tubes as gelling agents (Fig. 1.4a). Then, these 20 test tubes are placed in an oven and heated at 120 °C to concentrate the solution and promote polymerization (Fig. 1.4b). The polymerizable complex method [20, 21] is a solution method, in which the polyester reaction between citric acid and glycol is allowed to proceed, and as a result, metal ions or metal–citric acid complexes are uniformly trapped in a polyester resin. The polyester reaction is a dehydration reaction; extensive bubbling occurs during the release of water from the highly viscous polyester resin, as shown in Fig. 1.4c. To prevent the overflow of these bubbles, tall test tubes are used as the reaction containers. Figure 1.4d shows one of the test tubes turns upside down after the reaction, and the solidified polyester resin
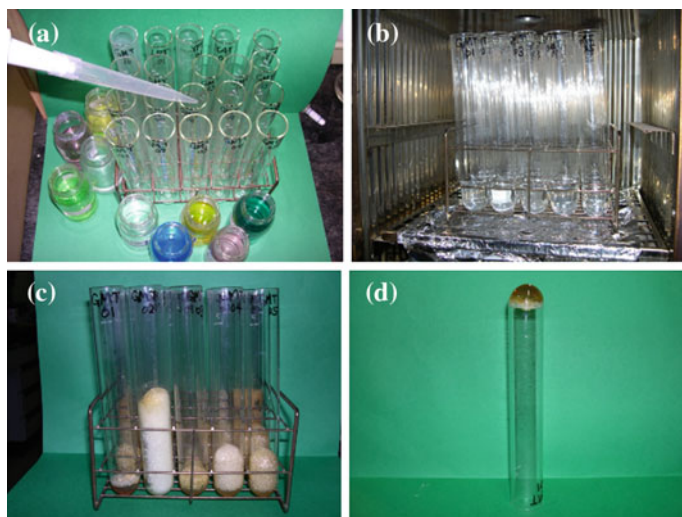
Fig. 1.4 Experimental view of the solution parallel synthesis method (part 1): **a** solution preparation; **b** polymerization in a dry box; **c** polyester reaction; and **d** solidified polyester resin
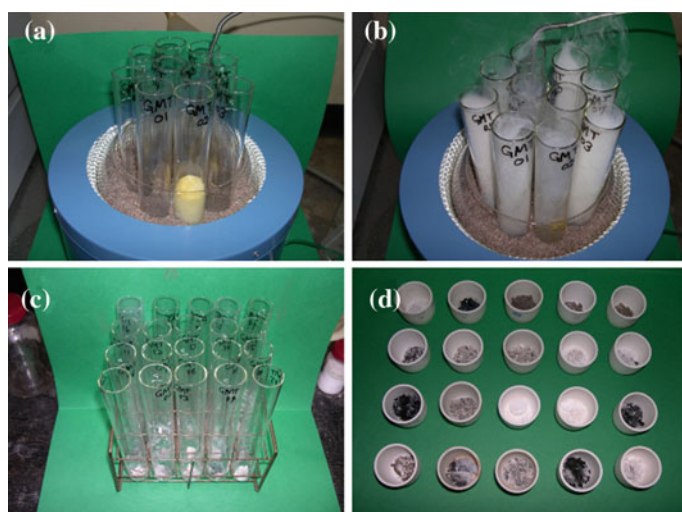
Fig. 1.5 Experimental view of the solution parallel synthesis method (part 2): resin decomposition in a sand bath **a** at the start time and **b** after 30 min; **c** degreasing product; and **d** calcination product at 500 °C

can be observed. The polyester resins are inserted into a sand bath at 300 °C to decompose the resins (Fig. 1.5a). The decomposition of the resins generates steam (Fig. 1.5b). Figure 1.5c shows the products after degreasing. Figure 1.5d shows the

Fig. 1.6 Experimental view of the solution parallel synthesis method (part 3): **a** products after firing at 1200 °C and **b** products irradiated with ultraviolet light (254 nm)
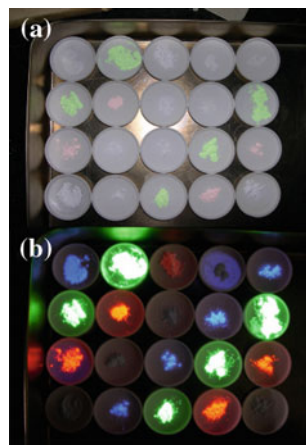
products obtained by putting the degreased products into crucibles and applying heat treatment in an electric furnace at 500 °C. Further heat treatment in an electric furnace at 1200 °C forms the fluorescent substances, i.e., "phosphors." Figure 1.6a shows the calcination products obtained after the treatment at 1200 °C. Figure 1.6b shows the emission from the resulting 20 samples when irradiated with ultraviolet light (254 nm) using a portable UV lamp. This enables visual confirmation of the substances that show strong blue, green, or red depending on the composition and the substances with no emission. A substance with strong light emission is then selected, a new composition library in the vicinity of its composition is constructed, and the solution parallel synthesis process is repeated to determine the optimum composition.

1.4 Exploration of New Phosphors Inspired by Minerals Using the Solution Parallel Synthesis Method

In contrast to the continual discovery of new organic compounds, new inorganic substances have not been discovered frequently. In the field of drug discovery, useful antibiotics are developed daily, so why is the development rate of new inorganic substance slow?

One reason for this is derived from the different essential principles of inorganic and organic synthesis. For inorganic synthesis reactions, slow diffusion of metal ions in solids is rate-limiting, whereas organic synthesis reactions are generally based on reactions between molecules. For this reason, it is thought that the efficiency of the exploration of inorganic substances is quite low, and the opportunity to discover new substance is reduced correspondingly. In addition to the difficulties associated with the synthesis itself, we think the selection of an appropriate lead substance, which is the starting point for exploration, is also a problem.

A lead substance is the substance from which the library for substance exploration is constructed. In the field of drug discovery, the lead substance is either a natural compound or a synthetic substance. Specifically, a synthetic substance is selected as a lead compound, and the required functional groups are introduced, for example, to construct a library consisting of a set of modifiers for combinatorial synthesis. It is possible to determine whether the modifiers can exist from the standpoint of organic synthetic chemistry. That is, it is possible to conduct substance exploration rationally, rather than by random combinatorial synthesis. On the other hand, with inorganic substances, it is difficult to predict whether the corresponding substances can exist for any composition. From the standpoint of crystal chemistry, a certain degree of prediction is possible, but, in many cases, it is difficult to be conclusive unless the actual synthesis is attempted. For this reason, the exploration of inorganic substances using a combinatorial method is likely to rely on exhaustive synthesis with no basis and, at this time, is far from rational. The fact that the number of new substance discoveries is limited, even when a combinatorial method with the advantage of concurrent synthesis of substances with tens or hundreds of thousands of compositions is used, may indicate the selection of inappropriate lead substances. That is, we think the answer to the question "Why are new inorganic substances not discovered frequently?" could be "There were problems selecting the lead substance."

We proposed to seek a lead substance for exploration of new inorganic substance in natural minerals. That is, exploration of new inorganic substances inspired by minerals using the solution parallel synthesis method. In this section, we introduce examples of the exploration of new phosphors based on this strategy.

1.4.1 Practical Exploration of Novel Phosphors Using a Mineral-Inspired Method with Solution Parallel Synthesis

Figure 1.7 shows a flowchart for the exploration of novel phosphors using a mineral-inspired method with solution parallel synthesis.

First, a mineral database provided by the International Mineralogical Association (IMA, http://www.ima-mineralogy.org/), Mindat (http://www.mindat.org/), etc. is accessed. Data on up to tens of thousands of kinds of basic minerals are available, so a search can be conducted by category, such as silicates, phosphates, and borates. Next, model minerals (lead substances) are selected, and a large-scale task of grouping is conducted. There are several possible ways of grouping. One is to group the minerals based on the characteristics of their crystal chemical structure. For example, in mineralogy, silicate minerals are classified into groups such as nesosilicates, sorosilicates, inosilicates, cyclosilicates, and phyllosilicates, as shown in Fig. 1.8, based on the way the silicate ion, which is the fundamental building unit of these structures, is bound. Therefore, using this method, minerals belonging to
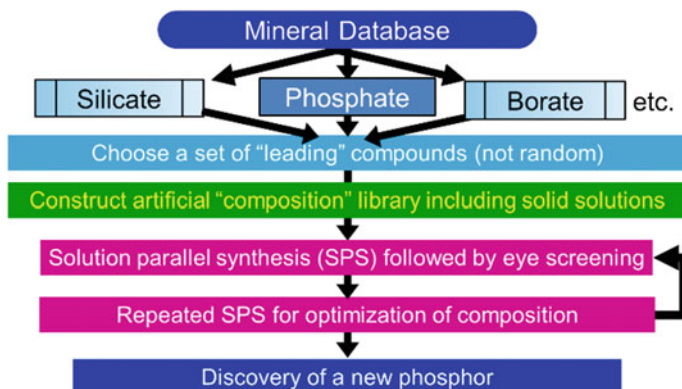
Fig. 1.7 Scheme of the search for novel phosphors inspired by minerals using the solution parallel synthesis method [23]
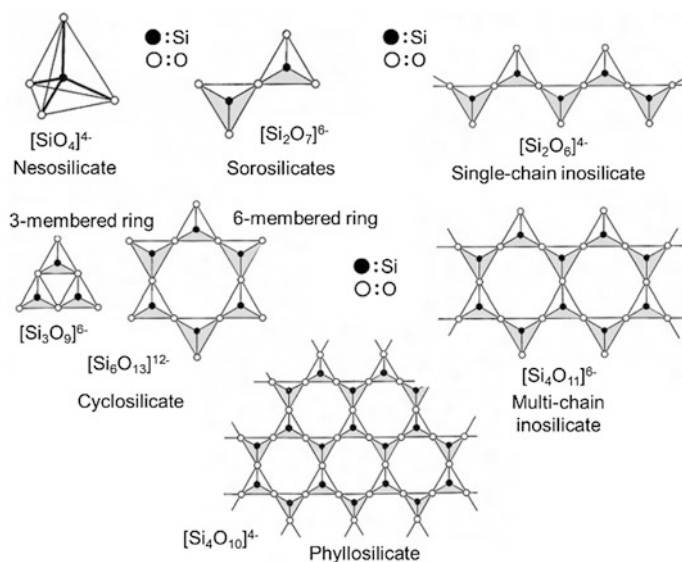
Fig. 1.8 A variety of silicates composed of $[SiO_4]^{4-}$ as a fundamental structural unit and the various binding modes of $[SiO_4]^{4-}$ [23]

each group are selected as lead substances to construct a library. Another method is to group the minerals by the element group. Here, we will describe this second method, using silicates as an example.

Figure 1.9 shows silicates classified into nine categories by elemental composition. Library 1 consists mainly of calcium silicate or magnesium silicate minerals, Library 2 of calcium–magnesium silicate minerals, Library 3 of calcium–aluminum

Library 1 ： Ca-silicate or Mg-silicate based minerals (39 compositions)
$CaSiO_3$, $CaSi_2O_5$, $MgSiO_3$ etc.
Library 2 ： Ca-Mg-silicate based minerals (37 compositions)
$CaMgSiO_4$, $Ca_2MgSi_2O_7$, $CaMg_2SiO_6$, $CaMg_6Si_3O_{16}$ etc.
Library 3 ： Ca-Al-silicate based minerals (48 compositions)
$Ca_2Al_2SiO_7$, $CaAl_2Si_2O_8$, $CaAl_2Si_3O_{10}$, $CaAl_2Si_6O_{16}$ etc.
Library 4 ： Na-Al-silicate based minerals (30 compositions)
$NaAlSi_2O_6$, $NaAlSi_3O_8$, $Na_2Al_2Si_3O_{10}$, $Na_2Al_2Si_7O_{18}$ etc.
Library 5 ： Ti-silicate based minerals (49 compositions)
$CaTiSiO_5$, $BaTiSi_3O_9$, $Ba_2MgTiSi_4O_{13}$, $Na_2Ba_2TiSi_4O_{14}$ etc.
Library 6 ： Zr-silicate based minerals (49 compositions)
$CaZrSi_6O_{15}$, $BaZrSi_3O_9$, $CaZrSi_3O_9$, $Na_6CaZrSi_6O_{18}$ etc.
Library 7 ： Zn-silicate based minerals (19 compositions)
$Ca_2ZnS_2iO_7$, $CaZnSi_2O_6$, $Na_3SrCeZnSi_6O_{17}$, $Na_4Zn_2Si_7O_{18}$ etc.
Library 8 ： B-silicate based minerals (20 compositions)
$NaBSi_3O_8$, $CaB_2Si_2O_8$, $KBSi_2O_6$, $NaBSiO_4$ etc.
Library 9 ： Other silicates (22 compositions)
$Na_3ScCeMgSi_6O_{17}$, $Na_3CaPSiO_7$, $Na_2Si_2O_5$, $NaScSi_2O_6$ etc.

Fig. 1.9 Nine artificial composition libraries used in the solution parallel synthesis inspired by silicate minerals [23]

silicate minerals, Library 4 of sodium–aluminum silicate minerals, Library 5 of titanium silicate minerals, Library 6 of zirconium silicate minerals, Library 7 of zinc silicate minerals, Library 8 of silicoborates minerals, and Library 9 of other silicate minerals.

Figure 1.10 shows the composition library for calcium silicate or magnesium silicate minerals (Library 1). The number in the first column is the classification number from the mineral database and has no special meaning. The second column shows the name of the mineral. The third column shows the original composition of the mineral. Original minerals contain small amounts of many impurity elements, and it is generally not useful to synthesize a substance with such an original composition. For example, when a radioactive element is contained, it is not realistic to synthesize a substance with the composition as is. In addition, phosphors should not be synthesized with an original composition containing transition metal elements, such as iron and manganese, because many transition metal elements suppress the desired luminescence. Therefore, for minerals that contain such transition metal elements in their original composition, an "artificial composition," in which the element is replaced with a different element with a similar ionic radius, is constructed, and the substance with this new composition is named the "standard substance."

As an example, we look at No. 92, augite, in Fig. 1.10. The original composition of augite is $(Ca, Mg, Fe)_2Si_2O_6$ (or to be more precise $(Ca, Na, Mg, Fe, Al, Ti)_2Si_2O_6$). Augite is a calcium silicate mineral, but it contains a small amount of magnesium and iron as impurities, the contents of which vary depending on the
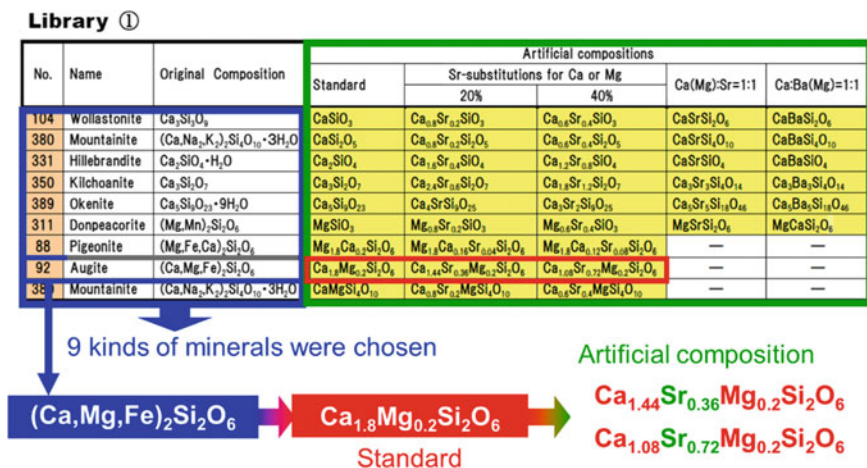
Fig. 1.10 Artificial composition Library 1 based on calcium or magnesium silicate minerals [23]

locality. For phosphors, the iron impurity is replaced by divalent magnesium (Mg^{2+}), which is an optically transparent element with an ionic radius close to that of divalent iron (Fe^{2+}). As they have a similar effective ionic radius (1.06 Å for eight-coordinate Fe^{2+} and 1.03 Å for eight-coordinate Mg^{2+}), it is crystal-chemically reasonable to assume that this replacement can be made (see table of Shannon ionic radii [24]). Therefore, $Ca_{1.8}Mg_{0.2}Si_2O_6$ was artificially created as a standard substance for augite with a hypothetical composition (bottom of Fig. 1.10). The proportions of calcium and magnesium are arbitrary. The amount of magnesium is set to 10 % of that of calcium only for convenience.

Similarly, artificial compositions were constructed for the rest of the minerals in Fig. 1.10 by necessary element substitution or by removing unnecessary crystallization water, and each of these is called the "standard substance." Next, using these standard substances as a starting material, various solid solutions, which do not exist naturally, were created. For augite, we artificially made the solid solutions $Ca_{1.44}Sr_{0.36}Mg_{0.2}Si_2O_6$ and $Ca_{1.08}Sr_{0.72}Mg_{0.2}Si_2O_6$ with hypothetical compositions in which 20 or 40 % of calcium is substituted with strontium (bottom of Fig. 1.10). A solid solution containing barium instead of strontium can also be created (not shown in Fig. 1.10). For No. 104 in Fig. 1.10, wollastonite, the artificial substances $CaSrSi_2O_6$ and $CaBaSi_2O_6$ were created based on Ca(Mg):Sr = 1:1 and Ca:Ba (Mg) = 1:1. When two elements with different ionic radii exist in a 1:1 ratio, it is not crystal-chemically rare that these two ions form a new structure, often by ordered arrangement. Therefore, it is reasonable to create artificial compositions with equal proportions of alkaline earth metals. With sulfides, which have been extensively studied by the present authors [25–33], new sulfide structures with equal proportion of alkaline earth metals, such as $CaBaSiS_4$ and $CaSrSiS_4$ [33],

have been discovered. In total, Library 1 consists of 39 kinds of artificial compositions inspired by 9 calcium silicate or magnesium silicate minerals (Fig. 1.10).

For Libraries 2–9 in Fig. 1.9, artificial composition libraries were constructed in the same way as for Library 1. In Libraries 1–9, 313 kinds of artificial composition libraries were constructed by selecting 144 silicate minerals as standard substances and artificially creating solid solutions or substances with equal compositions. Solution parallel synthesis was applied to each library (corresponding to the experiment in the latter half of Fig. 1.7). The candidate substances were narrowed down by visual observation with light irradiation and detailed analysis. Further solution parallel synthesis was carried out to optimize the composition of the screened candidate substances, and repletion of these steps can lead to the discovery of new phosphors.

By using this method, we succeeded in discovering several promising new phosphors. The new phosphors, $NaAlSiO_4:Eu^{2+}$ (Sect. 1.4.2), $BaZrSi_3O_9:Eu^{2+}$ (Sect. 1.4.3), $Na_3ScSi_3O_9:Eu^{2+}$ (Sect. 1.4.4), $CaSrSiO_4:Eu^{2+}$, and $Ca_2SiO_4:Eu^{2+}$ (Sect. 1.4.5), were all inspired by silicate minerals.

1.4.2 NaAlSiO₄:Eu²⁺ from Sodium–Aluminum Silicate Minerals [34]

The details of Library 4 (Fig. 1.9) are shown in Fig. 1.11. This library consists of sodium–aluminum (No. 97, 159, 171, 187, 195, and 201), potassium–aluminum (No. 155, 172, 173, and 366), lithium–aluminum (No. 396), sodium–barium–aluminum (No. 167), and sodium–strontium–aluminum (No. 168) silicate-based

Fig. 1.11 Artificial composition Library 4 based on sodium–aluminum silicate minerals [23]

minerals. Figure 1.11 shows the composition library in which compounds with 1:1 composition of the reference substance and solid solutions were artificially made. Here, in the artificial solid solutions that substitute strontium for sodium, the valences of the elements are different (2 and 1, respectively). Therefore, to compensate for electrical charge, the ratio of trivalent aluminum and quadrivalent silicon was regulated. In addition, on the assumption of a phosphor in which divalent europium ion is activated (Eu^{2+}), compositions in which 2 mol% europium was added were prepared for alkaline earth metal ions.

For this composition library, the solution parallel synthesis was conducted. To reduce europium from Eu^{3+} to Eu^{2+}, which is the activator, a final heat treatment was conducted at 1200 °C for 2 h in graphite. Fig. 1.12 shows the appearance of the light emission from the samples synthesized in this way when irradiated at 254, 365, and 400 nm. The branch numbers shown in Fig. 1.12 correspond to standard substance and solid solution compositions in Fig. 1.11. That is, 97-1, 97-2, and 97-3 are $NaAlSi_2O_6$(standard), $Na_{0.95}Sr_{0.05}Al_{1.05}Si_{1.95}O_6$, and $Na_{0.9}Sr_{0.1}Al_{1.1}Si_{1.9}O_6$, respectively. Interesting light emission was observed from these samples, but in order to completely reduce europium from Eu^{3+} to Eu^{2+}, several samples (171-1, 171-3, 187-1, 187-3, 155, 168-1) were subjected to a re-reducing heat treatment conducted under a nitrogen/ammonia (N_2/NH_3)atmosphere, which has a stronger reducing power than that of graphite, at 1200 °C for 2 h. Figure 1.13 shows the appearance of light emission from the samples following the re-reducing heat treatment when irradiated at 254, 365, and 400 nm. For comparison, the light
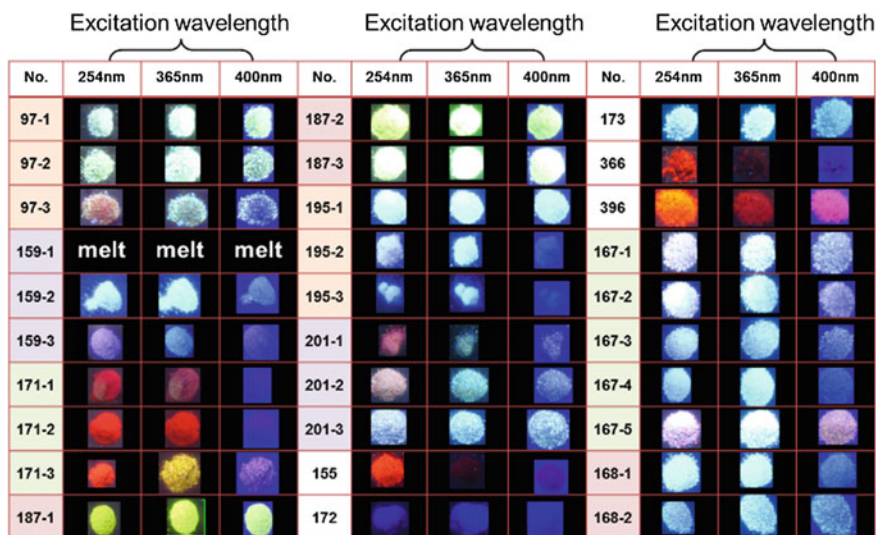
Fig. 1.12 Light emission of samples based on sodium–aluminum silicate minerals from artificial composition Library 4 when irradiated with ultraviolet and near-ultraviolet lights (2 mol% of Eu^{2+} relative to alkali metal was added to each sample). Some samples were further subjected to a stronger reduction treatment under N_2/NH_3 to strengthen the emission (see Fig. 1.13) [23]

Fig. 1.13 Comparison of the emission of $NaAlSiO_4$, $Na_{0.9}Sr_{0.1}Si_{0.95}O_4$, $Na_2Al_2Si_3O_{10}$, $Na_{1.8}Sr_{0.2}Al_{2.2}Si_{2.8}O_{10}$, $KAlSi_3O_8$, and $SrNa_2Al_4Si_4O_{16}$ before and after a strong reduction treatment under N_2/NH_3. The appearance of the emission before this treatment is shown on the left for each sample [23]

emission under the same conditions prior to the re-reducing heat treatment is shown on the left side of each sample. Generally, for most of the samples, an increase in light emission intensity was observed. In addition, samples 171-1, 171-3, and 155, which had red light emission when irradiated at 254 nm prior to the re-reducing heat treatment, showed white (actually, strong yellow-green) or blue emission following this treatment, indicating that Eu^{3+}, which was the source of the red emission was sufficiently reduced to Eu^{2+}.

Figure 1.14 shows the excitation and emission spectra of sample 171-1 ($NaAlSiO_4$:Eu^{2+}) to which strong reducing heat treatment was applied, and the light emission when irradiated with near-ultraviolet light (365 nm). $NaAlSiO_4$:Eu^{2+} is a phosphor with strong yellow-green emission that is excited by light in the near-UV region. The most effective excitation wavelength is 320 nm, and the maximum intensity in the emission spectrum occurs at 553 nm. The host $NaAlSiO_4$ originates from a nepheline mineral, which was not previously known to be an effective host for phosphors. However, at almost the same time as the authors, Professors Yoon and Masaki at, Sungkyunkwan University, South Korea, and Professor Toda's group at Niigata University found the same phosphor [35].
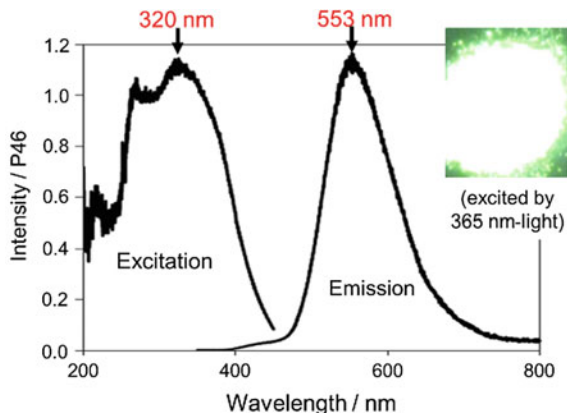
Fig. 1.14 Excitation and emission spectra and appearance of the light emission when irradiated at 365 nm for $NaAlSiO_4:Eu^{2+}$, which is derived from a nepheline mineral [34]

1.4.3 BaZrSi₃O₉:Eu²⁺ from Zirconium Silicate-Based Minerals

The details of Library 6 (Fig. 1.9) are shown in Fig. 1.15. The first three minerals (No. 253, 269, and 288) are silicates containing alkaline earth metals and zirconium, and the following six minerals (No. 421, 291, 314, 392, 412, and 418) are sodium–zirconium silicates. The remaining substances are various silicates

Library ⑥

No.	Name	Original Composition	Standard	Sr-substitutions for Ca, Ba or Mg 20%	Sr-substitutions for Ca, Ba or Mg 40%	Ca(Ba):Sr=1:1	Ca(Ba):Ba(Ca)=1:1
253	Armstrongite	$CaZrSi_6O_{15} \cdot 2.5H_2O$	$CaZrSi_6O_{15}$	$Ca_{0.8}Sr_{0.2}ZrSi_6O_{15}$	$Ca_{0.6}Sr_{0.4}ZrSi_6O_{15}$	$CaSr_2ZrSi_{12}O_{30}$	$CaBaZr_2Si_{12}O_{30}$
269	Benitoite	$BaZrSi_3O_9$	$BaZrSi_3O_9$	$Ba_{0.8}Sr_{0.2}ZrSi_3O_9$	$Ba_{0.6}Sr_{0.4}ZrSi_3O_9$	$BaSrZr_2Si_6O_{18}$	$BaCaZr_2Si_6O_{18}$
288	Calciohilairite	$CaZrSi_3O_9 \cdot H_2O$	$CaZrSi_3O_9$	$Ca_{0.8}Sr_{0.2}ZrSi_3O_9$	$Ca_{0.6}Sr_{0.4}ZrSi_3O_9$	$CaSrZr_2Si_6O_{18}$	—
421	Zirsinalite	$Na_6(Ca,Mn,Fe)ZrSi_6O_{18}$	$Na_6CaZrSi_6O_{18}$	$Na_6Ca_{0.8}Sr_{0.2}ZrSi_6O_{18}$	$Na_6Ca_{0.6}Sr_{0.4}TiSi_6O_{18}$	$Na_{12}CaSrZr_2Si_{12}O_{36}$	$Na_{12}CaBaZr_2Si_{12}O_{36}$
291	Cataplelite	$Na_2ZrSi_3O_9 \cdot 2H_2O$	$Na_2ZrSi_3O_9$	—	—	—	—
314	Elpidite	$Na_2ZrSi_6O_{15} \cdot 3H_2O$	$Na_2ZrSi_6O_{15}$	—	—	—	—
392	Parakeldyshite	$Na_2ZrSi_2O_7$	$Na_2ZrSi_2O_7$	—	—	—	—
412	Terskite	$Na_4ZrSi_6O_{16} \cdot 2H_2O$	$Na_4ZrSi_6O_{16}$	—	—	—	—
418	Vlasovite	$Na_2ZrSi_4O_{11}$	$Na_2ZrSi_4O_{11}$	—	—	—	—
32	Titanite	$CaTiSiO_5$	$CaZrSiO_5$	$Ca_{0.8}Sr_{0.2}ZrSiO_5$	$Ca_{0.6}Sr_{0.4}ZrSiO_5$	$CaSrZr_2Si_2O_{10}$	$CaBaZr_2Si_2O_{10}$
261	Barrio-ortho-joaquinite	$(Ba,Sr)_4Fe_2Ti_2Si_8O_{26} \cdot H_2O$	$Ba_2MgZrSi_4O_{13}$	$Ba_{1.6}Sr_{0.4}MgZrSi_4O_{13}$	$Ba_{1.2}Sr_{0.8}MgZrSi_4O_{13}$	$BaSrMgZrSi_4O_{13}$	$BaCaMgZrSi_4O_{13}$
266	Batisite	$Na_2BaTi_2(Si_2O_7)_2$	$Na_2BaZr_2Si_4O_{14}$	$Na_2Ba_{0.8}Sr_{0.2}Zr_2Si_4O_{14}$	$Na_2Ba_{0.6}Sr_{0.4}Zr_2Si_4O_{14}$	$Na_4BaSrZr_4Si_8O_{28}$	$Na_4BaCaZr_4Si_8O_{28}$
242	Aenigmatite	$Na_2Fe_5TiSi_6O_{20}$	$Na_2Mg_5ZrSi_6O_{20}$	$Na_2Mg_4SrZrSi_6O_{20}$	$Na_2Mg_3Sr_2ZrSi_6O_{20}$	—	—
367	Lorenzenite	$Na_2Ti_2Si_2O_9$	$Na_2Zr_2Si_2O_9$	—	—	—	—
387	Natisite	Na_2TiSiO_5	Na_2ZrSiO_5	—	—	—	—
395	Penkvilksite	$Na_4Ti_2Si_8O_{22} \cdot 4H_2O$	$Na_2ZrSi_4O_{11}$	—	—	—	—
364	Lintisite	$Na_3LiTi_2Si_4O_{14} \cdot 2H_2O$	$Na_3LiZr_2Si_4O_{14}$	—	—	—	—
416	Umbite	$K_2(Zr,Ti)Si_3O_9 \cdot H_2O$	$K_2ZrSi_3O_9$	—	—	—	—
64	Berezanskite	$KLi_3Ti_2Si_{12}O_{30}$	$KLi_3Zr_2Si_{12}O_{30}$	—	—	—	—
398	Pyatenkoite-Y	$Na_5(Y,Dy,Gd)TiSi_6O_{18} \cdot 6H_2O$	$Na_5YZrSi_6O_{18}$	—	—	—	—

Fig. 1.15 Artificial composition Library 6 based on zirconium silicate minerals [23]

containing titanium, sodium, barium, potassium, or lithium, and silicates containing iron and rare earth elements. Figure 1.15 shows the composition library of reference substances, solid solutions, and compounds with 1:1 compositions. Here, zirconium was used in the artificial compositions for the minerals that include titanium. As with the example in the previous section, assuming a phosphor in which Eu^{2+} is activated, compositions to which 1 mol% europium was added were prepared for alkali metal or alkaline earth metal ions.

For this composition library, the solution parallel synthesis method was conducted. As with the example in the previous section, europium was reduced from Eu^{3+} to Eu^{2+}, which acts as an activator, using a final heat treatment at 1200 °C for 2 h in graphite. Figure 1.16 shows the appearance of the light emission from the samples synthesized in this way when irradiated at 254, 365, and 400 nm. Here, only typical samples are shown. The most interesting result was obtained for a benitoite-based mineral, $BaZrSi_3O_9$ (benitoite or bazirite), and as shown in Fig. 1.16, $BaZrSi_3O_9$:Eu^{2+} showed visible green emission under ultraviolet or near-ultraviolet irradiation. When such significant emission is observed, the next step is to begin the process of optimizing the composition of the screened candidate (parallel synthesis), as shown in Fig. 1.7.
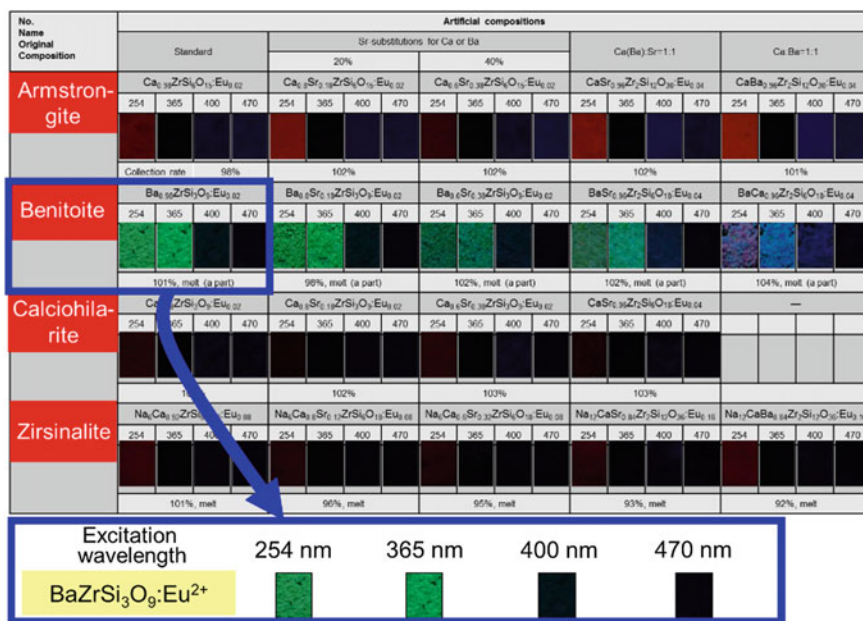
Fig. 1.16 Light emission of Eu^{2+}-activated samples selected from artificial composition Library 6 based on zirconium silicate-based minerals when irradiated with ultraviolet and near-ultraviolet light. Extract:benitoite (bazirite) $BaZrSi_3O_9$:Eu^{2+} showed interesting emission under near-ultraviolet excitation [23]

Step 1				
No.	Ba	Zr	Si	Eu
1	1.98	2	3	0.02
2	1.98	2	3.3	0.02
3	1.98	2	3.6	0.02
4	1.98	2	4.5	0.02
5	1.98	2	5	0.02
6	1.98	2	5.5	0.02
7	1.98	2	6	0.02
8	1.98	2	6.6	0.02
9	1.98	2	7.2	0.02
10	1.98	2	8	0.02
11	1.98	2	9	0.02
12	1.98	2	10	0.02
Solution parallel synthesis				

Step 2				
No.	Ba	Zr	Si	Eu
1	1.99	2	6.6	0.01
2	1.98	2	6.6	0.02
3	1.97	2	6.6	0.03
4	1.96	2	6.6	0.04
5	1.95	2	6.6	0.05
6	1.94	2	6.6	0.06

Step 3				
No.	Ba	Zr	Si	Eu
1	1.97	2	6.1	0.03
2	1.97	2	6.2	0.03
3	1.97	2	6.4	0.03
4	1.97	2	6.6	0.03
5	1.97	2	6.8	0.03
6	1.97	2	7.0	0.03

Fig. 1.17 Determination of the optimum composition of the new phosphor $BaZrSi_3O_9:Eu^{2+}$ inspired by benitoite using solution parallel synthesis [36]

Figure 1.17 shows the optimization of the composition using three steps (three solution parallel synthesis experiments). In the first solution parallel synthesis experiment, the Ba:Zr:Eu ratio was fixed at 1.98:2:0.02, and the amount of Si was varied widely in the range from 3 to 10. The maximum emission intensity was obtained for the No. 8 composition of Ba:Zr:Si:Eu = 1.98:2:6.6:0.02. Then, in the second solution parallel synthesis experiment, the Zr:Si ratio was fixed at 2:6.6, and to determine the optimal concentration of Eu, the amount of Eu was varied in the range from 0.01 to 0.06. To maintain electrical charge neutrality, the amount of Ba was decreased from 1.99 to 1.94 in response to the increase in Eu. The maximum emission intensity was obtained for the No. 2 composition of Ba:Zr:Si: Eu = 1.97:2:6.6:0.03. Then, in the third solution parallel synthesis experiment, the Ba:Zr:Eu was fixed at 1.97:2:0.03, and the amount of Si was varied in the range from 6.1 to 7 to determine the optimum Si concentration. The maximum emission intensity was obtained for the No. 4 composition of Ba:Zr:Si:Eu = 1.97:2:6.6:0.03.

Figure 1.18 shows the excitation and emission spectra of the sample with the optimized composition ($Ba_{0.97}ZrSi_3O_9:0.03Eu + 0.3SiO_2$). For comparison, the excitation and emission spectra of $BaMgAl_{10}O_{17}:Eu^{2+}$ (commonly called BAM), which is used as a blue phosphor for plasma TV displays, are also shown. The photographs on the right side in Fig. 1.18 show the appearance of $Ba_{0.97}ZrSi_3O_9:0.03Eu + 0.3SiO_2$ and its light emission when irradiated at 405 nm. The white powdered sample of $Ba_{0.97}ZrSi_3O_9:0.03Eu + 0.3SiO_2$ showed strong light emission. In fact, this novel phosphor has strong emission comparable to that of the commercially available BAM phosphor, as clearly shown by the comparison of the emission spectra. The emission wavelength is 480 nm and is located on the green
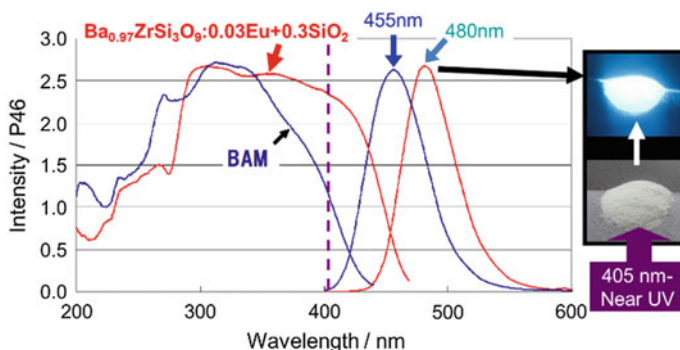
Fig. 1.18 Excitation and emission spectra of the optimal composition of $BaZrSi_3O_9:Eu^{2+}$ and a commercial phosphor (BAM, $BaMgAl_{10}O_{17}:Eu^{2+}$). *Right photograph* the appearance of $BaZrSi_3O_9:Eu^{2+}$ as a white powder and its strong emission when irradiated with near-ultraviolet light of 405 nm [36]

side of the emission wavelength of BAM (455 nm). The shape of the excitation spectrum differs greatly from that of BAM. Importantly, the $Ba_{0.97}ZrSi_3O_9:0.03Eu + 0.3SiO_2$ phosphor can be excited effectively using near-ultraviolet light, and at the practically important excitation wavelength of 405 nm, the light emission intensity of this phosphor is twice that of BAM.

Common white LEDs are two-wavelength systems that emit a pseudo-white color obtained by mixing light from a blue LED and a yellow phosphor (blue light and yellow light). This type of LED is referred to as 2-wavelength white LED system (Fig. 1.19). However, in 2-wavelength systems, the red and green components are insufficient. Therefore, viewing an object using the pseudo-white color shows an unnatural color (expressed as "color rendering is low (bad)"). To avoid this problem, a 3-wavelength white LED system, as shown in Fig. 1.20, has been used. A near-ultraviolet light LED with a wavelength of 395–405 nm is used as an excitation light source instead of a blue LED, and phosphors that efficiently emit blue, green, and red light following excitation using the near-ultraviolet light source are used to realize high color rendering. Thus, phosphors that can be excited effectively by wavelengths of ~ 400 nm are important for practical applications.

The 480-nm emission wavelength of the $Ba_{0.97}ZrSi_3O_9:0.03Eu + 0.3SiO_2$ phosphor is quite rare. The development of LD (laser diode) lighting and ultrahigh

Fig. 1.19 Schematic illustration of a 2-wavelength white LED system using a blue LED as an excitation light source
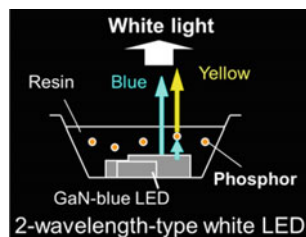
Fig. 1.20 Schematic illustration of a 3-wavelength white LED system using a near-ultraviolet LED as an excitation light source
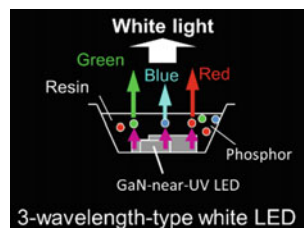
color rendering surface light sources has generated a demand for cyan blue-green phosphors that emit light near 480 nm, in addition to red phosphors excited either by blue or near-ultraviolet light. The wavelength of 480 nm is positioned between those of green light (510 nm) and blue light (450 nm). When a blue laser with a narrow line width is used as the excitation source, a cyan blue-green phosphor that is excited by blue light is indispensable, and to realize "ultrahigh" color rendering surface light (a light source with a level >95, when solar illumination is considered the standard of 100), a cyan blue-green phosphor (emitting at ∼480 nm) that can be excited by near-ultraviolet or blue light is essential to supplement the red component. An investigation of the literature reveals that such cyan blue-green phosphors are not commonly known [36–38].

1.4.4 $Na_3ScSi_3O_9:Eu^{2+}$ from Sodium–Scandium Silicate-Based Minerals

The details about the other silicate-based minerals contained in the Library 9 (Fig. 1.9) are omitted, but the solution parallel synthesis method using 22 artificial compositions revealed that $NaScSi_2O_6$ in which Eu^{2+} was activated functioned as a phosphor [39, 40]. Therefore, it was decided to explore Na–Sc–Si–O:Eu-based phosphors.

Figure 1.21a shows the composition library for the solution parallel synthesis method. The amount of Na (1, 2, 3, 4), Sc (0.5, 1, 2), and Si (1, 2, 3) was varied in the given ranges to construct a total of 36 artificial compositions. As with the examples in the previous sections, assuming a phosphor in which Eu^{2+} is activated, the compositions in which 2 mol% europium was added to sodium were prepared for the solution parallel synthesis method. A selection of these results is shown in the X-ray diffraction (XRD) pattern in Fig. 1.21b, c. At first, the formation of a single phase of $NaScSi_2O_6$ was confirmed in the XRD pattern (Fig. 1.21b), and our group's report [39] as well as Professor Xia's report [40] revealed that $NaScSi_2O_6$:Eu^{2+} is a phosphor that emits yellow-green light when excited by near-ultraviolet light (see the excitation and emission spectra in Fig. 1.22a). Interestingly, the XRD pattern of the sample treated with a flux (50 wt% of Na_2CO_3) with the expectation of increasing the emission intensity gave new peaks (marked with red ● in the XRD pattern in Fig. 1.21c) derived from an unknown phase (i.e., a new substance)
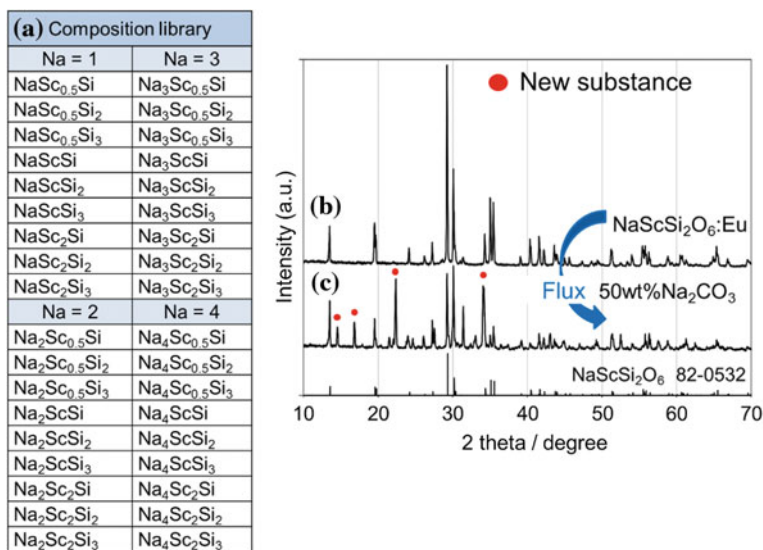
Fig. 1.21 **a** Composition library used for the exploration of new phosphors in Na–Sc–Si–O:Eu systems and X-ray diffraction patterns of **b** $NaScSi_2O_6$:Eu^{2+} and **c** a sample obtained by post-flux treatment (with 50 wt% Na_2CO_3) of $NaScSi_2O_6$:Eu^{2+}. Reprinted from Ref. [41], copyright 2014, with permission from Elsevier

in addition to the peaks derived from $NaScSi_2O_6$. The peaks derived from this unknown phase were also observed following the hydrogen reduction treatment of the sample with composition of $Na_4Sc_2Si_3O_{11}$ prepared using the graphite-reducing condition (XRD patterns in Fig. 1.22d, e). Following a detailed examination, the composition of this unknown phase was identified as $Na_3ScSi_3O_9$. $Na_3ScSi_3O_9$ has the same structure as $Na_3YSi_3O_9$ and had not been previously examined as a phosphor host until very recently [39, 41, 42]. Thus, $Na_3ScSi_3O_9$ in which Eu^{2+} is activated is a novel phosphor.

The left side of Fig. 1.22 shows the excitation and emission spectra of the $Na_4Sc_2Si_3O_{11}$:Eu^{2+} sample prepared using the graphite-reducing condition, as well as those of the sample containing $Na_3ScSi_3O_9$:Eu^{2+} as the main phase obtained by hydrogen reduction of $Na_4Sc_2Si_3O_{11}$:Eu^{2+}. For comparison, the excitation and emission spectra of the sample with the composition $NaScSi_2O_6$:Eu^{2+} are also shown. Compared with that of $NaScSi_2O_6$:Eu^{2+}, the excitation spectrum of $Na_3ScSi_3O_9$:Eu^{2+} is shifted to longer wavelengths (a redshift) and shows that this sample can be excited with blue light (450 nm) in addition to the useful near-ultraviolet light excitation at 400 nm. The emission wavelength of $Na_3ScSi_3O_9$: Eu^{2+} shifted from about 555 nm for $NaScSi_2O_6$:Eu^{2+} to 520 nm (a blueshift). $NaScSi_2O_6$ naturally exists as a jervisite pyroxene mineral (with calcium, iron, and magnesium impurities, i.e., $(Na,Ca,Fe^{2+})(Sc,Mg,Fe^{2+})Si_2O_6)$, but $Na_3ScSi_3O_9$ is a novel compound of artificial composition that does not exist in nature. The crystal structure, crystal system, and lattice constants of $Na_3ScSi_3O_9$ are shown in Fig. 1.23.
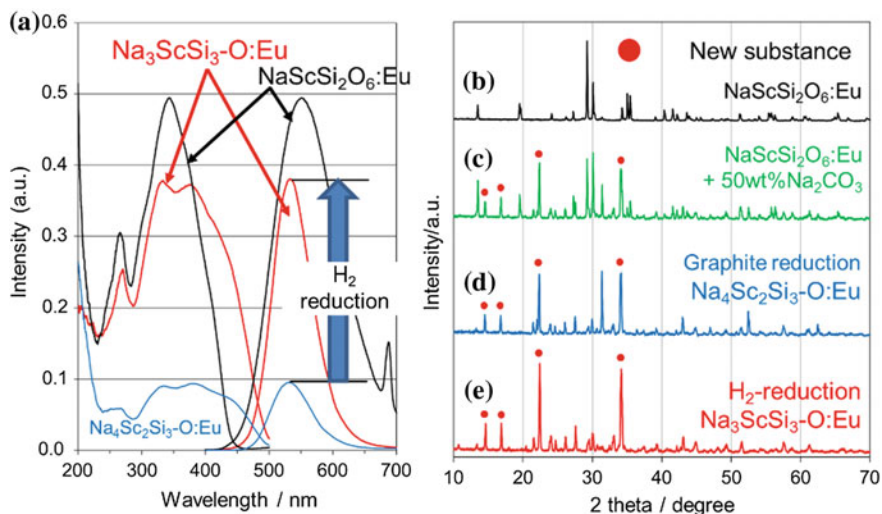
Fig. 1.22 **a** Excitation and emission spectra of NaScSi$_2$O$_6$:Eu^{2+} (*black*) and Na$_3$ScSi$_3$O$_9$:Eu^{2+} (*red*), and X-ray diffraction patterns of **b** NaScSi$_2$O$_6$:Eu^{2+}, **c** a sample obtained by post-flux treatment (with 50 wt% Na$_2$CO$_3$) of NaScSi$_2$O$_6$:Eu^{2+}, **d** a sample obtained by graphite reduction treatment of Na$_4$Sc$_2$Si$_3$O$_{11}$:Eu^{2+}, and **e** a sample obtained by a post-heat treatment of the Na$_4$Sc$_2$Si$_3$O$_{11}$:Eu^{2+} sample under H$_2$ atmosphere. Peaks marked with *red* ● correspond to reflections from the new phosphor Na$_3$ScSi$_3$O$_9$:Eu^{2+}. Reprinted from Ref. [41], copyright 2014, with permission from Elsevier
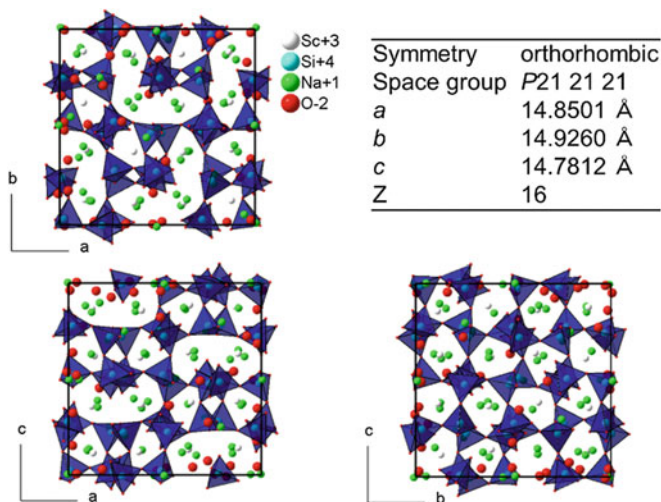
Fig. 1.23 Crystal structure and lattice constants of the new phosphor host Na$_3$ScSi$_3$O$_9$ inspired by a jervisite mineral. Reprinted from Ref. [41], copyright 2014, with permission from Elsevier

1.4.5 CaSrSiO$_4$:Eu^{2+} and Ca$_2$SiO$_4$:Eu^{2+} from Alkaline Earth Metal Silicate Minerals

1.4.5.1 Background

A huge number of silicates that contain alkaline earth metals (M = Ba, Sr, Ca, Mg) are known to function as phosphor hosts. As shown in the table in Fig. 1.24a, substances with five compositions (MSi$_2$O$_5$ [45], MSiO$_3$ [46], M$_3$Si$_2$O$_7$ [47], M$_2$SiO$_4$ [48], and M$_3$SiO$_5$ [49]) are known to be effective phosphor hosts with emission wavelengths ranging from 440 to 600 nm. In particular, research on Eu^{2+}-activated phosphors using M$_2$SiO$_4$ as a host has progressed. Figure 1.24b shows the excitation and emission spectra of the phosphors Ba$_2$SiO$_4$:Eu^{2+}, Ca$_2$SiO$_4$:Eu^{2+}, and Sr$_2$SiO$_4$:Eu^{2+}. Ba$_2$SiO$_4$:Eu^{2+} is a green phosphor (514 nm) that can be excited with near-ultraviolet (400 nm) and blue light (450 nm), whereas the excitation spectrum of Sr$_2$SiO$_4$:Eu^{2+} is shifted to longer wavelengths (redshift), giving an emission color between yellow and orange (581 nm). Ca$_2$SiO$_4$:Eu^{2+} is a green phosphor emitting light at 521 nm; however, the practicability of the phosphor is poor because it cannot be excited by blue light (450 nm). For that reason, it is a phosphor drew little attention until now. However, as described later, by designing based on crystal site engineering [44, 50], our research group found, for the first time, that Ca$_2$SiO$_4$:Eu^{2+} is a phosphor that strongly emits red light (650 nm) with blue light excitation. Similarly, CaSrSiO$_4$:Eu^{2+} was found to be a phosphor that strongly emits red light (615 nm) with blue light excitation [43]. The details of the discovery of these red-emitting phosphors are introduced in the next section.

(a) M-Si-O:Eu^{2+} Phosphors (M = Ba, Sr, Ca, Mg)

No.	Phosphor	Excitation		Emission / nm
		Near-UV	Blue	
1	MSi$_2$O$_5$	O	×	465–520
2	MSiO$_3$	O	×	440–555
3	M$_3$Si$_2$O$_7$	O	O	505–600
4	M$_2$SiO$_4$	O	O	514–581
5	M$_3$SiO$_5$	O	O	561–591

(b)
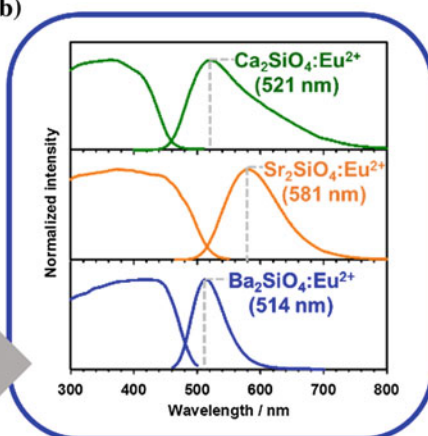
Fig. 1.24 **a** Emission wavelengths of known binary alkaline earth orthosilicates, and **b** excitation and emission spectra of M$_2$SiO$_4$:Eu^{2+} (M = Ba, Sr, Ca)

1.4.5.2 Exploration of Ganomalite: Discovery of a Phosphor that Emits Yellow-Orange Light

As shown in Fig. 1.25, the original composition of ganomalite is $Pb_9Ca_5MnSi_9O_{33}$. Lead and manganese are undesirable as elements in phosphor hosts. Therefore, the construction of an artificial composition was carried out by element substitution. In other words, divalent Pb (effective ionic radius of 8-coordinate Pb^{2+} is 1.29 Å) was substituted with divalent Sr (effective ionic radius of 8-coordinate Sr^{2+} is 1.26 Å) and divalent Mn (effective ionic radius of 8-coordinate Mn^{2+} is 0.96 Å) was substituted with divalent Mg (effective ionic radius of 8-coordinate Mg^{2+} is 0.89 Å) to construct a hypothetical substance with a composition of an artificial ganomalite: $Sr_9Ca_5MgSi_9O_{33}$ (Fig. 1.25) (see table of Shannon ionic radii [24]).

Unfortunately, the synthesis of $Sr_9Ca_5MgSi_9O_{33}$ could not be achieved. XRD analysis indicated that the obtained sample was a mixture of alkaline earth metal silicates containing $Sr_{1.16}Ca_{0.84}SiO_4$ as the main phase. The excitation and emission spectra of this sample activated by Eu^{2+} shown in Fig. 1.26. Interestingly, in the multi-phase sample containing $Sr_{1.16}Ca_{0.84}SiO_4$ as the main phase, yellow-orange emission was observed with maximum intensity at 605 nm using blue light excitation. As shown in the table on the left of Fig. 1.24, silicate-based phosphors of alkaline earth

Fig. 1.25 Composition of a typical ganomalite-based mineral ($Pb_9Ca_5MnSi_9O_{33}$) and a hypothetical artificial ganomalite ($Sr_9Ca_5MgSi_9O_{33}$) [23]
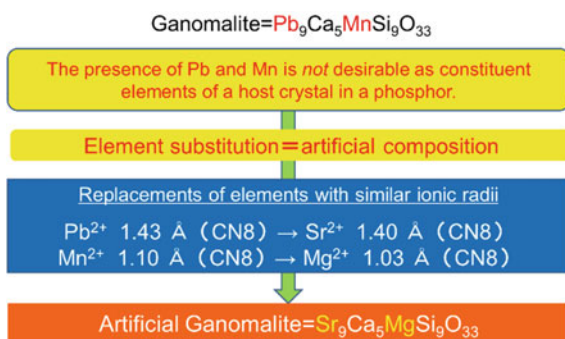
Fig. 1.26 Excitation and emission spectra of the as-prepared Eu^{2+}-doped sample synthesized according to the artificial ganomalite composition ($Sr_9Ca_5MgSi_9O_{33}$), and the appearance of its emission when irradiated with near-ultraviolet light (250 and 320 nm) [23]
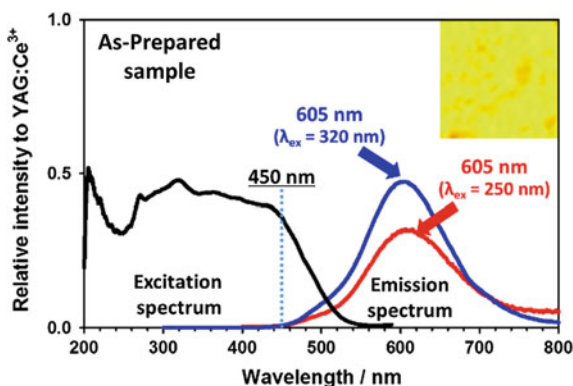
metals that emit light at wavelengths exceeding 600 nm are quite unusual. Therefore, the emission spectrum shown in Fig. 1.26 is considered an interesting and uncommon result.

1.4.5.3 Synthesis of $M_{1.9}Eu_{0.1}SiO_4$ Phosphors: Red-Orange-Emitting $CaSrSiO_4:Eu^{2+}$

The above phosphor, $Sr_{1.16}Ca_{0.84}SiO_4$, is a substance based on M_2SiO_4. To confirm the existence of a phosphor that emits orange-red light, $M_{1.9}Eu_{0.1}SiO_4$ (M = Ba, Sr, Ca) phosphors with different ratios of Ba, Sr, and Ca were synthesized by the solution parallel synthesis method. The solution parallel synthesis method was carried out by introducing the gel freeze-drying method as shown in Fig. 1.27. A selection of the sample compositions subjected to the solution parallel synthesis is shown in Fig. 1.28.

In the first experiment, four types of samples were considered as targets to investigate the mutual dependence of Ba/Sr/Ca on the emitting color ($Ba_{0.95}Sr_{0.95}Eu_{0.1}SiO_4$ in which 50 % Sr was substituted against $Ba_{1.9}Eu_{0.1}SiO_4$, and $Sr_{0.95}Ca_{0.95}Eu_{0.1}SiO_4$ in which 50 % Ca were substituted against $Sr_{1.9}Eu_{0.1}SiO_4$). In the second experiment, $Sr_{1.9}Eu_{0.1}SiO_4$ was used as a reference material to investigate the mutual dependence of Sr/Ca on the emitting color, with Sr substituted by Ca in the target samples $Sr_{1.7}Ca_{0.2}Eu_{0.1}SiO_4$, $Sr_{1.2}Ca_{0.7}Eu_{0.1}SiO_4$, $Sr_{0.95}Ca_{0.95}Eu_{0.1}SiO_4$, and $Sr_{0.7}Ca_{1.2}Eu_{0.1}SiO_4$. The excitation and emission spectra of the samples in Experiment 1 are shown in Fig. 1.29. The emission wavelength of maximum intensity for $Ba_{0.95}Sr_{0.95}Eu_{0.1}SiO_4$ was 533 nm, which is red-shifted about 19 nm compared with that of $Ba_{1.9}Eu_{0.1}SiO_4$. On the other hand, the emission wavelength of maximum intensity at 615 nm for $Sr_{0.95}Ca_{0.95}Eu_{0.1}SiO_4$ exhibited a large redshift of about 34 nm compared with that of $Sr_{1.9}Eu_{0.1}SiO_4$. Figure 1.30

Fig. 1.27 Solution parallel synthesis of $M_{1.9}Eu_{0.1}SiO_4$ (M = Ba, Ba–Sr, Sr, Sr–Ca) based on a gel freeze-drying method

PGMS, $(CH_3COO)_2Eu$, $(CH_3COO)_2M$ (M = Ca, Sr, Ba)

├ Heat at 323 K

Gel

├ Freeze dry at 243 K → 303 K

Powder

├ Calcination at 1273 K for 12 h

M_2SiO_4: Eu^{3+}

Flux →├ Reduction at 1573 K for 4 in a flow of 4%-H_2/Ar

├ Wash with warm water and ethanol

$M_{1.9}Eu_{0.1}SiO_4$ (M = Ca, Sr, Ba)
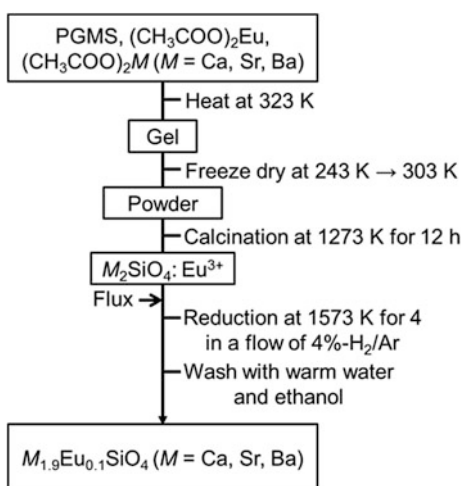
Fig. 1.28 An excerpt of the compositional library of $M_{1.9}Eu_{0.1}SiO_4$ (M = Ba, Ba–Sr, Sr, Sr–Ca) used for the solution parallel synthesis

Experiment-1: Dependence of Ba/Sr/Ca
$Ba_{1.9}Eu_{0.1}SiO_4$
$Sr_{0.95}Ba_{0.95}Eu_{0.1}SiO_4$
$Sr_{1.9}Eu_{0.1}SiO_4$
$Sr_{0.95}Ca_{0.95}Eu_{0.1}SiO_4$

Experiment-2: Dependence of Ba/Sr/Ca
$Sr_{1.9}Eu_{0.1}SiO_4$
$Sr_{1.7}Ca_{0.2}Eu_{0.1}SiO_4$
$Sr_{1.2}Ca_{0.7}Eu_{0.1}SiO_4$
$Sr_{0.95}Ca_{0.95}Eu_{0.1}SiO_4$
$Sr_{0.7}Ca_{1.2}Eu_{0.1}SiO_4$
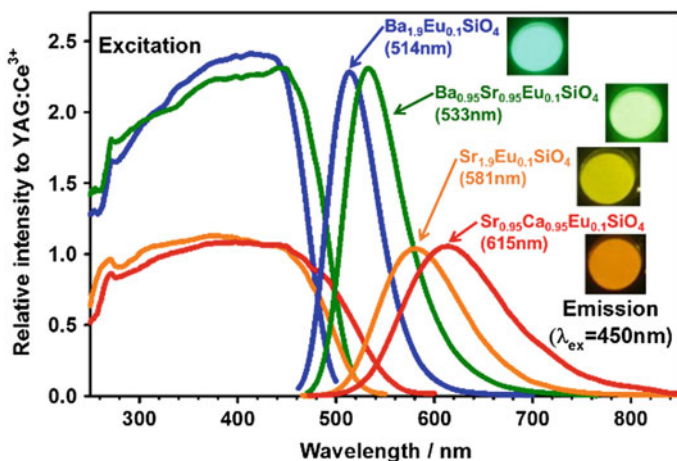
Fig. 1.29 Excitation and emission spectra of $Ba_{1.9}Eu_{0.1}SiO_4$, $Sr_{0.95}Ba_{0.95}Eu_{0.1}SiO_4$, and $Sr_{1.9}Eu_{0.1}SiO_4$, $Sr_{0.95}Ca_{0.95}Eu_{0.1}SiO_4$

shows the excitation and emission spectra of both $Sr_{0.95}Ca_{0.95}Eu_{0.1}SiO_4$ and YAG: $Ce^{3+}(Y_3Al_5O_{12}:Ce^{3+})$.

It can be seen that, unlike the yellow emission of YAG:Ce^{3+}, $Sr_{0.95}Ca_{0.95}Eu_{0.1}SiO_4$ is a phosphor that emits light into the red region beyond 600 nm. The internal quantum efficiency of $Sr_{0.95}Ca_{0.95}Eu_{0.1}SiO_4$ is 65 %, which still leaves room for improvement, but it is notable as the first M_2SiO_4-based phosphor to exceed 600 nm, with significant red light emission at 615 nm. The excitation and emission spectra of the $Sr_{1.9-y}Ca_yEu_{0.1}SiO_4$ samples in Experiment 2
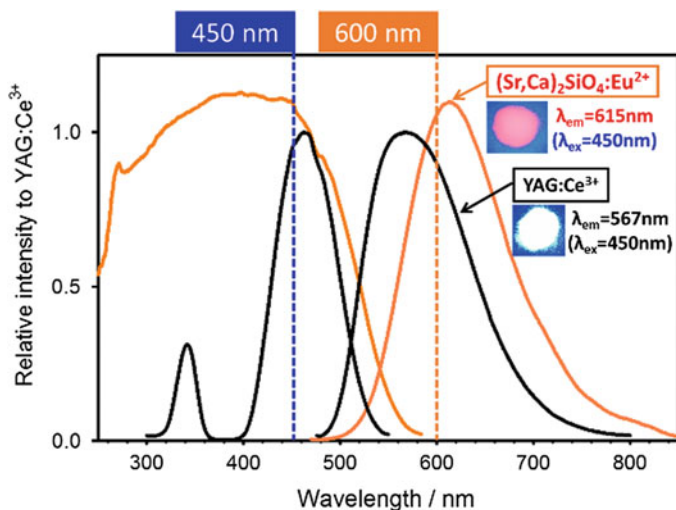
Fig. 1.30 Excitation and emission spectra of $Sr_{0.95}Ca_{0.95}Eu_{0.1}SiO_4$, which emits *red-orange light* under excitation with *blue light*, and its comparison with the spectra of commercially available YAG $(Y_3Al_5O_{12})$:Ce^{3+} [43]

are shown in Fig. 1.31. As the amount of Ca (y) increased, the emission wavelength (581 nm for $Sr_{1.9}Eu_{0.1}SiO_4$) experienced a large redshift, reaching 615 nm at $y = 0.95$. The emission wavelength did not show any further shifts when y was further increased ($y = 1.2$).

The positions of $Ba_{1.9}Eu_{0.1}SiO_4$, $Ba_{0.95}Sr_{0.95}Eu_{0.1}SiO_4$, $Sr_{1.9}Eu_{0.1}SiO_4$, $Sr_{0.95}Ca_{0.95}Eu_{0.1}SiO_4$, and YAG:$Ce^{3+}$ in a chromaticity diagram are shown in
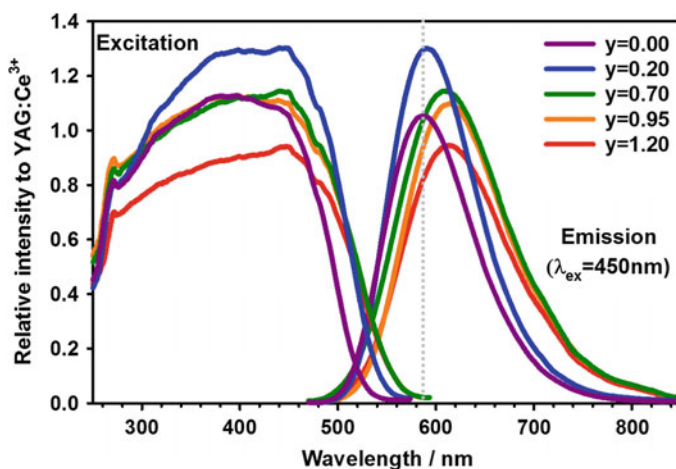
Fig. 1.31 Excitation and emission spectra of $Sr_{1.9-y}Ca_yEu_{0.1}SiO_4$ ($y = 0, 0.2, 0.7, 0.95, 1.2$)
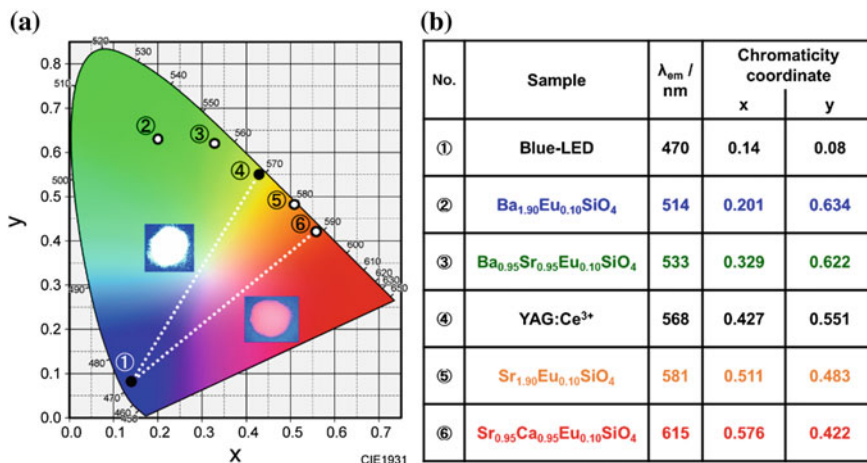
Fig. 1.32 a Positions of the emission colors of $Ba_{1.9}Eu_{0.1}SiO_4$, $Sr_{0.95}Ba_{0.95}Eu_{0.1}SiO_4$, YAG $(Y_3Al_5O_{12}):Ce^{3+}$, $Sr_{1.9}Eu_{0.1}SiO_4$, and $Sr_{0.95}Ca_{0.95}Eu_{0.1}SiO_4$ on a chromaticity diagram (CIE1931) and **b** their emission wavelengths and color coordinates. The appearance of the emission of YAG $(Y_3Al_5O_{12}):Ce^{3+}$ and $Sr_{0.95}Ca_{0.95}Eu_{0.1}SiO_4$ when irradiated with *blue light* of 470 nm (photographs on the diagram (**a**))

Fig. 1.32a with the emission wavelength and chromaticity coordinates shown in Fig. 1.32b. The chromaticity coordinates of $Sr_{0.95}Ca_{0.95}Eu_{0.1}SiO_4$ are (0.576, 0.422), and the color on the line linking to a blue LED with chromaticity coordinates (0.14, 0.08) can be represented (the red-purple color in Fig. 1.32a is the appearance when the blue LED was used to irradiate $Sr_{0.95}Ca_{0.95}Eu_{0.1}SiO_4$). Similarly, the chromaticity coordinates of YAG:Ce^{3+} are (0.427, 0.551), and the color on the line linking to the blue LED with the chromaticity coordinates (0.14, 0.08) can be represented (the white color in Fig. 1.32a is the appearance when the blue LED was used to irradiate YAG:Ce^{3+}). Fig. 1.32a shows that the pseudo-white color made by combining the blue LED with YAG:Ce^{3+} lacks red components. By incorporating $Sr_{0.95}Ca_{0.95}Eu_{0.1}SiO_4$ into the pseudo-white LED system (Fig. 1.32a), it becomes possible to express the light in the area of the triangle formed by the three points in Fig. 1.32a (④ YAG:Ce^{3+}, ⑥ $Sr_{0.95}Ca_{0.95}Eu_{0.1}SiO_4$, and ① blue LED). Therefore, adjustments of the ratio of these components would bring us closer to ideal white light.

1.4.5.4 Red-Emitting Ca_2SiO_4:Eu^{2+}: The Importance of Crystal Site Engineering

Ca_2SiO_4:Eu^{2+} is known as a phosphor that emits green light under ultraviolet to near-ultraviolet light excitation. Because it cannot be excited effectively by blue light, Ca_2SiO_4:Eu^{2+} cannot be used as a phosphor for white LEDs (see Fig. 1.24).

Considering that emission characteristics can change in accordance with polymorphism, we focused on the polymorphism of Ca_2SiO_4 (phases with the same Ca_2SiO_4 notation but different crystal structures). A number of polymorphs of Ca_2SiO_4 exist, including the $\alpha'l$-phase, β-phase, and γ-phase, with the stability of each phase depending on the temperature and composition (the composition can be changed by element substitution) [51, 52]. Green-emitting $Ca_2SiO_4:Eu^{2+}$ is equivalent to the addition of a small amount of Eu^{2+} to the β-phase of Ca_2SiO_4. Here, if $Ca_2SiO_4:Eu^{2+}$ is rewritten with notation $Ca_{2-x}Eu_xSiO_4$, the β-phase is stable when the Eu concentration (x) is below 0.1. However, when $x > 0.1$, a $\beta \rightarrow \alpha'l$ phase transition occurs, and the light emission changes dramatically. For example, in the $\alpha'l$ single-phase sample with $x = 0.2$ ($Ca_{1.8}Eu_{0.2}SiO_4$), green light emission disappears, and yellow light emission with a maximum at ~ 560 nm is observed instead. The changes in the excitation and emission spectra of $Ca_{2-x}Eu_xSiO_4$ owing to the $\beta \rightarrow \alpha'l$ phase transition are shown in Fig. 1.33. In addition, significantly increasing the europium concentration, for example, in the sample with $x = 0.8$ ($Ca_{1.2}Eu_{0.8}SiO_4$), surprisingly, results in the emission of deep-red light with a maximum intensity at 650 nm. Fig. 1.34 shows the excitation and emission spectra of this sample and its appearance when irradiated with near-ultraviolet light at 365 nm. These changes in the light emission characteristics can be interpreted as follows from the viewpoint of crystal site engineering (engineering to control the position that the light emission center ion (activator) occupies in crystal) [44, 50].

First, we examine the crystal structures of the β- and $\alpha'l$-phases of Ca_2SiO_4. Figure 1.35a shows the crystal structure of β-$Ca_{1.9}Eu_{0.1}SiO_4$ ($x = 0.1$) seen from the direction perpendicular to the ab plane. Here, a threefold expansion of the b-axis of the unit cell is shown for comparison with the crystal structure of the $\alpha'l$-phase
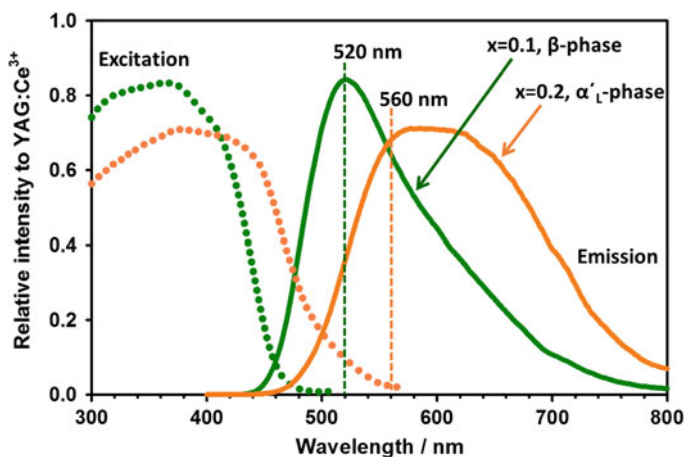
Fig. 1.33 Excitation and emission spectra of $Ca_{1.9}Eu_{0.1}SiO_4$ ($x = 0.1$, β-phase) and $Ca_{1.8}Eu_{0.2}SiO_4$ ($x = 0.2$, $\alpha'l$-phase). Reproduced from Ref. [44] by permission of John Wiley & Sons Ltd.
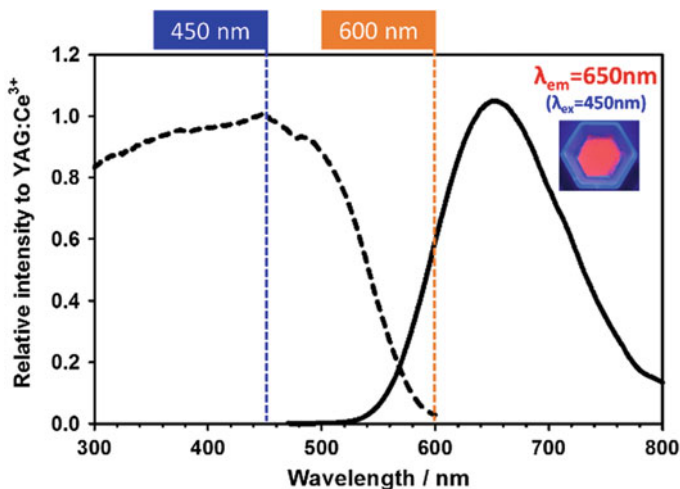
Fig. 1.34 Excitation and emission spectra of $Ca_{1.8}Eu_{0.2}SiO_4$ ($x = 0.2$, $\alpha' l$-phase) and the appearance of the emission when irradiated with near-ultraviolet light of 365 nm. Reproduced from Ref. [44] by permission of John Wiley & Sons Ltd.

described later.β-$Ca_{1.9}Eu_{0.1}SiO_4$ contains two calcium sites, the 10-coordinate Ca(1) site and 8-coordinate Ca(2) site (Fig. 1.35b, c, respectively). Similarly, the crystal structure of $\alpha' l$-$Ca_{1.8}Eu_{0.2}SiO_4$ seen from the direction perpendicular to the *ac* plane is shown in Fig. 1.36a. $\alpha' l$-$Ca_{1.8}Eu_{0.2}SiO_4$ contains six calcium sites, the 10-coordinate Ca($1n$) sites ($n = 1, 2, 3$) and 8-coordinate Ca($2n$) sites ($n = 1, 2, 3$). When categorized generally, $\alpha' l$-$Ca_{1.8}Eu_{0.2}SiO_4$ can be said, like β-$Ca_{1.9}Eu_{0.1}SiO_4$, to contain two types of sites: a 10-coordinate Ca(1) site and 8-coordinate Ca(2) site.

In the coordination structures of the Ca(1) and Ca(2) sites shown in Fig. 1.35b, c, respectively, the red-purple marking on the central metal (calcium) shows the percentage of europium ions that occupy that site. That is, in the sample with $x = 0.1$ (β-$Ca_{1.9}Eu_{0.1}SiO_4$), Eu^{2+} as the emission center ion (activator) exists almost exclusively in the Ca(1) site. Because the ionic radius of Eu^{2+} is greater than that of Ca^{2+}, Eu^{2+} can occupy the 10-coordinate Ca(1) site with sufficient spatial room. That is, the green emission of β-$Ca_{1.9}Eu_{0.1}SiO_4$ observed in Fig. 1.33 is considered to be emission from Eu^{2+} that occupies the 10-coordinate Ca(1) site. On the other hand, an examination of the sample with $x = 0.2$ ($\alpha' l$-$Ca_{1.8}Eu_{0.2}SiO_4$) revealed the occupancy rate of europium ions in the Ca(13) and Ca(23) sites of the coordination structure shown in Fig. 1.36b, c, respectively. Even in this sample, Eu^{2+} as the emission center ion (activator) exists almost exclusively in the 10-coordinate Ca($1n$) site. Therefore, the yellow emission of $\alpha' l$-$Ca_{1.8}Eu_{0.2}SiO_4$ observed in Fig. 1.33 is emission from Eu^{2+} that occupies the 10-coordinate Ca($1n$) site. Although in both cases Eu^{2+} occupies a 10-coordinate calcium site, the difference in emission color between β-$Ca_{1.9}Eu_{0.1}SiO_4$ (green emission) and $\alpha' l$-$Ca_{1.8}Eu_{0.2}SiO_4$ (yellow emission) is derived from the different crystal phases (i.e., crystal structures).
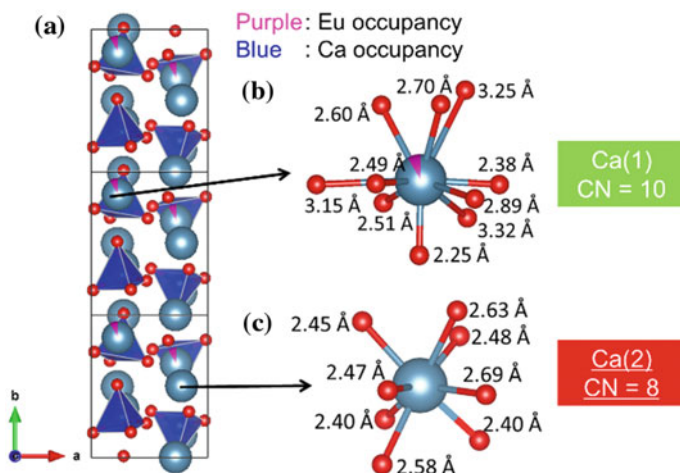
Fig. 1.35 **a** Crystal structure of β-Ca$_{1.9}$Eu$_{0.1}$SiO$_4$ seen from the direction perpendicular to the *ab* plane and two different calcium sites: **b** 10-coordinate Ca(1) site and **c** 8-coordinate Ca(2) site. Reproduced from Ref. [44] by permission of John Wiley & Sons Ltd.
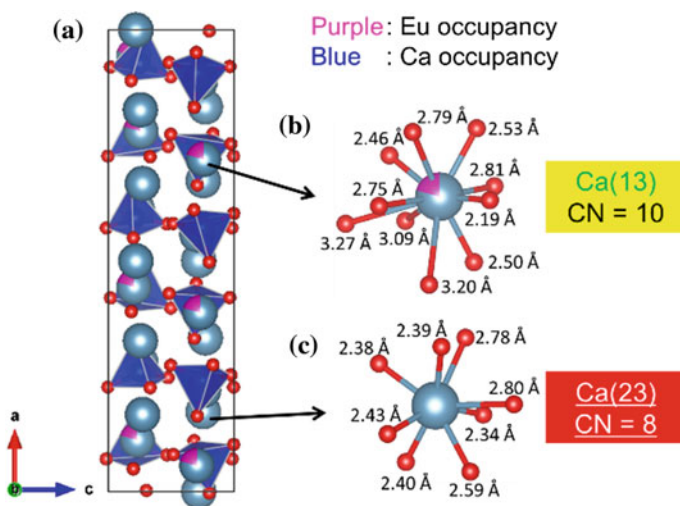
Fig. 1.36 **a** Crystal structure of $\alpha' l$-Ca$_{1.8}$Eu$_{0.2}$SiO$_4$ seen from the direction perpendicular to the *ac* plane and two representatives of six different calcium sites: **b** 10-coordinate Ca(13) site and **c** 8-coordinate Ca(23) site. Reproduced from Ref. [44] by permission of John Wiley & Sons Ltd.

The origin of the unusual deep-red emission at 650 nm in the sample with $x = 0.8$ ($\alpha' l$-Ca$_{1.2}$Eu$_{0.8}$SiO$_4$) can also be discussed in terms of crystal site engineering.
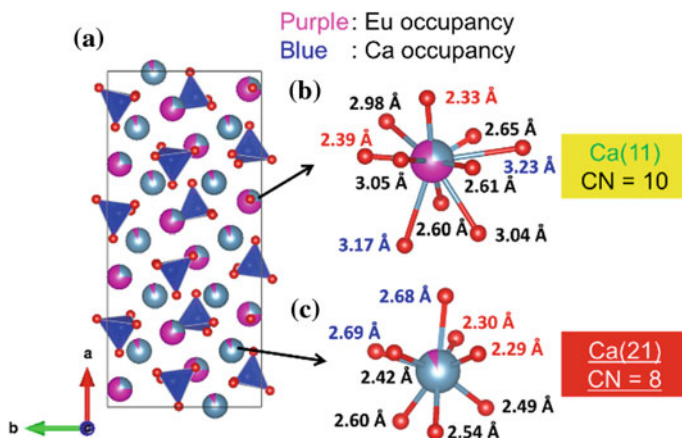
Fig. 1.37 **a** Crystal structure of $\alpha' l$-$Ca_{1.2}Eu_{0.8}SiO_4$ seen from the direction perpendicular to the *ab* plane and two representatives of six different calcium sites: **b** 10-coordinate Ca(11) site and **c** 8-coordinate Ca(21) site. Reproduced from Ref. [44] by permission of John Wiley & Sons Ltd.

Figure 1.37a shows the crystal structure of $\alpha' l$-$Ca_{1.2}Eu_{0.8}SiO_4$ seen from the direction perpendicular to the *ab* plane. As revealed from the occupancy rate of europium ions in the Ca(11) and Ca(21) sites of the coordination structure shown in Fig. 1.37b, c, respectively, most Eu^{2+} (90 %) as the emission center ion (activator) occupies the 10-coordinate Ca(1n) site. Importantly, a small amount of Eu^{2+} (10 %) also occupies the 8-coordinate Ca(2n) site. We presume that emission from Eu^{2+} occupying the 10-coordinate Ca(1n) site (yellow emission) was not observed owing to Eu^{2+} concentration quenching, as well as reabsorption of the yellow emission light from Eu^{2+} at Ca(1n) by Eu^{2+} at Ca(2n) (note that the excitation spectrum of $Ca_{1.2}Eu_{0.8}SiO_4$ in Fig. 1.34 covers the yellow light region around 560 nm). That is, the deep-red emission of $\alpha' l$-$Ca_{1.2}Eu_{0.8}SiO_4$ observed in Fig. 1.34 is considered to be emission from Eu^{2+} occupying the 8-coordinate Ca(2n) site.

Thus, the emission characteristics of $Ca_{2-x}Eu_xSiO_4$ are strongly related to not only the crystalline phase (β-phase or $\alpha' l$-phase), but also the structure of the two types of calcium sites present in the crystal. In particular, by substituting Eu^{2+} into the 8-coordinate Ca(2n) site, deep-red emission can be obtained. It may be concluded that crystal site engineering plays an important role in understanding the emission characteristics of a given phosphor and controlling its emission color.

1.4.6 A New Oxide Up-Conversion Phosphor of YTa_7O_{19}: Er^{3+},Yb^{3+} Derived from Tantalite-Based Minerals

This section introduces some research results on the oxide up-conversion phosphor developed by Professor Tomita's group at Tokai University [19].

In a normal phosphor, light with high energy (short wavelength), such as ultraviolet light, is used for excitation and light with energy lower than that of the exciting light (longer wavelength) is emitted. On the other hand, an up-conversion phosphor generates multiphoton excitation by low energy light (long wavelength), such as near-infrared light, and light with energy higher than that of the exciting light (shorter wavelength) is emitted. In the up-conversion phosphor, a sensitizer, most often Yb, is combined with an emission center ion (activator) to control the emission color and increase the emission intensity. The sensitizer is excited directly, and if its excited level overlaps with the excited level of the emission center ion, energy transfer from the sensitizer to the activator can occur. If the emission center ion is then excited to an upper excited level (two or three photons excitations), light with energy higher than that of the original exciting light will be observed when the phosphor returns from the excited state to the ground state.

Because the up-conversion phosphor relies on two and three photon excitations, the internal quantum efficiency is, even the best cases, as low as ~ 1 %. In contrast, the internal quantum efficiency of a normal phosphor is usually greater than 50 % and can sometimes exceed 90 %. Nevertheless, up-conversion phosphors are expected to find applications in bioimaging, energy conversion materials, optical communications, etc., because of its unique features that normal phosphors do not have, and, in recent years, there has been significant research and development with up-conversion phosphors. In particular, up-conversion phosphors that are characterized by excitation using near-infrared light, which has good biological permeability, are suitable for medical engineering applications, such as tumor detection by bioimaging, and research to achieve practical applications is being performed.

The obstacles to the development of oxide up-conversion phosphors are considered to include: (1) difficulties in determining the optimal concentrations of two types of additives: sensitizer and activator, and (2) difficulties in efficiently locating a host crystal among the various types of available compounds. Therefore, the benefits of applying the solution parallel synthesis method to search for the up-conversion phosphors and optimize the concentrations of both sensitizer and activator are overwhelming. Because the solution parallel synthesis method enables uniform dispersion of trace amounts of sensitizer as well as activator into a given host crystal, the determination of their optimum concentrations and the search for appropriate host crystals should not be very time-consuming.

Professor Tomita's group at Tokai University has studied mineral-derived complex oxide up-conversion phosphors, as well as simple oxides, such as CeO_2. They constructed 24 types of composition library for the general chemical formula $(Y, La, Gd)_x(Nb, Ta)_yO_z$ ($x{:}y$ = 3:1, 1:1, 1:3, 1:7) using niobates or tantalates of rare earth elements (inspired by minerals) as synthetic targets and conducted the solution parallel synthesis. In addition, Er and Yb concentrations were fixed at 5 and 10 %, respectively. There were 19 compositions from the composition library that could be synthesized (inset of Fig. 1.38). The bar graph in Fig. 1.38 indicates the relative emission intensities of the tested samples corresponding to these 19 compositions when excited by a near-infrared light with a wavelength of 980 nm.
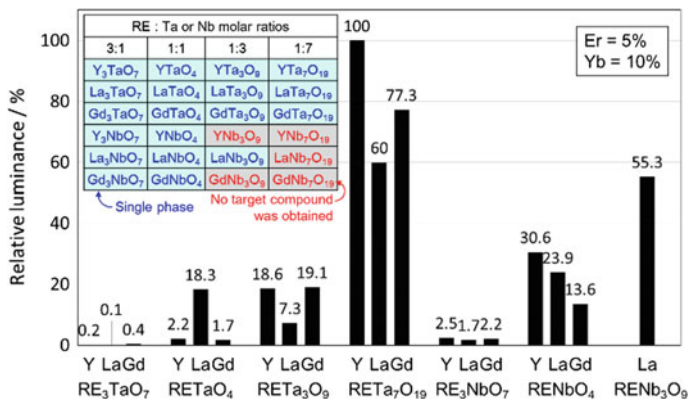
Fig. 1.38 Exploration of new up-conversion phosphors based upon (Y, La, Gd)$_x$(Nb, Ta)$_y$O$_z$ (x: y = 3:1, 1:1, 1:3, 1:7) inspired by rare earth niobate and tantalite minerals; relative emission intensities of the 24 different compounds tested [19]
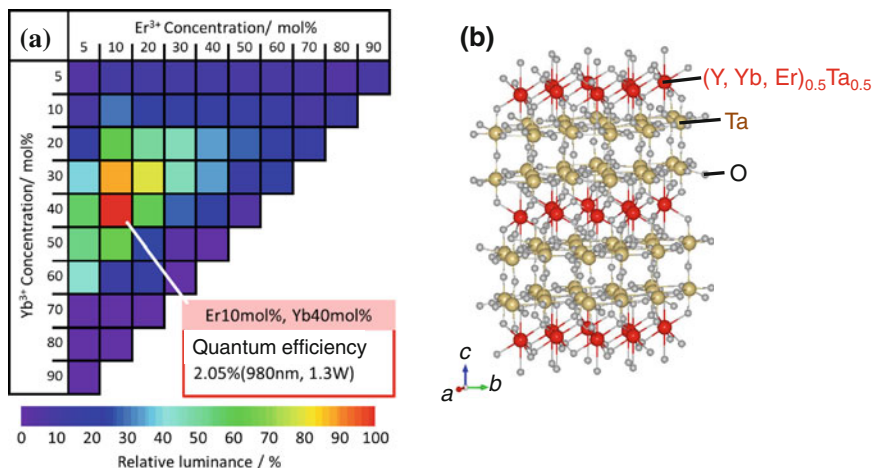
Fig. 1.39 **a** Dependence of Yb and Er concentrations on the up-conversion emission intensities of (Y, Yb, Er)Ta$_7$O$_{19}$ and **b** its crystal structure [19]

At a glance, RETa$_7$O$_{19}$ (RE = Y, La, Gd) has the highest emission intensities, and YTa$_7$O$_{19}$ is especially prominent. Therefore, the optimum concentration of Er and Yb in YTa$_7$O$_{19}$: Er, Yb that gave the strongest green emission was determined by the solution parallel synthesis method. Figure 1.39a shows the composition library and relative intensity of the emission for each composition when the Er and Yb concentrations were changed from 5 to 90 %. Of the 55 compositions, the highest emission intensity was achieved for Er:10 mol%–Yb:40 mol%, represented as Y$_{0.5}$Yb$_{0.4}$Er$_{0.1}$Ta$_7$O$_{19}$. The internal quantum efficiency of this compound is

2.05 %, which is high for an up-conversion phosphor. The reason for such high quantum efficiency is unclear, but it is thought to be associated with the two-dimensional structure of the rare earth site in YTa_7O_{19} found in the crystal structure shown in Fig. 1.39b. We plan to demonstrate the relationship between the structure and properties of such substances by further exploring novel complex oxide up-conversion phosphors in the future.

1.5   Summary and Future Prospects

In this chapter, we stressed that the mineral-inspired approach in combination with the solution parallel synthesis method is quite effective in the search for new phosphors. In particular, the importance of selecting the lead compound for a key search was emphasized, and using minerals as a guide showed that substance exploration could be conducted rationally and rapidly.

For silicate phosphors, it was difficult to apply the solution parallel synthesis method until recently. This is because, in the sol–gel method using the alkoxide of silicon (e.g., TEOS: tetraethoxysilane), the synthesis of oxides corresponding to a particular composition is possible, but it is difficult to simultaneously synthesize a series of samples with different compositions. Because the optimum synthesis conditions depend on the composition of the target, the solution parallel synthesis is impossible, and during the process of removing solvent by heating, which is essential for rapid synthesis, it is difficult to prevent deviations from the target composition owing to volatilization of silicon alkoxide. On the other hand, glycol-modified silane (GMS) is a silicon material that overcame the problems with silicon alkoxide for the solution parallel synthesis, and the advent of GMS has allowed anyone to perform solution parallel synthesis to explore new silicates [16–18, 23].

Especially important findings with silicate phosphors include the cyan blue-green emission (480 nm) of $BaZrSi_3O_9$:Eu^{2+} discovered after being inspired by benitoite and the deep-red emission (650 nm) of $\alpha'l$-Ca_2SiO_4:Eu^{2+} discovered after being inspired by ganomalite. These phosphors will help to improve the color rendering of white LED lamps using blue or near-ultraviolet LEDs as an excitation light source. An image picture of fruit shot under a conventional white LED (blue LED with a yellow phosphor) and the corresponding emission spectrum of the white LED are shown in Fig. 1.40a, b, respectively. As evident from the spectrum shape, the white LED lacks light components in the cyan blue-green and deep-red regions; therefore, the color of the object (the fruit) is unnatural. Such a condition is expressed as bad color reproducibility or low (bad) color rendering. Figure 1.40c shows an image picture of the fruit shot under a high-performance white LED, in which cyan blue-green and deep-red phosphors were added to the conventional white LED and the corresponding synthesized emission spectrum (Fig. 1.40d). This spectrum has a flatter shape with reasonably even intensity across the visible light
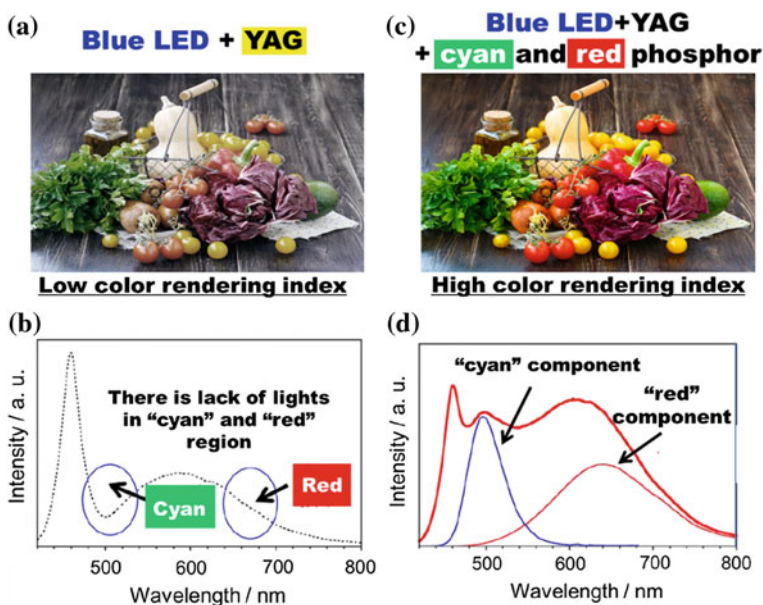
Fig. 1.40 **a** Image picture of objects (*fruit*) taken under a conventional *white* LED (*blue* LED with a *yellow* phosphor) and **b** its spectrum; **c** the corresponding image picture taken under an improved white LED (blue LED with *cyan blue-green* and *dark-red* phosphors in addition to a yellow phosphor) and **d** its synthesized spectrum. The difference in color is reproducibility due to the difference in the color rendering properties

region; therefore, color reproducibility and color rendering are improved significantly, and the color of the fruit is more natural. Thus, the cyan blue-green phosphor of $BaZrSi_3O_9:Eu^{2+}$ and deep-red phosphor of $\alpha'l\text{-}Ca_2SiO_4:Eu^{2+}$ discovered by our research group will contribute to the improvement of color rendering in white LED lighting.

For the further development of oxide up-conversion phosphors, we should notice that, in general, the emission color and intensity of a given up-conversion phosphor varies greatly with slight changes in the amount of the sensitizer and activator. For instance, in the known up-conversion phosphor $CeO_2:Er^{3+},Yb^{3+}$, precise control of the concentrations of both Er and Yb is crucial to obtain a sample that emits enough light for practical applications. For example, for green and red emission, the optimum concentrations of Er and Yb have been determined to be $Er_{0.03}Yb_{0.006}$ and $Er_{0.05}Yb_{0.06}$, respectively [19]. Thus, it can be said that the ultraprecise control (0.1 %) over the amount of sensitizer and activator in the solution parallel synthesis method is extremely important. It was virtually impossible to achieve the same control over the amount of sensitizer and/or activator using conventional methods, and this was a major factor that slowed down the development of oxide up-conversion phosphors until now.

References

1. Potyrailo R, Rajan K, Stoewe, K, TakeuchiI, Chisholm B, Lam H (2011)Combinatorial and high-throughput screening of materials libraries: Review of state of the art. ACS Comb Sci 13:579.
2. Kan D, SuchoskiR, Fujino S, TakeuchiI (2010) Combinatorial investigation of structural and ferroelectric properties of A- and B-site co-doped $BiFeO_3$ thin films. Integr Ferroelectr111: 116.
3. BealMS, HaydenBE, Le GallT, Lee CE, LuX, MirsanehM, MormicheC, Pasero D, SmithDCA, Weld A, Yada C, Yokoishi S (2011)High throughput methodology for synthesis, screening, and optimization of solid state lithium ion electrolytes. ACS Comb Sci 13:375.
4. ReiserM, Stöwe K, Maier WF (2012)Combinatorial development of novel Pd based mixed oxide catalysts for the CO hydrogenation to methanol. ACS Comb Sci 14:378.
5. KimDH, BiL, AimonNM, JiangP, Dionne GF, Ross CA (2012)Combinatorial pulsed laser deposition of Fe, Cr, Mn, and Ni-substituted $SrTiO_3$ films on Si substrates. ACS Comb Sci 14: 179.
6. Hawthorne FC (1981) Some systematics of the garnet structure. J. Solid State Chem 37:157.
7. Kim SW, Hasegawa T, Ishigaki T, Uematsu K, Toda K, Sato M (2013)Efficient red emission of blue-light excitable new structure type $NaMgPO_4$:Eu^{2+} phosphor. ECS Solid State Lett2: R49.
8. TangW, ZhengY (2010)Synthesis and luminescence properties of a novel blue emitting phosphor $NaMgPO_4$:Eu^{2+}. Luminescence 25: 364.
9. SohnKS, ParkDH, Cho SH, Kwak JS, Kim JS (2006)Computational evolutionary optimization of red phosphor for use in tricolor white LEDs. Chem Mater 18: 1768.
10. Sohn,KS, ParkDH, ChoSH, Kim BI, Woo SI (2006)Genetic algorithm − assisted combinatorial search for a new green phosphor for use in tricolor white LEDs. J Comb Chem 8: 44.
11. JungYS, KulshreshthaC, KimJS, Shin N, Sohn KS (2007)Genetic algorithm-assisted combinatorial search for new blue phosphors in a $(Ca,Sr,Ba,Mg,Eu)_xB_yP_zO_\delta$ system. Chem Mater 19: 5309.
12. Park WB, JeongYS, Singh SP, Sohn KS (2013)A yellow-emitting oxynitride phosphor: $Ce_{4-x}Ca_xSi_{12}O_{3+x}N_{18-x}$:$Eu^{2+}$. ECS J Solid State Sci Technol 2:R3100.
13. ParkWB, Shin N, Hong KP, Pyo M, Sohn KS (2012) A new paradigm for materials discovery: Heuristics-assisted combinatorial chemistry involving parameterization of material novelty. Adv Funct Mater 22: 2258.
14. Park WB, Singh SP, Sohn KS (2014) Discovery of a phosphor for light emitting diode applications and its structural determination, $Ba(Si,Al)_5(O,N)_8$:Eu^{2+}. J Am Chem Soc 136: 2363.
15. Park WB, Singh SP, Kim M, Sohn KS (2015) Phosphor informatics based on confirmatory factor analysis. ACS Comb Sci 17: 317.
16. KakihanaM (2009)Synthesis of high-performance ceramics based on polymerizable complex method. J Ceram Soc Jpn 117: 857.
17. Suzuki Y, Kakihana M (2009) Preparation of water soluble silicon compound and its application for synthesis of $(Y,Ce,Gd)_2SiO_5$ blue emission phosphor. J Ceram Soc Jpn117: 330.
18. Suzuki Y, Kakihana M (2009)Parallel Solution-Based Synthesis Approach for Search of Lanthanoid-Activated Ca_2SnO_4Phosphor Materials. J Am Ceram Soc92: S168.
19. Tomita K (2013)Synthesis of photofunctional ceramics by various solution processes.J Ceram Soc Jpn 121: 841.
20. Kakihana M (1996) Invited review "sol-gel" preparation of high temperature superconducting oxides. J Sol-Gel Sci Technol, 6: 7.

21. Kakihana M, Yoshimura M (1999)Synthesis and characteristics of complex multicomponent oxides prepared by polymer complex method. Bull Chem Soc Jpn 72: 1427.
22. Suzuki Y, Kakihana M (2007)Parallel synthetic exploration of Tm^{3+}-doped alkaline-earth gallate phosphors by use of polymerizable complex method. J Ceram Soc Jpn115: 612.
23. Kakihana M, Kim J, Komukai T, Kato H, Sato Y, Kobayashi M, Takatsuka Y (2013) Exploration of new phosphors using a mineral-inspired approach in combination with solution parallel synthesis. Opt Photonics J3: 5.
24. Shannon RD (1976)Revised effective ionic radii and systematic studies of interatomic distances in halides and chalcogenides. Acta Crystallogr A32: 751.
25. Lee CW, Petrykin V, Kakihana M (2009) Synthesis and effect of Sr substitution on fluorescence of new $Ba_{2-x}Sr_xZnS_3$: Eu^{2+} red phosphor: Considerable enhancement of emission intensity. J Cryst Growth311: 647.
26. Petrykin V, Okube M, Sasaki S, Kakihana M (2008) High pressure synthesis and analysis of new yellow emission Sr_2ZnS_3: Eu visible-light driven phosphor. Acta Crystallogr A64:C485.
27. Petrykin V, Kakihana M (2007) Synthesis of $BaAl_2S_4$:Eu phosphor using BaS:Eu precursor prepared by the polymerizable complex method. J Ceram Soc Jpn 115: 615.
28. Petrykin V, Kakihana M (2008)Direct synthesis of $BaAl_2S_4$:Eu^{2+} blue emission phosphor by one-step sulfurization of highly homogeneous oxide precursor prepared via a solution-based method. Chem Mater20: 5128.
29. Petrykin V, Kakihana M (2009)Synthesis of $BaAl_2S_4$:Eu^{2+} electroluminescent material by the polymerizable complex method combined with CS_2 sulfurization. J Am Ceram Soc92: S27.
30. Hasegawa T, Kato H, Takatsuka Y, Kobayashi M, Yamane H, Kakihana M (2013)Orange emission from $(Ba_{1-X}Sr_X)_4Al_2S_7$:Eu^{2+} thioaluminate phosphors with visible light excitation. ECS J Solid State Sci Technol2: R3107.
31. Petrykin V, Okube M, Yamane H, Sasaki S, Kakihana M (2010) Sr_2ZnS_3: Crystal structure and fluorescent properties of a new Eu(II)-activated yellow emission phosphor.Chem Mater22: 5800.
32. Nakamura M, Kato H, Takatsuka Y, Petrykin V, Tezuka S, Kakihana M (2010) Synthesis and luminescence properties of a cyan-blue thiosilicate-based phosphor $SrSi_2S_5$:Eu^{2+}. J Inf Disp 11: 135.
33. Ohara K, Petrykin V, Tezuka S, Kakihana M (2009) Luminescent properties of a new yellow phosphor $CaBaSiS_4$:Eu^{2+} synthesized by an advanced chemical solution method. Technical Digest of the 9th International Meeting on Information Display: 1274.
34. Kim J, Kato H, Kakihana M (2012)Control of NaAlSiO 4:Eu 2 + photoluminescence properties by charge-compensated aliovalent element substitutions. J Inf Disp13: 97.
35. Abe T, Toda K, Uehematsu K, Sato M, IshigakiT, Sung KB, Jo DS, Masaki T, Yoon DH (2014)Synthesis and the luminescent properties of silicate $NaAlSiO_4$:Eu^{2+}phosphor using SiO powder as a silica source. Key Eng Mater 582: 214.
36. KomukaiT, TakatsukaY, Kato H, KakihanaM (2015)Luminescence properties of $BaZrSi_3O_9$: Eu synthesized by an aqueous solution method. J Lumin 158: 328.
37. Kim M, KobayashiM, Kato H, Kakihana M (2014) The significance of phosphors source in the preparation of functional luminescent phosphate materials. J Ceram Soc Jpn 122: 626.
38. KimM, Kobayashi M, Kato H, Kakihana M (2013) A highly luminous $LiCaPO_4$:Eu^{2+} phosphor synthesized by a solution method employing a water-soluble phosphate ester. Opt Photonics J 3: 13.
39. MinJ, KatoH,KobayashiM, YamaneH, Kakihana M (2012)Synthesis of the new compound in a Na-Sc-Si-O system and luminescence properties activated by Eu^{2+}.Technical digest of the 12th International Meeting on Information Display (IMID2012): 638.
40. Xia Z, Zhang Y, Molokeev MS, Atuchin VV (2013) Structural and luminescence properties of yellow-emitting $NaScSi_2O_6$:Eu^{2+}phosphors: Eu^{2+}site preference analysis and generation of red emission by codoping Mn^{2+} for white-light-emitting diode applications. J Phys Chem C117: 20847.

41. MinJ, Yamaguchi T, Kato H, KobayashiM, Yamane H, Kakihana M (2014) Development of two novel Eu^{2+}-activated phosphors in the Na-Sc-Si-O system and their photoluminescence properties. J Lumin 154: 285.

42. Xia Z, Zhou J, Mao Z (2013) Near UV-pumped green-emitting $Na_3(Y,Sc)Si_3O_9$:Eu^{2+} phosphor for white-emitting diodes. J Mater Chem C 1: 5917.

43. Tezuka S, Sato Y, Komukai T, TakatsukaY, Kato H, Kakihana M (2013)Eu^{2+}-Activated $CaSrSiO_4$: a New Red-Emitting Oxide Phosphor for White-Light-Emitting Diodes. Appl Phys Express6: 072101.

44. SatoY, KatoH, KobayashiM, MasakiT, YoonDH, Kakihana M (2014)Tailoring of deep-red luminescence in Ca_2SiO_4:Eu^{2+}. Angew Chem Int Ed 53: 7756.

45. Nakanishi T, Tanabe S (2008) Preparation of $BaSi_2O_5$:Eu^{2+} glass ceramic phosphors and luminescent properties. J Light Visual Environ 32: 43.

46. Cui Z, Jia G, Deng D, Hua Y, Zhao S, Huang L, Wang H, Ma H, Xu S (2012) Synthesis and luminescence properties of glass ceramics containing $MSiO_3$:Eu^{2+} (M = Ca, Sr, Ba) phosphors for white LED. J Lumin 132: 153.

47. Qian F, Fu R, Agathopoulos S, Gu X, Song X (2012) Synthesis and luminescence properties of a broad-band red phosphor $Ca_3Si_2O_7$:Eu^{2+} for warm white light-emitting diodes. J Lumin 132: 71.

48. Barry TL (1968) Fluorescence of Eu^{2+}-activated phases in binary alkaline earth orthosilicate systems. J Electrochem Soc115: 1181.

49. Cheng G, Liu Q, Cheng L, Lu L, Sun H, Wu Y, Bai Z, Zhang X, Qiu G (2010) Synthesis and luminescence property of Sr_3SiO_5:Eu^{2+} phosphors for white LED. J Rare Earths 28: 526.

50. Kawano Y, KimSW, IshigakiT, UematsuK, TodaK, TakabaH, Sato M (2014)Site engineering concept of Ce^{3+}-activated novel orange-red emission oxide phosphors. Opt Mater Express 4: 1770.

51. Itoh H, Nishi F, Kuribayashi T, Kudoh (2009) Orientational ordering of three SiO_4 tetrahedra in $\alpha' l$-$Ca_{1.5}Sr_{0.5}SiO_4$ that satisfies bond-valence requirements and avoids O-O repulsion. J Mineral Petrol Sci 104: 234.

52. Fukuda K, Maki I, Ito S, Ikeda S (1996) Structural change in strontium oxide-doped dicalcium silicates. J Am Ceram Soc 79: 2577.

Chapter 2
Phosphors for Field Emission Display: Recent Advances in Synthesis, Improvement, and Luminescence Properties

Guogang Li and Jun Lin

Abstract Field emission displays (FEDs) have been considered as one of the most promising next-generation flat panel display (FPD) technologies due to its excellent display performances and low energy consumption. Phosphors are irreplaceable components for FEDs. The exploration of highly efficient low-voltage FED phosphors is the focus of enhancing energy efficiency and realizing high-quality display. This chapter summarizes the recent progress in chemical synthesis and improvement of rare earth and transition metal ion-activated inorganic FEDs phosphors with powder and thin film forms. Discussion is focused on the modification of morphology, size, surface, composition, conductivity of phosphors, and corresponding effects on their cathodoluminescent properties. Special emphases are given to the selection of host and luminescent centers, the adjustment of emission colors through doping concentration optimization, energy transfer, mono- or codoping activator ions, the improvement of chromaticity, color stability and color gamut as well as the saturation behavior and the degradation behavior of phosphors under the excitation of low-voltage electron beam. The authors also speak about the research prospects and future directions of FED phosphors and give some recommendations to facilitate the further exploration of new and highly efficient low-voltage FED phosphors.

G. Li

Faculty of Materials Science and Chemistry, China University of Geosciences, Wuhan 430074, People's Republic of China
e-mail: ggli8312@gmail.com

J. Lin (✉)
State Key Laboratory of Rare Earth Resource Utilization, Changchun Institute of Applied Chemistry, Chinese Academy of Sciences, Changchun 130022, People's Republic of China
e-mail: jlin@ciac.ac.cn

2.1 Introduction

So far, quite a few technologies have been developed for flat panel displays (FPDs), including plasma display panels (PDPs), electroluminescence (EL) devices, field emission displays (FEDs), and liquid crystal displays (LCDs). Of these display technologies, in recent years, FEDs have been considered as one of the most promising technologies for next-generation FPDs due to their potential advantages in aspects of display quality (brightness, contrast ratio, angle of viewing, response time), power consumption, stability, lifetime, etc. [1]. Currently, developing display panel technologies with enhanced energy efficiency and improved display quality is strongly stimulated, because people have more and more requirements for image quality. For FEDs, its basis is an array of field emitter tip cathodes aligned opposite to the phosphor anode, as shown in Fig. 2.1. Therefore, the development of FEDs mainly depends on the following aspects: electron-emitting microcathode arrays, the packaging of FED devices, and luminescent materials. Especially, the luminescent materials (or phosphors) are indispensable components of FED devices, whose luminescent efficiencies and properties not only determine the quality of images but also affect the energy efficiency of display devices [2–4]. Therefore, the selection of phosphors is critical for FEDs. In the past decade, the exploration and development of highly efficient low-voltage FED phosphors and improvement of existing FED phosphors have been becoming the focus of developing FED devices [5–10].

Basically, the operation principle of FEDs is similar to that of conventional cathode ray tubes (CRTs) in which the images originate from the excitation of electrons on phosphors (Fig. 2.1). However, requirements for phosphors applied in FEDs are greatly different from those used in CRTs due to the lower accelerating
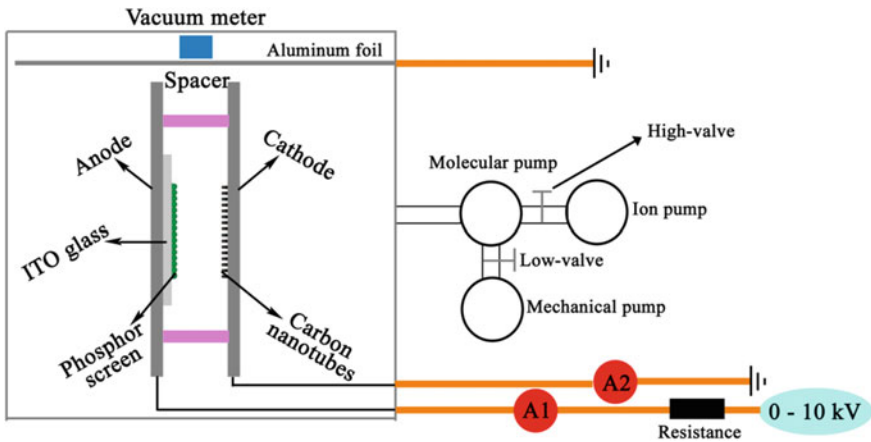
Fig. 2.1 A schematic model of analogue FEDs device. Adapted from Ref. [51] by permission of Optical Society of America

voltages and the higher current densities. One hand, FED phosphors should decrease or avoid the release of gasses in the FED devices [11]. On the other hand, it should posses excellent cathodoluminescent properties such as high emission intensity, high luminous efficiency, high saturation current density, high color purity, and good stability and durability under low accelerating voltages (≤ 7 kV) and high current density (≥ 100 μA/cm^2) [12, 13]. Therefore, the selection of suitable hosts and luminescent centers is very important for synthesis of FED phosphors [14]. As activator ions, rare earth (RE) ions have been playing an important role in modern lighting and display fields due to the abundant emission colors in the whole visible light range owing to their $4f \rightarrow 4f$ or $5d \rightarrow 4f$ transitions [15]. In addition, transition metal ion (Mn^{2+}), Bi^{3+} ion, and some groups (e.g., WO_4^{2-}, MoO_4^{2-}, GeO_4^{4-}, SnO_6^{2-}, TiO_6^{2-}, NbO_4^{2-}) are also efficient luminescent centers [16–20]. For host materials, so far many efficient sulfide-based phosphors such as $Y_2O_2S:Eu^{3+}$, $Gd_2O_2S:Tb^{3+}$, $SrGa_2S_4:Eu^{3+}/Ce^{3+}$, (Zn/Cd)S:Cu,Al, and ZnS:Ag,Cl have been explored as efficient low-voltage FED phosphors [21, 22]. Unfortunately, sulfide phosphors are easily decomposed and emit sulfide gases under electron bombardment due to dissociation of the cation–sulfur bonds, subsequently damage emission tips, shorten the device lifetime, and simultaneously contaminate environment. In avoidance of the above defects, oxide-based phosphors including rare earth and transition metal ion-doped garnets, oxides, silicates, phosphates, vanadates, and perovskites [23–29] have gained increasing concerns due to their better thermal stability, chemical stability, and environmental friendliness compared with sulfides. However, most of these phosphors are insulators, and negative loading is easy to accumulate on the grain surface in phosphor layer, which decreases cathodoluminescent efficiency. That is why the electrical conductivity of FED phosphors should be high enough to avoid charge accumulation [12]. In recent years, many semiconductor-based materials such as ZnO, Ga_2O_3, $(Gd,Lu)_3Ga_5O_{12}$, $Zn(Ga,In)_2O_4$, $(Ca,Sr)In_2O_4$, $Zn_3Ta_2O_8$, Zn_2GeO_4, $GaGe_2O_5$, Mg_2SnO_4, and $ZnGeN_2$ are explored as low-voltage FED phosphors through efficiently doping of RE^{3+}, Mn^{2+}, and Bi^{3+} ions [7, 23, 26, 28, 30–38]. Besides, the current low-voltage FED phosphors also suffer rough surfaces, irregular shape and size distribution, poor adherence to substrates, poor preparing of phosphor screens (thin films) from phosphor powders. Therefore, more efforts should explore excellent approaches for the fabrication of a variety of inorganic luminescence materials to improve their performance in applications. Finally, the color saturation and color index also need be further improved to enhance display quality. All these considerations and the ever-growing demand for highly efficiently low-voltage FED phosphors prompt researchers to reach a cognitive that more attention should be paid to improve existing phosphors and develop newly efficient low-voltage FED phosphors. This chapter mainly summarizes the recent progress in chemical synthesis and improvement of existing and new phosphors including RE^{3+} ions and transition metal ion-activated inorganic oxide-based luminescence materials, semiconductor-based luminescence materials, and self-activated luminescent materials. The authors discuss the modifications and optimizations in morphology,

size, composition, conductivity of phosphors, and their cathodoluminescent properties. Some emphases are also focused on the studies of selection of hosts and luminescent centers, enhancement of efficiency through energy transfer, adjustment and design of emission colors, improvement of color index, and color gamut as well as color stability and degradation behavior of phosphors.

2.2 Improvement of Current FED Phosphor Powders

2.2.1 Modification of Morphology, Surface, and Size of Phosphor Particles

It is well known that the most common form of phosphors is powders, which are conventionally prepared by the solid reaction process. Unfortunately, this process might result in a damage of luminescent performance of phosphors due to irregular shapes, wide size distribution, and serious aggregation of the final phosphor products [39]. Because the morphology, size, composition, surface, and crystallization have great effects on the cathodoluminescent properties of phosphors, many efforts have been made to explore suitable methods to control these factors for improving their cathodoluminescent performance, which has technological and fundamental scientific importance [40]. Among them, the soft-chemical methods (such as sol–gel, hydrothermal, spray pyrolysis, electrospinning, homogenous precipitation, high boiling solvent, combustion, and microwave) are intensively pursed as effective and convenient approaches to prepare various inorganic FED phosphors with controllable shape, size, surface form, composition, and luminescent properties [32, 41–45]. In general, soft-chemistry synthesis can produce future generation phosphors with better morphology and surface forms (more regular shape, spherical in some cases), and narrower size dispersions at moderate temperatures (<1000 °C). These factors can decrease the light scattering and non-radiative transitions of phosphors, which is conducive to enhance the cathodoluminescent performance.

On the other hand, for FED phosphor powders, the particle size is critical to loading on screens, which further influences their luminescent performance [12]. It is known that the cathodoluminescent emission intensities and brightness of FED phosphors increase with increasing the accelerating voltage and the filament current of anodes, which is attributed to the deeper penetration of the electrons into the phosphor body and the larger electron beam current density. The electron penetration depth can be estimated using the empirical formula:

$$L[\text{Å}] = 250\left(\frac{A}{\rho}\right)\left(\frac{E}{\sqrt{Z}}\right)^n, \quad n = \frac{1.2}{1 - 0.29\lg Z}$$

where $n = 1.2/(1 - 0.29 \lg Z)$, and A is the atomic or molecular weight of the material, ρ is the bulk density, Z is the atomic number or the number of electrons per molecule in the compounds, and E is the accelerating voltage (kV) [41]. The deeper the electron penetration depth, the more plasma will be produced, which results in the CL intensity increases. However, according to the above empirical formula, the electron penetration depth into phosphors are general tens of nanometers in FEDs devices due to the low excition voltage (1–7 kV), which makes activator ions in the inner of phosphor particles with big size (microsize) cannot be efficiently excited. So, reasonable particle size is important for improving their cathodoluminescent efficiencies. Nanoparticle phosphors might be more appropriate for low-voltage FED application in terms of the following aspects [12, 46]: (1) The resolution is inversely proportional to the particle size of the luminescent materials; (2) the use of such materials can optimize the packaging of grains, avoid cutting of the picture spot and decrease scattering of light-emitting; (3) phosphor powders with small grain size allow a fabrication of thin light-emitting film, which could extend the display operating time and fundamentally decreased the total resistance of phosphor layer. Therefore, some researchers try hard to obtain low-voltage FED phosphors in nanosize via various soft-chemical synthesis processes for improving their luminescence efficiency. Some possible routes to achieve the above improvements are presented in the following section.

Sol–gel process. The sol–gel technique is one of the most well-known soft-chemistry processes, which can be generally divided into three types judging by different use of precursors [47]: (a) sol–gel process under hydrolysis and condensation of molecular precursors; (b) gelation process under concentration of aqueous solutions into metal chelates, namely "chelate" route; (c) polymerization and complex process (called Pechini-type sol–gel process, and abbreviate as PSG). Among the three types, PSG process is frequently employed in the preparation of multicomponent metal oxide materials. This process commonly uses metal salts as precursors, citric acid (CA) as a chelating ligand of metal ions, and polyhydroxy alcohol such as ethylene glycol (EG) or poly(ethylene glycol) (PEG) as a cross-linking agent to form a polymeric resin on the molecular level, which can ensure compositional homogeneity and enhance dispersion of particles. After a heat treatment at moderate temperature (500–1000 °C) followed by PSG process, the organic additives can be removed and a pure phase of multiple-component metal oxide is obtained. The final materials (including luminescent materials) can be made into powder and thin film forms and others. By PSG process, the physical properties of materials can be improved with respect to the other routes such as solid-state reaction process and amorphous citrate process [47]. Recently, Lin's groups have derived multiformed FED phosphors from the PSG process, including nanocrystalline luminescent materials, monodisperse and spherical core–shell-structured phosphors, one-dimensional (1D) nanostructures (combined with the electrospinning process), thin film phosphors (via dip-coating), and their patterning (combined with the soft-lithography process). The basic principle is shown in Fig. 2.2. The purpose was to gain fine control of the material morphology, surface, and size, and to find novel FEDs phosphors and optimize their
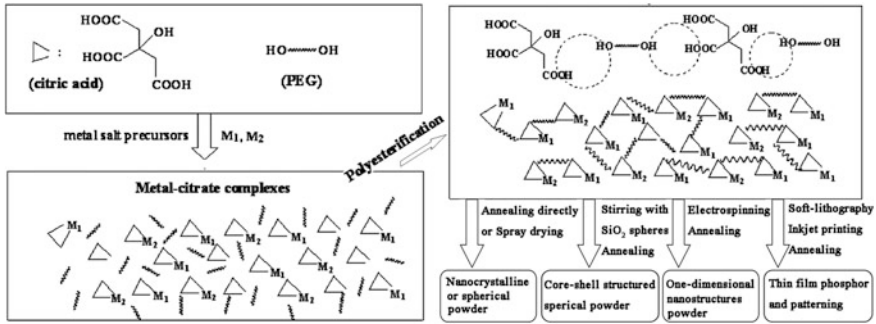
Fig. 2.2 Basic principle of Pechini-type sol–gel (PSG) process and multiform optical materials derived from it. Adapted from Ref. [47] by permission of American Chemical Society

cathodoluminescent performance. Typically, a series of oxide-based nanocrystalline phosphors from tens of nanometers to several hundred of nanometers have been prepared through the PSG process for FEDs, including LaOCl/LaGaO$_3$/LaAlO$_3$: RE^{3+} [41, 48, 49], Lu$_3$Ga$_5$O$_{12}$:RE^{3+} [50], (Ca,Sr)In$_2$O$_4$:RE^{3+} (RE = Pr, Sm, Eu, Tb, Dy, Ho, Er, Tm) [26, 36], NaCaPO$_4$:Mn^{2+} [51], KNaCa$_2$(PO$_4$)$_2$:A (A = Ce^{3+}, Eu^{2+}, Tb^{3+}, Mn^{2+}, Sm^{3+}) [52], K(Sr,Ca)Gd(PO$_4$)$_2$:RE^{3+}/Mn^{2+} (RE = Ce, Tb, Dy, Eu, Tm) [53], Ca$_2$Ba$_3$(PO$_4$)$_3$Cl:A [54], Ca$_8$Gd$_2$(PO$_4$)$_6$O$_2$:A (A = Eu^{2+}, Ce^{3+}, Dy^{3+}, Tb^{3+}, Mn^{2+}) [55]. It is found that the nanocrystalline phosphor layer could be much thinner compared to that consists of microsize phosphor grains, which can influence both total resistivity of the phosphor layer and amount of residual gasses bounded between the grains [12]. Then, it further influences the efficiency of the light source, longtime stability of the intensity of emitted light, and device lifetime. Psuja et al. [12] investigated the effect of grain sizes on emission yield of RE-doped nanophosphors in cases of Eu^{3+}:Y$_2$O$_3$, Tb^{3+}:Y$_2$O$_3$, Tb^{3+}:Y$_3$Al$_5$O$_{12}$ (Tb:YAG), Ce^{3+}:YAG, and Tb^{3+}:YAG/Eu^{3+}:YAG. It was found that the light-emitting efficiencies increase with grain size in the nanorange by a comparison of cathodoluminescent intensities of phosphor layer and powders, and Eu:Y$_2$O$_3$ nanopowder was more efficient than commercially available microsize phosphor grains. Xu et al. [33] demonstrated that these as-prepared nanocrystalline phosphors (Lu$_3$Ga$_5$O$_{12}$: Tb^{3+}) by PSG process can form a more compact phosphor screen, which exhibits an improved luminescent efficiency and stability under the bombardment of electron beam. Wakefield et al. [56] also confirmed that the nanocrystalline oxide-based phosphors (Y$_2$O$_3$:Eu and Zn$_2$SiO$_4$:Mn) had better luminescence efficiency than that of commercial FED phosphors, which show promising properties for use in low-voltage FEDs.

Homogenous precipitation process. Homogenous precipitation process is a simple, effective solution-based method for a large-scale fabrication of novel inorganic nano-/microstructured materials under template-free conditions. It is usually used to synthesize hydroxide materials under different precipitants using metal salts as precursors [42]. After an annealing process at moderate temperature,

the obtained hydroxides can be transformed to oxide materials with maintaining morphology. Over the past several years, monodisperse nano-/microstructures with controllable morphologies and sizes, which exhibit size-dependent luminescent properties, have been synthesized by the homogenous precipitation and investigated. For example, Li et al. have reported the simple synthesis of monodisperse β-Ga$_2$O$_3$:Dy^{3+} [32], La$_2$O$_3$/La$_2$O$_2$CO$_3$:RE^{3+} (RE = Eu, Tb, Yb, Ho, Er, Tm) [42], etc., with defined morphologies and narrow size dispersion (Fig. 2.3a, b) by optimizing the external experimental parameters. They demonstrated that the cathodoluminescent properties of phosphors can be improved by improving the morphologies and sizes of phosphors particles. As shown in Fig. 2.3c, the relative CL emission intensities of β-Ga$_2$O$_3$:Dy^{3+} phosphors are different with different morphologies/sizes, which are attributed to the difference in surface defects. The more defects on phosphor particles surface, the lower luminescent efficiency are obtained due to the increase in non-radiative transitions. The similar situation appears in the as-prepared La$_2$O$_3$/La$_2$O$_2$CO$_3$:RE^{3+} (RE = Eu, Tb) phosphor particles with different shapes and sizes (Fig. 2.3d). Jung et al. [57] also improved the
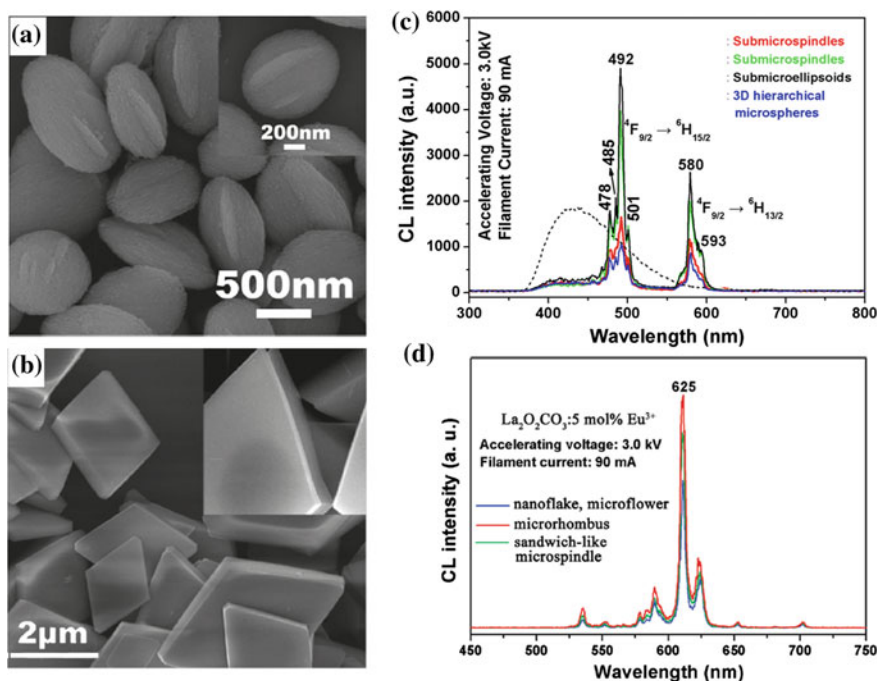
Fig. 2.3 SEM image of **a** GaOOH:Dy^{3+} and **b** LaCO$_3$OH:Eu^{3+} prepared at pH = 7. Following a heat treatment, the above samples are, respectively, transformed to β-Ga$_2$O$_3$:Dy^{3+} and La$_2$O$_2$CO$_3$/ La$_2$O$_3$:Eu^{3+} phosphors without changing morphologies. **c**, **d** show the comparison of CL and photoluminescent (PL) emission intensity of β-Ga$_2$O$_3$:Dy^{3+} and La$_2$O$_2$CO$_3$:Eu^{3+} at different morphologies and sizes. **a**, **c** Adapted from Ref. [32] by permission of American Chemical Society. **b**, **d** Adapted from Ref. [42] by permission of American Chemical Society

luminance of Zn_2SiO_4:Mn phosphors by homogenous precipitation process. The as-prepared Zn_2SiO_4:Mn phosphor particles present uniform spherical shape and have an enhanced emission intensity than commercial Zn_2SiO_4:Mn bulk phosphors. In addition, spherical sub-micrometer Y_2O_3:Eu^{3+} and cubic (Y, Gd)$_2O_3$:Eu^{3+} phosphor particles have been synthesized through a novel homogeneous precipitation method by Silver et al. [58]. These cubic-Y_2O_3:Eu^{3+} spherical phosphor particles (ca. 300 nm) will be ideal for FED devices as they can densely close-pack on screens and they display high luminous efficiency under low-voltage electron beam excitation. The above examples demonstrate through the modification of morphology, size, and surface, one can reduce surface defects and thus enhance the luminescent efficiencies of phosphors.

Hydro/solvothermal process. As a typical solution-based approach, hydro-/solvothermal process generally employs water or organic solvents under certain temperatures and pressures for synthesis of variously inorganic nano- and/or micro-crystals due to some acceptable advantages including relatively green synthesis, easily controllable reaction conditions, low reaction temperature (in general <250 °C) and cost, high yield, specially, easily controlled size, structure and shapes of the products. Shang et al. [38] developed a water-based hydrothermal system to prepare Zn_2GeO_4:Mn^{2+} phosphors with irregular submicrorods shape. Annealing at different temperatures can remove H_2O and organic components on surface, and then obtain Zn_2GeO_4:Mn^{2+} submicrorods phosphors, as shown in Fig. 2.4a–d. It is obviously seen that Zn_2GeO_4:Mn^{2+} submicrorod phosphor has smooth surface, regular shape, and narrow size distribution than bulk material prepared by solid-state reaction method. Under the same excitation conditions, Zn_2GeO_4:Mn^{2+} submicrorod phosphor has a higher CL emission intensity than that of bulk materials (Fig. 2.4e). Because of the optimal shape, size, and surface of particles, the cathodoluminescent efficiency of Zn_2GeO_4:Mn^{2+} phosphor was enhanced. During the process of hydro-/solvothermal reaction, selecting an
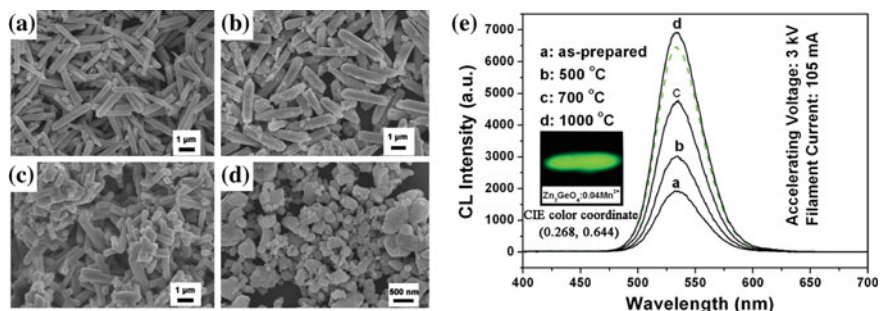
Fig. 2.4 **a–d** SEM images and **e** CL spectra of Zn_2GeO_4:Mn^{2+} submicrorods with different post-calcination temperatures: 500, 700, 1000 °C and Zn_2GeO_4:Mn^{2+} bulk material (solid-state reaction process), respectively. The *insets* in **e** show the luminescent photographs of Zn_2GeO_4:Mn^{2+} with highly pure *green light* emission. Adapted from Ref. [38] by permission of Royal Society of Chemistry

appropriate organic additive with functional groups is one of the promising and popular strategies to control shape and size. The organic additive generally acts as complex agent or structure-directing agent. Through using oleic acid in reaction system, Shang et al. [59] successfully prepared well-separated LaOF:RE^{3+} (RE = Eu^{3+}, Ho^{3+}, Tm^{3+}, Dy^{3+}, Sm^{3+}, Tb^{3+}) nanoparticles with sizes of about 30–50 nm. Due to the excellent dispersion and crystallinity, these as-prepared LaOF: RE^{3+} phosphor nanoparticles can also be compactly coated on screen to improve the intensity of emitted light, and device lifetime. Doping RE^{3+} ions into LaOF host, emission colors from blue to red with high color purity (4f–4f transition, Eu^{3+}, red; Ho^{3+}, green; Tm^{3+}, blue; Dy^{3+}, yellow; Sm^{3+}, orange) were obtained, which can be considered as potential full-color FED phosphors. In addition, the morphology and size of products can also be well controlled and modified by a combination of water and organic solvents in hydrothermal process. During these fabrication processes, organic solvents act as the "shape modifier" to either promote or inhibit crystal growth through modifying crystal growth dynamically and thus can adjust and control the morphology and size of the products. By the use of the above synthesis method, a series of FED phosphors such as β-Ga$_2$O$_3$:Dy^{3+} [32], Gd$_2$O$_3$:Eu^{3+} [60], Lu$_2$O$_3$:RE^{3+} (RE = Eu, Tb, Dy, Pr, Sm, Er, Ho, Tm) [61] with regular prism, rod, sphere shapes in nano- to microscale were synthesized, which not only improve the cathodoluminescent performances of phosphors but also meet some requirements in micromation of FED devices.

Electrospinning process. Because of some specific and fascinating luminescence properties, for example, various emission lifetimes and increased luminescence efficiencies, there is growing interest on exploring new luminescent materials on one-dimensional (1D) nanostructures [19, 62–65]. These one-dimensional luminescence nanomaterials possess diverse potential applications in nanoscale electronics, photonics, display and advanced bioanalysis [19]. The electrospinning technique is an effective and simple method for preparing one-dimensional (1D) nanomaterials. It is a process that uses the strong electrostatic force from a high static voltage act on a polymer solution placed in a container with a millimeter diameter nozzle. Under applied electrical force, the polymer solution is ejected from the nozzle. After the solvents are evaporated during the course of jet spraying, the fibers are collected on a grounded collector. The electrospinning setup and formation process of 1D luminescent nano-/microstructures is shown in Fig. 2.5a. 1D nanomaterials synthesized by this method followed an annealing process usually have exceptional long length, uniform diameter, and diverse composition. Through the electrospinning process, a variety of RE^{3+} ions doped 1D fiber-, tube- and belt-like cathodoluminescence materials including LaOCl [40], CaTiO$_3$ [63], LaPO$_4$ [64], YVO$_4$ [65], Y$_2$SiO$_5$ [66] etc. have been derived and/or optimized, especially morphology-/size-dependent luminescence were investigated and color tuning by doping different kinds of RE^{3+} ions, changing RE^{3+} ions concentrations, codoping and/or energy transfer were designed. For example, the as-prepared LaOCl:Eu^{3+} 1D nanofiber, nanotube, and microbelt phosphors are all composed of nanoparticles with perfect crystallinity, as shown in Fig. 2.5a. The comparison of CL spectra of 1D LaOCl:Eu^{3+} nanomaterials with three different
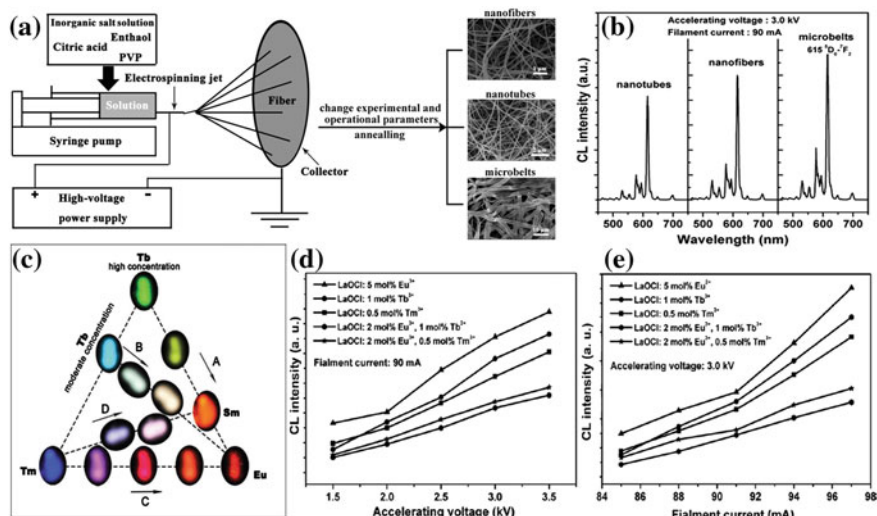
Fig. 2.5 **a** Scheme of the electrospinning setup and the formation process of 1D luminescence nano-/microstructures. SEM images of LaOCl:Eu^{3+} nanofiber, nanotube and microbelt phosphors are also shown in (**a**). **b** The CL spectra of LaOCl:Eu^{3+} phosphors with fiber, tube, and belt-like morphologies. **c** The CL photos of LaOCl:RE^{3+} (RE = Sm, Eu, Tb, Dy, Tm) 1D nanomaterials. The dependence of CL intensities of LaOCl:RE^{3+} 1D nanomaterials of **d** accelerating voltage (kV) and **e** filament current (mA). Adapted from Ref. [40] by permission of Wiley

morphologies/sizes is shown in Fig. 2.5b, and it can be seen that the belt-like sample has a higher CL intensity than that of fiber-like and tube-like samples. This is because that the LaOCl:Eu^{3+} nanofibers and nanotubes produce more surface defects than microbelts due to smaller nanoparticles and larger surface area. However, defects have serious drawback for luminescent intensity of phosphors as they provide non-radiative recombination routes for electrons and holes. The same morphology- and size-dependent luminescence performance appears in systems of LaPO$_4$:Ce^{3+}/Tb^{3+} [64], YVO$_4$:RE^{3+} (RE = Eu, Tb, Dy, Sm) [65], CaWO$_4$:Tb^{3+} [19], and so on. Therefore, controllable modification of morphology and size of 1D luminescent materials can elevate their luminous efficiencies. Via the electrospinning process, RE^{3+} (Eu^{3+}, Tb^{3+}, Tm^{3+}, Sm^{3+}) can be homogenously dispersed in LaOCl systems and the luminescence colors can be tuned in a wide range through changing RE^{3+} concentrations and codoping RE^{3+} ions (Eu^{3+}/Tb^{3+}, Eu^{3+}/Tm^{3+}, Eu^{3+}/Tb^{3+}/Tm^{3+}) as shown in Fig. 2.5c. In addition, the increase in CL intensity (brightness) with an increase in electron energy and filament current are attributed to the deeper penetration of the electrons into the phosphor body and the larger electron beam current density. However, a larger current density may result in the accumulation of excess electrons on phosphor surface. If these electrons could not be promptly transferred, the cathodoluminescent efficiency will be reduced due to a saturation behavior. Under low-voltage electron beam excitation, the CL emission intensities of 1D LaOCl:RE^{3+} nanophosphors gradually elevate with raising

accelerating voltage and filament current without obvious saturation behavior (Fig. 2.5d, e), which is beneficial to apply in FED devices.

Hydrolysis Sol–gel method. According to the previous research, the emission performances can be improved in spherical phosphors with respect to the irregular ones, which are basically attributed to the high packing densities and low scattering of light [12, 56]. Therefore, there is a growing interesting on synthesizing inorganic phosphors with spherical morphologies in recent years [66]. As one of the most well-known hydrolysis method, Stöber method [67] that based on hydrolysis of tetraethylorthosilicate (TEOS) in an alcohol medium in the presence of water and ammonia has been extensively employed to prepare the monodisperse silica (SiO_2) spheres with different sizes from nano- to micron meter by a modified procedure. Some research groups developed a combination of these monodisperse SiO_2 spheres and the PSG process following suitable annealing temperatures to synthesize a series of monodisperse and spherical core–shell-structured phosphors [47]. The concrete experimental process is extremely simple as follows (Fig. 2.6): first, stir the as-formed SiO_2 particles in corresponding PSG precursor solutions of the phosphors (composing of metal ions, citric acid, and PEG) and then separate the SiO_2 particles by centrifugation following a heat treatment at certain temperature to obtain the final phosphor products. The size for the phosphor particles can be controlled by the ones of the silica cores and the number of coating cycles [66]. By the above method, a variety of precursor solutions of phosphors can be coated on the surface of SiO_2 spheres to form the desirable spherical phosphors. More important, the luminescent properties of core–shell-structured phosphor particles can be tuned and optimized by changing the size of SiO_2 cores and thickness of phosphor shells [68]. In summary, it is a general method to prepare spherical phosphors for almost all of the inorganic salt phosphors.

Spray pyrolysis process. Except for hydrolysis sol–gel method, other better morphology of the spherical shape with a size around 0.5–3 μm for phosphors can be obtained by the spray drying process [43]. It needs a combination of PSG precursor solutions and subsequent annealing process to obtain final phosphor products. By loading the corresponding precursor solution on a spray drying apparatus and a following annealing process at high-temperature (600–1200 °C),

Fig. 2.6 Hydrolysis-Sol/gel synthesis of spherical core-shell-structured phosphors
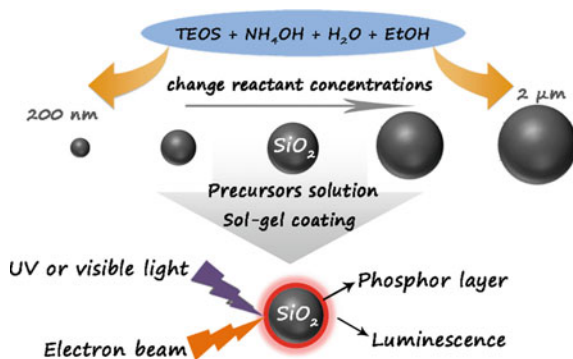
the representative red-emitting Y_2O_3:Eu^{3+} [47], red-emitting $CaTiO_3$:Pr^{3+} [69], green-emitting YBO_3:Tb^{3+} [70], and blue-emitting Sr_2CeO_4:Ce^{3+} [43] FED phosphors were also prepared to spherical particles with sizes ranging from 0.6 to 3.0 μm. It is demonstrated that the as-prepared spherical phosphors indeed improve their emission intensity over the other irregular ones, which is also due to high packing densities and low scattering of light. It is noticed that the disadvantages of phosphors prepared by spray pyrolysis are that the optimal heating temperature was generally higher than that for the solid-state reaction. Moreover, it also has a bigger size distribution than that prepared by homogenous precipitation or hydrolysis Sol–gel methods. Therefore, it will be further improved.

2.2.2 Modification of Phosphor Composition

For phosphors, it frequently involves in the substitution of cations in host lattice with activator ions to produce luminescence, which easily results in a mismatch of charge and crystal lattice due to different valence state and ion radius. These mismatches will generate many defects (vacancy, gap, crystal lattice distortion, and strain) to decrease the luminescent efficiency of phosphors and as a result need to be avoided or reduced. By modifying phosphor composition, the luminescent performance of phosphors can be efficiently improved. Generally, composition modifications of phosphors mainly focus on two aspects: the one is to conduct charge compensations for relaxing charge mismatch, and the other one is to relieve crystal lattice strain by introducing other cations with complementary radius. Based on the above consideration, representative Ca_2GeO_4:Eu^{3+} and Zn_2GeO_4:Mn^{2+} phosphors have been optimized, and the effect of composition modification on cathodoluminescent efficiencies of phosphors has been elaborately investigated. In Mg-doped $Zn_{1.96}GeO_4$:$0.04Mn^{2+}$ systems, it shows the maximum emission at 532 nm under the excitation of 3 kV accelerating voltage, which corresponds to the characteristic emission of Mn^{2+} from $^4T_1$ to $^6A_1$. The CL intensity increases with the replacement of Mg^{2+} ions. The possible reason is the join of Mg^{2+} ions ($r = 0.57$ nm, and coordination number (CN) = 4) decreases the crystal lattice strain due to mismatched ions radius with Zn^{2+} ($r = 0.60$ nm, CN = 4) and Mn^{2+} ($r = 0.66$ nm, CN = 4) ions. The relaxing of crystal lattice strain can efficiently suppress non-radiative processes and finally result in the improvement of cathodoluminescent efficiency [20]. For $Ca_{1.99}GeO_4$:$0.01Eu^{3+}$ systems, there is a charge mismatch between Eu^{3+} and Ca^{2+} ions. According to the electroneutrality theory, two Eu^{3+} ions will replace three Ca^{2+} ions to obtain charge balance, and as a result, two positive defects of $[Eu_{Ca}]^{\cdot}$ and one negative Ca^{2+} vacancy of $[V_{Ca}]''$ would form. These defects and vacancies may capture excited electron to proceed to non-radiative transitions and damage the luminous efficiency. Codoping Li^+ ions can help to incorporate the Eu^{3+} ions into Ca^{2+} sites by compensating for the different charges between Eu^{3+} and Ca^{2+} ions, and the red light emission intensity of $Ca_{1.98}Li_{0.01}Eu_{0.01}GeO_4$ is elevated with respect to $Ca_{1.99}Eu_{0.01}GeO_4$ [72].
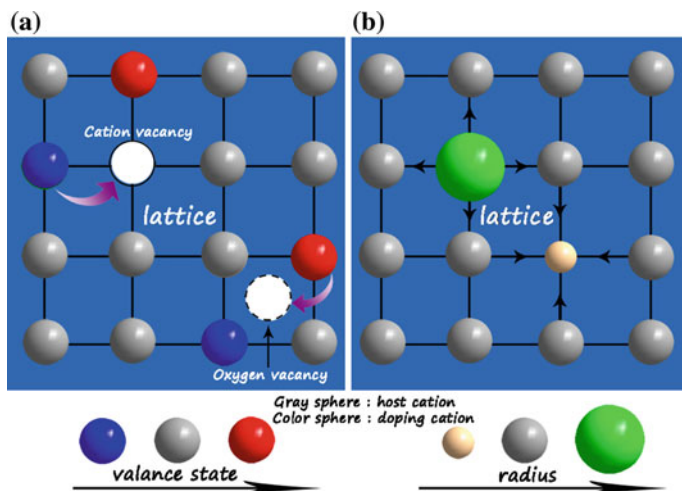
Fig. 2.7 A simple model to illustrate the possible increasing mechanism of luminescent efficiency by composition modification (charge compensations and crystal lattice strain relaxing)

A simple model to illustrate the possible increasing mechanism of luminescent efficiency by composition modification is shown in Fig. 2.7. During the process of doping cations into host lattice, if its valence state is higher than that of host cations, cation vacancies will be produced, whereas oxygen vacancies will appear (Fig. 2.7a). These vacancies, namely crystal lattice defects, increase the probability of non-radiative transitions and thus decrease luminescent efficiency. When introducing charge compensator ions into the host lattice, it will reduce charge defects and thus can improve luminescent performance. On the other hand, cationic replacements with different radius in one matrix will result in crystal expansion or shrinkage. This will generate strain or many defects due to the distorted crystal lattice, which also increases the possibility of non-radiative transitions. By doping other ions with complementary radius, it can relieve lattice strain and then decrease defects, which finally enhance luminescence efficiency of phosphor (Fig. 2.7b). In general, the cathodoluminescent efficiency of FEDs phosphors can be optimized by composition modification including charge compensations and crystal lattice strain relaxing, which promotes a potential application of phosphors in FED devices.

2.2.3 Improvement of Conductivity

It is well known that electron beam is used as excitation source in FED technology. In order to realize highly efficient FED, phosphors should be efficiently excited by low-voltage electrons. Although the accelerating voltage employed in FEDs is much less than that worked in CRTs, its energy is still much higher than UV or

visible light radiation, which is around a few thousand to thousands of eV [71]. If could not be promptly transferred, these electrons very easily accumulate on the phosphor surface to recombine with holes/surface defects, which increase non-radiative transitions and thus decrease cathodoluminescent efficiency. In addition, excessive electrons staying on the phosphor surface also easily reach charge saturation. The tendency for the brightness to plateau even when the current is increased at a fixed electron voltage; this is a serious concern especially for FEDs since the voltage is normally low (<4 kV). Requiring high current for high power and brightness. Accordingly, an important question for FEDs is how to eliminate or weaken charging and surface recombination effects, and improve the saturation. One of the most promising and efficient approach is to improve the conductivity of FED phosphors. This approach can efficiently and opportunely release the accumulated charges on phosphors and thus improve the saturation of phosphors and enhance their cathodoluminescent efficiency. Generally, there are two main routes to increase the conductivity of FED phosphors: the one is the selection of semiconductor materials as host lattice, and the other one is to mix transparent and conductive nanocrystalline powders with FED phosphors. For the selection of hosts, it is known that the compounds composed of elements with small differences in electronegativity should have a narrower band gap [72]. Moreover, the band gap of oxide-based phosphor systems is related to crystal structures of hosts [23, 38]. Generally, reticular acid radical-coordinated polyhedrons in host easily result in a narrow band gap of host. While the band gap of host has great effects on the conductivity and luminescent efficiency of phosphors. A narrow gap can lead to higher conductivity which is beneficial to the cathodoluminescence. On the other hand, luminescence quenching will occur if the energy levels of excited states of activator ions are located among the conduction band of host. Only the excited states of activator ions locate below the conduction band of host, the phosphors present excellent luminescent performance. Therefore, appropriate hosts with reasonable band gap should be considered during the exploration and design of novel FED phosphors, which could merge the luminescence performance and conductivity of phosphors. According to the first route, a series of RE^{3+} ions or Mn^{2+} ions activate Ga_2O_3 [32], $(Ca,Sr)In_2O_4$ [35, 36], $La(Ga,In)O_3$ [49], $Mg_2(Sn,Ti)O_4$ [30], $(Zn,Mg)_2GeO_4$ [38], Li_2ZnGeO_4 [20]. FED phosphors were derived, as summarized in Table 2.1. Except for the efficient transport of electrons, semiconductor hosts (emission from UV to bluish-green light region) generally have a sensitive enhancement for luminescent efficiency of RE^{3+} ions.

Another route toward increasing phosphor conductivity is a mixing of conductive nanocrystalline powders like In_2O_3, SnO_2, ZnO, and Au [12, 33, 73–75]. Zhang et al. [76] encapsulated In_2O_3 layer on $Y_2O_3:Eu^{3+}$ phosphor particles and concluded positive effect on the cathodoluminescent performance. They found that the luminous efficiency of $Y_2O_3:Eu^{3+}@In_2O_3$ phosphor screens was obviously improved with respect to uncoated $Y_2O_3:Eu^{3+}$, as shown in Fig. 2.8a. Moreover, the luminous efficiency of the former improves much more than the latter with an increase in the accelerating voltage. This is attributed to the increased electrical conductivity of $Y_2O_3:Eu^{3+}$ phosphors with increasing In_2O_3 coating. In_2O_3-coated

Table 2.1 CIE chromaticity coordinates, emission colors of color gamut enlarged phosphors under low-voltage electron beam excitation

Sample	Color coordinates	Color	Refs.
$Mg_{2(1-y)}Sn_{(1-x)}O_4$: x% Ti^{4+}, y% Mn^{2+}			
$x = 2.0$, $y = 0.01$	(0.1637, 0.2574)	Cyan	[30]
Li_2CaSiO_4:Eu^{2+}	(0.119, 0.203)	Cyan	[85]
$BaZrSi_3O_9$:Eu^{2+}		Cyan	[86]
$BaSi_2O_2N_2$:Eu^{2+}		Cyan	[87]
$NaCaPO_4$:Mn^{2+}	(0.428, 0.552)	Yellow	[51]
$LaGaO_3$:0.5 %Sm^{3+}	(0.4880, 0.4153)	Yellow	[71]
$ZnGeN_2$		Yellow	[7]
$LaAlO_3$:0.25 %Sm^{3+}	(0.5133, 0.4625)	Yellow	[48]
$Ca_2Gd_8(SiO_4)_6O_2$:5 %Ce^{3+}, 25 %Mn^{2+}	(0.545, 0.415)	Yellow	[88]
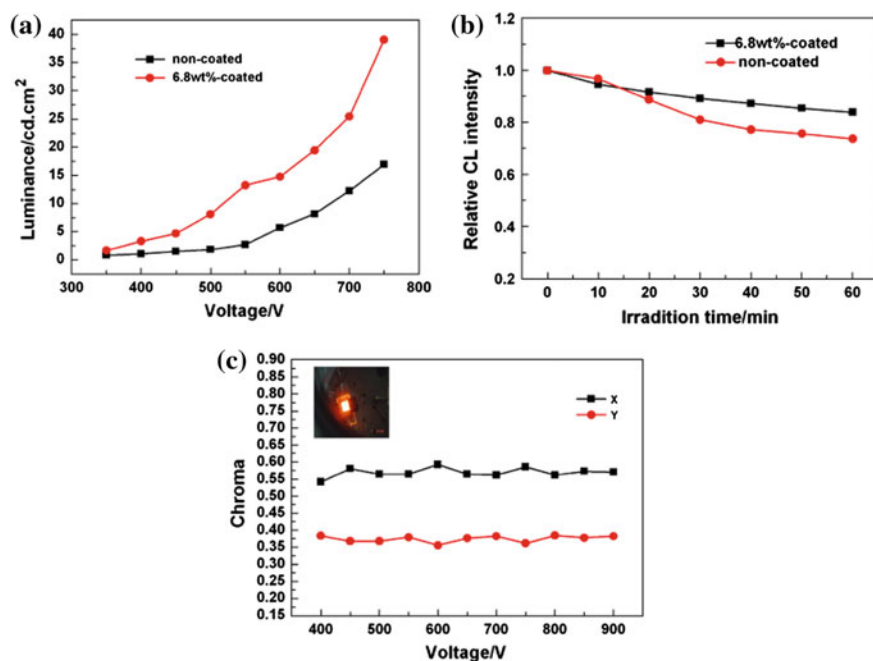
Fig. 2.8 **a** Dependence of luminous efficiency of Y_2O_3:Eu^{3+} phosphor screens before and after In_2O_3 coating on the excitation voltage. **b** Comparison of the relative CL degradation behavior and of uncoated and In_2O_3-coated Y_2O_3:Eu^{3+} phosphor screens. **c** The variation of chromaticity of In_2O_3-coated phosphor screen with an accelerating voltage. The *inset* shows a macrophotograph of the Y_2O_3:Eu^{3+} phosphors coated with 6.8 wt% In_2O_3 on excitation at 700 V. Adapted from Ref. [76] by permission of Wiley

Y_2O_3:Eu^{3+} phosphor screens have a better stability than uncoated one under 700 V accelerating voltage (Fig. 2.8b). This is because that the conductive In_2O_3 nanoparticles not only can reduce surface charge accumulation but also may serve as protective layer on phosphor surface to prevent chemical degradation caused by the direct electron beam bombardment. Finally, the aging rate of the low-voltage CL efficiency is suppressed, and as a result, the lifetime and stability of the phosphor screens are improved evidently. In addition, the Commission International del'Eclairge (CIE) chromaticity coordinate values of Y_2O_3:Eu^{3+}@In_2O_3 phosphors are nearly invariable (x and y keeps at about 0.575 and 0.375) with changing accelerating voltage (Fig. 2.8c), maintaining a color stability. The similar improvement for cathodoluminescent efficiency and luminance appears in In_2O_3-coated $ZnGa_2O_4$ and $ZnGa_2O_4$:Mn^{2+} phosphors [73, 74]. Therefore, employing some conductive materials on the surface of phosphor indeed can reduce the accumulated electrons on the surface of phosphor and improve the cathodoluminescent efficiency of phosphors. This may also act as a bridge to drain the Coulomb charge to the ITO substrate efficiently, which decreases the excited voltage and improves the lifetime, stability, and efficiency of the phosphor screen.

2.2.4 Improvement of Electron-Stimulated Degradation Behavior

It is known that most phosphors will degrade upon exposure to large doses of electrons (>50 C/cm^2). The luminescent degradation property of phosphors under electron beam bombardment is very important for their FED application. The origin of this degradation is now becoming clear, which is generally considered to be related to the stability of crystal structures and electron-stimulated surface chemical reaction of phosphor grains [78, 79]. Because prolonged electron beam irradiation commonly can decompose phosphors into volatile atomic species through the surface chemical reaction and then a possible formation of new layers on the surface. While the decomposition and hence the formation of the new layers has negative effects on both the chemical stability and luminescent intensity of the FEDs phosphors. To prevent the phosphors from decomposition, two strategies can be employed: first, selecting hosts with excellent chemical stability under electron beam irradiation; second, coating Al_2O_3, In_2O_3, ZnO, SiO_2, BN and organic polymers on phosphor surface [80]. The formers require stable crystal phases and crystal structures for phosphors, which can endure continuous electron beam irradiation. The rare earth ion-activated semiconductor materials and (oxo)nitridosilicates are possible selections [81]. The use of coatings can also yield excellent stability to the phosphors when exposed to moisture and other atmospheric components, and to protect phosphors from irradiation damage. For example, Xu et al. [33] investigated the degradation properties after mixing the representative $Lu_3Ga_5O_{12}$:Tb^{3+} phosphor with In_2O_3 nanoparticles. Figure 2.9a shows that the
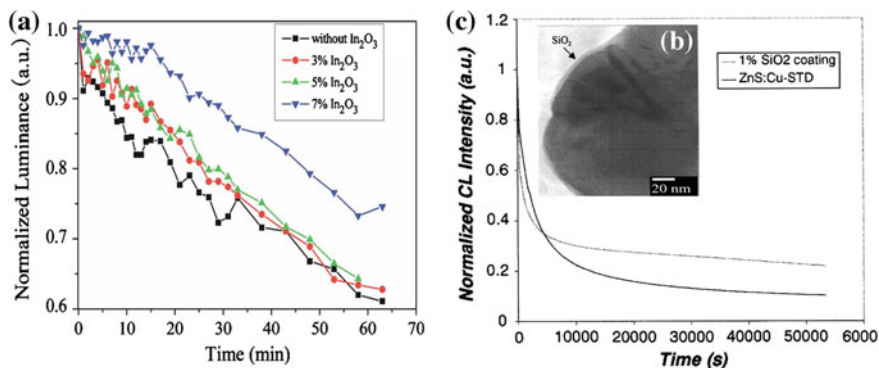
Fig. 2.9 **a** Normalized luminance decay of $Lu_3Ga_5O_{12}:Tb^{3+}$ phosphor mixed with and without In_2O_3 nanoparticles as a function of bombardment time. **b** TEM cross-sectional micrographs of 1.0 wt% SiO_2-coated ZnS:Cu phosphors. **c** Normalized CL intensity at 2 kV of 1.0 wt% SiO_2-coated and uncoated ZnS:Cu phosphors as a function of time. **a** Adapted from Ref. [33] by permission of American Vacuum Society. **b**, **c** Adapted from Ref. [77] by permission of The Electrochemical Society

degradation of the phosphor film becomes slow after being mixed with In_2O_3. Moreover, it becomes slower with increasing In_2O_3 contents. The decay is partially due to the charge-up of the phosphor. The improvement of the conductivity of $Lu_3Ga_5O_{12}:Tb^{3+}$ phosphor film by mixing with In_2O_3 eases the charge-up effect, and thus, the slower decay can be observed. After stopping bombardment for a while, however, the luminance could not restore to the initial value, indicating besides the charge-up effect, permanent damage to the phosphor occurs. This may be due to the accumulation of carbon at the surface during electron bombardment. This carbon contamination will prevent low-energy electrons from reaching the phosphor grains and also exacerbate surface charging, and thus lower the luminance. In addition to the mixing with semiconductive materials, Do et al. confirmed that coating SiO_2 on phosphor surface can also efficiently improve their electron-stimulated stability [82]. Figure 2.9b shows the formation of thin and uniform coatings on ZnS:Cu powders with a thickness of 5 nm. They founded that the SiO_2-coated phosphors were far more resistant to the loss of S species and to the formation of oxide dead layer. The CL aging study (Fig. 2.9c) showed much improved CL efficiency curves for the coated phosphors, confirming that the encapsulation of thin and uniform SiO_2 coatings on ZnS:Cu served as protective layers retarding the surface-related degradation, which is critically important for the development of commercial FEDs. On the other hand, the surface protective species need not necessarily be always externally applied, they can also originate from electron-stimulated surface chemical reaction [78]. This is attributed to surface disassociates partially of a phosphor compound. Pitale et al. found that a thermodynamically stable Al_2O_3 layer could be formed on the surface of lithium aluminate family like $LiAl_5O_8:Tb$ as a result of the electron-stimulated surface chemical reactions [78, 82]. Moreover, it generates a positive contribution to the CL stability

of the $LiAl_5O_8$:Tb phosphor. In general, the stable crystal structures and the surface protective species indeed can enhance the time stability of phosphors under electron beam irradiation to some extent. It is noticed that although the improvement can simply attribute to electron-stimulated surface chemical reaction, the more exact degradation mechanism is not clear and need to be further studied.

2.2.5 Enlarge Color Gamut

The resolution is a vital parameter for display devices, which is strongly related to the color gamut of phosphor [12, 40]. Generally, the wider of color gamut of phosphor, the higher picture quality can be achieved. The typical color gamut for FEDs is made up of a triangle region enclosed by three chromaticity coordinate points of trichromatic (red, green, and blue, RGB) FED phosphors, (0.647, 0.343) (Y_2O_2S:Eu^{3+}; red), (0.298, 0.619) (ZnS:Cu,Al; green), and (0.146, 0.056) (ZnS:Ag, Al; blue). In order to realize high-quality full-color FEDs, it is necessary to enlarge the color gamut of these phosphors. There are two main strategies to reach this goal. The one is to develop FED phosphors with higher color purity with respect to current trichromatic FED phosphors. The other one is to explore some novel phosphors with their CIE chromaticity coordinates locating out of the above triangle area. According to the first strategy, a series of RGB phosphors with high color purity have been developed. For example, blue-emitting Tm^{3+}-doped La_2O_3, LaOCl, LaOF, $LaGaO_3$, and so on were prepared and investigated [41, 49, 59, 71]. These phosphors demonstrate more higher color purities than commercial FED blue phosphor Y_2SiO_5:Ce due to main $^1D_2$–$^3F_4$ (around 458 nm) transition emission of Tm^{3+} ions (Table 2.1). Some Tb^{3+}-activated phosphors such as Tb^{3+}-doped LaOCl, $LaGaO_3$, and $KNaCa_2(PO_4)_2$ can also give highly pure blue emission through a low Tb^{3+} doping content due to the main $^5D_3$–$^7F_{6-0}$ transitions [83]. For these $4f$–$4f$ transitions of RE ions, the emission spectra are narrow and the peak positions are basically stable in different hosts because the electrons in $4f$ orbits are strongly shielded by the outside $5s$ and $5p$ electrons. As a result, they can maintain a high color purity. However, for $5d$–$4f$ transitions of RE ions, the energy level of the excited state $4f^{n-1}5d$ is commonly lower than that of the lowest excited state, which generally presents a broadband emission. Due to the bare electrons in $5d$ states, the different coordination surroundings of hosts have a prominent influence on the luminescence of RE ions, which can tune the emission colors from ultraviolet to red light region. For example, Hirosaki et al. [84] reported a highly pure blue emission of Eu^{2+} in AlN host with CIE coordinate (0.139, 0.106). Under electron beam excitation, it showed better saturation behavior, brightness, and degradation behavior than that of Y_2SiO_5:Ce. So it is an excellent blue-emitting FED phosphor. Mn^{2+} is a transition metal ion with $3d^5$ electronic configuration, and its emission, corresponding to $^4T_1 \rightarrow {}^6A_1$ transition, consists of a broad band whose position depends strongly on the host lattices. If the crystal field around Mn^{2+} ion is weak, the splitting of the excited energy levels in 3d orbits will be small resulting in Mn^{2+}

emission with higher energy, whereas it will give lower energy emission. Due to the weak crystal field surroundings, the as-prepared Mn^{2+}-activated Mg_2SnO_4, $(Zn, Mg)_2GeO_4$ and Li_2ZnGeO_4 phosphors give Brilliant green emission with narrow band width, which makes them have higher green purity than commercial green ZnO:Zn phosphors (Table 2.1). Therefore, they are promising green-emitting FED phosphors, while $Mg_2Y_8(SiO_4)_6O_2:Ce^{3+}/Mn^{2+}$ and $Ca_4Y_6(SiO_4)_6O:Ce^{3+}/Mn^{2+}$ show excellent red emission of Mn^{2+} due to the strong crystal field surroundings, which can be used for highly efficient red-emitting FED phosphors. Other promising red-emitting phosphors like $Ca_2GeO_4:Eu^{3+}$ and $CaTiO_3:Pr^{3+}$ also have potential application in FEDs due to high color purity (Table 2.1) [63, 72]. In general, developing phosphors with higher color purity than commercial RGB FED phosphors is a feasible strategy to improve display quality.

On the other hand, the colors observed by the human eye are those depicted in the whole 1931 CIE chromaticity diagram according to the colorimetry theory. At a four-color system, if four points are selected as red, yellow, green, and blue (RYGB) or red, green, cyan, and blue (RGCB), they would surround a larger color gamut than the three-color system [7, 71]. Therefore, these four-color systems will display more natural color than RGB system, and thus better meet people's individual requirements. Moreover, four-color system has a higher "information density" (namely, the pixels per unit area) compared with three-color system. Accordingly, the second strategy to enhance the display quality is to explore suitable four-color (RYGB) or (RGCB) systems phosphors such as cyan- or yellow-emitting phosphors. As mentioned in the previous section, the emission of Eu^{2+} ion can vary from ultraviolet to red light which depends on the host lattice. Therefore, Eu^{2+} ion can obtain cyan emission by selecting suitable host. Xie and Wang et al. realized cyan emission of Eu^{2+} ions in $Li_2CaSiO_4:Eu^{2+}$ [85] and $BaZrSi_3O_9:Eu^{2+}$ [86] systems, respectively, as shown in Table 2.1. Eu^{2+}-activated $BaSi_2O_2N_2$ can also be developed as cyan-emitting FED phosphor due to its excellent stability and high color purity (Table 2.1) [87]. In addition, Li et al. designed a highly pure cyan light emission by mixing blue light (Ti^{4+}) and green light (Mn^{2+}) in Ti^{4+}, Mn^{2+}-codoped Mg_2SnO_4 system, as shown in Fig. 2.10a, b. The as-prepared cyan-emitting phosphors have good stability under low-voltage electron beam excitation. After continuous electron beam excitation for an hour, it still keeps 92 % of its original intensity, with little change in their CIE chromaticity coordinates [30]. Therefore, it is promising phosphor for use in FEDs. Based on the second strategy, $NaCaPO_4:Mn^{2+}$ shows bright yellow emission under electron beam excitation with the CIE chromaticity coordinate (0.428, 0.552), which has a higher color purity than commercial yellow-emitting FED phosphor $(Zn, CdS):Ag^+$, as shown in the inset of Fig. 2.10c, d [51]. Under different voltages and continuous electron beam bombardment, its CIE chromaticity coordinates present a good stability. Moreover, there is no obvious saturation effect for the CL intensity of these phosphors with the increase in V_a and J_a. So the as-prepared $NaCaPO_4:Mn^{2+}$ phosphors have potential to be used as yellow-emitting phosphor in four-color system (RGBY) FEDs. Other yellow-emitting $ZnGeN_2$ [7], $LaAlO_3:Sm^{3+}$ [48], $LaGaO_3:Sm^{3+}$ [71], and $Ca_2Gd_8(SiO_4)_6O_2:Ce^{3+}/Mn^{2+}$ [88] also demonstrate
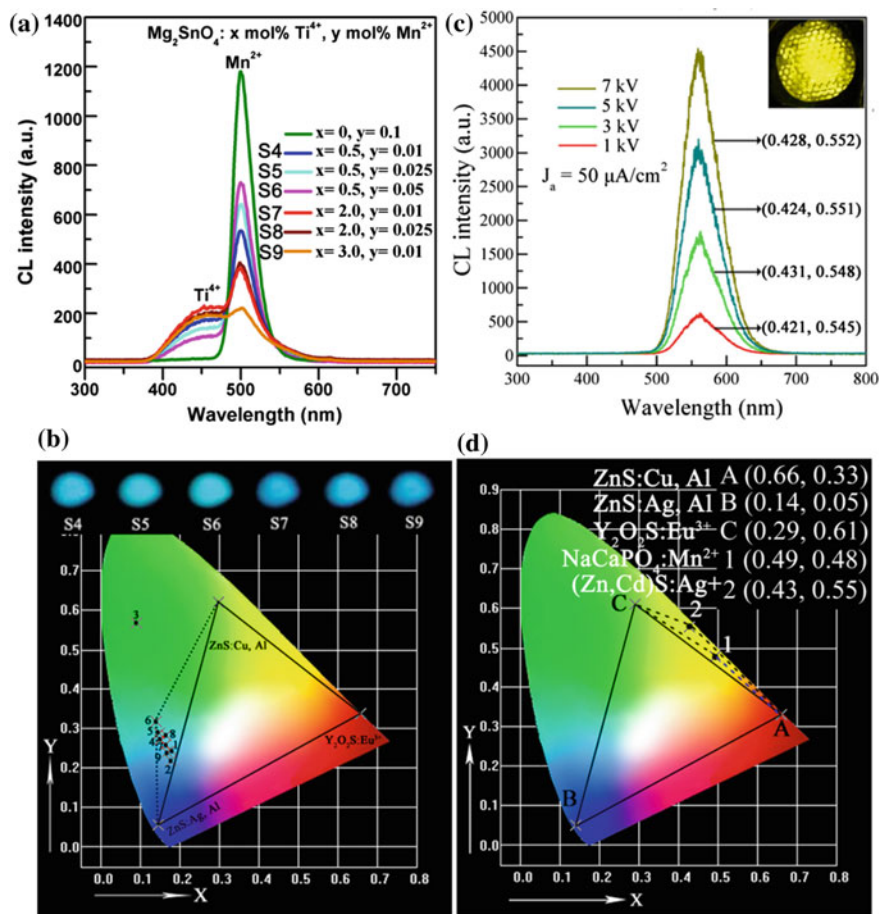
Fig. 2.10 CL spectra of **a** Mg_2SnO_4:xTi^{4+}, yMn^{2+} ($x = 0$–0.03, $y = 0.0001$–0.001) and **c** $NaCaPO_4$:$0.03Mn^{2+}$ samples. The CIE chromaticity coordinates of **b** Mg_2SnO_4:xTi^{4+}, yMn^{2+} ($x = 0$–0.03, $y = 0.0001$–0.001) and **d** $NaCaPO_4$:$0.03Mn^{2+}$ samples. The *triangle* and *quadrangle* in **b** and **d** show the typical and enlarged color gamut for FEDs phosphors, respectively. The *insets* in **b** and **c** are cathodoluminescent photographs. **a**, **b** Adapted from Ref. [30] by permission of Royal Society of Chemistry. **c**, **d** Adapted from Ref. [51] by permission of Optical Society of America

excellent chromaticity coordinates and stability (Table 2.1), which are also potential RYGB system phosphors in FED devices. In general, the development of highly pure RGB phosphors and appropriate four-color system (cyan or yellow-emitting phosphors) phosphors can efficiently enlarge color gamut and improve color saturation, and further to realize high-quality FED.

2.2.6 Design of White Light Emission

It is well known that excellent white light emission can supply excellent backlights in the display fields like LED, LCD, PDP, and FEDs, which has a positive effect on display quality. In recent years, there is an increasing focus on obtaining white light emission in single-phase host due to some potential advantages in luminous efficacy, chromatic stability, color-rendering index, and cost against the mixing of two or three different phosphors [89]. Many excellent and tunable white-light-emitting materials for FEDs can be obtained via designing co-emission (mono- or codoping RE^{3+} ions) and energy transfer (from hosts or RE ions to RE ions or Mn^{2+} ions) in single-phase hosts. The basic guiding principle mainly involves in a complex of complementary luminescence such as blue and yellow light, red, green, and blue light to obtain white light emission. A schematic illustration of generation of white light via co-emission and energy transfer in single-phase host is shown in Fig. 2.11. Due to abundant emission colors from blue to red based on $4f$–$4f$ transitions of trivalent RE^{3+} ions, white light emission in co-emission systems can be realized through mono-doping Eu^{3+} or Dy^{3+} ions, and codoping Tm^{3+}/Dy^{3+}, Tb^{3+}/Sm^{3+}, Tb^{3+}/Eu^{3+}, $Tm^{3+}/Tb^{3+}/Eu^{3+}$ ions, etc., into single matrix (Fig. 2.11a), while white light emission in energy transfer systems mainly results from the $Ce^{3+} \rightarrow Mn^{2+}$ (blue–yellow light complex) and $Ce^{3+} \rightarrow Tb^{3+}$, Mn^{2+} (red–green–blue light complex) energy transfers, as shown in Fig. 2.11b. The summary of luminescent properties for single-phase white-emitting phosphors via co-emission and energy transfer under low-voltage electron beam excitation is shown in Table 2.2. It is noticed that the energy can also be transferred to the lower energy excited state among the RE ions, depending on the RE concentration, energy transfers rates, and phonon energy. Moreover, the more energy transfer occur among the RE ions, the lower the luminescence efficiency. Therefore, it is important to optimize RE ion-doping concentrations and select suitable hosts. The elaborate discussions are shown as follows.
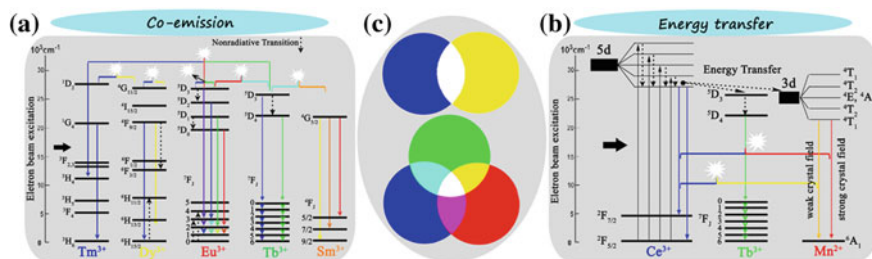
Fig. 2.11 Schematic mechanisms of generation of white light via **a** co-emission (mono-/codoping RE^{3+} ions) and **b** energy transfer (from hosts or RE ions to RE ions or Mn^{2+} ions) in single-phase host. **c** A generation of white light through the complex of different colors, *Blue-Yellow* (BY) or *Red–Green–Blue* (RGB). *Colored straight lines with arrows* represent different luminescence. The *horizontal braces* with different colors represent different light emission and *white stars* represent white light by the complex of different light emission

1. Singly doping RE^{3+} ions like Eu^{3+} or Dy^{3+} into appropriate single host.

The trivalent Eu^{3+} ion is well known as a red-emitting activator due to its $^5D_0$–^7F_J transitions based on $4f^6$ configuration with the most prominent $^5D_0$–$^7F_2$ emission group around 610–625 nm [35]. Except for the essential red emission, some other emission lines located in blue-green region from higher ^5D levels, such as $^5D_1$ (green), $^5D_2$ (green, blue), and $^5D_3$ (blue) can also appear at the low phonon frequencies of the host lattices and the low doping concentration of Eu^{3+} (Fig. 2.11a). That is attributed to the avoidance of the multiphonon relaxation and cross-relaxation occurring among the energy levels of Eu^{3+}, respectively. If the phonon energy (highest vibration frequency, v_{max}) of the host lattice is high enough to cause multiphonon relaxation, it will quench the higher-level $^5D_{1,2,3}$ emission of Eu^{3+}. Moreover, if the doping concentration of Eu^{3+} is high, the $^5D_{1,2,3}$ emission might be quenched by cross-relaxation between two neighboring Eu^{3+} ions, such as Eu^{3+} ($^5D_1$) + Eu^{3+} ($^7F_0$) → Eu^{3+} ($^5D_0$) + Eu^{3+} ($^7F_3$) and Eu^{3+} ($^5D_3$) + Eu^{3+} ($^7F_0$) → Eu^{3+} ($^5D_2$) + Eu^{3+} ($^7F_4$). So whether the emission can occur from higher excited states $^5D_1$, $^5D_2$, and $^5D_3$ or not for Eu^{3+} ion depends critically upon the highest vibration frequencies (v_{max}) available in the host lattice and the doping concentration of Eu^{3+}. In other words, an appropriate selection of the host lattice and doping concentration of Eu^{3+} is possible to yield simultaneously the red emission from $^5D_0$ energy level and the blue and green emissions from the higher $^5D_{1,2,3}$ energy levels of Eu^{3+} with comparable intensity, thus generating a white light emission from Eu^{3+}-monodoped materials. This situation has been confirmed in Eu^{3+}-doped $CaIn_2O_4$ system. Under low-voltage electron beam excitation, the emission spectra of $CaIn_2O_4$:0.01Eu^{3+} consist of all the emission lines from the $^5D_{0,1,2,3}$ excited states to the ^7F_J ground states of Eu^{3+}, i.e., $^5D_3$–$^7F_1$ (418 nm), $^5D_3$–$^7F_2$ (431 nm), $^5D_3$–$^7F_3$ (447 nm), $^5D_2$–$^7F_0$ (467 nm), $^5D_2$–$^7F_2$ (492 nm), $^5D_2$–$^7F_3$ (512 nm), $^5D_1$–$^7F_1$ (537 nm), $^5D_1$–$^7F_2$ (555 nm), $^5D_0$–$^7F_1$ (588 nm), $^5D_0$–$^7F_2$ (616 nm), and $^5D_0$–$^7F_4$ (700 nm), as shown in Fig. 2.12a. These emission lines of Eu^{3+} cover the whole visible spectral region and have comparable intensities resulting in a brilliant white light emission. Moreover, tunable white light emission can be obtained by precisely controlling the doping concentration of Eu^{3+} ions, as shown in Table 2.2. According to the same approach, $LaInO_3$:Eu^{3+}, LaOF: Eu^{3+} and β-$NaYF_4$:Eu^{3+} have been developed as single-phase white-light-emitting FEDs phosphors (Table 2.2) [90].

For Dy^{3+} ions, its emission spectrum is mainly separated into two groups, the blue emission from 460 to 505 nm and the yellow emission from 570 to 600 nm accompanied by a group of weak lines in the red region from 650 to 700 nm based in its $4f^9$ configuration. These emissions correspond to the transitions from $^4F_{9/2}$ to $^6H_{15/2}$, $^6H_{13/2}$ and $^6H_{11/2}$ of Dy^{3+} (Fig. 2.11a), respectively [74]. The yellow-emitting $^4F_{9/2}$–$^6H_{13/2}$ transition is hypersensitive transition, which is susceptible to the crystal environment. However, the blue emission is basically invariant with the surrounding environment. In composite oxides, the covalency between Dy^{3+} and O^{2-} has an important effect on the ratio of yellow-to-blue emission. Generally, the bigger covalency, the stronger yellow emission of Dy^{3+}

Table 2.2 Summary of cathodoluminescent properties for single-phase white-emitting phosphors via co-emission and energy transfer systems

Phosphor	Emission peaks (nm)/Transitions/Colors	CIE (x, y)	Refs.
Monodoping systems			
$CaIn_2O_4$:0.5 %Eu^{3+}	All the emissions from Eu^{3+}: ^5D_J–$^7F_{J'}$ $^5D_0$–$^7F_{J'}$, orange-red; $^5D_1$–$^7F_{J'}$, green $^5D_2$–$^7F_{J'}$, green-blue; $^5D_3$–$^7F_{J'}$, blue ($J = 0, 1, 2, 3; J' = 0, 1, 2, 3, 4$)	(0.290, 0.310)	[26]
$CaIn_2O_4$:1 %Eu^{3+}		(0.324, 0.323)	
$CaIn_2O_4$:1.5 %Eu^{3+}		(0.358, 0.345)	
$LaInO_3$:0.5 %Eu^{3+}		(0.369, 0.404)	[90]
$LaOF$:0.2 %Eu^{3+}		(0.291, 0.340)	[59]
$SrIn_2O_4$:1.5 %Dy^{3+}	491, 580/$^4F_{9/2}$ to $^6H_{15/2}$, blue; $^6H_{13/2}$, yellow	(0.302, 0.329)	[36]
Ga_2O_3:3 %Dy^{3+}	492, 580/$^4F_{9/2}$ to $^6H_{15/2}$, blue; $^6H_{13/2}$, yellow	(0.299, 0.333)	[32]
Codoping systems			
$LaOCl$:Tm^{3+},Dy^{3+}	458/$^1D_2$–$^3F_4$ (Tm^{3+}), blue 480, 571/$^4F_{9/2}$ to $^6H_{15/2}$, $^6H_{13/2}$ (Dy^{3+}), yellow	(0.318, 0.329)	[41]
$LaOCl$:Tb^{3+},Sm^{3+}	384, 417, 438, 486, 543/$^5D_{3,4}$–$^7F_{6-2}$ (Tb^{3+}), bluish green 565, 607, 650/$^4G_{5/2}$–$^6H_{5/2, 7/2, 9/2}$ (Sm^{3+}), orange	(0.341, 0.321)	[83]
$LaGaO_3$:Tb^{3+},Sm^{3+}	414, 437/$^5D_3$–$^7F_{5,4}$; 414, 437/$^5D_4$–$^7F_5$ (Tb^{3+}), bluish green 561, 597, 642/$^4G_{5/2}$–$^6H_{5/2}$, $^6H_{7/2}$, $^6H_{9/2}$ (Sm^{3+}), yellow	(0.341, 0.334)	[71]
$LaOCl$:Tb^{3+},Eu^{3+}, Tm^{3+}	416, 438, 543, 486/$^5D_{3,4}$–$^7F_{6-4}$ (Tb^{3+}), bluish green 577, 594, 615/$^5D_0$–$^7F_{0,1,2}$ (Eu^{3+}), red 458/$^1D_2$–$^3F_4$ (Tm^{3+}), blue	(0.291, 0.312)	[40]
Energy transfer systems			
$Mg_2Y_8(SiO_4)_6O_2$: Ce^{3+},Mn^{2+},Tb^{3+}	425, 455/$5d^1$–$4f^1$(Ce^{3+}) blue; 613/$^4T_1$–$^6A_1$ (Mn^{2+}) red; 544/$^5D_4$–$^7F_5$ (Tb^{3+}), green	(0.332, 0.337)	[91]
$Ca_2Ca_8(SiO_4)_6O_2$: Ce^{3+},Mn^{2+}	403, 428/$5d^1$–$4f^1$(Ce^{3+}) blue; 590/$^4T_1$–$^6A_1$ (Mn^{2+}) yellow	(0.342, 0.318)	[88]
$Sr_3In(PO_4)_3$:Ce^{3+}, Mn^{2+}	375/$5d^1$–$4f^1$(Ce^{3+}) blue; 568/$^4T_1$–$^6A_1$ (Mn^{2+}) yellow	(0.331, 0.319)	[96]
$Ca_3Sc_2Si_3O_{12}$:Ce^{3+}, Mn^{2+}	450, 505/$5d^1$–$4f^1$(Ce^{3+}) blue to green; 574, 680/$^4T_1$–$^6A_1$ (Mn^{2+}) red		[97]

ion will be achieved. Moreover, the covalency of Dy^{3+}–O^{2-} is different in different host matrix due to the local variation of the symmetry and coordination environment of crystal structure. Therefore, the ratio of yellow-to-blue emission can be adjusted by doping into different host lattice, resulting in a possible to obtain white light emission in Dy^{3+}-monodoped luminescence material. For example, for
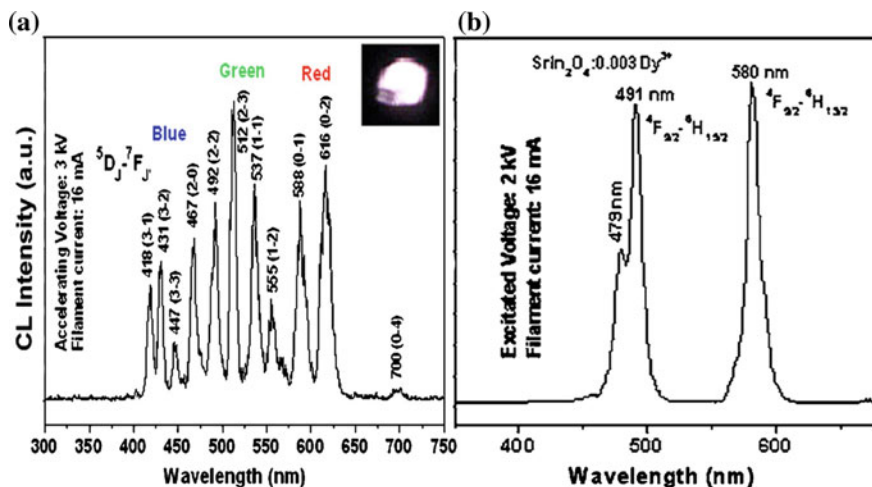
Fig. 2.12 Emission spectrum of **a** $CaIn_2O_4:0.01Eu^{3+}$ under the excitation of electron beam. The *inset* shows luminescent photograph with white light emission. **c** Typical cathodoluminescence spectra of $SrIn_2O_4:0.003Dy^{3+}$ with CIE chromaticity coordinates $x = 0.3019$ and $y = 0.3291$. **a** Adapted from Ref. [26] by permission of American Institute of Physics. **b** Adapted from Ref. [36] by permission of The Electrochemical Society

$SrIn_2O_4:0.015Dy^{3+}$ phosphor, its CL spectrum (Fig. 2.12b) is made up of the characteristic emission lines of Dy^{3+}, i.e., $^4F_{9/2}$–$^6H_{15/2}$, 491 nm and $^4F_{9/2}$–$^6H_{15/2}$, 580 nm. It has a suitable yellow-to-blue intensity ratio and thus appears a white emission of Dy^{3+} in $SrIn_2O_4$ with CIE chromaticity coordinates $x = 0.3019$ and $y = 0.3291$. The Dy^{3+}-doped $CaIn_2O_4$, $LaGaO_3$ and Ga_2O_3 are also considered as excellent single-phase white-emitting FEDs phosphors with tunable chromaticity coordinates in white light region, as shown in Table 2.2.

2. Codoping different RE^{3+} ions such as Tm^{3+}/Dy^{3+}, Tb^{3+}/Sm^{3+}, Tb^{3+}/Eu^{3+}, $Tm^{3+}/Tb^{3+}/Eu^{3+}$ etc., into single matrix.

Due to the abundant energy levels in $4f$ orbits of RE^{3+} ions such as Tm^{3+}, Dy^{3+}, Tb^{3+}, Sm^{3+}, Eu^{3+} ions, they produce various luminescence colors covering the whole visible light region. Tm^{3+} ion mainly emits blue light around 458 nm due to $^1D_2$–$^3F_4$ transition. Dy^{3+} ion usually exhibits two main emissions in the visible region: one in the blue region (470–500 nm) and one in the yellow region (570–600 nm), which originate from $^4F_{9/2} \rightarrow ^6H_{13/2}$ and $^4F_{9/2} \rightarrow ^6H_{15/2}$ transitions of Dy^{3+} ions, respectively. The emission of Eu^{3+} ion mainly appears in red region with the maximum between 610 and 625 nm due to $^5D_0$–$^7F_2$ emission. The emission of Sm^{3+} is situated in the orange spectral region and consists of transitions from the excited $^4G_{5/2}$ level to the ground-state $^6H_{5/2}$ and higher levels ^6H_J ($J > 5/2$). Tb^{3+} ion has a low-energy ground-state ^7F_J ($J = 6, \ldots 0$) and excited states $^5D_3$ and $^5D_4$. Generally, with a low doping concentration of Tb^{3+} in host matrix, the transitions of $^5D_3$ to ^7F_j dominate and produce the blue emissions. As Tb^{3+} concentration
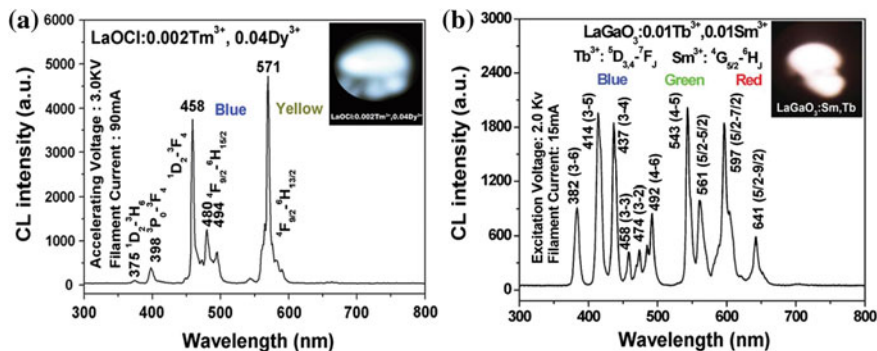
Fig. 2.13 CL spectra and corresponding luminescence photographs of RE^{3+} codoped phosphor systems. **a** LaOCl:Tm^{3+},Dy^{3+} and **b** LaGaO$_3$:Tb^{3+},Sm^{3+}. **a** Adapted from Ref. [41] by permission of Royal Society of Chemistry. **b** Adapted from Ref. [71] by permission of Royal Society of Chemistry

increases, the cross-relaxation from $^5D_3$ to $^5D_4$ occurs owing to the interaction between Tb^{3+} ions, which enhances the transitions of $^5D_4$ to ^7F_j with a green emission. Although these RE^{3+} ions generally are used as single activator in single host, they also generate highly efficient luminescence when coexisting in single matrix. Accordingly, many RE^{3+} ions codoped single-phase phosphor systems were designed to realize white light emission, for example, Tm^{3+}/Dy^{3+}, Tb^{3+}/Sm^{3+}, Tb^{3+}/Eu^{3+}, Tm^{3+}/Tb^{3+}/Eu^{3+} systems, as shown in Table 2.2. Figure 2.13 exhibits the CL spectra and corresponding luminescent photographs of codoping phosphor systems. Under electron beam excitation, LaOCl:Tm^{3+} and LaOCl:Dy^{3+} emit blue light (458 nm, $^1D_2$–$^3F_4$) and yellow light (571 nm, $^4F_{9/2}$–$^6H_{13/2}$), respectively. When codoping Tm^{3+} and Dy^{3+} ions into LaOCl host, it simultaneously gives blue and yellow emission with comparable, which results in a white light emission (CIE coordinates, $x = 0.318$, $y = 0.329$) by the complex of blue and yellow lights (Fig. 2.13a; Table 2.2). For Tb^{3+}/Sm^{3+}-codoped LaGaO$_3$, the white emission is realized by the complex of red, green and blue components. The red component comes from the characteristic transitions of Sm^{3+} (561, 597, 642 nm/$^4G_{5/2}$–$^6H_{5/2}$, $^6H_{7/2}$, $^6H_{9/2}$), while the green and blue components result from the mixing emissions of 414, 437 nm/$^5D_3$–$^7F_{5,4}$; 414, 437 nm/$^5D_4$–$^7F_5$ at a moderate Tb^{3+} doping concentration (Fig. 2.13b; Table 2.2). Based on the same complex method, LaOCl:Tb^{3+}/Eu^{3+}, LaOCl:Tb^{3+}/Sm^{3+}, LaOCl:Tb^{3+}/Eu^{3+}/Tm^{3+} phosphor system also obtained excellent white light emission (Table 2.2). The wide range adjustment of emission colors by precisely controlling the doping contents of RE^{3+} ions makes RE^{3+}-codoped single-phase white light emission have potential application as backlights in FEDs devices.

3. Designing energy transfers from host or RE ions to RE ions or Mn^{2+} ions to in single host.

It is well known that energy transfer plays an important role in the optical properties of luminescent materials both from theoretical and practical points of view, because it can not only enhance the luminescent efficiency but also tune the luminescent color in the single-phase host [92]. The Ce^{3+} with the $4f^1$ configuration in solids shows efficient broad band luminescence due to the $4f$–$5d$ parity allowed electric dipole transition. It can also act as an efficient sensitizer by transferring a better part of its excitation energy to coactivators. Because the d–d transition of Mn^{2+} is forbidden and difficult to pump, the emission of Mn^{2+} ions is generally excited by energy transfer from the host or the sensitizer. Caldiño [93] reported the spectral overlap between $5d^1 \rightarrow 4f^1$ Ce^{3+} emission and $^6A_1 \rightarrow {}^4T_2$ Mn^{2+} absorption. So far, the $Ce^{3+} \rightarrow Mn^{2+}$ energy transfers have been reported in many inorganic hosts, such as fluorides, phosphates, and borates, and the corresponding mechanisms have been extensively investigated [94, 95]. Ce^{3+} ion can also efficiently transfer energy to Tb^{3+} ions in single host to generate efficient green emission [91]. In these systems, there is a common feature that Ce^{3+} and Mn^{2+}/Tb^{3+} ions simultaneously substitute one or two lattice sites and the Ce^{3+} ions serve as effective sensitizer ions for Mn^{2+}/Tb^{3+}, transferring the energy from the 5D level of the Ce^{3+} to the 4G level of the Mn^{2+} or $^5D_4$–^7F_j level of Tb^{3+} by a process of resonance transfer via a spin exchange mechanism, which not only help Mn^{2+}/Tb^{3+} ions to emit efficiently but also tune their emission colors from blue to yellow or orange/red for $Ce^{3+} \rightarrow Mn^{2+}$, and from blue to green for $Ce^{3+} \rightarrow Tb^{2+}$, across the whole white light region, as shown in Fig. 2.11 and Table 2.2. Some research groups have demonstrated the above situation in many Ce^{3+}–Mn^{2+} (blue-yellow) or Ce^{3+}–Mn^{2+}–Tb^{3+} (blue–red–green) codoped systems such as $Ca_2Ca_8(SiO_4)_6O_2$ [88], $Mg_2Y_8(SiO_4)_6O_2$ [91], $Sr_3In(PO_4)_3$ [96], $Ca_3Sc_2Si_3O_{12}$:Ce^{3+}, Mn^{2+} [97] and so on (Table 2.2). For example, there is an efficient energy transfer from Ce^{3+} to Mn^{2+} in $Ca_2Ca_8(SiO_4)_6O_2$:Ce^{3+}, Mn^{2+}. This phosphor simultaneously emits blue light of Ce^{3+} ions (428 nm) and yellow light of Mn^{2+} ions (490 nm) (Fig. 2.14a), respectively. By changing the relative doping concentration of Ce^{3+} and Mn^{2+}, the ratio of blue to yellow is controllable and thus obtains an excellent white light emission with CIE coordinates (0.342, 0.318). For Ce^{3+}–Mn^{2+}–Tb^{3+}-codoped systems, there simultaneously exist two energy transfer processes of $Ce^{3+} \rightarrow Mn^{2+}$ and $Ce^{3+} \rightarrow Tb^{3+}$, which emit red light and green light, respectively (Fig. 2.14b). Because these energy transfer processes can be controlled via tuning the relative doping concentrations of Ce^{3+}, Tb^{3+} and Mn^{2+} ions. Therefore, the relative emission intensities of blue, green, and red light can be adjusted in single-phase phosphor, resulting in the controllable white light emission (Fig. 2.14b). In summary, by designing efficient energy transfer process $Ce^{3+} \rightarrow Mn^{2+}$ or $Ce^{3+} \rightarrow Mn^{2+}$, Tb^{3+} in single host lattices, excellent white light emission with tunable chromaticity coordinates and high efficiency can be obtained, which is promising in FED backlights. Except for the above energy transfer processes, other energy transfer routes like from Eu^{2+} to Mn^{2+}/Tb^{3+} or from host or self-activated
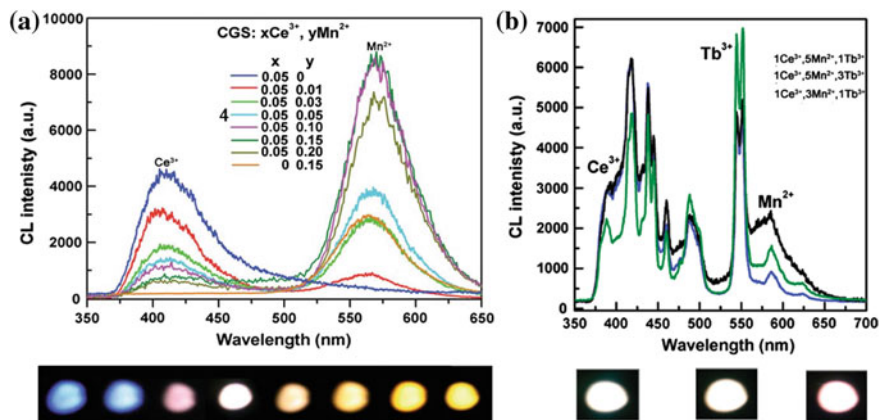
Fig. 2.14 CL spectra and corresponding luminescence photographs of energy transfer phosphor systems: **a** $Ca_2Ca_8(SiO_4)_6O_2:Ce^{3+},Mn^{2+}$ and **b** $Mg_2Y_8(SiO_4)_6O_2:Ce^{3+},Mn^{2+},Tb^{3+}$. **a** Adapted from Ref. [88] by permission of American Chemical Society. **b** Adapted from Ref. [91] by permission of Royal Society of Chemistry

luminescent center to RE^{3+} ions also can gain excellent white light emission, as shown in Table 2.2.

2.3 Development of Novel FEDs Phosphor Powders

Due to a relatively severe operation environment (low-voltage and high current density) in FEDs, future generation phosphors should possess better low-voltage efficiencies, chromaticity (high color purity and wide color gamut), saturation and degradation behavior, and maintenance. Possible routes to achieve these improvements include optimizing morphology, size, surface and crystallization of phosphor grains, enhancing electrical conductivity of phosphors particles, modifying composition of phosphors, enlarging color gamut, designing energy transfers and so on. On the basis of these approaches, in the past decade, a series of novel FEDs phosphors have been developed, as collected in Table 2.3, which shows excellent low-voltage cathodoluminescent properties and has promising application in FED devices. Although most of the newly developed low-voltage FEDs phosphors commonly have the higher color purity and color stability than traditional FEDs phosphors, for examples, $LaOCl:Tm^{3+}$ and $LaGaO_3:Tb^{3+}$ than $Y_2SiO_5:Ce$ (blue) [41]; $LaOCl:Tb^{3+}$ than $ZnO:Zn$ (green) [83]; $(Zn,Mg)_2GeO_4:Mn^{2+}$ and $Mg_2SnO_4:Mn^{2+}$ than $Y_2SiO_5:Tb^{3+}$ (green) [30, 38]; $NaCaPO_4:Mn^{2+}$ than $(Zn, CdS):Ag^+$ (yellow) [51], their luminescent efficiencies are still lower than the latters. Fortunately, these luminescent disadvantages of the newly developed

Table 2.3 Some newly developed rare earth ions or Mn^{2+} ions activated low-voltage FEDs phosphors and their luminescent properties

Sample	Emission peaks (nm)/main transition	Color	Refs.
$Ga_2O_3:Dy^{3+}$	$438/^4T_1-^4A_2$ (GaO_6)	Blue	[32]
	492, $580/^4F_{9/2}$ to $^6H_{15/2}$, $^6H_{13/2}$ (Dy^{3+})	White	
$CaIn_2O_4:Eu^{3+}$	431, 447, 467, 492, 512, 537, 588, $616/^5D_{0,1,2,3}-^7F_{0,1,2,3}$ (Eu^{3+})	White	[26]
	$588/^5D_1-^7F_2$; $619/^5D_0-^7F_2$ (Eu^{3+})	Red	
$SrIn_2O_4:Dy^{3+},Pr^{3+},Tb^{3+}$	$493/^4F_{9/2}-^6H_{15/2}$, $582/^4F_{9/2}-^6H_{13/2}$ (Dy^{3+})	Bluish white	[36]
	$494/^3P_0-^3H_4$ (Pr^{3+})	Orange	
	$487/^5D_4-^7F_6$, $544/^5D_4-^7F_5$ (Tb^{3+})	Green	
$LaOCl:Tm^{3+},Dy^{3+},Sm^{3+},Tb^{3+},Eu^{3+}$	$458/^1D_2-^3F_4$ (Tm^{3+})	Blue	[40, 41, 83]
	480, $571/^4F_{9/2}$ to $^6H_{15/2}$, $^6H_{13/2}$ (Dy^{3+})	Yellow	
	565, 607, $650/^4G_{5/2}-^6H_{5/2, 7/2, 9/2}$ (Sm^{3+})	Orange	
	384, 416, 437, 486, $543/^5D_{3,4}-^7F_j$ (j = 6-0) (Tb^{3+})	Blue, green	
	$615/^5D_0-^7F_2$ (Eu^{3+})	Red	
$LaGaO_3:Tm^{3+},Sm^{3+},Tb^{3+},Dy^{3+},Eu^{3+}$	$458/^1D_2-^3F_4$ (Tm^{3+})	Blue	[49, 71]
	561, 597, $642/^4G_{5/2}-^6H_{5/2, 7/2, 9/2}$ (Sm^{3+})	Yellow	
	414, 437, 414, $437/^5D_{3,4}-^7F_{5,4}$ (Tb^{3+})	Blue, green	
	480, $572/^4F_{9/2}$ to $^6H_{15/2}$, $^6H_{13/2}$ (Dy^{3+})	Yellowish white	
	590, $614/^5D_0-^7F_{1, 2}$ (Eu^{3+})	Red	
$LaInO_3:Eu^{3+}$	465, 491, 512, 534, 588, $610/^5D_{0,1,2,3}-^7F_{0,1,2,3}$ (Eu^{3+})	Yellowish white	[90]
	588, $610/^5D_0-^7F_{1,2}$ (Eu^{3+})	Red	
$Mg_2(Sn,Ti)O_4:Mn^{2+}$	$465/$(SnO_6)	Blue	[30]
	$456/$(TiO_6)	Blue	
	$499/^4T_1-^6A_1$ (Mn^{2+})	Green	
$Li_2ZnGeO_4:Mn^{2+}$	$530/^4T_1-^6A_1$ (Mn^{2+})	Green	[20]
$(Zn,Mg)_2GeO_4:Mn^{2+}$	$460/$(GeO_6); $531/^4T_1-^6A_1$ (Mn^{2+})	Blue, green	[38]
$NaCaPO_4:Mn^{2+}$	$560/^4T_1-^6A_1$ (Mn^{2+})	Yellow	[51]
$Ca_2GeO_4:Eu^{3+}$	$613/^5D_0-^7F_2$ (Eu^{3+})	Red	[72]
$CaYAlO_4:Tb^{3+},Eu^{3+}$	383, 416, 468, 537, $548/^5D_{3,4}-^7F_j$ (j = 6-0) (Tb^{3+})	Blue, green	[44]
	593, $623/^5D_0-^7F_{1,2}$ (Eu^{3+})	Red	

low-voltage FEDs phosphors can be reduced or eliminated to some extent through process optimization, including improves the morphology, size and crystallization of phosphors. Therefore, it is very necessary to explore appropriate preparation processes of these phosphors.

2.4   Phosphor Thin Films and Patterning

Except for powders, phosphor thin films that are formed by depositing phosphor precursor on a substrate following a subsequent annealing are the other important form to apply in display faceplates. It appears more attractive for FEDs, because they could be operated at lower voltage and endure much higher power densities without degradation than those powder phosphors [47]. Moreover, phosphor thin films offer advantages such as higher contrast and resolution, better thermal stability, superior thermal conductivity, a high degree of uniformity and better adhesion to the substrate, and reduced outgassing for FEDs compared with the conventional display screen prepared by the direct deposition of phosphor grains [98]. In order to define a smaller pixel spot size, thin film phosphors should possess uniform thickness, smoother surface form and small grain size. To date, phosphor thin films have been prepared by a variety of deposition techniques, such as chemical vapor deposition (CVD), physical vapor deposition (PVD), ion beam sputtering, filtered arc deposition, electrophoretic deposition (EPD), and pulsed laser ablation [99, 100]. These techniques are time-consuming or need expensive and complicated equipment setups. Therefore, a simple and economical method for making high-quality phosphor thin films is desirable, in which the preparation of oxide phosphor films by a PSG process is an excellent candidate [101–103]. This PSG process mainly involve in three steps: the first step is the preparation of a precursor solution with certain viscosity, including the dissolution of the starting materials, formation of metal chelates with citric acid (CA) and their polyesterification with PEG; the second step is the preparation of the amorphous precursor film by a dip-coating or spin-coating process on the desired substrates (silica glasses, silicon wafers, ITO and quartz plates, some ceramics slides, etc.); finally, crystalline phosphor films are produced by the post-annealing process at moderate temperature (500–1000 °C) with a slow heating rate to avoid the cracking and peeling of the films. The as-prepared phosphor thin films via the PSG process have some advantages, as follow: (a) simple process and equipment; (b) low processing temperature, making it possible to prepare films on glass, semiconductor, and integrated photoelectronic devices; (c) films can be coated on substrates with a large area, various shape and different material compositions; (d) a easy control of homogeneity, constituents and microstructure; (e) a controllable thickness by adjusting the viscosity of the coating solution or the repeating number of the coating process. Generally, the phosphor thin films prepared via PSG process are smooth and consist of nanocrystalline grains ranging from 100 to 500 nm. It is noted that the thin film phosphors have lower emission intensity due to the light trapping inside the luminescent layer. Therefore, such films cannot presently compete with powder phosphors in applications phosphors in applications that require high brightness.

On the other hand, full-color displays generally need to deposit the three-color modules (red, green, blue) on the desired regions to form pixels [47]. Therefore, during the fabrication of display devices, patterning luminescent materials on screen

to form pixel matrixes is an essential and critical technique. An accurate patterning technology and screening process for phosphor screen has a vital effect on the resolution of display devices. For instance, pitches of phosphor lines for a super-video graphics adapter with 800×600 lines, video graphics adapter with 640×480 lines, and quarter video graphics adapter with 320×240 lines in 6 in. color displays are defined as 50.8, 63.5, and 127 μm, respectively [47, 104]. So far, electrophoretic deposition, screen printing, vacuum deposition, etc., based on photolithographic patterning technologies have been employed to fabricate FPDs devices [105]. Unfortunately, these patterning techniques for a phosphor screen frequently require expensive photolithographic and etching equipment, complicated layout, and excessive loss of expensive phosphor materials during the fabrication process. Based on these considerations, a growing interest has been focused to soft-lithography patterning techniques, which has the potential of becoming versatile and low-cost methods for creating submicrometer and micrometer size structures [106]. Soft-lithography technique uses a soft and flexible poly (dimethylsiloxane) (PDMS) elastomer that can exactly replicate the surface features of the master mold and transfer them in the patterning process instead of rigid materials as the stamp or mold, and it is carried out by casting the prepolymer on a master with relief structure. Recently, several soft-lithography techniques including micromolding in capillaries (MIMIC), inkjet printing (IP), microtransfer molding (μTM), and microcontact printing (μCP) to realize the pattering of thin film phosphors have been well explored and developed. The detailed introductions are demonstrated in the following sections.

2.4.1 Micromolding in Capillaries (MIMIC)

As soft-lithography technique, MIMIC can pattern a material based on a low-viscosity solution. Phosphor thin films also can be patterned by the MIMIC technique. The basic principle of this process is shown in Fig. 2.15(left). First, polydimethylsiloxane (PDMS) stamp modes (with different channel widths 5–50 μm) were fabricated by casting PDMS on masters having desired patterns [101, 102]. Then the PDMS modes were placed in conformal contact with thoroughly cleaned silicon wafer substrates. The channels of the mode thus formed capillaries with the silicon wafer substrate. The phosphor precursor sol was then dropped at the open end with a transfer pipet. The capillary force made the sol flow into the mold. Then the modes and substrates were dried. After carefully removing the modes, the resulted patterned gel films were heated to high-temperature (500–1000 °C depending on the host compositions) with a slow heating rate (1 °C/min) and held for several hours. In this way, phosphor films with patterning were obtained. Figure 2.15(right) shows optical micrographs of the as-prepared patterned $LaPO_4$: Ce^{3+}, Tb^{3+} gel films. The dark and white regions correspond to the film strips and spaces, respectively. It is clearly seen from a to d in Fig. 2.15(right) that film strips have widths of 5, 10, 20, and 50 μm, respectively, with smooth and perfect
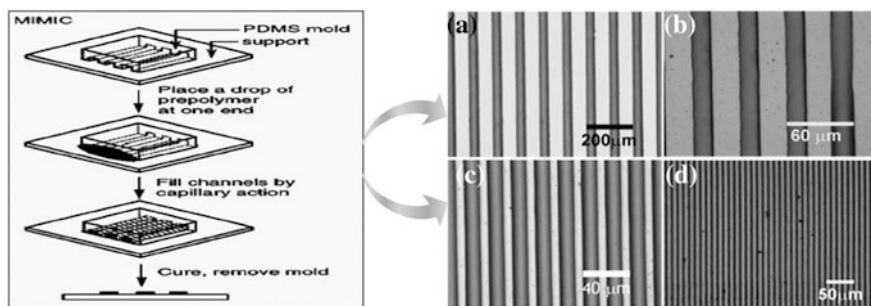
Fig. 2.15 Schematic procedures of MIMIC for patterning of phosphor films (*left*) and the optical photographs for patterned $LaPO_4:Ce^{3+}$, Tb^{3+} phosphor films with different stripe width (*right*, *a* 50 μm, *b* 20 μm, *c* 10 μm, *d* 5 μm). Adapted from Ref. [47] by permission of American Chemical Society

surfaces. Patterned phosphor films were formed after a subsequent annealing of these patterned gel films [101, 102]. According to the MIMIC technique, many other kinds of patterned phosphor films, such as $Y_2O_3:Eu^{3+}$, $Gd_2O_3:Eu^{3+}$, (Y, La, Gd)$VO_4:Eu^{3+}$ etc., can be prepared, which are promising for applications in the FED fields [107, 108].

2.4.2 Inkjet Printing (IP)

Recently, inkjet printing has attracted substantial interest as a pathway to make display devices, in which the material deposition and patterning can be performed within a single step by a fully digital driven process [109–111]. This direct-writing technique has many advantages such as simple, fast, large area, and low material consumption. There are many reports for the applications of inkjet printing on the fabrication of polymer light-emitting diodes (PLED) [112, 113]. The deposition of light-emitting polymers as pixels or conducting polymer PEDOT:PSS as the hole transportation layer can be carried out by inkjet printing in the PLED fabrication process. The bottleneck of the inkjet printing technique in organic electronics is being exceeded, and some prototypes of full-color organic light-emitting televisions have been demonstrated. Some attempts have also been made to pattern inorganic phosphor materials for the applications of a field emission flat display by the inkjet printing technique. The inkjet printing system consists of a piezoelectric type printing head with a nozzle (Fig. 2.16a). The microdrops were squeezed out by applying a voltage to the glass capillary inside the dispenser head. A computer-controlled motorized translation stage can move in the X–Y directions relative to the dispenser head which provide the patterns on the substrate such as dots and lines. Using $YVO_4:Eu^{3+}$ as a representative example, the patterning of phosphor thin films through inkjet printing technique can be realized. First, the
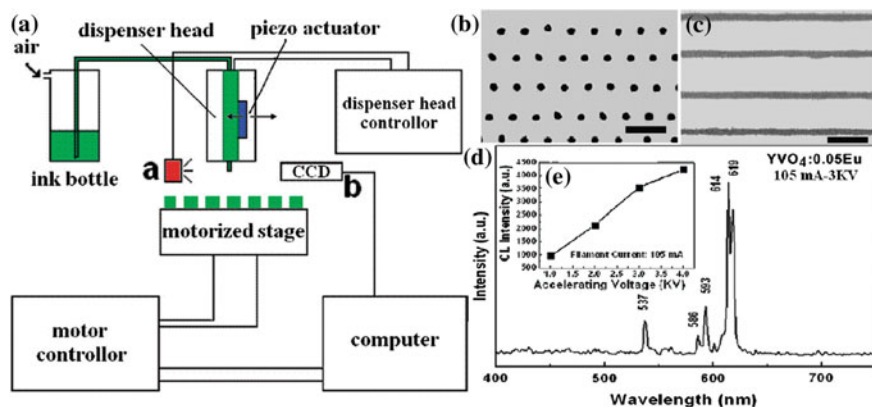
Fig. 2.16 a Schematic representation of the inkjet printing setup. **a** The inkjet printing system was manufactured by Microdrop Technique GmbH (Germany), which consists of a piezo-actuated inkjet dispenser head and its controller. A motorized stage under the inkjet printing head equipped with the computer and software provides the precise position of substrate; **b, c** microscopy photographs of the as-inkjet-printed *dots* and *lines* of crystalline $YVO_4:0.05Eu^{3+}$, the *scale bars* represent 200 μm; **d** the CL spectrum of patterned $YVO_4:0.05Eu^{3+}$ on ITO glass excited by electron beam; **e** the CL intensity of the $YVO_4:0.05Eu^{3+}$ pattern as a function of electron beam voltage. Adapted from Ref. [109] by permission of American Chemical Society

$YVO_4:Eu^{3+}$ ink precursor solution was prepared. Then, it was loaded on the inkjet printing system to produce the dots or lines pattern on the ITO glass. After setting driven voltage, pulse width and inkjetting frequency, the $YVO_4:Eu^{3+}$ patterned thin films were obtained. After being dried, the resulting pattern-formed substrates were baked to form the light-emitting $YVO_4:Eu^{3+}$ pixels. Figure 2.16b, c shows the microscopy image of as-inkjet-printed dots array after annealing. Obviously, the as-inkjet-printed dots arrays are highly uniform. Under the excitation of low-voltage electron beam, the patterned $YVO_4:0.05Eu^{3+}$ film can also give red light emission centered at 614 and 619 nm due to the $^5D_0-^7F_2$ transition, as shown in Fig. 2.16d. Moreover, the CL intensity increases quickly upon raising the accelerating voltage from 1 to 4 kV when the filament current is fixed on 105 mA, indicating the light-emitting intensity of $YVO_4:0.05Eu^{3+}$ is strongly dependent on the accelerating voltage, which is in line with FEDs working principle. In summary, the preparation of patterning $YVO_4:Eu^{3+}$ light-emitting pixels by a combination of inkjet printing and the PSG method show a feasible scheme for patterning inorganic thin film phosphors by the inkjet printing route (Fig. 2.16e). This facile and quick method has the potential to be used in the fabrication of FEDs devices by continuing efforts to further improving the properties of ink solution and prestructuring substrate, modifying the layout, and so forth.

2.4.3 Microtransfer Molding (μTM)

Microtransfer molding (μTM) is one of the most popular and typical soft-lithography techniques. This technique can directly replicate the feature of the stamp and form the pattern in accordance with the geometry of the stamp. By introducing $YVO_4:Eu^{3+}$ as an example can illustrate the fabrication of light-emitting arrays via μTM technique, as shown in the left of Fig. 2.17a [114]. First, the PDMS stamps were fabricated by casting the PDMS prepolymer, a mixture of Sylgard silicone elastomer and its curing agent over a relief master. The elastomer was degassed and cured and then peeled gently from the master. In this way, PDMS stamps with microwells were obtained. Second, the quartz plates were transformed to hydrophilic properties by immersing them in a piranha solution of concentrated sulfuric acid and hydrogen peroxide. Next, the $YVO_4:Eu^{3+}$ precursor solution was cast on the patterned side of the PDMS mold and the excess solution was removed by scraping with a flat PDMS block. By spin-coating, the $YVO_4:Eu^{3+}$ precursor solution was deposited into the recessed square regions of the PDMS mold, and the mold was brought into contact with the quartz substrate. Then, the mold and substrate were dried. When the mold was peeled away carefully, patterned squares of the $YVO_4:Eu^{3+}$ precursor gels were left on the surface of the quartz substrate. Finally, the patterned substrate was calcined to pyrolyze the organic components and the precursor gel was transformed into crystalline $YVO_4:Eu^{3+}$. The as-prepared $YVO_4:Eu^{3+}$ precursor gel pattern by the μTM technique
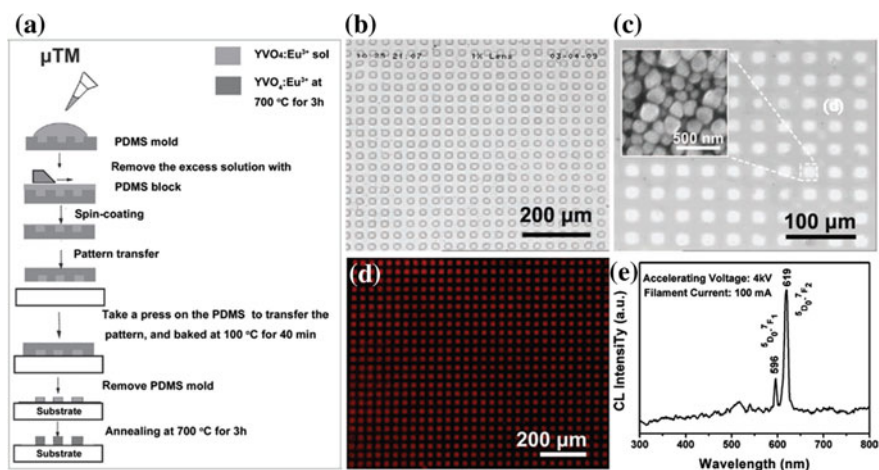
Fig. 2.17 **a** Schematic diagram of the experimental microtransfer molding (μTM) process used for patterning $YVO_4:Eu^{3+}$ films. Optical image of the patterned $YVO_4:Eu^{3+}$ precursor gel film fabricated by **b** μTM, **c** after calcination at 700 °C, and **d** the corresponding luminescent image under 254-nm UV light excitation. The *inset* in **c** SEM image of the patterned $YVO_4:Eu^{3+}$ film, indicative of the morphology of the crystalline $YVO_4:Eu^{3+}$ particles after firing at 700 °C. **e** The CL spectra of the patterned $YVO_4:Eu^{3+}$ film. Adapted from Ref. [114] by permission of Wiley

(Fig. 2.17b) exhibits ordered square arrays without obvious swelling or deformation. After calcination at 700 °C in air, the patterned YVO$_4$:Eu^{3+} crystalline film was formed on the quartz plate and the corresponding optical microscope image is shown in Fig. 2.17c. A size shrinkage of the square gels was observed after firing, which is attributed to the pyrolysis and evaporation of the organic compounds in the gel. The red luminescent image (Fig. 2.17d) and CL spectrum (Fig. 2.17e) of YVO$_4$:Eu^{3+} phosphor films indicated that the as-prepared YVO$_4$:Eu^{3+} phosphor films can be efficiently excited by UV light and low-voltage electron beam.

2.4.4   Microcontact Printing (μCP)

Microtransfer printing (μCP) is another one of the most popular and typical soft-lithography techniques [114]. On the contrast to μTM, the μCP technique prints the self-assembled monolayer (SAM) pattern on the substrate in the first step, which makes the substrate change from being chemically homogeneous into chemically heterogeneous. Then other functional materials can be grown or deposited on the desired patterned regions. Although μCP requires multiple steps and the final pattern formation depends on the chemical heterogeneity of the substrate's surface, these techniques are continuously being developed and improved. For example, a self-assembled monolayer can be firstly transferred onto a substrate and its end group can then be modified through organic synthesis to generate well-defined surfaces with a broad range of characteristics. Therefore, μCP is an improved technique based on μTM. Figure 2.18a shows the process of fabricating a representative YVO$_4$:Eu^{3+} arrays of dots via μCP. First, the PDMS molds and the quartz plates were carried out the same treatment as μTM technique. The PDMS mold was subsequently flooded with specific organic solvent and blown dry with N$_2$; then, the PDMS mold was placed in contact with the as-cleaned quartz substrate to print the self-assembled PFOTS monolayer (SAM). Next, the patterned substrate was used as a template for the selective deposition of the metal salts solution by spin-coating. During this spin-coating process, the precursor solution was selectively deposited on the hydrophilic regions because of the poor adhesion between the solution and the SAM. Finally, the substrate with the patterned gel was calcined to obtain the crystalline YVO$_4$:Eu^{3+} film. The optical microscopy image in Fig. 2.18b shows an ordered dot-patterned YVO$_4$:Eu^{3+} precursor gel arrays were transferred from the PDMS stamp to the quartz substrate by the μCP technique. After calcination, the patterned YVO$_4$:Eu^{3+} crystalline film was formed on the quartz plate and the corresponding optical microscope image is shown in Fig. 2.18c. Similarly, the calcination reduces the size of the dot gel spots owing to the pyrolysis and evaporation of the organic species and the edges of the calcined square spots are not as clear as that of the uncalcined gel spots because of the shrinkage during the heat treatment process. Under 254 nm UV light excitation, the patterned YVO$_4$:Eu^{3+} thin film phosphors show bright red light emission, as shown in Fig. 2.18d. The CL spectra of patterned YVO$_4$:Eu^{3+} films in Fig. 2.18e also
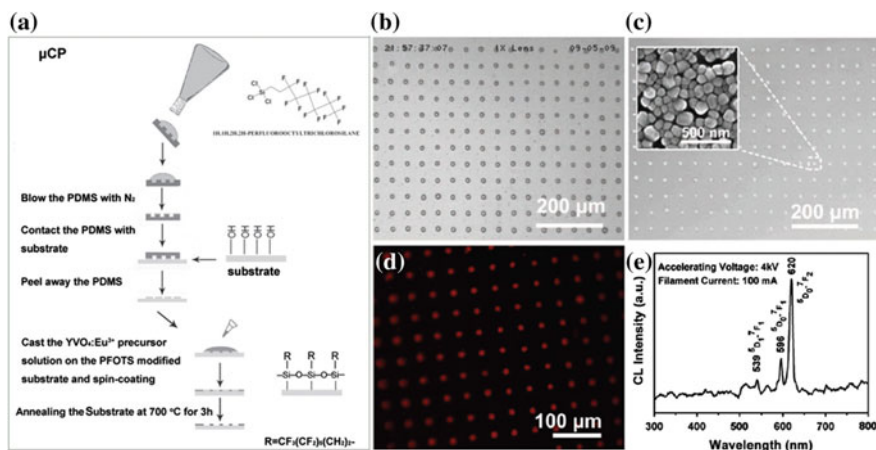
Fig. 2.18 **a** Schematic diagram of the experimental microcontact printing (μCP) process used for patterning YVO$_4$:Eu^{3+} films. Optical image of the patterned YVO$_4$:Eu^{3+} precursor gel film fabricated by **b** μCP, **c** after calcination at 700 °C, and **d** the corresponding luminescent image under 254-nm UV light excitation. The *inset* in **c** SEM image of the patterned YVO$_4$:Eu^{3+} film, indicative of the morphology of the crystalline YVO$_4$:Eu^{3+} particles after firing at 700 °C. **e** The CL spectra of the patterned YVO$_4$:Eu^{3+} film. Adapted from Ref. [114] by permission of Wiley

shows the characteristic Eu^{3+} emission at 596 and 619 nm, which correspond to the Eu^{3+} transitions of $^5D_0$–$^7F_1$, and $^5D_0$–F$_2$, respectively.

Except for YVO$_4$:Eu^{3+}, many other kinds of patterned phosphor films, such as CaWO$_4$:Ln^{3+} (Ln = Tb, Eu), Gd$_2$(WO$_4$)$_3$:Ln^{3+} (Ln = Eu, Tb) were also prepared based on the μTM and μCP methods, indicating that soft-lithography (μTM and μCP) techniques could be used at all for the patterning of inorganic rare earth salts [115, 116]. These results demonstrate that the Pechini-type sol–gel process has a good compatibility with soft-lithography techniques for patterning inorganic phosphor materials, which holds potential for fabricating new-generation field emission display devices. Moreover, these results can guide us in future research and be helpful to others who have interest in these types of devices.

2.5 Summary and Outlook

Phosphors are irreplaceable components in FEDs devices. The exploring of highly efficient FEDs phosphors has been becoming the focus of realizing high-quality FED. This chapter has summarized the recent progress in chemical synthesis and improvement of FEDs phosphors including rare earth and transition metal ions activated inorganic solid-state luminescent materials, semiconductor-based luminescence materials, self-activated luminescent materials etc. The common strategies for the modifications and optimizations of morphology, size, composition,

conductivity of phosphors, and corresponding effects on their cathodoluminescent properties have also been outlined. Special emphases are mainly focused on the studies of selection of hosts and luminescent centers, enhancement of efficiency through energy transfer, adjustment and design of emission colors, improvement of color index and color gamut as well as color stability and degradation behavior of phosphors. Based on the above modifications and optimizations, the cathodoluminescent performances of phosphors like emission intensity, brightness, color purity, and degradation behaviors can be obviously improved, indicating potential application in full-color FEDs. In addition, single-phase white-light-emitting phosphors with excellent emission properties and tunable CIE chromaticity coordinates have also been developed through designing co-emission and energy transfer between hosts or RE ions and RE ions or Mn^{2+} ions, which are promising backlights in FEDs devices.

Although rapid progress have been achieved in the synthesis, properties, and applications of FEDs phosphors, developing better synthetic routes to further optimize the luminescent performances and more detailed fundamental studies of luminescent mechanisms have a level of urgency. Thus there are still much room for improvement in the future. First, further investigations for optimization the morphology, size, surface state and crystallization of FEDs phosphors need be exactly explored; Secondly, making the matrix maintain a proper electrical conductivity is also a difficult issue; Thirdly, exact degradation mechanism of phosphors under low-voltage electron beam bombardment should be further investigated; Fourthly, researchers with various backgrounds like electronic technology and process optimization may be needed to develop multicolor-system display units and color gamut enlarged phosphors. Finally, numerous efforts need to be made to further develop the single-phase white-emitting luminescence materials based on the energy transfer from sensitizer to activator to contain the advantages of a controllability of emission colors and high luminous efficiency. In addition, the processes and methods for preparing phosphor thin films and screen should be optimized. From a long-term point of view, some emerging phosphors like defect-related environment-friendly phosphors that have high luminous efficiency should be actively explored to open the door to novel display applications. From the point of view of application, the development of highly efficient low-voltage FEDs phosphors might not only promote their application in daily display fields but also offer possibilities for FEDs devices into exploration, expedition, aviation, marine and military fields due to the perfect adaptation of some extremely harsh environment such as very cold or hot conditions. In summary, a large amount of newer improvement methods and novel low-voltage FEDs phosphors are still in the research stage. There is a long way in achieving the high-quality FED and thus need more efforts to pay attention to it.

References

1. Waser, R (2003) Nanoelectronics and Information Technology. chapter 39, Wiley-Vch, Weinheim, Germany
2. Holloway, PH, Trottier, TA, Abrams B, Kondoleon C, Jones SL, Sebastian JS, Thomes WJ, Swart H (1999) Advances in field emission displays phosphors. J Vac Sci Technol B 17: 758–764
3. Höppe, HA (2009) Recent Developments in the Field of Inorganic Phosphors. Angew Chem Int Ed 48: 3572–3582,
4. Jüstel T, Nikol H, Ronda C (1998) New Developments in the Field of Luminescent Materials for Lighting and Displays. Angew Chem Int Ed 37: 3084–3103
5. Hao JH, Gao J, Cocivera M (2003) Green, blue, and yellow cathodoluminescence of $Ba_2B_5O_9Cl$ thin-films doped with Tb^{3+}, Tm^{3+}, and Mn^{2+}. Appl Phys Lett 82: 2224–2226
6. Liu TC, Kominami H, Greer HF, Zhou W, Nakanishi Y, Liu RS (2012) Blue emission by interstitial site occupation of Ce^{3+} in AlN. Chem Mater 24: 3486–3492
7. Zhang QH, Wang J, Yeh CW, Ke WC, Liu RS, Tang JK, Xie MB, Liang HB, Su Q (2010) Structure, composition, morphology, photoluminescence and cathodoluminescence properties of $ZnGeN_2$ and $ZnGeN_2:Mn^{2+}$ for field emission displays. Acta Mater 58: 6728–6735
8. Zhang S, Liang HB, Liu CM, Qi ZM, Shao T, Wang YY (2013) High color purity red-emission of $NaGdTiO_4:Pr^{3+}$ Via quenching of $^3P_0$ emission under low-voltage cathode ray excitation. Opt Lett 38: 612–614
9. Jing YD, Zhang F, Summers CJ, Wang ZL (1999) Synthesis and properties of Sr_2CeO_4 blue emission powder phosphor for field emission displays. Appl Phys Lett 74: 1677–1679
10. Itoh M, Ozawa L (2006) Cathodoluminescent phosphors. Annu Rep Prog Chem Sect C 102:12–42
11. Han JI, Kwak MG, Park YK, Lim SC, Lee IK, Cho KI, Yoo HJ (1998) Experimental and theoretical considerations on evacuation of vacuum package for field emission display. J Vac Sci Technol B 16: 1236–1238
12. Psuja P, Hreniak D, Strek W (2007) Rare-Earth Doped Nanocrystalline Phosphors for Field Emission Displays. J Nanomater 2007: 81350
13. Wang ZL, Chan HLW, Li HL, Hao JH (2008) Highly efficient low-voltage cathodoluminescence of $LaF_3 :Ln^{3+}$ (Ln = Eu^{3+}, Ce^{3+}, Tb^{3+}) spherical particles. Appl Phys Lett 93: 141106
14. Sharma AK, Son KH, Han BY, Sohn KS (2010) Simultaneous optimization of luminance and color chromaticity of phosphors using a nondominated sorting genetic algorithm. Adv Funct Mater 20: 1750-1755
15. Blasse G, Grabmaier BC (1994) Luminescence Materials (Springer-Verlag, Berlin, Heideberg), ch. 4–5
16. Shi L, Huang YL, Seo HJ (2010) Emission Red Shift and Unusual Band Narrowing of Mn^{2+} in $NaCaPO_4$ Phosphor. J Phys Chem A 114: 6927–6934
17. Liu XM, J. Lin (2007) Enhanced luminescence of gadolinium niobates by Bi^{3+} doping for field emission displays. J Lumin 122–123: 700–703
18. Yamashita T, Ueda K (2007) Blue photoluminescence in Ti-doped alkaline-earth stannates. J Solid State Chem 180: 1410–141319
19. Hou ZY, Li GG, Lian HZ, Lin J (2012) One-dimensional luminescent materials derived from the electrospinning process: preparation, characteristics and application. J Mater Chem 22: 5254–5276
20. Shang MM, Li GG, Yang DM, X. J. Kang, Peng C, Lin J (2012) Luminescence properties of Mn^{2+}-doped Li_2ZnGeO_4 as an efficient green phosphor for field-emission displays with high color purity. Dalton Trans 41: 8861–8868

21. Zhang F L, Yang S, Stoffers C, Penczek J, Yocom PN, Zaremba D, Wagner BK, Summers CJ (1998) Low voltage cathodoluminescence properties of blue emitting $SrGa_2S_4$: Ce^{3+} and ZnS:Ag,Cl phosphors. Appl Phys Lett 72: 2226–2228.

22. Vecht A, Gibbons C, Davies D, Jing X, Marsh P, Reland T, Silver J, Nowport A, Barber D (1999) Engineering phosphors for field emission displays. J Vac Sci Technol B 17: 750–757

23. Guo P, Zhao F, Li G, Liao F, Tian S, Jing X (2003) Novel phosphors of Eu^{3+}, Tb^{3+} or Bi^{3+} activated Gd_2GeO_5. J Lumin 105: 61–67

24. Nagpure IM, Pitale SS, Coetsee E, Ntwaeaborwa OM, Terblans JJ, Swart HC (2011) Low voltage electron induced cathodoluminescence degradation and surface characterization of $Sr_3(PO_4)_2$:Tb phosphor. Appl Surf Sci 257: 10147–10155

25. Srivastava AM, Ronda CR (2003) Phosphors. Electrochem Soc Interface 12: 48–51

26. Liu X, Lin C, Lin J (2007) White light emission from Eu^{3+} in $CaIn_2O_4$ host lattices. Appl Phys Lett 90: 081904

27. Wakefield G, Holland E, Dobson P J, Hutchison JL (2000) Luminescence properties of nanocrystalline Y_2O_3:Eu. Adv Mater 13: 1557–1560

28. Yang SH, Hsueh TJ, Chang SJ (2005) Cathodoluminescence of a white $ZnGa_2O_4$/ZnO phosphor screen. J Electrochem Soc 152: H191–H195

29. Jang HS, Kang JH, Won YH, Lee S, Jeon DY (2007) Mechanism for strong yellow emission of $Y_3Al_5O_{12}$:Ce^{3+} phosphor under electron irradiation for the application to field emission backlight units. Appl Phys Lett 90: 071908

30. Li GG, Zhang X, Peng C, Shang MM, Geng DL, Cheng ZY, Lin J (2011) Cyan-emitting Ti^{4+}- and Mn^{2+}-coactivated Mg_2SnO_4 as a potential phosphor to enlarge the color gamut for field emission display. J Mater Chem 21: 6477–6479

31. Lin CH, Chiou BS, Chang CH, Lin JD (2003) Preparation and cathodoluminescence of ZnO phosphor. Mater Chem Phys 77: 647–654

32. Li GG, Peng C, Li CX, Yang PP, Hou ZY, Fan Y, Lin J (2009) Shape-controllable synthesis and morphology-dependent luminescence properties of GaOOH:Dy^{3+} and β-Ga_2O_3:Dy^{3+}. Inorg Chem 49: 1449–1457

33. Xu XG, Chen J, Deng SZ, Xu NS, Lin J (2010) Cathodoluminescent properties of nanocrystalline $Lu_3Ga_5O_{12}$:Tb^{3+} phosphor for field emission display application. J Vac Sci Technol B 28: 490–494

34. Liu BD, Bando Y, Dierre B, Sekiguchi T, Tang CC, Mitome M, Wu AM, Jiang X, Golberg D (2009) The synthesis, structure and cathodoluminescence of ellipsoid-shaped $ZnGa_2O_4$ nanorods. Nanotechnology 20: 365705–365711

35. Liu XM, Li CX, Quan ZW, Cheng ZY, Lin J (2007) Tunable Luminescence Properties of $CaIn_2O_4$:Eu^{3+} Phosphors. J Phys Chem C 111: 16601–16607

36. Liu XM, Lin CK, Luo Y, Lin J (2007) Host-sensitized luminescence of Dy^{3+}, Pr^{3+}, Tb^{3+} in polycrystalline $SrIn_2O_4$ for field emission displays. J Electrochem Soc 154: J21–J27

37. Jiao H, Wang JG, Liao FH, Tian SJ, Jing XP (2004) Cathodoluminescence of Eu^{3+}, Tb^{3+}, and Tb^{3+}-Eu^{3+} pair-activated $Zn_3Ta_2O_8$. J Electrochem Soc 151: H49–H51

38. Shang MM, Li GG, Yang DM, Kang XJ, Peng C, Cheng ZY, Lin J (2011) $(Zn, Mg)_2GeO_4$: Mn^{2+} submicrorods as promising green phosphors for field emission displays: hydrothermal synthesis and luminescence properties. Dalton Trans 40: 9379–9387

39. Xu XR, Su MZ (2014) Luminescence Science, Luminescent Materials (in Chinese); Chemical Industry Publisher: Beijing

40. Li GG, Hou ZY, Peng C, Wang WX, Cheng ZY, Li CX, Lian HZ, Lin J (2010) Electrospinning derived one-dimensional LaOCl:Ln^{3+} (Ln = Eu/Sm, Tb, Tm) nanofibers, nanotubes and microbelts with multicolor-tunable emission properties. Adv Funct Mater 20: 3446–3456

41. Li GG, Li CX, Zhang CM, Cheng ZY, Quan ZW, Peng C, Lin J (2009) Tm^{3+} and/or Dy^{3+} doped LaOCl nanocrystalline phosphors for field emission displays. J Mater Chem 19: 8936–8943

42. Li GG, Peng C, Zhang CM, Xu, ZH, Shang MM, Yang DM, Kang XJ, Wang WX, Li CX, Cheng ZY, Lin J (2010) Eu^{3+}/Tb^{3+}-doped $La_2O_2CO_3$/La_2O_3 nano/microcrystals with

multiform morphologies: facile synthesis, growth mechanism, and luminescence properties. Inorg Chem 49: 10522–10535

43. Liu XM, Y. Luo, Lin J (2006) Synthesis and characterization of spherical Sr_2CeO_4 phosphors by spray pyrolysis for field emission displays, J Crystal Growth 290: 266–271

44. Geng DL, Li GG, Shang MM, Peng C, Zhang Y, Cheng ZY, Lin J (2012) Nanocrystalline $CaYAlO_4:Tb^{3+}/Eu^{3+}$ as promising phosphors for full-color field emission displays. Dalton Trans 41: 3078–3086

45. Zhang Y, Geng DL, Shang MM, X. Zhang, Li XJ, Cheng ZY, Lian HZ, Lin J (2013) Soft-chemical synthesis and tunable luminescence of Tb^{3+}, Tm^{3+}/Dy^{3+}-doped SrY_2O_4 phosphors for field emission displays. Dalton Trans 42: 4799–4808

46. Mao YB, Tran T, Guo X, Huang JY, Shih K Wang KL, Chang JP (2009) Luminescence of nanocrystalline erbium-doped yttria. Adv Funct Mater 19: 748–754

47. Lin J, Yu M, Lin CK, Liu XM (2007) Multiform oxide optical materials via the versatile Pechini-type Sol-Gel process: synthesis and characteristics. J Phys Chem C 111: 5835–5845

48. Liu XM, Zou J P, Lin J (2009) Nanocrystalline $LaAlO_3:Sm^{3+}$ as a promising yellow phosphor for field emission displays. J Electrochem Soc 156: P43–P47

49. Liu XM, Lin J (2007) Nanocrystalline $LaGaO_3:Tm^{3+}$ as an efficient blue phosphor for field emission displays with high color purity. Appl Phys Lett 90: 184108

50. Liu XM, ZhuL, Wang LL, Yu CC, Lin J (2008) Synthesis and luminescent properties of $Lu_3Ga_5O_{12}:RE^{3+}$ (RE = Eu, Tb, and Pr) nanocrystalline phosphors via sol-gel process. J Electrochem Soc 155: P21-P27

51. Li GG, Xu XG, Peng C, Shang MM, Geng DL, Cheng ZY, Chen J, Lin J (2011) Yellow-emitting $NaCaPO_4:Mn^{2+}$ phosphor for field emission displays. Opt Exp 19: 16423–16431

52. Geng DL, Shang MM, Zhang Y, Lian HZ, Lin J (2013) Color-tunable and white luminescence properties via energy transfer in single-phase $KNaCa_2(PO_4)_2:A$ (A = Ce^{3+}, Eu^{2+}, Tb^{3+}, Mn^{2+}, Sm^{3+}) phosphors. Inorg Chem 52: 13708–13718

53. Geng DL, Shang MM, Yang DM, Zhang Y, Cheng ZY, Lin J (2012) Tunable luminescence and energy transfer properties in $KCaGd(PO_4)_2:Ln^{3+}/Mn^{2+}$ (Ln = Tb, Dy, Eu, Tm; Ce, Tb/Dy) phosphors with high quantum efficiencies. J Mater Chem 22: 23789–23798

54. Shang MM, Geng DL, Yang DM, Kang XJ, Zhang Y, Lin J (2013) Luminescence and energy transfer properties of $Ca_2Ba_3(PO_4)_3Cl$ and $Ca_2Ba_3(PO_4)_3Cl:A$ (A = $Eu^{2+}/Ce^{3+}/Dy^{3+}/Tb^{3+}$) under UV and low-voltage electron beam excitation. Inorg Chem 52: 3102–3112

55. Shang MM, Geng DL, Zhang Y, Li GG, Yang DM, Kang XJ, Lin J (2012) Luminescence and energy transfer properties of $Ca_8Gd_2(PO_4)_6O_2:A$ (A = $Ce^{3+}/Eu^{2+}/Tb^{3+}/Dy^{3+}/Mn^{2+}$) phosphors. J Mater Chem 22: 19094–19104

56. Wakefield G, Williams DM, Harris CG, Dobson PJ (2000) Nanocrystalline phosphors for low voltage excitation applications. SID Symposium Digest of Technical Papers 31: 691-693

57. Jung HK, Sohn KS, Sung BY, Park HD (2000) High Luminance $Zn_2SiO_4:Mn$ phosphors prepared by homogeneous precipitation method. J Soc Inf Disp 1: 35-41

58. Silver J, Withnall R, Lipman A, Ireland TG, Fern GR (2007) Low-voltage cathodoluminescent red emitting phosphors for field emission displays. J Lumin 122-123: 562-566

59. Shang MM, Geng DL, Kang XJ, Yang DM, Zhang Y, Lin J (2012) Hydrothermal derived $LaOF:Ln^{3+}$ (Ln = Eu, Tb, Sm, Dy, Tm, and/or Ho) nanocrystals with multicolor-tunable emission properties. Inorg Chem 51: 11106–11116

60. Yang J, Li CX, Cheng ZY, Zhang XM, Quan ZW, Zhang CM, Lin J (2007) Size-tailored synthesis and luminescent properties of one-dimensional $Gd_2O_3:Eu^{3+}$ nanorods and microrods. J Phys Chem C 111: 18148–18154

61. Yang J, Zhang CM, Wang LL, Hou ZY, Huang SS, Lian HZ, Lin J (2008) Self-assembled 3D flowerlike Lu_2O_3 and $Lu_2O_3:Ln^{3+}$ (Ln = Eu, Tb, Dy, Pr, Sm, Er, Ho, Tm) microarchitectures: ethylene glycol-mediated hydrothermal synthesis and luminescent properties. J Phys Chem C 112: 12777-12785

62. Dong GP, Xiao XD, LiuXF, Qian B, Ma ZJ, Chen DP, Qiu JR (2009) Preparation and optical properties of long afterglow europium-doped Ca(Sr)Al$_2$Si$_2$O$_8$ electrospun nanofibers. J Electrochem Soc 156: J356–J360

63. Peng C, Hou ZY, Zhang CM, Li GG, Lian HZ, Cheng ZY, Lin J (2010) Synthesis and luminescent properties of CaTiO$_3$:Pr^{3+} microfibers prepared by electrospinning method. Opt Exp 18: 7543–7553

64. Song HW, Yu LX, Lu SZ (2005) Improved photoluminescent properties in one-dimensional LaPO$_4$:Eu^{3+} nanowires. Opt Lett 30: 483–485

65. Hou ZY, Yang PP, Li CX,Wang LL, Lian HZ, Quan ZW, Lin J (2008) Preparation and Luminescence Properties of YVO$_4$:Ln and Y(V, P)O$_4$:Ln (Ln = Eu^{3+}, Sm^{3+}, Dy^{3+}) Nanofibers and Microbelts by Sol-Gel/Electrospinning Process. Chem Mater 20: 6686–6696

66. Yu M, Lin J, Fang J (2005) Silica spheres coated with YVO$_4$:Eu^{3+} layers via Sol-Gel process: A simple method to obtain spherical core-shell phosphors. Chem Mater 17: 1783–1791

67. Stöber W, Fink A, Bohn E (1968) Controlled growth of monodisperse silica spheres in the micron size range. J Colloid Interface Sci 26: 62–69

68. Lin CK, Kong DY, Liu XM, Wang H, Yu M, Lin J (2007) Monodisperse and Core-Shell-Structured SiO$_2$@YBO$_3$:Eu^{3+} Spherical Particles: Synthesis and Characterization. Inorg Chem 46: 2674–2681

69. Tan SY, Yang PP, Li CX, Wang WX, Wang J, Zhang ML, Jing XY, Lin J (2010) Preparation, characterization and luminescent properties of spherical CaTiO$_3$:Pr^{3+} phosphors by spray pyrolysis. Solid State Sci 12: 624–629

70. Jung KY, Kim EJ, Kang YC (2004) Morphology control and optimization of luminescent property of YBO$_3$:Tb phosphor particles prepared by spray pyrolysis. J Electrochem Soc 151: H69-H73

71. Liu XM, Lin J (2008) LaGaO$_3$:A (A = Sm^{3+} and/or Tb^{3+}) as promising phosphors for field emission displays. J Mater Chem 18: 221–228

72. Shang MM, Li GG, Yang DM, Kang XJ, Zhang CM, Lin J (2011) Red emitting Ca$_2$GeO$_4$: Eu^{3+} phosphors for field emission displays. J Electrochem Soc 158: J125–J131

73. Yang SH (2004) Indium- and tungsten-doped ZnGa$_2$O$_4$ phosphor. J Electron Mater 33: L1-L4

74. Kim JY, Jeon DY, Yu I, Yang HG (2000) A study on correlation of low voltage cathodoluminescent properties with electrical conductivity of In$_2$O$_3$-coated ZnGa$_2$O$_4$:Mn phosphors. J Electrochem Soc 147: 3559-3563

75. Xie LP, Song HW, Wang Y, Xu W, Bai X, Dong B (2010) Influence of concentration effect and Au coating on photoluminescence properties of YVO$_4$:Eu^{3+} nanoparticle colloids. J Phys Chem C 114: 9975-9980

76. Zhang MC, Wang XJ, Ding H, Li HL, Pan LK, Sun Z (2011) The enhanced low-voltage cathodoluminescent properties of spherical Y$_2$O$_3$:Eu^{3+} phosphors coated with In$_2$O$_3$ and its application to field-emission displays. Int J Appl Ceram Technol 8: 752–758

77. Do YR, Park DH, Yang HG, Park W, Wagner BK, Yasuda K, Summers CJ (2001) Uniform nanoscale SiO$_2$ encapsulation of ZnS phosphors for improved aging properties under low voltage electron beam excitation. J Electrochem Soc 148: G548-G551

78. Pitale SS, Kumar V, Nagpure IM, Ntwaeaborwa OM, Coetsee E, Swart HC (2011) Cathodoluminescent properties and surface characterization of bluish-white LiAl$_5$O$_8$:Tb phosphor. J Appl Phys 109: 013105

79. Holloway PH, Swart HC, Ntwaeaborwa OM (2013) Electro-stimulated surface chemical reactions on phosphors. J Vac Sci Technol A 31, 050808.

80. Rag D, Park D, Kim Y (2004) Al$_2$O$_3$ Nanoencapsulation of BaMgAl$_{10}$O$_{17}$: Eu^{2+} phosphors for improved aging properties in plasma display panels. J Electrochem Soc 151: H210-H212

81. Song YH, Xu XC, Zou HF, Sheng Y, You HP (2012) MSi$_2$O$_{2-\delta}$N$_{2+2/3\delta}$:Eu (M = Sr, Ba) phosphors for field emission displays. J Alloys Comp 513: 86-90

82. Hetaba W, Mogilatenko A, Neumann W (2010) Electron beam-induced oxygen desorption in γ-LiAlO$_2$. Micron 41: 479-483

83. Li GG, Li CX, Hou ZY, Peng C, Lin J (2009) Nanocrystalline LaOCl: Tb^{3+}/Sm^{3+} as promising phosphors for full-color field-emission displays. Opt Lett 34: 3833–3835

84. Hirosaki N, Xie RJ, Inoue K, Sekiguchi T, Dierre B, Tamura K (2007) Blue-emitting AlN: Eu^{2+} nitride phosphor for field emission displays. Appl Phys Lett 91: 061101

85. Xie MB, Liang HB, Su Q, HuangY , Gao ZH, Tao Y (2011) Intense cyan-emitting of $Li_2CaSiO_4:Eu^{2+}$ under low-voltage cathode ray excitation. Electrochem Solid-State Lett 14: J69-J72

86. Wang DY, Huang CM, Wu YC, Chen TM (2011) $BaZrSi_3O_9:Eu^{2+}$: A cyan-emitting phosphor with high quantum efficiency for white light-emitting diodes. J Mater Chem 21: 10818-10822

87. Bachmann V, Ronda C, Ceckler O, Schnick W, Meijerink A (2009) Color point tuning for $(Sr,Ca,Ba)Si_2O_2N_2:Eu^{2+}$ for white light LEDs. Chem Mater 21: 316-325

88. Li GG, Peng C, Li CX, Yang PP, Hou ZY, FanY, Lin J (2011) Tunable luminescence of Ce^{3+}/Mn^{2+}-coactivated $Ca_2Gd_8(SiO_4)_6O_2$ through energy transfer and modulation of excitation: Potential single-phase white/yellow-emitting phosphors. J Mater Chem 21: 13334–13344

89. Huang CM, Wu PJ, Lee JF, Chen TM (2011) $(Ca,Mg,Sr)_9Y(PO_4)_7:Eu^{2+},Mn^{2+}$: Phosphors for white-light near-UV LEDs through crystal field tuning and energy transfer. J Mater Chem 21: 10489–10495

90. Liu XM, Yan LS, Lin J (2009) Tunable photoluminescence and cathodoluminescence properties of Eu^{3+}-doped $LaInO_3$ nanocrystalline phosphors. J Electrochem Soc 156: P1–P6

91. Li GG, Geng DL, Shang MM, Zhang Y, Peng C, Cheng ZY, Lin J (2011) Color tuning luminescence of $Ce^{3+}/Mn^{2+}/Tb^{3+}$-triactivated $Mg_2Y_8(SiO_4)_6O_2$ via energy transfer: Potential single-phase white-light-emitting phosphors. J Phys Chem C 115: 21882–21892

92. Shang MM, Li CX, Lin J (2013) How to produce white light in a single-phase host? Chem Soc Rev 43: 1372-1386

93. Caldiño U (2003) On the Ce-Mn clustering in CaF_2 in which the $Ce^{3+} \rightarrow Mn^{2+}$ energy transfer occurs. J Phys Condens Matter 15: 3821–3830

94. Zhang CM, Huang SS, Yang DM, Kang XJ, Shang MM, Peng C, Lin J (2010) Tunable luminescence in Ce^{3+}, Mn^{2+}-codoped calcium fluorapatite through combining emissions and modulation of excitation: A novel strategy to white light emission. J Mater Chem 20: 6674–6680

95. Huang CM, Chen TM (2011) A novel single-composition trichromatic white-light $Ca_3Y(GaO)_3(BO_3)_4:Ce^{3+},Mn^{2+},Tb^{3+}$ phosphor for UV-light emitting diodes. J Phys Chem C 115: 2349–2355

96. Geng DL, Li GG, Shang MM, Yang DM, Zhang Y, Cheng ZY, Lin J (2012) Color tuning via energy transfer in $Sr_3In(PO_4)_3:Ce^{3+}/Tb^{3+}/Mn^{2+}$ phosphors. J Mater Chem 22: 14262–14271

97. Liu YF, Zhang X, Hao ZD, Wang XJ, Zhang JH (2011) Tunable full-color-emitting $Ca_3Sc_2Si_3O_{12}:Ce^{3+}$, Mn^{2+} phosphor via charge compensation and energy transfer. Chem Commun 47: 10677-10679

98. Choe JY, Ravichandran D, Biomquist SM, Morton DC, Kirchner KW, Ervin MH, Lee U (2001) Alkoxy sol-gel derived $Y_{3-x}Al_5O_{12}:Tb_x$ thin films as efficient cathodoluminescent phosphors. Appl Phys Lett 78: 3800–3802

99. Li W, Mao DS, Zhang FM, Liu XH, Zou SC, Zhu YK, Li Q, Xu JF (2000) ZnO:Zn phosphor thin films prepared by ion beam sputtering. J Vac Sci Technol A 18: 2295–2301

100. Yum JH, Sung YE (2004) Full color screen by EPD combined with photolithography for flat panel displays. J Electrochem Soc 151: H27–H32.

101. Yu M, Lin J, Wang Z, Fu J, Wang S, Zhang HJ, Han YC (2002) Fabrication, patterning, and optical properties of nanocrystalline $YVO_4:A$ ($A = Eu^{3+}$, Dy^{3+}, Sm^{3+}, Er^{3+}) phosphor films via Sol-Gel soft lithography. Chem Mater 14: 2224–2231

102. Yu M, Lin J, Fu J, Zhang HJ, Han YC (2003) Sol–gel synthesis and photoluminescent properties of $LaPO_4:A$ ($A = Eu^{3+}$, Ce^{3+}, Tb^{3+}) nanocrystalline thin films. J Mater Chem 13: 1413–1419

103. Pang ML, Shen WY, Lin J (2005) Enhanced photoluminescence of Ga_2O_3:Dy^{3+} phosphor films by Li^+ doping. J Appl Phys 97: 033511

104. Jang JE, Gwak JH, Jin YW, Lee SJ, Park SH, Jung JE, Lee NS, Kim JM (2000) High resolution phosphor screening method for full-color field emission display applications. J Vac Sci Technol B 18: 1106–1110

105. Ying GY, Hu WB, Qiu Y (2002) In The Technology of Flat Panel Displays; Fu, J. Ed.; Post & Telecom Press: Bejing, China

106. Xia Y, Whiteside GM (1998) Soft lithography. Annu Rev Mater Sci 28: 153–184

107. Pang ML, Lin J, Cheng ZY, Fu J, Xing RB, Wang SB (2003) Patterning and luminescent properties of nanocrystalline Y_2O_3:Eu^{3+} phosphor films by sol–gel soft lithograph. Mater Sci Eng B 100: 124–131

108. Pang ML, Lin J, Fu J, Xing RB, Luo CX, Han YC (2003) Preparation, patterning and luminescent properties of nanocrystalline Gd_2O_3:A (A = Eu^{3+}, Dy^{3+}, Sm^{3+}, Er^{3+}) phosphor films via Pechini sol-gel soft lithography. Opt Mater 23: 547–558

109. Cheng ZY, Xing RB, Hou ZY, Huang SS, Lin J (2010) Patterning of light-emitting YVO_4:Eu^{3+} thin films via ink-jet printing. J Phys Chem C 114: 9883–9888

110. Tekin E, Smith PJ, Schubert US (2008) Inkjet printing as a deposition and patterning tool for polymers and inorganic particles. Soft Mater 4: 703–713

111. Singh M, Haverinen HM, Dhagat P, Jabbour GE (2010) Inkjet printing-process and its applications. Adv Mater 22: 673–685

112. Xia YJ, Friend RH (2007) Nonlithographic patterning through inkjet printing via holes. Appl Phys Lett 90: 253513

113. Dijksman JF, Duineveld PC, Hack MJJ, Pierik A, Rensen J, Rubingh JE, Schram I, Vernhout MM (2007) Precision ink jet printing of polymer light emitting displays. J Mater Chem 17: 511–522

114. Wang WX, Cheng ZY, Yang PP, Hou ZY, Li CX, Li GG, Dai YL, Lin J (2011) Patterning of YVO_4:Eu^{3+} luminescent films by soft lithography. Adv Funct Mater 21: 456–463

115. Wang WX, Yang PP, Cheng ZY, Hou ZY, Li CX, Lin J (2011) Patterning of red, green, and blue luminescent films based on $CaWO_4$:Eu^{3+}, $CaWO_4$:Tb^{3+}, and $CaWO_4$ phosphors via microcontact printing route. ACS Appl Mater & Interfaces 3: 3921–3928

116. Wang D, Yang PP, Cheng ZY, Wang WX, Hou ZY, Dai YL, Li CX, Lin J (2012) Patterning of $Gd_2(WO_4)_3$:Ln^{3+} (Ln = Eu, Tb) luminescent films by microcontact printing route. J Coll Inter Sci 365: 320–325

Chapter 3
Phosphors with a 660-nm-Featured Emission for LED/LD Lighting in Horticulture

Dajian Wang, Zhiyong Mao and B.D. Fahlman

Abstract Photosynthetically active radiation (PAR) of lighting sources is a prerequisite to match well with the absorption spectrum of photoreceptors in plants. Light-emitting diodes (LED) or laser diodes (LD) or its combination with phosphor can be used to construct the 660-nm-featured simultaneous emission of both red and blue light for PAR. A variety of rare earth (RE) ion-doped phosphors such as nitride, silicate, sulfide allow a 660-nm-peaked broadband emission with proper composition and preparation, as illustrated by a highly efficient $A_3MgSi_2O_8$ (AMS, A = Ba, Sr, Ca) phosphor with a dual band emission at both 660 and 430 nm. These phosphors are excitable by sunlight, near ultraviolet (NUV), blue LED, or LD light sources as applied in the forms of particle, film, or transparent ceramics, providing a great potential to construct the artificial lighting sources in the closed, open, or their combined cultivation system with a customized, precise composition of light to achieve high photosynthetic efficiency.

3.1 Introduction

Photosynthesis is that some living organisms such as plants and algae gather and convert the harvested energy into chemical energy, which is the oldest but is the most important biochemical reaction on earth [1, 2]. Photosynthesis produces oxygen (O_2) and biomass in the form of carbohydrates such as glucose ($C_6H_{12}O_6$) by decomposing water (H_2O) and reducing carbon dioxide (CO_2) in the atmosphere. The incident energy of solar radiation is harvested by specific photoreceptors such as

D. Wang (✉) · Z. Mao · B.D. Fahlman
School of Materials Science and Engineering, Tianjin University of Technology,
Tianjin 300384, People's Republic of China
e-mail: djwang@tjut.edu.cn

Z. Mao
e-mail: mzhy1984@163.com

B.D. Fahlman
e-mail: fahlm1b@cmich.edu

chlorophylls in plants or algae. The maximum conversion efficiency of this natural photosynthesis is as low as to be 4.6–6 % [3]. Artificial photosynthesis [4–6] tends to mimic the natural process of photosynthesis via plants or artificial leaf [7–9], algae [10, 11], and bacteria by splitting water into hydrogen or solidifying carbon dioxide into carbohydrates by taking use of artificial lighting sources with higher efficiency.

Photosynthetically active radiation (PAR) in the incident energy of light toward photosynthesis is generally defined as the portion of the solar spectrum extending from 400 to 700 nm [12, 13], even though this wavelength range is still controversial owing to the newly discovered red-shifted chlorophyll photoreceptor [14] and some new observations on the roles of yellow-green [15, 16] and ultraviolet light [17]. PAR is critical for photosynthesis as it offers energy source used by plants for photosynthesis reactions that partially convert physical solar energy into bioenergy-carrying biomass. The flux density-based PAR is defined as photosynthetic photon flux densities (PPFD) [18].

The photosynthetic pigments such as chlorophylls and carotenoids are closely relevant to light harvesting and energy transduction during photosynthesis. Chlorophylls have maximum sensitivities in the blue and red regions, around 300–400 and 600–700 nm, respectively. Carotenoids such as xanthophylls and carotenes absorb mainly blue light and are thought as auxiliary photoreceptors of chlorophyll.

Cryptochromes are verified to be blue, ultraviolet-A photoreceptors [19] that have capability to sense and respond to blue light (400–500 nm) throughout the biological kingdom. Blue- and ultraviolet-A-sensitive photoreceptors are observed in the cryptochrome signal transduction system. Such responses include the production of anthocyanins and carotenoids in plants and fungi and the entrainment of behavioral rhythms in flies and mammals. UV-B plays a role in affecting the growth and development of plants [17].

The phytochrome photosystem consists of the two interconvertible forms of phytochromes, P_r and P_{fr}, with their respective sensitivity peaks in the red region at 660 nm and in the far-red (700- to 800-nm) region at 730 nm. Photomorphogenetic responses controlled by phytochromes are usually related to the red (R)/far-red (FR) ratio (R/FR) [14, 20]. In particular, the long-wavelength light excitation at 660 nm in red band (640–660 nm) results in a maximum photosynthetic efficiency, coinciding closely with the absorption bands of chlorophyll a and chlorophyll b [21], while that at above ~680 nm the quantum yield declines rapidly, i.e., Emerson's effect [22]. It is indicated that from Emerson's effect, only slight shift of peak wavelength at red band emission in a scale from 10 to 20 nm for LED or packaged phosphor may impact greatly the maximum absorbance of chlorophylls and photosynthetic efficiency.

Although it is known that the photosynthesis efficiency drops rapidly under the long-wavelength light excitation above 680 nm, it is also found that the initial fall is replaced by an unexpected increase at much longer wavelengths, so that a detectable O_2 evolution is remained till 780 nm. The quantum yield of O_2 evolution at the local maximum at 745 nm reaches almost 20 % of the yield at 650 nm. The extreme long-wavelength chlorophylls are probably present in the intact

photosystem II antenna system, similar to photosystem I [23]. More specifically, the effects of different red (660 ± 30 nm)/far-red (730 ± 30 nm) radiation ratios (R/FR) on the photosynthetic characteristics and chlorophyll fluorescence parameters play important roles to achieve the high photosynthesis efficiency [24, 25]. The effects of yellow-green (500- to 600-nm) light on plant development have not been well established [15, 16]. It was found that yellow (580- to 600-nm) light appears to inhibit lettuce growth by suppressing chlorophyll or chloroplast formation, while it was also observed that green light can revert the blue light-stimulated stomatal opening. In general, the existing knowledge supports the conclusion that green light sensory systems adjust the development and growth together with red and blue photoreceptors. Therefore, the combination of simultaneous red and blue light is vital for effective photosynthetic reactions, but does not alone provide the ultimate solution for the optimal growth of some specific plants. To achieve the maximum photosynthetic yield, an even distribution of absorbed light quanta between the photosystem is also required [23]. To trade off both the photosynthetically efficient irradiation for photosynthetic pigments in plants and vision-friendly lighting for human's eyes, the combination of multi-wavelength chip-typed LEDs is proposed by using four-package purplish white LEDs (630, 590, 520, and 450 nm) [26] or even five-wavelength (405, 460, 630, 660, and 735 nm) LEDs with a uniformly distributed spectral PFD (SPFD) [27].

Similar to the sunlight energy, many artificial illumination sources such as commonly used incandescent and fluorescent lamps for plant illumination suffer not only spectral mismatch, but also high energy consumption or environmental threat. Meanwhile, the energy-saving, environmental-friendly light-emitting diodes (LEDs) in solid-state lighting emerge recently as a very effective means to achieve the specific PAR in the year-around horticulture. LEDs play a variety of roles in horticultural lighting, including the use in controlled environment research, lighting for tissue culture, and supplemental and photoperiod lighting for greenhouses or called plant factory and 'vertical farm' in the future [28]. In principle, LED lighting systems have several unique advantages over existing horticultural lighting, including the ability to control spectral composition, the ability to produce very high light levels with low radiant heat output if cooled properly, and the ability to maintain useful light output for years without replacement. LEDs are the first light source to have the capability of true spectral composition control, allowing wavelengths to be matched to plant photoreceptors to provide more optimal production and to influence the plant morphology and composition.

Light-emitting diodes (LEDs) in solid-state lighting have gained wide applications in horticultural lighting in decades. Those semiconductor lighting devices generally use a combination of individual red (AlGaInP) and blue (AlInGaN) chip LEDs to construct PAR for plants. The 'light recipe' in horticulture refers to lighting aspects (spectrum, light level), required uniformity, position and duration, environmental aspects such as climate conditions, and expected results besides energy saving. The spectral influence of light on plant development has long been

investigated [1, 19], but was not understood fully, due to the complexity of the mechanisms mediating the plant responses to light and the differences among diversified plant species. In this chapter, we pay close attention to lighting aspects in specific spectrum requirements of several phosphors relevant to PAR in light recipe.

The issues of the presently used red and blue LED combination mainly include different working lifetimes of LEDs having different emission wavelengths, where the highest reported values of internal quantum efficiencies (QE) are plotted against wavelength for blue- and near ultraviolet-emitting LEDs, and it is apparent that the highest efficiencies are in the 380- to 410-nm range, allowing for the fact that the latter is based on external QE values; it appears that in addition to the green window, there is also a problem with blue and UV InGaN LED performance at wavelengths shorter than 360 nm in the near ultraviolet region of the electromagnetic spectrum.

For the purpose of lighting in horticulture, there are some drawbacks by using only these two kinds of LEDs without phosphor conversion (pc). A relatively broad wavelength red emission of RE ion-doped phosphor covers well the absorption spectrum of plants, compared with the narrow spectrum band of costly AlGaInP red chips. A broad excitation band of RE ion-doped phosphor easily avoids the problems of the efficiency and temperature dependence of the emission wavelength of AlGaInP red and InGaN blue LEDs as well. One blue or NUV chip-excited phosphor conversion lighting overcomes the inconsistence of forward bias driving current in between red and blue chips. The production of AlGaInP/GaAs red chips consumes much rare metal sources and produces toxic exhaust emission, allowing the blue- or UV-excitable red-emitting phosphor to be developed.

Despite the great success in the present pc-LED architecture, blue LEDs have another well-known limitation: a nonthermal drop in efficiency with increasing input power density, namely 'efficiency droop.' This droop limits operation to relatively lower input power densities, and thus, it is hard to achieve high light level for artificial crops cultivation [31]. Therefore, laser diode (LD) of solid-state lighting (SSL) is expected to become next semiconductor lighting technology to be free of 'efficiency droop' with high light level.

Blue-emitting LED or LD is commercially available allowing a cost-effective excitation source for red-emitting phosphor to construct PAR. To advance the cost-effective lighting in horticulture with semiconducting devices, an option of phosphor conversion (pc) typed light sources with adjustable band breadth and intensity ratio of PAR. Fortunately, there is large quantity of phosphor candidates available for that 660-nm-featured broadband emitter to construct PAR for horticulture lighting. In principle, any red-emitting phosphors with the features mentioned above can be used. Those phosphors mainly include RE-doped inorganic hosts such as silicate, nitride, sulfide, phosphate, but we confine the contents more to silicate and sulfide as examples in this chapter.

3.2 The 660-nm-Featured Dually Emitting Silicate-Hosted Phosphor

An inorganic silicate host, $A_3MgSi_2O_8$ (AMS, A = Ba, Sr, Ca), has drawn a long-lasting, intensive interest of the researchers in phosphor development, due to its high quantum efficiencies (η) of phosphor, e.g., η = 80 % for BMS-Eu (E) and 60 % for SMS-E upon UV irradiation [32], and its abundant, nontoxic host materials. A red emitter of Mn ion has long been investigated by using lesser amount or the absence [33] of RE ions as sensitizers through well-recognized principle of energy transfer to Mn ion, e.g., Eu^{2+} (E), Ce^{3+} ions via host lattice.

A variety of compositions have been intensively investigated such as in $Sr_3MgSi_2O_8$: Eu^{2+}, Mn^{2+}, Dy^{3+}, $Ca_3MgSi_2O_8$: Ce^{3+}, Eu^{2+} [34], $(Sr,Ca)_2BaMg$ Si_2O_8: Ce^{3+}, Mn^{2+} [35], $BaCa_2MgSi_2O_8$: Eu [36], $(Sr,Ba)_3MgSi_2O_8$: Eu^{2+} [37], $Ba_3MgSi_2O_8$: Eu^{2+}, $Ba_3MgSi_2O_8$: Eu^{2+}, Mn^{2+} [38], $Sr_3MgSi_2O_8$: Eu^{2+} [39], $Ba_3MgSi_2O_8$: Eu^{2+}, Mn^{2+} [38, 40–43], $(Ba,Sr)_3MgSi_2O_8$: Eu^{2+} [44], $Sr_3MgSi_2O_8$: Eu [45, 46], (Ba, Sr, Ca)$_3MgSi_2O_8$: Eu^{2+} [47], $Sr_3MgSi_2O_8$: Eu^{2+}, Dy^{3+} [48], $Ca_3MgSi_2O_8$: Eu^{2+}, Dy^{3+} [49].

Because the sub-binary or ternary system in Ba–Sr–Ca of AMS does not exhibit simple complete solid solution in all composition range [50], there more likely exist some intermediate or metastable phases in as-prepared phosphors depending on the preparation process parameters and composition derivation. There exists some uncertainty or discrepancy with respect to the crystallographic structure of AMS host [36, 51–55] and the identification of a easily formed impurity phase (A_2SiO_4) coexisting with AMS host that is responsible for a highly efficient ~ 505-nm-peaked green band emission [56, 57].

By effectively suppressing the formation of green-emitting A_2SiO_4 host phase with the aid of flux addition [56, 58] or sol spray-combustion pyrolysis process [59–61] in the preparation, a simultaneous red/blue broadband emission and a LED prototype [43] by combining AMS: Eu^{2+}, Mn^{2+} (AMS-EM, A = Ba, Sr, Ca) phosphor with NUV chip were used to mimic the PAR. The 660-nm-featured red band emission for PAR other than 610–640 nm for human eye is of significance to achieve potentially the desired photosynthetic quantum yield.

3.2.1 Adjustable Control Of ~505-nm Emitting Phase

Figure 3.1 depicts the typical photoluminescence (PL) and photoluminescence excitation (PLE) spectrum of a $Ba_{1.24}Sr_{1.7}Mg_{0.9}Si_2O_8$: $0.06Eu^{2+}$, $0.1Mn^{2+}$ sample with an optimized composition, exhibiting a distinct band emission peaked at around 660 and 430 nm concurrently. A significant overlap is observed between PL of Eu^{2+} and the enlarged PLE of Mn^{2+}, indicating an occurrence of effective resonant energy transfer from Eu^{2+} to Mn^{2+}. The broadband PLE of Eu^{2+} covers the wavelength range from 250 to 400 nm, indicating a strong absorption for UV light.
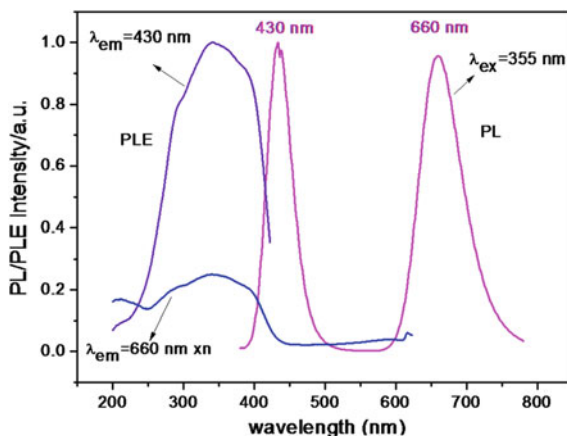
This excitation band can be fitted into three Gaussian components with maxima at 290, 350, and 400 nm that correspond to the electronic transition absorption of $^8S_{7/2} \rightarrow {}^2t_{2g}$ (350, 400 nm) and $^8S_{7/2} \rightarrow {}^2e_g$ (290 nm) for Eu^{2+}, respectively [32]. The crystal field splitting and the center of gravity are thus estimated to be 9300 and 29,800 cm^{-1}, respectively. The excitation spectrum of Mn^{2+} consists of five bands peaked at 317, 372, 411, 452, and 561 nm, corresponding to the transitions of energy levels from $^6A_1(^6S)$ to $^4E(^4D)$, $^4T_2(^4D)$, $[^4A_1 \ (^4G)$, $^4E(^4G)]$, $^4T_2(^4G)$, and $^4T_1(^4G)$ for Mn^{2+}, respectively.

Figure 3.2a depicts the typical emission spectra of $(Ba,Sr)_3MgSi_2O_8$: Eu^{2+}, Mn^{2+} with varied ratios of Ba to Sr. It is noted that no green band emission peaked at around 505 nm was detected in the solid solution composition range of Ba–Sr. As mentioned previously, [56, 57] many researchers experienced the coexistence of Ba_2SiO_4 impurity phase with $Ba_3MgSi_2O_8$ host phase, responsible for a highly efficient green emission of doped divalent Eu ion. In the present cases in a proper composition range of Ba–Sr solid solution, suppression of forming Ba_2SiO_4 impurity phase can be realized in high reproducible experiments most likely owing to phase equilibrium relation of Ba–Sr solution. It is observed that the emission peak of Eu^{2+} exhibits a red-shift from 436 nm for $Ba_3MgSi_2O_8$: Eu^{2+}, Mn^{2+} to 457 nm for $Sr_3MgSi_2O_8$: Eu^{2+}, Mn^{2+}, while that of Mn^{2+} shows a red-shift from 623 to 683 nm. The composition variation in Ba–Sr leads to disturbing crystal field around activators in host lattice and promoting the efficiency of energy transfer from Eu to Mn ions via host lattice, enabling the change in peak position of Eu and Mn ions and, in particular, broadening of band for Mn^{2+} ion in the red and far-red spectral range at around 660 nm. This adjustable feature offers a possibility to obtain an optimal combination of different photonic energy in longer- and shorter-wavelength red light to achieve a high photosynthetic efficiency by simply changing the composition of Ba–Sr in $(Ba,Sr)_3MgSi_2O_8$.

Figure 3.2 depicts the PL spectra and the photographs of $Ba_{1.24}Sr_{1.7}Mg_{1-x}Si_2O_8$: $0.06Eu^{2+}$, xMn^{2+} samples with varied Mn^{2+} contents. It is observed that as long as
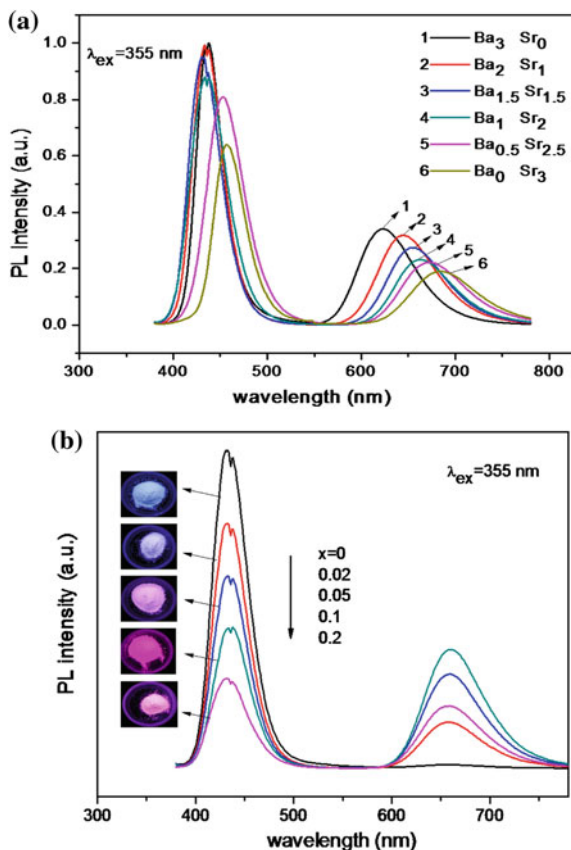
the proper composition of Ba–Sr was fixed, the peak position of red remains at
660 nm and that of blue at 430 nm regardless of the content change in Mn ion. As
the content of Mn^{2+} increases from 0 to 0.2 mol, the PL intensity of Eu^{2+} decreases
monotonically, whereas that of Mn^{2+} increases obviously at beginning, then gets to
a maximum owing to quenching effect. The intensity ratio of red to blue is
adjustable by changing the doping concentrations of Mn ions up to a maximum
value at 5:1 as $x = 0.1$, which is sufficient for the optimal photosynthetic photon
flux fraction of red to blue ration of PAR in horticulture lighting.

Figure 3.3 depicts the XRD patterns of $(Ba,Sr)_3MgSi_2O_8$: Eu^{2+}, Mn^{2+}. The
diffraction patterns of $(Ba,Sr)MgSi_2O_8$: Eu^{2+}, Mn^{2+} samples show a variety of solid
solution compositions formed by varying the Ba/Sr ratio. XRD patterns of the
samples with Ba = 3, Sr = 0 to Ba = 0, Sr = 3 are similar to those in JCPDS
10-0075 card for $Sr_3MgSi_2O_8$, but a slight shift tends to the small angle owing to
solid soluble effect of site substitution in the lattice. A detailed analysis reveals the
changes in diffraction peaks at [101] and [130] crystal planes of $(Ba,Sr)_3MgSi_2O_8$:
Eu^{2+}, Mn^{2+} phosphors with different Ba/Sr ratios to indicate an enlargement of cell

Fig. 3.3 XRD patterns of $(Ba,Sr)MgSi_2O_8$: Eu^{2+}, Mn^{2+} samples with different Ba/Sr ratio. Reprinted from Ref. [58], copyright 2013, with permission from Elsevier
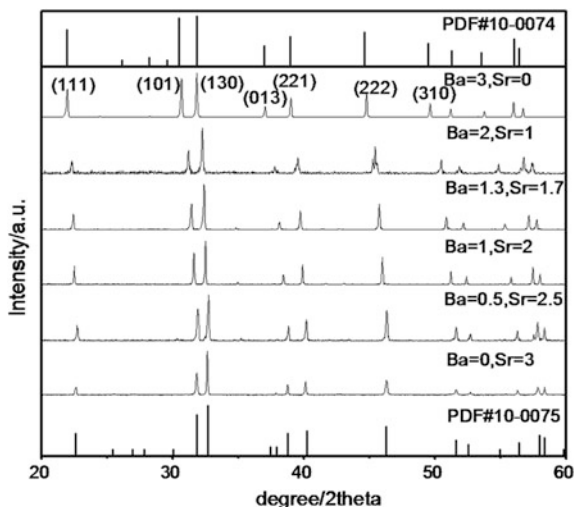
volume owing to the substitution of smaller Sr ions (144 Å, $n = 12$) with the larger Ba ions (1.61 Å, $n = 12$). The 2-theta value of [101] crystal plane peak increases from 30.92° to 32.02°, while the [130] crystal plane peaks increase from 31.82° to 32.91°. It is confirmed that the samples in the designated composition of Ba–Sr could be in phase-pure $(Ba,Sr)_3MgSi_2O_8$ since no trace of impurity phase $(Ba, Sr)_2SiO_4$ or $(Ba,Sr)MgSiO_4$ can be identified from the diffraction patterns, and a more convincing fact lies in the absence of green band emission peaked at ~ 505 nm that is much sensitive to any trace impurity phase as Eu^{2+} doped.

Im et al. [37] refined the neutron powder diffraction data of $(Ba,Sr)MgSi_2O_8$: Eu^{2+} samples by varying Ba content and ascribed thermal stability improvement to Ba substitution on preferential Sr sites and Ba-induced shortening of interatomic distance of Eu and O. Okamoto et al. [39] used X-ray fine structure measurements to show a suppression of Eu ion from thermal degradation in Ba-substituted composition, $Sr_{2.48}Ba_{0.5}MgSi_2O_8$: $0.02Eu^{2+}$. Yonesaki et al. [52] verified that different molar ration of Ba, Sr, Ca ions in Eu^{2+}-doped $A_3MgSi_2O_8$ may vary with different crystal structure and the intensive blue emission of 5d–4f electron transition at about 435 nm can be achieved. For Ba–Ca binary in $(Ba, Ca)_3MgSi_2O_8$, there probably exist some chemically stable compounds, e.g., $BaCa_2MgSi_2O_8$ [35, 51, 53]. Thus, each binary composed by any two of Ba, Sr, and Ca components in $A_3MgSi_2O_8$ exhibits different equilibrium-phase relationship and their crystal structure needs to be investigated further. For the presently studied Ba–Sr composition in $(Ba,Sr)_3MgSi_2O_8$: Eu^{2+}, Mn^{2+}, the pure host phase was obtained to be free of any green-emitting intermediate phases.

The quantum efficiency of Eu^{2+} single-doped $(Ba,Sr)_3MgSi_2O_8$ was much higher than that of codoped with Eu^{2+}, Mn^{2+} (Fig. 3.4). The Eu^{2+}, Mn^{2+}-codoped samples of B, C, E all exhibit a 660-nm red light emission, while that of $Ba_{1.24}Sr_{1.7}Mg_{0.9}Si_2O_8$: $0.06Eu^{2+}$, $0.1Mn^{2+}$ shows a maximum quantum efficiency.
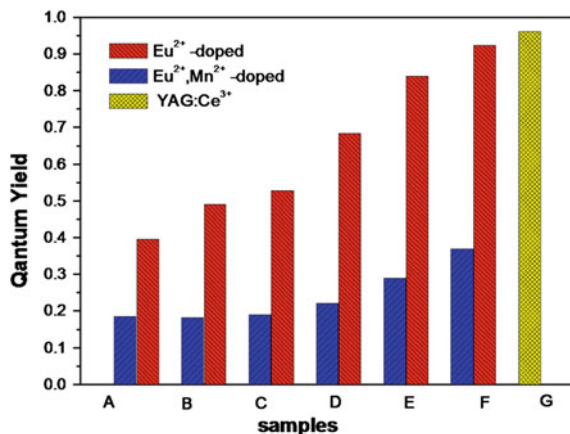
Fig. 3.4 The evaluations of the quantum yield of $Ca_3MgSi_2O_8$ (*A*), $Ba_{1.75}Ca_{1.25}MgSi_2O_8$ (*B*), $Ba_{1.8}Sr_{0.6}Ca_{0.6}MgSi_2O_8$ (*C*), $Sr_3MgSi_2O_8$ (*D*), $Ba_{1.3}Sr_{1.7}MgSi_2O_8$ (*E*), $Ba_3MgSi_2O_8$ (*F*), YAG: Ce^{3+} (*G*). Reprinted from Ref. [58], copyright 2013, with permission from Elsevier

The regime of energy transfer from Eu^{2+} to Mn^{2+} in AMS-EM has been confirmed in a manner of resonant energy transfer that usually accompanies with energy exchange with the surrounding lattice environment [62]. The energy exchange promotes a transfer of the excited energy into the vibration energy of crystal lattice to enable the energy transfer in some specific direction. The energy transferred will be relaxed in such kind of variation process across the lattices, leading to a decrease in quantum efficiency for Eu^{2+}, Mn^{2+}-doped than for Eu^{2+}-doped samples highly dependent on intrinsic symmetry feature of host lattice [62].

Figure 3.5a shows the temperature dependence of relative emission intensity for BMS, SMS, CMS, and BSMS samples as heated from room temperature to 220 °C. The emission intensity of each sample at 300 K is set to be 100 % for different samples and compared with others at higher temperature. The relative emission intensity of BSMS does not decrease, but shows a significant increase with increasing temperature that does not follow the general rule. Similar results are observed for BMS and SMS. This phenomenon is due to eye's visibility function for human being. The relative emission intensities of Eu^{2+}, Mn^{2+} exhibit an obvious thermal quench with increasing temperature. However, the peak position of blue emission spectra shows a little red-shift and the red emission spectra show obvious blue shift. Thus, it is inferred that although the emission intensity of Eu^{2+}, Mn^{2+} decreases, the brightness of sample increases. Figure 3.5b depicts the temperature-dependent external quantum efficiency of BMS, SMS, CMS, and BSMS, indicating a decrease with increasing temperature. BSMS shows the highest thermal stability that is owing to an effective incorporation of the Ba^{2+} ions into the crystal structure of Ba–Sr solid solution host. As more amount of Ba^{2+} ions were incorporated into the sites in the host lattice, the structure could not be subjected to a distinct change, but the Sr site was substituted by Ba^{2+}, especially at the Sr(I) site
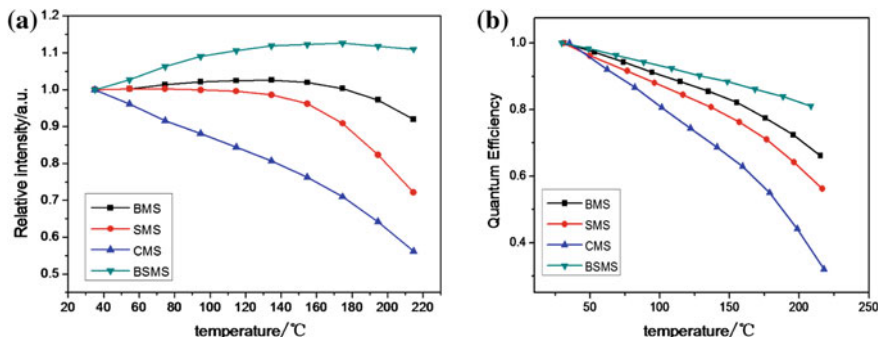
Fig. 3.5 Temperature-dependent PL intensity of BSMS ($Ba_{1.24}Sr_{1.7}Mg_{0.9}Si_2O_8$: $0.06Eu^{2+}$, $0.1Mn^{2+}$), BMS ($Ba_{2.94}Mg_{0.9}Si_2O_8$: $0.06Eu^{2+}$, $0.1Mn^{2+}$), SMS ($Sr_{2.94}Mg_{0.9}Si_2O_8$: $0.06Eu^{2+}$, $0.1Mn^{2+}$), CMS ($Ca_{2.94}Mg_{0.9}Si_2O_8$: $0.06Eu^{2+}$, $0.1Mn^{2+}$) (**a**), Temperature-dependent external quantum efficiency of BSMS, BMS, SMS, CMS (**b**). Reprinted from Ref. [58], copyright 2013, with permission from Elsevier

[37]. As a result, Eu^{2+} will substitute the low-coordinated and smaller-sized sites for Sr(II) and Sr(III) and favor a high thermal stability of the phosphor. The intensity will decrease to the values by 70, 62, 44, and 82 % of initial value at 200 °C for BMS, SMS, CMS, and BSMS samples, respectively. These values agree with common observation that the emission peak with smaller Stokes shift has higher activation energy and higher quenching temperature, as the Stokes shift of $Ba_{1.24}Sr_{1.7}Mg_{0.9}Si_2O_8$: $0.06Eu^{2+}$, $0.1Mn^{2+}$ was calculated to be around 4900 cm^{-1}.

The role of Ba substitution for Sr is similar to those discovered elsewhere. For instance, Yonesaki et al. [52] revealed that the amount variation of Ba ions in A ($A_3MgSi_2O_8$) corresponds to different crystal types in glaserite-type trigonal or merwinite-type monoclinic structure. Im et al. [37] revealed that the substitution of Ba on Sr sites adjusts the average interatomic distances between Eu^{2+} and O (d(Eu-o)) of the different Sr sites and enables Eu^{2+} occupying preferred Sr sites among three possible locations. Okamoto et al. [39] ascribed the improvement of thermal degradation to be closely correlated with the oxidation of Eu^{2+} ion into Eu^{3+} ion.

The absorption spectrum of light harvesting by green plants such as chlorophyll (a, b) carotenoids, and allophycocyanin was concentrated in blue-violet light of 660-nm red and 430-nm blue band. In terms of Emerson's effect that the quantum efficiency drops sharply beyond 685 nm, the emission spectrum of as-fabricated LED prototype matches well with the absorption spectrum of chlorophyll a, chlorophyll b, and chlorophyll c. This feature of asymmetric broad red emission band in the simultaneous red and blue band emission is of great significance to compromise the strong absorption at far-red band and low conversion efficiency at shorter-wavelength band of red. Furthermore, this 660-nm-featured band emission spectrum of $Ba_{1.3}Sr_{1.7}MgSi_2O_8$: Eu^{2+}, Mn^{2+} phosphor is also found to match well with the absorption spectrum of microalgae [63–65] so as to be able to construct a specific PAR for cultivating microalgae [66]. The advantages of this single-chip
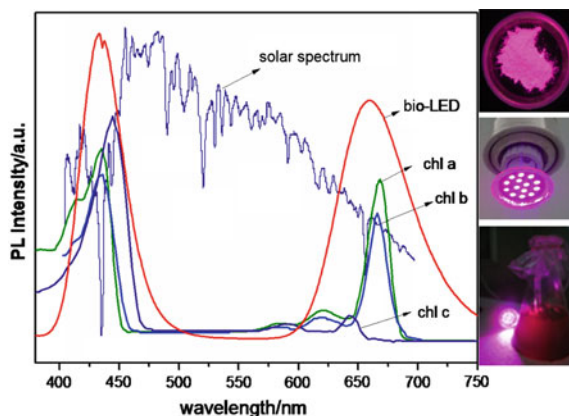
Fig. 3.6 A broad emission spectrum of this artificial sunshine emitter perfectly covers the absorption spectrum of chlorophyll a, chlorophyll b, and chlorophyll c of plants. The *insert* shows photographs of irradiated phosphor of $Ba_{1.24}Sr_{1.7}Mg_{0.9}Si_2O_8$: $0.06Eu^{2+}$, $0.1Mn^{2+}$ in *violet*, a as-fabricated LED lamp with this phosphor, and a microalgae cultivation setup upon NUV irradiation. Reprinted from Ref. [58], copyright 2013, with permission from Elsevier

single-phosphor-converted red/blue LED enable an option for the energy-saving illuminating phosphor materials and lighting devices in the application of plant cultivation or bioreactors (Fig. 3.6).

3.2.2 Microwave-Induced Small-Sized Phosphor Particles

Microwave processing [67, 68] may lead to the formation of small-sized and agglomeration-free phosphor particles probably resulted from suppressing the grain growth in as-formed host particles, compared with conventional high-temperature solid-state (SS) reaction firing procedure.

Figure 3.7 depicts the dependence of photoluminescence (PL) and PL of excitation (PLE) spectra of BSMS-EM on the holding temperature as fired by MW and SS. PLE shows that all samples are excitable in the wavelength range from UV to NUV, while the PL spectrum exhibits a dual peak band emission consisting of a blue emission band peaked at 432 nm from 4f–5d transition of Eu^{2+} and a red band emission peaked at 660 nm from the 4T–6A transition of $3d^5$ energy level of Mn^{2+} in the host of AMS-EM. It has been well verified that the excitation energy of Mn ion for 660-nm-peaked red is transferred from Eu^{2+} through lattice vibration [50]. In general, the intensity of PL increases with increasing MW holding temperature from 900 to 1000 °C.

Figure 3.8 depicts the diffuse reflection spectra (DRS) of as-fired BSMS-Eu, Mn samples. The absorption of incident photonic energy by Mn^{2+} is, however, very weak in most host lattices due to its spin and parity forbidden d–d transitions. An
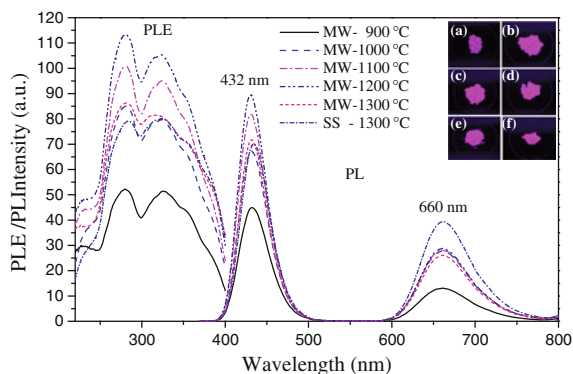
Fig. 3.7 Photoluminescence of excitation (*PLE*) monitored at 432 nm and photoluminescence (*PL*) excited at 350 nm of the $Ba_{1.14}Sr_{1.7}MgSi_2O_8$: $0.06Eu^{2+}$, $0.1Mn^{2+}$ (BSMS-EM) samples prepared by *MW* and *SS*, respectively. The *inset* represents the photographs of $Ba_{1.14}Sr_{1.7}MgSi_2O_8$: $0.06Eu^{2+}$, $0.1Mn^{2+}$ phosphors under 365-nm excitation. Reprinted from Ref. [60], copyright 2013, with permission from Elsevier
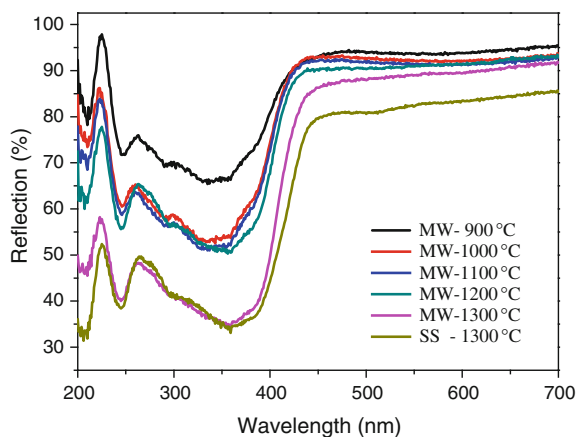
Fig. 3.8 Diffuse reflection spectra of $Ba_{1.14}Sr_{1.7}MgSi_2O_8$: $0.06Eu^{2+}$, $0.1Mn^{2+}$ (BSMS-EM) samples. Reprinted from Ref. [60], copyright 2013, with permission from Elsevier

efficient sensitizer such as Eu is generally needed as a dopant pair to promote the green-red emission of Mn. It was observed that there exists an absorption band peaked at around 250 nm corresponding to the valence-to-conduction band transitions of the BSMS host lattice. In the Eu^{2+} and Mn^{2+}-codoped BSMS, two absorption bands are in the wavelength range from 200 to 430 nm, which can be ascribed to the charge transfer band absorption and the transition absorption from the ground-state $4f^7$ of Eu^{2+} to its excited state $4f^65d^1$, respectively. No distinct transition absorption can be observed for Mn ion, indirectly confirming an

Fig. 3.9 XRD patterns of
$Ba_{1.14}Sr_{1.7}MgSi_2O_8$:
$0.06Eu^{2+},0.1Mn^{2+}$ samples
prepared by MW at
(a) 900 °C; (b) 1000 °C;
(c) 1100 °C; (d) 1200 °C;
(e) 1300 °C and SS at
(f) 1300 °C. Reprinted from
Ref. [60], copyright 2013,
with permission from Elsevier
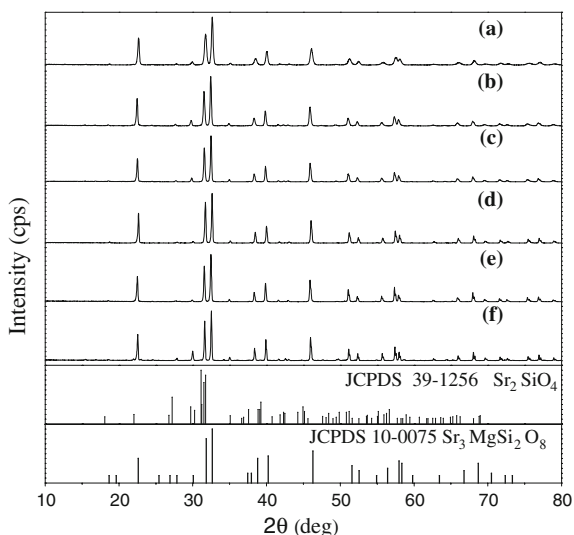
occurrence of effective energy transfer in between Eu–Mn ions via the lattice. These results from the DRS agree well with those from the PLE spectra.

Figure 3.9 depicts the XRD patterns for $Ba_{1.14}Sr_{1.7}MgSi_2O_8$: $0.06Eu^{2+}$, 0.1 Mn^{2+} samples, verifying the formation of phase-pure host phases of (BSMS-EM). In this Ba–Sr solid solution system of host phase, no trace phase of $Ba_3MgSi_2O_8$ was identified from the measured diffraction patters. The crystallographic frame agrees well with those of $Sr_3MgSi_2O_8$ (JCPDS 10-0075), indicating a partial substitution of Ba at Sr lattice sites in a solid solution form for the above-mentioned composition. More importantly, we observed the size effect of phosphor particles versus MW power as fired with MW procedure. As shown in Fig. 4, the particle exhibits a D_{50} value of around 8–10 μm in a uniform size distribution from 900 to 1200 W for MW-derived particles, while that for SS-derived particles is greater than ten micrometers. The phosphor particles by MW exhibit a smooth surface for the majority of particles than those by SS (Fig. 3.10).

The size effects of smaller MW-derived particles than SS-derived particles more likely reveal the underlying mechanism of nonthermal effects as affected by MW magnetic field with crystalline solids. A nonthermal mechanism for MW-enhanced surface diffusion and the reduction in activation for diffusion and overall faster kinetics might be responsible for the suppression of grain growth during MW firing process. The mechanism of the microwave processing of BSMS-EM samples is owing to the dielectric properties of the raw materials and varied intermediate products. In general, for the ceramics, the dielectric loss factor of inorganic materials becomes larger with an increase in temperature. Since most ceramic materials interact only very weakly with microwave radiation at room temperature, to the BSMS-EM samples, the auxiliary heating parts such as SiC or ZrO_2 are widely used to improve the uniform temperature distribution in the whole sample.
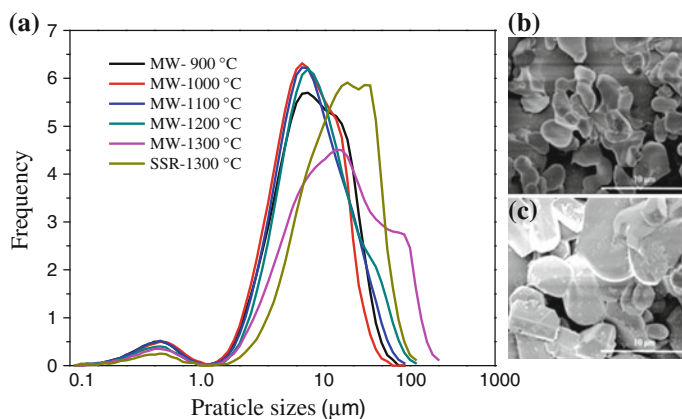
Fig. 3.10 Particle size (**a**) and morphology of BSMS-EM samples as fired by MW (**b**) and SS (**c**). Reprinted from Ref. [60], copyright 2013, with permission from Elsevier

Direct heating of the reactants by the microwaves is believed to lead to a more homogeneous heat distribution and potentially rapid and defect-free grain growth of the product due to the very efficient transfer of thermal energy.

3.2.3 Sol Spray-Microwave-Induced Cage-like Phosphor

Template-free assembling of cage-like $(Ba,Sr)_3MgSi_2O_8$: Eu, Mn phosphor with simultaneous 660-/430-nm-featured band emission was investigated through microwave firing as-sprayed hollow xerogel sphere. At a critical firing temperature at around 650 °C, the pure host phase of $(Ba,Sr)_3MgSi_2O_8$ forms and the release of decomposed gas of precipitated nitrates determines the morphology of as-fired particles. The results suggest that by using microwave firing procedure, it is possible to construct multi-scale cage-like phosphor particle in meso-, nano-, and submicrometers as long as the process parameters can be properly controlled so as to achieve enhancing the PL of simultaneous red/blue emission.

Figure 3.11 depicts the XRD patterns of the as-sprayed $Ba_{1.14}Sr_{1.7}MgSi_2O_8$: $0.06Eu^{2+}$, $0.1Mn^{2+}$ xerogel samples. The diffraction patterns of the nitrate precipitates of Ba, Sr, and Ba–Sr upon drying agree well with those in JCPDS cards (nos. 26-0187, 25-0746, and 24-0053). Other compounds relevant to Mg, Mn, Si, and Eu elements were not detected probably owing to instrument precision for trace amounts. The SEM images of $Ba_{1.14}Sr_{1.7}MgSi_2O_8$: $0.06Eu^{2+}$, $0.1Mn^{2+}$ xerogel particles. The xerogel particles exhibit a hollow, spherical shape with an average size of around 15 μm in diameter.

Figure 3.12 demonstrates schematically the evolution processes of $Ba_{1.14}Sr_{1.7}MgSi_2O_8$: $0.06Eu^{2+}$, $0.1Mn^{2+}$ phosphor particle in the spray-microwave
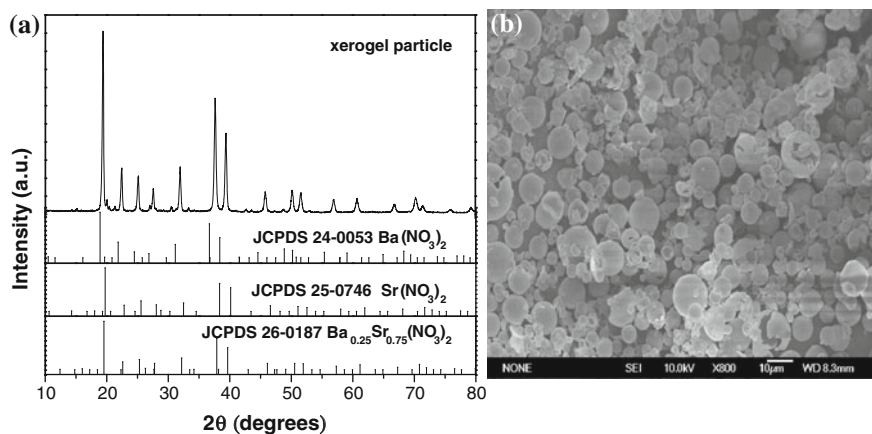
Fig. 3.11 **a** XRD patterns of xerogel particles in stoichiometric $Ba_{1.14}Sr_{1.7}MgSi_2O_8$: $0.06Eu^{2+}$, $0.1Mn^{2+}$ upon spraying, together with those from JCPDS cards no. 26-0187 for $Ba_{0.25}Sr_{0.75}$ $(NO_3)_2$,25-0746 for $Sr(NO_3)_2$, and 24-0053 for $Ba(NO_3)_2$. **b** SEM image of typical $Ba_{1.14}Sr_{1.7}MgSi_2O_8$: $0.06Eu^{2+}$, $0.1Mn^{2+}$ xerogel particles. Reprinted from Ref. [59], copyright 2013, with permission from Elsevier
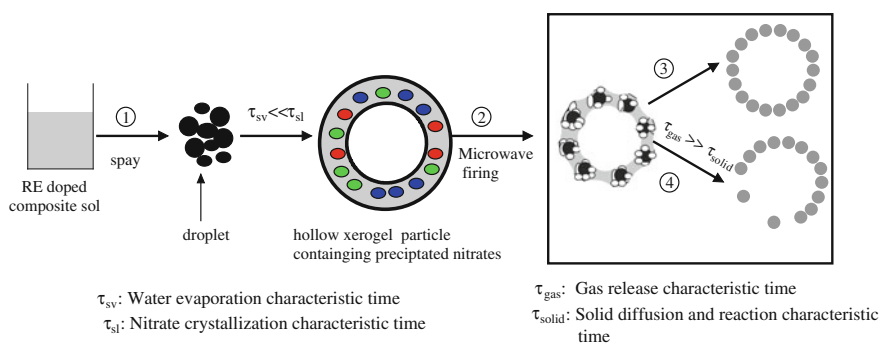
Fig. 3.12 A proposed morphology evolution regime from one-droplet-one particle model for micrometer-sized $Ba_{1.14}Sr_{1.7}MgSi_2O_8$: $0.06Eu^{2+}$, $0.1Mn^{2+}$ phosphor particle with mesopores and nanocrystals embedded on the coarse surface of the particle during spray-microwave firing morphology control of as-fired particles. Reprinted from Ref. [59], copyright 2013, with permission from Elsevier

firing procedure. In general, as the characteristic time of nitrate crystallization is much longer than that of the water evaporation during droplet flying process in the chamber, the xerogel particle in a hollow morphology will be formed. The crystals like nitrates will be precipitated from oversaturated droplet microreactor and migrated outward to the surface of hollow particles owing to Oswald effect, leading to the formation of xerogel particle in hollow. During the microwave firing process followed by spraying, the nitrates in hollow xerogel particles are subjected to

Fig. 3.13 Simultaneous
TG/DSC measurement of
xerogel sample in a
composition of
$Ba_{1.14}Sr_{1.7}MgSi_2O_8$:
$0.06Eu^{2+}$, $0.1Mn^{2+}$. Reprinted
from Ref. [59], copyright
2013, with permission from
Elsevier
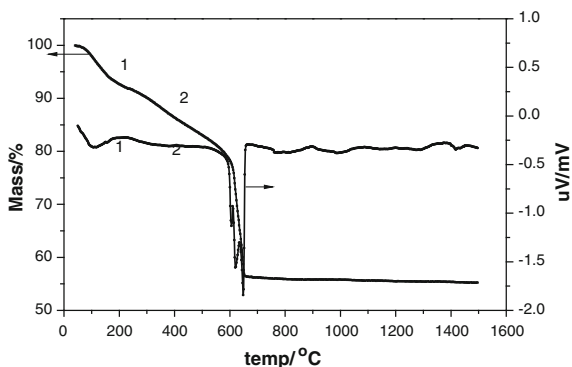
decomposition upon heating. The decomposition reaction involved could be represented as $M(NO_3)\cdot nH_2O \rightarrow MO + NO_x + nH_2O$, where M represents Ba or Sr, indicating the key role of the release of decomposed gas of NO_x and H_2O in the morphology evolution.

Figure 3.13 depicts the simultaneous TG/DSC measurement of the as-sprayed xerogel sample in a nominal composition of $Ba_{1.14}Sr_{1.7}MgSi_2O_8$: 0.06Eu, 0.1Mn. A distinct change in heat and weight in both TG and DSC occurs between the temperature range from 600 to 650 °C, indicating a decomposition of nitrate compound of Ba and Sr. The decomposition procedure was completed at 650 °C. By keeping the heating rate of 6.7 °C/m and the initial temperature of 650 °C, the firing temperature variation leads to the formation of phase-pure $Ba_{1.14}Sr_{1.7}MgSi_2O_8$ host. The XRD patterns of the sample powders upon firing beyond the temperature convince the formation of desired host phase. Since strontium is a major component of the solid solution, we compared $Ba_{1.14}Sr_{1.7}MgSi_2O_8$: $0.06Eu^{2+}$, $0.1Mn^{2+}$ with $Sr_3MgSi_2O_8$ from JCPDS card. All the peaks shift slightly to the lower-angle side. The reason is the substitution of Sr sites by Ba. No impurity peaks were detected, indicating an ease of formation of pure host phase upon firing with microwave heating in both chemistry and crystalline phase. It was observed that the dominant host phase of $Sr_3MgSi_2O_8$ starts to form as low as at 650 °C, indicating a very low formation temperature of desired host phase for as-sprayed xerogel particles owing to nanometer-sized effect from highly dispersed aerogel of sol precursor. Also, the crystallinity of crystals on the surface of the particles was observed to be improved continuously with further increasing the firing temperatures.

It was observed that at around 650 °C, the nitrates on the shell of xerogel particles were decomposed to the corresponding oxides completely. The shrinkage of those newly formed oxides and such desired host phase in nanometer and pores in meso scale result in the formation of coarse surface of particles. Thus, we could conclude that the release of decomposed gas of NO_x and water vapor eventually determines the morphology of spherical particles as long as the characteristic time of gas release is much shorter than that of solid diffusion and reaction. In practice, by microwave

firing procedure at a specific temperature, the heating rate is relatively easy to control so as to let the morphology control flexible through optimizing the process parameters. The PL emission wavelength of $Ba_{1.14}Sr_{1.7}MgSi_2O_8$: $0.06Eu^{2+}$, $0.1Mn^{2+}$ was observed at different annealing temperatures. The emission spectra of particles had two peaks at 430 and 660 nm, respectively. The emission peak at 430 nm was due to the transition of Eu^{2+} from 5d to 4f energy level, while the peak at 660 nm is ascribed to the transition of Mn^{2+} ions from ^4T to ^6A of $^3d_5$ energy level. The peak at 660 nm was necessary for plant growth. As the firing temperature increases from 1000 to 1200 °C, the intensity of the peaks increases from 1000 to 1100 °C and declines at 1200 °C. The firing temperature is optimized to be at 1100 °C. As there is no luminescence detected for these samples upon microwave firing at 650, 700, 800, and 900 °C, we assume that prerequisites have not met such that in the substitution of either Eu for Ba, Sr or Mn for Mg in the lattice, reduction of Eu, Mn to low valence state, formation of suitable crystallinity of crystals relevant to crystal field for ion transition and transfer of energy from Eu to Mn ion.

3.2.4 Adjustment of Phase and Morphology by Microwave Combustion

Dual band emissions positioned at both 660 and 430 nm of $(Ba,Sr)_3MgSi_2O_8$: Eu^{2+}, Mn^{2+} phosphor can also be achieved via spray-combustion synthesis procedure [61]. At a specific limited solid solubility composition $Ba_{1.3}Sr_{1.7}MgSi_2O_8$, the secondary green-emitting phases of $(Ba,Sr)_2SiO_4$ or $(Ba,Sr)MgSiO_4$ were effectively suppressed to give out the desired 660-nm broad emission. An enhancement of PL intensity for 660-nm red emission originated from Mn transition was observed for combustion synthesis samples, indicating an intrinsic promotion of energy transfer from Eu^{2+} to Mn^{2+} in $(Ba,Sr)_3MgSi_2O_8$ host. This PL enhancement for 660-nm emission is probably ascribed to an effective reduction in Mn ion in the combustion process with the aid of decomposed reductive radicals formed in situ upon fuel ignition. The particle crystallizes depending on process parameter variation locates in a size range from 5 to 20 μm.

The phosphor samples of $A_3MgSi_2O_8$: Eu^{2+}, Mn^{2+} were synthesized by spray-combustion and direct firing procedure. A precursor of aqueous solution was made from the stoichiometric amount of phosphor by using $Ba(NO_3)_2$ (99.99 %), $Sr(NO_3)_2$ (99.99 %), $Mg(NO_3)_2·6H_2O$ (analytical reagent), $C_4H_6MnO_4·4H_2O$ (analytical reagent), and tetraethoxysilane (TEOS). The citric acid (99.99 %) as fuel was mixed in the above solution only for combustion process. The volume of the precursor solution is 400 ml, and the concentration of the solution is 0.075 mol/L. The precursor solution was sprayed by an atomizer (LabPlant, UK) to obtain the xerogel particles by controlling spray parameter of 175 °C for the spray temperature, 2 L/min for the flow rate of carrier gas. As-sprayed xerogel particles with fuel was ignited at 1000 °C in a muffle furnace, followed by postfiring in a horizontal furnace
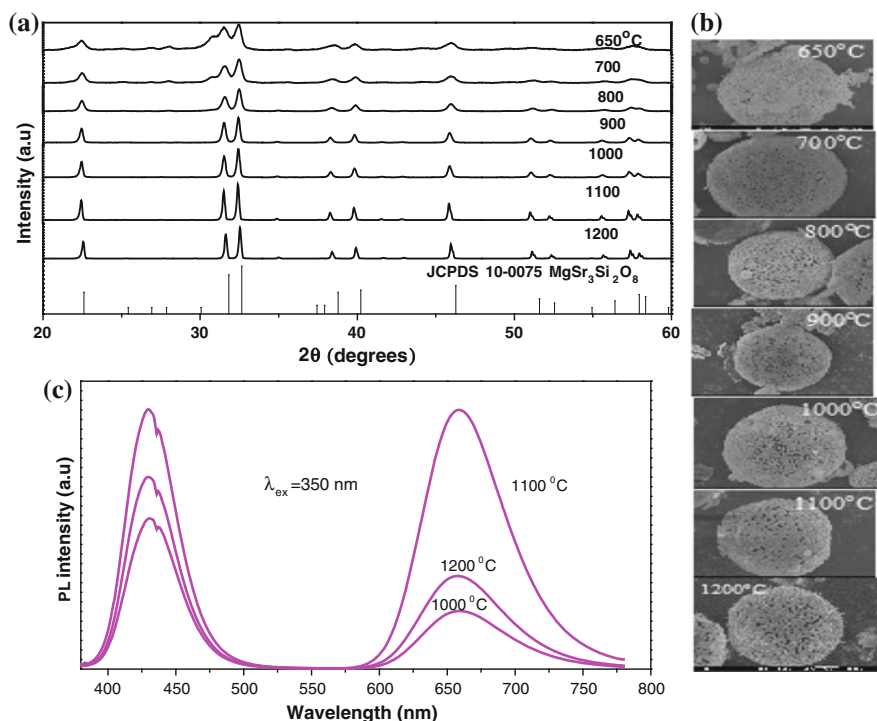
Fig. 3.14 a XRD patterns of $Ba_{1.14}Sr_{1.7}MgSi_2O_8$: $0.06Eu^{2+}$, $0.1Mn^{2+}$ powders prepared at different reaction temperatures. **b** SEM images of microwave-fired particles in stoichiometric $Ba_{1.14}Sr_{1.7}MgSi_2O_8$: $0.06Eu^{2+}$, $0.1Mn^{2+}$ at different temperatures. **c** PL spectra of $Ba_{1.14}Sr_{1.7}MgSi_2O_8$: $0.06Eu^{2+}$, $0.1Mn^{2+}$ under 350-nm light excitation at different microwave firing temperature (concentration = 0.01 mol/l). Reprinted from Ref. [61], with kind permission from Springer Science+Business Media

at 1250 °C for 3 h under the atmosphere of a mixed flowing gas of N_2 95 vol.%/H_2 5 vol.%; we designated this operation as combustion process. Other as-sprayed xerogel particles without fuel were fired directly under the same conditions. We designated this operation as direct firing process. No flux such as NH_4Cl or NH_4F was mixed with the as-sprayed xerogel particles before firing in a horizontal furnace. Figure 3.14 shows the XRD patterns, PL, and particle morphology of $Ba_{1.24}Sr_{1.7}Mg_{0.9}Si_2O_8$: $0.06Eu^{2+}$, $0.1Mn^{2+}$ phosphor samples prepared by the combustion process and by direct firing process, respectively. It was illustrated that both the phosphor samples obtained are crystallized in $Sr_3MgSi_2O_8$ phase to be in well coincidence of the diffraction patterns in PDF card 10-0075.

Figure 3.15 depicts the full-spectrum scanning X-ray photoelectron spectroscopy (XPS) for the two tested samples corresponding to different firing processes. The XPS measurement results of Mg1s to Si2P show that the mass ratio of Mg to Si is evaluated to be 0.55 and 0.52 for two samples, respectively, which are
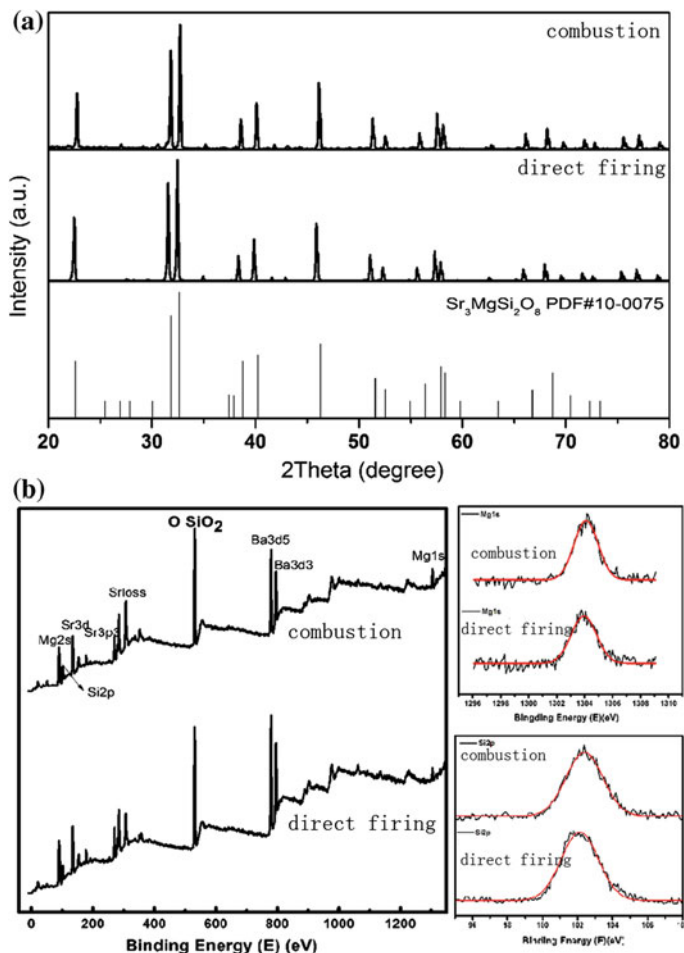
Fig. 3.15 **a** XRD patterns and **b** X-ray photoelectron spectroscopy (XPS) profiles of $Ba_{1.24}Sr_{1.7}Mg_{0.9}Si_2O_8$: $0.06Eu^{2+}$, $0.1Mn^{2+}$ prepared by combustion and direct firing. Reprinted from Ref. [61], with kind permission from Springer Science+Business Media

larger than that of the theoretical value 0.43 for $A_3MgSi_2O_8$. It is inferred that this higher value is probably owing to the occurrence of a small quantity of elemental silicon probably originating from a reduction reaction of silica on the surface of phosphor particle under an instant strong reductive atmosphere in combustion process.

Figure 3.16 depicts TEM images of phosphor samples prepared by combustion (a, b) and by direct firing procedure (c, d). It is observed that both samples achieved nearly the same high degree of crystallinity and the lattice perfection. Figure 3d depicts SEM images for the as-sprayed xerogel particles that exhibit uniform hollow sphere with an average size of around 12 μm in diameter. As-sprayed particles
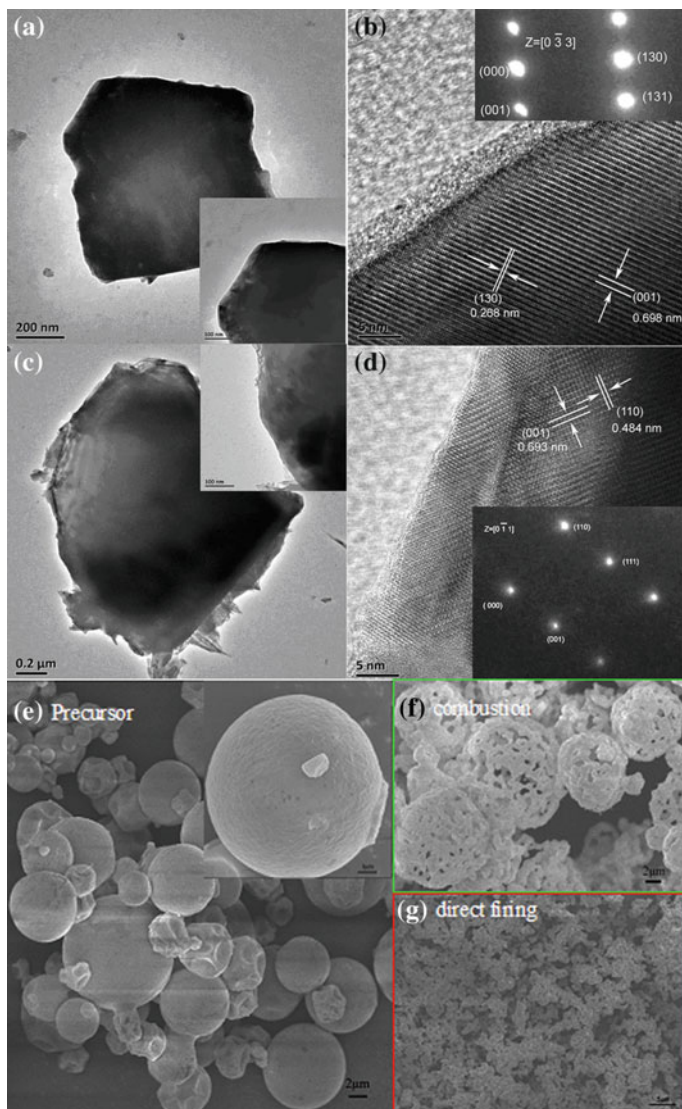
Fig. 3.16 TEM images of phosphor samples prepared by combustion (**a**, **b**) and direct firing process (**c**, **d**), SEM images (**d**) for as-sprayed with a constant particle size of around 12 μm, (**e**) SEM images of hollow cage-like phosphors for $Ba_{1.24}Sr_{1.7}Mg_{0.9}Si_2O_8$: $0.06Eu^{2+}$, $0.1Mn^{2+}$ after firing at 1250 °C in a reducing atmosphere of 5 % H_2, (**f**) SEM images highly dispersed phosphor for $Ba_{1.24}Sr_{1.7}Mg_{0.9}Si_2O_8$: $0.06Eu^{2+}$, $0.1Mn^{2+}$ powders prepared by combustion after firing at 1250 °C in a reducing atmosphere of 5 % H_2. Reprinted from Ref. [61], with kind permission from Springer Science+Business Media

were subjected to firing at 1250 °C in a reducing atmosphere of N_2 95 vol.%/H_2 5 vol.%; then, cage-like morphology of phosphor particles is observed (Fig. 3e), while those obtained by combustion exhibit highly dispersed particles with relatively smaller sizes. The as-fired phosphor particles with distribution of pores were said to be beneficial to harvest incident photons efficiently [29]. For the samples in Fig. 3d, smaller-sized particles are obtained owing to the crushing effect of evaporated vapor or decomposed gas from as-sprayed particles during the combustion procedure. Citric acid as fuel premixed in the precursor was decomposed in air to produce various reductive radicals in gas phase, leading to crash of as-sprayed hollow morphology and promotion of reduction in doping ions of Mn ions and Eu ions as well.

Figure 3.17a depicts PL spectra of samples obtained by combustion and direct firing procedure. Blue emission at 440 nm from the $4f^65d^1 \rightarrow 4f^7$ transition of Eu^{2+} and red emission at 660 nm resulted from the spin-forbidden $4T^1(4G) \rightarrow 6A^1(6S)$ transition of Mn^{2+} were observed on the PL spectra for these two samples. It is

Fig. 3.17 **a** PL spectra of samples with or without combustion synthesis, illustration (*I*) showing SEM images of well-dispersed phosphor particles with combustion synthesis, illustration (*II*) showing SEM images of hollow cage-like phosphor via direct firing, **b** diffuse reflection spectrum (DRS) of samples via combustion synthesis or direct firing. Reprinted from Ref. [61], with kind permission from Springer Science+Business Media
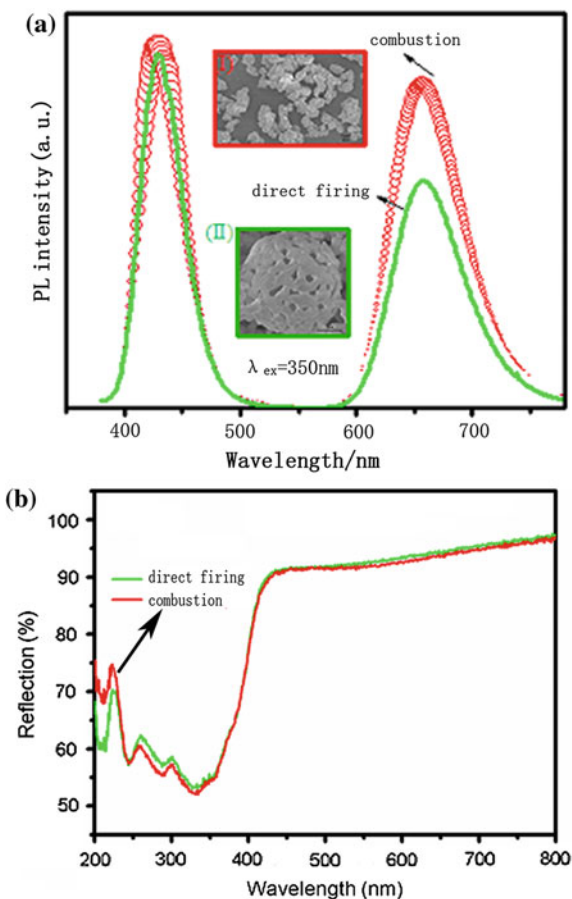
noted that an enhancement of PL intensity of the Mn^{2+} red emission for the sample obtained by combustion procedure is observed distinctly comparing to that of the counterpart sample obtained by direct firing. The enhancement of PL intensity in the sample synthesized with combustion route is more likely owing to the complete annealing or combustion that yields samples with lesser defects. Additionally, the diffuse reflection patterns of the prepared samples in Fig. 4b exhibit a slight difference in absorption efficiency; small particles prepared by combustion synthesis seem to reflect less incident photons energy so as to contribute a little bit to the red-emitting enhancement in this case. In Eu^{2+}-Mn^{2+}-codoped phosphor systems, the Mn^{2+} emission is commonly pumped by the excitation energy of Eu^{2+} through the energy transfer between Eu^{2+} and Mn^{2+}. Therefore, we speculate that the essential reason for the enhancement of Mn^{2+} red emission is possibly ascribed to the improvement of energy transfer process between Eu^{2+} and Mn^{2+} owing to the effective reduction of Mn ion with the aid of strong reductive radicals produced in combustion process.

Figure 3.18 depicts the X-ray photoelectron spectroscopy (XPS) of Mn element in $Ba_{1.24}Sr_{1.7}Mg_{0.9}Si_2O_8$: $0.06Eu^{2+}$, $0.1Mn^{2+}$ phosphor samples prepared by combustion and direct firing. It is found that the Mn element exists in variable valence in the samples from the XPS profiles. Peaks positioned at 641.4 eV correspond to Mn^{2+}, while the peaks positioned at 639.6 eV (Mn), 641 eV (Mn_3O_4), and 642.2 eV (MnO_2) were assigned to other valence of Mn. An obvious increasing trend of peaks positioned at 641.4 eV (Mn^{2+}) is observed for the sample obtained by combustion comparing with the sample obtained by direct firing, indicating that the amount of Mn^{2+} for the combustion sample is higher that of the counterpart sample. The luminescence center concentration that determines the distance between sensitizers and activators plays an important role in the energy transfer. Commonly, energy transfer efficiency increases with the increasing of the

Fig. 3.18 X-ray photoelectron spectroscopy (XPS) of Mn element in $Ba_{1.24}Sr_{1.7}Mg_{0.9}Si_2O_8$: $0.06Eu^{2+}$, $0.1Mn^{2+}$ phosphor samples prepared by combustion and direct firing. Reprinted from Ref. [61], with kind permission from Springer Science+Business Media
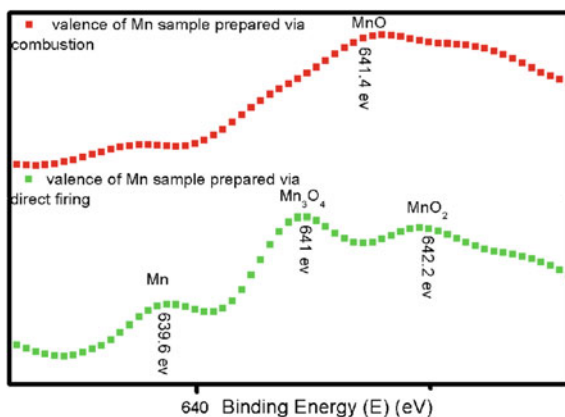
luminescence center before the occurrence of concentration quenching. Thus, the increasing amount of Mn^{2+} (positioned at 641.4 eV) in the combustion sample is the dominant reason for the enhancement of Mn^{2+} red emission, owing to the increasing of energy transfer efficiency between Eu^{2+} and Mn^{2+}.

Figure 3.19a depicts powder XRD patterns of $Ba_{1.24}Sr_{1.7}Mg_{0.9}Si_2O_8$: $0.06Eu^{2+}$, $0.1Mn^{2+}$ prepared by combustion at different temperatures, illustrating the well-defined $Sr_3MgSi_2O_8$ phase without Sr_2SiO_4 phase. It has been reported [30] that $M_3MgSi_2O_8$ (M = Ba,Sr) has a layer structure with glaserite type, which is considered to be highly order structure of merwinite type. The layer consists of
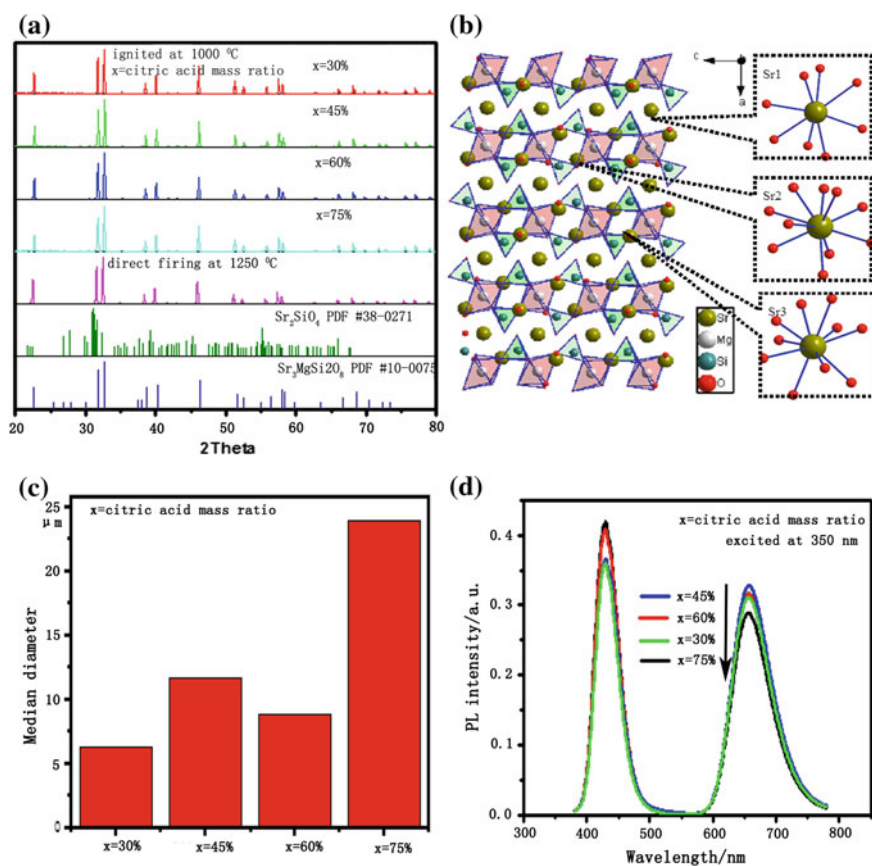
Fig. 3.19 **a** shows powder XRD patterns of $Ba_{1.24}Sr_{1.7}Mg_{0.9}Si_2O_8$: $0.06Eu^{2+}$, $0.1Mn^{2+}$ combusted 1000° with different citric mass ratio of the starting materials, illustrates the well-defined $Sr_3MgSi_2O_8$ phase without Sr_2SiO_4 phase, **b** layer types of crystal structure of $Sr_3MgSi_2O_8$ originating from ICDC-35666. **c** shows the median diameters for phosphors of $Ba_{1.24}Sr_{1.7}Mg_{0.9}Si_2O_8$: $0.06Eu^{2+}$, $0.1Mn^{2+}$ with different citric addition, **d** PL spectra of $Ba_{1.24}Sr_{1.7}Mg_{0.9}Si_2O_8$: $0.06Eu^{2+}$, $0.1Mn^{2+}$ phosphor with different mass ratio. Reprinted from Ref. [61], with kind permission from Springer Science+Business Media

polymerization of MgO_6 octahedra and SiO_4 tetrahedra. There are three sites for Eu^{2+} between the layers with 8, 10, 10 coordinates, respectively. The cage-like phosphor prepared in this laboratory consists of many small crystallites with varying sizes, depending on process parameters such as concentration of the precursor. Proper amount of citric acid added to the starting solution and the ignition temperature for combustion greatly affect the size and morphology of phosphor product. The particle size distribution of the pure phosphor $Ba_{1.24}Sr_{1.7}Mg_{0.9}Si_2O_8$: $0.06Eu^{2+}$, $0.1Mn^{2+}$, indicating that when the fuel was added at 60 % citric mass ratio, phosphor particle size in around 7 µm was obtained. Through the comparison of samples with varied amount of the fuel in the range of 30, 45, 60, and 75 %, we observed that the overall intensity of red emission increases and then reaches a maximum at 45 % citric acid concentration, while that of the blue emission declines. It reveals that the energy transfer process in turn depends on citric acid concentration. Samples with appropriate citric acid addition yield lesser defects, which may cause lesser nonradiation decay [31]. The excessive or insufficient citric addition generates more defective luminance centers, and the nonradiation decay occurs when the relaxed excited state may return to the ground state through the centers mentioned above. The nonradiation decay may increase the energy loss during the energy transfer process for Eu^{2+} to Mn^{2+}.

Phosphor in the absence of green light emission was obtained through optimizing temperature and duration of firing and post-treatment. Figure 3.20 depicts photoluminescence spectrum upon excitation by 350-nm light, PLE spectrum as monitored at 430 and 660 nm and diffuse reflection spectrum (DRS) of $Ba_{1.24}Sr_{1.7}Mg_{0.9}Si_2O_8$: $0.06Eu^{2+}$, $0.1Mn^{2+}$ prepared by combustion synthesis with
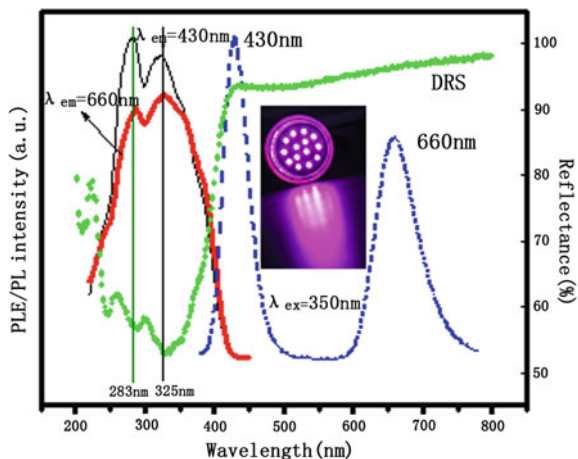
Fig. 3.20 Photoluminescence (PL), photoluminescence excitation (PLE), and diffuse reflection (DRS) and a 400-nm LED illumination prototype packaged with as-synthesized $Ba_{1.24}Sr_{1.7}Mg_{0.9}Si_2O_8$: $0.06Eu^{2+}$, $0.1Mn^{2+}$ phosphor prepared by combustion synthesis. Reprinted from Ref. [61], with kind permission from Springer Science+Business Media

45 % citric acid concentration. Excitation spectrum exhibits band emission ranging from 250 to 400 nm with two peaks at 283 and 325 nm; 430-nm blue emission band of specimen is resulted from $4f^65d^1 \rightarrow 4f^7$ electron transition of Eu^{2+}, in which the outer 5d orbitals is strongly impacted by the crystal field. Spin-forbidden $^4T(^4G) \rightarrow {}^6A_1(^6S)$ transition of Mn^{2+} is in charge of the 660-nm red emission band. The 8 and 10 coordination numbers of doping Eu^{2+} account for the two excitation peaks. The PLE spectrum and DRS contain the band that is the consequence of Eu^{2+} from $4f^7$ to $4f^65d(t_{2g})$ and $4f^65d(eg)$ energy levels, separately. The similarity of PLE shape for Eu^{2+} and Mn^{2+} indicates the excitation energy of Mn^{2+} transfers from Eu^{2+}. Efficient excitation band is monitored at 283 and 325 nm, which correspond well to the lower band of DRS. The excitation spectrum monitored at 660 nm is similar but weaker than that of spectrum monitored at 430 nm, which indicates the correlation between red and blue emission. It is red-orange light positioned at 660 nm and blue-violet light positioned at 450 nm that compose the major absorption light for the plant in the visible light range. Prepared phosphor could be encapsulated to be a LED prototype for plant illumination as illustrated in Fig. 7.

The simultaneous emission of blue and red light of $Ba_3MgSi_2O_8$: Eu^{2+}, Mn^{2+} can be enhanced by the metal-enhanced fluorescence (MEF) through assembling sliver island films [69]. The maximal enhancement factor was achieved as the thickness of silver films is around 50 nm upon annealing. The enhancement of blue emission by MEF leads to the enhancement of the red emission via transfer of energy in between Eu and Mn activator, exhibiting a simultaneous intensification effect of both blue and red emissions in such an indirect path.

3.3 Microwave Solvothermal Growth of 660-nm-Featured Sulfide Phosphor

A very classical RE-doped alkaline earth sulfide phosphor has long been recognized in its blue-excitable, red emission features. For instance, europium-doped calcium sulfide (CaS: Eu) [70] or α-(Y,Gd)FS: Ce^{3+} [71] is sufficiently excited by ultraviolet (UV) to visible light up to 600 nm. Lian [72] reported that CaS: Cu^+, Eu^{2+} polycrystalline possesses an emission band at 450 and 645 nm to enable a sunlight conversion to 650-nm wavelength red. Those RE-doped CaS phosphors were generally prepared by high-temperature solid-state synthesis procedure through sulfurizing calcium salts with RE activator in a hydrogen sulfide or a carbon disulfide atmosphere. The drawbacks exist in its sulfur-containing emission threat to the environment and poorly crystallized phosphor particles. High light conversion efficiency is highly dependent on crystalline degree and morphology. Some results have also been reported recently by adopting morphologically different phosphor crystallites to minimize the scattering loss through controllable solvothermal synthesis means so as to control well the particle size, morphology,

and structure. The exceptional advantages for synthesizing sulfide-hosted phosphor with solvothermal approach may lie in that those sulfur-containing pollutants are effectively limited to a closed autoclave, while the desired morphology or grain size could be obtained. Qian et al. [73] pioneered the solvothermal synthesis of CaS nanocrystalline. Poelman [74, 75] based on Qian's work successfully obtained the well-crystallined RE-doped (Ca,Sr)S: Eu crystals and proposed a prototype with solvothermally grown 650-nm emission crystals in arrays to construct electroluminescence (EL) devices. This idea is probably in clue of the route in more controlled selective area growth of GaN nanorods by using patterned substrates with metal organic chemical vapor deposition (MOCVD) or molecular beam epitaxy (MBE) to overcome present issues in lattice mismatch between substrate and epitaxy layer. For the present interest of 660-nm-featured red emission in PAR, it is noticed that a phenomenon in Poelman's work that a red-shift emission of phosphor crystal to 663 nm was observed even though that was only observed by accident in their experiments. This 660-nm or beyond emission of blue-excitable RE sulfide phosphor crystals is of critical importance in the consideration of its counterparts including either costly AlGaInP by MOCVD or severely prepared RE nitride phosphors.

MW solvothermal procedure was carried out to grow CaS: Eu crystals and repeatable red-shift phenomenon to 660-nm-featured emission for phosphor crystals with an average size of around 200 nm was observed [76]. Generally, MW processing procedure enables uniform heating and shortened reaction duration for synthesizing nanocrystalline. Organic solvent such as ethanol in MW field is of high dielectric loss substance that is easy to create homogeneous distribution in temperature and concentration. The MW solvothermal growth process was carried out in a commercial MW autoclave setup (2.45 GHz, Sineo MW Chem. Tech. Co., LTD., China). An optimized chemical composition in a formula of $Ca_{0.994-x}Mg_xS$: $0.004Mn^{2+}$, $0.002Eu^{2+}$ (x is denoted in atomic fraction) phosphors allows us possibly to concentrate on phenomenon observation of red-shift by using MW solvothermal process. The starting materials were of analytical purity $CaCl_2 \cdot 2H_2O$, $MnCl_2 \cdot 4H_2O$, $MgCl_2 \cdot 6H_2O$, $EuCl_3 \cdot 6H_2O$, $Na_2S \cdot 9H_2O$ and absolute ethanol as solvents.

Figure 3.21a shows the PL spectrum of CaMgS: Mn^{2+}, Eu^{2+} crystals prepared by solid-state reaction and MW solvothermal synthesis. The CaMgS: Mn^{2+}, Eu^{2+} crystal prepared by solid-state reaction exhibits a broad emission spectrum with a peak around 650 nm under the excitation of 450-nm blue light. However, the position of PL peak of CaMgS: Mn^{2+}, Eu^{2+} crystal prepared by MW solvothermal synthesis has a pronounced red-shift to 660 nm. According to previous research results, MW more likely promoted the formation of small particles [26]. Thus, it is inferred that the presence of small grains of MW solvothermal crystal could induce the red-shift of the emission. Figure 3.21b shows that the PL spectrum of MW solvothermal grown crystals was recorded at 450 nm. As shown in Fig. 1b, the host matrix remains unchanged, and Mn^{2+} ion doped into CaMgS: Eu^{2+} improves the intensity of PL. As established in general, incident photonic energy absorbed by Mn^{2+} is transferred to luminous center Eu^{2+}, leading to the red emission band to
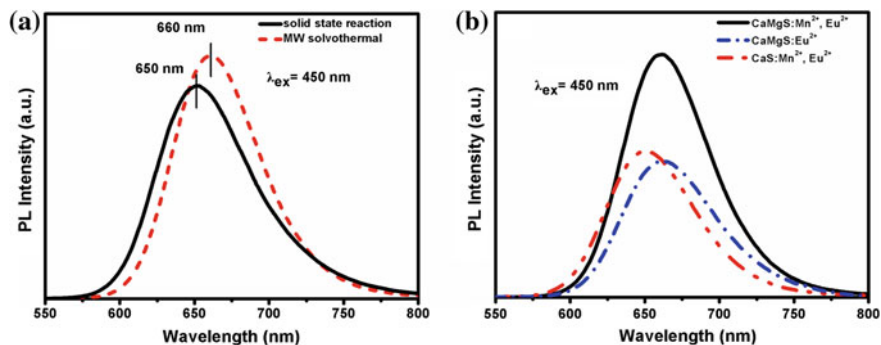
Fig. 3.21 **a** PL excited at 450 nm of CaMgS: Mn^{2+}, Eu^{2+} crystals prepared by solid-state reaction and MW solvothermal method, respectively. **b** PL excited at 450 nm of CaMgS: Mn^{2+}, Eu^{2+}, CaMgS: Eu^{2+}, and CaS: Mn^{2+}, Eu^{2+} crystals prepared by MW solvothermal method. Reprinted from Ref. [76], copyright 2014, with permission from Elsevier

enhance the PL intensity. It can be seen that the intensity of PL is enhanced as Mg^{2+} doped into CaS: Mn^{2+}, Eu^{2+} crystal. This result is in agreement with what was reported previously that a suitable substitution of Ca by Mg was beneficial to enhance the intensity of emission. However, we note that there exists a red-shift of the position of PL peak, which appears as Mg^{2+} codoping in the MW solvothermal crystal. As we have demonstrated that Mg^{2+} codoping crystal was prepared by solid-state reaction, not distinct red-shift was observed. Hence, we infer that Mg^{2+} codoping and MW disturbance exhibit a combination effect relevant to red-shift of the position of 660-nm-peaked PL.

Figure 3.22 depicts the PLE and PL spectra of MW solvothermal $Ca_{0.994-x}Mg_xS$: $0.004Mn^{2+}$, $0.002Eu^{2+}$ ($x = 0.1, 0.2, 0.3, 0.4, 0.5$) crystals with different contents of Mg^{2+} ion. The particles absorbed excitation energy from 250 to 600 nm and had the

Fig. 3.22 PLE monitored at 660 nm and PL excited at 450 nm of $Ca_{0.994-x}Mg_xS$: $0.004Mn^{2+}$, $0.002Eu^{2+}$ ($x = 0.1, 0.2, 0.3, 0.4, 0.5$) crystals. Reprinted from Ref. [76], copyright 2014, with permission from Elsevier
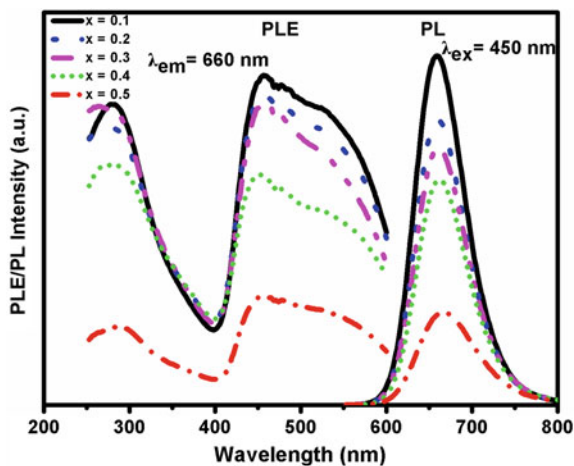
optimum excitation wavelength at 280 and 450 nm. The emission spectra show a broadband feature and the fluorescence intensity decreases with x until a maximum at a value of $x = 0.1$. The peak wavelengths vary from 660 to 666 nm. This result can be attributed to Mg^{2+} codoping and MW disturbance caused strain effect at grain boundaries owing to the formation of small-sized grains in nanometer- to micrometer-sized particles. It is known that Eu^{2+} with a transition between the excited state $4f^65d(T_{2g})$ and the ground-state $4f^7(^8S_{7/2})$. The split energy levels or the splitting patterns are determined by the chemical environment and the symmetry of the host matrix around the Eu^{2+} ion. In this case, Mg^{2+} codoping and the formation of small grain have a dominant effect on the emission spectra, which ascribed to enhance the crystal field at the boundaries from increasing the amount of nanosized grains. Consequently, Mg^{2+} codoping and a decrease in grain size lead to increased crystal field strength around the activators, resulting in decrease in the energy difference between the ground-state $4f^7$ and the excited state $4f^65d$, so that there will be stronger splitting of the T_{2g} and E_g levels. Although the 4f electrons of Eu^{2+} are not sensitive to a lattice environment due to the shielding function of the electrons in the outer shell, the 5d electrons are split by the crystal field, which may lead to the shift of the emission band. In a word, this red-shift probably resulted from the codoping of Mg^{2+} and the formation of nanosized grains in micrometer-sized particle upon disturbing by MW electromagnetic field in solvothermal growth environment.

3.4 660-nm-Featured Nitride-Based and Other Phosphors

The blue-excitable nitride-based nitride luminescent materials have emerged as a very efficient red-emitting phosphor [77, 78]. This variety of phosphor is investigated intensively worldwide owing to the primary motivation to add red component to construct warm white in LED lighting [79]. The host lattice of $CaAlSiN_3$ features in its coordination asymmetric geometry, strong covalency or local polarization and lower 5d energy level [80], allowing this phosphor in deep red emission. The peak wavelength of emission shows high dependence on the content of Eu dopant. The synthesis route for $CaAlSiN_3$: Eu^{2+} phosphor mainly includes a solid-state reaction, gas-reduction nitridation, and carbothermal reduction nitridation. For instance, a typical method used metal nitrides of Ca_3N_2, AlN, Si_3N_4, and EuN as starting materials under severe conditions (e.g., 0.9 MPa, 1800 °C) [77]. A lot of new synthesis routes have been explored [77, 81–99] and more detailed contents relevant can be found in the previous chapters. The peak wavelength of the broadband emission for $CaAlSiN_3$: Eu^{2+} is precisely adjustable to achieve the broad 660-nm or beyond emission to construct PAR in horticulture lighting. The unique properties of $CaAlSiN_3$: Eu^{2+} in its low thermal quenching and high chemical stability offer lots of advantages for LED/LD lighting sources in horticulture that is generally in service under severe environmental conditions.

A variety of RE-free phosphors with red emission draw much interests particularly by taking use of transition emission of Mn ion in some specific hosts. Red emissions of Mn^{4+} at 620–700 nm originate from the transitions $^4A_2 \rightarrow {}^4T_2$ and $^2E \rightarrow {}^4A_2$ depending on specific hosts. Mn^{4+}-activated fluoride hosts [33, 100–104] such as $BaGeF_6$, K_2MF_6 (M = Ge, Si), $BaTiF_6$, Na_2SiF_6, $K2TiF6$, $K2SiF6$, $K2GeF6$, $NaGdF$, $NaYF4$, and oxide hosts [105, 106] such as $CaAl_{12}O_{19}$, La_2MgGeO_6, $CaMg_2Al_{16}O_{27}$, $Ca_{14}Al_{10}Zn_6O_{35}$ are emerging as a new class of rare earth-free red-emitting phosphors. For instance, Mn^{4+}-activated $K2TiF6$: Mn^{4+} microcrystals were synthesized by the cation-exchange reaction and a photoluminescence quantum yield as high as 98 % for [33]. There are three intense excitation bands of K_2TiF_6: Mn^{4+} (0.72 at.%) in the range of 200–550 nm. The 468-nm-peaked band with around 50 nm of full-width at half-maximum is owing to the spin-allowed $^4A_2$–$^4T_2$ transition and indicates that this phosphor is excitable by blue InGaN LED. The red emission originating from the spin-forbidden ^2E_g–$^4A_2$ transition features in several sharp lines distributed in the spectral range of 610–650 nm with the strongest peak at 631.5 nm. Upon blue LED excitation, the combination by blending K_2TiF_6: Mn^{4+} with YAG: Ce^{3+} phosphor generates warm white, or by using single K_2TiF_6: Mn^{4+} phosphor. Similarly, a Mn^{4+}-activated phosphor $Ca_{14}Zn_6M_{10}O_{35}$: Mn^{4+} (M = Al^{3+} and Ga^{3+}) [106] that was prepared by high-temperature synthesis exhibits a longer-wavelength red emission at around 713 nm, which is excitable at 450-nm blue light. These Mn^{4+}-activated phosphors can also be considered as phosphor candidates to generate desired red light of the PAR for lighting in horticulture.

3.5 Summary and Prospective

The wavelength range of PAR in lighting sources is recognized to mainly locate at red and blue band for photosynthetic reaction, but the role of green-yellow band needs to be further evaluated. High-power LEDs are limited to achieve high irradiation intensity of lighting relevant to PPFD owing to 'efficiency droop' of semiconductor chip and thermal dissipation. LD technology featured in its high brightness is evolving into next-generation lighting technology, applicable to horticulture lighting. Blue LD-excited luminous glass in phosphor-in-glass is an important option. Therefore, significance of red-emitting phosphors is important to meet the requirements to achieve warm white or high color rendering index. Properly designed red light peaked at 660 nm with a proper full-width at half-maximum is important by combining with 430-nm blue to cover beneficial 730 nm.

References

1. Ceriani MF, Darlington TK, Staknis D, Mas P, Petti AA, Weitz CJ, Kay SA (1999) Light-dependent sequestration of TIMELESS by CRYPTOCHROME. Science 285 (5427):553-556. doi:10.1126/science.285.5427.553
2. Ahmad M, Jarillo JA, Smirnova O, Cashmore AR (1998) Cryptochrome blue-light photoreceptors of Arabidopsis implicated in phototropism. Nature 392 (6677):720-723. doi:10.1038/33701
3. Zhu X-G, Long SP, Ort DR (2008) What is the maximum efficiency with which photosynthesis can convert solar energy into biomass? Current Opinion in Biotechnology 19 (2):153-159. doi:10.1016/j.copbio.2008.02.004
4. Scholes GD, Fleming GR, Olaya-Castro A, van Grondelle R (2011) Lessons from nature about solar light harvesting. Nat Chem 3 (10):763-774. doi:10.1038/nchem.1145
5. Dugar D, Stephanopoulos G (2011) Relative potential of biosynthetic pathways for biofuels and bio-based products. Nature Biotechnology 29 (12):1074-1078. doi:10.1038/nbt.2055
6. Sheehan J (2009) Engineering direct conversion of CO(2) to biofuel. Nature Biotechnology 27 (12):1128-1129. doi:10.1038/nbt1209-1128
7. Liu C, Hwang YJ, Jeong HE, Yang PD (2011) Light-Induced Charge Transport within a Single Asymmetric Nanowire. Nano Lett 11 (9):3755-3758. doi:10.1021/nl201798e
8. Li CH, Wang F, Yu JC (2011) Semiconductor/biomolecular composites for solar energy applications. Energy Environ Sci 4 (1):100-113. doi:10.1039/c0ee00162g
9. Zhou H, Li XF, Fan TX, Osterloh FE, Ding J, Sabio EM, Zhang D, Guo QX (2010) Artificial Inorganic Leafs for Efficient Photochemical Hydrogen Production Inspired by Natural Photosynthesis. Adv Mater 22 (9):951-+. doi:10.1002/adma.200902039
10. Chisti Y, Yan J (2011) Energy from algae: Current status and future trends Algal biofuels - A status report. Applied Energy 88 (10):3277-3279. doi:10.1016/j.apenergy.2011.04.038
11. Torkamani S, Wani SN, Tang YJ, Sureshkumar R (2010) Plasmon-enhanced microalgal growth in miniphotobioreactors. Applied Physics Letters 97 (4):043703. doi:10.1063/1.3467263
12. McCree KJ (1972) The action spectrum, absorptance and quantum yield of photosynthesis in crop plants. Agric Meteorol 9 (5):191-216
13. Pinho P, Jokinen K, Halonen L (2012) Horticultural lighting - present and future challenges. Lighting Research & Technology 44 (4):427-437. doi:10.1177/1477153511424986
14. Fankhauser C (2001) The phytochromes, a family of Red/Far-red absorbing photoreceptors. Journal of Biological Chemistry 276 (15):11453-11456. doi:10.1074/jbc.R100006200
15. Folta KM, Maruhnich SA (2007) Green light: a signal to slow down or stop. Journal of experimental botany 58 (12):3099-3111. doi:10.1093/jxb/erm130
16. Kim HH, Goins GD, Wheeler RM, Sager JC (2004) Green-light supplementation for enhanced lettuce growth under red- and blue-light-emitting diodes. Hortscience 39 (7):1617-1622
17. Waring J, Underwood GJC, Baker NR (2006) Impact of elevated UV-B radiation on photosynthetic electron transport, primary productivity and carbon allocation in estuarine epipelic diatoms. Plant Cell Environ 29 (4):521-534. doi:10.1111/j.1365-3040.2005.01429.x
18. Ge S, Smith RG, Jacovides CP, Kramer MG, Carruthers RI (2011) Dynamics of photosynthetic photon flux density (PPFD) and estimates in coastal northern California. Theor Appl Climatol 105 (1-2):107-118. doi:10.1007/s00704-010-0368-6
19. Cashmore AR, Jarillo JA, Wu YJ, Liu DM (1999) Cryptochromes: Blue light receptors for plants and animals. Science 284 (5415):760-765. doi:10.1126/science.284.5415.760
20. Pettai H, Oja V, Freiberg A, Laisk A (2005) Photosynthetic activity of far-red light in green plants. Biochimica Et Biophysica Acta-Bioenergetics 1708 (3):311-321. doi:10.1016/j.bbabio.2005.05.005

21. Wendler J, Holzwarth AR (1987) State transitions in the green alga scenedesmus obliquus probed by time-resolved chlorophyll fluorescence spectroscopy and global data analysis. Biophysical journal 52 (5):717-728

22. Emerson R, Chalmers R, Cederstrand C (1957) Some factors influencing the long-wave limte of photosynthesis. Proceedings of the National Academy of Sciences of the United States of America 43 (1):133-143. doi:10.1073/pnas.43.1.133

23. Pettai H, Oja V, Freiberg A, Laisk A (2005) The long-wavelength limit of plant photosynthesis. Febs Letters 579 (18):4017-4019. doi:10.1016/j.febslet.2005.04.088

24. Lee MJ, Park SY, Oh MM (2015) Growth and cell division of lettuce plants under various ratios of red to far-red light-emitting diodes. Horticulture Environment and Biotechnology 56 (2):186-194. doi:10.1007/s13580-015-0130-1

25. Finlayson SA, Hays DB, Morgan P (2007) phyB-1 sorghum maintains responsiveness to simulated shade, irradiance and red light: far-red light. Plant Cell Environ 30 (8):952-962. doi:10.1111/j.1365-3040.2007.01695.x

26. Oh JH, Kang H, Park HK, Do YR (2015) Optimization of the theoretical photosynthesis performance and vision-friendly quality of multi-package purplish white LED lighting. Rsc Advances 5 (28):21745-21754. doi:10.1039/c4ra13853h

27. Yano A, Fujiwara K (2012) Plant lighting system with five wavelength-band light-emitting diodes providing photon flux density and mixing ratio control. Plant Methods 8:46. doi:10.1186/1746-4811-8-46

28. D.Despommier (2010) The vertical farm: feeding the world in the 21st century St. Martin's Press

29. Morrow RC (2008) LED Lighting in Horticulture. Hortscience 43 (7):1947-1950

30. Kitai A (ed) (2008) Luminescent Materials and Applications. John Wiley & Sons, Ltd

31. Wierer JJ, Jr., Tsao JY, Sizov DS (2013) Comparison between blue lasers and light-emitting diodes for future solid-state lighting. Laser & Photonics Reviews 7 (6):963-993. doi:10.1002/lpor.201300048

32. Blasse G, wanmaker.w.L (1968) Fluorescence of Eu^{2+} activated silicates. Philips Res Repts 23:189-200

33. Zhu H, Lin CC, Luo W, Shu S, Liu Z, Liu Y, Kong J, Ma E, Cao Y, Liu R-S, Chen X (2014) Highly efficient non-rare-earth red emitting phosphor for warm white light-emitting diodes. Nature Communications 5:4312. doi:10.1038/ncomms5312

34. Thiyagarajan P, Rao MSR (2010) Cool white light emission on $Ca_3MgSi_2O_8:Ce^{3+}$ Eu^{2+} phosphors and analysis of energy transfer mechanism. Appl Phys A-Mater Sci Process 99 (4):947-953. doi:10.1007/s00339-010-5702-4

35. Yonesaki Y, Takei T, Kumada N, Kinomura N (2010) Sensitized red luminescence from Ce^{3+}, Mn^{2+}-doped glaserite-type alkaline-earth silicates. J Solid State Chem 183 (6):1303-1308. doi:10.1016/j.jssc.2010.04.004

36. Yonesaki Y, Takei T, Kumada N, Kinomura N (2008) Crystal structure of $BaCaMgSi_2O_8$ and the photoluminescent properties activated by Eu2+. Journal of Luminescence 128 (9):1507-1514. doi:10.1016/j.jlumin.2008.02.011

37. Im WB, Kim YI, Yoo HS, Jeon DY (2009) Luminescent and Structural properties of $(Sr_{1-x}, Ba_x)_3MgSi_2O_8:Eu^{2+}$: Effects of Ba Content on the Eu2 + Site preference for Thermal Stability. Inorg Chem 48 (2):557-564. doi:10.1021/ic8012798

38. Umetsu Y, Okamoto S, Yamamoto H (2008) Photoluminescence properties of $Ba_3MgSi_2O_8$: Eu^{2+} blue phosphor and $Ba_3MgSi_2O_8$: Eu^{2+},Mn^{2+} blue-red phosphor under near-ultraviolet-light excitation. Journal of the Electrochemical Society 155 (7):J193-J197. doi:10.1149/1.2908877

39. Okamoto S, Nanba Y, Honma T, Yamamoto H (2008) Ba-substitution effect on luminescent properties and thermal degradation of $Sr_3MgSi_2O_8$: Eu^{2+} blue phosphor under Vacuum-UV-Light excitation. Electrochemical and Solid State Letters 11 (6):J47-J49. doi:10.1149/1.2894909

40. Kim JS, Jeon PE, Choi JC, Park HL, Mho SI, Kim GC (2004) Warm-white-light emitting diode utilizing a single-phase full-color $Ba_3MgSi_2O_8$: Eu^{2+}, Mn^{2+} phosphor. Applied Physics Letters 84 (15):2931. doi:10.1063/1.1695441

41. Kim JS, Kwon AK, Park YH, Choi JC, Park HL, Kim GC (2007) Luminescent and thermal properties of full-color emitting $X_3MgSi_2O_8$:Eu^{2+}, Mn^{2+} (X = Ba, Sr, Ca) phosphors for white LED. Journal of Luminescence 122-123:583-586. doi:10.1016/j.jlumin.2006.01.231

42. Cai Y, Lu QF, Li J, Qiu K, Wang P, Ding M, Wang DJ (2012) Intensification of the Photosynthetic Action Spectrum of $Ba_3MgSi_2O_8$: Eu^{2+}, Mn^{2+} Phosphor with Metal-Enhanced Fluorescence. Electrochem Solid State Lett 15 (2):P1-P4. doi:10.1149/2.014202esl

43. Ma L, Wang D-j, Mao Z-y, Lu Q-f, Yuan Z-h (2008) Investigation of Eu–Mn energy transfer in $A_3MgSi_2O_8$:Eu^{2+}, Mn^{2+} (A = Ca,Sr,Ba) for light-emitting diodes for plant cultivation. Applied Physics Letters 93 (14):144101. doi:10.1063/1.2996256

44. Jung HK, Seo KS (2006) Luminescent properties of Eu^{2+}-activated $(Ba,Sr)_3MgSi_2O_8$ phosphor under VUV irradiation. Opt Mater 28 (6-7):602-605

45. Sun XYY, Zhang JH, Zhang X, Lu SZ, Wang XJ (2007) A white light phosphor suitable for near ultraviolet excitation. Journal of Luminescence 122:955-957. doi:10.1016/j.jlumin.2006.01.336

46. Hwangbo S, Jeon YS, Kang BA, Kim YS, Hwang KS, Kim JT (2010) Sol-gel derived blue-emitting $Sr_3MgSi_2O_8$:Eu^{2+} oxide phosphor for ultraviolet emitting diodes. J Ceram Process Res 11 (4):513-515

47. Jung KY, Han KH, Jung HK (2009) Luminescence Optimization of $M_3MgSi_2O_8$:Eu^{2+} Phosphor by Spray Pyrolysis Combined with Combinatorial Chemistry for UV-LED Application. Journal of the Electrochemical Society 156 (6):J129-J133

48. Pan W, Ning GL (2007) Synthesis and luminescence properties of $Sr_3MgSi_2O_8$:Eu^{2+}, Dy^{3+} by a novel silica-nanocoating method. Sensors and Actuators a-Physical 139 (1-2):318-322. doi:10.1016/j.sna.2006.12.021

49. Lin YH, Zhang ZT, Tang ZL, Wang XX, Zhang JY, Zheng ZS (2001) Luminescent properties of a new long afterglow Eu^{2+} and Dy^{3+} activated $Ca_3MgSi_2O_8$ phosphor. Journal of the European Ceramic Society 21 (5):683-685

50. Barry TL (1968) Equilibria and Eu^{2+} luminescence of subsolidus phases bounded by $Ba_3MgSi_2O_8$, $Sr_3MgSi_2O_8$ and $Ca_3MgSi_2O_8$. JElectrochemSoc: Solid State Science 115:733-738

51. Park C-H, Kim T-H, Yonesaki Y, Kumada N (2011) A re-investigation of the crystal structure and luminescence of $BaCa_2MgSi_2O_8$:Eu^{2+}. J Solid State Chem 184:1566-1570

52. Yonesaki Y, Takei T, Kumada N, Kinomura N (2009) Crystal structure of EU2 + -doped $M_3MgSi_2O_8$ (M: Ba, Sr, Ca) compounds and their emission properties. J Solid State Chem 182 (3):547-554

53. Park CH, Hong ST, Keszler DA (2009) Superstructure of a phosphor material $Ba_3MgSi_2O_8$ determined by neutron diffraction data. J Solid State Chem 182 (3):496-501. doi:10.1016/j.jssc.2008.11.024

54. Iwata T, Horie T, Fukuda K (2009) Reinvestigation of crystal structure and structural disorder of $Ba_3MgSi_2O_8$. Powder Diffr 24 (3):180-184

55. Aitasalo T, Hietikko A, Holsa J, Lastusaari M, Niittykoski J, Piispanen T (2007) Crystal Structure of the $Ba_3MgSi_2O_8$: Mn^{2+},Eu^{2+} phosphor for white light emitting diodes. Z Kristallogr:461-466

56. Ma L, Wang DJ, Zhang HM, Gu TC, Yuan ZH (2008) The origin of 505 nm-peaked photoluminescence from $Ba_3MgSi_2O_8$: Eu^{2+}, Mn^{2+} phosphor for white-light-emitting diodes. Electrochemical and Solid State Letters 11 (2):E1-E4. doi:10.1149/1.2817472

57. Kim JS, Jeon PE, Park YH, Choi JC, Park HL, Kim GC, Kim TW (2004) White-light generation through ultraviolet-emitting diode and white-emitting phosphor. Applied Physics Letters 85 (17):3696. doi:10.1063/1.1808501

58. Lu Q-F, Li J, Wang D-J (2013) Single-phased silicate-hosted phosphor with 660 nm-featured band emission for biological light-emitting diodes. Current Applied Physics 13 (7):1506-1511. doi:10.1016/j.cap.2013.05.013

59. Wang L, Lu Q, Li J, Lin C, Cao L, Wang D (2013) Microwave firing-incubation of cage-like $(Ba,Sr)_3MgSi_2O_8$:0.06Eu^{2+},0.1Mn^{2+} sphere from sprayed template-free xerogel particles. J Rare Earths 31 (6):541-545. doi:10.1016/s1002-0721(12)60316-0

60. Cao L-s, Lu Q-f, Wang L-c, Li J, Song J, Wang D-J (2013) Microwave-induced small size effect of $(Ba,Sr)_3MgSi_2O_8$:0.06Eu^{2+}, 0.1Mn^{2+} phosphor for 660 nm-featured bio-lighting. Ceram Int 39 (7):7717-7720. doi:10.1016/j.ceramint.2013.03.026

61. Sun L, Lu Q, Mao Z, Wang D (2015) Enhancement of photosynthetic action spectrum for 660 nm-featured phase-pure $(Ba,Sr)_3MgSi_2O_8$: Eu^{2+}, Mn^{2+} phosphor by spray-combustion synthesis. J Mater Sci-Mater Electron 26 (4):2647-2653. doi:10.1007/s10854-015-2739-3

62. Li X, Fan T (2011) Artificial Photosynthesis. Prog Chem 23 (9):1841-1853

63. Posten C (2009) Design principles of photo-bioreactors for cultivation of microalgae. Eng Life Sci 9 (3):165-177. doi:10.1002/elsc.200900003

64. Pienkos PT, Darzins A (2009) The promise and challenges of microalgal-derived biofuels. Biofuels Bioprod Biorefining 3 (4):431-440. doi:10.1002/bbb.159

65. Lardon L, Helias A, Sialve B, Stayer JP, Bernard O (2009) Life-Cycle Assessment of Biodiesel Production from Microalgae. Environ Sci Technol 43 (17):6475-6481. doi:10.1021/es900705j

66. Zemke PE, Wood BD, Dye DJ (2010) Considerations for the maximum production rates of triacylglycerol from microalgae. Biomass Bioenerg 34 (1):145-151. doi:10.1016/j.biombioe.2009.10.012

67. Das S, Mukhopadhyay AK, Datta S, Basu D (2009) Prospects of microwave processing: An overview. Bull Mat Sci 32 (1):1-13. doi:10.1007/s12034-009-0001-4

68. Agrawal DK (1998) Microwave processing of ceramics. Curr Opin Solid State Mat Sci 3 (5):480-485. doi:10.1016/s1359-0286(98)80011-9

69. Yi Cai Q-FLJL, Kun Qiu, Peng Wang, Mei Ding, Da-Jian Wang (2012) Intensification of the Photosynthetic Action Spectrum of $Ba_3MgSi_2O_8$:Eu^{2+}, Mn^{2+} Phosphor with Metal-Enhanced Fluorescence. Electrochemical and Solid State Letters 15 (2) (1099-0062/2012/15(2)/P1/4/$28.00):P1-P4

70. Guo C, Huang D, Su Q (2006) Methods to improve the fluorescence intensity of CaS: Eu^{2+} red-emitting phosphor for white LED. Materials Science and Engineering: B 130 (1):189-193

71. Wu YC, Chen YC, Wang DY, Lee CS, Sun CC, Chen TM (2011) alpha-(Y,Gd)FS:Ce^{3+}: a novel red-emitting fluorosulfide phosphor for solid-state lighting. J Mater Chem 21 (39):15163-15166. doi:10.1039/c1jm12819a

72. Lian S, Qi Y, Rong C, Yu L, Zhu A, Yin D, Liu S (2010) Effectively Leveraging Solar Energy through Persistent Dual Red Phosphorescence: Preparation, Characterization, and Density Functional Theory Study of $Ca_2Zn_4Ti_{16}O_{38}$:Pr^{3+}. Journal of Physical Chemistry C 114 (15):7196-7204. doi:10.1021/jp911885c

73. Wang C, Tang K, Yang Q, An C, Hai B, Shen G, Qian Y (2002) Blue-light emission of nanocrystalline CaS and SrS synthesized via a solvothermal route. Chem Phys Lett 351 (5):385-390

74. Avci N, Cimieri I, Smet PF, Poelman D (2011) Stability improvement of moisture sensitive CaS:Eu^{2+} micro-particles by coating with sol–gel alumina. Opt Mater 33 (7):1032-1035. doi:10.1016/j.optmat.2010.07.021

75. Avci N, Musschoot J, Smet PF, Korthout K, Avci A, Detavernier C, Poelman D (2009) Microencapsulation of Moisture-Sensitive CaS:Eu^{2+} Particles with Aluminum Oxide. Journal of The Electrochemical Society 156 (11):J333. doi:10.1149/1.3211959

76. Dong X, Lu Q, Lu Z, Mao Z, Wang D (2014) Investigation of the red-shift of the emission of microwave solvothermally-grown europium doped calcium sulphide crystals. J Rare Earths 32 (8):702-708

77. Uheda K, Hirosaki N, Yamamoto Y, Naito A, Nakajima T, Yamamoto H (2006) Luminescence properties of a red phosphor, CaAlSiN$_3$: Eu^{2+}, for white light-emitting diodes. Electrochemical and Solid State Letters 9 (4):H22-H25. doi:10.1149/1.2173192

78. Xie RJ, Hirosaki N (2007) Silicon-based oxynitride and nitride phosphors for white LEDs - A review. Sci Technol Adv Mater 8 (7-8):588-600. doi:10.1016/j.stam.2007.08.005

79. Mueller-Mach R, Mueller GO, Krames MR, Shchekin OB, Schmidt PJ, Bechtel H, Chen CH, Steigelmann O (2009) All-nitride monochromatic amber-emitting phosphor-converted light-emitting diodes. Physica Status Solidi-Rapid Research Letters 3 (7-8):215-217. doi:10.1002/pssr.200903188

80. Xie; R-J, Li; YQ, Hirosaki; N, Yamamoto H (eds) (2011) Nitride Posphors and Solid-State Lighting. CRC Press

81. Zhu J, Wang L, Zhou T, Cho Y, Suehiro T, Takeda T, Lu M, Sekiguchi T, Hirosaki N, Xie R-J (2015) Moisture-induced degradation and its mechanism of (Sr,Ca)AlSiN$_3$:Eu^{2+}, a red-color-converter for solid state lighting. Journal of Materials Chemistry C 3 (13):3181-3188. doi:10.1039/c4tc02824d

82. Wang J, Zhang H, Lei B, Xia Z, Dong H, Liu Y, Zheng M, Xiao Y (2015) Enhanced photoluminescence and phosphorescence properties of red CaAlSiN$_3$:Eu^{2+} phosphor via simultaneous UV-NIR stimulation. Journal of Materials Chemistry C 3 (17):4445-4451. doi:10.1039/c5tc00236b

83. Liu G, Tian Z, Chen Z, Wang H, Zhang Q, Li Y (2015) CaAlSiN3:Eu2+ phosphors bonding with bismuth borate glass for high power light excitation. Opt Mater 40:63-67. doi:10.1016/j.optmat.2014.11.047

84. Kim HS, Machida K-i, Horikawa T, Hanzawa H (2015) Luminescence properties of CaAlSiN$_3$:Eu^{2+} phosphor prepared by direct-nitriding method using fine metal hydride powders. Journal of Alloys and Compounds 633:97-103. doi:10.1016/j.jallcom.2015.01.069

85. Suehiro T, Xie R-J, Hirosaki N (2014) Gas-Reduction-Nitridation Synthesis of CaAlSiN$_3$: Eu^{2+} Fine Powder Phosphors for Solid-State Lighting. Industrial & Engineering Chemistry Research 53 (7):2713-2717. doi:10.1021/ie4038455

86. Kim HS, Machida K-i, Itoh M, Hanzawa H (2014) Synthesis and Luminescence Properties of (Sr, Ca)AlSiN$_3$:Eu^{2+} Phosphors under Atmospheric-Pressure. Ecs Journal of Solid State Science and Technology 3 (12):R234-R237. doi:10.1149/2.0061412jss

87. Kim HS, Machida K-i, Horikawa T, Hanzawa H (2014) Carbothermal Reduction Synthesis Using CaCN$_2$ as Calcium and Carbon Sources for CaAlSiN$_3$:Eu^{2+} Phosphor and Their Luminescence Properties. Chem Lett 43 (4):533-534. doi:10.1246/cl.131050

88. Jo DS, Senthil K, Song YH, Masaki T, Yoon D-H (2014) Synthesis of CaSiAlN$_3$: Eu^{2+} phosphor by liquid phase precursor method. J Ceram Process Res 15 (4):259-261

89. Hu W-W, Cai C, Zhu Q-Q, Xu X, Hao L-Y, Agathopoulos S (2014) Preparation of high performance CaAlSiN$_3$:Eu^{2+} phosphors with the aid of BaF$_2$ flux. Journal of Alloys and Compounds 613:226-231. doi:10.1016/j.jallcom.2014.06.026

90. Cho J, Bang BK, Jeong SJ, Kim CH (2014) Synthesis of red-emitting nanocrystalline phosphor CaAlSiN$_3$:Eu^{2+} derived from elementary constituents. Rsc Advances 4 (44):23218-23222. doi:10.1039/c4ra02550d

91. Kubus M, Meyer HJ (2013) A Low-Temperature Synthesis Route for CaAlSiN$_3$ Doped with Eu^{2+}. Zeitschrift Fur Anorganische Und Allgemeine Chemie 639 (5):669-671. doi:10.1002/zaac.201200533

92. Piao X, Machida K-i, Horikawa T, Yun B (2010) Acetate reduction synthesis of Sr$_2$Si$_5$N$_8$: Eu^{2+} phosphor and its luminescence properties. Journal of Luminescence 130 (1):8-12. doi:10.1016/j.jlumin.2009.03.008

93. Lei B, Machida K-i, Horikawa T, Hanzawa H (2010) Synthesis and Photoluminescence Properties of CaAlSiN$_3$:Eu^{2+} Nanocrystals. Chem Lett 39 (2):104-105. doi:10.1246/cl.2010.104

94. Watanabe H, Imai M, Kijima N (2009) Nitridation of AEAlSi for Production of AEAlSiN$_3$: Eu^{2+} Nitride Phosphors (AE=Ca, Sr). J Am Ceram Soc 92 (3):641-648. doi:10.1111/j.1551-2916.2009.02945.x

95. Li J, Watanabe T, Wada H, Setoyama T, Yoshimuraz M (2009) Synthesis of Eu-Doped CaAlSiN$_3$ from Ammonometallates: Effects of Sodium Content and Pressure. J Am Ceram Soc 92 (2):344-349. doi:10.1111/j.1551-2916.2008.02883.x

96. Watanabe H, Wada H, Seki K, Itoua M, Kijima N (2008) Synthetic method and luminescence properties of Sr$_x$Cal$_{(1-x)}$AlSiN$_3$: Eu^{2+} mixed nitride phosphors. Journal of the Electrochemical Society 155 (3):F31-F36. doi:10.1149/1.2829880

97. Li J, Watanabe T, Sakamoto N, Wada H, Setoyama T, Yoshimura M (2008) Synthesis of a multinary nitride, Eu-doped CaAlSiN$_3$, from alloy at low temperatures. Chem Mater 20 (6):2095-2105. doi:10.1021/cm071612m

98. Uheda K, Hirosaki N, Yamamoto H (2006) Host lattice materials in the system Ca$_3$N$_2$-AlN-Si$_3$N$_4$ for white light emitting diode. Phys Status Solidi A 203 (11):2712-2717. doi:10.1002/pssa.200669576

99. Piao XQ, Horikawa T, Hanzawa H, Machida K (2006) Photoluminescence properties of Ca$_2$Si$_5$N$_8$: Eu^{2+} nitride phosphor prepared by carbothermal reduction and nitridation method. Chem Lett 35 (3):334-335. doi:10.1246/cl.2006.334

100. Zhou Q, Zhou Y, Liu Y, Luo L, Wang Z, Peng J, Yan J, Wu M (2015) A new red phosphor BaGeF$_6$:Mn^{4+}: hydrothermal synthesis, photo-luminescence properties, and its application in warm white LED devices. Journal of Materials Chemistry C 3 (13):3055-3059. doi:10.1039/c4tc02956a

101. Wei L-L, Lin CC, Fang M-H, Brik MG, Hu S-F, Jiao H, Liu R-S (2015) A low-temperature co-precipitation approach to synthesize fluoride phosphors K$_2$MF$_6$:Mn^{4+} (M = Ge, Si) for white LED applications. Journal of Materials Chemistry C 3 (8):1655-1660. doi:10.1039/c4tc02551b

102. Wang Y, Wen T, Tang L, Yang L, Yang W, Zhao Y (2015) Impact of hydrostatic pressure on the crystal structure and photoluminescence properties of Mn^{4+}-doped BaTiF$_6$ red phosphor. Dalton Transactions 44 (16):7578-7585. doi:10.1039/c5dt00426h

103. Oh JH, Kang H, Eo YJ, Park HK, Do YR (2015) Synthesis of narrow-band red-emitting K$_2$SiF$_6$:Mn^{4+} phosphors for a deep red monochromatic LED and ultrahigh color quality warm-white LEDs. Journal of Materials Chemistry C 3 (3):607-615. doi:10.1039/c4tc02042a

104. Hoang-Duy N, Lin CC, Fang M-H, Liu R-S (2014) Synthesis of Na$_2$SiF$_6$:Mn^{4+} red phosphors for white LED applications by co-precipitation. Journal of Materials Chemistry C 2 (48):10268-10272. doi:10.1039/c4tc02062f

105. Wang B, Lin H, Xu J, Chen H, Wang Y (2014) CaMg$_2$Al$_{16}$O$_{27}$:Mn^{4+}-based Red Phosphor: A Potential Color Converter for High-Powered Warm W-LED. Acs Applied Materials & Interfaces 6 (24):22905-22913. doi:10.1021/am507316b

106. Lu W, Lv W, Zhao Q, Jiao M, Shao B, You H (2014) A Novel Efficient Mn4+ Activated Ca$_{14}$Al$_{10}$Zn$_6$O$_{35}$ Phosphor: Application in Red-Emitting and White LEDs. Inorg Chem 53 (22):11985-11990. doi:10.1021/ic501641q

Chapter 4
The Application of Phosphor in Agricultural Field

Xiaotang Liu, Bingfu Lei and Yingliang Liu

Abstract The applications of phosphor in agricultural field mainly include light conversion film (LCF) to cover greenhouse and LED plant lamp (LED-pl). For light conversion agent (LCA), phosphors are obviously indispensable for the devices and therefore influence their eventual performances such as light conversion efficiency and life of devices. For LCA, the phosphors should be able to be excited by the lights with wavelengths from 290 to 350 nm and/or from 510 to 580 nm and emit 400- to 480-nm blue light and 600- to 680-nm red light at the same time. This can match with the absorption peak of chlorophyll photosynthesis and therefore increase the overall efficiency of the plant photosynthesis and then increase yield and quality of crops. In this chapter, mechanisms and typical phosphors are reviewed, and some examples of practical application in vegetable and tea cultivation are exhibited. At the end, future challenges to research and development of these phosphors are discussed.

4.1 Mechanisms of Luminescent Materials Applied in Agriculture

About 95 % of dry matters of plants are organic materials which were synthesized by photosynthesis. Crop productivity depends basically on the photosynthetic efficiency and economic factors. In the absence of significant adverse conditions, the highest energy efficiency of sunlight utilized by crops in field can be up to 5 %, but generally the utilization rate is only about 1.1 %. So to improve the photosynthetic efficiency is the critical way to significantly improve crop yields [1].

X. Liu (✉) · B. Lei · Y. Liu
Guangdong Provincial Engineering Technology Research Center
for Optical Agriculture, College of Materials and Energy,
South China Agricultural University, Guangzhou 510642, China
e-mail: xtliu@scau.edu.cn

Leaves are plant organs for photosynthesis. When the sunlight shines onto the surface of a leaf, it will be absorbed by the pigment in plants. Those pigments which can absorb light energy for photosynthesis are chlorophyll α and β, α-carotene and lutein. Figure 4.1 shows that there are two absorption ranges which are benefit to photosynthesis: (1) blue light (400–500 nm). The strongest absorption peak of chlorophyll α is at 425 nm, and the strongest absorption peak of chlorophyll β, α-carotene and lutein is at 440 nm; (2) red-orange light area (600–680 nm). 645 and 660 nm are the strongest absorption peak of chlorophyll β and chlorophyll α, respectively. Solar average relative spectral energy distribution tells us that not all bands of the sun rays are useful for plant growth because green light is unnecessary to plants growth and ultraviolet light is even harmful to that [2]. If the ultraviolet and green light of sunlight can be converted into blue and/or red-orange light which are necessary to the photosynthesis of plants by a certain method, the composition of sunlight will be changed and be conducive to the photosynthesis. Therefore, the more efficient utilization of sunlight is quite valuable to increasing biomass production. Numerous studies indicate that by increasing the irradiation of blue or red light on the plants, the crop root system will be more developed, stems and leaves will be denser, and therefore ensure superior quality and higher production of the crops. Scientists called the blue and red light as "light fertilizer," which is a new type of environmental friendly "physical fertilizer" after the widely used "chemical fertilizers." In addition, if the 320- to 350-nm UV light can be absorbed before reaching the field, some harmful pests and diseases of plants will be inhibited. This technique is called as "physical pesticides."

Fig. 4.1 The absorption spectra of chlorophyll α and chlorophyll β. Reproduced from Ref. [3] by permission of spectroscopy and spectral analysis
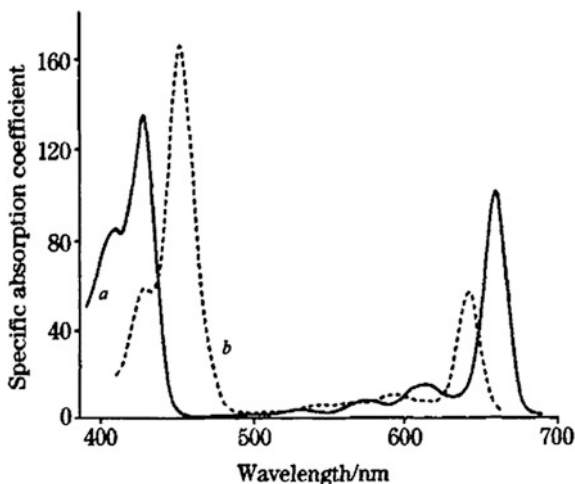
4.2   Phosphors Applied in Agriculture

The absorption spectra of chlorophyll α and chlorophyll β are slightly different, but they mainly absorb blue and red light and hardly absorb green and ultraviolet light [4, 5]. Therefore, as a light conversion material, the excitation spectra of the material must match with part of the solar spectrum that is not utilized by the plants, while the emission spectrum of materials must match with the absorption spectrum of plant chlorophyll. So, the basic requirements of light conversion agent are: (1) The main peak of excitation spectrum is 520- to 589-nm yellow-green light and/or 280- to 380-nm UV light; (2) the main peak of emission spectrum is 600- to 680-nm red light and/or 400- to 470-nm blue light.

The applications of light conversion agents in agriculture can be categorized into two major fields: light conversion greenhouse film and LED plants lamp.

The phosphors as light conversion agent for greenhouse film were organic light conversion agents [6, 7] at earliest stage and are still in use nowadays [8–12] because of their high luminous efficiency and good compatibility. But these light conversion agents mainly convert UV light to red light, and their emission spectra poorly match with absorption wavelength of plants. They are also of high cost and short fluorescence lifetime, fast decayed intensity, which further lower their value for practical applications.

In order to improve the characteristics of phosphors for greenhouse film, inorganic light conversion agents were researched. Scientists focused their interests on sulfide matrix doped with rare-earth ions and other metal ions [13–22]. This kind of materials can convert UV and green light to red light, while being maintained at a competitive price level. But they often suffer from deliquescence in the atmosphere and are easily oxidized under the sunlight. So its stability has to be improved by appropriate modifications.

4.3   The Application of Phosphor in Greenhouse Film

Light conversion film (LCF) is a kind of functional plastic film which was added with light conversion agent to improve composition of light through the film to be benefit to plants photosynthesis. LCF can absorb 290- to 350-nm UV light and 510- to 580-nm green light which are undesired for photosynthesis to emit 400- to 480-nm blue light and 600- to 680-nm red light. LCF can promote plant uptake of nitrogen, phosphorus, potassium, zinc and other nutrients, and improve the area and expending degree of leaf, and increase plant height and petiole length, thereby increasing the content of chlorophyll, which raises leaves photosynthesis products content, and finally promote crop growth [23–25]. Practices have proved that LCF has a more significant effect in enhancing photosynthesis of plants and the effective utilization of light, and then to promote crops early maturing to increase production and improve quality [1, 4, 26–28].

The application of synthetic resin for light conversion material in plant culti-vation has been patented in 1970s, Japan. The earliest concept of agricultural conversion film was proposed by former Soviet Academy of Sciences LN Golodkava and AF Lepaev [6, 7], who synthesized light conversion agent and added them to PE, PP, PVC, PMMA and other polymer materials to manufacture LCF and finished a series of experiments in farms. The results showed effects of LCF on increasing yield, quality and early maturing of crops significantly [1, 4, 26–28]. LCF was recommended as "the most promising film" in the International Horticulture High-tech Conference in Tokyo in 1988. Since then, some groups of Chinese institute, such as Institute of Physics Chinese Academy of Science, Hunan Normal University, Beijing Technology and Business University and South China Agriculture University, have done a lot of research and application experiments in this area [29–32], such as vegetable, tobacco, fruits and horticultural flowers [33–37]. Here, we just introduce the application of LCF in vegetable planting and tea cultivation.

In our experiments [32], low-density polyethylene (LDPE), red and blue light conversion agents and other additions were stirred into homogenization in the high-speed mixer and then squeezed out as masterbatch by twin-screw extrusion granulating. The masterbatch and LDPE were mixed, squeezed out by single screw and then blown into films at 190–200 °C. Greenhouses covered by the light con-version film were put up, and some vegetables were planted in them compared with blank greenhouse covered by commercial plastic film.

The excitation and emission spectra of two types of blue conversion agents are shown in Fig. 4.2. The absorption peak of them is at 375 nm, and their emission peaks are at 435 and 424 nm, respectively. Figure 4.3 shows the excitation spec-trum of red light conversion agent monitored with 640 nm (as line a) and the emission spectrum of it excited by 570 nm (as line b). The results indicated that these phosphors can absorb UV light and green light and then emit blue light and red light which match exactly with the absorption wavelength of chlorophyll as shown in Fig. 4.1.

Fig. 4.2 The excitation (λ_{em} = 435 nm) and emission (λ_{ex} = 375 nm) spectra of *a* blue light conversion agent I and *b* blue light conversion agent II
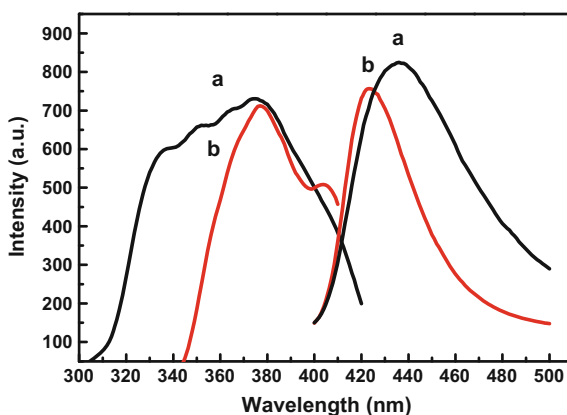
Fig. 4.3 The excitation (λ_{em} = 640 nm) and emission (λ_{ex} = 570 nm) spectra of red light conversion agent
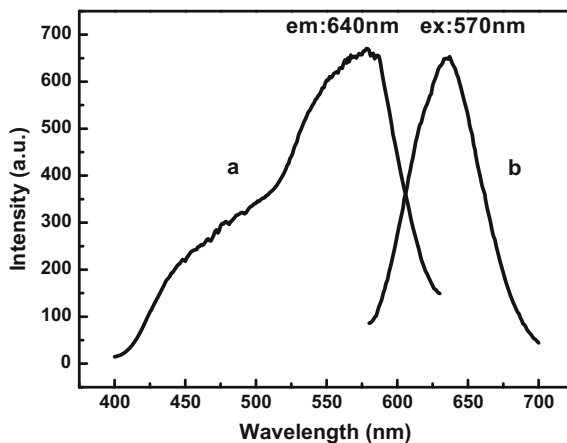
Fig. 4.4 (*1*) The excitation (λ_{em} = 435 nm) and emission (λ_{ex} = 375 nm) spectra of blue conversion film and blank film. (*2*) The excitation (λ_{em} = 640 nm) and emission (λ_{ex} = 570 nm) spectra of red conversion film and blank film
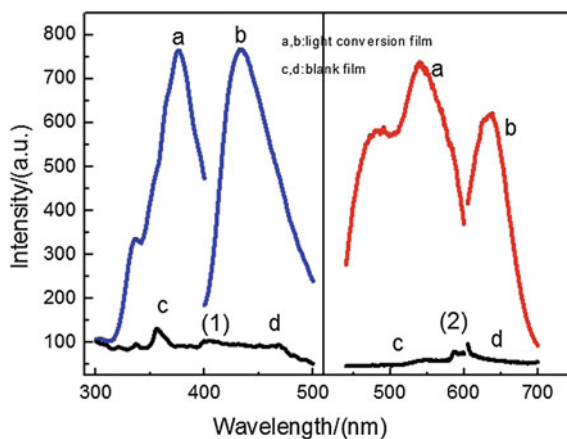
The spectra of light conversion films in Fig. 4.4 were measured under the same conditions as the light conversion agents. The results are in agreement with Figs. 4.2 and 4.3. It is obvious that the blank film has almost no luminescence. We can conclude that the light conversion agents, that preferably absorbed the UV and green light of sunlight to emit blue light and red light fitting the light input of plants' photosynthesis, were successfully added into the LDPE matrix. Pictures of LCF under UV lamp can be excited to emit blue light and red light, shown in Fig. 4.5, which were direct evidences. So these light conversion films are the best choices to exploit the solar energy and promote plants' photosynthesis.

Fig. 4.5 LCF with light conversion agents under UV lamp

4.4 The Application of LCF in Vegetable Planting

LCF was firstly applied in vegetable planting, which then attracted most researchers' attention. Some examples are given below to show the LCF's effects on vegetable. References [34, 38] show that tomato and cucumber planted in greenhouse covered with LCF were rareriper 3 and 4 days, respectively. Tables 4.1 and 4.2 indicate that LCF can increase yield and improve quality of vegetables [33, 38–40]. Therefore, LCF can make the vegetables planting in greenhouse early maturity, increase yield and increase the nutritional ingredients of vegetables. In addition, some reported that LCF was of benefit to reducing pests [34, 41–44].

4.4.1 Effect of Heat Preservation

All of our trials were three different treatments. CK is a part of an open-air farm as the control case which area is approximately the same as the area of a greenhouse. CF is the greenhouse which covered by commercial plastic film, sometimes called as ordinary film. LCF is the greenhouse covered by light conversion films which were added with our light conversion agents.

The temperature and humidity of all trials were recorded. As shown in Fig. 4.6, the monthly mean temperature in LCF was 1.6–3.4 °C higher than that in CF. It indicated that LCF had effect of heat preservation and its effect was better than CF.

4.4.2 Early Maturity Effect

In our earlier researches [45], we observed the yields of greens and mustard in LCF were 11.5–19.6 and 13.6–20.8 % higher than that in CF, respectively, and early maturity 5–7 days and 5–8 days, respectively. In LCF, the vegetable leaves were

Table 4.1 The amount of yield increased by using LCF

Varieties	Tomato	Eggplant	Cucumber	Green pepper	Chinese cabbage
Yield increase (%)	13	20.8	21.6	15.1	7.35–13.7

Table 4.2 The amount of content increased by using LCF

Varieties	Dry materials (%)	Soluble sugar (%)	Vc/mg 100 g^{-1}	Fresh weight (%)
Chinese cabbage	57.24	70.34	9.61	
Cucumber		9.7	31.4	40
Pakchoi		20.8	4.73	6.65

Fig. 4.6 Monthly mean temperature of greenhouses covered LCF and CF (test time: 1:00 p.m.)
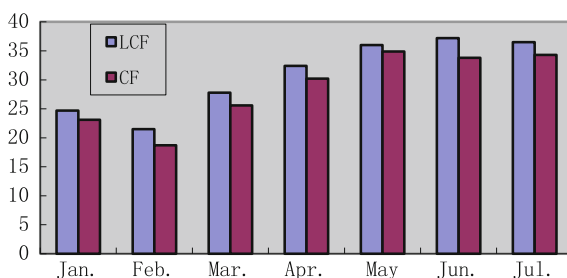
fresh and larger, and their color and taste were also significantly better than those in the comparative films.

4.4.3   Increasing Production Effect

The results of covering film trials on vegetables are shown in Table 4.3. The vegetable production increased significantly (19.8–56.0 %) after covered by LCF while maintaining the same other experimental conditions. It indicates that the light conversion films can make full use of solar energy. Therefore, it is a safe and efficient way to increase yield. Table 4.4 shows the results of another vegetable trails which is in agreement with Table 4.3. Compared with CF, the yield of

Table 4.3 The results of covering film trials on vegetables

Varieties	Average fresh weight (g)		Increase in yield (%)
	CF	LCF	
Japanese Pakchoi	197.8	264.4	33.7
Cabbage	97.1	116.3	19.8
Mustard	232.2	283.1	21.9
Lettuce	192.9	300.9	56.0

vegetables in greenhouse covered by LCF increases by 20.3–52.4 %. Furthermore, the vegetables in LCF have stronger growth and had thicker and brighter leaves.

4.4.4 Improving Quality Effect

Table 4.5 shows the production of cherry tomato in different treatments. The production significantly increased in LCF greenhouse than that in CF greenhouse and CK, or the yield increasing was 91.4 % versus CF and 71.9 % versus CK.

LCF not only increases production of vegetables but also can improve the quality of vegetables. As shown in Table 4.6, soluble sugar and free amino acid of cherry tomato in LCF were higher than those in CF and CK. Free amino acid of cherry tomato in LCF greenhouse was 1.6 times higher than that in CF and 1.2 times higher than that in CK. The Vc content of cherry tomato in greenhouses was above 3.26 times higher than that in CK, and that in LCF was comparable with that in CF.

In pimiento planting trials, we observed significant growth difference of pimiento between LCF and CF. Firstly, pimiento in LCF grew quicker, and the foliage lusher and chlorophyll were better than those in CF, as shown in Fig. 4.7. Secondly, the fully mature period in LCF was more than 20 days earlier than that in CF. Thirdly, the production of pimiento in LCF increased up to 40 %. Furthermore, the quality of pimiento was improved (as shown in Table 4.7) and of good taste. Finally and the most importantly, there were less pests found in LCF.

Table 4.7 shows that Vc, soluble sugar and free amino acid of pimiento in LCF were higher than those in CF. Meanwhile, nitrate and soluble phenol of pimiento in LCF decreased significantly. The pimiento in LCF had good taste, not only because of higher soluble sugar but also because of lower soluble phenol which leads to a stringent taste. The results suggested that LCF is of benefit to the accumulation of organic matter and improvement of quality.

4.4.5 Development of Root System

Figures 4.8 and 4.9 show two seeding trails. Obviously, the seeding in LCF generated more developed root system and wider and thicker leaves than that in CF. These indicated that the seeding cultivated in LCF was healthier, and then, they would grow more quickly and healthily. So plant diseases and pests would decrease, and production would increase and quality would improve.

Table 4.4 Comparison of yield of different vegetables in different treatments

Treatment	Yield	Pictures		
		LCF	CF	CK
Lettuce				
LCF	218			
CF	143			
CK	100			
Japanese Pakchio				
LCF	345			
CF	258			
CK	100			
Cabbage				
LCF	172			
CF	143			
CK	100			
Mustard				
LCF	326			
CF	259			
CK	100			

4.5 The Application of Phosphor in Tea Cultivation

In order to advance the spring tea start-picking period and increase the production of the high-quality spring tea, especially Mingqian tea, the experiment of tea garden covered by plastic film during cold period in winter to preserve heat has been studied to shorten the period of dormancy of tea tree and advance spring tea spout stage and start-picking period [46]. However, many experiments [47–50] show that

Table 4.5 The production of cherry tomato in different treatments

Treatment	Production (g)				
	May 5	May 9	May 15	May 13	Total
LCF	941.8	2127.1	9732.7	6560.2	19368.8
CF	1235.3	1821.3	2045.1	5016.2	10117.9
CK	148.2	1134.4	2917.4	7067.9	11267.9

Table 4.6 Quality and composition content of cherry tomato in different treatments

	Vc/mg 100 g^{-1}	Soluble sugar (%)	Free amino acid/mg 100 g^{-1}
LCF	19.107 ± 3.896[a]	34.926 ± 0.466[a]	1.428 ± 0.023[a]
CF	19.356 ± 1.125[a]	32.185 ± 2.136[a]	0.882 ± 0.051[c]
CK	5.86 ± 1.125[b]	34.530 ± 1.395[a]	1.203 ± 0.057[b]

Note Statistical analysis was performed by the statistical software SPSS. p values of less than 0.05 were considered significant

Fig. 4.7 Comparison of pimiento growth (*left* in LCF greenhouse, *right* in CF greenhouse)

Table 4.7 Composition content of pimiento in different greenhouses

	Vc (mg g)$^{-1}$	Soluble protein (mg g)$^{-1}$	Soluble sugar (mg g)$^{-1}$	Free amino acid (mg 100 g)$^{-1}$	Nitrate (mg g)$^{-1}$	Soluble pheno (U g)$^{-1}$ Fw
LCF	3.86	0.997	20.2	4.31	0.262	226.7
CF	2.19	1.11	17.7	3.64	0.331	333.3
Change (%)	+76.3	−10.2	+14.1	+18.4	−20.8	−32.0

ordinary plastic film had a significant effect on the early spring tea sprout, but the photosynthesis of tea tree was weaker than open-air tea garden because of the decrease in solar light illumination, and then yield and quality of tea were slightly lower than open-air tea garden. LCF can overcome ordinary film's shortages since
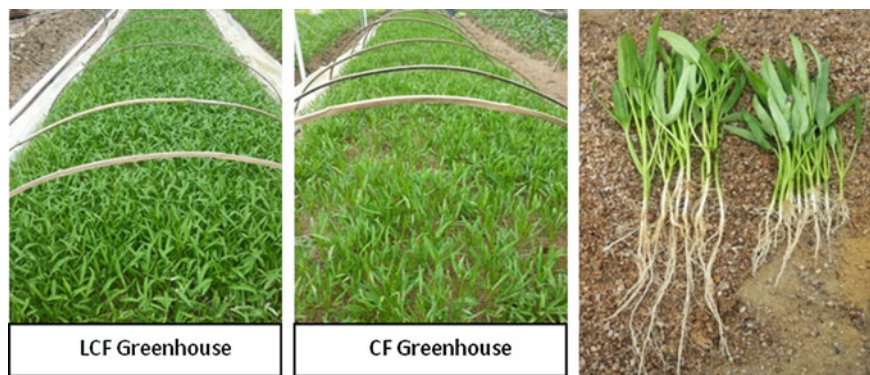
Fig. 4.8 Seeding of water spinach (for the seeding picture: *left* is in LCF greenhouse, and *right* is in CF greenhouse)

Fig. 4.9 Seeding of rice (*left* in CK greenhouse, *right* in LCF greenhouse)

its light conversion function. In our experiments [51], open-air tea garden and ordinary film greenhouse tea garden were used as the controls, and physiological and ecological effects of tea garden greenhouse covered by LCF with CO_2 gas supply during the cold period in winter and spring have been studied for 3 years. The greenhouses and their internal facilities are shown in Fig. 4.10.

4.5.1 Impacts of Different Treatments on Tea Garden Microclimate and Tea Tree Phenological Phase

Table 4.8 shows that the monthly mean temperature difference is very small between greenhouses covered by LCF and CF. In other words, there was no significant difference for heat preservation between LCF and CF. During the period covered by films (from January to March), the heat preservation effect was

Fig. 4.10 Greenhouses and the internal facilities for tea cultivation

Table 4.8 Comparison of monthly mean temperature in different treatments (^{o}C)

Month	T1(LCF)	T3(CF)	CK
January	11.5	12.1	8.7
February	17.1	17.6	13.7
March	21.5	21.8	19.9

Table 4.9 Comparison of monthly average relative humidity in different treatments (%)

Month	T1(LCF)	T3(CF)	CK
January	80.9	78.3	73.1
February	75.6	73.5	64.7
March	70.8	67.7	60.4

significant because the temperature in greenhouses was 2.8–3.4, 3.1–3.9, 1.3–1.9 °C higher than open-air tea garden (CK) in the three months, respectively. Table 4.9 shows that humidification effect of LCF was much better than that of CF. The average humidity of LCF was 0.30–0.97 and 5.0–10.4 % higher than that of CF and CK, respectively. Some studies suggested that air of relative humidity of 80–90 % was the most suitable for the growth and development of tea tree. Table 4.10 shows that the illumination inside greenhouses was 7.9–30.2 % lower than in CK because the films reflect and/or absorb some of light, and the illumination of LCF was slightly lower than that of CF since inorganic light conversion agent was added in LCF. Tea shoots sprout stage (more than 20 % of the over wintering paleae expand) and spring tea start-picking period (more than 20 % of one shoot and one leaf first expand) are the main indices of concern during the phenological period of tea. The effects of the covering films on heat preservation and humidity lead to some changes of the phenological period, such as shortening the winter break and early shoots sprout. Table 4.11 shows that the tea shoots sprout stage and spring tea start-picking period of LCF were 6–7 days earlier than in CF and 23–27 days earlier than in CK.

Table 4.10 Comparison of the average illumination in different treatments (lux)

Month	$T1$(LCF)	$T3$(CF)	CK
January	1764.0	1836.6	1916.9
February	5025.2	5105.5	6273.5
March	8581.6	8652.2	12396.5

Table 4.11 Comparison of tea tree phenophase in different treatments (2012)

	$T1$(LCF)	$T3$(CF)	CK
Tea shoots sprout stage	February 13	February 19	March 12
Spring tea start-picking period	March 5	March 12	March 30

4.5.2 Comparison of Tea Yield in Different Treatments

Table 4.12 shows that the effect on increasing yield was significant in the LCF or CF during spring tea production period. $T1$, $T2$ and $T3$ increased by 11.6, 59.2 and 24.6 % than CK, respectively. Mingqian tea (which is picked before the Ching Ming festival) is of high-quality and good economic value, and earlier spring tea start-picking period will increase the yield of Mingqian tea. The yield of Mingqian tea from $T1$ and $T2$ was 13.7–17.4 % higher than from $T3$ and 56.2 and 51.2 % higher than from CK, respectively.

The total yield of $T1$ was 11.58 % less than $T3$, and that of $T2$ was 27.8 % higher than $T3$. The reasons are: LCF can enhance the effective amount of light which participates in plants' photosynthesis; however, CO_2 and H_2O as photosynthesis substrates must be also supplemented in addition to light enhancement if enhanced photosynthesis is expected. Otherwise, the higher amount of effective light is not sufficient to the formation and accumulation of photosynthesis products because the photosynthesis reaction will cause the substrates in an unbalance state. Therefore, it is needed to add CO_2 gas to greenhouse-covered LCF, especially on the leaf crop, to play a role in promoting photosynthesis.

Table 4.12 Comparison of yield in different treatments (kg)

Tea-picking period	$T1$(LCF)	$T2$(LCF + CO_2)	$T3$(CF)	CK
Mingqian tea	15.85	15.35	13.50	10.15
Second round	8.90	21.25	12.55	16.25
Third round	14.10	18.80	17.30	8.40
Total yield	38.85	55.4	43.35	34.8
Increase yield %	11.63	59.20	24.56	0

4.5.3 Comparison of Tea Quality in Different Treatments

Effect of film covered tea garden on tea quality is the most important matter to the producers. Tables 4.13, 4.14 and 4.15 show that tea water extracts and tea polyphenols of spring tea in LCF greenhouses were significantly higher than those in CF greenhouses, while amino acids and caffeine were slightly lower from mid-March. The quality data of the second batch of tea in the end of March indicated that polyphenols, amino acids, caffeine and water extracts of tea differ in contents slightly between the LCF and CF. However, polyphenol content of tea in greenhouses was significantly higher than that in CK, and amino acid content of tea in greenhouses was significantly lower. The reason is that enhanced carbon assimilation will lead to suppressed nitrogen assimilation. Enhanced photosynthesis causes higher carbon assimilation and more products, so soluble sugar content of tea in LCF was 11.8–15.6 % higher than that in CF and CK, and there was no

Table 4.13 Tea quality composition content from different treatments (March 12, 2012)

Treatment	Water extra (%)	Polyphenols (%)	Amino acids (%)	Caffeine (%)
LCF + CO_2	35.85 ± 1.31^a	26.63 ± 1.39^b	3.48 ± 0.01^a	3.91 ± 0.18^a
LCF	35.24 ± 0.05^a	24.87 ± 0.25^a	3.52 ± 0.03^a	3.79 ± 0.36^a
CF	34.90 ± 0.72^a	24.34 ± 0.58^a	3.59 ± 0.08^a	4.43 ± 0.65^a

Note At this time tea cannot be picked in the open-air, so no sample; Statistical analysis was performed by the statistical software SPSS. p values of less than 0.05 were considered significant

Table 4.14 Tea quality composition content from different treatments (March 30, 2012)

Treatment	Water extra (%)	Polyphenols (%)	Amino acids (%)	Caffeine (%)	Soluble sugar (%)
LCF + CO_2	33.90 ± 0.10^a	21.94 ± 0.34^a	2.06 ± 0.02^b	3.31 ± 0.07^a	3.51 ± 0.27^a
LCF	34.37 ± 0.46^a	21.91 ± 0.13^a	2.16 ± 0.09^b	3.16 ± 0.09^a	3.63 ± 0.11^a
CF	33.97 ± 0.29^a	22.03 ± 0.17^a	2.09 ± 0.01^b	3.36 ± 0.15^a	3.15 ± 0.12^a
CK	33.91 ± 0.07^a	19.70 ± 0.07^b	2.79 ± 0.10^a	3.22 ± 0.03^a	3.14 ± 0.13^a

Note Statistical analysis was performed by the statistical software SPSS. p values of less than 0.05 were considered significant

Table 4.15 Tea quality composition content from different treatments (April 4, 2012)

Treatment	Water extra (%)	Polyphenols (%)	Amino acids (%)	Caffeine (%)	Soluble sugar (%)
LCF + CO_2	35.16 ± 0.39^a	22.76 ± 0.21^a	1.871 ± 0.05^a	2.938 ± 0.00^a	3.38 ± 0.07^a
LCF	34.42 ± 0.30^a	24.75 ± 0.29^b	1.687 ± 0.02^a	3.347 ± 0.00^b	3.10 ± 0.01^a
CF	33.09 ± 0.25^a	23.59 ± 0.26^b	1.783 ± 0.06^a	3.571 ± 0.06^b	3.32 ± 0.11^a
CK	33.94 ± 0.32^a	20.57 ± 0.62^c	1.915 ± 0.16^a	3.446 ± 0.05^b	2.93 ± 0.18^b

Note Statistical analysis was performed by the statistical software SPSS. p values of less than 0.05 were considered significant

significant difference between CF and CK. From quality ingredients comparison of the third round tea in early April, water extracts, polyphenols and soluble sugar content of tea in LCF were higher than in CF and CK, and amino acids and caffeine content of tea in greenhouses were slightly lower than those of tea in CK. In summary, tea garden covered by plastic film is in favor of carbon assimilation, increases of water extracts, polyphenols and soluble sugar content, thus promoting tea's sweetness. So quality of the overall taste of tea is almost unchanged, although amino acids, caffeine of tea in greenhouses were slightly lower than those of tea in an open-air tea garden.

4.5.4 Effect of LCF on Photosynthetic Characteristics of Tea Trees

Table 4.16 shows that the photosynthetic active radiation of tea crown was significantly decreased because the light transmittance would decrease after film covered. Therefore, the photosynthetic active radiation of tea in greenhouses was significantly lower than that in CK, especially greater decrease in CF. But the net photosynthetic rate of tea in LCF was significantly higher than that in CK and CF because LCF significantly enhances amount of effective light. So the stomatal conductance and transpiration rate of tea in LCF greenhouses were significantly higher than that in CK and CF. The results show LCF increases the amount of effective light for photosynthesis, which makes up for the decline in photosynthetic radiation through the film, thus contributing to the photosynthesis of tea tree.

4.5.5 Influence of LCF on Pest Occurrence of Tea Tree

Figure 4.11 shows after the LCF covered, tea leafhopper (*Empoasca vitis Gothe*) occurrence trend has not been changed, but the insect population density in greenhouses was lower than in CK, and the difference between the LCF and CF is small. Tea aphid (*Toxoptera aurantii boyer*) presented consistent trend in all treatments, or May is peak time for tea aphid growth and insect population increase rapidly. The amount of tea aphid in CK was significantly higher than greenhouses,

Table 4.16 Comparison of photosynthetic characteristics in different treatments

	Photosynthetic active radiation (PAR)	Net photosynthesis rate (Pn)	Stomatal conductance (C)	Transpiration rate (W)
LCF + CO_2	938.09	8.18	83.28	2.33
LCF	1010.59	8.20	80.97	2.41
CF	753.76	8.14	61.66	1.56
CK	1151.32	7.90	27.69	0.71
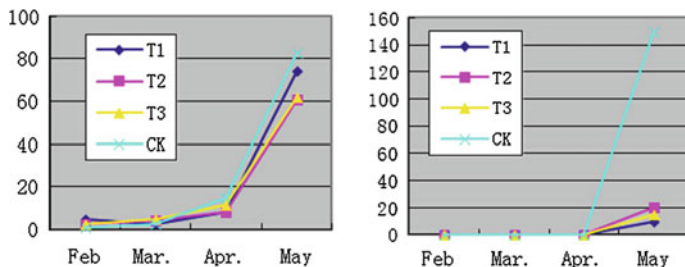
Fig. 4.11 Comparison of prevalence of natural enemy spiders in different treatments

Fig. 4.12 Comparison of prevalence of natural enemy spiders in different treatments
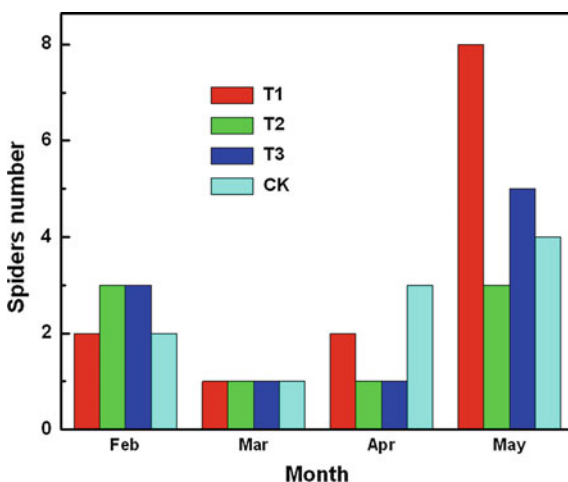
but there is smaller difference between the LCF and CF. Films would lead to increased temperature and humidity of small variation range and decreased illumination. All of these results would not be conducive to tea leafhopper and tea aphid reproduction. Figure 4.12 shows that spiders increased after film covered because the warm and moist atmosphere is conducive to spider reproduction. The insect population density of tea leafhopper and tea aphid decreased with the amount of natural enemies spiders increase. So greenhouse climate change can inhibit reproduction of tea leafhopper and tea aphid.

4.6　Summary and Perspectives

This chapter briefly reviewed the mechanism of phosphors applied in agriculture and then described the effects of light conversion films (LCFs) on vegetable planting and tea cultivation. We found that LCF has a more significant effect on

promoting crops rareripe, increasing production and improving quality. These are because they can be excited by UV and/or green light and emit blue and red light that are desired for photosynthesis, and they can enhance photosynthetic rate of plants and the effective utilization of light. We have synthesized blue and red light conversion agents and made light conversion films (LCFs) added with these phosphors. The emission peak of these LCFs matches with the absorption peak of chlorophyll for photosynthesis. In the future of practical application of the LCFs, challenges exist and a thorough study is needed. Firstly, how to stabilize the chemical characteristics of different phosphors since the stability affects the life of LCF. Secondly, how to enhance the emission intensity of phosphors. Currently, there is no problem that these phosphors can be excited by UV and green lights, but the problem is that the emission is not strong in the effecting area, as shown in Fig. 4.5. So once applied in farm, it cannot be guaranteed that higher light conversion efficiency is realized to increase effective utilization of sunlight. Thirdly, how the phosphors decays in longer periods. Because we must make sure that LCF can be used for 3 years in practice. Preliminary study has shown it might be correlated with the intrinsic defects inside the phosphor compounds. The fourth challenge is how to slow down the degradation of the phosphors. After these, the authors believe the future of phosphors is bright in the agricultural applications.

References

1. Xu DQ (2002) Photosynthesis efficiency. Shanghai Science and Technology Press.
2. Pierce AK (1954) Relative solar energy distribution in the spectral region 10000-2500 a. Astrophys J 119: 312.
3. Dong JY, Cheng XF, Fu TR, Ding JL, Fan XL (2008) Determination of chlorophyll a and b using absorption spectrum. Spectrosc Spect Anal 28: 141.
4. Pierce AK (1954) Relative solar energy distribution in the spectral region 10000-2500 a. Astrophys J 119: 312.
5. Ruban AV, Phillip D, Young AJ, Horton P (1997) Carotenoid-dependent oligomerization of the major chlorophyll a/b light harvesting complex of photosystem II of plants. Biochemistry-US 36: 7855.
6. Markvart T (2000) Light harvesting for quantum solar energy conversion. Prog Quant Electron 24: 107.
7. Golodkava LN, Lepave AF, Dmitriev EV (1985) Polymer material for coating hot greenhouse . UK Patent GB A 2158833.
8. Lepaev AF, Leplyan NGV (1983) Polymermaterial for coating hot greenhouse. USSR Patent SU 8300041.
9. Zhang SP, Liu YJ, Zhang PZ (1999) Progress of plastic film fluorescent light conversion technology. Modern Plastic Processing and Application 11: 58.
10. Li CZ, Lian SX, Liu FH, Mao XH (2006). Synthesis and luminescence properties of agriculture-used red photo-conversion materials. Chemical Engineer (China) 12: 16.
11. Ni YR, Xu C, Lu CH, Xu ZZ (2010) Synthesis of Rare Earth Complexes $Sm_{1-x}Tb_x(TTA)_3$phenas Light Conversion Agent and Surface Modification by SiO_2. ACTA Phtonica Sinica 39: 1424.

12. Luo GL, Xiao ZH, Tan GH (2010) Synthesis and characterization of novel blue light-conversion agents: 2-pentylene-4, 6-di((1-phenyl)-1, 3-butadiene)-1, 3, 5-s-triazine. J Guizohu Normal University (Natural Science) 3: 93.

13. Adachi G (1988) Fluorescence of a Eu^{2+} (M a thacryloyt-Oxymethyl-15-crown-5-oligoether) polymer complex. Chem Express 3: 97.

14. Park HL, Chung CH, Hong KS, Yuan SI, Moon BG (1988) $Ce^{3+} \rightarrow Eu^{3+}$ energy transfer in CaS phosphor. J Lumin 40-41: 647.

15. Park HL, Kim HK, Chung CH, Chang SK, Yu JT (1989) Valence state of europium in CaS:Eu phosphor. Solid State Commun 69: 765.

16. Ando M, Ono YA (1992) Temperature effects in the emission characteristics of CaS:Eu thin-film electroluminescent devices. J Cryst Growth 117: 969.

17. S´wiątek K, Karpin´ska K, Godlewski M, Niinisto L, Leskela M (1994) Influence of Eu concentration on recombination processes in CaS : Eu^{2+} thin films. J Lumin 60-61: 923.

18. Poelman D, Vercaemst R, Van Meirhaeghe RL, Laflere WH, Cardon F (1997) Influence of the growth conditions on the properties of CaS:Eu electroluminescent thin films. J Lumin 75: 175.

19. Cho A, Kim SY, Lee MY, Kim SJ, Kim CH, Pyun CH (2000) Fast luminescence decay processes of photoexcited Eu^{3+} in CaS:Eu,La. J Lumin 91: 215.

20. Wu JW, Newman D, Viney LVF (2002) Study on relationship of luminescence in CaS:Eu,Sm and dopants concentration. J Lumin 99: 237.

21. Suchea M, Christoulakis S, Androulidaki M, Koudoumas E (2008). CaS:Eu,Sm and CaS:Ce, Sm films grown by embedding active powder into an inert matrix. Mater Sci Eng: B150: 130.

22. Liu YP, Chen ZY, Ba WZ, Fan YW, Guo Q, Yu XF, Ghang AM, Lu W, Du YZ (2008) Optically stimulated luminescence dosimeter based on CaS:Eu,Sm. Nucl Science Tech 19: 113.

23. Lu LP, Zhang XY, Bai ZH, Mi XY (2009) Synthesis and characterization of IR up-conversion material CaS:Eu,Sm by low-temperature combustion synthesis method. Mater Res Bull 44: 207.

24. Meng JW (1992) High-efficiency fluorescent agricultural plastic film. China Patent 91106112.

25. Meng JW, Hou SG, Yang YH, Pang BC, Zhou M, Piao YJ, Peng YZ (1993) Effect of high efficiency plastic film on ginseng ecology. J Appl Ecol 4: 102.

26. Lv JG, Wen FY (1994) Application of Agricultural multi-light plastic film on vegetable production. Tianjin Agricultural Sciences 4: 19.

27. Fu MiH, Wang XD, Gu ZL (2000) Study on application of multifunction light conversion plastic film. J. Agr Eng 16: 81.

28. Bushmanm C, Meier D, Kleudgen HK, Lichtenthaler HK (1978) Regulation of chloroplast development by red and blue light . Photochem. Photobio. 27: 195.

29. Macc CC (1999) Crop scientists seeks a new revolution. Science 283: 310.

30. Li WL, Wang QR, Wei GD (1993) Study on containing rare earth complexes convert light energy conversion vegetable greenhouse film. Chinese Rare Earths14: 25.

31. Lian SX (2007) Synthesis of sunlight conversion composites and their chemical and biological effects of crop growth. Thesis, Hunan Normal University.

32. Zhang SP, Li JY, Chen J, Xiao Y, Sun YE (2004) Research of spectrum characteristics for light conversion agricultural films. Spectrosc Spect Anal 24: 1180.

33. Sun QM, Hu GQ, Lin ZX, Yu LL, Liu XT, Yu YS (2014) Preparation and application of light conversion film for exploiting solar energy. Advanced Materials Research 827: 44.

34. Wang YX, Xu K, Mi QH, Kong XB, Shang QW (2006) Effect of spectrum conversion film on temperature, light and growth of Chinese cabbage. China Vegetables 9: 9.

35. Wang JQ, Dong HG, Ji GC, Lan XB (2004) Test of tomato cultivation in greenhouse covered ecological conversion film. Chinese Agricultural Technology Extension 6: 34.

36. Pu WX, Yi JH, Sun ZJ, Liu JF, Lian SX, Li CZ, Yin DL (2008) Effect of sunlight-cloud-conversion film on the growth and physiological characteristics of tobacco seeding of temperature of greenhouse. Chinese Agricultural Science Bulletin 24: 407.

37. Lu GJ, Yu GX (2007) Test summary of application of light conversion film on greenhouses grapes. Modern Agricultural Science and Techonology 9: 20.

38. Xu JY (2008) Application and Extension of light conversion film in cotton. Rural Technology 11: 13.
39. Xu W (2005) Significant effects of early mature and yield increase using light conversion film. Modern Technology 3: 18.
40. Wang H, Xu WL (2011) Preliminary application of light conversion film on horticultural crops. Hunan Agricultural Science 18: 35.
41. Luo GL, Zhang L, Xiao ZH (2011) Influence on growth and nutritional quality of Pakchoi of blue light-conversion agent. Hubei Agricultural Science 50: 749.
42. Yuichi H, Toshifumi Y (1978) Action spectrum for photosporogenesis in botrytis cinerea pers. ex fr. Plant Physiol 61: 711.
43. Kumagai T, Oda Y (1969) Blue and near ultraviolet reversible photoreaction in conidial development of the fungus. Development, Growth and Differentiation 11: 130.
44. Rahman MZ, Khanam H, Ueno M, Kihara J, Honda Y, Arase S (2010) Suppression by red light irradiation of corynespora leaf spot of cucumber caused by corynespora cassiicola. J Phytopathol 158: 378.
45. Feng Y, Gao ZJ, Zu YQ, Li Y (2008) The potential effects of UV-radiation on plant diseases. Acta Phytophylacica Sinica 35: 88.
46. Hu GQ (2010) The preparation, characterization and application of red and blue light conversion agent and it's composite conversion film. Thesis, South China Agriculture University.
47. Han WY, Wang GQ, Xu YW (2003) Climate microdomains, tea tree growth and physiological changes in tea garden greenhouse. Third Symposium Cross-Strait on Tea Industry .
48. Huang SB (1997) Micrometeorological characteristics of plastic greenhouses and Longjing tea production. J Zhejiang Forestry College 14: 58.
49. Kumar RR (1999) Tea leaf photosynthesis in relation to light. J Plantation Crops 27: 93.
50. Lin JK, Lai MZ (2000) Preliminary analysis for the relationship between eco-physiological factors and net photosynthetic rate of tea leaves. Acta Agronomica Sinaca 26: 110.
51. Tang H, Liu XT, Chen ZD, Tang JC, Li JL (2014) Comprehensive effect of greenhouse tea garden covered with light conversion film during low temperature period in winter and spring. Guangdong Agricultural Science 41: 18.

Chapter 5
Rare Earth Solar Spectral Convertor for Si Solar Cells

Jing Wang, Xuejie Zhang and Qiang Su

Abstract The goal of current energy policy worldwide is to develop clean renewable energy capable of powering the world household and economy, now and in the future. Photovoltaics (PV) is an advanced technique that can directly convert clear and sustainable solar energy into electricity, which makes it a promising candidate for achieving this goal. Currently, PV devices fabricated from silicon (Si) wafers dominate the marketplace. Unfortunately, current silicon-based PV products are expensive and suffer poor efficiency when converting solar energy to electricity. The mismatch between the solar photon flux spectrum and the spectral response of Si solar cells is one of the main drawbacks greatly limiting the power energy efficiency of Si solar cell. In recent years, rare earth-activated luminescent materials, which are capable of converting lights of higher energy into near-infrared (NIR) photons of lower energy by means of downshifting (DS) and downconverting (DC), have been designed and systematically investigated with aim to minimize the charge thermalization of Si solar cell in the process of photoelectric conversion. In this review, we will survey recent progress in the development of such kinds of rare earth solar spectral converters for Si solar cells as well as rare earth-converted Si solar cells (REC-Si solar cells). In addition, future challenges of these rare earth solar spectral converters will be briefly discussed toward REC-Si solar cells.

5.1 Introduction

One of the most pressing issues of our time is clean energy. The basis of the problem lies not only in the fact that we have limited fossil fuel resources, but also in the greenhouse gas emissions created by burning these fuels, which is creating a

J. Wang (✉) · X. Zhang · Q. Su
State Key Laboratory of Optoelectronic Materials and Technologies,
School of Chemistry and Chemical Engineering, Sun Yat-Sen University,
Guangzhou 510275, People's Republic of China
e-mail: ceswj@mail.sysu.edu.cn
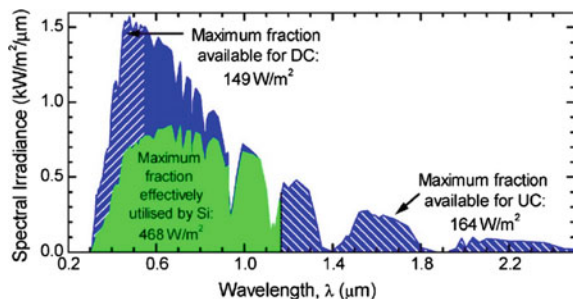
Fig. 5.1 AM 1.5G spectrum showing the fraction (highlighted in *green*) absorbed by a typical Si-based PV cell and the spectral regions that can be utilized through DS as well as DC and UC processes. Reprinted from Ref. [1]. Copyright 2006, with permission from Elsevier

growing problem in global warming. The goal of current energy policy worldwide is to develop clean renewable energy capable of powering the world household and economy, now and in the future. PV is an advanced technique that can directly convert clear and sustainable solar energy into electricity, which makes it a promising candidate for achieving this goal. Currently, PV devices fabricated from Si wafers dominate the marketplace. Unfortunately, current Si-based PV products are expensive and suffer poor efficiency when converting solar energy to electricity. Consequently, only a small fraction of current electrical energy generation comes from PV systems despite the fact that PVs have long been an important component of this strategy [1–3]. In order for PVs to play a major role in future energy generation, it is necessary that the efficiency of these systems is improved. At present, the mismatch between the solar photon flux spectrum and the spectral response of Si solar cells is one of the main drawbacks greatly limiting the efficiency of Si solar cell. As shown in Figs. 5.1 and 5.2, the incident solar spectrum dominates in the UV–visible region, whereas Si solar cells most effectively convert NIR photons of lower energy close to the semiconductor band gap ($E_g \approx 1.12$ eV, $\lambda \approx 1000$ nm). Consequently, this mismatch leads to about 70 % energy loss of solar light in the form of heat. This extra heat energy significantly causes the charges thermalization of Si solar cell and the transmitted IR lights do not show any contribution in the process of photoelectric conversion, as shown in Fig. 5.3a, which limits the energy efficiency of the state of the art of current commercial c-Si solar cell to be about 15–20 % though its theoretical maximum efficiency is about ~ 30 % [1, 3].

As shown in Fig. 5.3b, if UV–visible photons of high energy can be converted into visible-NIR photons of low energy prior to being absorbed into Si solar cell by means of DS with a theoretical maximum quantum efficiency of 100 %, the charges thermalization of Si solar cells will be greatly decreased due to the energy matching between the incident NIR lights and the spectral response of Si solar cells. Consequently, the power conversion efficiency of Si solar cell will be slightly enhanced but not beyond the theoretical maximum efficiency of ~ 30 %. As shown in Fig. 5.3c, if UV-green photons of high energy can be twice converted into NIR
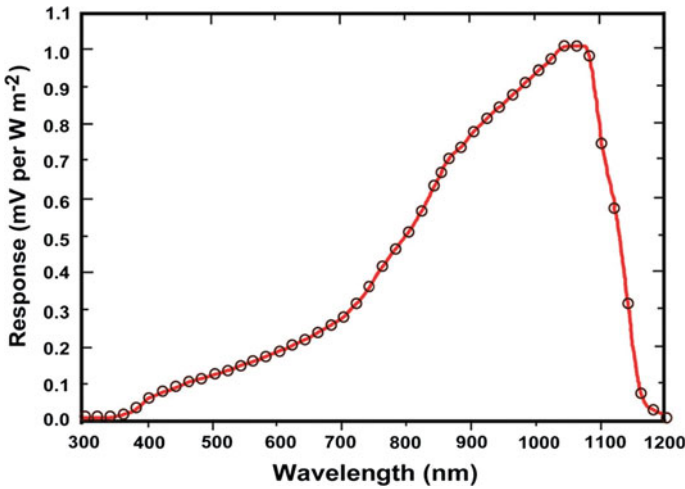
Fig. 5.2 Normalized spectral response of a typical c-Si solar cell pyranometer (courtesy of Apogee Instruments, Inc., 2008). Reproduced from Ref. [4] by permission of The Royal Society of Chemistry
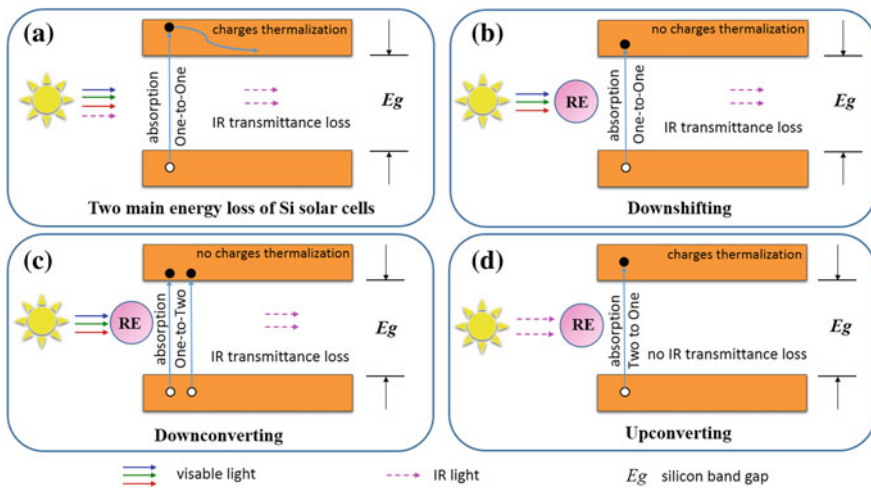
Fig. 5.3 The schematic diagram on energy loss of Si solar cells (**a**) and three of important methods of modifying the solar photon flux spectrum including DS (**b**), DC (**c**), and UC (**d**)

photons of low energy prior to being absorbed into Si solar cell by means of DC with a theoretical maximum quantum efficiency of 200 %, the utilization efficiency of high energy photons in the UV-green fraction of solar spectrum will be greatly enhanced and the charges thermalization of Si solar cells will be greatly decreased due to the perfect energy matching between the incident NIR lights and the spectral response of Si solar cells. Comparatively, the power conversion efficiency of Si

solar cell will be greatly enhanced and theoretically up to $\sim 40~\%$. Additionally, if IR photons of low energy that was originally not used can be converted into visible photons of high energy prior to being absorbed into Si solar cell by means of UC, the transmission loss will be greatly decreased, as shown in Fig. 5.3d.

Rare earth luminescent materials are expected to be important solar spectral convertors to modify the solar photon flux spectrum. In the past decade, many efforts have been made to develop rare earth solar spectral convertor involving the ions couple (RE_s–RE_a) or ions triple (RE_s–RE_m–RE_a) system. Among the RE_s–RE_a and RE_s–RE_m–RE_a systems, DC and DS are two of the most interesting approaches to modify the solar spectrum. Hereafter, we will focus on such kinds of rare earth solar spectral convertors. In a typical couple system, inorganic compounds with excellent chemical stability and "green" composition are usually selected as luminescent matrices. RE_s ion acts as a sensitizer facilitating utilization of the high energy fraction of the solar spectrum and RE_a ion serves as an activator converting high energy photon into low energy photon that matches the spectral response of Si solar cells. Hereafter, the recent developments of rare earth solar spectral convertor will be reviewed mainly based on the type of spectral transition of RE_s and the species of RE_a. Then, we will survey recent progress in the development of REC-Si solar cells. Finally, future challenges of these rare earth solar spectral converters will be discussed toward REC-Si solar cells.

5.2 Rare Earth Solar Spectral Convertor for Si Solar Cell

5.2.1 *Narrow Band NIR DC Phosphors Activated by RE_{sn}–Yb^{3+} (RE_{sn} with 4f–4f Transitions)*

Trupke et al. already demonstrated that, for a band gap similar to that of Si, a conversion efficiency of 39 % can be achieved using a Si solar cell with a DC convertor under unconcentrated sunlight [3], as compared to an efficiency of 30 % (Shockley–Queisser limit) for the same solar cell without a DC layer [5]. Thereafter, many efforts have been made to develop NIR DC phosphors codoped with the RE_{sn}^{3+}–Yb^{3+}(RE_{sn} = Tb, Pr, Tm, Er, Nd, Ho, Dy; here, RE_{sn} denotes rare earth narrow band sensitizer) couple [4, 6, 7]. In these systems, Yb^{3+} ion is used as NIR emitting centers due to the $^2F_{5/2} \rightarrow {}^2F_{7/2}$ transition at about 1000 nm, perfectly matching with the band gap of c-Si. It is well known that Yb^{3+} ion only has a single 4f excited $^2F_{5/2}$ state approximately 1000 nm above the ground $^2F_{7/2}$ state, and therefore, it usually has no direct absorptions in the UV–visible (300–800 nm) range [8]. It is necessary to codope RE_{sn}^{3+} as sensitizer to absorb UV–visible photons and transfer the energy to Yb^{3+} ions. RE_{sn}^{3+} ions commonly have narrow absorption peaks in the UV–visible region, due to 4f–4f transitions. DC process occurs between RE_{sn}^{3+} and Yb^{3+} ions. Based on different DC mechanisms, the

RE_{sn}^{3+}–Yb^{3+} couples can be further divided into two groups: cooperative NIR DC and sequential NIR DC.

Cooperative NIR DC. If overlap between sensitizer emission and activator absorption is absent and no intermediate energy level exists for the sensitizer, second-order energy transfer (ET), also called cooperative DC, may become the dominant relaxation process, which competes with spontaneous emission. In the RE_{sn}^{3+}–Yb^{3+} couple, cooperative NIR DC may happen if the emitting level of RE_{sn}^{3+} is located at about 20,000 cm^{-1}, twice the $^2F_{5/2}$ excited state of Yb^{3+} around 10,000 cm^{-1}. In such a typical process, a sensitizer excites two activators simultaneously [4, 6, 7, 9–14]. A well-known example of cooperative NIR DC is $Yb_xY_{1-x}PO_4$:Tb^{3+} reported by Vergeer in 2005 [9], as shown in Fig. 5.4. Emission, excitation, and time-resolved luminescence measurements show the occurrence of ET from the $^5D_4$ level of Tb^{3+} around 20,000 cm^{-1} to two Yb^{3+} ions, exciting both ions from the $^2F_{7/2}$ ground state to the $^2F_{5/2}$ excited state around 10,000 cm^{-1}. ET mechanism between Tb^{3+} and Yb^{3+} was investigated by luminescence measurements on $Yb_xY_{1-x}PO_4$ doped with 1 % Tb^{3+}. Time-resolved luminescence experiments were analyzed using Monte Carlo simulations based on theories for phonon-assisted, cooperative, and accretive ET. The luminescence decay curves of the $^5D_4$ emission from Tb^{3+} show an excellent agreement with simulations based on cooperative ET via dipole–dipole interaction, while a phonon-assisted or an accretive ET mechanism cannot explain the experimental results. The ET rate to two nearest-neighbor Yb^{3+} ions is 0.26 ms^{-1}. This corresponds to an upper limit of the ET efficiency of 88 % in $YbPO_4$. This yields an upper limit for the quantum efficiency (visible + IR) of 188 %. Application of cooperative ET has prospects for
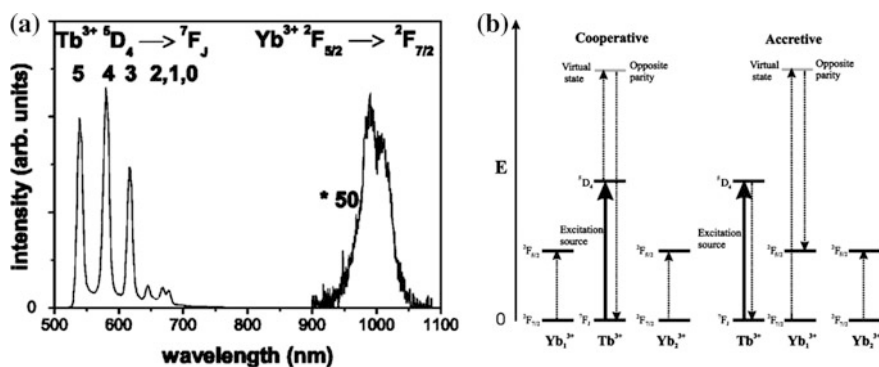
Fig. 5.4 a Visible/NIR photoluminescence (PL) spectrum of $Y_{0.74}Yb_{0.25}Tb_{0.01}PO_4$ upon $Tb^{3+7}F_6 \rightarrow {}^5D_4$ excitation (λ_{ex} = 489 nm). The spectral region between 900 and 1100 nm is amplified by a factor of 50. **b** Schematic representation of the cooperative and accretive pathways for ET from Tb^{3+} to Yb^{3+}. The *bold arrows* indicate excitation of Tb^{3+} into the $^5D_4$ state, after which ET may occur. The ET processes are depicted by the *dotted lines*. In mechanism, a virtual state is involved. For the cooperative mechanism, the virtual state is located on Tb^{3+}. Reprinted from Ref. [9] by permission of American Physical Society

increasing the power conversion efficiency of crystalline Si solar cells by photon doubling of the high energy part of the solar spectrum.

Sequential NIR DC. If overlap between sensitizer emission and activator absorption is absent and there exists intermediate energy level for the sensitizer, first-order ET, also called sequential DC, may become the dominant relaxation process. Efficient NIR DC using Yb^{3+} as an activator requires sensitizer ion with an energy level at about 20,000 cm^{-1} and an intermediate level at approximately 10,000 cm^{-1}. Evaluation of the Dieke Diagram reveals that potential couples are Er^{3+}–Yb^{3+}, Nd^{3+}–Yb^{3+}, and Pr^{3+}–Yb^{3+} [15–17]. A well-known example of cooperative DC is SrF_2:Pr^{3+}, Yb^{3+} [15] reported by Meijerink in 2009, as shown in Fig. 5.5. They demonstrated efficient NIR DC of one visible photon into two NIR photons in SrF_2:Pr^{3+}, Yb^{3+}. Comparison of absorption and photoluminescence excitation (PLE) spectra provided direct evidence that the NIR DC efficiency was close to 200 %, which is consistent with a two-step ET process that can be expected based on the energy level diagrams of Pr^{3+} and Yb^{3+}. This first-order ET process was effective at relatively low Yb^{3+} concentrations (5 mol%) where concentration quenching of the Yb^{3+} emission was limited. Comparison of emission spectra for SrF_2:Pr^{3+} (0.1 mol%) and SrF_2:Pr^{3+} (0.1 mol%), Yb^{3+} (5 mol%), which were corrected for any instrumental response, revealed an actual conversion efficiency of 140 %. Comparatively, the actual quantum efficiency in $Yb_xY_{1-x}PO_4$:Tb^{3+} is strongly reduced or much lower than the theoretical upper limit for the quantum efficiency (visible + IR) of 188 % by concentration quenching of the IR emission from Yb^{3+}. In other word, high concentrations of Yb^{3+} are needed for efficient cooperative ET from Tb^{3+} to 2 Yb^{3+} [9, 15].

It is worth to note that why SrF_2 was chosen as a host lattice to investigate whether efficient sequential NIR DC happens, as the authors noted, was motivated by its low
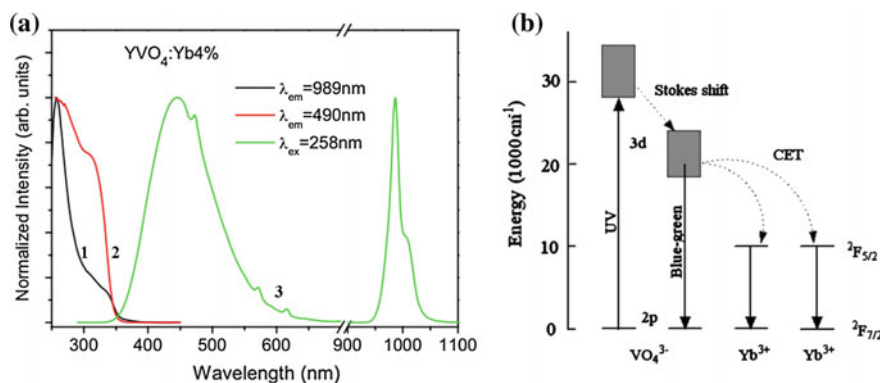
Fig. 5.5 **a** PLE and PL spectra of YVO_4 doped with 4 mol% Yb^{3+} monitored at 989 nm (*1*) and 490 nm (*2*), and excited at 258 nm (*3*). **b** Schematic energy level diagrams of VO_4^{3-} and Yb^{3+} in YVO_4:Yb^{3+} and the cooperative ET (CET) mechanism for the NIR DC emission under UV excitation. Reprinted with permission from Ref. [31]. Copyright 2010, American Institute of Physics

phonon energy [18]. Theoretically, low phonon energy will suppress undesired multiphonon relaxation processes of Pr^{3+} at ^3P_J ($J = 0, 1, 2$) at about 20,000 cm^{-1} and intermediate $^1D_4$ level at about 10,000 cm^{-1}. Otherwise, multiphonon relaxation processes of Pr^{3+} from the upper ^3P_J or $^1D_4$ level to the nearest lower $^1D_2$ or $^3F_{3,4}$ level will dominate and consequently sequential NIR DC from Pr^{3+} to Yb^{3+} will be not efficient and even not happen. The host compounds with low phonon energy are usually fluorides, which is necessary to observe sequential NIR DC in Er^{3+}–Yb^{3+} or Nd^{3+}–Yb^{3+} couple like Pr^{3+}–Yb^{3+} [4, 19–26]. In oxides with high phonon energy, e.g., $GdAl_3(BO_3)_4$, cooperative NIR DC instead of sequential NIR DC between Pr^{3+}–Yb^{3+} commonly occurs as reported by Zhang in 2007.

Although NIR DC phosphors codoped with the RE_{sn}^{3+}–Yb^{3+} have been investigated worldwide in the past decade, these kinds of NIR DC systems, whatever cooperative NIR DC or sequential NIR DC, still encounter one main drawback, i.e., its poor absorption efficiency, which greatly limits its potential application in Si solar cells. The reason why RE_{sn}^{3+}–Yb^{3+} couples show low absorption efficiency is that the sensitizer RE_{sn}^{3+} (RE = Pr, Tb, Tm, Er, Nd, and Ho) has only a series of narrow and weak absorption peaks in the UV–visible fraction of solar spectrum, due to forbidden 4f–4f absorption transitions, of which the optical oscillator strength is so small. Consequently, actual external quantum efficiency for NIR DC systems mentioned above is much lower.

5.2.2 Broadband NIR DC and DS Phosphors Activated by RE_{sb}–Yb^{3+} (RE_{sb} with non-4f–4f Transitions)

Compared to the RE_{sn}–Yb^{3+} couple, the RE_{sb}–Yb^{3+} couple has attracted more and more attention worldwide. Here, the sensitizer RE_{sb} denotes metal ion with broadband and intensive absorption transitions, due to non-4f–4f transitions. Hereafter, we will review recent developments on broadband NIR DC and DS phosphors activated by RE_{sb}–Yb^{3+}, based on the nature of optical transitions of RE_{sb} ion, charge transfer state (CTS), 6s–6p transition, and 4f–5d transition.

Charge Transfer State. CTS is generally associated with an electron transfer from the ligand's orbital to an orbital of the metal. It is allowed by the spin and parity selection rules and consequently has strong and broadband absorption [27]. The charge transfer state is important in applications. For example, in the red phosphor commercially used in fluorescent tubes (Y_2O_3:Eu^{3+}), UV radiation ($\lambda = 254$ nm) is efficiently absorbed by a transition to the CTS of the Eu^{3+} ion, i.e., Eu^{3+}–O^{2-} charge transfer transition. After nonradiative decay to the lower 4f levels, luminescence occurs from the ^5D_J states of Eu^{3+} [28].

For potential application in Si solar cells, three types of CTSs have been reported to sensitize Yb^{3+} ion, including CTS of V^{5+}–O^{2-}, Yb^{3+}–S^{2-}, and Mo^{6+}–O^{2-} till now [29–33]. In 2010, Yin et al. reported photoluminescence properties and ET mechanism of NIR DC YVO_4:Yb^{3+} phosphor. As shown in Fig. 5.5a, an intense

NIR emission of Yb^{3+} $\left({}^2F_{5/2} \rightarrow {}^2F_{7/2}\right)$ around 980 nm is observed in YVO_4:Yb^{3+} phosphors upon UV light excitation. Owing to CT absorption of V^{5+}–O^{2-}, a broad excitation band ranging from 250 to 350 nm is recorded when the NIR emission of Yb^{3+} was monitored, suggesting an efficient ET from host to Yb^{3+} ions. The decay curve of vanadate emission is measured under the excitation of a 266-nm pulsed laser. The lifetime of the vanadate emission at 500 nm is remarkably reduced with increasing amount of Yb^{3+} ions, further verifying that the ET from the vanadate to the Yb^{3+} ions is very efficient. Cooperative DC was proposed as a possible mechanism for the NIR emission, as shown in Fig. 5.5b. The YVO_4:Yb^{3+} phosphor can convert each UV photon into two NIR photons via cooperative DC. The calculated quantum efficiency was roughly estimated to be as high as 185.7 % for the sample doped with 16 mol% Yb^{3+} [31].

In 2011, our group reported photoluminescence properties of NIR DS $CaLaGa_3S_6O$:Yb^{3+} phosphor [30]. It is well known that the position of the CTS is determined mainly by the optical electronegativity of the ligand and the metal ion. CTS of Yb^{3+} ion in many compounds was experimentally reported [8]. For fluorides and oxides, the position of the CTS of Yb^{3+} usually lies in high energy scales of the solar spectrum [34, 35]. It is obvious that it cannot effectively harvest UV–visible (300–500 nm) photons. For Si solar cells, we proposed that it is strongly expected that the CTS of Yb^{3+} in the oxysulfides might shift toward longer wavelength and more effectively absorb UV–Vis (300–500 nm) photons because oxysulfides have higher covalency, compared to fluorides and oxides. As shown in Fig. 5.6a, NIR phosphors $CaLaGa_3S_6O$:Yb^{3+}:xYb^{3+} (x = 0, 0.001, 0.002, 0.004,

Fig. 5.6 The PLE (**a**) and PL (**b**) of $CaLaGa_3S_6O$:xYb^{3+} (x = 0, 0.001, 0.002, 0.004, 0.006, 0.008, 0.010); the *inset* of **b** shows the concentration dependence **c** of the integrated NIR emission intensity of Yb^{3+}

0.006, 0.008, 0.010) have an efficient broad absorption band dominating at around 345 nm and extending from 250 to 500 nm. In general, the next nearest excited level of Yb^{3+} is the CTS of Yb^{3+} and the $4f^{12}5d^1$ configuration of Yb^{3+} lying in higher energy (around 70,000 cm^{-1}, i.e., ~ 140 nm) [8] beside the first excited $^2F_{5/2}$ level situated near 1000 nm. In $CaLaGa_3S_6O$, the host absorption edge is around 250 nm [36]. Therefore, it is reasonable to assign the prominent broadband at 345 nm to the CTS of Yb^{3+} rather than $4f \rightarrow 5d$ transition of Yb^{3+}. In $CaLaGa_3S_6O$, there is only one cation site available for Yb^{3+}, i.e., La^{3+}, which are surrounded octahedrally by seven S^{2-} and one O^{2-} [37]. Consequently, the prominent broadband at 345 nm is probably ascribed to the CTS of Yb^{3+}–S^{2-} and/or Yb^{3+}–O^{2-}, involving an electron transfer from the surrounding $3p^6$ (or $2p^6$) orbital of S^{2-} (or O^{2-}) to the $4f^{13}$ orbital of Yb^{3+}. In general, the position of the CTS of Yb^{3+}–O^{2-} usually lies in the range of 194–262 nm [34, 35, 38]. So we finally concluded that broad absorption band dominating at around 345 nm mainly ascribes to the CTS of Yb^{3+}–S^{2-}. The NIR emission intensity of $CaLaGa_3S_6O$:Yb^{3+} is 12 times as intense as that of a NIR DC phosphor Ca_2BO_3Cl:Ce^{3+}, Tb^{3+}, Yb^{3+} upon 4f–5d excitation of Ce^{3+} [39]. The relatively low phonon frequency of oxy-sulfides [40] may dramatically reduce the probabilities of nonradiative transition and increase the fluorescence emission efficiencies. These results demonstrate that the allowed CTS of Yb^{3+}–S^{2-} with high absorption cross section can be an efficient and direct sensitizer harvesting UV-blue photons and greatly enhancing the NIR emission of Yb^{3+} ion.

For the solar spectral converter based on the DC process as shown in Fig. 5.3, only solar photons of high energy in the wavelength of 300–500 nm can be used in theory. In such a wavelength range, the photon flux of the AM1.5 solar spectrum almost increases linearly as the wavelength increases as shown in Fig. 5.1. The fractions of the integrated intensity of light in 300–400 and 400–500 nm are about 21 and 79 %, respectively, when compared with that in 300–500 nm [41]. Although the CTS of Yb^{3+}–S^{2-} can efficiently absorb the shorter wavelength UV light (300 nm $< \lambda <$ 350 nm) but still fail to harvest the longer wavelength UV light ($\lambda >$ 350 nm). Therefore, we further developed a NIR cooperative DC Sr_2CaMoO_6:Yb^{3+} [29]. Figure 5.7a shows the absorption spectra of $Sr_2Ca_{1-x}MoO_6$:x mol%Yb^{3+} (x = 0, 2, 4, 6, and 8), obtained from the diffuse reflection spectra using the Kubelka–Munk function: $F(R) = (1 - R)^2/2R = K/S$ (R, K, and S are the reflectivity, the absorption coefficient, and the scattering coefficient, respectively). For the Sr_2CaMoO_6 host lattice, there are three obvious absorption bands, a strong band at ~ 250 nm ascribed to the interband transition, an intense broad CTS of the MoO_6 groups extending from 270 to 420 nm [42–44] and a weak shoulder at ~ 470 nm probably due to the cooperative absorption of Yb ion pair [45, 46]. By subtracting the absorption curve of Sr_2CaMoO_6 from $Sr_2Ca_{0.92}MoO_6$:$0.08Yb^{3+}$, it is clearly observed in Fig. 5.7b that the cooperative absorption of Yb ion pair is prominent at 470 nm. And its absorption intensity becomes more and more intense as the concentration of Yb^{3+} ion increases. Comparatively, the intensity of the cooperative absorption of Yb ion pair is
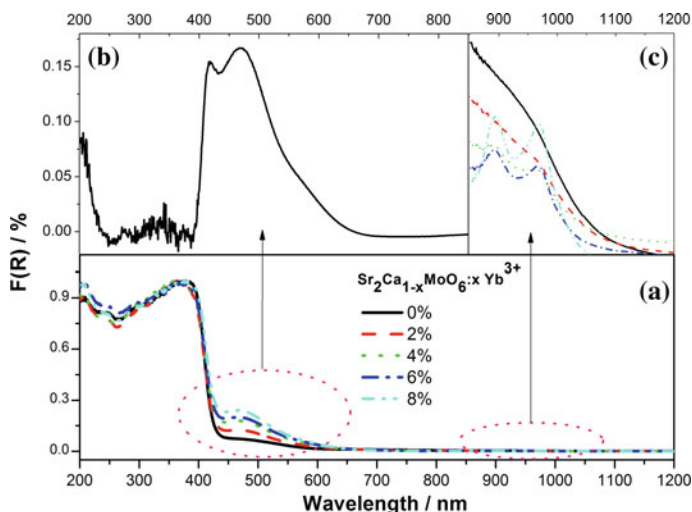
Fig. 5.7 Absorption spectra **a** of $Sr_2Ca_{1-x}MoO_6$:$x$mol% Yb^{3+} (x = 0, 2, 4, 6, and 8); **b** the *curve* subtracting Sr_2CaMoO_6 from $Sr_2Ca_{0.92}MoO_6$:0.08 Yb^{3+}; **c** the magnified *curve* of $Sr_2Ca_{0.92}MoO_6$:0.08 Yb^{3+} in the wavelength of 850–1050 nm

relatively lower than the CTS of the MoO_6 groups. The later shows an absorption efficiency of above 90 %. Additionally, two obvious broadband appear in the range of 850–1050 nm, due to the intra-transitions of Yb^{3+} ion between $^2F_{7/2}$ and $^2F_{5/2}$, as shown in Fig. 5.7c. These results indicate that it is possible to directly sensitize Yb^{3+} ion by the CTS of Mo^{6+}–O^{2-}.

Figure 5.8 presents the NIR emission and PLE spectra of Sr_2CaMoO_6 and Sr_2CaMoO_6:Yb^{3+} at room temperature. For Sr_2CaMoO_6, no NIR emissions are observed. For Sr_2CaMoO_6:Yb^{3+}, the characteristic broad NIR emissions of Yb^{3+} ion dominating at 900–1100 nm are obviously seen, of which the full width at half maximum (FWHM) is about 1635 cm^{-1}, almost comparable to the 5d–4f

Fig. 5.8 The NIR emission (λ_{ex} = 397 nm) and PLE (λ_{em} = 1012 nm) spectra of $Sr_2Ca_{1-x}MoO_6$:xYb^{3+} (x = 0, 2, 4, 6, 8 mol%) at room temperature
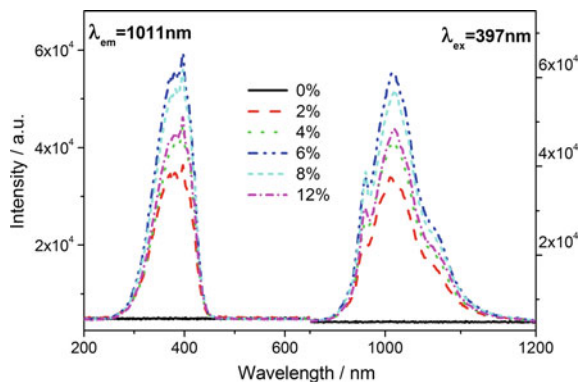
transitions. This phenomenon is mainly due to the lanthanide contraction that weakens the screening of the $4f^n$ shell by the filled 5s and 5p electron shells [47]. Monitoring the prominent emission at 1012 nm, only an intense broad excitation band extending from 270 to 450 nm dominates. With careful comparison with Fig. 5.7, this broad excitation band is probably assigned to the CTS of Yb^{3+}–O^{2-} or Mo^{6+}–O^{2-}. The CTS of Yb^{3+}–O^{2-} was experimentally reported in many oxidic lattices (phosphates, oxides, and aluminates). They are situated at from 195 nm in $ScPO_4$ to 262 nm in $NaLaO_2$ [35]. Consequently, the prominent excitation band located at 397 nm should be ascribed to the CTS of Mo^{6+}–O^{2-} rather than Yb^{3+}–O^{2-}. Moreover, it is clearly observed in Fig. 5.8 that the NIR emission intensity of Yb^{3+} ion exhibits concentration dependence, and the optimal Yb^{3+} ion concentration is 6.0 mol%.

Theoretically, the electronic configuration of Yb^{3+} ion has a unique spectral term, ^2F that is split by the spin–orbit interaction into two energy manifolds, $^2F_{7/2}$ (ground manifold) and $^2F_{5/2}$; in crystal fields of symmetry lower than cubic, the ground manifold $(^2F_{7/2})$ of Yb^{3+} ion is split in four Stark levels and the excited manifold $(^2F_{5/2})$ in three levels [8]. Unfortunately, the NIR emission of Yb^{3+} ion does not present a fine structure at room temperature as shown in Fig. 5.8. In order to verify our assignment of Yb^{3+} energy levels, the NIR excitation and emission spectra of Yb^{3+} ion were detected at 3 K and compared with the DRS in the NIR region as shown in Fig. 5.9. It is obviously seen in NIR emission spectrum that one broad emission band dominating at 1011 nm at room temperature (Fig. 5.8) is split into four sharp peaks at 972 nm (5 → 1), 1011 nm (5 → 2), 1028 nm (5 → 3), and 1068 nm (5 → 4) at 3 K. Whereas there are two broad absorption bands at ~890 nm (1 → 7 and 1 → 6) and 972 nm (1 → 5). Importantly, the $^2F_{7/2} \leftrightarrow ^2F_{5/2}$ lowest energy resonant transition line (5 ↔ 1), also known as zero phonon line, is estimated to be at 972 cm using the barycentre plot method [35, 48]. Based on the spectra data above, the fine energy level structure of Yb^{3+} ion is built as shown in Fig. 5.10.

Fig. 5.9 The diffuse reflection spectra (DRS, *dot*, room temperature) and the NIR excitation (*solid*, 3 K) and emission (*dash*, 3 K) spectra of $Sr_2Ca_{0.94}MoO_6$:0.06 Yb^{3+} in the wavelength range of 700–1200 nm
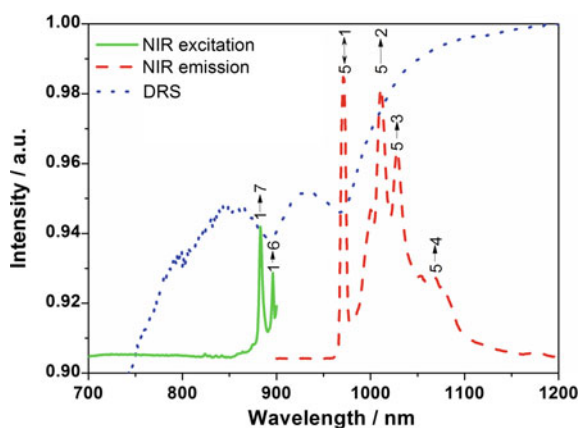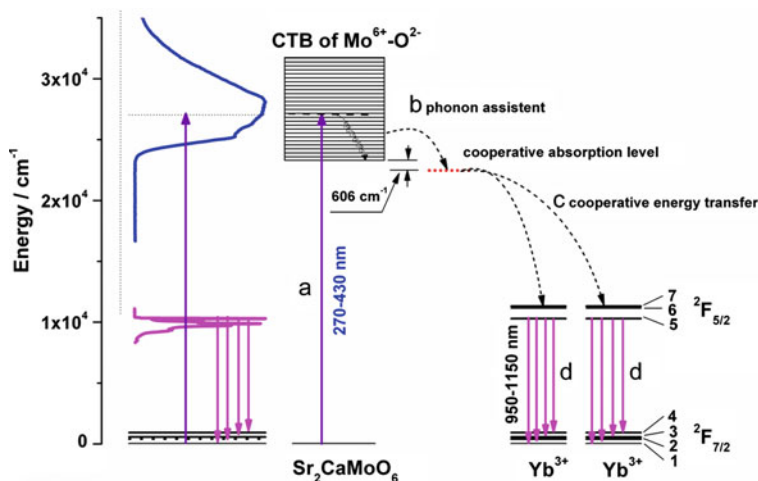
Fig. 5.10 The schematic diagram for NIR cooperative DC processes in Sr_2CaMoO_6:Yb^{3+}

The appearance of the CTS of the MoO_6 group in the excitation spectrum (λ_{em} = 1012 nm) of Yb^{3+} ion strongly suggests that efficient energy transfer from the CTS of Mo^{6+}–O^{2-} to Yb^{3+} occurs. As shown in Fig. 5.10, the energy difference between the bottom of the CTS of Mo^{6+}–O^{2-} and the $^2F_{5/2}(7)$ level of Yb^{3+} ion is about 11,931 cm^{-1}, which is 15.1 times as large as the vibration energy of YbO_6 ($\upsilon \approx 790$ cm^{-1}, Yb^{3+} at Ca site) in Sr_2CaMoO_6 [29]. So it is impossible to bridge such a huge energy gap via assistance of multi-phonons in present case [39]. Therefore, the direct energy transfer from the CTS of Mo^{6+}–O^{2-} to Yb^{3+} is excluded. On the other hand, the difference between the bottom of the CTS of Mo^{6+}–O^{2-} and the cooperative absorption level $\left[^2F_{5/2}(7) + {}^2F_{5/2}(7)\right]$ of Yb^{3+} ion pair is only about 606 cm^{-1}, which is almost as large as the vibration energy of YbO_6($\upsilon \approx 790$ cm^{-1}, Yb^{3+} at Ca site). Therefore, it is reasonable to bridge such a small energy gap via the assistance of about one phonon. Herein, a one phonon-assisted cooperative DC process involving Yb^{3+} ion pair is proposed. First, the MoO_6 group directly absorbs a UV or blue photon via the intense and allowed ligand-to-metal transitions (a). Subsequently, the excitation energy in the lowest vibration level of the CTS of Mo^{6+}–O^{2-} quickly transfers to the absorption level of Yb^{3+} ion pair via the assistance of about one phonon (b) [49]. Thereafter, the energy of the excited Yb^{3+} ion pair is transferred to two Yb^{3+} ions by cooperative energy transfer process. Consequently, the $^2F_{5/2}$ levels of two Yb^{3+} ions are simultaneously populated. Finally, Yb^{3+} ions give the NIR emissions (d) at 972 nm (5 → 1), 1012 nm (5 → 2), 1028 nm (5 → 3), 1068 nm (5 → 4).

It is obviously seen that Sr_2CaMoO_6:Yb^{3+} exhibits much broader and more intense excitation band than $CaLaGa_3S_6O$:Yb^{3+}. We also compared Sr_2CaMoO_6: Yb^{3+} with Ca_2BO_3Cl:Ce^{3+}, Tb^{3+}, Yb^{3+}. When excited upon broadband excitation of Mo–O charge transfer at 397 nm, the former is about 113 times as intense as the

latter. Unfortunately, the experimental quantum efficiency is estimated to be only about 9 %. Even so, these results demonstrate that the allowed CTS of Mo^{6+}–O^{2-} with high absorption cross section can be an efficient and direct sensitizer harvesting UV-blue photons and greatly enhancing the NIR emission of Yb^{3+} ion.

6s–6p transition. Ions with an electronic configuration of *6s*^{2}, for instance, Bi^{3+}, have the excited states with an electronic configuration of *6s6p*. Among *6s–6p* transitions of Bi^{3+}, the transition of $^1S_0 \rightarrow {}^3P_1$ is broad and relatively has high absorption efficiency [50]. Therefore, Bi^{3+} usually acts as a sensitizer for Eu^{3+} in a variety of hosts. For instance, in the commercial red phosphor used in fluorescent tubes (Y_2O_3:Eu^{3+}), the absorption of Eu^{3+} ion in UV region is broaden and enhanced and its red emission is improved by codoping Bi^{3+} ion into the matrix [51]. For potential application in Si solar cells, Zhang et al. reported broadband DC of UV light to NIR emission in Bi^{3+}–Yb^{3+} codoped RE_2O_3 (RE = Y and Gd) phosphors [52]. Gd_2O_3:Bi^{3+}, Yb^{3+} phosphor possesses a broadband absorption in the UV region of 320–390 nm, ascribed to the $^1S_0 \rightarrow {}^3P_1$ transition of Bi^{3+} and exhibits an intense visible emission centered at around 506 nm and NIR emission around 1000 nm, due to the $^3P_1 \rightarrow {}^1S_0$ transitions of Bi^{3+} and $^2F_{5/2} \rightarrow {}^2F_{7/2}$ transitions of Yb^{3+}. The PLE, PL spectra, and lifetime data evidence the occurrence of CET from one Bi^{3+} to two Yb^{3+} ions. The highest quantum efficiency of the calculated NIR DC reaches up to 173.92 %.

4f–5d transition. Compared to the 4f shell, an electron in a 5d orbital is not shielded from the environment by the filled $5p^6$ and $5s^2$ outer shells of the [Xe] configuration, and the energies of 5d levels are much influenced by the crystalline environment. Therefore, 4f–5d transitions are allowed by the spin and parity selection rules and usually have strong and broadband absorptions in UV-to-visible region [53]. These characteristics make them the ideal broadband sensitizers for Yb^{3+} in RE_{sb}–Yb^{3+} for solar spectral convertor. Up to now, many broadband sensitizers (RE_{sb}) with 4f–5d transitions for Yb^{3+} have been reported, including Ce^{3+}, Eu^{2+}, and Yb^{2+}. Hereafter, we will review recent developments on broadband NIR phosphors activated by RE_{sb}–Yb^{3+} including Ce^{3+}–(Tb^{3+})–Yb^{3+}, Eu^{2+}–Yb^{3+}, and Yb^{2+}–Yb^{3+}. Additionally, broadband NIR phosphors activated by Ce^{3+}/Eu^{2+}–Pr^{3+} will also be reviewed.

Ce^{3+}–(Tb^{3+})–Yb^{3+}. In 2009, our group reported broadband NIR cooperative DC Ca_2BO_3Cl:Ce^{3+}, Tb^{3+}, Yb^{3+}, Na^+ [39]. As shown in Fig. 5.11, the Tb^{3+}–Yb^{3+} couple can convert one blue photon into two NIR photons in Ca_2BO_3Cl like the other compounds previously reported. It is very interesting that upon 369-nm excitation of Ce^{3+}, Ca_2BO_3Cl:Ce^{3+}, Tb^{3+}, Yb^{3+}, Na^+ exhibits intense NIR emissions, 10.5 times as intense as Ca_2BO_3Cl:Tb^{3+}, Yb^{3+}, Na^+ upon 484-nm excitation of Tb^{3+}. They are rare but desirable characteristics that are not present in the previously identified Tb^{3+}, Yb^{3+} couple system with high NIR quantum efficiency (>100 %). It demonstrates for the first time that Ce^{3+} ion can be an efficient sensitizer harvesting UV photons and greatly enhancing the NIR emission of Yb^{3+} ion through efficient energy feeding by the allowed 4f–5d absorption of Ce^{3+} ion with high oscillator strength. An assisted cooperative NIR DC mechanism was proposed based on the results and discussions of the PLE, PL, and lifetime. Thereafter, the Ce^{3+}–Tb^{3+}–Yb^{3+} triple has been reported in various powder ($GdBO_3$ and $KSrPO_4$) and glass (borate) systems [54–56].
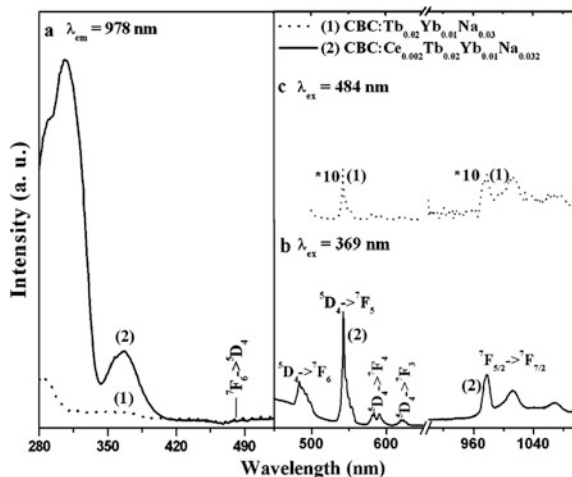
Meantime, many researchers focused on broadband NIR phosphors activated by the Ce^{3+}–Yb^{3+} couple since the two-step ET between Ce^{3+}–Tb^{3+} and Tb^{3+}–Yb^{3+} contributes a little to the total NIR emission efficiency of Yb^{3+} in the Ce^{3+}–Tb^{3+}–Yb^{3+} triple system even if Ce^{3+} ion indirectly broaden and improve the absorption of Yb^{3+} ion in UV–visible region. Till now, broadband NIR phosphors activated by the Ce^{3+}–Yb^{3+} couple have been systematically investigated in various powders, glasses and glass ceramics, and films [57–64]. As a representative, $Y_3Al_5O_{12}:Ce^{3+}$, Yb^{3+} glass ceramic reported by Ueda et al. will be reviewed here [64]. As shown in Fig. 5.12a, it gives intense emission bands peaked at 550 nm from 5d → 4f transition of Ce^{3+} and 1030 nm from $^2F_{5/2} \rightarrow {}^2F_{7/2}$ transition of Yb^{3+} when excited into the 5d level of Ce^{3+} with 450-nm light. And it has two broad excitation bands dominating at 330 and 450 nm whenever the visible of Ce^{3+} at 550 nm or NIR emissions of Yb^{3+} at 1030 nm were monitored. Such a broad spectral converting properties from UV-to-green light to NIR light is rare but desirable characteristics that are not present in the previously identified Ce^{3+}, Yb^{3+} couple systems. About the ET mechanism in Ce^{3+}, Yb^{3+} couple systems, there still remains controversial. Cooperative DC $\left[Ce^{3+}(5d \rightarrow 4f):2Yb^{3+}\left(^2F_{7/2} \rightarrow {}^2F_{5/2}\right)\right]$ appears to be the dominant relaxation route to achieve the NIR emission of Yb^{3+}. However, some researchers believe that the energy transfer from Ce^{3+} to Yb^{3+} is possibly due to metal-to-metal charge transfer (MMCT) through the facile redox reaction of $Ce^{3+}+Yb^{3+}$–$Ce^{4+}+Yb^{2+}$ [4]. In ceramic $Y_3Al_5O_{12}:Ce^{3+}$, Yb^{3+}, Ueda et al. calculated its highest quantum efficiency of 96 % ($x = 0.05$) from ET efficiency with the measured lifetime of Ce^{3+} in $(Y_{0.995-x}Ce_{0.005}Yb_x)_3Al_5O_{12}$ ($x = 0, 0.005, 0.02, 0.05$, and 0.1) as shown in Fig. 5.12b. The authors also experimentally estimated the highest quantum efficiency of 12.8 % ($x = 0.05$) from the total radiant flux spectrum by 440-nm laser diode excitation as shown in Fig. 5.12c. Such a distinguishable difference between the experimental and theoretical values was considered to be due to the existence of other nonradiative processes. Based on
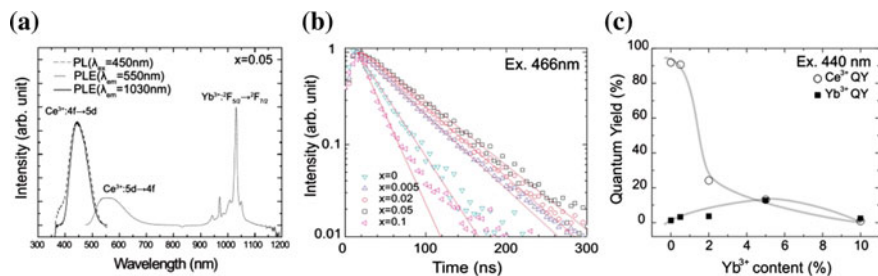
Fig. 5.12 **a** The PLE (λ_{em} = 550 and 1030 nm) and PL (λ_{ex} = 450 nm, laser diode) spectra, **b** decay curves and **c** quantum yield of $Y_3Al_5O_{11}$:Ce^{3+}, Yb^{3+}. Reprinted with permission from Ref. [64]. Copyright 2009, American Institute of Physics

those results mentioned above, the authors concluded that the ET from Ce^{3+} to Yb^{3+} may be caused through a CTS of Ce^{4+}–Yb^{2+} [64].

Eu^{2+}–Yb^{3+}. Beside Ce^{3+} ion, Eu^{2+} ion is one of the most promising sensitizer with 4f–5d transitions for Yb^{3+} ion in broadband NIR RE_{sb}–Yb^{3+} systems. Till now, broadband NIR phosphors activated by the Eu^{2+}–Yb^{3+} couple have been mainly investigated in glass as well as powder [65–69]. As a representative, CaO–Al_2O_3–SiO_2–GeO_2:Eu^{2+}, Yb^{3+} reported by Qiu et al. will be reviewed here. As shown in Fig. 5.13, it has a broad excitation band extending from 250 to 500 nm when the visible of Eu^{2+} at 504 nm or NIR emissions of Yb^{3+} at 980 nm were monitored. And it gives an intense emission band peaked at 504 nm from 5d → 4f transition of Eu^{2+} and 980 nm from $^2F_{5/2}$ → $^2F_{7/2}$ transition of Yb^{3+} when excited into the 5d level of Eu^{2+} with 360 nm light. Based on the dependence of the
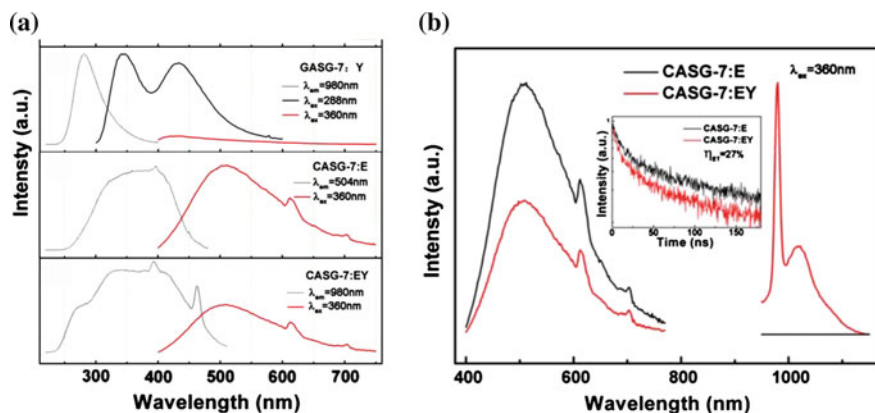
Fig. 5.13 **a** The PLE spectra of a series of CaO–Al_2O_3–SiO_2–GeO_2:Yb^{3+} (CASG-7:Y), CaO–Al_2O_3–SiO_2–GeO_2:Eu^{2+} (CASG-7:E) and CaO–Al_2O_3–SiO_2–GeO_2:Eu^{2+}, Yb^{3+}(CASG-7:EY) glasses in UV/visible region and **b** PL spectra of CASG-7:E and CASG-7:EY in visible/NIR region. The *inset* shows the decay curves. Reproduced from Ref. [66] by permission of The Electrochemical Society

emission intensity and lifetime of Eu^{2+} on the appearance of Yb^{3+} ion, the authors concluded that cooperative DC occurs in aluminosilicate glasses and its efficiency was estimated to reach 27 % [66].

$Yb^{2+}–Yb^{3+}$. Similar to Ce^{3+} and Eu^{2+} ions, Yb^{2+} also has allowed 4f–5d transitions, which makes it potentially an ideal sensitizer for Yb^{3+} ion in broadband NIR $RE_{sb}–Yb^{3+}$ systems. In 2010, Qiu et al. reported NIR phosphor $CaAl_2O_4$:Yb^{2+}, Yb^{3+}. As shown in Fig. 5.14a, it has an intense broad excitation band dominating at 310 nm as well as a weaker shoulder at 275 nm, ascribed to the 4f–5d transition of Yb^{2+} and the CTS of $Yb^{3+}–O^{2-}$, respectively, when the NIR emissions of Yb^{3+} at 980 nm were monitored. And it gives intense emissions centered at 980 nm from $^2F_{5/2} \rightarrow {}^2F_{7/2}$ transition of Yb^{3+} when excited into the 5d level of Yb^{2+} with 310-nm light. Two kinds of cooperative NIR DC processes, i.e., three-photon NIR DC process and phonon-assisted two-photon DC process, were proposed by the authors to explain the ET from Yb^{2+} to Yb^{3+}, as shown in Fig. 5.14b, c [70]. It demonstrates that Yb^{2+} ion can be also an efficient sensitizer harvesting UV photons and greatly enhancing the NIR emission of Yb^{3+} ion through efficient energy feeding by the allowed 4f–5d absorption of Yb^{2+} ion with high oscillator strength. Unfortunately, the probability of these cooperative NIR DC processes, especially three-photon NIR DC process, may be theoretically much low and Yb^{2+} ion can only convert short wavelength UV light into NIR light, which greatly limits it potential application in Si solar cells.

$Ce^{3+}/Eu^{2+}–Pr^{3+}$. Compared to simple energy level structure of Yb^{3+}, Pr^{3+} ion has a rich energy level structure, allowing for direct absorption of visible photons, for instance, the $^3H_4 \rightarrow {}^2D_2$ (~ 600 nm), $^3P_J (J = 0, 1, 2)$, $^1I_6$ (440–490 nm) transitions, and allowing for the NIR emission at ~ 1000 nm from the $^3P_0 \rightarrow {}^1G_4$ and/or $^1G_4 \rightarrow {}^3H_4$ transitions, which matches the optimal spectral response of the Si solar cells. Furthermore, Pr is relatively abundant and inexpensive compared to Yb. These motivations prompted us to explore novel NIR DC or DS materials activated by Pr^{3+} ions for Si solar cell applications [15, 71].

In 2012, our group developed a dual-mode solar spectral converter $CaLaGa_3S_6O$:Ce^{3+}, Pr^{3+} for Si solar cells. Figure 5.15a shows the PLE and NIR
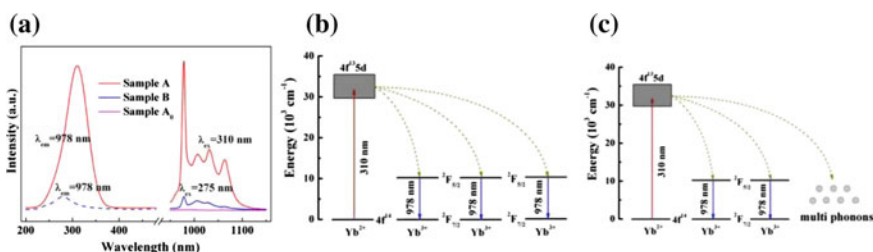
Fig. 5.14 **a** The PLE and PL spectra of $CaAl_2O_4$:x Yb (A_0 for $x = 0$; A for $x = 4$ mol%; A_0 and A sintered in reducing atmosphere; B for $x = 4$ mol% sintered in air) and **b** schematic cooperative DC diagrams of Yb^{2+} and Yb^{3+}: **b** three-photon NIRDC process and **c** phonon-assisted two-photon DC process. Reprinted from Ref. [70] by permission of OSA Publishing
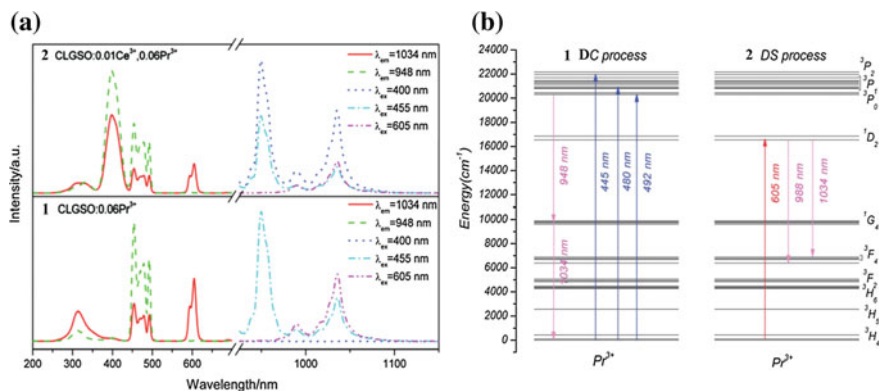
Fig. 5.15 **a** The PLE and NIR emission spectra of $CaLaGa_3S_6O:xCe^{3+}$, $0.06Pr^{3+}$ [$x = 0$ for (*1*) and 0.01 for (*2*)] and **b** the schematic diagram on the NIR emission mechanism of $CaLaGa_3S_6O:0.06\ Pr^{3+}$ under excitation into the $^3P_J(J = 0, 1, 2)$ (*1*, DC process) and $^1D_2$(*2*, DS process) levels. Reproduced from Ref. [71] by permission of The Royal Society of Chemistry

emission spectra of $CaLaGa_3S_6O:Pr^{3+}$ (1) and $CaLaGa_3S_6O:Ce^{3+}$, Pr^{3+} (2). It is obviously seen in (1) that Pr^{3+} ion exhibits distinct PLE and NIR emission features. Monitoring the NIR emission at 948 nm, the PLE spectrum comprises a number of absorption lines of Pr^{3+} dominating in the 440- to 500-nm region and a weak band peaking at about 305 nm. These are due to $^3H_4 \rightarrow {}^3P_0$, $^3P_1/{}^1I_6$, and $^3P_2$ transitions of Pr^{3+} and the host absorption, respectively. The PLE spectra, recorded at $\lambda_{em} = $ 1034 nm, are almost identical to that recorded at 948-nm emission, except the prominent $^3H_4 \rightarrow {}^1D_2$ excitation lines at 594 and 605 nm. Under excitation of 455 nm ($^3H_4 \rightarrow {}^3P_2$), the NIR emission spectrum mainly consists of one prominent emission peak at 948 nm as well as a shoulder at 1034 nm, due to $^3P_0 \rightarrow {}^1G_4$ and $^1G_4 \rightarrow {}^3H_4$ transitions, respectively. When excited by 605 nm ($^3H_4 \rightarrow {}^1D_2$), there is mainly one prominent emission at 1034 nm and a shoulder at 988 nm, assigned to $^1D_2 \rightarrow {}^3F_4$ and $^1D_2 \rightarrow {}^3F_3$ transitions, respectively [71].

In order to prove the above NIR assignments of Pr^{3+}, the decay curves of $CaLaGa_3S_6O:0.06Pr^{3+}$ were measured and the lifetimes of visible and NIR emissions from $^3P_0$ and $^1D_2$ were presented in Table 5.1. In general, the decay time of the emission from $^3P_0$ is 0.135–50 μs, shorter than that from $^1D_2$, which is about 50–250 μs [72]. In $CaLaGa_3S_6O:0.06Pr^{3+}$, the lifetimes of NIR emissions at 948 nm ($\lambda_{ex} = 492$ nm), 988, and 1034 nm ($\lambda_{ex} = 605$ nm) are evaluated to be 10.0, 49.1, and 55.2 ms, respectively. They are almost the same as the 10.1 and 53.2 ms evaluated for visible emissions of Pr^{3+} from $^3P_0$ at 492 nm ($\lambda_{ex} = 454$ nm) and $^1D_2$ at 605 nm ($\lambda_{ex} = 594$ nm). These results strongly prove that the NIR emissions at 948 nm ($\lambda_{ex} = 492$ nm), 988, and 1034 nm ($\lambda_{ex} = 605$ nm) are ascribed to $^3P_0 \rightarrow {}^1G_4$ and $^1D_2 \rightarrow {}^3F_{3,4}$ transitions. Additionally, the lifetimes of NIR emissions at 1034 nm ($\lambda_{ex} = 492$ nm) are estimated to be 23.8 ms (shown in Table 5.1), which is obviously smaller than 55.2 ms for the same NIR emission

Table 5.1 The lifetimes of the $^3P_0$, $^1D_2$, and $^1G_4$ level of Pr^{3+} in $CaLaGa_3S_6O$ and $LiYF_4$ and BaY_2F_8

Pr^{3+}	$^3P_0 \rightarrow {}^3H_4$	$^3P_0 \rightarrow {}^1G_4$	$^1D_2 \rightarrow {}^3H_4$	$^1D_2 \rightarrow {}^3F_4$	$^1D_2 \rightarrow {}^3F_4$
λ_{ex}	454 nm	492 nm	594 nm	605 nm	605 nm
λ_{em}	492 nm	948 nm	605 nm	988 nm	1034 nm
τ	10.1 μs	10.0 μs	53.2 μs	49.1 μs	55.2 μs
$^1G_4$ level of Pr^{3+}	LiYF$_4$	CLGSO			BaY$_2$F$_8$
Photon energy/cm	566	~500			415
τ/μs	17	23.8			38

Reproduced from Ref. [71] by permission of The Royal Society of Chemistry

(λ_{ex} = 605 nm). The NIR emission at 1034 nm (λ_{ex} = 492 nm) may be due to the $^1G_4 \rightarrow {}^3H_4$ transition of Pr^{3+}. In general, the decay rate of the $^1G_4$ level of Pr^{3+} is determined mainly by the maximum phonon energy of the host. For some fluorides with relatively low phonon frequency ($\sim$500 cm^{-1}), the lifetime of the $^1G_4$ level of Pr^{3+} is about 15–38 ms, for example, 17 ms for LiYF$_4$ (566 cm^{-1}) and 38 ms for BaY$_2$F$_8$ (415 cm^{-1}), as shown in Table 5.1 [73]. The maximum phonon frequency is usually about 500 cm^{-1} in oxysulfides [40]. Therefore, it is reasonable to observe comparable lifetime of the $^1G_4$ level of Pr^{3+} in $CaLaGa_3S_6O$ with similar maximum phonon frequency. This also support the assignment of the NIR emission at 1034 nm (λ_{ex} = 492 nm) to the $^1G_4 \rightarrow {}^3H_4$ transition of Pr^{3+}. Based on the above analysis, $CaLaGa_3S_6O:Pr^{3+}$ has dual-mode spectral converting behaviors, NIR DC process $\left(^3P_{J=0,1,2} \rightarrow {}^1G_4 \rightarrow {}^3H_4 \right)$, and NIR DS process $\left(^1D_2 \rightarrow {}^3F_{J=3,4} \right)$, depending on different excited levels of Pr^{3+}. Here dual-mode photoluminescence come from the same luminescence center (Pr^{3+}), which differs to those based on two different luminescent centers, for example, Eu-doped nanocrystalline Li$_2$ZnSiO$_4$ glass ceramics reported by Zhang et al. [71].

Figure 5.15b, 1 shows the NIR emission mechanism of $CaLaGa_3S_6O:0.06Pr^{3+}$ under excitation into the $^3P_{J=0,1,2}$ levels. Electrons are pumped from the ground $^3H_4$ level into the excited $^3P_{J=0,1,2}$ and $^1I_6$ levels, respectively, under 455, 480, and 492 nm excitation. They then relax to the emitting level of $^3P_0$, from which the process of NIR DC $\left(^3P_0 \rightarrow {}^1G_4 \rightarrow {}^3H_4 \right)$ occurs. Therefore, the NIR emission peaking at 948 and 1034 nm was observed. Figure 5.15b, 2 presents the NIR emission mechanism of $CaLaGa_3S_6O:0.06Pr^{3+}$ under excitation into the $^1D_2$ level. Under 594 and 605 nm excitation, electron is directly jumped into the $^1D_2$ level and then radioactively relax back to $^3F_{J=3,4}$, which reasonably gives the NIR emissions at 988 nm $\left(^1D_2 \rightarrow {}^3F_3 \right)$ and 1034 nm $\left(^1D_2 \rightarrow {}^3F_4 \right)$. From Fig. 5.15a, 1, it is obviously seen that $CaLaGa_3S_6O:Pr^{3+}$ meets the requirement of excitation and emission characteristics of NIR DC material. But it can only absorb blue and red photons in the solar photon flux spectrum. In order to widen the utilization of the solar photon flux spectrum toward UV region, we further investigated the luminescent properties of $CaLaGa_3S_6O:Ce^{3+}, Pr^{3+}$ and explored the possibility of Ce^{3+} ion as a donor utilizing UV photons and enhancing the NIR emission of Pr^{3+} ion.

As shown in Fig. 5.15a, 2, it is very interesting that upon 400-nm excitation of Ce^{3+} ion, $CaLaGa_3S_6O:0.01Ce^{3+}$, $0.06Pr^{3+}$ exhibits intense NIR emissions of Pr^{3+} ion around 948, 988, and 1034 nm. Monitoring the NIR emission at 948 and 1034 nm, it shows the same PLE features as the allowed 4f–5d transitions of Ce^{3+} [74] and the forbidden 4f $\rightarrow$ 4f transitions of Pr^{3+} ion (shown in Fig. 5.15a, 1). Additionally, the appearance of 4f $\rightarrow$ 5d transitions of Ce^{3+} ion in the PLE spectrum (λ_{em} = 948, 1034 nm) of Pr^{3+} suggests UV-to-NIR ET from Ce^{3+} to Pr^{3+} occurs. These results successfully demonstrated that Ce^{3+} ion can be used as a donor utilizing UV photons and greatly enhancing the NIR emission of Pr^{3+} ion through efficient energy feeding by allowed 4f–5d absorption of Ce^{3+} ion with high oscillator strength [71].

Further, our group also investigated NIR emission mechanism of Pr^{3+} in $LiSrPO_4$, of which the maximum phonon frequency (~ 1037 cm^{-1}) is two times as large as that of $CaLaGa_3S_6O$ (~ 500 cm^{-1}) discussed above. And we found that the maximum phonon frequency of the host compound occupied by Pr^{3+} plays a key role in whether NIR DCof Pr^{3+} happens or not. The lower the maximum phonon frequency of the host compound, the higher the probability of the NIR DC of Pr^{3+}.

Hereafter, luminescence properties and NIR emission mechanism of Pr^{3+} in $LiSrPO_4$ will be discussed in detail [75]. Figure 5.16a, b presents the PLE and PL spectra of $LiSrPO_4 : Pr^{3+}_{0.0045}$ invisible region at 3 K. PLE consists of a series of typical 4f–4f transitions of Pr^{3+} (Fig. 5.16a). Under excitation into the $^3P_2$ sand $^1D_2$ levels, respectively, Pr^{3+} ion exhibits distinct emission features (Fig. 5.16b). The PL spectrum (λ_{ex} = 581 nm) only consists of several emission peaks in the wavelength range of 590–630 nm, due to the transitions from $^1D_2$ to the Stark levels of $^3H_4$. Whereas the PL spectrum (λ_{ex} = 443 nm) presents not only weak emission peaks at 482, 640, and 724 nm, assigned to $^3P_0 \rightarrow {}^3H_4, {}^3P_0 \rightarrow {}^3F_{2,4}$, but also the dominant emission peaks in the wavelength range of 590–630 nm. The decay curves (Fig. 5.16c, d) are almost identical, and the average decay time is about 105.3 and 106.5 µs when excited to $^3P_0$ and $^1D_2$ levels, respectively. Therefore, it is reasonable to assign the emissions between 590 and 630 nm to the $^1D_2$ levels.

It is interesting to note that not only the shapes but also the position of the emission peaks between 590 and 630 nm are exactly the same when excited into either $^3P_2$ or $^1D_2$ levels. Why can the radiative transitions from $^1D_2$ to $^3H_4$ be observed when excited into $^3P_2$ level [Fig. 5.17 (process 2a)]? There are two possible ways as shown in Fig. 5.17(process 2b and 2c). One is nonradiative relaxation process (2b) directly from $^3P_0$ to $^1D_2$ level assisted by phonons. The energy gap between $^3P_0$ and $^1D_2$ levels is about 3449 cm^{-1}. The maximum vibration frequency of phosphate is about 1037 cm^{-1} [76]. That is to say at least three phonons are needed to bridge this energy gap. In general, if the energy gap is more than 5 times the energy of the highest energy phonon, phonons assisting nonradiative relaxation process from the upper level to the lower level is impossible. In the present case, it is therefore expected that multiphonon relaxation process from $^3P_0$ to $^1D_2$ level may occur but its possibility is relatively low. The
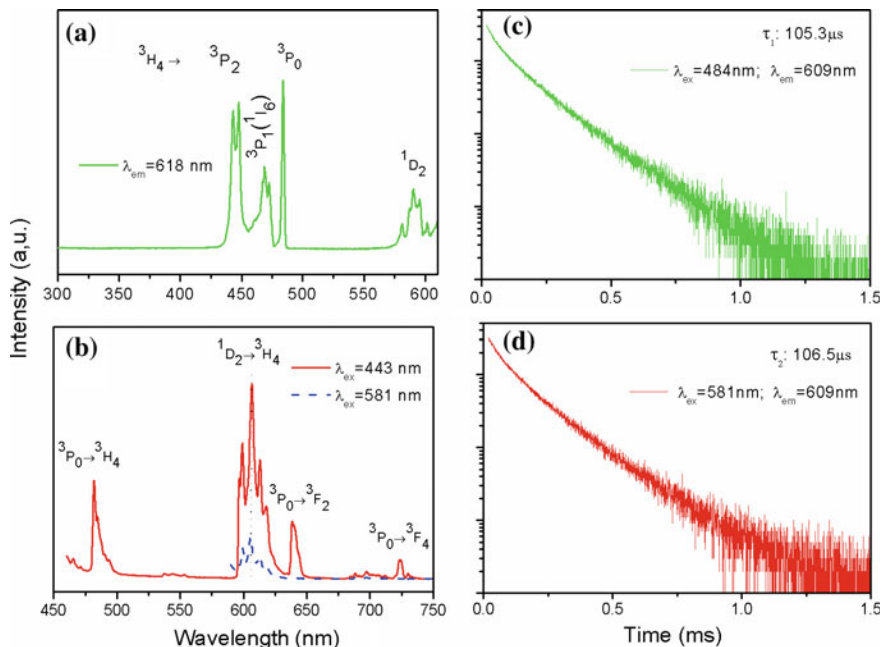
Fig. 5.16 PLE (**a** λ_{em} = 618 nm) and PL (**b** *solid*, λ_{ex} = 443 nm; *dash*, λ_{ex} = 581 nm) spectra of LiSrPO$_4$: Pr$^{3+}_{0.0045}$ at 3 K and the luminescence decay curves (**c** λ_{ex} = 484 and 581 nm, **d** λ_{em} = 609 nm) of LiSrPO$_4$: Pr$^{3+}_{0.0045}$ at room temperature. Reprinted from Ref. [75] by permission of the OSA Publishing
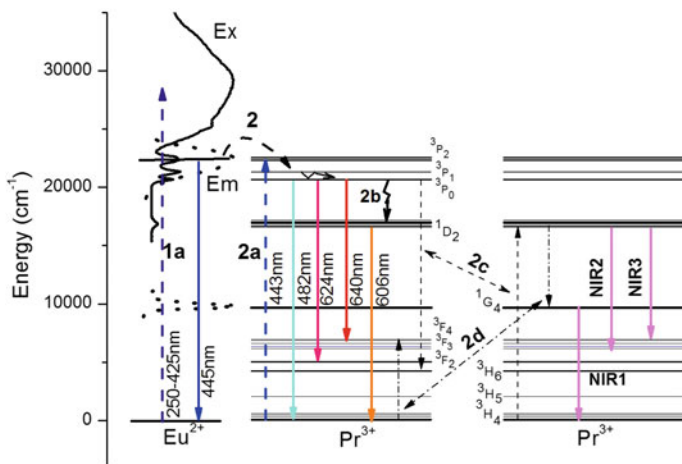
Fig. 5.17 The schematic diagrams of the cross-relaxation processes and energy transfer from Eu^{2+} to Pr^{3+} in LiSrPO$_4$ and from Pr^{3+} to Si solar cells. (**2c** [$^3P_0$, $^3H_4$] → [$^3H_6$, $^1D_2$]; **2d** [$^1D_2$, $^3H_4$] → [$^1G_4$, $^3F_4$]; **2b** the lattice thermalization loss). Reprinted from Ref. [75] by permission of the OSA Publishing

other is cross-relaxation process (**2c**), $[^3P_0, ^3H_4] \rightarrow [^3H_6, ^1D_2]$. The energy gaps between $^3P_0$ and $^3H_6$ levels, and $^1D_2$ and $^3H_4$ levels are 16,421 and 16,622 cm^{-1}, respectively. The difference between them is only about 201 cm^{-1}. Therefore, the cross-relaxation $[^3P_0, ^3H_4] \rightarrow [^3H_6, ^1D_2]$ is considered to be relatively more efficient than multiphonon relaxation process directly from $^3P_0$ to $^1D_2$ levels. Through the cross-relaxation (**2c**), it is reasonable to observe the prominent red emissions from the $^1D_2$ level as well as the $^3P_0$ level upon being pumped into the $^3P_2$ level (λ_{ex} = 443 nm). In summary, the whole blue-to-red energy transfer process could be expressed as (**2a** $\rightarrow$ **2c** $\rightarrow$ 606 nm) for the prominent red emissions from the $^1D_2$ level [75].

As shown in Fig. 5.17, the energy gaps between $^1G_4$ and $^1D_2$, and $^3H_4$ and $^3F_4$ are 6622 and 6163 cm^{-1}, respectively. The difference is only about 459 cm^{-1}. Therefore, it is theoretically expected that the cross-relaxation (**2d**), $[^1D_2, ^3H_4] \rightarrow [^1G_4, ^3F_4]$ occurs. That is to say the $^1G_4$ level can be populated via two steps of cross-relaxation (**2c** and **2d**) when excited into $^3P_0$ levels. Consequently, the NIR emissions from the $^1G_4$ level are expected. Figure 5.18a presents the emission spectra of $LiSrPO_4 : Pr^{3+}_{0.0045}$ in NIR region at 3 K. Under 484 nm ($^3P_0$) and 590 nm ($^1D_2$) excitation, Pr^{3+} ion shows almost the same NIR emission except the emission intensity. The sharp NIR1 emissions at 1042, 1053, and 1064 nm are due to the transitions from the excited $^1G_4$ level to the different Stark levels of the ground $^3H_4$ level. These results further prove that the cross-relaxation (**2d**), $[^1D_2, ^3H_4] \rightarrow [^1G_4, ^3F_4]$, is efficient in $LiSrPO_4$. Additionally, there are some other sharp emissions between 950 and 1040 nm. The NIR2 emissions at 969, 978, 982, and 989 nm, and the other NIR3 emissions at 1007, 1017 and 1025, 1028 and
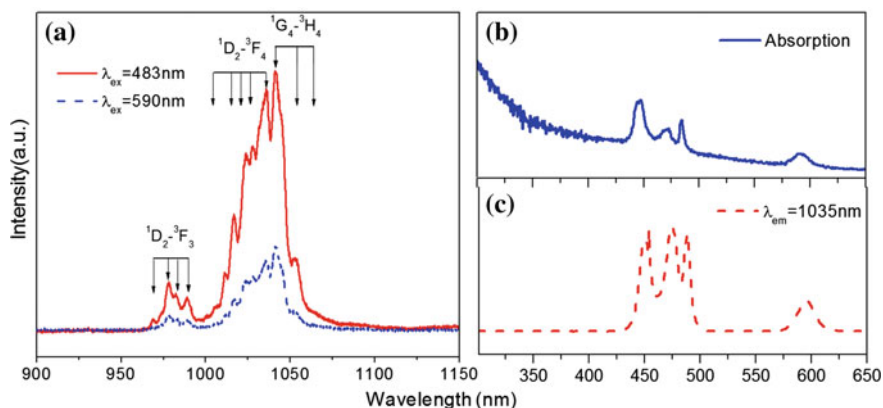
Fig. 5.18 a The PL spectrum of $LiSrPO_4 : Pr^{3+}_{0.0045}$ in near-infrared region (λ_{ex} = 484 and 590 nm) at 3 K; **b** the diffuse reflection spectrum and **c** PLE spectra (λ_{em} = 1035 nm) of $LiSrPO_4 : Pr^{3+}_{0.0045}$ at room temperature. Reprinted from Ref. [75] by permission of the OSA Publishing

1035 nm are attributed to the transitions from the excited $^1D_2$ level to the different Stark levels of $^3F_3$ and $^3F_4$, respectively. In summary, the whole blue-to-NIR ET process could be expressed as $\left(2a \to 2c \subset_{\mathrm{NIR1+NIR3}}^{2d \to \mathrm{NIR1}}\right)$ for the prominent NIR emissions from the $^1G_4$ and $^1D_2$ levels [75].

In order to prove the existence of quantum cutting, Meijerink et al. compared the diffuse reflection and excitation spectra of $SrF_2:Pr^{3+}$ and found the ratio of the total area of the peaks due to the $^3H_4 \to {}^3P_J$ and $^3H_4 \to {}^1I_6$, transitions relative to that of the $^3H_4 \to {}^1D_2$ peak in the excitation spectrum should be twice as large as the ratio similarly obtained in the diffuse reflectance spectra [15]. In $LiSrPO_4:Pr^{3+}$, as shown in Fig. 5.18b, c, the ratio of the total absorption (integrated spectral area) of the $^3H_4 \to {}^3P_J$ and $^3H_4 \to {}^1I_6$ transitions relative to that of the $^3H_4 \to {}^1D_2$ transition was determined to be 4.88. From the PLE of $LiSrPO_4 : Pr_{0.0045}^{3+}$, the ratio for the same transition is 4.91. Within experimental uncertainty, this ratio is equal to the value of that of the absorption strengths (from diffuse reflectance), confirming that for every photon absorbed into the ^3P_J and $^1I_6$ levels, only one NIR photon was generated. Therefore, the blue-to-NIR quantum cutting process from the $^3P_0$ level does not occur in $LiSrPO_4$ [75].

5.2.2.1 Summary and Outlook

In the past decade, rare earth ion-activated NIR DC and DS phosphors in form of powder, glass and glass ceramic, and film have been focused worldwide and deeply investigated from the viewpoint of spectroscopy of materials. Unfortunately, no proof-of-concept experiments have been reported for these kind of rare earth solar spectral convertors to answer whether they can really work in improving the spectral response of Si solar cells and enhancing the energy conversion efficiency of Si solar cells or not. Hereafter, recent proof-of-concept experiments for rare earth ion-activated visible DS phosphor, including complex and submicron spherical phosphor-polyvinylpyrrolidone (PVP) composite film, in Si solar cells will be representatively reviewed. Finally, we will discuss the possibility or potential of rare earth ion-activated NIR DC and DS phosphors on the way to the success of high performance and low cost Si solar cells in the future.

In 2015, Chen et al. reported DS $Gd_2O_2S:Eu^{3+}$phosphor-polyvinylpyrrolidone (PVP) composite film and explored its proof-of-concept experiments in rare earth-converted Si solar cells application [77], as shown in Fig. 5.19a. All the sub-micrometer spherical $Gd_2O_2S:Eu^{3+}$ phosphors with different concentration and particle size show the same spectral characteristic of Eu^{3+} ion except the intensity. They exhibit a broad excitation band extending from 250 to 400 nm and give intense red emission at 624 nm, due to typical 4f–4f transition of Eu^{3+} ion. The PL intensity of GS125, GS290 and GS419 was found to be 30.7, 35.7, and 45.8 % with respect to commercial Y_2O_2S: Eu^{3+} bulk phosphor, respectively. The quantum efficiency of $Gd_2O_2S:Eu^{3+}$ submi-crometer spheres with different particle size is ranging from 26.6 to 36.2 %, which are lower than 63.9 % of commercial $Y_2O_2S:Eu^{3+}$ bulk phosphor [77].
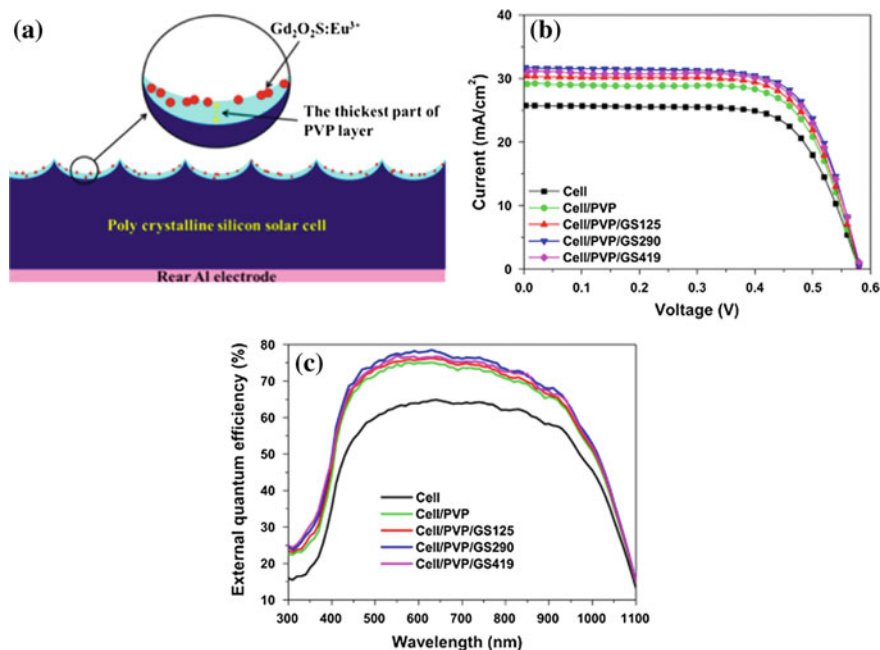
Fig. 5.19 **a** The schematic structure of proof-of-concept rare earth-converted Si solar cells (REC-Si Solar Cells), **b** J–V characteristics of the REC-Si solar cells before and after coating with PVP and PVP/Gd$_2$O$_2$S:Eu^{3+} and **c** EQE as a function of illumination wavelength for solar cells before and after coating with PVP and PVP/Gd$_2$O$_2$S:Eu^{3+}. Reprinted from Ref. [77]. Copyright 2014, with permission from Elsevier

Figure 5.19b shows the current density–voltage (J–V) characteristics of the REC-Si solar cells coated with PVP and PVP/Gd$_2$O$_2$S:Eu^{3+} under air mass 1.5 global illumination conditions and compared to the untreated cell. The bare Si solar cell exhibited a power conversion efficiency (PCE) of about 10.44 %, a short-circuit current density (J_{sc}) of about 25.76 mA/cm^2, an open-circuit voltage (V_{oc}) of about 0.5798 V, and a fill factor (F.F.) of about 69.9 %. After coating PVP and PVP/Gd$_2$O$_2$S:Eu^{3+} on the textured surface, the J–V curves showed a distinct increase in J_{sc}. The highest increase in J_{sc} of about 6 mA/cm^2, corresponding to a 23 % enhancement compared with that of the bare cell, was achieved by integrating PVP/GS290 on the cell surface. The enhancement was found to be 8.9 % for the devices coated with PVP/GS290, compared to PVP solely. The authors believed that these results come from an enhancement of light absorption and photo response. The reflection intensity can be further reduced by embedding Gd$_2$O$_2$S: Eu^{3+} phosphors into the PVP layer, in particular for the coating with PVP/GS290. The authors thought that the increase in light trapping, which is achieved by light scattering from the spherical Gd$_2$O$_2$S:Eu^{3+} particles, is a more reasonable explanation for the reduced reflectance. The solar cells covered with PVP/Gd$_2$O$_2$S:Eu^{3+} layers achieved better enhancement of photocurrent in the measured spectral range,

particularly in the UV region, compared to the PVP-coated device. The author concluded that this is not only because of the better anti-reflection properties of PVP/Gd_2O_2S:Eu^{3+}, but also because of the luminescent DS behavior of Gd_2O_2S: Eu^{3+} [77].

For practical application, the c-Si solar cells have to be encapsulated into modules for protection from moisture and impact. Such a kind of the modules structure leads to the quite difference between the spectral responses of commercial c-Si PV modules with that of c-Si solar cells because of the additional photo losses caused by absorption and reflection by the front glass and absorption by the encapsulation material [78]. Therefore, recent developments on REC-Si solar cells via rare earth ion-activated luminescent DS as mentioned above seem not enough for further practical application. In 2013, Li et al. reported a series of luminescent DS Eu^{3+} complexes and explored their proof-of-concept experiments in rare earth-converted Si solar cell modules application [78]. The as-tested Eu^{3+} complex shows typical PLE and PL of Eu^{3+} similar to Gd_2O_2S:Eu^{3+}. After simple coating of polyvinyl acetate film (PVA) doped with this complex onto the surface of c-Si PV module, the short-circuit current density (J_{sc}) increases from 35.67 to 36.38 mA/cm^2, whereas the overall energy conversion efficiency (η) increases from 16.05 to 16.37 % as shown in Fig. 5.20a. Also, the increase of the external quantum efficiency (EQE) in the UV region can be observed for c-Si PV module coated by PVA films doped with Eu^{3+} complexes, as shown in Fig. 5.20b. The best improvement of EQE is achieved for c-Si PV module coated by PVA film doped with 5: The EQE at 300–400 nm is higher than 50 % although no decrease of EQE at l > 400 was presented. The increase of EQE of c-Si PV module after coating with PVA doped with complexes 1–5 can be ascribed to the photo-conversion effect of complexes 1–5. The authors thought that the reduction in reflection upon coating of PVA films should contribute little [78].
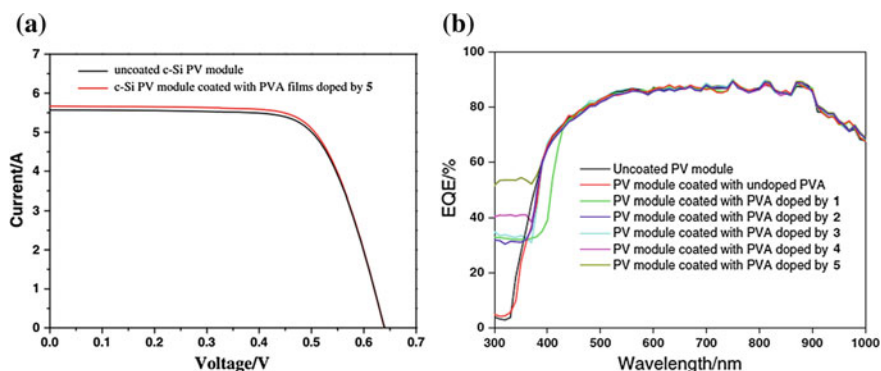
Fig. 5.20 **a** J–V characteristics of the REC-Si solar cells before and after coating with polyvinyl acetate (PVA) and PVA/Eu^{3+} complex 5 and **b** EQE as a function of illumination wavelength for solar cells before and after coating with PVA and PVA/Eu^{3+} complex 1, 2, 3, 4, and 5. Reprinted from Ref. [78]. Copyright 2006, with permission from Elsevier

These results mentioned above suggest that the simple luminescent DS technique with Eu^{3+} complexes or a suitable inorganic phosphorus luminescent DS species is promising for improving the spectral response of c-Si solar cell or PV modules to UV photons. Even so, this kind of traditional luminescent DS complex or inorganic phosphor is theoretically not the most ideal solar spectral convertor from the viewpoint of the spectral response of Si solar cells, as firstly discussed in the introduction of this chapter. Firstly, they can only work in UV fraction of solar spectrum, which contributes a little to the AM 1.5 solar spectral. Second, they can only convert UV photons into red photons, which do not match well with the optimal spectral response of Si solar cell. Comparatively, there leaves a great space for rare earth ion-activated NIR DC or DS to improve the spectral response of Si solar cells and to enhance the power conversion efficiency of Si solar cells. The challenges for rare earth ion-activated NIR DC or DS materials in the future are the following: (1) up to now, the spectral convertor performance, especially the external quantum efficiency of NIR DC or DS materials is not good enough although the shape of absorption and emission spectral is better than traditional luminescent DS as mentioned above. Therefore, the first task should be done is to further design and develop advanced NIR DC or DS materials with high external quantum efficiency; (2) for future practice application, the transparency of NIR DC or DS materials should be focused. Consequently, glass or composite polymer film with high efficient NIR DC or DS performance and high transparency will be hot topic in the future. (3) How to use these spectral converting materials for PV devices and systems will certainly be hot issue in the future. The proof-of-concept experiments on the device structure of REC-Si solar cells or modules should be explored. In summary, I believe the future of rare earth ion-activated NIR DC or DS materials is bright in the application of REC-Si solar cells or modules.

References

1. Richards BS (2006) Enhancing the performance of silicon solar cells via the application of passive luminescence conversion layers. Sol Energ Mat Sol C 90: 2329.
2. Gratzel M (2007) Photovoltaic and photoelectrochemical conversion of solar energy. Philos T Roy Soc A 365: 993.
3. Trupke T, Green MA, Wurfel P (2002) Improving solar cell efficiencies by downconversion of high-energy photons. J Appl Phys 92: 1668.
4. Huang XY, Han SY, Huang W, Liu XG (2013) Enhancing solar cell efficiency: the search for luminescent materials as spectral converters. Chem Soc Rev 42: 173.
5. Shockley W, Queisser HJ (1961) Detailed Balance Limit of Efficiency of P-N Junction Solar Cells. J Appl Phys 32: 510.
6. Zhang QY, Huang XY (2010) Recent progress in quantum cutting phosphors. Prog Mater Sci 55: 353.
7. Chen DQ, Wang YS, Hong MC (2012) Lanthanide nanomaterials with photon management characteristics for photovoltaic application. Nano Energy 1: 73.
8. Boulon G (2008) Why so deep research on Yb^{3+}-doped optical inorganic materials? J Alloy Compd 451: 1.

 9. Vergeer P, Vlugt TJH, Kox MHF, den Hertog MI, van der Eerden JPJM, Meijerink A (2005) Quantum cutting by cooperative energy transfer in $Yb_xY_{1-x}PO_4:Tb^{3+}$. Phys Rev B: Condens Matter 71: 014119.
10. Zhang QY, Yang CH, Jiang ZH, Ji XH (2007) Concentration-dependent near-infrared quantum cutting in $GdBO_3$:Tb,Yb nanophosphors. Appl Phys Lett 90: 061914.
11. Huang XY, Zhang QY (2009) Efficient near-infrared down conversion in Zn_2SiO_4:Tb,Yb thin-films J Appl Phys 105: 053521.
12. Zhang QY, Yang GF, Jiang ZH (2007) Cooperative downconversion in $GdAl_3(BO_3)_4$:RE, Yb (RE=Pr, Tb, and Tm) Appl Phys Lett 91: 051903.
13. Ye S, Zhu B, Luo J, Chen JX, Lakshminarayana G, Qiu JR (2008) Enhanced cooperative quantum cutting in Tm^{3+}-Yb^{3+}codoped glass ceramics containing LaF_3 nanocrystals. Opt Express 16: 8989.
14. Chen XP, Huang XY, Zhang QY (2009) Concentration-dependent Pr^{3+}-Yb^{3+} down conversion phosphor. J App Phys 106: 063518.
15. van der Ende BM, Aarts L, Meijerink A (2009) Near-Infrared Quantum Cutting for Photovoltaics. Adv Mater 21: 1.
16. Dieke GH (1968) Spectra and Energy Levels of Rare Earth Ions in Crystals, Interscience. New York 142.
17. Wegh RT, Meijerink A, Lamminma RJ, Hölsä J (2000) Extending Dieke's diagram. J Lumin 87-89: 1002.
18. Denham P, Field GR, Morse PLR, Wilkinson GR (1970) Optical and Dielectric Properties and Lattice Dynamics of Some Fluorite Structure Ionic Crystals. Proc R Soc London A 317: 55.
19. Zheng W, Zhu H, Li R, Tu D, Liu Y, Luo W, Chen X (2012) Visible-to-infrared quantum cutting by phonon-assisted energy transfer in YPO_4:Tm^{3+},Yb^{3+} phosphors. Phys ChemChem Phys 14: 6974.
20. Aarts L, van der Ende BM, Meijerink A (2009) Downconversion for solar cells in $NaYF_4$:Er, Yb. J Appl Phys 106: 023522.
21. Eilers JJ, Biner D, van Wijngaarden JT, Kraemer K, Guedel HU Meijerink A (2010) Efficient visible to infrared quantum cutting through downconversion with the Er^{3+}–Yb^{3+} couple in $Cs_3Y_2Br_9$. Appl Phys Lett 96: 151106.
22. Meijer JM, Aarts, van der Ende BM, Vlugt TJH, Meijerink A. (2010) Downconversion for solar cells in YF_3:Nd^{3+}, Yb^{3+}. Phys Rev B: Condens Matter 81: 035107.
23. Lin H, Chen D, Yu Y, Yang A, Wang Y (2011)Near-infrared quantum cutting in Ho^{3+}/Yb^{3+} codoped nanostructured glass ceramic. Opt Lett 36: 876.
24. Yu DC, Huang XY, Ye S, Zhang QY (2011) Efficient first-order resonant near-infrared quantum cutting in β-$NaYF_4$:Ho^{3+},Yb^{3+}. J Alloys Compd 509: 9919.
25. Deng K, Gong T, Hu L, Wei X, Chen Y, Yin M (2011) Efficient near-infrared quantum cutting by resonance energy transfer in $NaYF_4$:Ho^{3+}, Yb^{3+}. Opt Express 19: 1749.
26. Bai Z, Fujii M, Hasegawa T, Imakita K, Mizuhata M, Hayashi S (2011) Efficient ultraviolet-blue to near-infrared downconversion in Bi–Dy–Yb-doped zeolites. J Phys D: Appl Phys 44: 455301.
27. Jørgensen CK (1970) Electron transfer spectra. Prog Inorg Chem 12: 101.
28. Bae JS, Park JC, Park JM, Seo HJ, Choi BC, Jeong JH, Kim YS, Yi SS (2004) Morphology-dependent luminescence behavior of $Y_{2-x}Gd_xO_3$:Eu^{3+} thin-film phosphors grown by a laser ablation. Appl Phys A-Mater 78: 877.
29. Wang EY, Zhou WL, Liu CM, Wang J, Kuang XJ, Ye YM, Tang JK, Su Q (2014) Yb^{3+} site occupation and host sensitization luminescence of a novel near-infrared emitting Sr_2CaMoO_6:Yb^{3+} phosphor, Phys Status Solidi-R 8: 202.
30. Zhang GG, Liu CM, Wang J, Kuang XJ, Su Q (2011) An intense charge transfer broadband sensitized near-infrared emitting $CaLaGa_3S_6O$:Yb^{3+} phosphor suitable for solar spectral convertor. Opt Express 19: 24314.
31. Wei X, Huang S, Chen Y, Guo C, Yin M, Xu W (2010) Energy transfer mechanisms in Yb^{3+} doped YVO_4 near-infrared downconversion phosphor. J Appl Phys 107: 103107.

32. Peng Y, Liu J, Zhang K, Luo H, Li J, Xu B, Han L, Li X, Yu X (2011) Near-infrared luminescent and antireflective in $SiO_2/YVO_4:Yb^{3+}$ bilayer films for c-Si solar cells. Appl Phys Lett 99:121110.
33. Cheng X, Su L, Wang Y, Zhu X, Wei X, Wang Y (2012) Near-infrared quantum cutting in $YVO_4:Yb^{3+}$ thin-films via downconversion. Opt Mater 34: 1102.
34. Sablayrolles J, Jubera V, Guillen F, Garcia A (2008) Charge transfer emission of ytterbium-doped oxyborates. Spectrochim Acta A Mol Biomol Spectrosc 69: 1010.
35. van Pieterson L, Heeroma M, de Heer E, Meijerink A (2000) Charge transfer luminescence of Yb^{3+}. J Lumin 91: 177.
36. Yu RJ, Wang J, Zhang M, Zhang JH, Yuan HB, Su Q (2008) A new blue-emitting phosphor of Ce^{3+}-activated $CaLaGa_3S_6O$ for white-light-emitting diodes. Chem Phys Lett 453: 197.
37. Teske CL (1985) Überoxidsulfidemit Åkermanitstruktur $CaLaGa_3S_6O$, $SrLaGa_3S_6O$, $La_2ZnGa_2S_6O$ and $Sr_2ZnGe_2S_6O$," Z AnorgAllgChem 531: 52.
38. Sablayrolles J. Jubera V, Guillen F, Garcia A (2008) Charge transfer emission of ytterbium-doped oxyborates. Spectrochim. Acta A Mol BiomolSpectrosc 69:1010.
39. Zhang QH, Wang J, Zhang GG, Su Q (2009) UV photon harvesting and enhanced near-infrared emission in novel quantum cutting $Ca_2BO_3Cl:Ce^{3+}$, Tb^{3+}, Yb^{3+} phosphor. J Mater Chem 19: 7088.
40. De Mello Donega C, Meijerink A, Blasse G (1995) Nonradiative Relaxation Processes of the Pr^{3+} Ion in Solids. J Phys Chem Solids 56: 673.
41. Li Y, Wang J, Zhou WL, Zhang GG, Chen Y, Su Q (2013) UV-Vis-NIR luminescence properties and energy transfer mechanism of a novel 5d broadband sensitized $Sr_3SiO_5:Ce^{3+}$, Yb^{3+} suitable for solar spectral convertor. Appl Phys Express 6: 082301.
42. Ye S, Wang CH, Jing XP (2008) Photoluminescence and Raman Spectra of Double-Perovskite $Sr_2Ca(Mo/W)O_6$ with A- and B-Site Substitutions of Eu^{3+}. J Electrochem Soc 155: 148.
43. Ye S, Wang CH, Liu ZS, Lu J, Jing XP (2008) Photoluminescence and energy transfer of phosphor series $Ba_{2-z}Sr_zCaMo_{1-y}W_yO_6:Eu$, Li for white light UVLED applications. Appl Phys B 91:551.
44. Sivakumar V, Varadaraju UV (2006)A Promising Orange-Red Phosphor Under Near UV Excitation. Electrochem Solid-State Lett 9: 35.
45. Auzel F, Goldner P (2001) Towards rare-earth clustering control in doped glasses. Opt Mater 16: 93.
46. Lai B, Wang J, Su Q (2010)Ultraviolet and visible upconversion emission in Tb^{3+}/Yb^{3+} co-doped fluorophosphate glasses. Appl Phys B 98: 41.
47. Deng ZP, Kang W, Huo LH, Zhao H, Gao S (2010) Rare-earth organic frameworks involving three types of architecture tuned by the lanthanide contraction effect: hydrothermal syntheses, structures and luminescence. Dalton Trans 39: 6276.
48. Legendziewicz J, Guzik M, Szuszkiewicz W (2008)Charge transfer and f–f emission of trivalent ytterbium observed in double phosphates $M^IM^{III}(PO_4)_2$ (M^I=Na, Rb; M^{III}=Lu, Y). J Alloys Compd 451: 165.
49. Ye S, Li Y, Yu D, Yang Z, Zhang Q (2011)Structural effects on Stokes and anti-Stokes luminescence of double-perovskite $(Ba,Sr)_2CaMoO_6$: Yb^{3+},Eu^{3+}. J Appl Phys 110: 013517.
50. Peng MY, Wondraczek L (2009) Bismuth-doped oxide glasses as potential so-lar spectral converters and concentrators. J Mater Chem 19: 627.
51. Wang DM, Tie SL, Wan X (2015) White light emitting from $YVO_4/Y_2O_3:Eu^{3+}$, Bi^{3+} composite phosphors for UV light-emitting diodes. Ceram Int 41: 7766.
52. Huang XY, Zhang QY (2010) Near-Infrared Quantum Cutting via Cooperative Energy Transfer in $Gd_2O_3:Bi^{3+}$, Yb^{3+} Phosphors. J Appl Phys 107: 063505.
53. Dorenbos P (2003) f→d transition energies of divalent lanthanides in inorganic compounds. J Phys: Condens Matter 15:575.
54. Huang XY, Yu DC, Zhang QY (2009) Enhanced Near-Infrared Quantum Cutting in $GdBO_3$: Tb^{3+},Yb^{3+} Phosphors by Ce^{3+} Codoping. J Appl Phys 106: 113521.
55. Zhou JJ, Teng Y, Ye S, Zhuang YX, Qiu JR (2010)Enhanced downconversion luminescence by co-doping Ce^{3+} in $Tb^{3+}–Yb^{3+}$ doped borate glasses. Chem Phys Lett 486: 116.

56. Liu TC, Zhang GG, Qiao XB, Wang J, Seo HJ, Tsai DP, Liu RS (2013) Near-Infrared Quantum Cutting Platform in Thermally Stable Phosphate Phosphors for Solar Cells. InorgChem 52: 7352.
57. Chen D, Wang Y, Yu Y, Huang P, Weng F (2008) Quantum cutting downconversion by cooperative energy transfer from Ce^{3+} to Yb^{3+} in borate glasses. J Appl Phys 104: 116105.
58. Chen J, Guo H, Li Z, Zhang H, Zhuang Y (2010) Near-infrared quantum cutting in Ce^{3+}, Yb^{3+} co-doped YBO_3 phosphors by cooperative energy transfer. Opt Mater 32: 998.
59. Chen J, Zhang H, Li F, H. Guo (2011) High efficient near-infrared quantum cutting in Ce^{3+}, Yb^{3+} co-doped $LuBO_3$ phosphors. Mater Chem Phys 128: 191.
60. Liu X, Teng Y, Zhuang Y, Xie J, Qiao Y, Dong G, Chen D, Qiu J (2009) Broadband conversion of visible light to near-infrared emission by Ce^{3+}, Yb^{3+}-codoped yttrium aluminum garnet. Opt Lett 34: 3565.
61. Lin H, Zhou SM, Teng H, Li YK, Li WJ, Hou XR, Jia TT (2010) Near infrared quantum cutting in heavy Yb doped transparent ceramics for crystalline silicon solar cells. J Appl Phys 107: 043107.
62. Zhou WL, Li Y, Zhang RH, Wang J, Zou R, Liang HB (2012) Ultraviolet to near-infrared downconversion of Y_2SiO_5:Ce^{3+}, Yb^{3+}nanobelt-poly-EVA films. Opt Lett 37: 4437.
63. Zhou WL, Yang J, Wang J, Li Y, Kuang XJ, Tang JK, Liang HB (2012) Study on the effects of 5d energy locations of Ce^{3+} ions on NIR quantum cutting process in Y_2SiO_5:Ce^{3+}, Yb^{3+}. Opt Express 20: 510.
64. Ueda J, Tanabe S (2009) Visible to near infrared conversion in Ce^{3+}-Yb^{3+} Co-doped YAG ceramics. J Appl Phys 106: 043101.65.
65. Zhou J, Zhuang Y, Ye S, Teng Y, Lin G, Zhu B, Xie J, Qiu J (2009) Broadband downconversion based infrared quantum cutting by cooperative energy transfer from Eu^{2+} to Yb^{3+} in glasses. Appl Phys Lett 95: 141101.
66. Zhou J, Teng Y, Lin G, Xu X, Ma Z, Qiu J (2010) Broad-Band Excited Quantum Cutting in Eu^{2+}–Yb^{3+} Co-doped Aluminosilicate Glasses. J Electrochem Soc 157: 1146.
67. Teng Y, Zhou J, Ye S, Qiu J (2010)Broadband Near-Infrared Quantum Cutting in Eu^{2+} and Yb^{3+} Ions Co-doped $CaAl_2O_4$ Phosphor. J Electrochem Soc 157: 1073.
68. Lin H, Chen D, Yu Y, Shan Z, Huang P, Yang A, Wang Y (2011)Broadband UV excitable near-infrared downconversion luminescence in Eu^{2+}/Yb^{3+}:CaF_2 nanocrystals embedded glass ceramics. J Alloys Compd 509: 3363.
69. Smedskjaer MM, Qiu J, Wang J, Yue Y (2011)Near-infrared emission from Eu–Yb doped silicate glasses subjected to thermal reduction. Appl Phys Lett 98: 071911.
70. Teng Y, Zhou J, Liu X, Ye S, Qiu J (2010)Efficient broadband near-infrared quantum cutting for solar cells. Opt Express 18: 9671.
71. Zhang GG, Liu CM, Wang J, Kuang XJ, Su Q (2012) A dual-mode solar spectral converter $CaLaGa_3S_6O$:Ce^{3+},Pr^{3+}: UV-Vis-NIR luminescence properties and solar spectral converting mechanism. J Mater Chem 22: 2226.
72. Moune OK, Faucher MD, Edelstein N (2002)Spectroscopic investigations and configuration-interaction-assisted crystal field analysis of Pr^{3+} in YPO_4 single crystal. J Lumin 96: 51.
73. Garapon C, Malinowski M, Joubert MF, Kaminskii AA, Jacquier B (1994) IR luminescence from the $^1G_4$ multiplet of Pr^{3+} in various doped crystals. J. De Physique IV C4: 349.
74. Zhang GG, Wang J, Chen Y, Su Q (2010) Two-color emitting of Ce^{3+} and Tb^{3+} co-doped $CaLaGa_3S_6O$ for UV LEDs. Opt Lett 35: 2382.
75. Chen Y, Wang J, Liu CM, Tang JK, Kuang XJ, Wu MM, Su Q (2013) UV-Vis-NIR luminescence properties and energy transfer mechanism of $LiSrPO_4$:Eu^{2+}, Pr^{3+} suitable for solar spectral convertor. Opt Express 21: 3161.
76. Paques-Ledent MT (1978) Vibrational spectra and structure of $LiB^{2+}PO_4$ compounds with B=Sr, Ba, Pb. J Solid State Chem 23(1-2): 147.
77. Hung WB, Chen TM (2015) Efficiency enhancement of silicon solar cells through a downshifting and antireflective oxysulfide phosphor layer. Sol Energ Mat Sol C 133: 39.
78. Liu J, Wang K, Zheng W, Huang W, Li CH, You XZ (2013)Improving spectral response of monocrystalline silicon photovoltaic modules using high efficient luminescent down-shifting Eu^{3+} complexes. Prog Photovolt: Res Appl 21: 668.

Chapter 6
Persistent Luminescent Materials

Yingliang Liu and Bingfu Lei

Abstract Persistent luminescent materials have become an important class of multi-functional materials and have a broad application in many fields. The persistent luminescent materials have been mainly used as luminous materials. Besides, as for the photocatalysis, the persistent luminescent materials act as the light source for the photocatalysis in dark environment; as for sensing, the persistent luminescent materials use their temperature change and mechanoluminescence features to measure the environment temperature and pressure; the application of the persistent luminescent materials in biomedical study lies in the luminescent marker, tumor diagnostics and analysis, as well as photodynamic therapy of cancer; as for the application in solar energy, the persistent luminescent materials can be used in photoelectron nano-devices, fiber amplifier, and photovoltaic materials; the persistent luminescent materials can also be used in agriculture, as the light source for plant growth, and enhance the photosynthesis of the plants. Combining the published work with our research, this chapter will include: the basic concepts and history of persistent luminescent materials, the classification of the persistent luminescent materials, the luminescent mechanism and model, and the basic methods and conditions to realize the persistent luminescence, the applications of the persistent luminescent materials, and the prospects of the persistent luminescent materials in the end.

6.1 Introduction

The persistent luminescent materials are an important class of light-induced energy storage materials, which have undertaken a long development process. The luminescent system developed from irradiative materials to sulfide system and then to

Y. Liu (✉) · B. Lei
Guangdong Provincial Engineering Technology Research Center for Optical Agriculture,
College of Materials and Energy, South China Agricultural University, Guangzhou 510642,
China
e-mail: tliuyl@scau.edu.cn

oxide and nitride system; from inorganic system to organic system [1]; and from non-carbon system to carbon quantum dot system [2, 3]; and the luminescence lifetime ranges from a few seconds and minutes to more than 10 h. The persistent luminescent materials have become an important class of multi-functional materials, whose applications spread beyond the traditional luminous material, but across to the pressure sensing material, biomedical marking material, photocatalysis source material, solar cell photovoltaic material, photoconversion material for agriculture, etc., and have a wide range of applications and application prospects.

There have been several valuable review articles describing the persistent luminescent material, including the persistent luminescent material activated by Eu^{2+} [4], non-Eu^{2+}-activated persistent luminescent material [5], sulfide persistent luminescent material [6], nitride and nitrogen oxide persistent luminescent material [7], red and near-infrared persistent luminescent materials and their biomedical applications [8, 9], the history, application, and mechanism of persistent luminescent materials [10, 11], and so on. Wang et al. [12] published the research progress of multi-color persistent luminescent materials. Su et al. [13] recently published a very instructive summary about the persistent luminescent materials. Combining the published work with our research, this chapter will include: the basic concepts and history of persistent luminescent materials, the classification of the persistent luminescent materials, the luminescent mechanism and model, and the basic methods and conditions to realize the persistent luminescence, the applications of the persistent luminescent materials, and the prospects of the persistent luminescent materials in the end.

6.2   The Concepts and History of Persistent Luminescence

When the light illumination, applied electric fields, or the electron beam bombardment exert on the material, and as long as the material does not undertake any chemical reactions, it will recover to its original equilibrium, during which some excess energy will be released in the forms of light or heat. If this part of energy is released by visible or near-visible lights, this phenomenon is called luminescence [14]. There is a large diversity of luminescence forms, and the luminescence types are mainly photo-luminescence, cathodo-luminescence, electroluminescence, thermoluminescence, and radio-luminescence.

It is not a simple energy conversion process in luminescence. Another important characteristic is the persistency, which means besides the conversion from absorbed energy to radiation, the resulted radiation can also persist for a certain period after the applied excitation stops, which is named persistent luminescence.

We usually call the emission light when the material gets excited as 'fluorescence,' and the emission light after the excitation stops as 'phosphorescence.' The boundary between fluorescence and phosphorescence is the persistent lifetime of 10^{-8} s, with a persistent lifetime shorter than which is generally called 'fluorescence,' longer than which is called 'phosphorescence.' Any kinds of luminescence

can show its decay process in the form of luminescence. The decay period can be extremely short (shorter than 10^{-8} s) and can also be very long (several minutes to even more than 10 h). The materials with long persistent luminescence lifetime after the excitation stops are called persistent luminescent materials [4].

The persistent luminescent materials are a class of photo-luminescent materials. When excited by light irradiation, the persistent luminescent materials absorb light energy and store in the matrix. After the excitation stops, the stored energy will be gradually released in the form of light emission, and this luminescence lifetime can last long. This type of energy absorption–storage–emission–re-excitation–re-emission can repeat indefinitely, is similar to the battery's charge-discharge-re-charge-re-discharge process, and can thus be called 'light-storing material.'

The persistent luminescent materials can also be called luminous materials. In China, they are commonly named luminous powder or persistent luminescent powder, while academically they are called persistent phosphorescent fluorescent body or long-time luminescent materials. This type of materials can store the solar energy or natural light during the day time and gradually release during the night, irradiating bright light in the dark or in the night and having the function of lighting. They do not consume electric energy and therefore become a type of light–light-converting material, energy-saving material, as well as green energy material [15–17]. As a result, persistent luminescent materials are widely applied in industrial and agricultural production, military, firefighting, people's daily life, and many other fields, especially in the safety indicator field. As reported, in '911' accident in USA, persistent luminescent materials indicators played an important role in people evacuation process.

More generally speaking, the persistent luminescence is a very special optical phenomenon, and a luminescence resulted from the material being excited by high-energy sources such as visible light, ultraviolet, X-ray, γ-ray, and electron beams. This luminescence can last for a few seconds, hours, or even days after the excitation stops. And this phenomenon can be named by persistent luminescence, persistent phosphor, phosphorescence, afterglow, long-lasting phosphorescence, etc. [18]. Usually, this persistent luminescence phenomenon is considered to be due to the trapped electrons slow release under the heat excitation.

The persistent luminescence intensity and lifetime are the two important parameters to evaluate the persistent luminescent properties of materials. We expect the materials to have very high luminescence intensity and long persistent lifetime. The persistent luminescence lifetime is defined as the time length from the excitation stops to the luminescence intensity drops to 0.32 mcd/m^2, which is 100 times more sensitive than human eyes in the dark.

Reports show that the earliest persistent luminescence phenomenon can be dated back to prehistoric civilization. Relevant descriptions were found in ancient Chinese records of luminous oil paintings and luminous night pearls. According to the history books, as early as the prehistoric times such as Yan and Huang times, there were reports about the luminous night pearls, which have been proved to be a kind of fluorite mineral [4]. The first systematical introduction for the persistent luminescence phenomenon showed up in the year of 1602, when an Italian

shoemaker Vincenzo Casciarolo discovered the persistent luminescence phenomenon in barites (barium sulfate) [11]. Unfortunately, this persistent luminescence actually did not come from barium sulfate, but from barium sulfide, and some natural impurities' existence played an important role in the generation of the persistent luminescence [19]. Later on, although the persistent luminescence intensity and lifetime of ZnS:Cu, Co can hardly fulfill the practical application needs, due to the lack of the persistent luminescent materials, ZnS:Cu, Co as the only persistent luminescent materials was still widely used. For example, it was used in the clock dials, luminescent paints, and some crafts [20, 21]. To improve the persistent luminescence intensity and lifetime, some radioactive elements (promethium, tritium, etc.) were usually introduced. For a long time before 1990s, because there was no breakthrough in the persistent luminescent materials study and application, the research interest about persistent luminescent materials gradually decreased.

In 1996, Matsuzawa et al. [22] reported a new type of green persistent luminescent materials $SrAl_2O_4$:Eu^{2+},Dy^{3+} and realized a breakthrough in persistent luminescent materials development. This finding also marked the new round of intensive study of persistent luminescent materials. At the beginning of the investigation, the major research focused on aluminate substrates, such as $CaAl_2O_4$, $SrAl_2O_4$, $BaAl_2O_4$, and other systems [23, 24]. Until 2001, Lin et al. reported a type of high-intensity persistent luminescent materials $Sr_2MgSi_2O_7$:Eu^{2+},Dy^{3+}. After that, many silicate persistent luminescent materials with comparable luminescent properties were reported one by one [25, 26]. From the discovery of $SrAl_2O_4$:Eu^{2+}, Dy^{3+} until now, almost 20 years passed, and the research of persistent luminescent materials has made significant progresses. Till now, various kinds of persistent luminescent materials have been discovered, from simple luminescent substrates, to rare-earth and non-rare-earth elements ions-doped solid materials, and their luminescent properties are improving all the time. The studies of persistent luminescent materials progressed from the sulfide persistent luminescent materials, aluminates, silicates, titanates, sulfur oxides, and nitride (oxide) persistent luminescent materials, in a time order.

Persistent luminescent materials with different luminescent substrates have their own advantages and disadvantages (as given in Table 6.1).

6.3 The Categorization of Persistent Luminescent Materials

The persistent luminescent materials can be divided into different categories. According to different matrixes, persistent luminescent materials can be divided into aluminates, silicates, and non-oxides; based on their luminescence wavelengths, persistent luminescent materials can be divided into visible persistent luminescent materials (including blue, green, and red) and near-infrared persistent

Table 6.1 Properties and characteristics of different persistent phosphors

Host material	Color	Composition	Emission (nm)	Afterglow duration (min)	Characteristics
Sulfides	Red	CaS:Eu,Tm	650	45	Rich colors, but poor chemical stability, shorter afterglow time
	Yellow	CaSrS:Bi	450	90	
	Yellow-green	ZnS:Cu,Co	530	500	
Sulfur oxides	Red	Y_2O_2S:Eu, Ti,Mg	625	300	longer afterglow time, but poor chemical stability and single color
Alkaline earth aluminates	Yellow-green	$SrAl_2O_4$:Eu, Dy	520	2000	High luminous intensity, long afterglow time, good chemical stability, but poor water resistance, lack of red color
	Blue-green	$Sr_4Al_{14}O_{25}$: Eu,Dy	490	2000	
Alkaline earth silicates	Blue	$Sr_2MgSi_2O_7$: Eu,Dy	469	300	High luminous intensity, better chemical stability, water resistance, but shorter afterglow time and fewer emitting colors
	Blue-green	$Ca_2MgSi_2O_7$: Eu,Dy	535	200	
Titanates	Red	$CaTiO_3$:Pr	613	60	Purer color, good chemical stability, but single emitting colors, shorter afterglow time
Gallates	Blue-green	$ZnGa_2O_4$:Mn	503	60	
Nitrides	Red	$Ca_2Si_5N_8$:Eu, Tm	620	60	

luminescent materials; based on the different activating ions, persistent luminescent materials can be divided into rare-earth ions-activated persistent luminescent materials and non-rare-earth ions (transition metal ions and defects)-activated persistent luminescent materials. Besides, persistent luminescent materials can also be categorized according to their applications.

From the activating ions point of view, the most studied and applied activating ion so far is the Eu^{2+}, followed by other rare-earth ions and transition metal ions (such as Mn^{2+} and Cr^{3+}) and main group metal ions (such as Bi^{3+} and Pb^{2+}). From the matrix point of view, the aluminates and silicates matrixes are the most widely and thoroughly studied persistent luminescent materials systems. As for the colors, green persistent luminescence and blue persistent luminescence are the most abundant categories, some of which have reached the practical application level, such as $SrAl_2O_4$:Eu^{2+},Dy^{3+} (yellow-green), $CaAl_2O_4$:Eu^{2+},Nd^{3+} (blue), $Sr_2MgSi_2O_7$:Eu^{2+},Dy^{3+} (blue), and $Sr_4Al_{14}O_{25}$:Eu^{2+},Dy^{3+} (blue-green), while the red and near-infrared persistent luminescent materials are relatively less abundant,

with their luminescence intensity and persistent lifetime far from being practically applied.

Here, we introduce some categories according to the matrix, activating ions, and colors as follows.

6.3.1 Sulfide System

The sulfide system of transition metals is the earliest discovered and investigated persistent luminescent materials. The research, production, and application have been over a 100 years. This category of persistent luminescent materials usually uses sulfide MS (M as one or two elements of Zn, Cd, Mg, Ca, Sr, Ba) as matrix, with small amount of addition of variable valence elements (transition metal ions or rare-earth ions), and then firing to a series of persistent luminescent materials under certain conditions, such as $ZnS:Cu^+$, $CaS:Bi^{3+}$, $CaSrS:Bi^{3+}$, $CaS:Eu^{2+},Tm^{3+}$ [27–29].

As the first generation of persistent luminescent materials, since the first preparation of ZnS:Cu [30] fluorescent powder by a French Sidot in 1866, the sphalerite ZnS in the sulfide system has been an important material to be investigated. Along with the more investigation into the luminescence mechanism, matrix structure, the activating agent function, and synthesis procedure, a series of practical persistent luminescent materials of ZnS, ZnS–CdS, ZnS–ZnSe, and alkaline earth sulfides were further developed. $ZnS:Cu,Co$ and $CaS:Eu^{2+}$ are the representatives of the sulfide persistent phosphorescent materials. This category of materials has the characteristics of simple preparation, broad excitation band, fast light absorption, variety of luminescent colors, and other advantages. The luminescent color covers the entire visible light range, from blue to red, which the aluminates system persistent luminescent materials cannot compare. This category is the major products of persistent phosphorescence materials from 1960s to 1990s.

However, due to the poor chemical stability, tendency of aging and deliquescence, low persistent luminescence intensity, short persistent lifetime, and other apparent disadvantages of the sulfide system persistent luminescent materials, further coating process is needed to make them practically used [31], and even radioactive materials are doped to meet the needs for practical application, such as tritium H-3 and Pm-147, to improve the luminescence and persistent properties. In the meanwhile, it brings the problem of radioactive pollution and causes damage for both human health and the environment. These disadvantages largely limit the application range of the sulfide system persistent luminescent materials.

6.3.2 The Aluminates System

Besides the sulfide system, aluminates are the mostly studied and applied persistent luminescent materials matrix in recent years. The aluminates persistent luminescent materials usually use the rare-earth ions to excite, and the matrix material is usually alkaline earth aluminates MAl_2O_4 (M = Ca, Sr, Ba). The research of the aluminates phosphorescent material doped with rare-earth and alkaline earth elements can be dated back as early as 1960s. In the year 1968, Palilla el al. [32] for the first time discovered its persistent luminescence decay characteristic when studying the persistent luminescence of $SrAl_2O_4:Eu^{2+}$. After being illuminated, this material will undertake a rapid decay process (lifetime is 10 μs) and a slow decay process (lifetime is several minutes). But at that time people were mainly using the high quantum efficiency of $SrAl_2O_4:Eu^{2+}$ to make the fluorescent lamps, low-pressure mercury lamp as well as the fluorescent powder for the copier and display screens. In the year of 1996, Matsuzawa et al. [22] from Japan Osaka University, by doping co-activating ion Dy^{3+} in the $SrAl_2O_4:Eu^{2+}$, successfully developed a new generations of high-efficiency photo-energy storage persistent luminescent materials. With the excitation of ultraviolet or sunlight, $SrAl_2O_4:Eu^{2+},Dy^{3+}$ phosphorescent material can illuminate bright and long-lasting green persistent luminescence, with the emission peak at 520 nm, and the intensity, persistent lifetime, and chemical stability are far better than the sulfide persistent luminescent materials, opening a new chapter for the rare-earth persistent luminescent materials.

Besides the $SrAl_2O_4:Eu^{2+},Dy^{3+}$, researchers further developed a series of aluminates persistent phosphorescence systems activated by rare-earth materials, such as $CaAl_2O_4:Eu^{2+},Nd^{3+}$ [33], $BaAl_2O_4:Eu^{2+},Dy^{3+}$ [34], $Sr_4Al_{14}O_{25}:Eu^{2+},Dy^{3+}$ [35], $Ca_{12}Al_{14}O_{33}:Eu^{2+},Nd^{3+}$ [36], and $CaYAl_3O_7:Ce^{3+}$ [37]. Besides, researchers also observed the persistent luminescence of these rare-earth ions in the aluminates system doped with Ce^{3+} [38], Tb^{3+} [39] and further developed this system.

The aluminates system as the second generation of persistent luminescent materials, their luminescence efficiency, luminescence intensity, persistent lifetime, and material stability all exceed the sulfide system persistent luminescent materials to a large extent and have become a new category of energy-saving, high-efficiency, chemically stable luminescent materials. The study on aluminate materials have also been developed from the powder toward glass, single crystal, thin film, and microcrystal glass ceramics, and other directions and has shown promising prospectus in the photo-electro-conversion and two-dimensional image storage and other high technology fields, causing interests and attentions from researchers and industry from various countries. The excitation spectrum of aluminates phosphorescent materials is very broad. Lamp light, sunlight, ultraviolet, and natural room light can all excite them, but the emission lights are mostly green or blue-green, with a lack of yellow, orange, red, and other long-wavelength colors. In the meantime, the alkaline earth aluminates have poor water resistance and are prone to form hard knots when confronted with water and cause the luminescence efficiency to decrease, making its application very limited.

6.3.3 The Silicates System

The silicates system is another category of important persistent luminescent materials, mainly divided into binary silicates system and ternary silicates system. The binary system mainly includes the orthosilicates and metasilicates. The research about the ternary silicates system mainly focuses on the disilicates and metasilicates containing Mg. As early as 1949, Smith [40] reported the luminescent properties of $CaMgSi_2O_6:Eu^{2+}$, but after which the persistent luminescent properties of the silicates system were not reported. Until 1975, Chiba Institute of Technology and Dental University in Japan discovered that the persistent luminescence time of $Zn_2SiO_4:Mn^{2+},As^{3+}$ could reach 30 min, which was the first discovery of the persistent luminescence of the orthosilicates system [30].

In recent years, the silicates system persistent luminescent materials research has progressed a lot. In 2001, Lin et al. [25] used the high-temperature solid-state method prepared a series of $Sr_2MgSi_2O_7:Eu^{2+},Dy^{3+}$, by firing for 3 h at 1300 °C, in 5 % H_2–95 % N_2 atmosphere. When Eu^{2+}/Dy^{3+} is 1/3, the persistent luminescence lifetime exceeds 10 h. In 2004, Lei et al. [41] realized pink color persistent luminescence by doping Sm^{3+} into $CdSiO_3$, with the persistent luminescence lifetime reaching 5 h. At the same time, $Cd_{1-x}Dy_xSiO_3$ was synthesized using the high-temperature solid-state method [42]. The spectrum analysis showed that there was a characteristic peak of Dy^{3+} in the $Cd_{1-x}Dy_xSiO_3$ system. After removing the 254-nm excitation source, it can continuously produce a 5 h of white persistent luminescence in the dark. In 2007, Ji et al. [43] used sol–gel method prepared flower-shaped $Sr_2MgSi_2O_7:Eu^{2+},Dy^{3+}$ at 1250 °C for the first time, whose initial luminescent intensity reached as high as 7230 mcd/m^2 and persistent lifetime reached 690 min when compared with the powder product. Because the silicates and aluminates systems are the same, that no matter their persistent luminescence properties or the chemical stability are both better than that of the traditional sulfides. Therefore, the silicates system and the aluminates system persistent luminescent materials are together called the second generation of persistent luminescent materials.

The silicates system persistent luminescent materials have excellent optical properties and special grid structures, and the raw materials are cheap and easy to obtain, non-toxic, and easy to be synthesized. The doping ions can be present with different valences in the grid and matrix holes and occupy different lattice positions. Their chemical stability is excellent, and water resistance is strong. Soaked in 5 % NaOH solution, the aluminates persistent luminescent materials stop the luminescence after 2–3 h at room temperature, while the silicates can maintain their luminescent properties even after 20 days. At the same time, the silicates are resistant to ultraviolet radiation, have various colors, and can complement with aluminates system persistent luminescent materials with each other. The silicates

have a wide application range and are superior to the aluminates system persistent luminescent materials especially in the glass and ceramics. Right because of these advantages, the silicates system persistent luminescent materials are now a hot spot for the current research.

6.3.4 The Red Color Persistent Luminescence System

From the trichromatic theory point of view, mixing the red, green, and blue persistent luminescent materials at a certain ratio can generate output with any colors. The alkaline earth aluminates (silicates) green color persistent luminescent materials doped with rare-earth ions have entered the application stage, while the red materials are still at the research and development stage, for its luminescence lifetime and intensity and other properties are still far below the blue and yellow-green color materials and thus cannot fulfill the practical application needs. Therefore, we specifically categorized the red color persistent luminescent materials. Besides the previously introduced metal sulfide series, the red persistent luminescent materials also include the alkaline earth titanates, oxides, sulfur oxides, and nitrides series.

6.3.4.1 The Alkaline Metal Titanates System

At the end of 1990s, Yamamoto et al. [44] reported the red persistent luminescence with stable properties in $CaTiO_3:Pr^{3+}$, after which the research about this system gradually increased. The alkaline earth metal titanates $MTiO_3$ (M = Ca, Sr, Ba) activated by Pr^{3+} as a red persistent luminescent material, for its chemical properties are stable and persistent luminescence decays slowly, caused a broad attention, and have become the hot spot for the research of red persistent luminescent materials in recent years.

The alkaline earth metal titanates system persistent luminescent materials are a new category of red persistent luminescent materials. So far, the matrix is mainly $MTiO_3$ (M = Mg, Ca, Sr, Ba), and the activating agent is mainly Pr^{3+} ion. $MTiO_3$: Pr^{3+} all emit red light (615 nm) with the ultraviolet light excitation, corresponding to the characteristic emission of $^1D_2$–$^3H_4$ in Pr^{3+}. To increase the luminescence intensity of alkaline earth metal titanates red persistent luminescent materials and further improve the luminescent properties, substantial research focuses on changing titanates matrix, doping and improvement of the synthesis method, etc. Royce et al. [45] discovered that doping a certain amount of Zn or Mg ions into $CaTiO_3:Pr^{3+}$ can effectively increase the luminescent intensity and elongate its persistent time. Besides, Liang et al. [46] also thoroughly studied the effects of

doping with alkaline metal ions Li^+, Na^+, K^+, Rb^+, Cs^+, and Ag^+ into $Ca_{1-x}Zn_xTiO_3:Pr^{3+}$, on the luminescent properties.

Currently, the alkaline earth titanates red persistent luminescent materials with the $CaTiO_3:Pr^{3+}$ as the representative have not only stable chemical properties, but also pure emission colors. The biggest disadvantage in the alkaline earth titanates system is the low luminescence intensity and that the luminescence decay time cannot reach the requirement for practical application. The excitation intensity in the visible range is also to be further improved.

6.3.4.2 The Alkaline Earth Oxides System

The rare-earth ions-activated alkaline earth oxides $MO:Eu^{3+}$ (M = Ca, Sr, Ba, etc.) are a novel category of persistent luminescent materials developed in recent years [47]. This series of materials uses Eu^{3+}, Sm^{3+}, and Tm^{3+} as activating agents and H_3BO_3 as a fusion agent and is synthesized with traditional high-temperature solid-state reaction. The research shows the H_3BO_3 has positive effects on the luminescence intensity and persistent time for the luminescent materials. Entering the twenty-first century, Lin et al. [48] and Xie et al. [49] obtained red persistent luminescence by doping with red fluorescent powder $Y_2O_3:Eu^{3+}$ to the traditional tricolor light, and the persistent luminescence time reached 1 h and more.

6.3.4.3 The Rare-Earth Sulfur Oxides System

$Y_2O_2S:Eu^{3+}$ was initially a red cathode ray fluorescent material with very high luminescence efficiency and currently widely used in television, computer monitor, and other CRT display units. In 1999, Murazaki et al. [50] in Nichia Chemical Industries, Ltd, Japan, doped Mg^{2+} and Ti^{4+} when preparing $Y_2O_2S:Eu^{3+}$ and $Gd_2O_2S:Eu^{3+}$, observed the super persistent luminescence phenomenon of Eu^{3+} for the first time, and systematically studied their physical and chemical properties. After that, the research reports about the sulfur oxides system persistent luminescent materials gradually increased. The matrix materials exploited from the traditional Y_2O_2S to $(Y, Gd)_2O_2S$, Gd_2O_2S, and La_2O_2S [51–54]. The activating ions exploited from the initial single Eu^{3+} to Sm^{3+}, Tm^{3+} and doping with Mg^{2+}, Ti^{4+}, Sr^{2+}, Ca^{2+}, Ba^{2+}, and other ions.

The rare-earth sulfur oxides system persistent luminescent materials have excellent chemical stability, heat resistance, acid/base resistance, and optical stability and are an ideal type of luminescent matrix material. Although the rare-earth sulfur oxides system persistent luminescent materials have progressed a lot in their research and development, however, as for the aspect of the selection of the matrix

materials, the novel red persistent luminescent materials with stable chemical properties, strong luminescence intensity, and long persistent lifetime should be selected.

6.3.4.4 The Nitrides (Oxides) System

Regarding the persistent luminescence in the nitrides and the nitrogen oxides systems, Smet et al. [7] published a very good review. In these systems, the compounds that have red persistent luminescence are mainly $Ca_2Si_5N_8$:Eu,Tm, $Sr_2Si_5N_8$:Eu,Tm, and $SrCaSi_5N_8$:Eu,Tm, while the $Ca_2Si_5N_8$:Eu,Tm has reached the practical application level.

The biggest characteristic of the nitrides is the good stability of the luminescent properties. As shown in Fig. 6.1, compared with the commercially used green, blue, and red color persistent luminescent materials, $Ca_2Si_5N_8$:Eu,Tm has a persistent luminescence intensity only 2 % less after 2-year soaking in the water than in the sealed conditions, while for the other species the decrease can be more than 25 %.

Our team carried out a systematic research of the alkaline earth metal nitrides persistent luminescent materials and found that by doping Dy^{3+} into $Ca_2Si_5N_8$:Eu^{2+}, Tm^{3+}, the luminescence intensity and lifetime can dramatically increase. A solid solution is formed by the continuous substitution of Ca with Sr, and the emission wavelength shifts to the long-wave direction [55, 56].

6.3.5 The Near-Infrared Persistent Luminescent System

In recent years, the utilization of near-infrared radiation for biological tissue imaging, diagnostics, and detection has become a research hot spot. The major reason is that the living organisms and tissues have very little absorption in the near-infrared range, the penetration depth is large, and the radiation has barely any effect on the tissues and organisms. For example, there is a novel approach to studying the brain functions—functional near-infrared spectroscopy imaging technology (FNIRS), which can achieve non-invading measurements of the brain
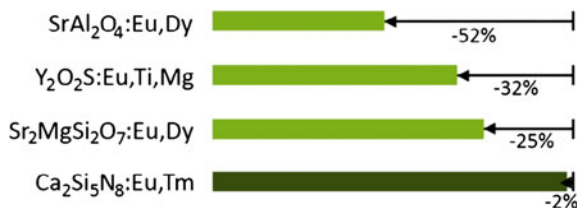
Fig. 6.1 Decrease in the persistent luminescence intensity after 2-year storage in (distilled) water for $Ca_2Si_5N_8$:Eu, Tm and selected common persistent phosphors, compared with samples stored in a sealed container. Reprinted from Ref. [7], copyright 2014, with permission from Elsevier

functions through the near-infrared spectrum. Because this technology has low costs and the device is portable, it is widely used in neuroscience, psychology, and other cutting-edge fields [57]. Using the near-infrared persistent luminescent materials to prepare biomarkers can help to realize external excitation and effectively avoid the difficulty of excitation for regular fluorescent materials, and therefore contributes to optical imaging of biological tissues and promotes the organism pathology research [58].

The transition metal ions and the rare-earth ions with persistent luminescence and emission in near-infrared range are mainly Cr^{3+}, Mn^{2+}, Yb^{3+}, Er^{3+}, Ni^{2+}, etc. [59–63]. Currently, the research about the near-infrared persistent luminescent materials focuses on the Cr^{3+} ion-doped gallogermanates. On the one hand, the transition metal ion Cr^{3+} has the $3d^3$ electron configuration, whose electron transition is largely affected by the matrix lattice crystal field environment. But the gallogermanates matrix material has the crystal field intensity that usually the Cr^{3+} ion can undergo the transition of $^2E(t^3) \rightarrow {}^4A_2(t^3)$, with the corresponding emission wavelength at around 700 nm in the near-infrared range [64]. On the other hand, the Cr^{3+} ion radius (0.0615 nm) is close to the Ga^{3+} ion radius (0.062 nm), making it easy to substitute the latter one with the former one as the doping ion. Bessiere et al. [65] found that the vacancy of Zn played a key role in the luminescent properties of the spinal-type material $ZnGa_2O_4:Cr^{3+}$. The gallogermanates material $Zn_3Ga_2Ge_2O_{10}:Cr^{3+}$ reported by Pan et al. [66] has high-intensity and long-lasting persistent luminescence, whose excellent luminescence properties have much to do with the Ge^{4+} ion. Pan et al. also reported the Cr^{3+}-doped $LiGa_5O_8$ whose super long-lasting near-infrared luminescence could last for more than 1000 h [67]. Abdukerim et al. used the sol–gel method and prepared the gallium zinc germanates material $Zn_{2.94}Ga_{1.96}Ge_2O_{10}:Cr^{3+}$. The persistent luminescent properties are significantly improved by co-doping with Pr^{3+}, making it produce super long-lasting near-infrared luminescence with high intensity in the biologically transparent window [68].

When Cr^{3+} is in a relatively strong crystal field, $^4T_2$ energy level is above the ^2E level, and the luminescence is mainly generated from the transition from ^2E to $^4A_2$ and is linear emission. Due to the crystal field and the self-spinning orbit coupling, ^2E energy level splits into a double energy level with narrow gaps, and thus, there are two sharp spectrum peaks produced with their wavelengths close to each other. But not in all the cases ^2E is the lowest excitation state. When the crystal field has relatively low intensity, the $^4T_2$ energy level is even lower, below the ^2E level, and results mainly the broadband emission from $^4T_2$ to $^4A_2$. Therefore, when doping the Cr^{3+} into different matrix materials, adjusting the crystal environment can generate light emissions with different wavelengths, i.e., can produce emissions from red to near-infrared [69]. Generally, the transition metal ions locating at the tetrahedral positions can generate near-infrared luminescence. Compounds that have this structure include $Y_3Ga_5O_{12}$, $La_3Ga_5GeO_{14}$, $ZnGa_2O_4$, $LiGa_5O_8$, and $LiGaO_2$, which when doped with transition metal ions could generate promising near-infrared persistent luminescence.

Another approach to obtaining the near-infrared persistent luminescent materials is to take advantage of the energy transfer of the green persistent luminescent materials. For example, in $SrAl_2O_4:Eu^{2+},Dy^{3+},Er^{3+}$ [70], the green color persistent luminescence of Eu^{2+} can be transferred to Er^{3+} through the energy transfer, so that the Er^{3+} ion can be excited and generate persistent luminescence at around 1530 nm in the near-infrared range.

6.4   The Mechanism and Models of Persistent Luminescence

The mechanism research of persistent luminescence has always been a hot spot and complex problems. At present, there is no consistent and convincing explanation regarding the persistent luminescence mechanism. After investigation and experiments of many researchers, there are now a recombination luminescence band model, the hole-transferring luminous model, and oxygen vacancies model. Different persistent luminescence systems have different mechanisms and models, among which the recombination luminescence band model is the most well-recognized one.

6.4.1   The Recombination Luminescence Band Model

The recombination luminescence band model theory indicates that [71] after the rare-earth ions are doped into the matrix materials, impurity levels form in the band gaps of the materials. One of the levels is the acceptor level, or electron traps (E-trap), and the other is the donor level, also known as hole traps (H-trap). The luminescence process is shown in Fig. 6.2. When the material is excited by light, the electrons jump from the valence bands to the conduction bands (process 1), and the electrons enter the conduction bands, leaving the holes in the valence bands. The electrons in the conduction bands directly return to the luminescent center excited state (E2) and recombine with the holes that return to the luminescent center ground state (G), and result in the transient luminescent phenomenon (processes 2 and 3), which is the fluorescence emission. Some electrons in the conduction bands and some holes in the valence bands can possibly be captured electron traps and hole traps (processes 4 and 5). After the termination of the excitation, with the thermal perturbation, the electrons and holes in the traps will reenter the conduction and valence bands (processes 6 and 7). The electrons entering the conduction bands and the holes entering the valence bands could be recaptured by the traps (processes 4 and 5). This is called the electron recapture effects. It is a very common phenomenon in the persistent luminescent materials. Alternatively, electrons jump to luminescent center excited state through the conduction band, and the holes return

Fig. 6.2 Composite persistent luminescence model
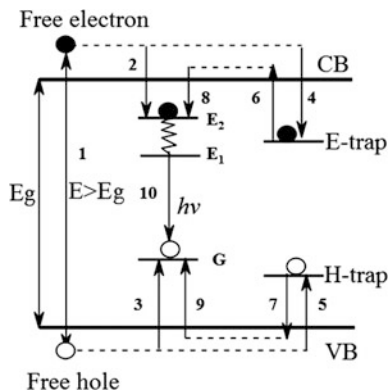
to the ground state of the luminescent center via the valence bands (processes 8 and 9) and recombine with the luminescent center to emit photons. This emission process is the persistent luminescence.

It is easy to see that, after the sample gets excited, the electrons being captured by the traps are very limited and decrease along with the increase in luminescence time length. Therefore, the persistent luminescence process is not sustained, but decays along with the time increase. The decay process usually has two modes, the exponential decay model and hyperbolic decay mode.

6.4.2 The Hole-Transferring Model (I)

The hole-transferring model is a luminescence mechanism model proposed by Matsuzawa et al. [22] based on the photoconductive experiments of persistent luminescent materials $MAl_2O_4:Eu^{2+},Re^{3+}$. The experiment results showed that the charge carriers generating the conductivity were the holes, and Eu^{2+} and Re^{3+} were the electrons trapping center and holes trapping center in $MAl_2O_4:Eu^{2+},Re^{3+}$. Subsequently, Jia et al. [72] also believed the Re^{3+} acted as the trapping center in the persistent luminescent materials $MAl_2O_4:Eu^{2+},Re^{3+}$. With the introduction of Re^{3+}, a new energy level can be generated in the original system. For the persistent luminescent materials $MAl_2O_4:Eu^{2+},Re^{3+}$, to give it persistent luminescent properties at room temperature, the key is that its trapping energy level exists at a depth with considerable thermal excitation rates. If the trapping energy level is too shallow, the persistent luminescence will not last long, and decay over rapidly; if the trapping energy level is too deep, the persistent luminescence cannot be generated at room temperature.

Figure 6.3 shows the illustration of the hole-transferring model of $MAl_2O_4:Eu^{2+}$, Re^{3+}. With the external light source excitation, the luminescence center of the matrix lattice absorbs light energy, and electrons can be excited from the ground state to excited state to produce holes in the ground energy level, which is further
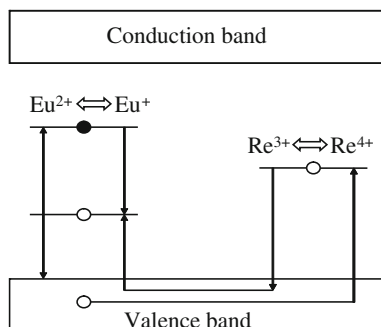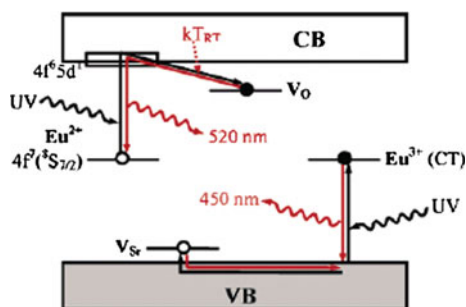
released to the valence band. In this process, the luminescent center ion Eu^{2+} becomes Eu^+, and the released holes are captured by Re^{3+} and become Re^{4+} during the transition process via the valence band. After the termination of the excitation, holes formed at the Re^{3+} location with certain trapping energy levels can return to the valence band due to the thermal perturbation. The holes, when captured when migrating to excited Eu^+ locations in the valence band and then migrating to Eu^{2+} ground state, will recombine with the Eu^{2+} luminescent center and produce the persistent luminescence.

Clabau et al. [73] proposed the new hole-transferring model in 2005, specifically for $SrAl_2O_4$:Eu^{2+},Dy^{3+},B^{3+} material, as shown in Fig. 6.4. They believed that, in the material synthesis process, Eu^{3+} was only partially reduced to Eu^{2+}, there remained a small amount of Eu^{3+}, and they also believed that the Eu^{2+} continuously converted to Eu^{3+} under the irradiation of ultraviolet light. With the ultraviolet light excitation, the electrons went through 4f–5d transition and were captured by trapping energy level V_o excited from valence band to the empty 4f level of Eu^{3+}, and followed by being captured by V_{Sr} or V_{Al} holes. After the excitation stops, the electrons can escape to 5d level at room temperature and can produce the 520-nm green color persistent luminescence. They also used this model to explain that the emission light at 450 nm at low temperatures was due to the combination of

electrons with Eu^{3+}. As for the secondary ions Dy^{3+} and B^{3+}, they are considered to play a role to increase the trapping energy level and electron density.

6.4.3 The Oxygen Vacancy Model

The oxygen vacancy model [74, 75] asserts that the persistent luminescence of $MAl_2O_4{:}Eu^{2+},Re^{3+}$ relates to the crystal lattice defects. Because the reduction atmosphere is used for the synthesis, there are O^{2-} vacancies V_o formed in the lattice. The V_o carrying two positively charged units has Coulomb attraction with the electrons in the crystal field and can capture electrons. When persistent luminescent materials are illuminated by ultraviolet or sun lights, the $4f^7$ electrons in the ground state of Eu^{2+} transit to excited-state $4f^6 5d^1$. The excited-state energy level has a certain width, and when the electrons enter the excited state, part of them will relax to the bottom of the energy level and transit back to ground state to form fluorescence, while another part will relax to the adjacent defect level V_o. When the electrons relax to the traps, they will be captured. After absorbing some energy from the environment, the captured electrons will escape from the traps and return to the excited state in the luminescent center, followed by transition back to the ground state and photon emission, which is called the persistent emission. After the persistent emission stops, Eu^{2+} is recovered. Figure 6.5 shows the oxygen vacancy luminescence model.

6.4.4 The Coordination Model

For the luminescence mechanism of persistent luminescent materials $MAl_2O_4{:}Eu^{2+}$, Re^{3+}, Qiu et al. [76] and Zhang et al. [77] proposed different opinions. Figure 6.6 shows their proposed coordination models. A and B are the ground and excited states of Eu^{2+}, respectively, C is the defect level, and E is the energy difference between the defect level and the excited energy level. They believed that in the

Fig. 6.5 Oxygen vacancies phosphorescent model [74]
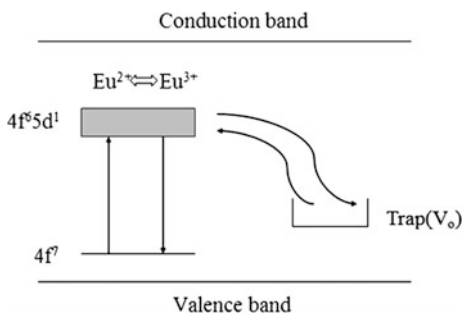
Fig. 6.6 Coordinates
phosphorescent model.
Reprinted from Ref. [76],
Copyright 1998, with
permission from Elsevier
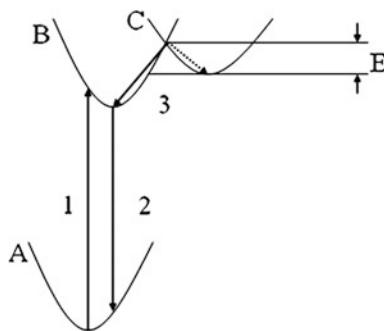
oxygen vacancy model the prepared $MAl_2O_4:Eu^{2+},Re^{3+}$ in the reduction atmosphere could generate certain oxygen vacancies, because they believed the defect level C is usually hole or oxygen vacancy, and the holes were resulted from the substitution of Eu^{2+} with Re^{3+}.

The coordination model believes that the whole luminescence and persistent emission process can be divided into three steps: (1) the external light excites the persistent luminescent materials, making the electrons transit from the ground state to the excited state; (2) part of the electrons transit back to the ground state and emit light; (3) another part of the electrons relax to the defect level C, in which the electrons absorb energy and return to the excited state, and then transit back to the ground state to realize the persistent luminescence.

This mechanism model believes the persistent luminescence lifetime length relates with the number and energy absorbed by the electrons that are stored in the defect level. The more the electrons exist in the defect level, the more the energy can be absorbed, and the longer the persistent luminescence time will be.

6.4.5   The Two-Photon Absorption Model

The excitation light wavelength of $CaAl_2O_4$ doped with Eu^{2+} and Dy^{3+} has an upper limit around 530 nm, which cannot generate Eu^+. Aitasalo et al. [78] proposed a energy transfer model which includes an absorption of two 530-nm photons through deep energy level excited state, together with the capture of two electrons by the shallow energy level. It is named as 'two-photon absorption model.' As shown in Fig. 6.7, Aitasalo et al. believed that, in $CaAl_2O_4:Eu^{2+}$, the defect formed a electron–hole recombination process in the band gap after two steps of excitation. Through the recombination process, the energy was finally transferred to Eu^{2+} to generate persistent luminescence.

The above model mainly focuses on the aluminates system. For the substantially studied silicates system, different mechanisms and models have also been proposed.

The 'hole-transferring model,' 'Dorenbos model,' 'composite luminescent model,' and other models have been proposed to explain the silicates persistent
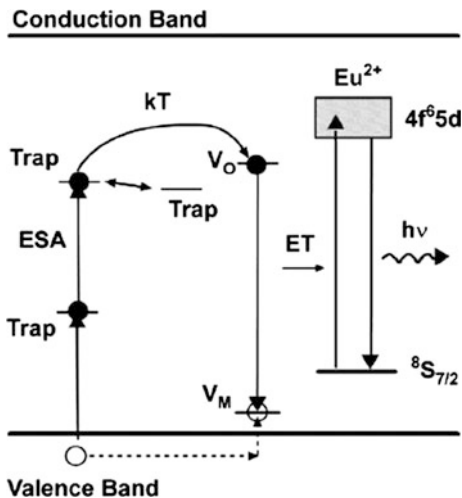
luminescent materials mechanisms. Due to the complexity of the mechanisms, different models can only partially explain one aspect of the persistent luminescence phenomenon and have certain limitations. And many theories hold only as assumptions and require further evidence of experiments to validate. However, for silicate persistent luminescent materials doped with rare-earth ions, one consistent opinion is that, due to the introduction of Dy^{3+} (or other assistant rare-earth ions), a new energy level—trapping level—is generated in the matrix, and after the termination of the excitation, the energy that is stored in the trapping level is transferred to the light-emitting ions, which eventually produces the luminescence characteristic emission.

6.4.6 The Hole-Transferring Model (II)

Pan, Lin, Wang, and Alvan et al. [79–83] believed Dy^{3+} was a hole trap when explaining the silicates persistent luminescent materials mechanism. The luminescence process mainly includes: (1) the excitation of luminescent center and the formation of electron–hole pair; (2) the recombination of part of the electrons and holes and the generation of fluorescence; (3) part of the holes entering the valence band; (4) the transportation of holes in the valence band and their capture by the trapping energy level; (5) with the thermal perturbation, the re-release of the holes captured by trapping energy level; (6) the transportation of released holes via the valence band, their recombination with free electrons, and the generation of the persistent luminescence; as shown in Fig. 6.8.

This is similar to the hole-transferring model proposed by Matsuzawa et al. [22] and thus can be called 'hole-transferring model' as well.
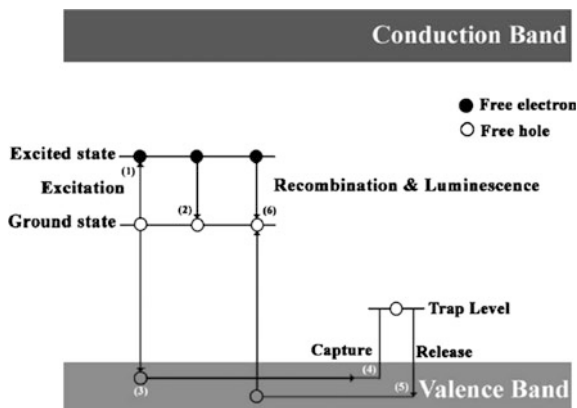
6.4.7 Dorenbos Model

As Fig. 6.9 shows, Dorenbos [84] based on Qi et al.'s [85, 86] research results and his own theoretical study of the relative energy level positions of divalent lanthanide ions in the matrix explained the luminescence mechanism of $Sr_2MgSi_2O_7$: Eu^{2+},Dy^{3+}. Dorenbos assumed that the persistent luminescence was generated as follows: First of all, Eu^{2+} absorbed a ultraviolet photon and transited to $4f^65d$ level in the conduction band, undertook photoionization, and generated one Eu^{3+} and an electron. The electron was captured by Dy^{3+} and became Dy^{2+}, which located at
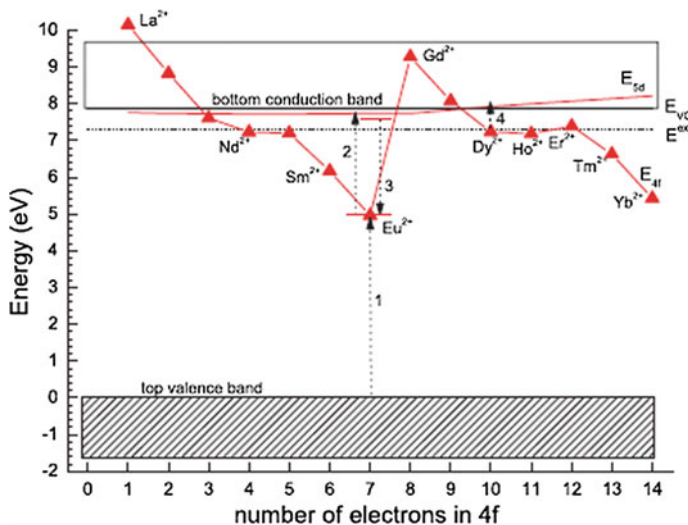
Fig. 6.9 Relative energy level of divalent lanthanide ions in $Sr_2MgSi_2O_7$ matrix. Reproduced from Ref. [84] with permission of John Wiley & Sons Ltd

0.66 eV position below the conduction band, playing a determining role in the persistent luminescence of the material.

Dorenbos made a prediction according to the relative energy level positions of divalent lanthanide ions in the matrix: Nd^{2+}, Ho^{2+}, and Er^{2+} which differed with Dy^{2+} trapping depth by 0.1 eV, when acted as co-activators, could generate good persistent luminescence, while Sm^{2+}, Tm^{2+}, and Yb^{2+} which differed with Dy^{2+} trapping depth by more than 0.3 eV could not. Seltur et al. [87] also showed experiments to support this model. Although Dorenbos's prediction is more or less consistent with the experimental evidences, it needs further experimental proof to conclude if Dy^{2+} actually exists or not.

6.4.8 The Recombination Luminescence Model

Our team [41] proposed the recombination luminescence model when explaining the pink persistent luminescence mechanism of $CdSiO_3:Sm^{3+}$. Because the $CdSiO_3$ matrix band gap is approximately 5.1 eV (41,000 cm^{-1}, 243 nm), we only need to consider the excitation, emission, and energy transfer process of Sm^{3+} in $CdSiO_3$. So we put the ground state of Sm^{3+} ion to a position slightly higher than the valence band and parallel with the self-captured exciton STE (i.e., localized electron–hole pair), as illustrated in Fig. 6.10.

With the irradiation of 243-nm ultraviolet light, electrons are excited from the valence band to the conduction band (process 1) and leave holes in the valence band at the same time. The processes 2a and 2b generate STE. STE is an energy state of the excited electron and can release some energy in the form of self-radiation
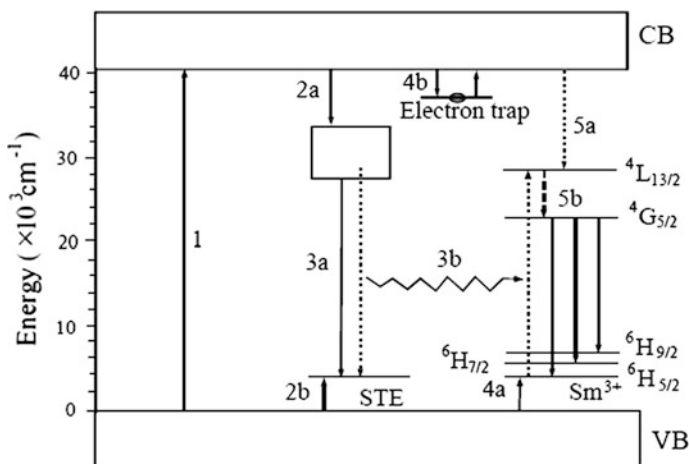
Fig. 6.10 Mechanism of $CdSiO_3$: Sm^{3+}. Reprinted from Ref. [41], Copyright 2004, with permission from Elsevier

(process 3a), as an energy storage system. Another part of the energy is transferred to Sm^{3+} ions for luminescence in the form of resonance energy transfer (process 3b). Since the maximum emission wavelength (~ 420 nm) of the STE self-radiation process matches well with the transition of Sm^{3+} ions $^4L_{13/2} \rightarrow {}^6H_{5/2}$(413 nm), it is considered to have a large ratio for this resonance transfer mode to happen. The emission of Sm^{3+} ion $^4G_{5/2} \rightarrow {}^6H_J$(J = 5/2, 7/2, 9/2) has a stronger emission when compared with the STE generated ~ 420-nm bandwidth emission, which further proved the existence of process 3b. The high energy state electrons located at $^4L_{13/2}$ in the Sm^{3+} ions transit to $^4G_{5/2}$ in a non-radiation manner and transit further below to produce luminescence.

In addition, in the year of 2005, Liu et al. [88] used the photo-stimulated luminescence (PSL) and thermoluminescence (TL) coordination models to confirm the relationship between PSL with TL and explained the higher energy required for photoexcitation than the thermal excitation for Eu^{2+}, Dy^{3+}-co-doped silicates persistent luminescent materials. Others [89–94] searched for white, green, red light silicates persistent luminescent materials according to the energy transfer model; especially Wang et al. [89] prepared red light $MgSiO_3$:Eu^{2+},Dy^{3+}, Mn^{2+} with the persistent luminescence lifetime exceeding 4 h. It is worth to note that it remains to be investigated whether the energy transfer modes are the same in persistent luminescent materials and regular fluorescent materials, since in persistent luminescent materials the defects play an important role in persistent luminescence, and the effects on energy transfer are not reported so far.

The above mechanisms and models are mainly for the inorganic systems. As we all know, there are always defects in the inorganic systems, and the persistent luminescence is dependent on the generation and transfer of the defects, or it can be said that the mechanism of the inorganic persistent luminescence mechanism is actually the defects mechanism. Right because the formation of the defects, the traps exist, which can capture electrons or holes, and generate the trapping energy level. The trapped electron and holes are further released upon the external perturbation, recombine, and generate the persistent luminescence. Therefore, the mechanism of the inorganic system can be also called trapping mechanism. The depth of the traps determines whether or not the persistent luminescence is visible or not at room temperature. Only the trapping system with the suitable depth could enable the visibility of the luminescence at room temperature. The number or density of the traps determines the lifetime of the persistent luminescence of the material.

Besides the inorganic system, we also observed the visible persistent luminescence in the organic coordinate compounds and in the composite system of the carbon quantum dots with polymers, with the persistent luminescence lifetime of the former to be 1 s [1] and 140 s for the latter [3]. This type of persistent luminescent system has newer and wider applications. Analysis showed that the persistent luminescence in the coordinate compounds and the carbon quantum dots composite system come from the excitation of the triplet energy level, and by controlling the structure and surface modification or hydrogen bonds protection, the fluorescence lifetime can be improved or elongated, so that the persistent

luminescence lifetime can be increased. Therefore, different from the inorganic system defects mechanism or trapping mechanism, the mechanism for the coordinate compounds and carbon quantum dots can be called triplet-state mechanism. Based on the current reports, the persistent luminescence lifetime of the trapping mechanism in the inorganic system is much longer than that of the triplet-state mechanism for the organic or carbon quantum dots system. We further combined the carbon quantum dots with amorphous SiO_2 and observed longer persistent luminescence lifetime. The thermoluminescent spectrum analysis showed there was trapping energy levels in the composite system, and the trapping energy levels could transfer the energy to the triplet-state energy level and thus generate the persistent luminescence, which eventually combined the trapping mechanism with the triplet-state mechanism. This is a new result and is finishing submission, waiting to be published.

6.5 The Conditions and Rules for Persistent Luminescence

In the practical applications of persistent luminescent materials, the lifetime of the persistent luminescence is always the first concern. More importantly, for the exploration of the persistent luminescence and its generation conditions, there is a lack of theoretical instruction currently, leaving the research direction vague. Here, by analyzing and summarizing the literature, as well as combining with our own work about how to elongate the persistent luminescence lifetime and the material luminescent property prediction, some instructive results and rules can be found.

6.5.1 Basic Methods to Realize the Persistent Luminescence

There are multiple approaches to elongating the persistent luminescence lifetime. It mainly includes the creation of more traps in the matrix, increasing trapping efficiency, and so on. Besides the persistent luminescent lifetime, the persistent luminescent materials light color is very important too. Because of the long emission time for persistent luminescent materials, the problem of the emission color is specially concerned. At least, the color needs to be stable during the decay process.

6.5.1.1 Co-doping

Co-doping is the most commonly used method to study the persistent luminescent materials. The co-doping ions act as trapping center or defects generating related trapping center in the matrix. Choosing the right doping ions can increase the persistent luminescence lifetime by an order. The principle of the doping lies in the

generation of defects-related trapping center by charge compensation. Generally speaking, doping of the ions that have charges different than that of the substrate cations or anions can substitute the cations or anions in the original lattices, and generating unbalanced changes. For example, the doping of Cl^- in CaS will replace S^{2-}, doping of Y^{3+} and Al^{3+} into CaS will replace Ca^{2+}, as well as the doping of Mg^{2+} and Ti^{4+} into $Y_2O_2S:Eu^{3+}$ [95]. In this way, a large amount of defects are generated in the matrix, and the traps relative to the defects will elongate the persistent luminescence lifetime of the material.

Some ions doped into the matrix can become trapping centers themselves. These ions can capture electrons or holes and may be reduced or oxidized to different ion metastable states, for example, the Nd^{3+} in $SrAl_2O_4:Eu^{2+},Nd^{3+}$ and the Dy^{3+} in $SrAl_2O_4:Eu^{2+},Dy^{3+}$ [96]. This type of co-doping will significantly generate a large amount of traps and increase the persistent luminescence lifetime. Most of the rare-earth ions have such applications.

The co-doping of ions in the matrix can not only increase the trapping centers, but also improve the capture efficiency. Some ions have larger transition probability; therefore, electrons can be pumped into the matrix conduction band through this ion pump, but not other ions. As a result, more electrons can be captured by the trap and generate the persistent luminescence. For example, by doping of Ce^{3+} in $SrAl_2O_4$, electrons that are pumped into the traps through the Ce^{3+} 4f–5d transition pump can be more than 30-fold abundant than the electrons absorbed into the substrate band gaps [97].

6.5.1.2   Energy Transfer

Not every ion can produce sustained persistent luminescence, so the persistent luminescence cannot include all the colors. The sustained energy transfer is one of the most novel approaches to studying persistent luminescent materials. It adopts the energy transfer mechanism, which is a process that using the known persistent luminescent materials to obtain some other persistent luminescent materials with different emission wavelengths. In the sustained energy transfer mechanism, the known persistent luminescent materials act as the donor, the selection of acceptor should base on whether the emission light color is the one needed and whether the transferred energy is large enough. In the sustained energy transfer process, the donor keeps using its persistent luminescence to support the acceptor's emission. Therefore, the donor's persistent luminescence converts to the acceptor's persistent luminescence. In this way, the new persistent luminescent materials acquire the color of the donor. This method easily relates to some persistent luminescent materials that need specific emission colors. There are examples of the sustained energy transfer, such as $CaAl_2O_4:Ce^{3+},Tb^{3+}$ and $CaAl_2O_4:Ce^{3+},Mn^{2+}$ that have successfully transferred their more than 10-h blue color persistent luminescence to Tb^{3+} and Mn^{2+} and generated 10-h Tb^{3+} green color persistent luminescence and Mn^{2+} yellow color luminescence [89, 98]. People have adopted this approach to obtaining near-infrared persistent luminescence in the nano-sized $SrAl_2O_4:Eu^{2+}$,

Dy^{3+}, Er^{3+}, whose decay time is very long and can be used for information storage and other daily applications. It could also generate near-infrared persistent luminescent material with the emission at 1200–1400 nm by transferring the energy from Cr^{3+} to Ni^{2+} in $LiGa_5O_8:Cr^{3+}$.

6.5.1.3 Multi-luminescence Center-Doped Material

Another approach to obtaining specific colored persistent luminescent materials is to mix two types of persistent luminescent materials at a certain ratio, which is quite similar to the trichromatic method. But there is a problem that each component has different persistent luminescence lifetimes, and the mixture's emission color will change along with time. To overcome this problem, according to the relationship between release mechanism and the substrates, various emission centers can be doped into the matrix.

For example, doping Eu^{2+} and Bi^{3+} in CaS will combine the Eu^{2+} red color and the Bi^{3+} blue color and generate a net purple emission. Because both have the same decay mechanism, the persistent luminescence is very stable. In the year 2007, Liu found that in the white persistent luminescent material $Sr_2MgSi_2O_7:Dy^{3+}$ doped solely with Dy^{3+}, Dy^{3+} played two roles: the trapping center and the luminescence center [70].

The interaction between electrons and the lattice in persistent luminescent materials is usually very strong and follows the electron capture and emission mechanism. Therefore, most of the emission of persistent luminescent materials is very sensitive to the environment. So the emission of each component changes a lot in multicenter materials.

6.5.1.4 Non-equivalent Substitution

We have pointed out previously that the defects and traps are the basic prerequisite and conditions for persistent luminescence. Then how are the defects generated? Su et al. [99] proposed that the non-equivalent substitution was the easiest and most important method to generate defects. With the non-equivalent ions substitution method, non-stoichiometry method, or high-energy radiation method, there can be generated defects, electrons, and holes inside of the luminescence matrix. The defects can form traps with different depths, and electrons or holes could be captured by these traps. When these electrons or holes are released from the traps with different depths and recombined, the emitted energy can be transferred to luminescence center to produce luminescence, such as rare-earth ions. Some luminescent materials doped with rare-earth ions, such as persistent luminescent materials, solid dosage units, and scintillators all belong to the electron capture materials.

Ever since 1990s the occurrence of alkaline earth aluminates $SrAl_2O_4:Eu^{2+},Dy^{3+}$ doped with rare-earth elements, due to their longer persistent luminescence time and intensity than ZnS:Cu, Co used in the past, they received lots of attention and

have been applied as low-light illumination indicators in the dark and information storage. The generation of persistent luminescence has a close relationship with the non-equivalent substitution of divalent alkaline earth ions (Sr^{2+}, Ca^{2+}, etc.) with trivalent rare-earth co-activator ions (Dy^{3+}, Nd^{3+}, Ho^{3+}, Er^{3+}, etc.). If the produced traps have suitable depth, the electrons and holes stored inside can be thermally excited and emitted at room temperature, transfer energy to Eu^{2+} and other variable valence activator ions, and produce persistent luminescence.

6.5.2 The Conditions and Basic Rules for the Generation of Persistent Luminescence

Till now, there have been hundreds of persistent luminescent materials discovered. The excitation ions include almost all the rare-earth ions and the common transition metal ions. It is worth to summarize and analyze what the rules of these persistent luminescent materials are and what the conditions of these persistent luminescent materials luminescence require to generate.

Qiang Su group, after many years of research, proposed some conditions to explore novel rare-earth persistent luminescent materials [13, 100]: (1) the variable valence rare-earth ions or d-transition ions are used as activators; (2) the non-equivalent ion substitution method or the non-stoichiometry synthesis to generate defects are used; (3) the defects generating traps with suitable depth, and the depth is the best to have the thermoluminescence spectrum peaks at 50–100 °C; (4) it might also be considered that the variable valence ions need to have suitable electro negativity so that the electrons (holes) in the traps can have suitable emission speeds. According to these conditions, aluminates, phosphates, silicates, borates, or glass were prepared with the non-equivalent ion substitution method or non-stoichiometry synthesis method, using Eu^{2+}, Tb^{3+}, Mn^{2+}, and other variable valence ions as activating agents, using Dy^{3+}, Nd^{3+}, Ho^{3+}, and other trivalent ions as co-activating agents, and non-equivalently substituted the divalent alkaline earth ions in the matrix. They measured and investigated the structures, excitation spectrum, fluorescent spectrum, thermoluminescence spectrum, persistent luminescence lifetime, intensity, color coordinates, and other properties, they developed some novel persistent luminescent materials that emit red, green, blue, and yellow lights (including powder, glass, ceramics, and enamel), they observed the phenomenon that the light-induced persistent luminescence, as well as the rare-earth persistent luminescent materials had the function to achieve information photo-storage.

Rare-earth persistent luminescent materials are the important aspect in the study of persistent luminescent materials, but the rare-earth ions mechanism in persistent luminescent materials remains unclear. Comparing its behavior with the rare-earth elements valence variability, some clues could be found. As we all know, Ce^{3+}, Pr^{3+}, Tb^{3+} are prone to be oxidized to tetravalent ions and Sm^{3+}, Eu^{3+}, Tm^{3+}, Yb^{3+} are prone to be reduced to divalent ions, while for Nd^{3+}, Dy^{3+}, the tendency to become tetravalent or divalent is the same and not strong; Ho^{3+} slightly inclines to be

divalent; Er^{3+} has very weak tendency to change the valence; La^{3+}, Gd^{3+}, Lu^{3+} barely have any valence change tendency. Among the rare-earth ions that are prone to change their valences, Ce^{3+}, Pr^{3+}, Tb^{3+}, Eu^{2+}, Eu^{3+}, Sm^{3+} all have shown persistent luminescence, as well as the materials doped with Tm^{3+}. The persistent luminescence of Yb^{3+} has not been reported yet, which is mainly due to the luminescence wavelength of Yb^{3+} locates at infrared range.

Using the rare-earth ions prone to change valences as activating ions and searching for co-activators from other rare-earth ions have instructive effect in the search for novel rare-earth persistent luminescent materials. Considered from the quantum efficiency of the rare-earth ions luminescence, Ce^{3+}, Eu^{2+}, Eu^{3+}, Pr^{3+}, Tb^{3+} are most suitable to be the activating ions.

In principle, when there are traps with suitable depth, and the traps can undertake effective energy transfer with the luminescent ions, any kind of the luminescent material could become persistent luminescent materials. Variable valence elements, especially the lanthanides, are more suitable to be the persistent luminescent ions. The key problems of the persistent luminescent materials are the defects chemistry and the energy transfer, and the variable valence chemistry (mainly the lanthanides) is the important aspect to investigate.

Our group summarized the basic rules and inner relationships [41, 42, 51, 90, 101–110] of the studied persistent luminescent materials through substantial work, which inspired a lot for the search of novel persistent luminescent materials.

We investigated systems mainly include, rare-earth sulfur oxides, $Cd_3Al_2Ge_3O_{12}$ with a garnet structure, $CdSiO_3$ with low-dimensional chain structure, and the series of $CaBO_3$ (B = Ti, Zr, Sn) with the perovskite structure.

With the rare-earth sulfur oxides Gd_2O_2S as a representative, the persistent luminescence excited by rare-earth ions has three cases as follows.

1. For Eu^{3+}, Sm^{3+}, Tm^{3+}, Er^{3+}, Ho^{3+}, Dy^{3+}, their persistent luminescence is composed by the broadband emission of the matrix with the characteristic linear emission of the activating ions;
2. For Yb^{3+}, Nd^{3+}, there is only Gd_2O_2S's own broadband emission in the persistent luminescent spectrum, but no characteristic emission of the activating ions;
3. For Ce^{3+}, Pr^{3+}, Tb^{3+}, no persistent luminescence can be detected, nor does the thermo-luminescent spectrum show up.

Due to the difference of the activating ions persistent luminescence intensity and effects on the matrix, Dy^{3+}, Er^{3+}, Ho^{3+}, Tm^{3+} and Nd^{3+}, Yb^{3+} recombine with the matrix Gd_2O_2S and generate orange persistent luminescence, similar with that of the matrix Gd_2O_2S. But Eu^{3+} and Sm^{3+} recombine with Gd_2O_2S and produce orange-red persistent luminescence.

The persistent luminescence of $Cd_3Al_2Ge_3O_{12}$ with the garnet structure that is activated by rare-earth ions is nearly opposite to that of the sulfur oxides.

1. Pr^{3+}, Tb^{3+} have very strong persistent luminescence, with the Dy^{3+} slightly weaker;
2. Eu^{3+}, Sm^{3+} have the characteristic emission, but there is no persistent luminescence;
3. Ce^{3+}, Nd^{3+}, La^{3+}, and other lanthanides themselves do not have luminescence, but have certain influence on the luminescent properties of the matrix.

In $CdSiO_3$, both rare-earth ions doping and some non-rare-earth ions doping generate different persistent luminescence. The analysis of the results of rare-earth doping shows, according to the different electronic configurations of the rare-earth ions, the luminescence of the rare-earth ions in the $CdSiO_3$ matrix can have three cases as follows.

1. Y^{3+}, La^{3+}, Gd^{3+}, Lu^{3+} all have all-empty $(4f)^0$, half-empty $(4f)^7$, and all-full $(4f)^{14}$ electronic configuration. Although these rare-earth ions do not have energy level transition in the visible range, they have suitable ion radii and charges, making the introduction of these ions able to generate traps with suitable depth in $CdSiO_3$ matrix, which could produce broadband luminescence with the wavelength peak at ~ 420 nm;
2. Ce^{3+}, Nd^{3+}, Ho^{3+}, Er^{3+}, Tm^{3+}, Yb^{3+} with complicated energy level configuration can also generate blue-purple luminescence at ~ 420 nm in the $CdSiO_3$ matrix, which is similar with the first case, both as defects luminescence;
3. Pr^{3+}, Sm^{3+}, Eu^{3+}, Tb^{3+}, Dy^{3+}, besides the observation of 420-nm blue-purple emission, could generate very strong rare-earth ion characteristic persistent luminescence at the same time. The combination of the two luminescence materials can produce various colors lights.

For the series of $CaBO_3$ (B = Ti, Zr, Sn) with the perovskite structure, it could also be divided into three cases for the rare-earth ions persistent luminescence.

1. Pr^{3+} and Tb^{3+} have the characteristic persistent luminescence and can generate strong green persistent luminescent with the ultraviolet excitation, with the Sm^{3+} slightly weaker;
2. Eu^{3+} and Dy^{3+} have the characteristic emission, but there is no characteristic persistent luminescence;
3. Ce^{3+}, La^{3+}, Gd^{3+}, Lu^{3+}, Yb^{3+} have no fluorescent emission.

For the perovskite structure, the thermo-luminescent spectra after the doping of the second and the third types of ions are the same with that of the matrix, with no thermo-luminescent spectra peaks showing up.

To summarize the above experimental results, we can further conclude the rules as follows.

1. For different luminescent matrixes, there are different persistent luminescence rules for the rare-earth ions. In the rare-earth sulfur oxides matrix, the trivalent rare-earth ions that are prone to be reduced such as Eu^{3+}, Sm^{3+}, Tm^{3+}, Yb^{3+} can all produce persistent luminescence, while the rare-earth ions prone to be

oxidized usually do not have persistent luminescence. In contrast, in $Cd_3Al_2Ge_3O_{12}$ with the garnet structure and the $CaBO_3$ (B = Ti, Zr, Sn) with perovskite structure, the trivalent rare-earth ions prone to be oxidized, such as Pr^{3+} and Tb^{3+}, show the persistent luminescence, while the rare-earth ions prone to be reduced usually do not have the persistent luminescence.

2. In the same matrix, the activating ions with the similar valence changing tendencies have similar persistent luminescent properties. It means that, in a certain matrix, if Pr^{3+} that is prone to be oxidized has the persistent luminescence, Tb^{3+} will then also have the persistent luminescence; if Eu^{3+} that is prone to be reduced has persistent luminescence, the Sm^{3+} will then also have the persistent luminescence.

We further divided the matrix into two classes based on the dependency on the optical electronegativity of the activating ions: the oxidizing matrix and the reducing matrix, as given in Table 6.2.

The ions with high optical electronegativity in the oxidizing matrix have better persistent luminescent properties, while the ions with low optical electronegativity in the reducing matrix have better persistent luminescent properties. In the trivalent rare-earth ions, Pr^{3+} and Tb^{3+} have similar optical electronegativity, prone to lose electrons, and usually present as the coexistence of trivalence and tetravalence. Summarizing our work, with the prerequisite of the fluorescence emission, as long as Pr^{3+} has the persistent luminescence, Tb^{3+} must have it, vice versa. In contrast, if Pr^{3+} or Tb^{3+} does not have persistent luminescence, Tb^{3+} or Pr^{3+} will not have persistent luminescence either. The optical electronegativity of Eu^{3+} and Sm^{3+} is similar, both of which are prone to obtain electrons and become positive divalent. Their persistent luminescent properties, though less similar as Pr^{3+} and Tb^{3+}, yet differ from Pr^{3+} and Tb^{3+} significantly. For example, in Y_2O_2S, both Eu^{3+} and Sm^{3+} have good persistent luminescence, but not for Pr^{3+} and Tb^{3+}; in $CaZrO_3$, Pr^{3+} and Tb^{3+} have good persistent luminescence, but not for Eu^{3+} and Sm^{3+}.

3. For $CdSiO_3$ matrix, the persistent luminescence rules are complicated for the rare-earth ions. In this matrix, the rare-earth ions with the characteristic emissions all have persistent luminescence, no matter the easily oxidized ions or easily reduced ions or any other ions. It can be considered that the sample generates electrons and holes under the ultraviolet light excitation, which are captured by different defects, respectively. After the termination of the excitation, part of the energy produced by the recombination of electrons and holes in

Table 6.2 General classification of the host

Matrix with oxidation	Matrix with reduction
$CaWO_4$	RAl_2O_4 (R = Ca, Sr)
Y_2O_2S	$R_2MgSi_2O_7$ (R = Ca, Sr)
La_2O_2S	$CaBO_3$ (B = Ti, Zr, Sn)
Gd_2O_2S	$MgSiO_3$
$CdSiO_3$	$Cd_2Ge_7O_{16}$
Y_2O_3	$Cd_3Al_2Ge_3O_{12}$

the defects can emit short-wavelength broadband emission in the manner of luminescence, and the other part of the energy is transferred to rare-earth ions to emit light. The energy emitted by the recombination of electrons with holes can match with the corresponding energy levels of Pr^{3+}, Sm^{3+}, Eu^{3+}, Tb^{3+}, Dy^{3+}, and thus the characteristic persistent luminescence of these rare-earth ions can be observed.

4. For the neutral rare-earth ions with characteristic emission or rare-earth ions with complex energy configurations, they play roles in the persistent luminescence in three aspects: First of all, if the matrix can have effective energy transfer, a characteristic persistent luminescence will be produced. For example, in the rare-earth sulfur oxides and $CdSiO_3$ matrix, due to the existence of the energy transfer between the matrix and the activating ions, the persistent luminescence of these ions can be observed. Secondly, as assistant activating ions, they themselves do not generate persistent luminescence. Thirdly, the defects energy levels that affect the matrix (including the energy level density and depth) can increase or decrease the persistent luminescence of the matrix. For the all-empty, half-full, and all-full rare-earth ions, the major function is the third case.

5. From the defects chemistry point of view, the defects to produce the persistent luminescence can be summarized to the following three cases: Firstly, defects are caused by the assistant ions. A typical example is $SrAl_2O_4$:Eu^{2+},Dy^{3+}, in which the addition of Dy^{3+} largely enhances the persistent luminescent properties of $SrAl_2O_4$:Eu^{2+}. Secondly, the activating ions cause some defects, which is the case for most single-doped persistent luminescent materials. The defects come from the substitution effect from the doping ions, such as $CaZrO_3$:Pr^{3+}. Thirdly, the matrix itself could have defects. We found that the compounds that contain Cd tend to produce persistent luminescence more easily, making the defects types of these compounds in a large variety. From the probability point of view, the matrix that easily produces defects could have larger probability for the persistent luminescence than the other matrixes.

6. Except for the perovskite-structured compound matrix which does not have persistent luminescence itself, in the three systems including rare-earth sulfur oxides, garnet-structured $Cd_3Al_2Ge_3O_{12}$, and low-dimensional chain-structured $CdSiO_3$, the matrixes themselves have broadband emission and persistent luminescent properties. The experiment shows that there is a common energy transfer between the matrix and the activating ions. We adopted time-resolved spectrum and fluorescence lifetime to analyze and demonstrate.

6.6 The Applications of the Persistent Luminescent Materials

As mentioned previously, the persistent luminescent materials have become an important class of multi-functional materials, as shown in Fig. 6.11. As the low-light display and lighting, the persistent luminescent materials have been mainly used as luminous materials; as for the photocatalysis, the persistent luminescent materials act as the light source for the photocatalysis in dark environment [111, 112]; as for sensing, the persistent luminescent materials use their temperature change and mechanoluminescence features to measure the environment temperature and pressure [113, 114]; the application of the persistent luminescent materials in biomedical study lies in the luminescent marker, tumor diagnostics and analysis, as well as photodynamic therapy of cancer [58, 115]; as for the application in solar energy, the persistent luminescent materials can be used in photoelectron nano-devices, fiber amplifier, and photovoltaic materials [18, 22, 116, 117]; the persistent luminescent materials can also be used in agriculture, as the light source for plant growth, and enhance the photosynthesis of the plants.

6.6.1 The Application of the Persistent Luminescent Materials in Traditional Fields

The persistent luminescent materials firstly as traditional luminous materials have very wide applications in industrial and agricultural manufacturing, military, fire-fighting and daily life. Specifically, they can be made into luminescent paints,
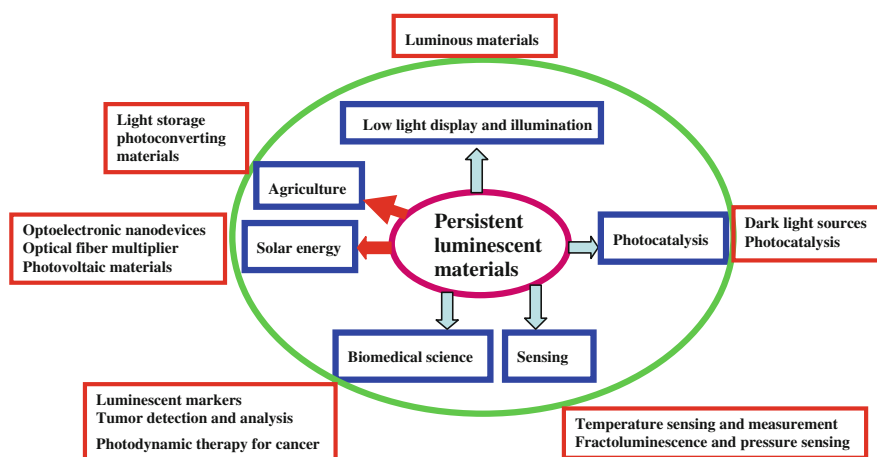
Fig. 6.11 Persistent luminescent materials are an important class of multi-functional materials

luminescent plastics, glass, ceramics, and luminous products, which are widely used in architecture decoration, traffic and transportation, military facilities, fire-fighting emergency, and many other aspects.

6.6.1.1 The Application of the Persistent Luminescent Materials in Luminescent Paints

Paint is a type of material that forms a continuous thin film that steadily attaches onto the object surfaces. Doping the persistent luminescent materials as functional pigments into the paints can generate the paints with persistent luminescence and can be coated onto architecture or decoration materials to generate surfaces with persistent luminescent functions, so as to achieve the decoration or emergency indicator purposes.

The luminescent paints usually use multiple types of varnishes and $SrAl_2O_4:Eu^{2+}$, Dy^{3+} to prepare. However, the solvent paints have severe pollutions to the environment. Since the aluminates persistent luminescent materials are prone to hydrolysis and lose the luminescent function in humid environment [118], pre-modification for the persistent luminescent material surfaces is necessary before the addition of aluminates into water-based paint. For example, nano-titanium dioxide can be a coating material for strontium aluminates persistent luminescence materials, to prepare water-based persistent luminescent paint. It could also be considered to coat a layer of polymer onto the persistent luminescent materials, to improve the stability of luminescent powder against hydrolysis in water-based paint and the compatibility with organic resin.

6.6.1.2 The Application of the Persistent Luminescent Material in Plastics

The application in plastics is one of the main applications of the persistent luminescent materials. The major substrates are polymethyl methacrylate, polyurethane, and other resins with high transparency. It could also be made into luminescent plastic mother particles and be added directly into other plastics, to prepare different types of plastic products. Mishra et al. [119–121] prepared a series of aluminates–polymer hybrid material by extrusion molding method and systematically studied the application of the aluminates persistent luminescent material in PVA, LDPE, PP, PMMA, HDPE, LDPE, and other polymer materials. They also carried out a comprehensive investigation into the luminescent property and mechanical property of the composite materials. After the surface modification with silane coupling agents, the compatibility of the persistent luminescent material with the organic system can be enhanced and the composite material could acquire good mechanical properties.

6.6.1.3 Persistent Luminescent Glass

Glass, with its high transparency, shaping versatility, and other characteristics, has become a suitable substrate for persistent luminescent materials' applications. The luminescent glass as a novel functional material also has wide applications in architecture, aviation, arts, and crafts. The investigation of persistent luminescent glass progressed slowly for quite a while after this discovery. The luminescence lifetime of most persistent luminescent glass was at millisecond level before 1996 [122].

However, since the luminescent glass has special characteristics that crystal materials do not have, in recent years, the research regarding the persistent luminescent glass gradually increased. Qiu et al. [76, 123, 124] did most of the research and investigated across a wide range, including the preparation of various ions-activated multiple substrates glass material through overall crystallization technology, for example, the $CaO–Al_2O_3–SiO_2–B_2O_3$ glass, $SrO–Al_2O_3–SiO_2$ glass, $CaO–Al_2O_3–SiO_2$ glass activated by Eu^{2+}, and the SiO_2 glass activated by Ge. Yamazaki et al. [125] prepared green color Tb^{3+}-doped $60ZnO–20SiO_2–20B_2O_3$ luminescent glass, with luminescent time longer than 1 h.

Lin et al. [126–128] applied two-step approach to preparing the persistent luminescent glass. In this process, luminescent glass was firstly made by melting method, and persistent luminescent glass was then generated by mixing the persistent luminescent powder with glass powder at low temperatures. This procedure is easy to apply, utilizes the excellent luminescent characteristics of the material, takes advantages of the lattice structure of the glass, and effectively solves the problem that the formation temperature affects the luminescent properties.

Su et al. [129–132] investigated the red, green, yellow color $SiO_2–B_2O_3–ZnO–MnO–Sm_2O_3$ system persistent luminescent glass, whose luminescence lifetime could reach 500 min, and realized multi-color Mn^{2+}-doped $ZnO–B_2O_3–SiO_2$ persistent luminescent glass.

Liu et al. [133, 134] prepared boron aluminates persistent luminescent glass with $SrAl_2O_4$ as the major crystal and investigated surface crystallizing $SrAl_2O_4$:Eu^{2+}, Dy^{3+} persistent luminescent glass. The process left out the heating process and showed the surface crystallizing $SrAl_2O_4$:Eu^{2+},Dy^{3+} persistent luminescent glass had apparent advantages, through comparison between transparent glass, surface crystallizing glass, and overall crystallizing $SrAl_2O_4$:Eu^{2+},Dy^{3+} glass.

6.6.1.4 Persistent Luminescent Ceramics

Luminescent ceramics generally have three major preparation approaches: the first of which is to mix the luminescent powder with ceramic aggregate and directly fired, so as to obtain whole-body persistent luminescent ceramic products; the second of which is to fire the luminescent material precursors under high-temperature to persistent luminescent ceramic pieces, and create persistent luminescent ceramic products through second time process; the third of which is to generate persistent luminescent glaze material followed by coating the glaze onto

the ceramic surfaces to obtain the surface luminescent ceramic products. The first two methods are both limited in industrial manufacture due to the poor resistance against high-temperature oxidation of persistent luminescent material. Therefore, the third method has the widest application [135]. Among the aluminates system persistent luminescent materials, $Sr_4Al_{14}O_{25}:Eu^{2+},Dy^{3+}$ has the best resistance against high-temperature oxidation. However, its limiting temperature is still lower than 1000 °C, and it is not suitable to fire high-temperature ceramics above 1000 °C. On the other hand, even if it is used for mid-low-temperature ceramics, the resulted products still have non-ideal luminescence intensity and lifetime. Therefore, in the preparation of luminescent ceramics, there is a large need for improvement of the resistance against high-temperature oxidation for the luminescent materials.

6.6.2 Biomedical Application of the Persistent Luminescent Materials

Optical imaging as an easy, fast, and sensitive method with low costs has been playing a more and more important role in early diagnostics and therapies of diseases. The development of highly efficient, multi-functional fluorescent imaging probes, to simultaneously monitor the variety intracellular locations of bioactive materials, interaction, and their dynamic changes, and to obtain 'the intracellular snapshots,' has drawn more and more attention.

The fluorescent probe technology has played an important role in immuno-analysis, cellular diagnostics, and other aspects and attracted lots of interest. Currently, the major fluorescent marker is fluorescein, and complexes and organic materials, which have poor photochemical stability, are prone to be photobleached and photodegraded. It is been a hot spot to search for a marker material with good stability and high luminescent efficiency. Persistent luminescence is a photo-luminescent phenomenon, a process that the materials continue to be luminescent after the excitation light stops illumination. Persistent luminescent material can be excited before detection and imaging, can realize biosensing and imaging without further excitation, and thus can effectively avoid the background interference during in situ excitation.

Chermont group [58] has used sol–gel method to prepare the silicate persistent luminescent nano-material $Ca_{0.2}Zn_{0.9}Mg_{0.9}Si_2O_6:Eu^{2+}/Dy^{3+}/Mn^{2+}$ with near-infrared fluorescence at high temperature. They used PEG to modify the material surface and enhance the in vivo biocompatibility and applied to mice in vivo imaging, as illustrated in Fig. 6.12. This method successfully avoided the potential damage from the light source to the organism in traditional fluorescent analysis methods and realized 'excitation free' in vivo imaging for the first time.

In 2011, Scherman group [136] studied the in vivo imaging distribution of silicate persistent luminescent materials after various modifications, and with
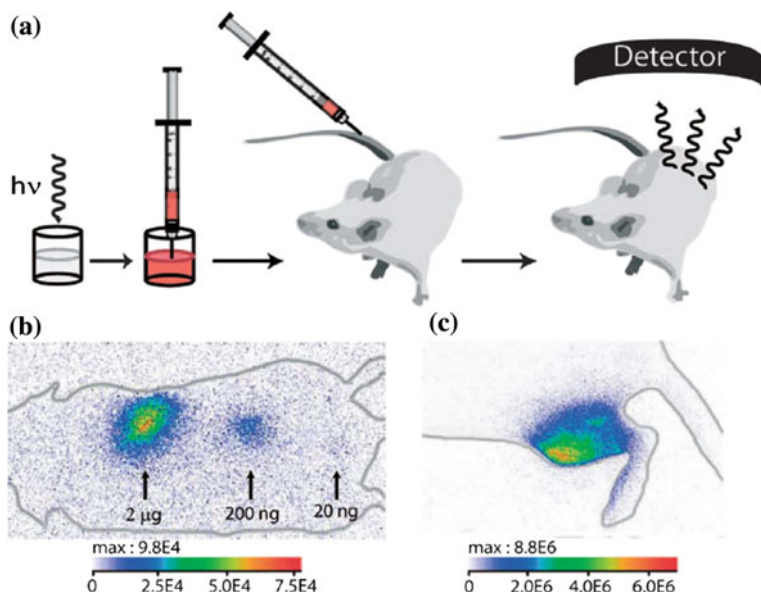
Fig. 6.12 Illustration of silicate persistent luminescent materials for mice in vivo imaging. Reprinted from Ref. [58] by permission of PNAS

different particle sizes. After 120-nm silicate persistent luminescent material surfaces that were hydroxylated and modified with PEG and 180-nm silicate persistent luminescent material surfaces that were modified with PEG, it was revealed that the in vivo circulation could be affected by different modification for the same sized particles, or by the same modification for different sized particles, as demonstrated in Fig. 6.13.

In 2012, Scherman group [137, 138] functionalized the silicate persistent luminescent material surfaces and functionalized with biotin and Rak-2. They further used TGA, FTIR, DLS, and other techniques to characterize the material surface functionalizations, investigated the targeting capability, and targeted on avidin that is secreted by gliomas. The study found that the targeting capability was not relevant to biotin, but also with the particle size.

Wu et al. [115] synthesized polyethyleneimine-coated $Ca_{1.86}Mg_{0.14}ZnSi_2O_7$ persistent luminescent material doped with Eu, Dy, and combined with gold nanoparticles that were functionalized by alpha-fetoprotein (AFP) to form a resonance energy transfer system. The generated nano-material can detect AFP in blood serum sensitively and selectively without excitation and enables the direct monitor of AFP secretion by liver cancer cells during growth, as illustrated in Fig. 6.14.

There remain the following questions to address to exploit the research and application of persistent luminescent materials in biological fields.
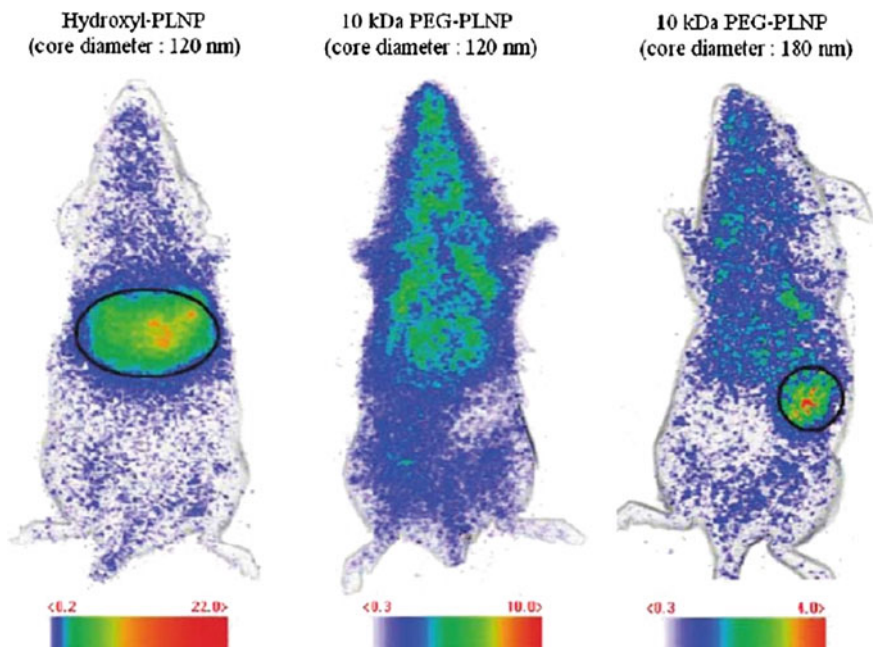
Fig. 6.13 Differently modified silicate persistent luminescent material used for mice in vivo imaging. Reprinted with the permission from Ref. [136]. Copyright 2011, American Chemical Society
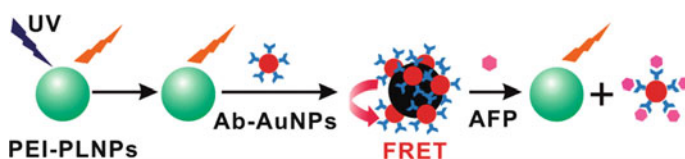
Fig. 6.14 Schematic illustration of the FRET inhibition assay for AFP based on the PL quenching of PEI-PLNPs by Ab-AuNPs. Reprinted with the permission from Ref. [115]. Copyright 2011, American Chemical Society

1. The synthesis of the persistent luminescent materials requires strict conditions, and high-temperature firing is required no matter in the traditional synthesis approach or sol–gel method, or chemical precipitation method. Some of the materials have the firing temperature over 1000 °C.
2. The dispersity of the material is very poor after high-temperature firing. Some materials that use silicate as substrates have large particle sizes after high-temperature firing, with size of some particles reaching micron level, with severe agglomerations and poor water dispersity, and thus are not suitable for biological applications.

3. The surface functionalization has large difficulties, especially that the surface of the silicate persistent luminescent material synthesized traditionally barely has any functional groups, making the further surface functionalization and increase in biocompatibility especially hard.

6.6.3 The Application of Persistent Luminescent Material in Sensing

There are not many applications of persistent luminescent materials in sensing. Here, we mainly introduced the application in temperature sensing and pressure sensing of persistent luminescent materials.

6.6.3.1 Temperature Sensing

By investigating the relationship between luminescence intensity and lifetime with temperature for the persistent luminescent materials, the material luminescent properties can be related to temperature and can be used for environment temperature sensing. The persistent luminescent materials used in temperature sensing have the following advantages and characteristics:

1. The materials can be used as passive sensors. The passive sensors belong to the energy control sensors. By controlling the input energy from the other end or excitation energy, they can realize the non-contact measurement, which is featured with no power and signal wires, small sizes, strong anti-interference, and other advantages that are suitable in complicated environment, such as the detection and analysis for sports and objects that cannot be contacted.

2. They have a wide application range. Compared with other temperature sensors, the persistent luminescent material could combine with optical fiber to create fluorescent temperature sensor, which not only can be used in high electromagnetic cases, but also can avoid the explosive danger due to the introduction of assistant power, suitable in explosive atmosphere. They can also be controlled remotely and thus become a promising sensitive temperature sensing material.

3. They have high sensitivity and accuracy. A large number of experiments have shown that: Within a certain temperature range, the temperature sensors made from persistent luminescent materials have excellent sensitivity and accuracy, themselves have long luminescence lifetime, strong luminescence intensity, and large temperature coefficients, and thus can be used as ideal probe materials in fluorescent temperature sensing system [103, 139, 140].

Persistent luminescent materials combine with optical fiber to create the fluorescent fiber temperature sensors, whose sensing system is usually composed of

a sensor probe that emits fluorescent signals by the light source that excites sensor elements, a photodetector receiving the fluorescent signals, as well as a signal analysis processor. The sensors complete the measurement through the detection of the intensity or lifetime changes of the objects to be analyzed (temperature or applied radiation) by the fluorescent material (persistent luminescent materials).

6.6.3.2 Mechanoluminescence and Pressure Sensing

Mechanoluminescence is an optical phenomenon discovered as early as the 1600s, which is a physical phenomenon that some materials could emit visible light under the effects of stress, friction, scratching, breakage, and ultrasonic oscillation. There are two other terms that hold similar physical natures, which are triboluminescence and fractoluminescence.

Although the mechanoluminescence phenomenon has been discovered for centuries, since the fluorescent materials usually have low-intensity mechanoluminescence, short lifetime, and the poor detection capability for weak light in the past, the mechanoluminescence was not practically applied until the end of 1990s. Because of the discovery of strong visible mechanoluminescence of persistent luminescent materials, as well as the improvement of weak light detection capability, the mechanoluminescence has drawn large attention and interests in mechanical engineering, material fracture, earthquake prediction and monitoring, life science, medical diagnostics, and other fields. The reports about utilizing mechanoluminescence for stress sensors have increased rapidly [114, 141–144].

Li et al. [145] developed a technique that utilizes the mechanoluminescent membrane to measure the stress distribution on the material surfaces. Wang et al. [146] fabricated a sensor to detect structure damages using the mechanoluminescence of $SrAl_2O_4$:Eu, to evaluate the fracture and stress intensity. Kim et al. [147] utilized persistent luminescent materials persistent luminescence characteristics and mechanoluminescent properties to study the rapid transmission process during the cracks of the concretes. They successfully recorded the formation and transmission of cracks during the concretes fracture process and also discovered some interesting phenomena between the crack transmission with the shedding speed during the concretes bending and fracture process. Therefore, the mechanoluminescent sensors are being emphasized, and their potential application prospects have called more and more attentions in architecture, mechanical engineering, material fracture, earthquake prediction and monitoring, life science, medical diagnostics, and many relevant fields that closely relate to people's livelihood.

A novel pressure sensor could be made based on the persistent luminescent materials mechanoluminescence phenomenon and can have potential applications in earthquake prediction, volcano forecast, building and bridges safety warnings, materials failure analysis, and other aspects.

Currently, the mechanism for the mechanoluminescence remains unclear. Two proposed mechanisms are typical and described as follows, one of which is induced by electricity and the other by heat [148].

1. Electricity mechanism: The mechanical force generates free electrons, which compress the crystals to generate electric field. The free electrons can be released when the local electric field forms at the crystal deformation area, and trigger the light emission.
2. Heat mechanism: The mechanical force causes the crystal deformation and generates free electrons, part of which (or holes) can be captured by traps in the crystal and emit light under heat disturbances.

6.6.4 The Application of Persistent Luminescent Materials in Photocatalysis

The photocatalysis of semi-conductor TiO_2 requires light and is lost in the dark. Utilizing the persistent luminescent materials—TiO_2 composite photocatalyst—has been a novel modification approach, and the study has shown that the persistent luminescent materials—TiO_2 photocatalyst—can effectively improve the photocatalysis capability of TiO_2, and realize the degradation of organic pollutes, formaldehyde, ammonia, and other gases in the dark environment [111, 112, 149–152], as shown in the photocatalysis decrease process and mechanism chart in Figs. 6.15 and 6.16.

In 2003, Ko [111] proposed using persistent luminescent materials as the light source for TiO_2, and realized the degradation of ammonia in the dark. In 2004, Zhang et al. [112] proposed the concept of energy storage photocatalysis materials.

The persistent luminescent process shares the similarity with TiO_2 photocatalysis in that they both utilize the light and both relevant to the charge carriers' generation and separation. The photocatalysis mechanism of persistent luminescent materials-modified TiO_2 has three arguments from the current studies, the first of which is the persistent luminescent materials facilitate the light absorption of TiO_2, while the second of which is that the combination of persistent luminescent materials with TiO_2 changes the Ti and O combination energy and the third of which is that there exists a transfer process for charge carriers between luminescent materials with TiO_2 that prevents the recombination of photo-induced electrons with holes and promotes the photocatalytic activity. Briefly, there are a carrier transfer mechanism and a light absorption mechanism in the persistent luminescent composite photocatalysis materials, which synergistically promote the photocatalytic activity.
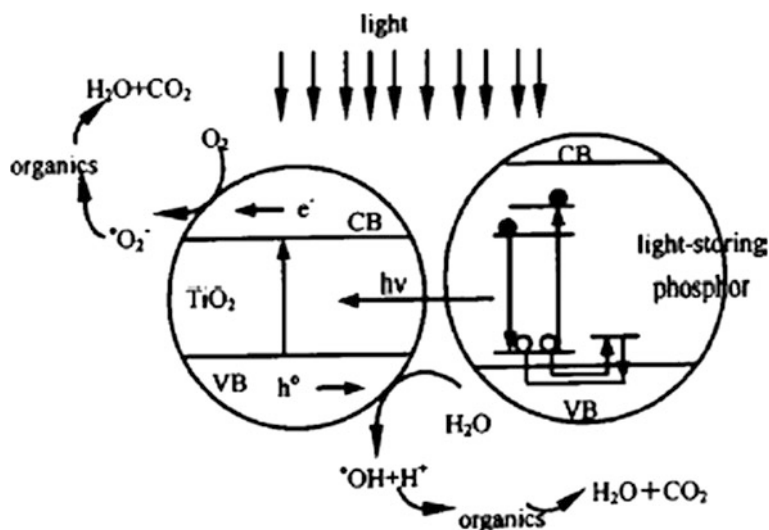
Fig. 6.15 Mechanism of the light-storing figure photocatalysis. Reprinted from Ref. [112] with permission of AIP Publishing LLC

Fig. 6.16 Persistent fluorescence-assisted $TiO_{2-x}N_y$-based photocatalyst for Gaseous acetaldehyde degradation. Reprinted with the permission from Ref. [152]. Copyright 2012, American Chemical Society
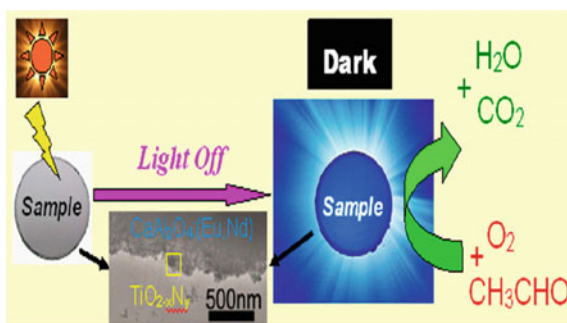
6.7 Prospects of Persistent Luminescent Materials

The research of persistent luminescent materials has made a lot of progress, but still faces strict challenges. There is a general lack of practical red persistent luminescent materials. The activation ions are mainly Eu^{2+} and the luminescent substrates are mainly aluminates and silicates, making the development of novel luminescent species very necessary. From the persistent luminescent materials luminescence mechanism point of view, some luminescence cannot be well explained by current models or mechanisms, and the prediction for the luminescence phenomena remains to be improved. The major application of persistent luminescent materials is the luminous material, while some new application fields need to be exploited.

Besides, the particle size, morphology, surface structure, and crystal states have effects on the luminescent properties of persistent luminescent materials, which has not been emphasized or studied. The luminescent intensity and lifetime (especially the intensity and lifetime of the second time application) of the materials, as well as the second time applications, need to be improved.

Based on the current research and development of persistent luminescent materials, the following aspects are necessary to be explored.

6.7.1 The Exploration of the Novel Persistent Luminescent Materials System

It is an important way out to search for persistent luminescent materials with excellent chemical stability, luminescence intensity, lifetime, and multiple colors. The aluminates persistent luminescent materials doped with rare-earth elements have already fulfilled the needs for blue and green persistent luminescence. Therefore, the searching for excellent red persistent luminescent materials is very important for the future work. Beside the powder material, glass has become another promising way out due to its own characteristics such as uniformity, transparency, and the ease of obtaining various shapes. Furthermore, the persistent luminescent thin film and fiber are also future directions, to exploit new application fields and enlarge the application range.

6.7.2 The Exploit of Persistent Luminescent Materials Application Fields

Beside the environmentally friendly energy-saving products and industrial crafts used for indication and illumination, along with the development of some new persistent luminescent materials such as the persistent luminescent glass, the major development direction for persistent luminescent materials should be in the high technology fields, such as information storage, radiation detection, and imaging. The key step to exploit the application of persistent luminescent materials lies in the tight fit between the material research and development with the following processing such as device fabrication.

Currently the biomedical application of persistent luminescent materials is an important development direction and is with unique advantages. However, it confronts the problem that nano-lization and surface modification are needed, and the research needs to be enhanced in these aspects. Nano-lization usually causes the luminescence to be severely decreased, which can potentially be addressed by using the plasmon resonance mechanism and energy transfer to enhance the luminescent properties.

6.7.3 The Mechanism Study of Persistent Luminescent Materials

The diversity of persistent luminescent materials has determined the complexity of their mechanisms. By summarizing the current progress, it can be seen that it is instructive to search for novel persistent luminescent materials by using abnormal rare-earth element ions as activation ions, and selecting the co-activating ions from other rare-earth element ions. The enrichment of mechanisms will largely promote the investigation and application of persistent luminescent materials.

At present, the mechanisms of persistent luminescent materials remain unclear. Most of the researchers agree that there exist some trapping energy levels in the band gaps, in which the free charge carriers will be trapped by these energy levels. But it remains unclear whether or not these charge carriers come from the luminescent center and whether or not they can be excited directly in conduction bands or valence bands. Another unclear point is that how the energy stored in the traps plays a role on the luminescent center: by direct energy transfer or by the migration of these charge carriers in the valence or conduction bands. The co-doping agent near the activation agent together with the crystal lattice deficiency has effects, causing other problems. The future experiments might be able to address these questions. Synchrotron radiation (e.g., XANES, ESAFS) and electron paramagnetic resonance (EPR) measurement can thoroughly reveal the material structure, composition, valence, and charge distribution and provide solutions to these theoretical problems that can only be solved by the light-induced luminescence and heat-induced luminescence phenomena.

References

1. Luo F, Sun GM, Zheng AM, Lian SX, Liu YL, Feng XF, Chu YY (2012) Promising long-lasting phosphor material: a novel metal-organic framework showing intriguing luminescent performance. Dalton T 43: 13280.
2. Deng YY, Zhao DX, Chen X, Wang F, Song H, Shen DZ (2013) Long lifetime pure organic phosphorescence based on water soluble carbon dots. Chem Commun 49: 5751.
3. Feng HB, Zhang HR, Dong HW, Lei BF, Xiao Y, Zheng MT, Liu YL (2014) Luminescence properties of silk cocoon derived carbonaceous fluorescent nanoparticles/PVA hybrid film. Opt Mater 36: 1787.
4. Van den Eeckhout K, Smet PF, Poelman D (2010) Persistent luminescence in Eu^{2+}-doped compounds: A review. Materials 3: 2536.
5. Van den Eeckhout K, Poelman D, Smet PF (2013) Persistent luminescence in non-Eu^{2+}-doped compounds: A review. Materials 6: 2789.
6. Smet PF, Moreels I, Hens Z, Poelman D (2010) Luminescence in sulfides: A rich history and a bright future. Materials 3: 2834.
7. Smet PF, Botterman J, Van den Eeckhout K, Korthout K, Poelman D (2014) Persistent luminescence in nitride and oxynitride phosphors: A review. Opt Mater 36: 1913.
8. Zhuang YX, Katayama Y, Ueda J, Tanabe S (2014) A brief review on red to near-infrared persistent luminescence in transition-metal-activated phosphors. Opt Mater 36: 1907.

9. Singh SK (2014) Red and near infrared persistent luminescence nano-probes for bioimaging and targeting applications. RSC Adv 4: 58674.

10. Lastusaari M, Laamanen T, Malkamäki M, Eskola KO, Kotlov A, Carlson S, Welter E, Brito HF, Bettinelli M, Jungner H, Hölsä J (2012) The Bologna Stone: history's first persistent luminescent material. Eur J Mineral 24: 885.

11. Brito HF, Hölsä J, Laamanen T, Lastusaari M, Malkamäki M, Rodrigues LCV (2012) Persistent luminescence mechanisms: human imagination at work. Opt Mater Express 2: 371.

12. Wang YH, Gong Y, Xu XH, Li YQ (2013) Recent progress in multicolor long persistent phosphors. J Lumin 133: 25.

13. Su Q, Li CY, Wang J (2014) Some interesting phenomena in the study of rare earth long lasting Phosphors. Opt Mater 36: 1894.

14. Xu XR, Su MZ (2004) Optical and luminescent materials. Chinese Chemical Industry Press.

15. Kang FW, Hu YH, Wu HY, Mu ZF, Ju GF, Fu CJ, Li NN (2012) Luminescence and red long afterglow investigation of Eu^{3+}–Sm^{3+} Co-doped $CaWO_4$ phosphor. J Lumin 132: 887.

16. Chang CK, Li W, Huang XJ, Wang ZY, Chen X, Qian X, Guo R, Ding YL, Mao D (2010) Photoluminescence and afterglow behavior of Eu^{2+}, Dy^{3+} and Eu^{3+}, Dy^{3+} in $Sr_3Al_2O_6$ matrix. J Lumin 130: 347.

17. Pang R, Li CY, Shi LL, Su Q (2009) A novel blue-emitting long-lasting proyphosphate phosphor $Sr_2P_2O_7$:Eu^{2+}, Y^{3+}. J Phys Chem Solids 70: 303.

18. Smet PF, Poelman D, Hehlen MP (2012) Focus issue introduction: persistent phosphors, Opt Mater Express 2: 452.

19. Harvey EN (1957) A history of luminescence from the earliest times until 1900. American Philosophical Society.

20. Hoogenstraaten W, Klasens H (1953) Some properties of zinc sulfide activated with copper and cobalt. J Electrochem Soc 100: 366.

21. Shionoya S, Yen WM, Hase T (2007) Phosphor handbook. CRC press.

22. Matsuzawa T, Aoki Y, Takeuchi N, Murayama Y (1996) A new long phosphorescent phosphor with high brightness, $SrAl_2O_4$:Eu^{2+}, Dy^{3+}. J Electrochem Soc 143: 2670.

23. Qiu Z, Zhou Y, Lu Zhang MA, Q. Ma (2007) Combustion synthesis of long-persistent luminescent MAl_2O_4:Eu^{2+}, R^{3+} (M = Sr, Ba, Ca, R = Dy, Nd and La) nanoparticles and luminescence mechanism research. Acta Mater 55: 2615.

24. Schweizer S, Henke B, U. Rogulis U, Yen WM (2007) Recombination processes in rare-earth doped MAl_2O_4 (M = Ca, Sr) persistent phosphors investigated by optically-detected magnetic resonance. Phys Stat Sol A 204: 677.

25. Lin Y, Tang Z, Zhang Z, Wang, X, Zhang J (2001) Preparation of a new long afterglow blue-emitting $Sr_2MgSi_2O_7$-based photoluminescent phosphor. J Mater Sci Lett 20: 1505.

26. Fei Q, Chang C, Mao D (2005) Luminescent properties of $Sr_2MgSi_2O_7$ and $Ca_2MgSi_2O_7$ long lasting phosphors activated by Eu^{2+}, Dy^{3+}. J Alloy Compd 390: 133.

27. Jia DD, Jiang LH, Liu YL, Zhu J (1998) The luminescent properties of Ca_xSr_{1-x}S: Bi, Tm, Cu and CaS: Eu. Chines J Lumin 19: 312.

28. Jia DD, Wu BQ, Jiang LH, Zhu J (2000) The luminescent properties of $Ca_{0.9}Sr_{0.1}$S: Bi^{3+}, Tm^{3+}. Chines J Lumin 21: 43.

29. Jia DD, Zhu J, Wu BQ (2000) Trapping processes in CaS: Eu^{2+}, Tm^{3+}. J Electrochem Soc 147: 386.

30. Xiao ZG, Luo XX (2005) Optical storage luminescent materials and their products (the second edition). Chinese Chemical Industry Press.

31. Guo CF, Chu BL, Xu J, Su Q (2004) Improving the stability of alkaline earth sulfide based phosphors by oxide coating. Chinese J Lumin 25: 449.

32. Palilla FC, Levine AK, M. R. Tomkus MR (1968) Fluorescent properties of alkaline earth aluminates of the type MAl_2O_4 activated by divalent europium. J Electrochem Soc 115: 642.

33. Aitasalo T, Durygin A, Holsa J, Lastusaari, M, Niittykoski J, Suchocki A (2004) Low temperature thermoluminescence properties of Eu^{2+} and R^{3+} doped $CaAl_2O_4$. J Alloy Compd 380: 4.

34. Sakai R, Katsumata T, Komuro S, Morikawa T (1999) Effect of composition on the phosphorescence from $BaAl_2O_4$: Eu^{2+}, Dy^{3+} crystals. J Lumin 85: 149.
35. Akiyama M, Xu C, Matsui H, Nonaka K, Watanabe T (2000) Photostimulated luminescence phenomenon of $Sr_4Al_{14}O_{25}$: Eu, Dy using only visible lights. J Mater Sci Lett 19: 1163.
36. Zhang JY, Zhang ZT, Wang TM, Hao WC (2003) Preparation and characterization of a new long afterglow indigo phosphor $Ca_{12}Al_{14}O_{33}$: Nd, Eu. Mater Lett 57: 4315.
37. Kodama N, Takahashi T, Yamaga M, Tanii Y, Qiu J, Hirao K (1999) Long-lasting phosphorescence in Ce^{3+}-doped $Ca_2Al_2SiO_7$ and $CaYAl_3O_7$ crystals. Appl Phys Lett 75: 1715.
38. Jia D, Yen WM (2003) Enhanced V^{K+} center afterglow in $MgAl_2O_4$ by doping with Ce^{3+}. J Lumin 101: 115.
39. Jia D, Wang XJ, Yen WM (2002) Electron traps in Tb^{3+}-doped $CaAl_2O_4$. Chem Phys Lett 363: 241.
40. Smith AL (1949) Some new complex silicate phosphors containing calcium, magnesium, and beryllium. J Electrochem Soc 96: 287.
41. Lei BF, Liu YL, Liu J, Shi CS (2004) Pink light emitting long-lasting phosphorescence in Sm^{3+}-doped $CdSiO_3$. J Solid State Chem 177: 1333.
42. Liu YL, Lei BF, Shi CS (2005) Luminescent properties of a white afterglow phosphor $CdSiO_3$: Dy^{3+}. Chem Mater 17: 2108.
43. Ji HM, Xie GJ, Y. Lv Y, Lu HX (2007) A new phosphor with flower-like structure and luminescent properties of $Sr_2MgSi_2O_7$: Eu^{2+}, Dy^{3+} long afterglow materials by sol-gel method. J Sol-Gel Sci Techn 44: 133.
44. Yamamoto H, Okamoto S, Kobayashi H (1997) Red luminescence in Pr^{3+}-doped calcium titanates. Phys Stat Soc 160: 255.
45. Royce MR, Matsuda S, Tamaki H (1997) Red emitting long decay phosphors. US Patent 5650094A.
46. Lian SX, Jin JH, Su MZ (2001) The synthesis and luminescent properties of $Ca_{1-x}Zn_xTiO_3$: Pr^{3+}, R^+ (R^+ = Li^+, Na^+, K^+, Rb^+, Cs^+, Ag^+). J Chin Soc Rare Earths 19: 602.
47. Fu J (2000) Orange and red emitting long-lasting phosphors MO: Eu^{3+}(M = Ca, Sr, Ba). Electrochem Solid State Lett 3: 350.
48. Lin YN, Nan CW, Cai N, Zhou XS, Wang HF, Chen DP (2003) Anomalous afterglow from Y_2O_3-based phosphor. J Alloy Compd 36: 92.
49. Xie W, Wang YH, Zou CW, Quan J, Shao LX (2015) A red-emitting long-afterglow phosphor of Eu^{3+}, Ho^{3+} co-doped Y_2O_3. J Alloy Compd 619: 244.
50. Murazaki Y, Arai K, Ichinomiya K (1999) A new long persistence red phosphor. Jpn Rare Earth 35: 41.
51. Lei BF, Liu YL, Zhang JW, Meng JX, Man SQ, Tan SZ (2010) Persistent luminescence in rare earth ion-doped gadolinium oxysulfide phosphors. J Alloy Compd 495: 247.
52. Zhang JW, Liu YL, Man SQ (2006) Afterglow phenomenon in Erbium and Titanium codoped Gd_2O_2S phosphors. J Lumin 117: 141.
53. Li W, Liu Y, Ai P (2010) Synthesis and luminescence properties of red long-lasting phosphor Y_2O_2S:Eu^{3+}, Mg^{2+}, Ti^{4+} nanoparticles. Mater Chem Phys 119: 52.
54. Song CY, Lei BF, Liu YL (2004) Long lasting phosphorescence of Eu^{3+} in La_2O_2S. Chinese J Inorg Chem 20: 89.
55. Zhang HR, Dong HW, Lei BF, Wang P, Li JF, Liu YL, Wang J, Xiao Y, Zheng MT, Meng JX (2014) Enhanced performance of $Ca_2Si_5N_8$:Eu^{2+}, Tm^{3+} reddish-orange afterglow phosphor by co-doping with Dy^{3+}. Opt Mater 36: 1846.
56. Wang J, Zhang HR, Lei BF, Dong HW, Zhang HM, Liu YL, Lai NL, Fang Y, Chen ZJ (2014) Red persistent and photo-stimulated luminescence properties of $SrCaSi_5N_8$: Eu^{2+}, Tm^{3+} solid solution. Opt Mater 36: 1855.
57. Rasmussen JC, Kwon S, Sevick-Muraca EM, Corrmier JN (2012) The role of lymphatics in cancer as assessed by near-infrared fluorescence imaging. Ann Biomed Eng 40: 408.

58. Chermont QM, Chanéac C, Seguin J, Pellé F, Maitrejean S, Jolivet JP, Gourier D, Bessodes M, Scherman D (2007) Nanoprobes with near-infrared persistent luminescence for *in vivo* imaging. Proc Natl Acad Sci USA 104: 9266.

59. Peng MY, Qiu JR, Zhang QY (2014) An introduction to the 2nd International Workshop on Persistent and Photostimulable Phosphors (IWPPP 2013). Opt Mater 36: 1769.

60. Li Y, Li YY, Sharafudeen K, Dong GP, Zhou SF, Ma ZJ, Peng MY, Qiu JR (2014) A strategy for developing near infrared long-persistent phosphors: taking $MAlO_3:Mn^{4+}$, Ge^{4+} (M = La, Gd) as an example. J Mater Chem C 2: 2019.

61. Caratto V, Locardi F, Costa GA, Masini R, Fasoli M, Panzeri L, Martini M, Bottinelli E, Gianotti E, Miletto I (2014) NIR persistent luminescence of lanthanide ion-doped rare-earth oxycarbonates: The effect of dopants. ACS Appl Mater Inter 6: 17346.

62. Chen DQ, Chen Y, Lu HW, Ji ZG (2014) A bifunctional $Cr/Yb/Tm:Ca_3Ga_2Ge_3O_{12}$ phosphor with near-infrared long-lasting phosphorescence and upconversion luminescence. Inorg Chem 53: 8638.

63. Basavaraju N, Priolkar KR, Gourier D, Sharma SK, Bessiere A, Viana B (2015) The importance of inversion disorder in the visible light induced persistent luminescence in Cr^{3+} doped AB_2O_4 (A = Zn or Mg and B = Ga or Al). Phys Chem Chem Phys 17: 1790.

64. Grinberg M (2002) Spectroscopic characterisation of disordered materials doped with chromium. Opt Mater 19: 37.

65. Bessiere A, Jacquart S, Priolkar K, Lecointre A, Viana B, Gourier D (2011) $ZnGa_2O_4:Cr^{3+}$: A new red long lasting phosphor with high brightness. Opt Express 19: 10131.

66. Pan ZW, Lu YY, Liu F (2012) Sunlight activated long persistent luminescence in the near infrared from Cr^{3+}-doped zinc gallogermanates. Nat Mater 11: 58.

67. Liu F, Yan WZ, Chuang YJ, Zhen ZP, Xie J, Pan ZW (2013) Photostimulated near-infrared persistent luminescence as a new optical read-out from Cr^{3+}-doped $LiGa_5O_8$. Sci Rep 3: 1554.

68. Abdukayum A, Chen JT, Zhao Q, Yan XP (2013) Functional near infrared-emitting Cr^{3+} Pr^{3+} co-doped zinc allogermanate persistent luminescent nanoparticles with superlong afterglow for *in vivo* targeted bioimaging. J Am Chem Soc 135: 4125.

69. Wang LL, Hou ZY, Quan ZW, Lian HZ, Yang PP, Lin J (2009) Preparation and luminescence properties of Mn^{2+}-doped $ZnGa_2O_4$ nanofibers via electrospinning process. Mater Res Bull 44: 1978.

70. Yu NY, Liu F, Li XF, Pan ZW (2009) Near infrared long-persistent phosphorescence in $SrAl_2O_4:Eu^{2+}$, Dy^{3+}, Er^{3+} phosphors based on persistent energy transfer. Appl Phys Lett 95: 231110.

71. Zhang XY, Lu LP, Bai ZH (2005) Rare earths luminescent materials. National Defence Industry Press of China.

72. Jia WJ, Yuan HB, Lu LZ, Liu HM, Yen WM (1998) Phosphorescent dynamics $SrAl_2O_4:Eu^{2+}$, Dy^{3+} single crystal fibers. J Lumin 76-77: 424.

73. Clabau F, Rocquefelte X, Jobic S, Deniard P, Whangbo MH, Garcia A, Mercier TL (2005) Mechanism of phosphorescence appropriate for the long-lasting phosphors Eu^{2+}-Doped $SrAl_2O_4$ with codopants Dy^{3+} and B^{3+}. Chem Mater 17: 3904.

74. Zhang RJ, Ning GL (2003) The mechanism of long afterglow phosphors $MAl_2O_4: Eu^{2+}$, RE^{3+}. Optoelectron Techn (in Chinese) 23: 30.

75. Liu YL, Ding H (2001) Advances in long lasting phosphorescent materials. Chinese J Inorg Chem 17: 181.

76. Qiu JR, Hirao K (1998) Long lasting phosphorescence in Eu^{2+}-doped calcium aluminoborate glasses. Solid State Commun 106: 795.

77. Zhang TZ, Su Q, Wang SB (1999) Luminescent properties of $MAl_2O_4: Eu^{2+}$, Re^{3+}, Chinese J Lumin 20: 170.

78. Aitasalo T, Holsa J, Jungner H, Lastusaari M, Niittykoski J (2001) Mechanisms of persistent luminescence in Eu^{2+}, RE^{3+} doped alkaline earth aluminates. J Lumin 94-95: 59.

79. Lin Y, Zhang ZL, Zhang ZT, Nan CW (2003) Influence of co-doping different rare earth ions on the luminescence of $CaAl_2O_4$-based phosphors. J. Eur Ceram Soc 23: 175.

80. Alvani AAS, Moztarzadeh F, Sarabi AA (2005) Effects of dopant concentrations on phosphorescence properties of Eu/Dy-doped $Sr_3MgSi_2O_8$. J Lumin 114: 131.

81. Pan W, Ning GL, Zhang X, Wang J, Lin Y, Ye JW (2008) Enhanced luminescent properties of long-persistent $Sr_2MgSi_2O_7$: Eu^{2+}, Dy^{3+} phosphor prepared by the co-precipitation method. J Lumin 128: 1975.

82. Lin YH, Tang ZL, Zhang ZT, Nan CW (2003) Luminescence of Eu^{2+} and Dy^{3+} activated $R_3MgSi_2O_8$-based (R = Ca, Sr, Ba) phosphors. J Alloy Compd 348: 76.

83. Wang XS, Lin YH, Zhang ZT (2002) Eu and Dy co-doped $Sr_2MgSi_2O_7$-based long afterglow photoluminescent materials. J Chin Ceram Soc 30: 216.

84. Dorenbos P (2005) Mechanism of persistent luminescence in $Sr_2MgSi_2O_7$:Eu^{2+}, Dy^{3+}. Phys Status Solidi B 242: R7.

85. Qi ZM, Shi CS, Liu M, Zhou DF, Luo XX, Zhang J, Xie YN (2004) The valence of rare earth ions in $R_2MgSi_2O_7$:Eu, Dy (R = Ca, Sr) long-afterglow phosphors. Phys Status Solidi A 201: 3109.

86. Zhang GB, Qi ZM, Zhou HJ, Fu YB, Huo TL, Luo XX, Shi CS (2005) Photoluminescence of (Eu^{2+}, Dy^{3+}) co-doped silicate long lasting phosphors. J Electron Spectrosc Relat Phenom 144-147: 861.

87. Setlur AA, Srivastava AM, Pham HL, Hannah ME, Hannek U (2008) Charge creation, trapping, and long phosphorescence in $Sr_2MgSi_2O_7$: Eu^{2+}, RE^{3+}. J Appl Phys 103: 053513.

88. Liu B, Shi CS, Yin M, Dong L, Xia ZG (2005) The trap states in the $Sr_2MgSi_2O_7$ and (Sr, Ca)$MgSi_2O_7$ long afterglow phosphor activated by Eu^{2+} and Dy^{3+}. J Alloy Compd 387: 65.

89. Wang XJ, Jia DD, Yen WM (2003) Mn^{2+} activated green, yellow, and red long persistent phosphors. J Lumin 102-103: 34.

90. Lei BF, Liu YL, Ye ZR, Shi CS (2004) Luminescence properties of $CdSiO_3$:Mn^{2+} phosphor. J Lumin 109: 215.

91. Abe S, Uematsu K, Toda K, Sato M (2006) Luminescent properties of red long persistence phosphors, $BaMg_2Si_2O_7$:Eu^{2+}, Mn^{2+}. J Alloy Compd 408-412: 911.

92. Ye S, Zhang J, Zhang X, Lu S, Ren X, Wang XJ (2007) Mn^{2+} activated red phosphorescence in $BaMg_2Si_2O_7$: Mn^{2+}, Eu^{2+}, Dy^{3+} through persistent energy transfer. J Appl Phys 101: 063545.

93. Aitasalo T, Hietikko A, Hreniak D, Holsa J, Lastusaari M, Niittykoski J, Strek W (2008) Luminescence properties of $BaMg_2Si_2O_7$:Eu^{2+}, Mn^{2+}. J Alloy Compd 451: 229.

94. Lin L, Yin M, Shi, CS, Zhang WP (2008) Luminescence properties of a new red long-lasting phosphor: Mg_2SiO_4: Dy^{3+}, Mn^{2+}. J Alloy Compd 455: 327.

95. Wang XX, Zhang ZT, Tang ZL, Lin YH (2003) Characterization and properties of a red and orange Y_2O_2S-based long afterglow phosphor. Mater Chem Phys 80: 1.

96. Yamamoto H, Matsuzawa H (1997) Mechanism of long phosphorescence of $SrAl_2O_4$:Eu^{2+}, Dy^{3+} and $CaAl_2O_4$:Eu^{2+}, Nd^{3+}. J Lumin 72: 287.

97. Jia DD, Wang XJ, Jia W, Yen WM (2007) Trapping processes of 5d electrons in Ce^{3+} doped $SrAl_2O_4$. J Lumin 122-123: 311.

98. Jia DD, Jia WY, Jia Y (2007) Long persistent alkali-earth silicate phosphors doped with Eu^{2+}, Nd^{3+}. J Appl Phys 101: 023520.

99. Su Q, Li CY, Wang J, Li J, Zhang YL, Guo CF, Lu YH (2005) Electron trapping materials doped with Rare Earth ions. Chinese J Lumin 26: 143.

100. Li CY, Su Q, Qiu JR (2003) Development of Long-lasting phosphorescent materials doped by RE ions. Chinese J Lumin 24: 19.

101. Lei BF, Liu YL, Ye ZR, Shi CS (2003) Multi-color long-lasting phosphorescence of rare earth ions in $CdSiO_3$ matrix. Chinese Science Bull 48: 2434.

102. Lei BF, Liu YL, ZYe ZR, Shi CS (2004) Upconversion of thulium-doped yttrium oxysulfide phosphor and its long-lasting phosphorescence. Electrochem Solid State Lett 7: G225.

103. Lei BF, Liu YL, Tang GB, Ye ZR, Shi CS (2004) Spectra and long-lasting properties of Sm^{3+}-doped yttrium oxysulfide phosphor. Mater Chem Phys 87: 227.

104. Lei BF, Liu YL, Liu J, Tang GB, Ye ZR, Shi CS (2004) Long-lasting properties of Rare Earth-doped Y_2O_2S phosphor. J Rare Earth Soc 22: 63.

105. Liu YL, Kuang JY, Lei BF, Shi CS (2005) Color-control of long-lasting phosphorescence (LLP) through rare earth ion-doped cadmium metasilicate phosphors. J Mater Chem 15: 4025.

106. Liu ZW, Liu YL (2005) Afterglow energy transfer in $Cd_3Al_2Ge_3O_{12}$: Dy. Phys Stat Sol A 202: 1814.

107. Liu ZW, Liu YL, Zhang JX, Rong JH, Huang LH, Yuan DS (2005) Long-lasting phosphorescence in Pr^{3+} and Li^+ co-doped $CaZrO_3$. Optics Commun 251: 388.

108. Liu ZW, Liu YL (2005) Synthesis and luminescent properties of a new green afterglow phosphor $CaSnO_3$:Tb. Mater Chem Phys 93: 129.

109. Kuang JY, Liu YL, Lei BF (2006) Effect of RE^{3+} as a co-dopant in long-lasting phosphorescence $CdSiO_3$:Mn^{2+} (RE = Y, La, Gd, Lu). J Lumin 118: 33.

110. Liu YL, Lei BF, Kuang JY, Shi CS, Meng JX, Man SQ, Tan SZ, Xiao Y, Yuan DS, Huang LH, Zhang JX (2009) Advances in Long Lasting Phosphorescent Materials. Chinese J Inorg Chem 25: 1323.

111. Ko JH (2003) Process for providing a titanium dioxide layer on material that contains a light absorbing substance and the product so formed. USA Patent US6569386.

112. Zhang JY, Pan F, Hao WC, Qi G, Wang TM (2004) Light-storing photocatalyst. Appl Phys Lett 85: 5778.

113. Aizawa H, Katsumata T, Takahashi J, Matsunaga K, Komuro S, Morikawa T, Toba E (2003) Long afterglow phosphorescent sensor materials for fiber-optic thermometer. Rev Sci Instrum 74: 1344.

114. Jia Y, Yei M, Jia WJ (2006) Stress-induced mechanoluminescence in $SrAl_2O_4$:Eu^{2+}, Dy^{3+}. Opt Mater 28: 974.

115. Wu BY, Wang HF, Chen JT, Yan XP (2011) Fluorescence resonance energy transfer inhibition assay for α-fetoprotein excreted during cancer cell growth using functionalized persistent luminescence nanoparticles. J Am Chem Soc 133: 686.

116. Geng BY, Ma JZ, Zhan FM (2009) A solution chemistry approach for one-dimensional needle-like $SrAl_2O_4$ nanostructures with Ln (Ce^{3+}, Eu^{2+} and Tb^{3+}) as activator/dopant. J Alloy Compd 473: 530.

117. Cheng BC, Fang LT, Zhang ZD, Xiao YH, Lei SJ (2011) $BaAl_2O_4$:Eu^{2+}, Dy^{3+} nanotube synthesis by heating conversion of homogeneous coprecipitates and afterglow characteristics. J Phys Chem C 115: 1708.

118. Guo CF, Luan L, Huang DX, Su Q, Lv YH (2007) Study on the stability of phosphor $SrAl_2O_4$:Eu^{2+}, Dy^{3+} in water and method to improve its moisture resistance. Mater Chem Phys 106: 268.

119. Mishra SB, Mishra AK, Revaprasadu N, Hillie KT, Steyn WJV, Coetsee E, Swart HC (2009) Strontium aluminate/polymer composites: morphology luminescent properties, and durability. J Appl Polym Sci 112: 3347.

120. Mishra SB, Mishra AK, Luyt AS, Revaprasadu N, Hillie KT, Steyn WJ, Coetsee E, Swart HC (2010) Ethyl vinyl acetate copolymer-$SrAl_2O_4$:Eu^{2+}, Dy^{3+} and $Sr_4Al_{14}O_{25}$: Eu^{2+}, Dy^{3+} phosphor-based composites: preparation and material properties. J Appl Polym Sci 115: 579.

121. Ben DB, Swart HC, Luyt AS, Coetzee E, Dejene FB (2010) Properties of green $SrAl_2O_4$ phosphor in LDPE and PMMA polymers. J Appl Polym Sci 117: 2635.

122. Sooraj HN, Prabhakara RY, Buddhudu Y (2001) Luminescence spectral of Eu^{3+} doped GeO_2-PbO-Bi_2O_3 glasses. Mater Res Bull 36: 1813.

123. Qiu JR, Kojima K, Miura, Mitsuyu T, Hirao K (1999) Infrared femtosecond laser pulse-induced permanent reduction of Eu^{3+} to Eu^{2+} in a fluorozirconate glass. Opt Lett 24: 786.

124. Qiu JR, Kawasaki M, Tanaka K, Shimizugawa Y, Hirao K (1998) Phenomenon and mechanism of long lasting phosphorescence in Eu^{2+}-doped calcium aluminoborate glasses. Phys Chem Solids 59: 1521.

125. Yamazaki M, Yamamoto Y, Nagahama S, Sawanobori N, Mizuguchi M, Hosono H (1998) Long luminescent glass: Tb^{3+} activated ZnO-B_2O_3-SiO_2 glass. J Non-Cryst Solids 241: 71.

126. Lin YH, Zhang ZT, Chen QM, Tang ZL, Gong JH (2000) A study on preparation of long afterglow photoluminescence glass and its properties. Mater Sci Technol (in Chinese) 8: 1.
127. Chen QM, Lin YH, Zhang ZT, Tang ZL (2001) Studies on preparation of long afterglow luminescent glass and its properties. Funct Mater (in Chinese) 32: 208.
128. Lin YH, Chen QM, Zhang ZT, Tang ZL (2002) Influence of sintering conditions on the optical properties of long afterglow luminescent glass. J Inorg Mater (in Chinese) 15: 982.
129. Li CY, Wang SB, Su J (2002) Long-lasting Phosphorescence in Eu^{2+}, Dy^{3+} Co-doped Strontium Aluminoborate Glass-ceramic. Chinese J Lumin 23: 233.
130. Su Q, Li CY, Lv YH (2001) Manufacturing method of Rare earth yellow-green long afterglow glass. China Patent 1305967.
131. Su Q, Li CY, Lv YH (2001) Manufacturing method of red, green, yellow, long afterglow from zinc borosilicate glass. China Patent 1317456A.
132. Li CY, Su Q, Wang SB (2002) Multi-color long-lasting phosphorescence in Mn^{2+}- doped ZnO-B_2O_3-SiO_2 glass ceramics. Mater Res Bull 37: 1443.
133. Huang LH, Chen WX, Liu YL (2006) Preparation and luminescent properties studies of strontium aluminoborate luminescent glasses. Funct Mater (in Chinese) 37: 861.
134. Xiao LY, Xiao Q, Liu YL, Ai PF, Li YD, Wang HJ (2010) A transparent sur-face-crystallized Eu^{2+}, Dy^{3+} codoped strontium aluminate long-lasting phosphorescent glass-ceramic. J Alloy Compd 495: 72.
135. Zhang XY, Guo Y, Bai CH, Wang XR, Cao ZF (2002) Preparation of $SrAl_2O_4$:Eu^{2+}, Dy^{3+}, photoluminescence enamel coating. Mater Sci Technol (in Chinese) 3: 314.
136. Maldiney T, Richard C, Seguin J, Wattier N, Bessodes M, Scherman D (2011) Effect of core diameter, surface, coating, and PEG chain length on the biodistribution of persistent luminescence nanoparticles in mice. ACS Nano 2: 854.
137. Maldiney T, Byk G, Wattier N, Seguin J, Khandadash R, Bessodes M, Richard C, Scherman D (2012) Synthesis and functionalization of persistent luminescence nanoparticles with small molecules and evaluation of their targeting ability. Int J Pharm 423: 102.
138. Maldiney M, Kaikkonen MU, Seguin J, Chermont QM, Bessodes M, Airenne KJ, Herttuala SY, Scherman D, Richard C (2012) In vitro targeting of avidin-expressing glioma cells with biotinylated persistent luminescence nanoparticles. Bioconjugate Chem 23: 472.
139. Takayama T, Katsumata T, Komuro S, Morikawa T (2005) Growth and characteristics of a new long afterglow phosphorescent yttrium tantalite crystal. J Cryst Growth 275: 2013.
140. Katsumata T, Kohno Y, Kubo H, Komuro S, Morikawa T (2005) Low temperature fluorescence thermometer application of long afterglow phosphorescent $SrAl_{12}O_{19}$:Eu^{2+}, Dy^{3+} crystals. Rev Sci Instrum 76: 084901.
141. Akiyama M, Nishikubo K, Nonada K (2003) Intense visible light emission from stress-activated $SrMgAl_6O_{11}$:Eu. Appl Phys Lett 83: 650.
142. Chandra VK, Chandra BP (2012) Dynamics of the mechanoluminescence induced by elastic deformation of persistent luminescent crystals. J Lumin 132: 858.
143. Fontenot RS, Hollerman WA, Bhat KN, Aggarwal MD (2012) Effects of Added Uranium on the Triboluminescent Properties of Europium Dibenzoylmethide Triethylammonium. J Lumin 134: 477.
144. Jha P, Chandra BP (2014) Survey of the literature on mechanoluminescence from 1605 to 2013. Lumin 29: 977.
145. Li CS, Xu CN, Zhang L, Yamada H, Imai Y, Wang WX (2008) Dynamic visualization of stress distribution on metal by mechanoluminescence images. J Visual-Japan 11: 329.
146. Wang WX, Imai Y, Xu CN, Matsubara T, Takao Y (2011) A new smart damage sensor using mechanoluminescence material. Mater Forum 675-677: 1081.
147. Kim WJ, Lee JM, Kim JS, Lee CJ (2012) Measuring high speed crack propagation in concrete fracture test using mechanoluminescent material, Smart structures and systems 10: 547.
148. Yang R, Yang YX, Hu DD, Cui B, Tang ZX (2001) Origins and mechanisms of the triboluminescence. Chem Res Appl (in Chinese) 13: 10.

149. Sun ZX, Liu YL, Huang LH, Chen WX (2004) Study of preparation and photocatalytic properties of new type complex material $CaAl_2O_4$: Eu^{2+}, Dy^{3+} coated by TiO_2. Huaxue Jiancai (in Chinese) 6: 46.
150. Zhong JB, Wang JL, Tao L, Gong MC, Liu ZM, Chen YQ (2007) Photocatalytic degradation of gaseous benzene over TiO_2/Sr_2CeO_4: preparation and photocatalytic behavior of TiO_2/Sr_2CeO_4. J Hazard Mater 140: 200.
151. Zhong JB, Ma D, He XY, Li JZ, Chen YQ (2009) Sol-gel preparation and photocatalytic performance of $TiO_2/SrAl_2O_4$: Eu^{2+}, Dy^{3+} toward the oxidation of gaseous benzene. J Sol-gel Sci Techn 52: 140.
152. Li HH, Yin S, Wang YH, Sato T (2012) Persistent fluorescence-assisted $TiO_{2-x}N_y$-based photocatalyst for gaseous acetaldehyde degradation. Environ Sci Technol 46: 7741.

Chapter 7
Foundations of Up-conversion Nanoparticles

Song Wang and Hongjie Zhang

Abstract Up-conversion is an anti-Stokes optical process that can emit ultraviolet/visible/near-infrared light by converting low-energy near-infrared excitation photon radiation. With the advent of nanotechnology and the inexpensive high-power infrared diode lasers, the rare earth-doped up-conversion luminescent nanoparticles have been extensively studied for its potential applications in various fields. In recent years, rare earth-doped up-conversion nanoparticles have been developed as a promising alternatives luminescent optical labels to organic fluorophores and quantum dots for applications in biological assays and medical imaging. The unique optical property of rare earth-doped up-conversion nanoparticles offers low autofluorescence, less scattering and absorption, and deep penetration in biological samples. In this chapter, we give a general introduction to rare earth up-conversion nanoparticles, including the rare earth up-conversion materials, up-conversion mechanisms, synthesis methods, surface modifications, optical properties tuning and so on.

7.1 Introduction

The up-conversion luminescence (UCL) refers to the nonlinear anti-Stokes optical process that converts two or more low-energy pump photons to a higher-energy output photon. Since the UC phenomena in 1959 were first discovered by Bloembergen [1], who proposed a conceptual device named "infrared quantum

S. Wang · H. Zhang (✉)
State Key Laboratory of Rare Earth Resource Utilizations, Changchun Institute
of Applied Chemistry, Chinese Academy of Sciences, Changchun 130022, Jilin, China
e-mail: hongjie@ciac.jl.cn

S. Wang
e-mail: wangsong1984@126.com

S. Wang
Hubei Key Laboratory of Low Dimensional Optoelectronic Materials and Devices,
Hubei University of Arts and Science, Xiangyang 441053, Hubei, China

counter" the UCL phenomenon has been observed in most rare earth (RE) elements, and a few transition metals, actinides and organic dyes [2]. The anti-Stokes process often occurs in following ways: simultaneous two-photon absorption (STPA), second-harmonic generation (SHG), excited-state absorption (ESA) and energy transfer UCL (ETU) (Fig. 7.1) [3, 4].

STPA is referred to the process in which two low-energy photons are absorbed simultaneously to get the two-photon absorption molecules excited. SHG happens under coherent radiation with highly hyper-polarizable materials, in which the emission doubles the frequency of the incident light. In 1961, SHG was first discovered by Franken et al. [5], who observed second-harmonic light (0.3471 μm) when ruby laser light (0.6943 μm) was getting through a quartz crystal. Simultaneous two-photon absorption (STPA) and second-harmonic generation (SHG) are two well-established methods for generating anti-Stokes emissions from organic dyes and semiconducting nanoparticles etc. However, either expensive pulsed lasers with high-density excitation (10^6–10^9 W/cm^2) or nonlinear optical materials with non-centrosymmetric atomic or molecular organization are required for these methods [6]. Alternatively, the UC process in rare earth-doped inorganic materials, classified by ESA or ETU, has emerged as a more efficient way. As the RE ions have special f-block electronic configuration, for which the 4f electrons at inner shells are effectively shielded by the closely lying 5 s and 5p sub-shells. This is responsible for the important optical phenomena of RE ions such as sharp and narrow f–f transition bands. And the f–f transitions are Laporte forbidden, resulting in low transition probabilities and long-lifetime (up to 0.1 s) excited states. Several metastable intermediate energy states of RE ions can participate in the typical up-conversion process. The long-lifetime metastable energy levels of the RE ions enable the sequential multiphoton (in microsecond time) to be pumped to the emission state and then produce the intense anti-Stokes photoluminescence under relatively low laser power (about 1 W/cm^2) [7–9].
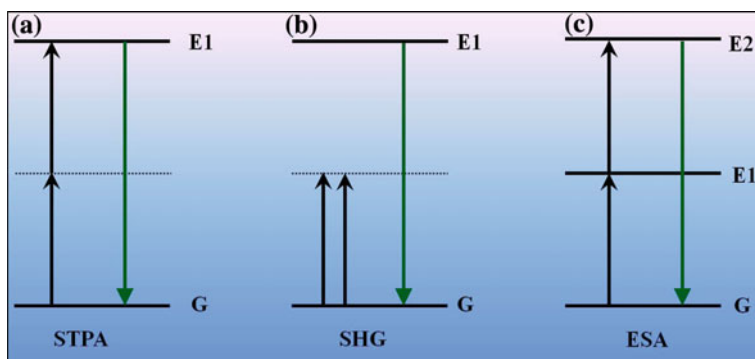
Fig. 7.1 Schematic representation of three common anti-Stokes processes that convert low-energy photon to higher energy emission output *SHG* Second-harmonic generation, *STPA* Simultaneous two-photon absorption, and *ESA* excited-state absorption

With the advent of nanotechnology and the inexpensive high-power infrared diode lasers, the RE^{3+}-doped up-conversion luminescent nanoparticles (UCNPs) have been extensively studied for its significant applications in the fields of analytical sensors, photodynamic therapy, solar energy conversion and especially for biological applications [10–14]. The UCNPs possess fascinating features, including low autofluorescence, less scattering and absorption, and deep penetration in biological samples. As a result, viable and robust methodologies have been developed to prepare RE UCNPs with uniform sizes and shapes, and sufficient brightness. In this chapter, we will focus on foundations of RE UCNPs, including the RE UC materials, UC mechanisms, synthesis methods, surface modifications, optical properties tuning of the UCNPs.

7.2   The RE Up-conversion Luminescent Materials

Typically, an UCL material is composed of inorganic host matrix and doping ions (usually including activator and sensitizer). The general strategy to get new up-conversion material involves the following two methods: changing the host materials and variation of the dopant ions in the host lattice [15, 16]. Changing the host materials (differing the phonon energy) may dramatically influence the multi-phonon relaxation as well as energy transfer process, which may lead to an entirely different up-conversion luminescence behavior. For example, one can reduce the efficiency of multi-phonon relaxation processes by changing from high phonon energy oxide to low phonon energy fluoride. The change of doping ions has a dramatic effect on the emission properties and energy transfer process of a material. The most obvious effect is a change in the color of the emitted light. For example, green up-conversion emission can be obtained in Er^{3+}/Yb^{3+}-doped $NaYF_4$ nanoparticles and blue emission can be obtained in Tm^{3+}/Yb^{3+}-doped $NaYF_4$ nanoparticles. Based on the abundant energy level RE ions, a possible broad up-conversion spectrum can be obtained by the appropriate selection of the host lattice, doping and codoping ions. This section will focus on doping ions (activators and sensitizers) and host materials of RE UCNPs.

7.2.1   Doping Ions

Theoretically, up-conversion emission can be realized in most lanthanide ions [16–18]. However, to get an efficient up-conversion emission, the energy difference between the excited level and its lower-lying level should be approached to excitation photon energy or energy transfer steps in up-conversion processes. Up to now, Er^{3+}, Tm^{3+}, and Ho^{3+} are recognized as the most effective activators in up-conversion materials due to their ladder-like arranged energy levels (Fig. 7.2). Particularly, the up-conversion efficiency of Er^{3+} is relative higher than the other

two ions due to its multiple gaps with similar photon energy (Fig. 7.2d). For example, the energy difference between the $^4I_{11/2}$ and $^4I_{15/2}$ level in Er^{3+} (about 10350 cm^{-1}) is similar to that between the $^4F_{7/2}$ and $^4I_{11/2}$ levels (about 10370 cm^{-1}). And the energy difference between $^4F_{9/2}$ and $^4I_{13/2}$ levels is in the same region, too. Thus, the energy levels of $^4I_{15/2}$, $^4I_{11/2}$, $^4F_{9/2}$ and $^4F_{7/2}$ can be used to generate up-conversion emission using 976 nm (10246 cm^{-1}) excitation. Hence, at least three different transitions in Er^{3+} ions can be induced by 976 nm laser diode excitation, leading to green ($^2H_{11/2}, ^4S_{3/2} \rightarrow ^4I_{15/2}$) and red ($^4F_{9/2} \rightarrow ^4I_{15/2}$) light emissions (Fig. 7.2a) [2, 16]. Moreover, if the pump power of laser is high enough, emission bands in the near violet region ($^2G_{7/2} \rightarrow ^4I_{15/2}$), 380 nm ($^4G_{11/2} \rightarrow ^4I_{15/2}$), the violet band ($^2H_{9/2} \rightarrow ^4I_{15/2}$) (Fig. 7.2d) and the blue band ($^4F_{7/2} \rightarrow ^4I_{15/2}$) can be obtained. The blue ($^1G_4 \rightarrow ^3H_6$ centered at 480 nm), red ($^1G_4 \rightarrow ^3H_5$ centered
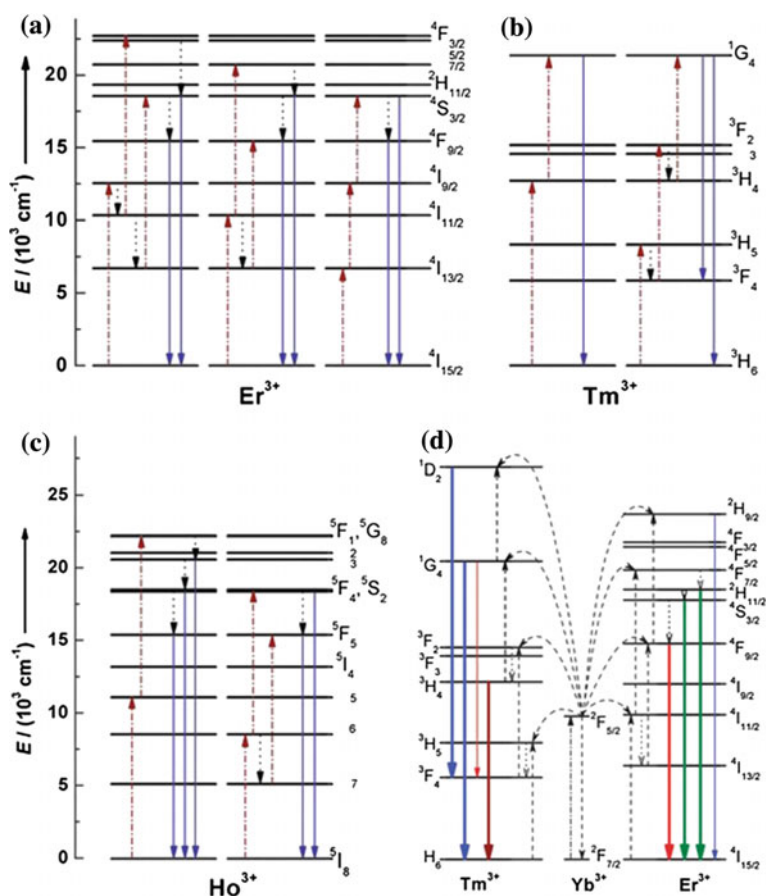
Fig. 7.2 Energy level diagram of the Er^{3+}, Ho^{3+}, Tm^{3+} and Yb^{3+} ions and corresponding typical UCL processes **a–d** Reprinted with the permission from Ref. [16]. Copyright 2009 Royal Society of Chemistry

at 650 nm) and near-infrared ($^3H_4 \rightarrow \, ^3H_6$ centered at 800 nm) emissions can be accomplished in the Tm^{3+}-doped materials (Fig. 7.2d), too. Generally, the NIR emission is significantly more intense than the blue and red up-conversion emissions. And, green emission centered at 545 nm ($^5F_4$, $^5S_2 \rightarrow \, ^5I_8$) and weak red emission centered at 650 nm ($^5F_5 \rightarrow \, ^5I_8$) can be obtained in Ho^{3+}-doped materials (Fig. 7.2c).

It is worth to note that the range of effective doping concentrations is severely limited due to the cross-relaxation process. High doping concentration will lead to the quenching of pump energy. But, the low doping levels will lead to low absorption of the pump light. Either of these two doping levels will result in low luminescence efficiency. So, a strong excitation light absorbing ions called sensitizers can be codoped in the host material to ensure efficient energy transfer to the activator [15, 16]. The sensitizer is usually codoped with the activator to enhance the efficient ETU process between the sensitizer and activator [18]. The most widely utilized sensitizer for Er^{3+}, Ho^{3+} and Tm^{3+} ions is Yb^{3+} ion. As Yb^{3+} ion possesses only one excited 4f level of $^2F_{5/2}$ (Fig. 7.2d). The energy difference between the ground state $^2F_{7/2}$ and excitation state $^2F_{5/2}$ (about 10000 cm^{-1}) of Yb^{3+} matches well with several emission energy of Er^{3+} mentioned above, allowing an efficient energy transfer process between the two ions. Usually, the concentration of codoped Yb^{3+} is relatively high (18–20 mol%) [2, 16].

7.2.2 Host Materials

The lattice and anions of the host materials have a significant influence on the up-conversion properties including emission intensity and color. The lattice of the host materials will determine the distance between the doping RE ions, relative spatial position and coordination numbers. Therefore, it is essential to choose an appropriate host material for favorable luminescent properties such as high up-conversion efficiency and controllable emission profiles. The general rule for selecting a host material is low phonon energy and close lattice match to the dopant ions as host lattice with low phonon energies can minimize nonradiative losses and maximize the radiative emission [16]. The close matching of lattice of the host materials to dopant ions is required to readily incorporate RE dopant ions. Moreover, an ideal host matrix should be easily obtained with small size, uniform shape and narrow size distribution.

Up to now, the UCL process has been widely studied in various nanoscale host materials, such as fluorides, oxides, heavy halides (chlorides, bromides and iodides), oxysulfide, phosphates and vanadates. The heavy halides generally exhibit low phonon energies no more than 300 cm^{-1}. However, they are hygroscopic, which will be of limited usage in wet chemical atmosphere. The oxides exhibit much higher chemical stability, but they have relatively high phonon energies larger than 500 cm^{-1} due to the stretching vibration of the host lattice. Alternatively, fluorides usually exhibit low phonon energies (about 350 cm^{-1}) and high chemical

stability [15, 16]. So, RE fluorides including binary REF_3 and complex $AREF_4$ (RE = rare earth; A = alkali) are considered as most commonly used host materials for the fabrication of UCNPs [19–25]. Up to now, Yb/Er co-doped hexagonal $NaYF_4$ nanocrystals are identified as the most efficient UCNPs. However, one challenge of $NaYF_4$-based UCNPs is that it is hard to obtain ideal nanocrystals with smaller size (less than 10 nm). So, extensive attention has also been paid to the fabrication of other fluoride, hybrid and composite materials incorporating RE fluoride UCNPs. For example, other fluorides such as $NaLuF_4$ [26–28], $BaLuF_5$ [29], $NaYbF_4$ [30], $KGdF_4$ [31], CaF_2 [32, 33] and Na_xScF_{3+x} [34] are recently additional choices as host materials to obtain small sized and bright UCNPs. Very recently, hybrid host materials such as Gd [35, 36], Mn [37], ^{18}F [38, 39] and ^{153}Sm [40–42] doped $NaREF_4$ (RE = Y, Yb, and Lu) have been well investigated as CT/MRI/PET/optical contrast agents.

7.2.3 The RE Up-conversion Nanoparticles

The RE-doped UCNPs are composed of trivalent RE ions dispersed in an appropriate host lattice with at least one dimension of less than 100 nm. The dopants of RE are optically active centers mentioned above, which produce UC emission. The UCNPs have similar optical properties to the corresponding bulk materials. They both produce the same up-conversion luminescence peaks due to the electronic transitions between 4f–4f orbitals which are well-shielded by the outer complete 5 s and 5p shells. However, the luminescent efficiency and the relative intensity between different emission peaks of UCNPs are quite different from their bulk materials. Due to the high surface-to-volume ratio of the nanoparticles, more RE dopants are exposed to surface deactivations (such as surface defects, ligands and solvents). Firstly, the dopants located on or near the surface of the UCNPs can be deactivated by neighboring quenching centers. Secondly, the dopants located in the center of NCUPs can randomly migrate and travel a long distance to the surface quenching sites. As a result, the luminescent efficiency of UCNPs is found much lower than their bulk materials. So, it is crucial to find a feasible way to enhance emission intensity of UCNPs in the synthesis procedure.

7.3 Mechanism of the RE UCNPs

Several mechanisms either alone or in combination have been recognized to be participate in the UC process of RE-doped materials, including excited-state absorption (ESA), energy transfer UC (ETU), cooperative sensitization up-conversion (CSU), photon avalanche (PA), and cross-relaxation (CR), and these are illustrated in Fig. 7.3 [43–46].
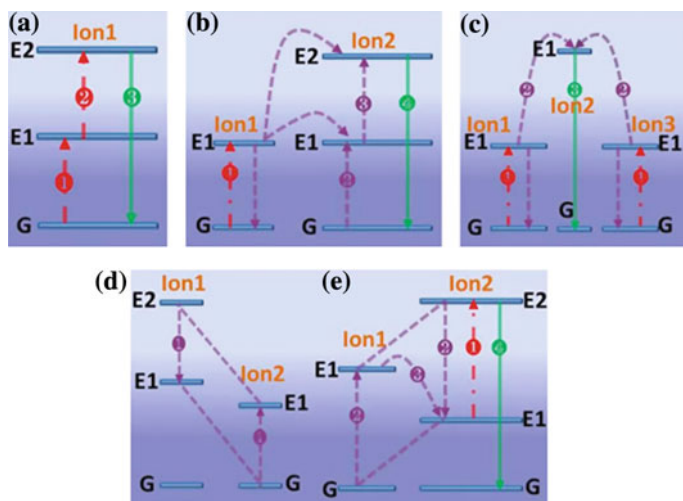
Fig. 7.3 Principal up-conversion processes for RE UCNPs **a** excited-state absorption (ESA), **b** energy transfer up-conversion (ETU), **c** cooperative sensitization up-conversion (CSU), **d** cross-relaxation (CR), and **e** photon avalanche (PA). The *red*, *violet*, and *green lines* represent photon excitation, energy transfer, and emission processes, respectively. **a–e** Reprinted with the permission from Ref. [47]. Copyright 2014 American Chemical Society

Excited-state Absorption. The universal energy diagram of the ESA process is a simple three-energy level system (Fig. 7.3a) [47]. The excitation is realized by successive absorption of pump photons by a single ground-state ion. Firstly, an ion is excited from the ground state to the E1 level. Before it decays to the ground state, a second pump photon promotes the ion from E1 to E2 level. Consequently, UC emission will occur by radiative transition from E2 level to the ground state. To achieve highly efficient ESA, a ladder-like energy level configuration of active ion is required.

Active ion with a long lifetime of energy levels is necessary to make sure the second photon can be pumped to a higher energy level. Some RE ions such as Er^{3+}, Ho^{3+}, Tm^{3+}, and Nd^{3+} own such energy level configurations [47]. The commercially available diode lasers with the wavelength at 976 or 808 nm match well with the excitation wavelength of these ions. It is worth to note that the ESA process is a single ions absorption process and thus independent on the doping concentrations. It is no need for the exciting source to strictly match the RE energy level in the ESA process, as the phonons of host materials can also participate in the process.

Energy Transfer Up-conversion. Similar to ESA process, the ETU process utilizes sequential absorption of two photons to populate the energy level with long lifetime. The essential difference is that ESA process occurs within a single RE ion, while ETU involves two neighboring ions [47]. In ETU process, an ion (1) known as the sensitizer is firstly excited from the ground state to its excited state E1 after absorbing a pump photon. Then energy is transferred from the excited state of ion1

to the ground state G of ion2, known as the activator. The ion2 will be excited to the state E1, while ion1 relaxes back to ground state G and the first step of energy transfer is fulfilled. The excited ion2 can be pumped to its upper emitting state E2 by second step energy transfer and finally fulfills the UC emission (Fig. 7.3b). Different from the ESA process, the dopant concentration has a strong influence on the UC efficiency in the ETU up-conversion process, as it determines the average distance between the neighboring doping ions. Generally speaking, an optimized UCNP should be a sensitizer–activator system containing a sensitizer Yb^{3+} with no more than 20 mol%, and an activator with the concentration below 2 mol%, to minimize the loss of excitation energy by cross-relaxation process. Actually, the ETU and ESA are concurrent or cooperated process in many up-conversion materials. The phonon in the crystal lattice is allowed to participate in the up-conversion process to make up for the energy mismatch.

Cooperative Sensitization Up-conversion. CSU is a process taking place by the interaction among three ions (Fig. 7.3c) [47]. When irradiated with excitation photons, both ion1 and ion3 (considered as sensitizers) can be excited to the state E1, respectively. Then ion1 and ion3 will interact with ion2 (activator) simultaneously and excite ion2 to a higher state E1. The excited ion2 relaxes to its ground state by emitting an up-conversion photon. But the CSU process is related to quasi-virtual pair levels during transitions, which is needed quantum mechanically in a higher order of perturbation. So the efficiency of CSU process is usually orders of magnitude lower than that of ESA or ETU process. For example, CSU process can be realized in Yb^{3+}/Tb^{3+}, Yb^{3+}/Eu^{3+} codoped materials [48, 49].

Cross-relaxation. Generally, CR is same as the ETU process. But it is considered as a detrimental process in up-conversion phosphors. It takes place from ion–ion interaction through an energy transfer process of E2 (ion1) + G (ion2) → E1 (ion1) + E1 (ion2) [47]. Ion1 and ion2 can be either the same or not, and the two ions can be in their excited state in some cases. If ions are same, CR process will cause "concentration quenching", which significantly decreases the emission intensity. But it can be intentionally used in up-conversion color-tuning materials or constructing efficient PA mechanism.

Photon Avalanche. The phenomenon of PA was first discovered in Pr^{3+}-doped $LaCl_3$ crystal-based infrared quantum counters by Chivian and coworkers in 1979 [50]. The PA is a looping process that involves processes of ESA for excitation light and an efficient energy transfer process that produces feedback. The PA process is initiated with excitation of level E1 of ion2 by ground-state absorption (GSA). By resonant ESA process to populate upper level E2. Then, an efficient energy transfer process of E2 (ion2) + G (ion1) → E1 (ion2) + E1 (ion1) between ion1 and ion2 occurs, resulting in both ions occupying the intermediate level E1. The two ions can be pumped to level E2 by further energy transfer. This will increase level E2 population by ESA exponentially, which produces strong UC emission as an avalanche process. In addition to high pump intensity, PA-induced up-conversion also requires long response time to excitation source (up to several seconds) [47, 50]. There are two important characteristics of the PA process. First, the pump energy matches energy gap between the excited stated to up higher

energy level other than it between the ground state to the excited state. Second, PA-induced up-conversion requires a pump intensity above a certain threshold value (Fig. 7.3e). When the pump intensity is below the threshold, little up-conversion luminescence can be detected, while the photoluminescence intensity will be increased by orders of magnitude when pump intensity is above the pump threshold.

7.4 Synthesis of Up-conversion Nanoparticles

In order to get high-quality lanthanide-doped up-conversion nanoparticles with controlled composition, crystalline phase, shape, and size, the design and controllable synthesis of high-quality UCNPs are very critical. There are two different approaches to fabricate nanocrystals: the physical "top-down" methods, and the solution-phase chemistry (wet chemistry) "bottom-up" approach [51]. The physical methods are the production of a large quantity of nanocrystals without uniform size and shape. In contrast, the wet chemical methods can be used to synthesize uniform nanocrystals with controlled particle size, but generally only sub-gram output can be obtained.

Even so, dramatic attentions of the synthesis of RE-based UCNPs have been devoted to the "wet chemical methods". The experimental parameters, such as temperature, reaction time, concentration of precursors, pH values of the system, templates, and mineralizer, can be precisely adjusted, which allows the fine control of size, shape and chemical homogeneity of the products. So far, the typical "wet" synthetic methods can be classified as follows: thermal decomposition, hydro (solvo) thermal reaction, coprecipitation, and newly developed methods including microwave-assisted synthesis and ionic liquid-based routes.

Thermal decomposition is one of the most popular methods to obtain high-quality UCNPs with well-defined shapes, easily controlled sizes and dispersed in nonpolar solvents. Generally, it involves two steps. Firstly, organic precursors are dissolved in organic solvents with a high boiling point under the assistance of surfactants. Secondly, those precursors will be decomposed at an elevated temperature afterward. Typically, the organic precursors are the RE organic acid compounds (e.g., trifluoroacetate, acetoacetate, oleate, etc.). The surfactants involve polar capping groups and long hydrocarbon chains, such as oleic acid (OA) and oleylamine (OM). Yan et al. [52] first reported the preparation of highly monodispersed LaF_3 triangular nanoplates from the single precursor La $(CF_3COO)_3$ in OA/1-octadecene (ODE) media (Fig. 7.4a, b). Then, this method was soon extended to the synthesis of $NaREF_4$ and $NaYF_4$-based UCNPs [54–56]. By the co-thermolysis of CF_3COONa, $Y(CF_3COO)_3$, $Yb(CF_3COO)_3$, and $Er(CF3COO)_3$ (or $Tm(CF_3COO)_3$) in OA/OM/ODE, high-quality $NaYF_4$:Yb,Er/Tm nanoparticles could be obtained (Fig. 7.4c,d) [53]. The mechanism of this method is referred to go through four stages: (1) the nucleation in the initial time, (2) the growth of nanoparticles supplied by monomer, (3) the size shrinkage by dissolution, and
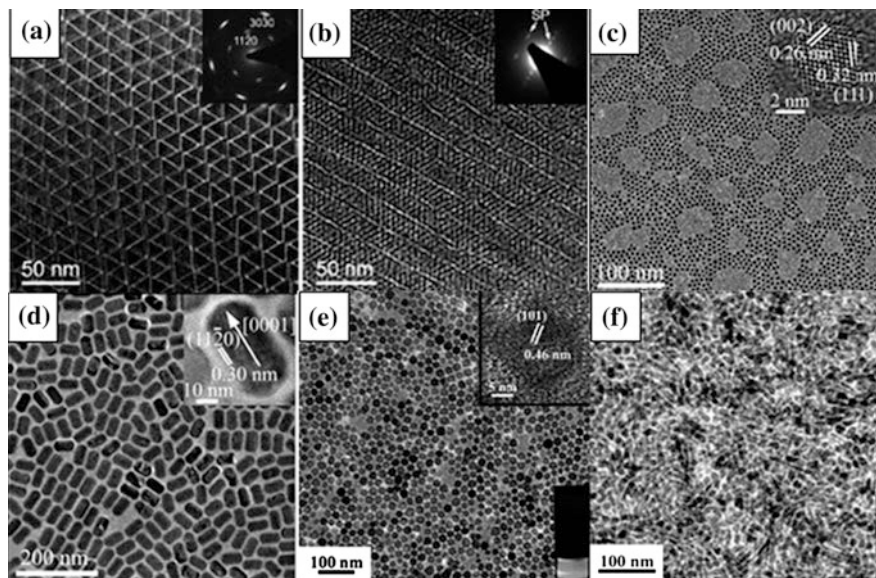
Fig. 7.4 Representative shapes of various rare earth fluoride nanoparticles by a single-source precursor or multiple-source precursors thermal decomposition of rare earth trifluoroacetate RE $(CF_3COO)_3$. TEM images (**a–f**) of typical fluoride nanoparticles **a** edge-to-edge and **b** face-to-face super lattices (SP) of LaF_3 nanoplates. Insets are the SAED patterns. (Adapted from Ref. [52], copyright 2005 American Chemical Society), **c** α-$NaYF_4$ nanopolyhedra and **d** β-$NaYF_4$ nanorods. (Adapted from Ref. [53], copyright 2006 American Chemical Society), **e** $LiYF_4$:20 % Yb^{3+},2 %Er^{3+} nanopolyhedra and **f** KYF_4 nanocrystals (Adapted from Ref. [57], copyright 2009 Royal Society of Chemistry)

(4) the aggregation [54]. This method was found to be viable for the synthesis of $LiREF_4$ and $KREF_4$ UCNPs (Fig. 7.4e, d) [57]. Similar synthetic methods were also reported individually by Yi's group [58] and Capobianco's group [59], and a wealth of representative research results were subsequently published [60–62]. Two/multi-step thermal decomposition is also developed for constructing core–shell structure of UCNPs to enhance the intensity of up-conversion emission and induce functional components [63–69]. For the first step, UCNPs cores are prepared through the thermal decomposition. Then, these cores are used as seeds and a homogeneous or heterogeneous layer grows around the cores to form core–shell structure via the similar procedure.

However, the thermal-decomposition method exhibits also some drawbacks, such as the high-cost and toxic precursors in some cases, the rigorous experimental conditions (relative high temperature, waterless, oxygen-free and inert gas protection). Moreover, the nanocrystals produced by the thermal decomposition method need be stabilized by surfactants and can only be dispersed in nonpolar or weak polar solvents. Therefore, post-modification processes are required to introduce hydrophilic and biocompatible coatings on those nanocrystals.

The hydro (solvo) thermal method is another typical solution-based approach, which features superheated solvents (water or organic solvents) and the autogenic high pressure in autoclaves to increase the solubility and reactivity of precursors. As a result, the products provided by this method usually exhibit high crystallinity and fewer defects than other wet chemistry methods. This method possesses several acceptable advantages, including the convenient operation condition, the relatively low reaction temperature (usually below 250 °C), fine controlled size and morphology of the products, etc. Generally, hydro(solvo) thermal reactions require the addition of an appropriate organic additive with functional groups known as the complex agent or structure-directing agents, such as polyvinylpyrrolidone [70], polyethylene glycol [71], polyethylenimine [72], ethylenediaminetetraacetic acid [73], cetyltrimethylammonium bromide [74], and trisodium citrate [75]. By utilizing this method, various kinds of UCNPs, such as oxide [76], fluoride [77, 78], oxyfluoride [79], vanadate [80], phosphate [81], and oxysulfide [82] with the fine control of size, shape and structures can be prepared. One representative example of hydrothermal synthesis for preparing high-quality RE UCNPs is a liquid–solid–solution strategy developed by Li's group. This strategy is based on a general phase transfer and separation mechanism that occurs at the interfaces of the liquid, solid, and solution phases present during the hydrothermal process [83]. Based on this strategy, UCNPs with various shapes, such as nanospheres, nanorods, nanospindles and nanotubes, were synthesized follow-up [84–87]. Lin's group systematically investigated the mechanism of hydrothermal synthesis for different shapes of RE-based nano-/microcrystals [87]. It was reported that the organic additive trisodium citrate, the fluoride source, and the pH value of the initial solution have great effects on the shapes of the product (Fig. 7.5). However, by using hydrothermal synthesis, it is hard to produce ultra-small (less than 10 nm) and monodispersed nanocrystals.

Coprecipitation is one of the classic methods, which usually provides favorable phase purity products by using simple procedures. This method can be easily scaled up for massive production. It is worth to note that different ions possess different precipitation rates due to their own chemical natures. Thus, coordination agents are usually introduced for adjusting the coprecipitation procedure. However, subsequent heat treatment is often necessary to improve the crystallinity of the products (ranging from 400 to 600 °C). For example, this method was adopted by Yi's group to prepare $LaF_3:Yb^{3+}$, $Er^{3+}/Ho^{3+}/Tm^{3+}$ UCNPs with particle sizes of 5.4 ± 0.9 nm [88]. By using ethylenediamine tetraacetic acid as the chelating reagent, they also prepared nearly monodispersed $NaYF_4:Yb^{3+}$, Er^{3+} nanoparticles. By adjusting the molar ratio of EDTA to RE ions, the particle size could be controlled in the range of 37–166 nm [89].

Recently, the green solvent ionic liquids (ILs) have been utilized in many synthesis fields due to their unique properties, such as non-volatilization, non-flammability and high thermally stability. The main advantage of using ILs as solvents or additives is their superior capability to dissolve and stabilize the metal ions. Particularly, some ILs contains fluorine atoms (e.g., tetrafluoroborates, hexafluorophosphates). They can serve as the fluoride source during the synthesis of RE fluorides. For example, Kong's group synthesized water-soluble and pure
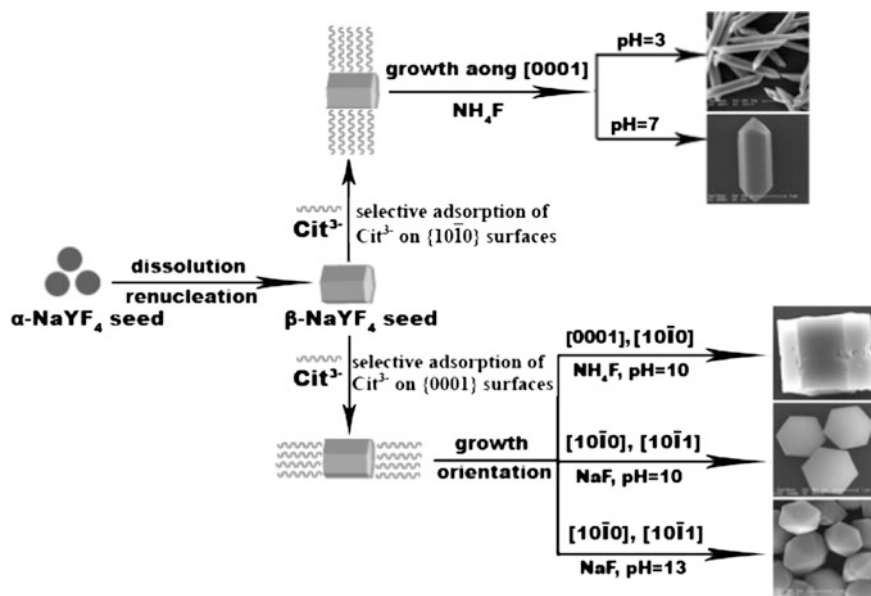
Fig. 7.5 Schematic illustration of the possible formation processes of the β-NaYF4 Microcrystals with various morphologies under different experimental conditions (Adapted from Ref. [87], copyright 2007 American Chemical Society)

β-NaYF$_4$:Yb^{3+}/Er^{3+} UCNPs for the first time by an ionothermal method. The key point to this method is the utilization of an ionic liquid, [BMIM] [BF$_4$], which acts as solvent and template, as well as fluoride source [90]. Yan's group also used this IL route to prepare NaYF$_4$ nanoclusters in combination with microwave irradiation [91].

As an efficient energy source, microwave irradiation can be employed in combination with other methods. Microwave heating systems hardly generate thermal gradient effects due to the high penetrability of microwaves, which ensures the energy to be absorbed almost simultaneously by the whole system. As a result, the nanoparticles can be obtained within a very short reaction time. Using this method, Nann's group synthesized a series of monodispersed AREF$_4$-based UCNPs within 5 min [92] and our group synthesized bifunctional lanthanide-doped 3D raisin-like GdF$_3$ nanocrystals [93].

As aforementioned, thermolysis, hydro-thermal and coprecipitation strategies are general approaches to synthesize RE UCNPs. However, the quality of the same RE UCNPs (the same size, morphology and doping ratios) produced by these approaches lacks comparison. Most of the equipment used to characterize the optical properties of UCL nanoparticles are based on the home-made instruments. Standard measurement facilities and protocols are highly required to allow the quantitative comparison of optical properties.

7.5 Surface Modifications of UCNPs

Due to surface-induced effect, nanochemistry for engineering the surface of UCNPs was developed to enhance the luminescent efficiency. Moreover, the UCNPs prepared by conventional methods have either no intrinsic aqueous solubility or a lack of functional organic moieties. Therefore, an additional surface modification step is required. During the fabrication process, the surface modifications by ligands engineering [94–97], surface polymerization [98–100], self-assembly [101–103] or layer-by-layer assembly technology [83] are often indispensable for tailoring the surface status of UCNPs so as to meet the technical requirements of the corresponding applications.

A well-established approach to obtain functional UC nanoparticles is "ligand engineering". It involves ligands exchange or oxidation of the native ligands on the surface of UCNPs. Utilizing ligand exchange reactions, the hydrophobic ligands can be replaced by hydrophilic organic molecules such as 6-aminohexanoic [104], poly-(ethylene glycol) diacid [58], polyacrylic acid [105], etc. Alternatively, if the native capping ligands contain mono-unsaturated carbon–carbon double bonds, they can also be directly oxidized to carboxylic acid groups [106, 107].

Surface functionalizations by using ligand attraction, electrostatic layer-by-layer assembly, and surface polymerization have been applied to form water-soluble core–shell UCNPs. These methods realize the surface coverage with molecules consisting of additional functional groups that allow further reactions with biological entities. Several materials including amphiphilic polymers [108], linear polyions [109], styrenes [110], and silanes [111–113] can be utilized. Further more, to improve the up-conversion efficiency, the layer-by-layer technology was developed, which was usually employed as two/multi-step thermal decomposition process.

Among these methods, silica coating is a well-established strategy for encapsulating nanoparticles into a silica shell for facile bioconjugation. Silica coating possesses following advantages: (i) silica is a highly biocompatible material; (ii) the silica shell greatly reduces the potential risk of toxic effect from RE ions; (iii) additional functional groups (such as—NH_2) that allow further conjugation with biological groups; and (iv) silica coating can be used to modify both hydrophilic and hydrophobic UCNPs via Stöber method [114] and reverse-micro-emulsion method [115], respectively. Recently, mesoporous silica coating has becoming a popular strategy for surface modification of UCNPs via the reverse-micro-emulsion method [116]. The porous silica provides the drug loading capability for UCNPs due to their porous structure. Various functional molecules, such as chemotherapy drugs, PS and organic dyes, could be tightly adsorbed on the surface of silica coating UCNPs, making them widely used for drug delivery, PDT and chemical sensors. There have been several comprehensive reviews published [117–119].

7.6   Optical Properties Tuning of the UCNPs

7.6.1   Enhancement of Up-conversion Luminescence Efficiency

The UCL efficiency is of critical importance in application field because the high UCL efficiency can improve the signal-to-noise ratio. There are three general routes to enhance the emission efficiency of UCNPs. First, doping impurities ions (such as alkaline, alkaline-earth ions, Gd^{3+}, Ti^{4+}, Mn^{2+} etc.) into the host matrix are a useful method to enhance the UCL [23, 24, 37, 120, 121]. Another useful strategy for the enhancement of the UCL intensity is to attach Ag or Au NPs onto UCNPs surfaces [122–124]. This enhancement is attributed to the surface-plasmon-coupled emission, which can increase the radiative decay rate and emission efficiency. The most widely used strategy to improve the luminescence of UCNPs is the fabrication of core–shell structures through layer-by-layer method. The shell with similar lattice constant with the core is grown around the UCNPs. In such structures, the activators are confined in the interior core of the UCNPs. The shell will effectively suppress surface-induced effect, resulting in enhancement of UC efficiency. A good deal of core–shell UCNPs, such as $NaYF_4$:Yb/Er(Tm)@$NaYF_4$ [125], $NaYF_4$: Yb/Er@$NaGdF_4$ [126], $NaGdF_4$:Yb/Tm@$NaGdF_4$ [127], and $NaYF_4$:Yb/Er@CaF_2 [128], has been fabricated to improve the corresponding UC efficiency. The charming advantage of this strategy is that it protects the activators from vibrational deactivation from water or biological fluids to enhance the UCL.

7.6.2   Tuning the Up-conversion Emission Colors

In recent years, a mass of efforts have been devoted to tune UC emissions output of UCNPs over a broad spectral range to get multicolor or high chromatic purity single-band UCL. The conventional strategies for tuning the color output of UCNPs typically involve adjust and control doping ions and dopant concentrations in different host materials. For instance, by adjusting the Tm and/or Er dopants and dopant concentration, the UCL could be tuned from UV-visible to NIR (around 800 nm of Tm^{3+} ion) under 980 nm laser diode excitation. Although different dopant-host combinations can lead to multiple UCL, the color output produced by this method is limited. For example, UCNPs show a limited number of efficient emission colors since only three typical activators (Tm^{3+}, Er^{3+}, and Ho^{3+} ions) are available for generating UCL emissions.

To broaden the emission color of UCNPs, fluorescence resonance energy transfer (FRET) system based on UCNPs (donors) and acceptors (such as organic dyes, quantum dots and other RE ions) have been employed for tuning the UCL spectra. For example, Li et al. [129] synthesized multicolor up-conversion nanocomposites by encapsulating organic dyes or QDs in the silica shell of the core–shell $NaYF_4$:

Yb/Er(Tm) nanospheres. Alternatively, Liu et al. [6] recently developed a novel intra-particle FRET system for fine-tuning UCL color output by elaborately designing core–shell nanostructure. By controlling Gd energy migration through a well-defined core–shell structure, RE ions (Tb^{3+}, Eu^{3+}, Dy^{3+} and Sm^{3+}) without long-lived intermediary energy states can generate tunable up-conversion emissions.

In addition to the multicolor up-conversion emissions, single-band UCL with high chromatic purity is also highly desirable. It was reported that increasing concentration of Yb^{3+} will be significantly enhance energy back-transfer from Er^{3+} to Yb^{3+} in some Er^{3+}/Yb^{3+} co-doped materials, thereby resulting in tunable color output from yellow to red [17]. In addition, the doping of Mn^{2+} in Yb/Er co-doped UCNPs have been shown to significantly increase red/green emission ratios [37]. The existing of Mn^{2+} ion disturbs the transition possibilities of green and red emissions of Er^{3+} and facilitates the occurrence of red emission.

7.7 Summery

This chapter primarily summarizes the foundations of RE-based UCNPs. A brief introduction on the RE-doped up-conversion materials, mechanisms, synthesis method, surface modifications, emission color tuning of the UCNPs was given. With the rapid development of nanoscience and nanotechnology since late 1990s, UCNPs have been a milestone of the nanomaterials world.

With nearly 20 years' development, up-conversion nanomaterials have been expanded from single host materials to hybrid and composite materials. And the activator RE-based up-conversion materials have been extended from typical Er^{3+}, Ho^{3+}, Tm^{3+} to Tb^{3+}, Eu^{3+}, Dy^{3+} and Sm^{3+} ions. As a result, multicolor or single band, the emission output of UCNPs with a broad spectral range can be obtained.

As aforementioned, thermolysis and hydro-thermal strategies are the most common used approaches to produce RE-based UCNPs. Although these synthesis methods are able to produce monodispersed UCNPs with a diameter of 20–100 nm, it remains a challenge to produce smaller (sub 10 nm) and efficient UCNPs. The ultra-small size UCNPs is always associated with a significant decrease of the luminescent efficiency due to the high "surface-to-volume" ratio. Hence, developing new or modified synthetic method to prepare sub-10-nm UCNPs is of crucial importance. Moreover, methodologies for fabricating high-quality water-soluble UCNPs by simple, low cost, and low-temperature pathways are still limited. Due to surface-induced effect, surface modification of UCNPs was developed to enhance the luminescent efficiency. Doping impurities ions attaching Ag or Au NPs onto UCNPs surfaces and core–shell construction were developed to enhance UCL efficiency. But the quantum yield of UCNPs is still relative low (usually less than 1 %). The fabrication of high efficient UCNPs still remains as a grand challenge. In addition, there are no commercial, ready-to-use instruments in the market for those applications based on UCNPs. And standard equipment and protocols are highly required to allow the quantitative measurement of UC properties.

References

1. Bloembergen N (1959) SOLID STATE INFRARED QUANTUM COUNTERS. Phys. Rev. Lett. 2: 84.
2. Auzel F (2004) Upconversion and anti-stokes processes with f and d ions in solids. Chem. Rev. 104: 139.
3. Gamelin DR, Gudel HU (2000) Design of luminescent inorganic materials: New photophysical processes studied by optical spectroscopy. Accounts. Chem. Res. 33: 235.
4. Jin J, Wong ET (2011) Encyclopedia of Inorganic and Bioinorganic Chemistry. Wiley, London.
5. Franken, PA, Weinreich G, Peters CW, Hill AE (1961) Generation of optical harmonics. Phys. Rev. Lett. 7: 118.
6. Wang F, Deng RR, Wang J, Wang QX, Han Y, Zhu HM, Chen XY, Liu XG (2011), Tuning upconversion through energy migration in core-shell nanoparticles. Nat. Mater. 10: 968.
7. Niedbala RS (2000) Multiphoton up-converting phosphors for use in rapid immunoassays Proc. SPIE–Int. Soc. Opt. Eng. 3913: 193.
8. Auzel F (2002) Up-conversion in rare-earth-doped systems: past, present and futureProc. SPIE–Int. Soc. Opt. Eng. 4766: 179.
9. Suyver J F, Aebischer A, Biner D, Gerner P, Grimm J, Heer S, Kramer KW (2005) Novel Materials Doped with Trivalent Lanthanides and Transition Metal Ions Showing near-Infrared to Visible Photon Upconversion Opt. Mater. 27: 1111.
10. Downing E, Hesselink L, Alston J, Macfarlane RR (1996) A three-color, solid-state, three-dimensional display. Science. 273: 1185.
11. Cohen BE (2010) Biological imaging: Beyond fluorescence. Nature, 467: 407.
12. VanderEnde BM, Aartsa L, Meijerink A (2009) Lanthanide ions as spectral converters for solar cells Phys. Chem. Chem. Phys. 11: 11081.
13. Wang G, Peng Q, Li YD (2011), Lanthanide-doped nanocrystals: synthesis, optical-magnetic properties, and applications. Acc. Chem. Res., 44: 322.
14. Chen J, Zhao XJ (2012), Upconversion Nanomaterials: Synthesis, Mechanism, and Applications in Sensing. Sensors. 12: 2414.
15. Haase M, Schafer H (2011) Upconverting nanoparticles. Angew. Chem. Int. Ed. 50: 5808.
16. Wang, F, Liu XG (2009) Recent advances in the chemistry of lanthanide-doped upconversion nanocrystals. Chem. Soc. Rev. 38: 976.
17. Wang F, Liu XG (2008) Upconversion Multicolor Fine-Tuning: Visible to near-Infrared Emission from Lanthanide-Doped $NaYF_4$ Nanoparticles. J. Am. Chem. Soc. 130: 5642.
18. Gnach A, Bednarkiewicz A (2012) Lanthanide-doped up-converting nanoparticles: merits and challenges. Nano Today. 7: 532.
19. Passuello T, Pedroni M, Piccinelli F, Polizzi S, Marzola P, Tambalo S, Conti G, Benati D, Vetrone F, Bettinelli M, Speghini A (2012) PEG-capped, lanthanide doped GdF_3 nanoparticles: luminescent and T_2 contrast agents for optical and MRI multimodal imaging. Nanoscale, 4: 7682.
20. Schäfer H, Ptacek P, Zerzouf O, Haase M (2008) Synthesis and Optical Properties of KYF_4/ Yb, Er Nanocrystals, and their Surface Modification with Undoped KYF_4. Adv. Funct. Mater. 18: 2913.
21. Chen C, Sun, LD, Li ZX, Li LL, Zhang J, and Zhang YW (2010) Ionic liquid-based route to spherical $NaYF_4$ nanoclusters with the assistance of microwave radiation and their multicolor upconversion luminescence. Langmuir. 26: 8797.
22. Schäfer H, Ptacek P, Eickmeier H, Haase M (2009) Synthesis of Hexagonal Yb^{3+}, Er^{3+}- Doped $NaYF_4$ Nanocrystals at Low Temperature. Adv. Funct. Mater. 19: 3091.
23. Chen DQ, Yu Huang Y, Wang FY (2011) Phase transition from hexagonal LnF_3 (Ln = La, Ce, Pr) to cubic $Ln_{0.8}M_{0.2}F_{2.8}$ (M = Ca, Sr, Ba) nanocrystals with enhanced upconversion induced by alkaline-earth doping. Chem. Commun. 47: 2601.

24. Yin W, Zhao L, Zhou L, Gu Z, Liu X, Tian, G, Jin S, Yan L, Ren W, Xing G, Zhao Y(2012) Enhanced Red Emission from GdF_3:Yb^{3+},Er^{3+} Upconversion Nanocrystals by Li^+ Doping and Their Application for Bioimaging Chem. Eur. J. 18: 9239.

25. Li F, Li C, Liu X, Bai T, Dong W, Zhang X, Shi Z, Feng S (2013) Microwave-assisted synthesis and up–down conversion luminescent properties of multicolor hydrophilic LaF_3:Ln^{3+} nanocrystals Dalton Trans. 42: 2015.

26. Liu Q, Sun Y, Yang TS, Feng W, Li CG, Li FY (2011) Sub-10 nm Hexagonal Lanthanide-Doped $NaLuF_4$ Upconversion Nanocrystals for Sensitive Bioimaging in Vivo. J. Am. Chem. Soc. 133: 17122.

27. Shi F, Wang J, Zhai X, Zhao D, Qin W (2011) Facile synthesis of beta-$NaLuF_4$:Yb/Tm hexagonal nanoplates with intense ultraviolet upconversion luminescence CrystEngComm. 13:3782.

28. Yang DM, Dai, YL, Ma PA, Kang XJ, Cheng ZY, Li CX, Lin J (2013) One-Step Synthesis of Small-Sized and Water-Soluble $NaREF_4$ Upconversion Nanoparticles for In Vitro Cell Imaging and Drug Delivery. Chem. Eur. J. 19: 2685.

29. Sarkar S, Meesaragandla, Hazra BC, Mahalingam, V (2013) Sub-5 nm Ln^{3+}-doped $BaLuF_5$ Nanocrystals: A Platform to Realize Upconversion via Interparticle Energy Transfer (IPET). Adv. Mater. 25: 856.

30. Chen G, Ohulchanskyy TY, Kumar R, Ågren H, Prasad PN (2010) Ultrasmall monodisperse $NaYF_4$:Yb^{3+}/Tm^{3+} Nanocrystals with enhanced near-infrared to near-infrared upconversion photoluminescence ACS Nano. 4: 3163.

31. Wong HT, Vetrone, Naccache F R, Chan HLW, Hao J, Capobianco, JA(2011) Water dispersible ultra-small multifunctional $KGdF_4$:Tm^{3+}, Yb^{3+} nanoparticles with near-infrared to near-infrared upconversion. J. Mater. Chem. 21: 16589.

32. Wang GF, Peng Q, Li YD (2009) Upconversion Luminescence of Monodisperse CaF_2:Yb^{3+}/Er^{3+}Nanocrystals J. Am. Chem. Soc. 131: 14200.

33. Dong NN, Pedroni M, Piccinelli F, Conti G, Sbarbati A, Ramírez-Hernández, Maestro JELM, Iglesias-de la Cruz MC, Sanz-Rodriguez, Juarranz FA, Chen F, Vetrone F, Capobianco JA, Solé JG, Bettinelli, Jaque MD, Speghini A (2011) NIR-to-NIR Two-Photon Excited CaF_2:Tm^{3+},Yb^{3+} Nanoparticles: Multifunctional Nanoprobes for Highly Penetrating Fluorescence Bio-imaging. ACS Nano. 5: 8665.

34. Teng X, Zhu Y, Wei W, Wang S, Huang J, Naccache R, Hu W, Tok A I Y, Han Y, Zhang Q, Fan Q, Huang W, Capobianco J A, Huang L (2011) Lanthanide-Doped Na_xScF_{3+x} Nanocrystals: Crystal Structure Evolution and Multicolor Tuning. J. Am. Chem. Soc. 134: 8340.

35. Chen F, Bu W, Zhang S, Liu J, Fan W, Zhou L, Peng W, Shi J (2013) Gd^{3+}-Ion-Doped Upconversion Nanoprobes: Relaxivity Mechanism Probing and Sensitivity Optimization Adv. Funct. Mater. 23: 298.

36. Chen D, Yu F, Huang Y, Lin H, Huang P, Yang A, Wang Z, Wang Y (2012) Lanthanide dopant-induced formation of uniform sub-10 nm active-core/active-shellnanocrystals with near-infrared to near-infrared dual-modal luminescence. J. Mater. Chem. 22: 2632.

37. Tian G, Gu Z, Zhou L, Yin W, Liu X, Yan L, Jin S, Ren W, Xing G, Li S, Zhao Y (2012) Mn^{2+} Dopant-Controlled Synthesis of $NaYF_4$:Yb/Er Upconversion Nanoparticles for in vivo Imaging and Drug Delivery. Adv. Mater. 24: 1226.

38. Zhou J, Yu MX, Sun Y, Zhang XZ, Zhu XJ, Wu ZH, Wu DM, Li FY (2011) Fluorine-18-labeled Gd^{3+}/Yb^{3+}/Er^{3+} codoped $NaYF_4$ nanophosphors for multimodality PET/MR/UCL imaging. Biomaterials. 32: 1148.

39. Sun Y, Yu M X, Liang S, Zhang Y J, Li C G, Mou TT, Yang WJ, Zhang XZ, Li B, Huang CH, Li FY (2011) Fluorine-18 Labeled Rare-Earth Nanoparticles for Positron Emission Tomography (Pet) Imaging of Sentinel Lymph Node. Biomaterials. 32: 2999.

40. Yang Y, Sun Y, Cao TY, Peng JJ, Liu Y, Wu YQ, Feng W, Zhang YJ, Li FY (2013) Hydrothermal Synthesis of $NaLuF_4$:^{153}Sm,Yb,Tm Nanoparticles and their Application in Dual-modality Upconversion Luminescence and SPECT Bioimaging. Biomaterials. 34: 774.

41. Yang Y, Sun Y, Liu Y, Peng JJ, Wu YQ, Zhang YJ, Feng W, Li FY (2013) Long-term in vivo biodistribution and toxicity of Gd(OH)$_3$ nanorods. Biomaterials. 34: 508.

42. Sun Y, Liu Q, Peng JJ, Zhou J, Yang PY, Zhang YJ, Li FY (2013) Radioisotope post-labeling upconversion nanophosphors for in vivo quantitative tracking. Biomaterials. 34: 2289.

43. Huang XY, Han SY, Huang W (2013) Enhancing solar cell efficiency: the search for luminescent materials as spectral converters. Chem. Soc. Rev. 42: 173.

44. Wang F(2015) Photon Upconversion Nanomaterials springer, chapter1.

45. Wang F, Liu XG (2009) Recent advances in the chemistry of lanthanide-doped upconversion nanocrystals. Chem. Soc. Rev. 38: 976.

46. Liu Y, Tu D, Zhu H Zhu H, Ma E, Chen X (2013) Lanthanide-doped luminescent nano-bioprobes: from fundamentals to biodetection. Nanoscale. 5: 1369.

47. Chen GY, Qiu HL, Prasad PN, Chen XY (2014) Upconversion nanoparticles: design, nanochemistry, and applications in theranostics. Chem. Rev. 114: 5161.

48. Martin I R, Yanes AC, Mendez-Ramos J, Torres M E Rodriguez VD (2001) Cooperative Energy Transfer in Yb-Tb Codoped Silica Sol-Gel Glasses. J. Appl. Phy. 89: 2520.

49. Dwivedi Y, Thakur SN, Rai SB (2007) Study of Frequency Upconversion in Yb^{3+}/Eu^{3+} by Cooperative Energy Transfer in Oxyfluoroborate Glass Matrix. Appl. Phys. B-Las. and Opt. 89: 45.

50. Chivian JS, Case WE, Eden DD (1979) The Photon Avalanche-a New Phenomenon in Pr^{3+} Based Infrared Quantum Counters. Appl. Phys. Lett. 35: 124.

51. Park J, Joo J, Kwon SG, Jang Y, Hyeon T (2007) Synthesis of monodisperse spherical nanocrystals. Angew. Chem. Int. Ed. 46: 4630.

52. Zhang YW, Sun X, Si R, You LP, Yan CH (2005) Single-Crystalline and Monodisperse LaF$_3$ Triangular Nanoplates from a Single-Source Precursor. J. Am. Chem. Soc. 127: 3260.

53. Mai H X, Zhang Y W, Si R Yan ZG, Sun LD, You LP, Yan CH (2006) High-quality sodium rare-earth fluoride nanocrystals: Controlled synthesis and optical properties. J. Am. Chem. Soc. 128: 6426.

54. Mai H, Zhang Y, Sun L, Yan C (2007) Size- and phase-controlled synthesis of monodisperse NaYF$_4$:Yb,Er nanocrystals from a unique delayed nucleation pathway monitored with upconversion spectroscopy. J. Phys. Chem. C 111: 13730.

55. Yin AX, Zhang YW, Sun LD, Yan CH (2010) Colloidal synthesis and blue based multicolor upconversion emissions of size and composition controlled monodisperse hexagonal NaYF$_4$: Yb,Tm nanocrystals. Nanoscale 2: 953.

56. Mai HX, Zhang YW, Sun LD, Yan CH (2007) Highly Efficient Multicolor Up-Conversion Emissions and Their Mechanisms of Monodisperse NaYF$_4$:Yb,Er Core and Core/Shell-Structured Nanocrystals. J. Phys. Chem. C 111: 13721.

57. Du YP, Zhang YW, Sun LD, Yan CH (2009) Optically active uniform potassium and lithium rare earth fluoride nanocrystals derived from metal trifluoroacetate precursors. Dalton Trans. 38: 8574.

58. Yi GS, Chow GM (2006) Synthesis of hexagonal-phase NaYF$_4$:Yb,Er and NaYF$_4$:Yb,Tm nanocrystals with efficient up-conversion fluorescence. Adv. Funct. Mater. 16: 2324.

59. Boyer JC, Vetrone F, Cuccia LA, Capobianco JA (2006) Synthesis of colloidal upconverting NaYF$_4$ nanocrystals doped with Er^{3+}, Yb^{3+} and Tm^{3+}, Yb^{3+} via thermal decomposition of lanthanide trifluoroacetate precursors. J. Am. Chem. Soc. 128: 7444.

60. Yi GS, Chow GM (2007) Water-Soluble NaYF$_4$:Yb, Er(Tm)/NaYF$_4$/Polymer Core/Shell/Shell Nanoparticles with Significant Enhancement of Upconversion Fluorescence. Chem. Mater. 19: 341.

61. Boyer JC, Cuccia LA, Capobianco JA (2007) Synthesis of colloidal upconverting NaYF$_4$: Er^{3+}/Yb3 + and Tm^{3+}/Yb^{3+} monodisperse nanocrystals. Nano Lett. 7: 847.

62. Boyer JC, Gagnon J, Cuccia LA, Capobianco JA (2007) Synthesis, Characterization, and Spectroscopy of NaGdF$_4$: Ce^{3+}, Tb^{3+}/NaYF$_4$ Core/Shell Nanoparticles. Chem. Mater. 19: 3358.

63. Pichaandi J, Boyer JC, Delaney KR, van Veggel FCJM (2011) Two-Photon Upconversion Laser (Scanning and Wide-Field) Microscopy Using Ln^{3+}-Doped NaYF4 Upconverting Nanocrystals: A Critical Evaluation of their Performance and Potential in Bioimaging. J. Phys. Chem. C 115: 19054.

64. Khan AF, Yadav R, Mukhopadhya PK, Singh S, Dwivedi C, Dutta V, Chawla S (2011) Core–shell nanophosphor with enhanced NIR–visible upconversion as spectrum modifier for enhancement of solar cell efficiency. J. Nanopart. Res. 13: 6837.

65. Chen G, Ohulchanskyy TY, Liu S, Law WC, Wu F, Swihart MT, Agren H, Prasad P N (2012) Core/Shell NaGdF$_4$:Nd^{3+}/NaGdF$_4$ Nanocrystals with Efficient Near-Infrared to Near-Infrared Downconversion Photoluminescence for Bioimaging Applications. ACS Nano. 6: 2969.

66. Chen G, Shen JT, Ohulchanskyy Y, Patel NJ, Kutikov AZ, Li Song J, Pandey RK, Ågren H, Prasad PN, Han G (2012) (α-NaYbF$_4$:Tm^{3+})/CaF$_2$ Core/Shell Nanoparticles with Efficient Near-Infrared to Near-Infrared Upconversion for High-Contrast Deep Tissue Bioimaging. ACS Nano 6: 8280.

67. Kar A, Patra A (2012) Impacts of core–shell structures on properties of lanthanide-based nanocrystals: crystal phase, lattice strain, downconversion, upconversion and energy transfer. Nanoscale 4: 3608.

68. Zhang C, Lee JY (2013) Prevalence of Anisotropic Shell Growth in Rare Earth Core–Shell Upconversion Nanocrystals. ACS Nano. 7: 4393.

69. Qian H-S, Zhang Y (2008) Synthesis of Hexagonal-Phase Core − Shell NaYF$_4$ Nanocrystals with Tunable Upconversion Fluorescence. Langmuir 24: 12123.

70. Tang Y, Di W, Zhai X, Yang R, Qin W (2013) NIR-Responsive Photocatalytic Activity and Mechanism of NaYF$_4$:Yb,Tm@TiO$_2$ Core–Shell Nanoparticles. ACS Catal. 3: 405.

71. Zeng S, Tsang MK, Chan CF, Wong KL, Hao J (2012) PEG modified BaGdF$_5$:Yb/Er nanoprobes for multi-modal upconversion fluorescent, in vivo X-ray computed tomography and biomagnetic imaging. Biomaterials. 33: 9232.

72. Wang F, Chatterjee DK, Li Z, Zhang Y, Fan X, Wang M (2006) Synthesis of polyethylenimine/NaYF$_4$ nanoparticles with upconversion fluorescence. Nanotechnology, 17: 5786.

73. Li CX, Quan ZW, Yang PP, Huang SS, Lian HZ, Lin J (2008) Shape-Controllable Synthesis and Upconversion Properties of Lutetium Fluoride (Doped with Yb^{3+}/Er^{3+}) Microcrystals by Hydrothermal Process. J. Phys. Chem. C, 112: 13395.

74. Liu J, Bu W, Zhang S, Chen F, Xing H, Pan L, Zhou L, Peng W, Shi J (2012) Controlled Synthesis of Uniform and Monodisperse Upconversion Core/Mesoporous Silica Shell Nanocomposites for Bimodal Imaging. Chem. Eur. J. 18: 2335.

75. Zhang CM, Hou ZY, Chai RT, Cheng ZY, Xu ZH, Li CX, Huang L, Lin J (2010) Mesoporous SrF$_2$ and SrF$_2$:Ln^{3+} (Ln = Ce, Tb, Yb, Er) Hierarchical Microspheres: Hydrothermal Synthesis, Growing Mechanism, and Luminescent Properties. J. Phys. Chem. C 114: 6928.

76. Dorman JA, Choi JH, Kuzmanich G, Chang JP (2012) Elucidating the Effects of a Rare-Earth Oxide Shell on the Luminescence Dynamics of Er^{3+}:Y$_2$O$_3$ Nanoparticles, J. Phys. Chem. C, 116: 10333.

77. Bogdan NE, Rodriguez, Sanz-Rodriguez MF, Iglesias de la Cruz MC, Juarranz A, Jaque D, Sole J G, Capobianco JA (2012) Bio-functionalization of ligand-free upconverting lanthanide doped nanoparticles for bio-imaging and cell targeting. Nanoscale 4:3647.

78. Wang S, SY Song, Deng RP, Guo HL, Lei YQ, Cao F, Li XY, Su SQ, Zhang HJ (2010) Hydrothermal synthesis and upconversion photoluminescence properties of lanthanide doped YF$_3$ sub-microflowers. CrystEngComm 12: 3537.

79. Wang S, Deng RP, Guo HL, Song SY, Cao F, Li XY, Su SQ, Zhang HJ (2010) Lanthanide doped Y$_6$O$_5$F$_8$/YF$_3$ microcrystals: phase-tunable synthesis and bright white upconversion photoluminescence properties. Dalton Trans. 39: 9153.

80. Yin WY, Zhou LG, Gu ZJ, Tian G, Jin S, Yan L, Liu XX, Xing GM, Ren WL, Liu F (2012) Pan, Z.W., Zhao, Y.L.: Lanthanide-doped GdVO$_4$ upconversion nanophosphors with tunable emissions and their applications for biomedical imaging. J. Mater. Chem. 22: 6974.

81. Ren WL, Tian G, Zhou LJ, Yin WY, Yan L, Jin S, Zu Y, Li SJ, Gu ZJ, Zhao YL (2012) Lanthanide ion-doped GdPO$_4$ nanorods with dual-modal bio-optical and magnetic resonance imaging properties. Nanoscale 4: 3754.

82. Song Y, Huang Y, Zhang L, Zheng Y, Guo N, You H (2012) Gd$_2$O$_2$S:Yb,Er submicrospheres with multicolor upconversion fluorescence. RSC Adv. 2:4777.

83. Wang X, Zhuang J, Peng Q, Li YD (2005) A General Strategy for Nanocrystal Synthesis. Nature 437: 121.

84. Wang X, Zhuang J, Peng Q, Li YD (2006) Hydrothermal Synthesis of Rare-Earth Fluoride Nanocrystals. Inorg. Chem. 45: 6661.

85. Zeng JH, Su J, Li ZH, Yan RX, Li YD (2005) Synthesis and Upconversion Luminescence of Hexagonal-Phase NaYF$_4$:Yb^{3+}, Er^{3+}, Phosphors of Controlled Size and Morphology, Adv. Mater. 17: 2119.

86. Zeng JH, Li ZH, Su J, Wang LY, Yan RX, Li YD (2006) Synthesis of complex rare earth fluoride nanocrystal phosphors. Nanotechnology. 17: 3549.

87. Li CX, Yang J, Quan Z, Yang PP, Kong DY, Lin J (2007) Different Microstructures of β-NaYF$_4$ Fabricated by Hydrothermal Process: Effects of pH Values and Fluoride Sources, Chem. Mater. 19: 4933.

88. Yi GS, Chow GM (2005) Colloidal LaF$_3$:Yb,Er, LaF$_3$:Yb,Ho and LaF$_3$:Yb,Tm nanocrystals with multicolor upconversion fluorescence. J. Mater. Chem. 15: 4460.

89. Yi G, Lu H, Zhao S, Ge Y, Yang W, Chen D, Guo L (2004) Synthesis, characterization, and biological application of size-controlled nanocrystalline NaYF$_4$:Yb,Er infrared-to-visible up-conversion phosphors. Nano Lett. 4: 2191.

90. Kong X, Zhang H (2009) Ionothermal synthesis of hexagonal-phase NaYF$_4$:Yb^{3+},Er^{3+}/Tm^{3+} upconversion nanophosphors. Chem. Commun. 6628.

91. Chen C, Sun LD, Li ZX, Li LL, Zhang J, and Zhang YW (2010) Ionic liquid-based route to spherical NaYF$_4$ nanoclusters with the assistance of microwave radiation and their multicolor upconversion luminescence. Langmuir 26: 8797.

92. Wang H Q, Nann T (2009) Monodisperse Upconverting Nanocrystals by Microwave-Assisted Synthesis. ACS Nano 3: 3804.

93. Wang S, Su SQ, Song SY, Deng RP, Zhang HJ (2012) Raisin-like rare earth doped gadolinium fluoride nanocrystals: microwave synthesis and magnetic and upconversion luminescent properties. CrystEngComm. 14: 4266.

94. Cao TY, Yang Y, Gao Y, Zhou J, Li ZQ, Li FY (2011) High-Quality Water-Soluble and Surface-Functionalized Upconversion Nanocrystals as Luminescent Probes for Bioimaging. Biomaterials. 32: 2959.

95. Hu H, Yu MX, Li FY, Chen ZG, Gao X, Xiong LQ, Huang CH (2008) Facile Epoxidation Strategy for Producing Amphiphilic Up-Converting Rare-Earth Nanophosphors as Biological Labels. Chem. Mater. 20: 7003.

96. Naccache R, Vetrone F, Mahalingam V, Cuccia LA, and Capobianco JA (2009) Controlled Synthesis and Water Dispersibility of Hexagonal Phase NaGdF$_4$:Ho^{3+}/Yb^{3+} Nanoparticles. Chem. Mater. 21: 717.

97. Boyer JC, Manseau MP, Murray JI, van Veggel FCJM (2010) Surface Modification of Upconverting NaYF$_4$ Nanoparticles with PEG − Phosphate Ligands for NIR (800 nm) Biolabeling within the Biological Window. Langmuir, 26: 1157.

98. Hu H, Xiong LQ, Zhou J, Li FY, Cao TY, Huang CH (2009) Multimodal-Luminescence Core–Shell Nanocomposites for Targeted Imaging of Tumor Cells. Chem.Eur. J. 15:3577.

99. Jiang S, Zhang Y, (2010) Upconversion Nanoparticle-Based FRET System for Study of siRNA in Live Cells. Langmuir. 26: 6689.

100. Li Z, Zhang Y, (2006) Monodisperse silica-coated polyvinylpyrrolidone NaYF$_4$ nanocrystals with multicolor upconversion fluorescence emission. Angew. Chem., Int. Ed. 45: 7732.

101. Liu Q, Li CY, Yang TS, Yi T, Li FY (2010) "Drawing" upconversion nanophosphors into water throughst guest interaction. Chem. Commun. 46: 5551.
102. Liu Q, Chen M, Sun Y, Chen G, Yang T, Gao Y, Zhang X, Li FY (2011) ^{18}F-labeled Rare-earth self-assemble nanosystem for dual-modal upconversion luminescence and positron emission tomography imaging in vivo. Biomaterials. 32: 8243.
103. Jalil R A, Zhang Y, (2008) Biocompatibility of Silica Coated $NaYF_4$ Upconversion Fluorescent Nanocrystals, Biomaterials. 29: 4122.
104. Meiser F, Cortez C, Caruso F (2004) Biofunctionalization of Fluorescent Rare-Earth-Doped Lanthanum Phosphate Colloidal Nanoparticles. Angew. Chem. Int. Ed., 43:5954.
105. Hilderbrand SA, Shao FW, Salthouse C, Mahmood U, Weissleder R (2009) Upconverting luminescent nanomaterials: application to in vivo bioimaging. Chem. Commun. 4188.
106. Chen Z, Chen H, Hu H, Yu MX, Li FY, Zhang Q, Zhou ZG, Yi T, Huang CH (2008) Versatile Synthesis Strategy for Carboxylic Acid-Functionalized Upconversion Nanophosphors as Biological Labels. J. Am. Chem. Soc. 130: 3023.
107. Zhou HP, Xu CH, Sun W, Yan CH (2009) Clean and Flexible Modification Strategy for Carboxyl/Aldehyde-Functionalized Upconversion Nanoparticles and Their Optical Applications. Adv. Funct. Mater. 19: 3892.
108. Kobayashi H, Kosaka N, Ogawa M, Morgan NY, Smith PD, Murray CB, Ye XC, Collins J, Kumar G A, Bell H, Choyke P L (2009) In vivo multiple color lymphatic imaging using upconverting nanocrystals. J. Mater. Chem. 19: 6481.
109. Wang LY, Yan RX, Hao ZY, Wang L, Zeng JH, Bao H, Wang X, Peng Q, Li YD (2005) Fluorescence Resonant Energy Transfer Biosensor Based on Upconversion-Luminescent Nanoparticles Angew. Chem., Int. Ed., 44: 6054.
110. Qian HS, Li ZQ, Zhang Y (2008) Multicolor polystyrene nanospheres tagged with up-conversion fluorescent nanocrystals. Nanotechnology, 19: 255601.
111. Lu HC, Yi GS, Zhao SY, Chen DP, Guo LH, Cheng J (2004) Synthesis and characterization of multi-functional nanoparticles possessing magnetic, up-conversion fluorescence and bio-affinity properties, J. Mater. Chem., 14:1336.
112. Liu ZY, Yi GS, Zhang HT, Ding J, Zhang YW, Xue JM (2008) Monodisperse silica nanoparticles encapsulating upconversion fluorescent and superparamagnetic nanocrystals, Chem. Commun. 694.
113. Ehlert O, Thomann R, Darbandi M, Nann T (2008) A Four-Color Colloidal Multiplexing Nanoparticle System ACS Nano, 2: 120.
114. Mi C, Tian Z, Cao C, Wang Z, Mao C, Xu S (2011) Novel Microwave-Assisted Solvothermal Synthesis of $NaYF_4$:Yb,Er Upconversion Nanoparticles and Their Application in Cancer Cell Imaging. Langmuir. 27: 14632.
115. Shan J, Ju Y (2007) Controlled synthesis of lanthanide-doped $NaYF_4$ upconversion nanocrystals via ligand induced crystal phase transition and silica coating. Appl. Phys. Lett. 91: 123103.
116. Yi G, Peng Y, Gao Z (2011) Strong Red-Emitting near-Infrared-to-Visible Upconversion Fluorescent Nanoparticles. Chem. Mater. 23: 2729.
117. Liu SH, Han MY (2010) Silica-Coated Metal Nanoparticles Chem. Asian J. 5: 36.
118. Caruso, F. (2001) Nanoengineering of Particle Surfaces, Adv. Mater., 13:11.
119. Piao YZ, Burns A, Kim J, Wiesner U, Hyeon T (2008) Designed Fabrication of Silica-Based Nanostructured Particle Systems for Nanomedicine Applications. Adv. Funct. Mater. 18:3745.
120. Wang F, Han Y, Lim C S, Lu YH, Wang J, Xu J, Chen HY, Zhang C, Hong M H, Liu X G (2010) Simultaneous phase and size control of upconversion nanocrystals through lanthanide doping. Nature. 463: 1061.
121. Chen D, Huang P, Yu Y, Huang F, Yang A, Wang Y (2011) Dopant-induced phase transition: a new strategy of synthesizing hexagonal upconversion $NaYF_4$ at low temperature. Chem. Commun. 47: 5801.
122. Liu N, Qin WP, Qin GS, Jiang T, Zhao D (2011) Highly plasmon-enhanced upconversion emissions from Au@β-$NaYF_4$:Yb,Tm hybrid nanostructures. Chem. Commun. 47: 7671.

123. Paudel HP, Zhong LL, Bayat K, Baroughi MF, Smith S, Lin CK, Jiang CY, Berry MT, May PS (2011) Enhancement of near-infrared-to-visible upconversion luminescence using engineered plasmonic gold surfaces.,J. Phys. Chem. C, 115: 19028.
124. Yuan PY, Lee YH, Gnanasammandhan MK, Guan Z, Zhang Y, Xu QH (2012) Plasmon enhanced upconversion luminescence of $NaYF_4$:Yb,Er@SiO_2@Ag core–shell nanocomposites for cell imaging. Nanoscale, 4: 5132.
125. Wang Y, Tu LP, Zhao, JW, Sun YJ, Kong XG, Zhang H (2009) Upconversion luminescence of β-$NaYF_4$:Yb^{3+},Er^{3+}@β-$NaYF_4$ core/shell nanoparticles: Excitation power density and surface dependence.,J. Phys. Chem. C, 113: 7164.
126. Zhang F, Che RH, Li XM, Yao C, Yang JP, Shen DK, Hu P, Li W, Zhao DY (2012) Direct Imaging the Upconversion Nanocrystal Core/Shell Structure at the Subnanometer Level: Shell Thickness Dependence in Upconverting Optical Properties. Nano Lett. 12: 2852.
127. Park YI, Kim JH, Lee KT, Jeon K-S, Na HB, Yu JH, Kim HM, Lee N, Choi SH, Baik S-I, Kim H, Park SP, Park B-J, Kim YW, Lee SH, Yoon SY, Song IC, Moon WK, Suh YD, Hyeon T (2009) Nonblinking and Nonbleaching Upconverting Nanoparticles as an Optical Imaging Nanoprobe and T1 Magnetic Resonance Imaging Contrast Agent. Adv. Mater. 21: 4467.
128. Wang YF, Sun LD, Xiao JW, Feng W, Zhou JC, Shen J, Yan CH. (2012) Rare-Earth Nanoparticles with Enhanced Upconversion Emission and Suppressed Rare-Earth-Ion Leakage Chem. Eur. J. 18: 5558.
129. Li Z, Zhang Y, Jiang S. (2008) Multicolor Core/Shell-Structured Upconversion Fluorescent Nanoparticles. Adv. Mater. 20: 4765.

Chapter 8
Lanthanide-Doped Upconversion Nanoprobes

Datao Tu, Wei Zheng, Ping Huang and Xueyuan Chen

Abstract Lanthanide-doped upconversion nanoparticles (UCNPs) have attracted considerable interest due to their superior physicochemical features, such as large anti-Stokes shifts, low autofluorescence background, low toxicity, and high penetration depth, which make them extremely suitable for use as alternatives to conventional downshifting luminescence bioprobes such as organic dyes and quantum dots for various biological applications. Fundamental understanding the photophysics of lanthanide-doped UCNPs is of vital importance for discovering novel optical properties and exploring their new applications. In this chapter, we focus on the most recent advances in the development of lanthanide-doped UCNPs as potential luminescent nanobioprobes by means of our customized lanthanide photophysics measurement platforms specially designed for upconversion luminescence, which covers from their fundamental photophysics to bioapplications, including electronic structures (energy levels and local site symmetry of emitters), excited-state dynamics, UC luminescence enhancement strategies, and their promising applications for biodetection and bioimaging. Some future prospects and efforts toward this rapidly growing field are also envisioned.

8.1 Introduction

Lanthanide (Ln^{3+}) activated upconversion (UC) materials, which are able to convert long-wavelength stimulation into short-wavelength emission, have been widely used in solid-state lasers, flat displays, optical communications, and other photonic devices. In comparison with the multiphoton absorption or second harmonic generation that require expensive ultrashort-pulse lasers (e.g., a femtosecond pulse

D. Tu · W. Zheng · P. Huang · X. Chen (✉)
Key Laboratory of Optoelectronic Materials Chemistry and Physics
and State Key Laboratory of Structural Chemistry, Fujian Institute of Research
on the Structure of Matter, Chinese Academy of Sciences, Fuzhou 350002,
Fujian, China
e-mail: xchen@fjirsm.ac.cn

laser) to perform the excitation, Ln^{3+}-doped UC materials generally take advantage of a more efficient energy transfer UC process and thus can be excited by a low-cost continuous-wave (CW) near-infrared (NIR) diode laser (e.g., 808 nm or 980 nm laser). It is their unique electronic structures that enable the Ln^{3+} ions in crystals to effectively emit photons from high energy levels through successive photon absorptions and energy transfers from their low-lying energy levels. Thanks to the pioneering work by Auzel and others in theoretical and experimental studies on UC within $4f^N$ electronic structure, much of the spectroscopy and mechanism involved in Ln^{3+}-doped UC materials are well understood [1–3]. With the rapid advances in nanotechnology and biotechnology, particularly the development of new methods for material synthesis, there has been growing interest in the controlled synthesis, optical properties, and bioapplications of Ln^{3+}-doped UC materials in nanoscale. Nanocrystalline and nanostructured UC materials, typically with particle sizes smaller than 100 nm, may exhibit novel electronic, magnetic, optical, or thermo-dynamic properties in comparison with their bulk counterparts [4–8].

As compared to conventional downshifting luminescence (DSL) bioprobes such as organic dyes and quantum dots (QDs), Ln^{3+}-doped UCNPs possess superior physicochemical features, such as large anti-Stokes shifts, high resistance to pho-tobleaching, low autofluorescence background, low toxicity, and high penetration depth, and thus are regarded as a new generation of luminescent bioprobes. These functional UCNPs, although most of their bulk counterparts were well studied previously, have attracted reviving interest for their biomedical applications in areas as diverse as biodetection [9–11], bioimaging [12–16], drug delivery [17–21], photodynamic therapy (PDT) [22–24], photothermal therapy (PTT) [25–27], and disease theranostics [28–30]. Despite extensive research, UCNPs still suffer from a low quantum yield (QY), which is currently the major bottleneck toward their commercialization. Therefore, pursuing a high QY for UC luminescence (UCL) becomes a goal of general concern. To realize this goal, a comprehensive survey on the photophysics of Ln^{3+}-doped UCNPs is essential.

Recently, with the rapid development in Ln^{3+}-doped UCNPs, many significant advances have been accomplished in the structure/morphology control, function-alization design, and optical performance optimization of these UC nanobioprobes for versatile biomedical applications, as summarized in many recent reviews and book chapters [31–47]. Rather than being exhaustive, this chapter is aimed at providing a comprehensive survey on the latest advances toward the developments of Ln^{3+}-doped UCNPs as potential luminescent nanobioprobes, which covers from their fundamental photophysics to biosensing, including electronic structures (en-ergy levels and local site symmetry of emitters), excited-stated dynamics, UCL enhancement strategies, and their promising applications for biodetection of bio-molecules, as well as bioimaging of cells and tissues. This chapter will be organized as follows (Fig. 8.1). To begin with, we briefly introduce our customized lanthanide photophysics measurement platforms specially designed for UCL in Sect. 8.2. The fundamental photophysics of Ln^{3+}-doped UCNPs, including UC mechanism, electronic energy levels, local site symmetry, and excited-state dynamics of Ln^{3+} emitters, are reviewed in Sect. 8.3. In Sect. 8.4, we highlight the QY improvement
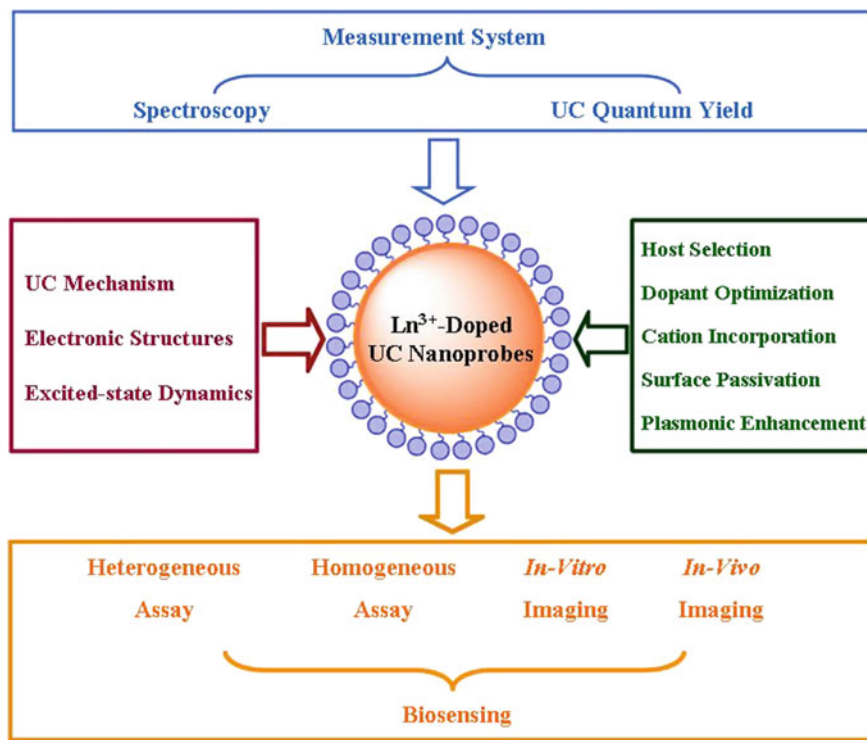
Fig. 8.1 Summary of luminescent biosensing based on Ln^{3+}-doped UCNPs

especially for biomedical applications. Sections 8.5 and 8.6 exemplify several key applications of Ln^{3+}-doped UC nanoprobes in homogeneous and heterogeneous bioassays, as well as in vitro and in vivo bioimaging, respectively. Finally, some future prospects and efforts toward this rapidly growing field are put forward.

8.2 Lanthanide Photophysics Measurement Platform for Upconversion Luminescence

Spectroscopic data such as photoluminescence (PL) excitation and emission spectra, PL transients, and the pump power dependence of PL intensities are essential to understanding the excitation mechanisms in UCNPs and improving their optical performance. Different from conventional DSL fluorophores that can be excited at UV or visible regions by using a xenon or tungsten lamp, Ln^{3+}-doped UCNPs usually require a high pump power density in the NIR to activate the UC process due to its nonlinear optical nature. As such, the optical measurement on UCNPs is normally carried out on a commercial fluorescence spectrometer with an

external NIR laser as the excitation source. A CW NIR diode laser with a medium power density is sufficient to trigger UCL for Ln^{3+}-doped UCNPs. The steady-state UC emission spectrum and UCL lifetime are most frequently recorded in routine optical characterization of UCNPs. In steady-state UCL measurement, the CW NIR diode laser is preferred to give a stable laser beam for the excitation, whereas in transient UCL measurement, a pulse laser is necessary to provide the time-dependent UCL signal within two pulses. Upon pulse excitation, time-resolved UC emission spectra can be obtained by setting appropriate delay time and gate time within the temporal domain of Ln^{3+} luminescence. Unlike the UC emission spectrum and PL lifetime that are commonly measured, the PL excitation spectrum of UCNPs is seldom recorded unless critically demanded, because it is often difficult and tedious to conduct such a measurement with the availability of tunable pulse lasers. Note that most of these optical measurements are conducted for the ensemble of NPs, and single NP measurement is now accessible by combining the optical instruments with diverse electronic micro-scopes [48–50].

Fundamental research on lanthanide spectroscopy in Ln^{3+}-doped UCNPs, for example, the localized electronic structure, local site symmetry, and excited-state dynamics of Ln^{3+} ions, is of vital significance for optimizing their optical perfor-mance and discovering novel optical properties, which relies on sophisticated optical measurement instruments and advanced spectroscopic methods. However, commercial and integrated fluorescence spectrometers could not satisfy the crucial demands for high-resolution and ultrafast spectroscopic measurements in view of their limited spectral resolution and expansibility. In this regard, we developed low-temperature and high-resolution spectroscopic measurement system equipped with a variety of laser sources (Fig. 8.2a). Based on modular and open optical path design by integrating various excitation sources and making full use of the four windows of the optical cryostat, the functionality of the system is maximally expanded. The techniques such as multiple grating design, microchannel plate photomultiplier tube, and time-correlated single photon counting are adopted in this spectroscopic measurement system, which greatly improve its detection sensitivity (10^{-18} W) and spectral resolution (0.0053 nm). Utilizing this system, the PL transients in the order of tens of picosecond can be detected, and the measurement is allowed to perform at a cryogenic temperature as low as 3 K.

Evaluation on the optical performance of Ln^{3+}-doped UCNPs is essential to the material optimization and application. However, currently, it still lacks a criterion for the quantitative comparison of optical performance among different Ln^{3+}-doped UCNPs. Due to the nonlinear nature of UC process, UCNPs exhibit a power density-dependent efficiency, which makes it difficult to compare the UC efficiency of the NPs measured under various conditions in the literature. To aim at providing such a standard for quantitative comparison of UC efficiency, we recently proposed the design of an absolute UC QY measurement system (Fig. 8.2b). With the sim-plified patented design (namely single grating + single detector configuration), this system enables the measurement in a broad emission wavelength range from 300 to 1700 nm and allows for fast and sensitive measurement of UC QY with a detection
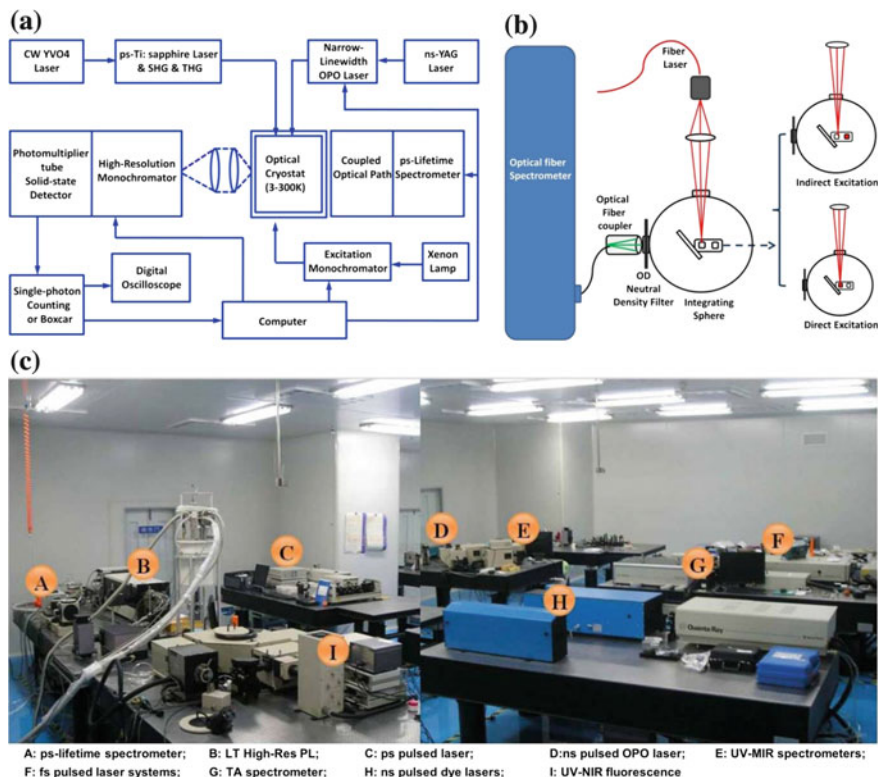
Fig. 8.2 **a** Schematic design of the low-temperature and high-resolution laser spectroscopic measurement system. **b** Schematic design of the absolute UC QY measurement system. **c** Panorama of the optical measurement platform for lanthanide photophysics and photochemistry of UCNPs

limit down to 0.01 %. Particularly, this system covers a wavelength range of 410–2400 nm in the UC excitation and an UCL lifetime range of 1 μs–100 ms. Based on the above instrument developments, we further constructed a state-of-the-art optical measurement platform for lanthanide photophysics (Fig. 8.2c). The platform shares various excitation sources (including femtosecond, picosecond, and nanosecond pulse lasers, CW lasers, and xenon lamps) and integrates diverse modules of the spectrometer systems (including UV to NIR steady-state and transient fluorescence, high-resolution fluorescence, UV to mid-infrared (MIR) steady-state and phosphorescence lifetime, picosecond fluorescence lifetime, femtosecond-to-submillisecond transient absorption (TA), and high-throughput UCL microplate reader) and the cryogenic systems (4 and 10 K), thus facilitating comprehensive study on lanthanide photophysics and photochemistry properties of UCNPs in the time, frequency, and/or space domains with high resolution.

8.3 Electronic Structures and Excited-State Dynamics

Ln^{3+} ions are excellent structural and spectroscopic probes, and their optical properties in diverse host materials are critically dependent on the localized electronic structures and excited-state dynamics. Comprehensive survey on the optics and photonics of Ln^{3+}-activated UCNPs is fundamentally important for discovering novelty optical properties and exploring their new applications. In this section, we will focus on the fundamental photophysics of Ln^{3+}-doped UCNPs, including UC mechanism, electronic energy levels, local site symmetry, and excited-state dynamics of Ln^{3+} ions involved in the UC process.

8.3.1 Upconversion Mechanism

The so-called UC refers to a nonlinear optical process that converts two or more low-energy pump photons into a higher-energy output photon. With the advent of inexpensive high-power infrared diode lasers (e.g., 980 or 808 nm NIR laser), the UC emission of Ln^{3+} ions, especially from NIR to visible, has been extensively studied for its significant applications in the field of biosensing. Several different mechanisms have been recognized to be involved in the UC process either alone or in combination, including excited-state absorption (ESA), energy transfer UC (ETU), photon avalanche (PA), cooperative UC (CUC), and energy migration-mediated UC (EMU) (Fig. 8.3) [1].

In the case of ESA, excitation takes the form of successive absorption of pump photons by a single ion (Fig. 8.3a). ETU processes also utilize sequential absorption of two photons to populate the metastable level, but differing from ESA, it is realized through energy transfer between two neighboring ions rather than successive absorption of two photons in a single ion (Fig. 8.3b). As a result, ETU can be distinguished from ESA by a rising edge in the initial stage of the PL decay curve, since the population of the luminescent level in the ETU process requires an energy transfer between two ions [51]. Although ESA takes effect in single Ln^{3+} ions (e.g., Er^{3+}), the weak absorption induced by parity-forbidden intra–4f transitions within Ln^{3+} strongly suppresses its efficiency. By contrast, the ETU takes advantage of the larger absorption cross section of a sensitizer (e.g., Yb^{3+}) and thus is established as the most efficient UC process in practical applications.

The phenomenon of PA was first discovered by Chivian and coworkers in Pr^{3+}-based infrared quantum counters [52]. The PA UC features an unusual pump mechanism that requires a pump intensity above a certain threshold. In the PA process (Fig. 8.3c), the intermediate reservoir level is initially populated by non-resonant weak ground-state absorption (GSA), followed by the resonant ESA or energy transfer from another excited ion (i.e., ETU) to populate the luminescent level from which UCL occurs. After this initial stage, an efficient cross-relaxation (CR) takes place between the excited ion and another adjacent ground-state ion,
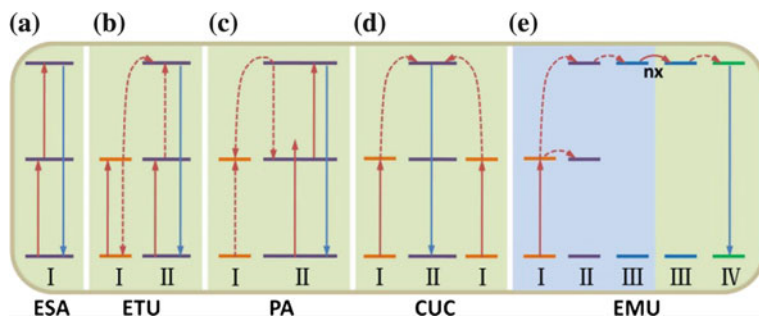
Fig. 8.3 Simplified energy level diagrams describing reported UC processes. *ESA*, *ETU*, *PA*, *CUC*, and *EMU* denote the excited-state absorption, energy transfer UC, photon avalanche, cooperative UC, and energy migration-mediated UC, respectively. Reprinted with the permission from Ref. [57]. Copyright 2011, Macmillan Publishers Limited

resulting in the population of reservoir level of two UC ions. Subsequently, the feedback looping of ESA (or ETU) and CR will exponentially increase the population of the reservoir and luminescent levels, thus producing strong UCL known as the PA UC [53]. Although the PA UC is considered to be the most efficient due to the feedback looping of ESA (or ETU) and CR in UC processes, its disadvantages including weak GSA, high pump threshold, and much longer rise time (even up to seconds) limit its commercial applications.

CUC is a three-body process, which involves the interaction of three ions and takes place with a much lower probability [54]. In the CUC process (Fig. 8.3d), the luminescent level is populated through cooperative energy transfer from two adjacent ions, where the emitters have no intermediate energy level matchable to that of the donors. CUC usually happens as cooperative luminescence in Yb^{3+} singly doped and as cooperative sensitization in Yb^{3+}/Tb^{3+} or Yb^{3+}/Eu^{3+} codoped bulk materials [55, 56], especially in those host matrices with Ln^{3+} heterovalently doping (e.g., CaF_2), in which Ln^{3+} clusters are easily formed. So far, no solid evidence has been provided to support CUC luminescence in monodisperse UCNPs and their potential bioapplications have not yet been explored.

The EMU process was first proposed by Liu and Wang in $NaGdF_4:Yb^{3+}, Tm^{3+}$ @$NaGdF_4:Ln^{3+}$ (Ln = Tb, Eu, Dy, and Sm) core/shell nanostructures (Fig. 8.4a) [57, 58]. In this novel UC process, Ln^{3+} ions designed for realizing EMU are classified into four types, i.e., sensitizers (type I), accumulators (type II), migrators (type III), and activators (type IV) (Fig. 8.3e). A sensitizer ion (Yb^{3+}) is used to harvest pump photons and subsequently promote a neighboring accumulator ion (Tm^{3+}) to the excited states. A migrator ion (Gd^{3+}) extracts the excitation energy from high-lying energy levels of the accumulator, followed by random energy hopping through the migrator ion sublattice and trapping of the migrating energy by an activator ion (e.g., Tb^{3+}, Eu^{3+}, Dy^{3+}, and Sm^{3+}) (Fig. 8.4b). To control the energy exchange interaction between the accumulator and the activator, the sensitizer/accumulator and the activator are spatially confined in different layers of the core/shell structure, which is
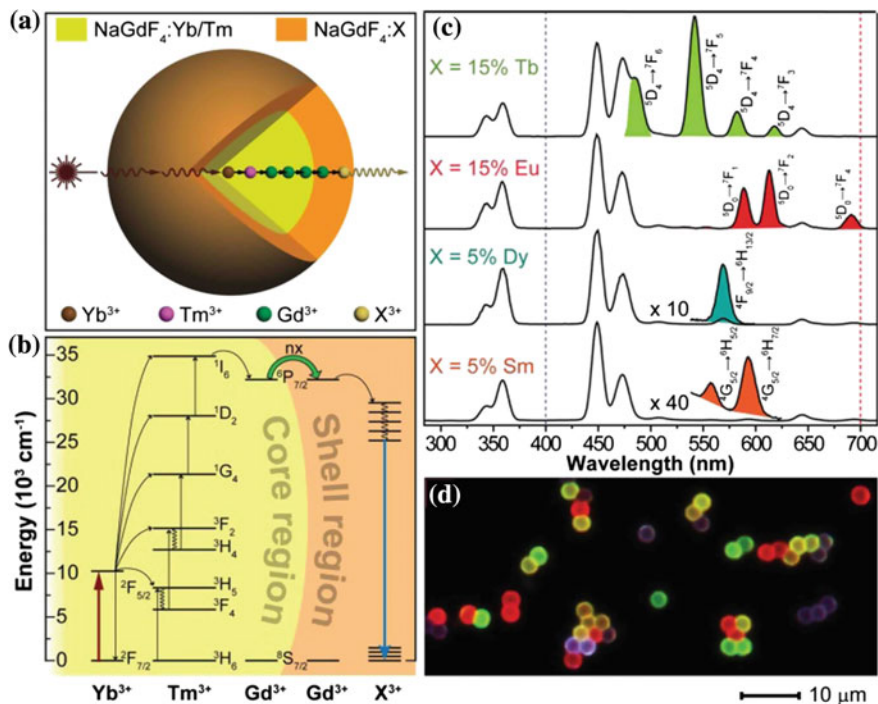
Fig. 8.4 Tuning UC through energy migration in core/shell NPs: **a** schematic design of a Ln^{3+}-doped $NaGdF_4@NaGdF_4$ core/shell NP for EMU (X: activator ions). **b** Proposed energy transfer mechanism in the core/shell NP. **c** Emission spectra of the as-prepared $NaGdF_4@NaGdF_4$ core/shell NPs doped with different activators. **d** Luminescence micrograph of polystyrene beads tagged with core/shell NPs doped with different activators. (Adapted with the permission from Ref. [57]. Copyright 2011, Macmillan Publishers Limited.)

essential for eliminating deleterious CR. To generate an efficient EMU process, arrays of migrator ions through the core/shell interface are needed to bridge the energy transfer from the accumulator to the activator. A key feature of the EMU design is that the excitation energy collected by the sensitizer can be amassed in the accumulator by successive energy transfer while enabling one-step energy transfer to the activator. Thus, stringent selection rules for activators (type IV ion) can be largely exempted, in parallel with the benefit of inherent high conversion efficiency of ETU for low-energy excitation photons. The core/shell layout also allows a facile modulation in activator composition and concentration while minimizing luminescence quenching. As a result, multicolor UCL from activators without long-lived intermediate energy levels can be realized (Fig. 8.4c, d). This novel UC mechanism is an important extension of traditional UC processes including ESA, ETU, CUC, and PA and thus may broaden the applications of Ln^{3+}-doped UCNPs.

Besides these established UC mechanisms, other new types of UC processes have been proposed recently. For example, a mechanism termed as

hetero-looping-enhanced energy transfer (hetero-LEET) was suggested for UC in LaF_3:Yb,Er NPs embedded in silica sol-gel thin films [59]. The combination of resonant GSA and ETU with a CR feedback looping makes it potentially more efficient than any other established UC processes. Meanwhile, a thermal avalanche process that involves a thermally induced production of free carriers was revealed to account for the broadband white-light UC emissions from several rare earth oxides (e.g., Yb_2O_3) [60]. Although the actual mechanisms remain to be confirmed, these UC processes produce intense UCL and thus may find potentials in the fields of lighting, imaging, and displays. More recently, the persistent luminescence nanophosphors were also demonstrated to function as UC materials [61]. By utilizing CaS:Eu^{2+}, Dy^{3+} NPs as energy reservoirs to store UV photon energy, red UC emission was observed upon NIR excitation.

8.3.2 Electronic Energy Levels and Local Site Symmetry of Lanthanide Ions in UCNPs

The intricate optical properties of Ln^{3+} ions originate from the unique features of their electronic $[Xe]4f^N$ configurations ($N = 0$–14). They are characterized by three quantum numbers: S, L, and J, within the framework of the Russel–Saunders spin–orbit coupling scheme [62, 63]. Since the energy levels of Ln^{3+} are well-defined due to the shielding of the $4f$ orbitals by the filled $5s^2 5p^6$ subshells, Ln^{3+} ions show little sensitivity to the chemical environments into which they are inserted. As such, inner-shell $4f$–$4f$ transitions of Ln^{3+} in nanocrystals resemble the spectra of their free ions and are sharp and easily recognized. On placing a Ln^{3+} ion in a dielectric crystal, the energy levels split under the influence of the electric field produced by the crystalline environment. The f-electrons have very localized states that are conventionally described within the framework of crystal field (CF) theory [64]. The electronic energy levels of Ln^{3+} and their CF parameters in a given host are usually obtained through the energy-level-fitting performed by parametrization of an effective operator Hamiltonian including free-ion and CF interactions. The commonly used effective operator Hamiltonian has been described by Crosswhite and Crosswhite [63], Wybourne [64], and Carnall et al. [65]. Once a set of experimental CF levels of Ln^{3+} occupying a single dopant site in a given host are identified from the high-resolution PL and/or absorption spectra, the energy-level-fitting can be performed by using f-shell empirical program suite, which enables a complete diagonalization without truncation of the $4f^n$ wave functions [35]. The computing programs have been widely spread and used for decades in the community of lanthanide spectroscopy, which are available upon request from Prof. M. F. Reid.

It is well known that the optical properties of Ln^{3+} are very sensitive to their local coordination environment, and the emission intensity of Ln^{3+}-doped NPs is critically dependent on the crystal structure and CF of the surroundings around Ln^{3+} emitters. A slight variation of local structure will bring about a significant change in

the optical properties of Ln^{3+} ions doped into NPs [66]. In general, host matrices with low site symmetries of dopants are more favorable for UCL than their higher symmetry counterparts, because low-symmetry hosts typically exert a CF containing more uneven components around the dopant ions. The uneven components enhance the electronic coupling between $4f$ energy levels and their higher electronic configuration and subsequently increase $4f$–$4f$ transition probabilities of the dopant ions [67]. For example, hexagonal-phase $NaYF_4$:Yb, Er bulk materials exhibit about one order of magnitude enhancement in UC efficiency relative to their cubic-phase counterparts that are higher in the site symmetries of Ln^{3+} dopants [68]. Therefore, it is fundamentally significant to determine the localized electronic structures and the site symmetries of Ln^{3+} in given UC host matrices, which are essential for optimizing their optical performance as well as exploring novel host materials for efficient UCL.

On the nanoscale, structure disordering and surface defects are inevitable upon the introduction of Ln^{3+} ions into the lattices of inorganic NPs. Consequently, multiple sites of Ln^{3+} with different CF surroundings come into being [69, 70]. In view of their different CF surroundings, Ln^{3+} ions possessing multiple sites in NPs will display distinct PL pattern and PL decay for each single site. These optical behaviors may facilitate the determination of local structures (or site symmetry) of Ln^{3+} ions embedded in NPs by means of high-resolution site-selective or time-resolved PL spectroscopy. Among all the Ln^{3+} ions, Eu^{3+} ion is considered to be the most useful spectroscopic probe due to its nondegenerate emissive state of $^5D_0$ and the ground state of $^7F_0$ [71–73]. The $^5D_0 \rightarrow {}^7F_2$ transition of Eu^{3+} is of electric dipole (ED) nature and hypersensitive to its local site symmetry, while the $^5D_0 \rightarrow {}^7F_1$ transition is of magnetic dipole (MD) nature and insensitive to the site symmetry. Thereby, the intensity ratio of the $^5D_0 \rightarrow {}^7F_2$ emission to $^5D_0 \rightarrow {}^7F_1$ emission of Eu^{3+} can provide site symmetry information [74, 75]. Moreover, according to the ED selection rule, the $^5D_0 \rightarrow {}^7F_0$ transition of Eu^{3+} induced by CF J-mixing may emerge in the emission spectrum, which is only allowed for the following 10 site symmetries, C_s, C_1, C_n, and C_{nv} (n = 2, 3, 4, 6) [76, 77]. Based on the above analysis as well as the Judd–Ofelt (JO) theory and the selection rules for ED and MD transitions, the allowed transition lines of $^5D_0 \rightarrow {}^7F_J$ (J = 0, 1, 2, 3, 4, 5, and 6) for Eu^{3+} ions at 32 crystallographic point groups are known [78–80]. By comparing the CF splitting numbers of the $^5D_0 \rightarrow {}^7F_J$ transitions with the theoretical predictions, multiple luminescent sites of Eu^{3+} within different CF surroundings can be easily identified in NPs.

Recently, by means of low-temperature and high-resolution PL spectroscopy that utilizes Eu^{3+} as the structural probe, we provided solid spectroscopic proof accounting for the universal breakdown of crystallographic site symmetry in Ln^{3+}-doped disordered crystals, in which two or more cations statistically occupy a single lattice site (Fig. 8.5a, b) [81]. $NaYF_4$ in the form of cubic (α) and hexagonal (β) phases was chosen as a model host, because the spectroscopic site symmetry of Ln^{3+} ions doped in $NaYF_4$, particularly in β-$NaYF_4$, has been the subject of much
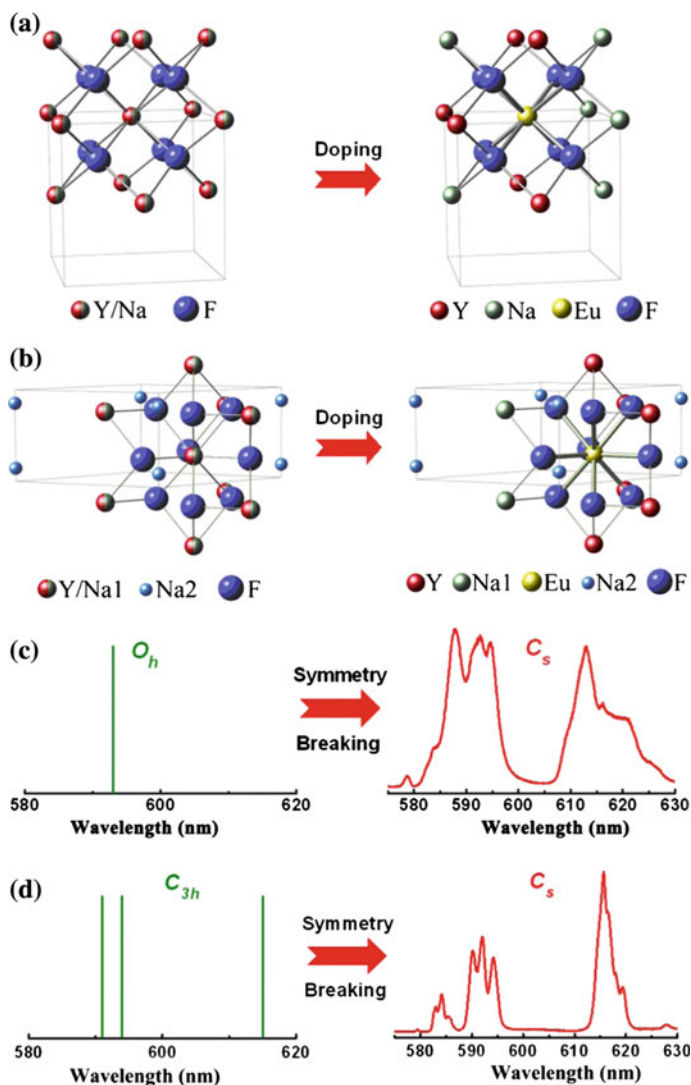
Fig. 8.5 Schematic illustration showing the breakdown of crystallographic site symmetry of Eu^{3+} in **a** α-NaYF$_4$ and **b** β-NaYF$_4$ crystals. Induced by Ln^{3+}-doping for the disordered Y/Na site, the original crystallographic site symmetries of O_h in (**a**) and C_{3h} in (**b**) are descended to C_s and C_s, respectively, as exemplified by the significant change in the observed and theoretical predicted spectral patterns for Eu^{3+} doped in **c** α-NaYF$_4$ and **d** β-NaYF$_4$ crystals. (Adapted with the permission from Ref. [81]. Copyright 2013, Wiley-VCH Verlag GmbH & Co. KGaA.)

debate [82–85]. The symmetry of spectroscopic sites for the Ln^{3+} dopants was observed to deviate from that of the crystallographic sites. Particularly, we found that the highest spectroscopic site symmetries of Eu^{3+} descended from crystallographic O_h to C_s (or C_2) in α-NaYF$_4$ and from crystallographic C_{3h} to C_s in β-NaYF$_4$
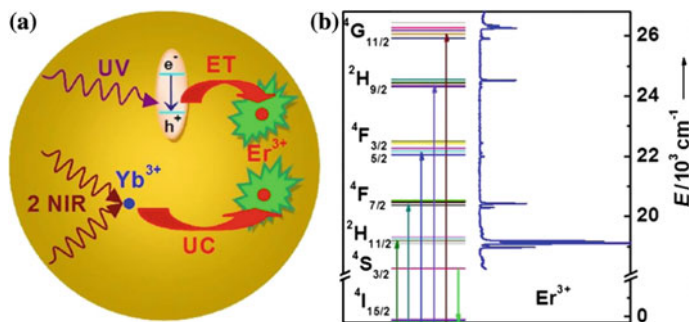
Fig. 8.6 **a** Schematic illustration showing the host-sensitized DSL and Yb^{3+}-sensitized UCL of Er^{3+}. **b** Low-temperature and high-resolution excitation spectrum of Er^{3+} and its corresponding electronic energy levels in anatase TiO_2 semiconductor nanocrystals. (Adapted with the permission from Ref. [51]. Copyright 2011, Wiley-VCH Verlag GmbH & Co. KGaA.)

(Fig. 8.5c, d), which was further supported by the corresponding CF-level-fitting that yielded a very small standard deviation from the experiments. A similar breakdown of crystallographic site symmetry was also observed in other disordered crystals, such as α-KLaF$_4$ and α-KGdF$_4$ [86, 87]. Meanwhile, a set of CF parameters and energy levels of Er^{3+} in both α- and β-NaYF$_4$, which are critically important and have long been sought for designing highly luminescent NaYF$_4$-based UC materials, were determined in our most recent work. The unambiguous spectroscopic identification of local site symmetry breakdown in this family of disordered crystals is crucial to optimizing their optical performance for further applications. Similar work was conducted for Er^{3+} in anatase TiO_2 semiconductor NPs (Fig. 8.6) [51]. A set of reliable CF parameters and energy levels of Er^{3+} assuming a site symmetry of C_{2v} were identified through CF-level-fitting. Both UCL and DSL were observed in Er^{3+} singly doped or Yb/Er codoped TiO_2 NPs. The UCL intensity of Er^{3+} in Yb/Er codoped NPs was found to be about five times higher than that of Er^{3+} singly doped counterparts as a result of efficient Yb^{3+} sensitization and ETU evidenced by its distinct UCL dynamics. These findings provide deep insights into the fundamentals of Ln^{3+}-doped semiconductor NPs like TiO_2 that may function as the spectral convertor in solar cells and are currently of great interest.

8.3.3 Excited-State Dynamics of Lanthanide Ions Involved in Upconversion Process

The excited-state dynamics of Ln^{3+} in UC process has been extensively investigated in bulk materials, most of which is also applicable to their nanoscale counterparts. In principle, the UC process can be quantitatively expressed by a set of rate

equations describing the population density (N_i) of each $4f^N$ manifold of Ln^{3+}, taking into account all population and depopulation paths involved [88–90]:

$$\frac{dN_i}{dt} = \sum \text{population rate} - \sum \text{depopulation rate}$$

$$= \sum_j N_j\left(A_{ji}^{ED} + A_{ji}^{MD}\right) + N_{i+1}W_{i+1,i}^{NR} + \sum_{ij,kl} N_j N_l C_{ji,lk}^{ET}$$

$$- \sum_j N_j\left(A_{ij}^{ED} + A_{ij}^{MD}\right) - N_i W_{i,i-1}^{NR} - \sum_{ij,kl} N_i N_k C_{ij,kl}^{ET}$$

where A_{ij}^{ED} and A_{ij}^{MD} are Einstein coefficients for ED and MD radiative transitions from manifold i to j; $W_{i,i-1}^{NR}$ is the nonradiative multiphonon relaxation rate from manifold i to $i-1$; $C_{ij,kl}^{ET}$ represents the microscopic parameter of the energy transfer involving the donor $i \rightarrow j$ and the acceptor $k \rightarrow l$ transitions. In this model, the interactions among more than two ions (e.g., cooperative sensitization) are not considered. The ED and MD transition rates and the energy transfer parameter $C_{ij,kl}^{ET}$ can be calculated using the JO theory [74, 75], while the nonradiative multiphonon relaxation rates can be treated with a modified energy gap law [91, 92]. The intensity of any given UC emission peak is proportional to the product of the population density of the emitting manifold and its radiative transition rates. Once the transition rates are determined, the UC characteristics, including spectral ratios, luminescent lifetimes, and QYs, can be calculated directly by solving these differential equations. The critical energy transfers involved in UC process can also be determined using this model. Although this model is usually simplified to include only the major transitions and nonradiative multiphonon relaxations, it remains challenging to give an accurate solution to these rate equations due to the difficulty in determining all the rate constants.

The rate equations for UC process are often built for theoretical analysis or prediction, but there are only very few reports on the use of this approach in UCNPs mainly because of the complexity of UC process in nanoscale [88, 89]. Instead, most of the optical characteristics of UCNPs were determined experimentally. The investigation on the time-dependent PL behavior (or luminescence lifetime) of UC emissions is a good way to verify the validity of the proposed UC processes, and the rate constants could be extracted by fitting the measured time-dependent emission intensity with transient rate equations [93, 94]. In a typical ETU process, energy transfer from the sensitizers (e.g., Yb^{3+}) will apparently lengthen the PL lifetimes of the activators (e.g., Er^{3+} and Tm^{3+}), which are intrinsically orders of magnitude shorter than that of the sensitizers, due to slow population of the activator's excited state from the long-lived sensitizer's excited state [95]. As a result, the apparent UCL lifetime of the activators strongly depends on those of the sensitizers, which differs markedly from its downshifting PL lifetime upon direct excitation to the high-lying states. It was predicted that the UCL lifetime of the activators for an n-photon UC process in bulk materials was $1/n$ of the sensitizer's

lifetime [96, 97]. However, in the nanosystems, the nonradiative deactivation plays a dominant role due to the surface quenching effect, and thus, the UCL lifetime of the NPs is closely related to their particle size and surface structure and usually deviates from the theoretical prediction [98, 99].

Owing to its nonlinear optical feature, UC displays a power density-dependent efficiency under CW laser excitation. The analysis on power dependence of UC emissions combined with the steady-state rate equations provides useful hints on UC kinetics. A theoretical model was proposed by Pollnau and Suyver et al. [2, 100], which is now frequently used as an evidence for UC processes in Ln^{3+}-doped UCNPs. Briefly, the UC emission intensity (I) is proportional to n orders of the pump power density (P): $I \propto P^n$. By plotting the emission intensity versus the pump power density in a double-logarithmic diagram, the order n of the UC process, i.e., the number of pump photons required to excite the emitting state, can be obtained by the slope of the power dependence curve (Fig. 8.7) [2]. This slope indicates the multiphoton nature of the UC emissions. It should be noted that the
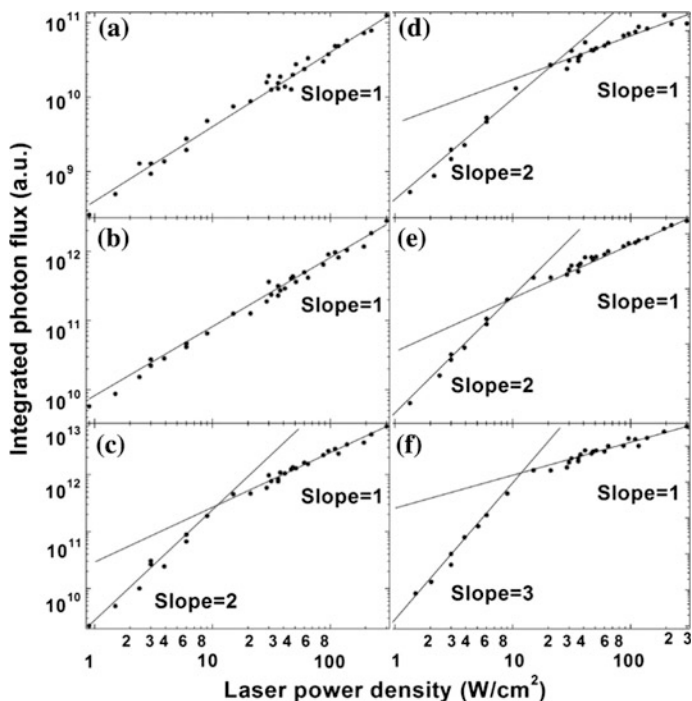
Fig. 8.7 UC excitation power dependence of the following transitions in NaYF$_4$:18 % Yb^{3+}, 2 % Er^{3+} powder samples: **a** $^4I_{13/2} \rightarrow {}^4I_{15/2}$, **b** $^2F_{5/2} \rightarrow {}^2F_{7/2}$ and $^4I_{11/2} \rightarrow {}^4I_{15/2}$, **c** $^4S_{3/2} \rightarrow {}^4I_{13/2}$, **d** $^4F_{9/2} \rightarrow {}^4I_{15/2}$, **e** $^4S_{3/2} \rightarrow {}^4I_{15/2}$, and **f** $^2H_{9/2} \rightarrow {}^4I_{15/2}$. The *lines* represent the calculations from the theoretical model in the high- and low-power limits. (Reprinted with the permission from Ref. [2]. Copyright 2005, American Physical Society.)

power density dependence of the UC emissions is valid only in the regime of low excitation power density and will turn more complicated for higher excitation power densities due to the competition between UC and linear decays in the individual excitation steps. The slope of the power dependence curve is known to decrease with increasing excitation power density. When the excitation intensity is high enough so that saturation of the intermediate energy state involved in the UC process occurs, the multiphoton UCL will appear with a slope of 1.

8.4 UCL Enhancement

The major bottleneck for the practical application of UCNPs lies in their low UC QYs. When compared with the conventional DSL bioprobes such as organic dyes or QDs, Ln^{3+}-doped UCNPs often suffer from low-to-medium brightness, which strongly restricts their commercial biomedical applications. Therefore, it is of fundamental significance to enhance the QY of UCNPs, in order to achieve high UCL output and promote their commercial applications. Apart from the manipulation of UC excitation (e.g., pulse excitation, multiwavelength excitation, and broadening the excitation band through the antenna effect), a variety of methods have been proposed to improve UCL, which can be classified into the following categories: (i) selection of the host materials, (ii) optimization of the dopant concentrations, (iii) intentional cation incorporation, (iv) surface passivation, and (v) plasmonic enhancement.

8.4.1 Selection of the Host Materials

The UC efficiency of Ln^{3+} is critically dependent on the structure, local site symmetry, CF strength, and phonon energy of the host materials. Careful selection of host materials is essential for achieving efficient UCL. Generally, desirable host materials should bear adequate transparency within the wavelength range of interest, low phonon energy, high optical damage threshold, and close lattice matches to Ln^{3+} dopants. In these regards, inorganic compounds of rare earth ions, alkaline earth ions, and a number of transition metal ions are suitable candidates for Ln^{3+} dopants to generate efficient UCL [47].

Phonon energy of the host matrix has a profound effect on UC efficiency. Host materials with low phonon energies are favorable for Ln^{3+} doping to achieve intense UCL, as the low-energy phonons assure low multiphonon relaxation rate and minimal nonradiative energy losses [101, 102]. Nevertheless, UC may sometimes require phonon assistance, and thus, there is a balance between phonon properties and UC efficiency. Among various inorganic materials, fluorides, owing to their high chemical stability and suitably low phonon energies (<350 cm^{-1}), are considered to be the most efficient host materials for Ln^{3+} doping to achieve

desirable UCL for versatile applications. Particularly, β-NaYF$_4$ has been recognized as the most efficient UC host materials for decades [44, 103]. Recently, some novel UC host materials such as β-NaLuF$_4$ and tetragonal-phase LiLuF$_4$ were found to yield higher UCL output than β-NaYF$_4$ [104–106]. Although the real UC efficiency of these materials needs to be confirmed, these studies greatly encourage researchers to find novel UC materials with QYs higher than β-NaYF$_4$.

In addition to phonon energy, crystal structure of the host matrix plays an important role in UC efficiency. The local site symmetry and CF strength around Ln^{3+} dopants determine their intrinsic electronic transitions. In general, low-symmetry hosts are more favorable for UCL than those high-symmetry counterparts, since low-symmetry hosts typically exert a CF containing more uneven components around the dopant ions, which would increase 4f–4f transition probabilities of the emitters. Besides, the lattice constants and the localized structure of the host matrix that influence the energy transfer between Ln^{3+} dopants have significant impact on UC efficiency. For instance, by preserving the excitation energy within Yb^{3+} sublattice, an unusual four-photon violet UC emission from Er^{3+} was observed in KYb$_2$F$_7$:Er NPs, with an intensity more than 8 times higher than the previously reported value in NaYF$_4$:Yb,Er NPs (Fig. 8.8) [107].

8.4.2 Optimization of the Dopant Concentration

The potentially easiest way to improve UC QY is the optimization of the dopant concentration within a single NP. The underlying mechanism for this approach involves the control over the distance-dependent energy transfer and CR as well as the concentration-dependent photon absorptions. UCL through GSA/ESA processes in Er^{3+} or Tm^{3+} singly doped NPs is often found too weak for bioapplications. To improve UC efficiency, Yb^{3+} ions with a larger absorption cross section in the NIR spectral region are codoped as sensitizers, as Yb^{3+} ions can effectively absorb NIR radiation and then transfer their energy to the activators through the ETU process.

Concentration quenching, a typical nonradiative process, should be avoided when optimizing the dopant concentration [108, 109]. Concentration quenching often occurs to those Ln^{3+} activators with rich energy levels (e.g., Tm^{3+}, Er^{3+}, Nd^{3+}, and Pr^{3+}) via a CR process at high doping concentration, resulting in nonradiative depopulation of the excited activator ions [110]. As a result, the UC QY and lifetime decrease with the increasing dopant concentration even though the UC emitter content increases. To this end, the doping level of the activators is usually kept low (typically below 2 mol%) to minimize the loss of excitation energy by CR. Unlike the activators, the sensitizer Yb^{3+} ion has a simple energy-level structure and thus is barely affected by CR, but luminescence quenching induced by energy migration from Yb^{3+} to the impurities, defects, or surface ligands increases with the Yb^{3+} concentration. To maximize the absorption, Yb^{3+} ions are often heavily doped. For example, the dopant concentrations of Er^{3+} and Yb^{3+} in NaYF$_4$ UCNPs
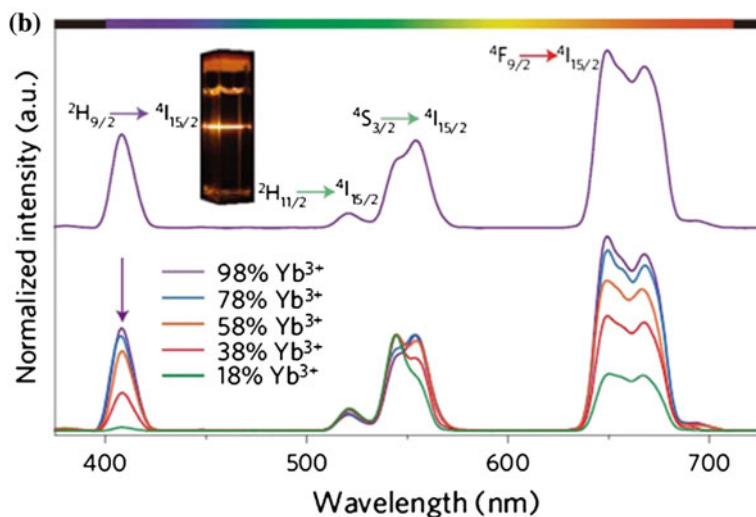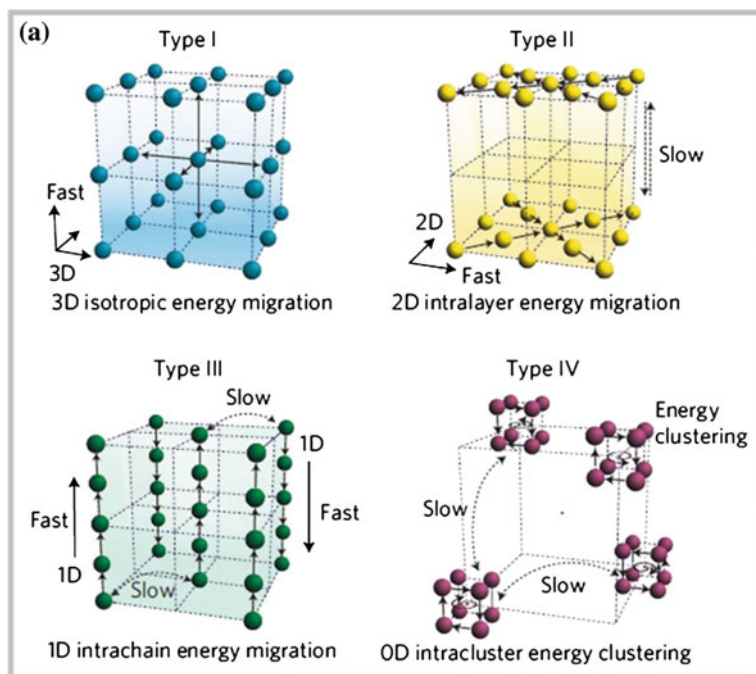
are optimized to be 2 mol% and 20 mol%, respectively [103, 111]. It is worthy of mentioning that in the hosts (e.g., CaF_2) heterovalently doped with Ln^{3+}, the optimized dopant concentration is usually lower than that in $NaYF_4$, because ion clusters are easily formed in Ln3+ heterovalently doped UCNPs, which might

◀ **Fig. 8.8 a** Schematic representation showing the topological energy migration pathways in different types of crystal sublattice. Type I to Type III schemes represent the random energy migration from an atom to its neighboring atoms in 3D, 2D, and 1D (space dimension), respectively. Type IV represents energy transfer within sublattice clusters. **b** UC emission spectra of KYb_2F_7:Er (2 mol%) (*top*) and KYb_2F_7:Er/Lu (2/0–80 mol%; *bottom*) nanocrystals recorded in cyclohexane solutions (0.2 wt%). All samples were excited with a 980-nm laser illumination at a power density of 10 W/cm². The emission spectra were normalized to the Er^{3+} emission at either 558 or 545 nm, whichever is stronger. The inset is a typical micrograph showing the UCL of KYb_2F_7:Er (2 mol%) nanocrystals. (Reprinted with the permission from Ref. [107]. Copyright 2014, Macmillan Publishers Limited.)

shorten the distance between Ln^{3+} ions and thus increase the energy losses through CR or energy transfer to defects [67].

Concentration quenching may be alleviated in some hosts by optimizing the synthesis and enhancing the excitation power density. It was demonstrated that monotonous increase of the Yb^{3+} concentration up to 100 mol% resulted in orders of magnitude enhancement of UCL in $NaYF_4$:Yb,Tm, $NaYF_4$:Yb,Tm@CaF_2, and KLu_2F_7:Yb,Er NPs [107, 112, 113]. Similarly, enormous UCL enhancement was found in LaF_3:Yb,Er NPs via a hetero-LEET UC process by simultaneously increasing the Yb^{3+} and Er^{3+} concentrations to 50 mol% and 5 mol%, respectively. Recently, Jin and coworkers demonstrated that high excitation irradiance (2.5×10^6 W/cm²) was able to alleviate concentration quenching in UCL when combined with higher activator concentration (Fig. 8.9) [48], which could be increased from 0.5 to 8 mol% for Tm^{3+} in $NaYF_4$. The UCL signals were significantly enhanced by up to a factor of 70. These unusual findings present a new approach for understanding and predicting the optical properties of Ln^{3+}-based UC systems.

8.4.3 Intentional Cation Incorporation

Cation incorporation is an effective way to enhance UCL through either controlling the energy transfer process or tailoring the local site symmetry and CF surrounding of Ln^{3+} dopants [114]. For instance, Yb^{3+} ions are usually codoped as sensitizers to harvest the excitation energy and improve UCL through ETU. Gd^{3+} ions serve as energy migrators in EMU to facilitate UCL for those Ln^{3+} ions without intermediate energy levels matchable to Yb^{3+} [57, 58]. Mn^{2+} ions enable excitation energy redistribution among different emitting levels of Er^{3+} and improve UC red emissions [115, 116]. Li^+ and Na^+ ions are excellent codopants or charge compensators to modify the CF surroundings of Ln^{3+} to improve their UCL [117, 118].

Cation incorporation also influences the synthesis of UCNPs, resulting in the change of the size, phase, and morphology of the NPs, which may in turn improve UC efficiency [119–121]. For instance, Liu and Wang reported that Gd^{3+} doping influenced the growth process of $NaYF_4$:Ln^{3+} NPs to give simultaneous control over the crystallographic phase, size, and UCL properties [121]. We recently found
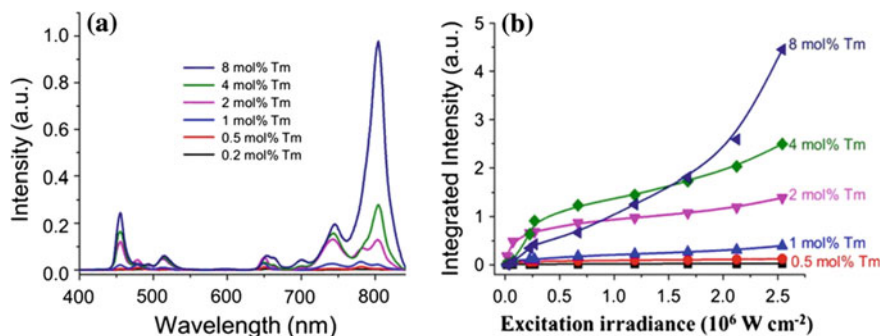
Fig. 8.9 a UC emission spectra of a series of $NaYF_4$:Yb,Tm NPs with varied Tm^{3+} concentrations under an excitation irradiance of 2.5×10^6 W/cm^2, showing a steady increase in UCL with increasing Tm^{3+} content from 0.2 mol% to 8 mol%. **b** Integrated UCL intensity (400–850 nm) as a function of excitation irradiance for a series of Tm^{3+}-doped nanocrystals. (Reprinted with the permission from Ref. [48]. Copyright 2013, Macmillan Publishers Limited.)

that the Na^+ doping had a significant effect on the growth of ultrasmall CaF_2:Ln^{3+} NPs, which significantly improved the crystallinity of the NPs as well as their DSL and UCL properties [66]. By recording the steady-state PL spectra and PL transients of CaF_2:Ce,Tb NPs, we showed solid spectroscopic evidence for the CF modification induced by Na^+ doping (Fig. 8.10). It was observed that the excitation band of Ce^{3+}, the spectral line splitting and branching ratio of Tb^{3+}, and their PL lifetimes varied significantly with the codoped Na^+ concentration, which unambiguously verified the modification of the CF environment around Ln^{3+} induced by Na^+ codoping. These DSL properties of Ln^{3+} are very sensitive to their local coordination environment and thus may be exploited to monitor the impurity-induced local structure and CF modification for Ln^{3+}-doped UCNPs.

8.4.4 Surface Passivation

The main reason for the low UC QY of Ln^{3+}-doped UCNPs lies in the deleterious surface quenching effect in colloidal dispersions deriving from their high surface-to-volume ratio. To overcome this shortcoming, surface passivation by growing a uniform shell with similar lattice constants is regarded as an effective way to improve UC QY of UCNPs. Several strategies have been explored for the fabrication of high-quality core/shell UCNPs, with either homogeneous or heterogeneous shells. An ideal shell coating is that all dopant ions are totally confined in the interior of the core particles and the shell is homogeneously grown around the core, thereby effectively suppressing the energy losses related to the crystal surface and eventually enhancing UCL [37].
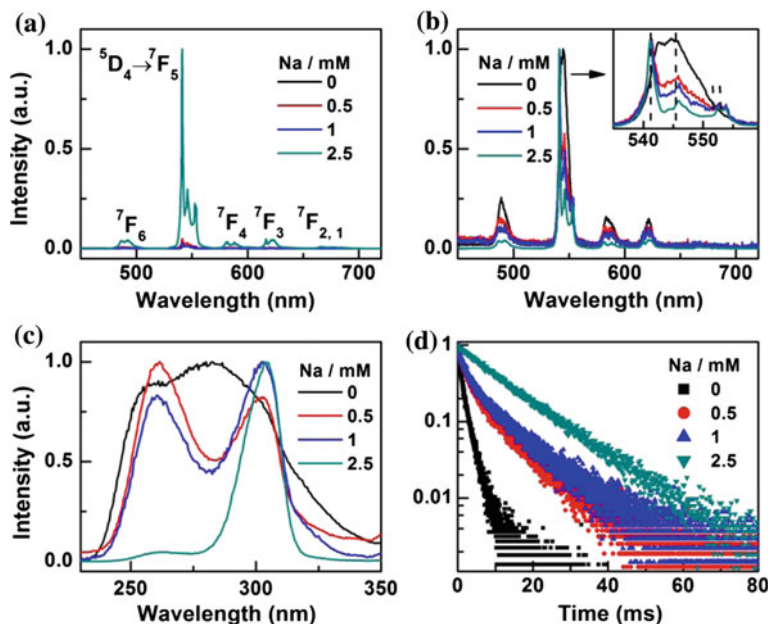
Fig. 8.10 a PL emission spectra and **b** the corresponding normalized emission spectra of CaF_2:5 %Ce^{3+}, 5 %Tb^{3+} NPs synthesized with different Na^+ concentrations upon excitation at 304 nm. The *inset* enlarges the spectral line splitting within 530–580 nm. **c** Normalized PL excitation spectra and **d** PL decay from $^5D_4$ by monitoring the Tb^{3+} emission at 541.2 nm for NPs synthesized with different Na^+ concentrations. (Reprinted with the permission from Ref. [66]. Copyright 2013, Wiley-VCH Verlag GmbH & Co. KGaA.)

In homogeneous core/shell architectures, the shell has similar compositions with the core. The first demonstration of UCL enhancement using homogeneous core/shell architectures was reported by Chow and coworkers in β-$NaYF_4$:Yb,Er(or Yb,Tm)@$NaYF_4$ NPs [122]. By growing an inert $NaYF_4$ shell with a thickness of 1.5 nm on the 7.7-nm core, the UCL intensity of the resulting NPs was enhanced by factors of 7.4 and 29.6 for Er^{3+} and Tm^{3+}, respectively. Since then, the concept of core/shell architectures has been established as the most general and effective strategy for UCL enhancement in UCNPs of varied hosts and Ln^{3+} compositions [123–125]. Core/shell structures bearing completely different chemical compositions (namely heterogeneous core/shell architectures), with matched lattice parameters, can also be constructed for UCL enhancement. To exemplify this, Yan et al. successfully realized a ∼300-fold enhancement of UCL intensity in 10–13 nm α-$NaYF_4$:Yb,Er@CaF_2 core/shell NPs relative to their core-only counterparts [126]. Similarly, Prasad et al. coated the hetero-shell of CaF_2 on α-$NaYbF_4$: Tm NPs, which yielded a 35-fold enhancement of NIR-to-NIR UCL intensity [113].

Apart from the inert shells without Ln^{3+} dopants, the active shells doped with Ln^{3+} activators or sensitizers are also designed in surface passivation for UCL enhancement. Capobianco et al. demonstrated that the growth of $NaGdF_4$:Yb active shell

around $NaGdF_4$:Yb,Er core was more effective in UCL enhancement than the growth of an inert $NaGdF_4$ shell, which was attributed to the increased Yb^{3+} absorption [127]. Later, the strategy of active-core/active-shell architecture was extensively applied to other Ln^{3+}-doped UCNPs for improving their UC efficiency, such as $LaPO_4$:Er@$LaPO_4$:Yb [128], $BaGdF_5$:Yb,Er@$BaGdF_5$:Yb [129], and BaF_2:Ln^{3+}@SrF_2:Ln^{3+} [130]. Such architecture may endow UCNPs with destined UC properties by incorporating Ln^{3+} dopants into different shell layers. The detrimental CR between Ln^{3+} dopants can be completely eliminated by the spatial confinement of Ln^{3+} ions in different layers. For instance, the design of $NaGdF_4$:Yb,Tm@$NaGdF_4$:Ln EMU NPs and the Nd^{3+}-sensitized $NaGdF_4$:Yb,Er@$NaGdF_4$:Nd,Yb UCNPs was based on the spatial separation of Ln^{3+} dopants in different layers of core/shell structures and the control over the energy transfer between the layers.

In most cases, the shell growth is not as ideal as expected and the dopant ions are often partially shielded by the shells; thus, the UC efficiency is strongly dependent on the thickness or number of shell monolayers. Zhang and coworkers established a linear link between the thickness of $NaGdF_4$ shell and the UCL intensity response of β-$NaYF_4$:Yb,Er@$NaGdF_4$ core/shell NPs [131]. Along with the homogeneous epitaxial shell growth layer-by-layer, surface defects of the cores were gradually passivated by the shells, which resulted in significant enhancement in the overall UCL intensity and the increase in UCL lifetime. With the development of the synthesis and characterization of core/shell nanostructures, ideal core/shell UCNPs with dopant ions totally confined in the core can now be readily fabricated. For instance, van Veggel et al. developed a facile approach based on self-focusing by Ostwald ripening for the synthesis of core/shell UCNPs that are tunable both in thickness and in compositions [132]. Zhang et al. reported one-pot successive layer-by-layer synthesis of 16-monolayer core/shell UCNPs by injecting the shell precursors into the reacting solution without the lengthy multicycle batch operation necessitated in conventional seed-mediated heat-up synthesis [133]. Similarly, we developed a unique strategy based on successive layer-by-layer injection of shell precursors for the synthesis of multishell $LiLuF_4$:Ln^{3+}@$LiLuF_4$ UCNPs through a thermal decomposition route (Fig. 8.11) [104]. Compared to the method reported by Zhang et al., our strategy is much easier to handle without the need for the precipitation of core NPs and the tedious alterative injection of different shell precursors, thus providing a more convenient and general synthetic method for core/shell UCNPs. Due to the successive shell growth, the overall UCL intensity was remarkably enhanced. The absolute UC QYs of Er^{3+} and Tm^{3+} were, respectively, improved from 0.11 and 0.61 % in the core-only NPs to 5.0 and 7.6 % in 16-monolayer core/shell counterparts, upon 980-nm NIR laser excitation at a power density of 127 W/cm². It is worthy of emphasizing that the UC QYs for Yb/Er (or Yb/Tm) codoped $LiLuF_4$ core/shell UCNPs with 16 monolayers are the highest among those Ln^{3+}-doped UCNPs ever reported, upon NIR excitation at equivalent power density. Moreover, due to the effective shell protection, these multishell UCNPs exhibited very high resistance to luminescence quenching in colloidal dispersions. These results clearly demonstrate that the $LiLuF_4$ crystal is a promising host material for UCL, and the strategy of successive surface passivation is effective for improving UC QY.
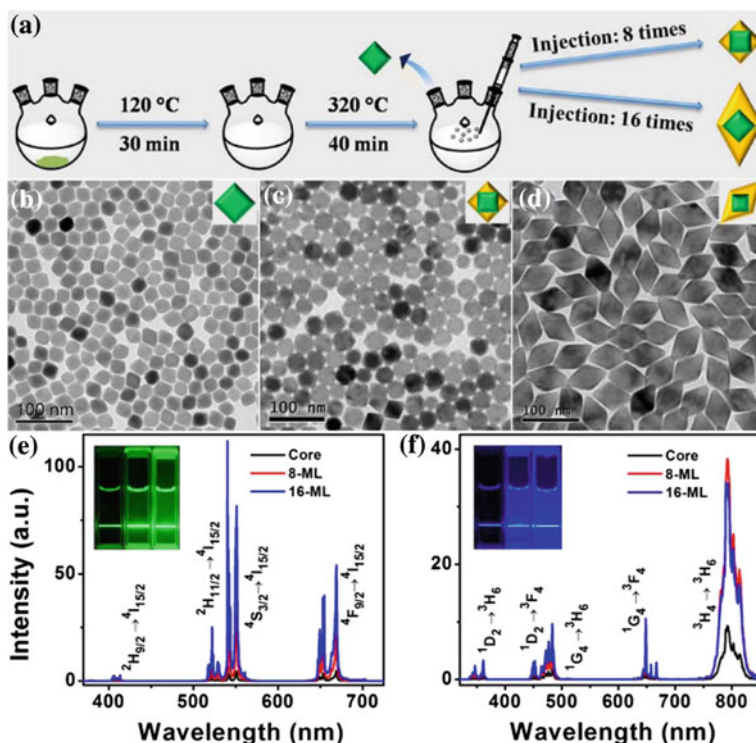
Fig. 8.11 **a** Schematic illustration of the synthesis of LiLuF$_4$:Ln^{3+} core-only and core/shell UCNPs. TEM images of LiLuF$_4$:Yb,Er core-only (**b**) and core/shell UCNPs with 8 (**c**) and 16 monolayers (**d**). UC emission spectra of (**e**) LiLuF$_4$:Yb,Er and (**f**) LiLuF$_4$:Yb,Tm core-only and core/shell UCNPs with different shell layers upon NIR excitation at 980 nm. The *insets* show the corresponding UCL photographs under 980-nm NIR laser irradiation at a power density of 20 W/cm^2. (Reprinted with the permission from Ref. [104]. Copyright 2014, Wiley-VCH Verlag GmbH & Co. KGaA.)

8.4.5 Plasmonic Enhancement

Surface plasmon resonance (SPR) is the collective oscillation of electrons at the interface of metallic structures and is produced by the electromagnetic interaction of the metals with lights of specific wavelengths within the skin depth of the metal surface [134, 135]. It is established that SPR of metallic structures can effectively enhance the fluorescence of the adjacent fluorophores such as organic dyes and QDs [136, 137]. Similarly, SPR can also be used to enhance the UC efficiency of Ln^{3+}-doped UCNPs. The coupling of UCNPs with SPR of noble metals is capable of amplifying the electromagnetic field acting on UCNPs, resulting in improved UC efficiency. Meanwhile, the electronic transitions of the Ln^{3+} ion and the energy transfer between ions may be affected by SPR under the resonant condition of UC emissions with SPR of noble metals, which also accounts for the improvement of

UC efficiency [138–141]. Note that the SPR effect is sensitive to the distance between UCNPs and the metal surface, which may also cause unwanted UCL quenching.

Generally, noble metals such as Au and Ag are employed to create SPR enhancement effect on UCNPs. For instance, Duan et al. reported a factor of ~ 2.6 enhancement of UCL intensity by SPR through the attachment of Au NPs onto $NaYF_4$:Yb,Tm NPs [138]. Kagan et al. designed a configuration in which close-packed monolayers of UCNPs were separated from a dense multilayer of metal NPs (Au or Ag) by a nanoscale Al_2O_3 spacer (Fig. 8.12a) [139]. UCL
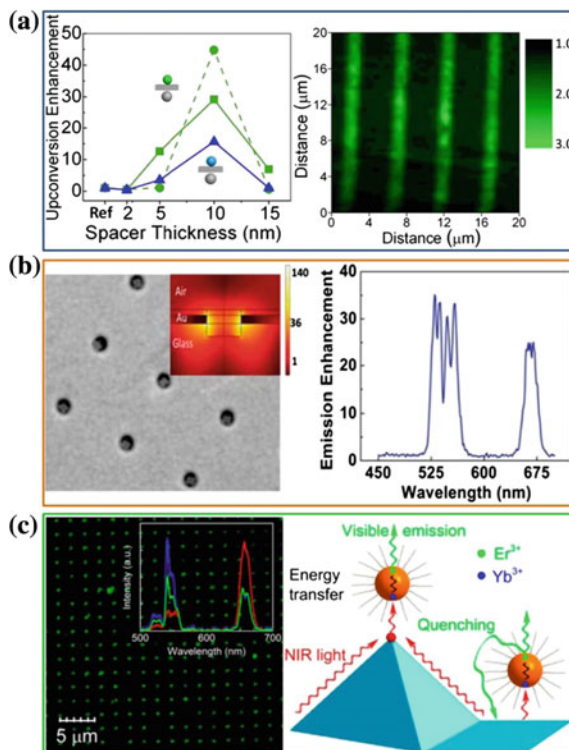
Fig. 8.12 **a** Metal-enhanced UCL tunable through metal nanoparticle–nanophosphor separation. *Left* integrated UCL intensity as a function of the Al_2O_3 layer thickness normalized to that of the pure UCNP sample for Ag NPs; *right* UCL mapping of Au NP-Al_2O_3-$NaYF_4$:Yb,Er UCNP films with an Al_2O_3 layer of 5 nm. **b** Plasmonic UCL enhancement in Au nanohole arrays. *Left* SEM image of the UCNP filled Au nanohole array, the *inset* shows the intensity enhancement inside an aperture in the nanohole array at its resonance normalized with respect to a similar array made in glass; *right* UC emission enhancement factor as a function of wavelength. **c** Plasmonic UCL enhancement on Au pyramid substrate. *Left* confocal images for the green emission on 29-nm $NaYF_4$:Yb,Er NPs, the *inset* shows the corresponding UC emission spectra of the NPs on the gold pyramid (*red curve*), flat gold (*green curve*), and glass substrate (*blue curve*), respectively; *right* schematic of the energy transfer, UC, and quenching processes on the top and bottom of the gold pyramid substrate. (Reprinted with the permission from Refs. [139–141], respectively. Copyright 2012, 2013, 2014, American Chemical Society.)

enhancements were found to be dependent on the thickness of Al_2O_3 spacers and the type of metal NPs with enhancements of up to 5.2-fold proximal to Au NPs and of up to 45-fold proximal to Ag NPs. They also fabricated a tunable plasmonic nanohole Au array that can accommodate only a single UCNP and be resonant at the excitation wavelength of $NaYF_4$:Yb,Er (Fig. 8.12b) [140]. UCL enhancements of up to 35-fold were observed and attributed to the combined effects of enhancement in the excitation of sensitizers and increase in radiative decay rate of emitters, as corroborated by the measured decrease in the rise and decay times of the UCNPs in nanohole arrays. Recently, Nagpal et al. reported the resonant surface-plasmon-polaritons waves enhanced UCL of $NaYF_4$:Yb,Er on Au pyramid substrate (Fig. 8.12c) [141]. Their analysis indicated that surface-plasmon-polaritons waves not only enhanced the electromagnetic field, but also increased the rate of resonant energy transfer from Yb^{3+} to Er^{3+} by sixfold. Despite the improvement observed, the underlying mechanism and the optimal design of such plasmonic-enhanced UC system remain obscure and thus deserve in-depth study.

Besides the above chemical routes, other approaches such as external electric field or magnetic field can also be applied to UCNPs for efficient UCL enhancement [142, 143]. For instance, by applying relatively low voltages to Yb/Er codoped $BaTiO_3$ thin films, an enhancement factor of ~ 2.7 was observed for Er^{3+} UCL [143]. Such an enhancement was revealed to originate from the increase in the radiative transition probabilities resulting from the lower symmetry of Er^{3+} sites which arises when an external electric field is applied. These findings will aid further investigations of luminescence and the widespread applications of UC materials because they provide an additional degree of freedom in the design of luminescent materials and devices.

8.5 Luminescent Biodetection

Sensitive and specific biodetection is essential for a variety of biomedical applications, including protein identification, DNA immunoassay, and early cancer theranostics [144–146]. Among diverse in vitro biodetection methods, luminescent bioassay is currently the primary analytical tool because of its convenient optical signal transduction, high sensitivity, and fast response [147, 148]. Conventional luminescent bioprobes such as organic dyes, Ln^{3+} chelates, and QDs might suffer from a series of disadvantages, such as high background noise and considerable photodamage to biological specimens associated with UV excitation, low photobleaching threshold, and potential long-term toxicity. In sharp contrast, Ln^{3+}-doped UCNPs show little damage to biological specimens and are free of background autofluorescence upon excitation at NIR, where the biological samples have nearly no response. The large anti-Stokes shift of UCL under NIR excitation produces neat emission spectrum without any interference from the excitation light. Moreover, the line-like multiwavelengths and single-band emissions of UCNPs are highly desired for multiplexed bioassay to avoid any fluorescent cross talk. These features promise

Ln^{3+}-doped UCNPs as a new generation of luminescent bioprobes to circumvent the above limitations of traditional ones. In the past decade, many novel and efficient bioassay techniques based on Ln^{3+}-doped UCNPs have been developed. According to their signal detection formats, two broad categories can be divided into heterogeneous and homogeneous luminescent bioassays. In this section, we will provide a brief overview on the most recent advances in the development of Ln^{3+}-doped nanobioprobes and their in vitro detection of biomolecules with an emphasis on tumor markers, based on both homogeneous and heterogeneous UCL assays.

8.5.1 Heterogeneous Assay

Heterogeneous assay commonly refers to a solid-phase assay and has the advantages of specific recognition and high binding affinity between target analytes and capture molecules anchored on a solid substrate carrying trace amounts of analyte for detection. The target analytes cover from small biomolecule to biomacromolecule including proteins and nucleic acids, and the capture molecules can be avidin, biotin, antigen, antibody, or aptamer, specific to the targeted analytes. Heterogeneous assays involve sandwich assay and competitive assay and usually require multiple washing steps to separate the probe–analyte complexes from the unreacted or unbound species for subsequent detection. In a typical procedure for a heterogeneous sandwich assay based on Ln^{3+}-doped UCNPs (Fig. 8.13a), the capture molecules are first immobilized on a solid substrate like a microtiter plate via incubation and then conjugated with the target analyte followed by a thorough washing step to avoid any negative effects of other biological species in the sample. Thereafter, a solution containing UCNP-labeled capture molecules is added to mark the analyte. As such, the analyte is sandwiched between the capture molecule immobilized on the solid phase and the UCNP-labeled capture molecule. After washing off excess unbound UCNP-labeled capture molecules, the substrate is subjected to UCL detection. The concentration of analyte can be quantified by directly measuring the optical signal of the UCNP label. For comparison, in a heterogeneous competitive assay, a solution containing UCNP-labeled analyte instead of UCNP-labeled capture molecule is added in the second step in order to compete with the free analyte to bind to the capture molecule anchored on the substrate, and therefore, the optical signal varies inversely with the concentration of the free analyte (Fig. 8.13b).

The first demonstration of UCL bioassay dated back in 1999 [149]. Since then, considerable efforts have been devoted to the use of UCNPs as sensitive bioprobes for diverse heterogeneous bioassays, including DNA microarrays, lateral-flow assays, microplate assays, and magnetic separation-assisted assays. Typical heterogeneous UCL bioassays based on Ln^{3+}-doped UCNPs are summarized in Table 8.1.
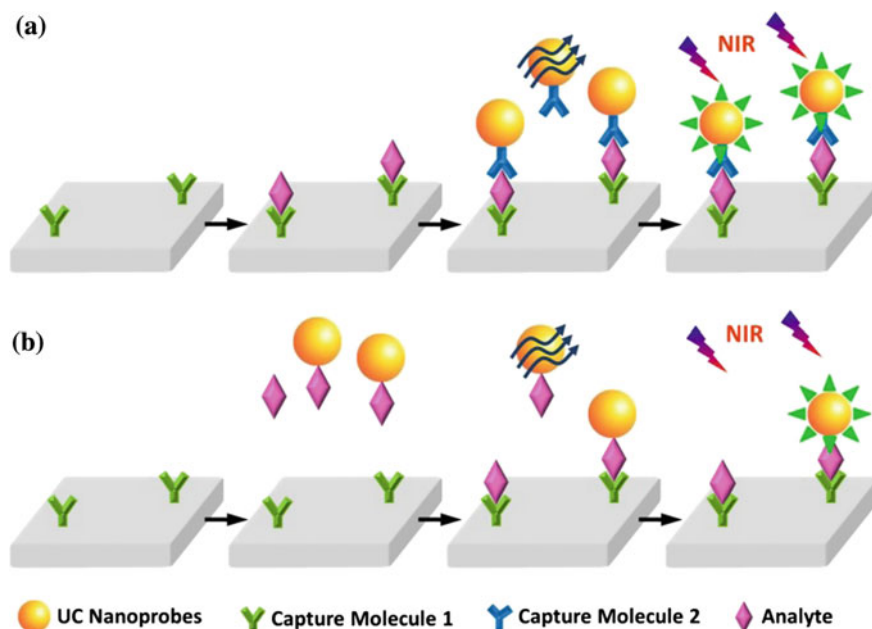
Fig. 8.13 Schematic illustration of typical heterogeneous UCL assays based on Ln^{3+}-doped UC nanoprobes: **a** sandwich assay and **b** competitive assay

One of the pioneering UCL bioassay applications based on Ln^{3+}-doped UCL probes was documented in DNA microarrays in order to improve their hybridization efficiency and detection sensitivity. For instance, Tanke and coworkers used biotinylated Y_2O_2S:Yb,Er submicron as UCL probes in DNA microarrays for the detection of nucleic acid hybrids [150]. Due to the absence of autofluorescence under NIR excitation, the use of UC phosphors yielded a fourfold lower limit of detection (LOD) than using conventional DSL probe cyanin 5. Zhang and coworkers developed UC microbarcodes based on multicolor $NaYF_4$:Yb,Ho,Tm UCNPs and combined them with organic dyes for multiplexed signaling and nucleic acid encoding [151]. Because there was no optical cross talk between the UC optical code and any reporter dyes under different excitation conditions, the target labels can be selected in a wide emission range, and thus, the code number was significantly increased. This kind of novel barcode material or biochips can be used for rapid and sensitive analysis of antigens and nucleic acids, which may have many potential applications in clinical, food, and environmental detection.

Another bioassay platform for Ln^{3+}-doped UCNPs is the lateral-flow assay, which is highly promising for point-of-care testing in community medical practice [164]. The lateral-flow platform typically consists of a sample pad, a nitrocellulose membrane, and an absorbent pad [153]. The nitrocellulose membrane provides one or more test lines for target capture, depending on the number of analyte species. These test lines contain antibodies specific to the target analyte of interest that is

Table 8.1 Typical heterogeneous UCL bioassays based on Ln^{3+}-doped UCNPs

Nanoprobes	Size (nm)	Bioconjugation	Analyte	LOD	Assay format	Ref.
Y_2O_2S:Yb,Er	400	DNA	DNA	~2 fM	Lateral-flow assay	[152]
$NaYF_4$:Yb,Er	Bulk	Antibody	E. coli O157:H7	1 pg/mL		[153]
Y_2O_2S:Yb,Er/Tm	Bulk	Antibody	hCG	10 pg/mL		[154]
$NaYF_4$:Yb,Er	200–300	Antibody	HBsAb	<20 mIU/mL		[155]
$NaYF_4$:Yb,Er	200	Antibody	V. anguillarum	10^2 CFU/mL		[156]
$NaYF_4$:Yb,Er	400	Antibody	Yersinia pestis	10^4 CFU/mL		[157]
$NaYF_4$:Yb,Er	20	Aptamer	CIAP	2 U/mL	Magnetic-separation-assisted assay	[158]
$NaYF_4$:Yb,Er	50	Avidin	EV71	20 pM		[159]
$NaYF_4$:Yb,Tm	50	Avidin	CV-A16	25 pM		[159]
$NaYF_4$:Yb,Tm	20–30	Aptamer	S. aureus	20 CFU/mL		[160]
$NaYF_4$:Yb,Ho	20–30	Aptamer	V. parahemolyticus	10 CFU/mL		[160]
$NaYF_4$:Yb,Er,Mn	20–30	Aptamer	S. typhimurium	15 CFU/mL		[160]
$NaYF_4$:Yb,Er	Bulk	Strepavidin	PSA	0.53 ng/L	Microplate assay	[161]
Y_2O_2S:Yb,Er	Bulk	Strepavidin	PSA	1.3 ng/L		[161]
$LiLuF_4$:Yb,Er@$LiLuF_4$	~50	Avidin	β-hCG	3.8 ng/mL		[104]
$NaScF_4$:Yb,Er	42	Biotin	Avidin	180 pM		[162]
$NaYF_4$:Yb,Er	30–40	Sugar	Lectin	1.3 nM		[163]

adsorbed onto the membrane. If the analyte is present in the sample, it will be captured and subsequently labeled by UCNPs at the test line. At least one additional control line captures any free UCNPs in order to confirm correct performance. Such UC lateral-flow bioassays have been extensively studied and established for the detection of several pathogenic microorganisms, nucleic acids, drugs of abuse, cytokines, and antibodies, through either a sandwich assay or a competitive one [153–155, 165–167]. For example, Corstjens et al. [165] applied UC phosphors to these test strips for the detection of human papillomavirus and achieved a 100-fold improved sensitivity as compared to established assays using Au NPs. Similarly, Lu et al. employed $NaYF_4$:Yb,Er microcrystals in an UC lateral-flow assay to detect hepatitis B surface antibody in standard positive sera and clinical sera, with distinctly higher sensitivities and reliability than those of conventional enzyme-linked immunosorbent assay (ELISA) [155]. Multiplex detection based on UC lateral-flow assays was conducted by Niedbala et al. for simultaneous detection of amphetamine, methamphetamine, phencyclidine, and opiates in saliva [153]. An important step toward point-of-care and on-site monitoring using UC lateral-flow assays was accomplished by the development of a portable UC reader (called Uplink) for scanning lateral-flow strips that were integrated in a disposable plastic cassette (a self-contained immunoassay device) [166, 167].

Magnetic separation and concentration are an effective way to amplify the optical signal and improve the detection sensitivity in heterogeneous UCL bioassays [159, 160, 168]. Li and Wang proposed a sandwich hybridization assay based on magnetic separation for the ultrasensitive detection of DNA using sub-50 nm $NaYF_4$:Yb,Er UCNPs [168]. In their study, a three-component sandwich assay was employed, in which capture DNA-modified Fe_3O_4 NPs were conjugated to probe DNA-modified $NaYF_4$:Yb,Er NPs through the hybridization of the target DNA. When combined with magnetic techniques for facile separation, this method produced an LOD of ~ 10 nM without polymerase chain reaction (PCR) amplification. Likewise, Wang and coworkers employed dual-color $NaYF_4$:Yb,Er,Tm UCNPs for quantitative analysis of viral loads in clinical samples with enterovirus 71 (EV-71) and coxsackievirus A16 (CV-A16) [159]. Through magnetic bioseparation and concentration using Fe_3O_4 NPs, extremely high sensitivity and selectivity were achieved with LODs of 20 and 25 pM for EV-71 and CV-A16, respectively. Based on this method, they further developed simultaneous aptasensors for multiplex pathogenic bacteria detection by using aptamer-functionalized multicolor $NaYF_4$: Ln^{3+} UCNPs as bioprobes and oligonucleotide-conjugated Fe_3O_4 NPs as magnetic separators [160]. The proposed simultaneous detection shows great potential to specifically detect various types of pathogenic bacteria coexisting in the food matrices through the substitution of suitable aptamers. The combination of UCNPs and magnetic NPs greatly simplifies the operations in sample separation and purification that are often tedious in a typical heterogeneous assay and thus provide a convenient approach for rapid and sensitive biodetection.

Recently, a novel heterogeneous UCL bioassay approach (i.e., UCL microplate assay) has been developed in our laboratory, which makes use of the surface-functionalized Ln^{3+}-doped UCNPs as bioprobes to detect trace amounts of
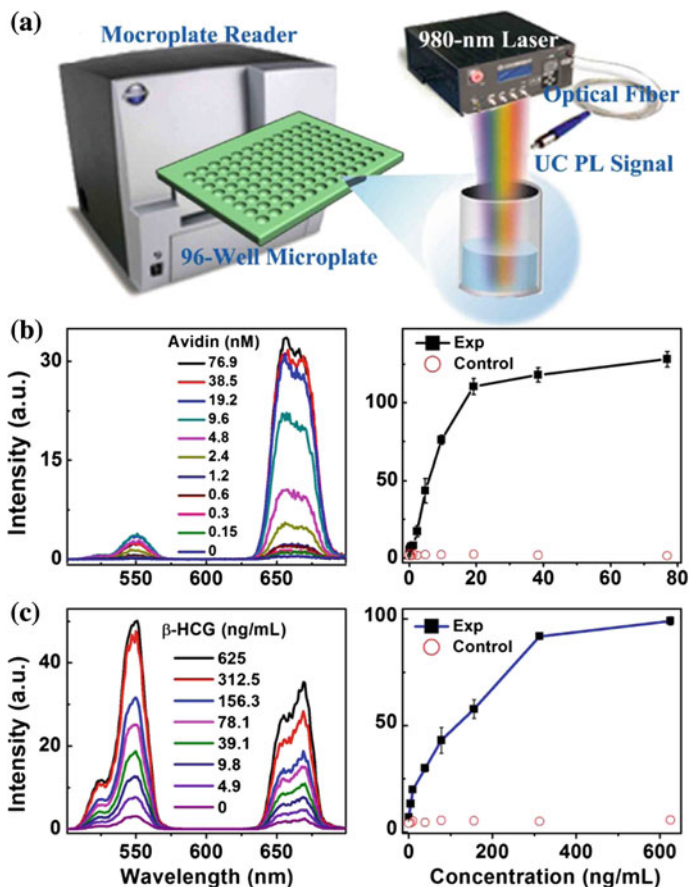
Fig. 8.14 a Experimental setup for heterogeneous UCL microplate assay based on Ln^{3+}-doped UCNPs. UC emission spectra of the bioassays for the detection of **b** avidin and **c** β-hCG as a function of the analyte concentrations by using $NaScF_4$:Yb,Er and $LiLuF_4$:Yb,Er@$LiLuF_4$ core/shell UCNPs as nanoprobes, respectively. In these detection processes, an external 0–4 W adjustable CW 980-nm laser was used as the excitation source, and the Synergy 4 multimode microplate reader (BioTek) was used as the signal collector. (**a**, **b**) Reprinted from Refs. [162, 169], respectively, by permission of The Royal Society of Chemistry. **c** Reproduced from Ref. [104] by permission of John Wiley & Sons Ltd.

analytes in fluid samples, ranging from model biomolecules like avidin to important tumor markers such as urokinase plasminogen activator receptor (uPAR), carcinoembryonic antigen (CEA), α-fetoprotein (AFP), prostate-specific antigens (PSA), and β subunit of human chorionic gonadotropin (β-hCG). The concentration of analytes is quantified by measuring the optical signals of UC nanoprobes bound to a 96-well microplate upon 980-nm laser excitation based on our customized UCL biodetection system equipped with a microplate reader (Fig. 8.14a). For instance, utilizing biotinylated $NaScF_4$:Yb,Er UCNPs as bioprobes, we realized the detection

of avidin protein in UCL microplate assays with an LOD of ~ 180 pM (Fig. 8.14b) [162]. More recently, we developed a novel and highly emissive avidin-functionalized $LiLuF_4$:Yb,Er@$LiLuF_4$ core/shell UCNPs and explored them as sensitive UC nanobioprobes for the detection of β-hCG [104]. It was observed that the UCL intensity of the nanoprobes exhibited a linear dependence with the concentration of β-hCG at 0-310 ng/mL. The LOD, defined as the concentration that corresponds to three times the standard deviation above the signal measured in the control experiment, was determined to be ~ 3.8 ng/mL, which is comparable to the β-hCG level in the serum of normal humans (Fig. 8.14c). These results reveal the great potential of the avidin-functionalized $LiLuF_4$:Ln^{3+} UCNPs as a sensitive UC nanobioprobe for the detection of diverse disease markers. More encouraging results were also obtained for the assay of uPAR, CEA, and AFP with LODs ranging from 1 to 20 pM, which are much lower than those in conventional fluorescence immunoassays like ELISA. Further work is underway on the analysis of human fluid samples such as serum and saliva, in order to fulfill the requirements in clinical applications.

8.5.2 Homogeneous Assay

Homogeneous assay is primarily based on the distance-dependent energy transfer (commonly FRET or LRET) from an energy donor to a nearby acceptor through long-range dipole–dipole interactions [170]. Unlike heterogeneous assay that involves laborious separation or washing operations, homogeneous assay is a liquid-phase assay and can be performed directly in the test solution through a simple "mix-and-read" step and thus is the most convenient bioassay method for fast detection in practical applications. The detection sensitivity in a homogeneous assay relies on the efficiency of the FRET process, which is critically dependent on the integral of spectral overlap between the emissions of the donor and the absorptions of the acceptor as well as the distance between the donor and acceptor molecules [171]. To maximize the FRET efficiency and achieve high detection sensitivity, the energy donors and acceptors in homogeneous FRET assays should be judiciously selected. Conventional DSL probes such as Ln^{3+} chelates and QDs as energy donors in the FRET system always suffer from serious background autofluorescence from the samples or assay plates in the test solutions, thus offering a low signal-to-noise ratio (S/N) and detection sensitivity. Moreover, the UV excitation of the energy donors is apt to simultaneously excite the energy acceptors, which could interfere with the FRET signal and give a fault detection result. Alternatively, Ln^{3+}-doped UCNPs are free of such background noise and coexcitation of energy acceptors under NIR irradiation, providing an improved S/N and high sensitivity for detection, and thus are regarded as ideal energy donors in homogeneous UC-FRET bioassays. The multiwavelength emissions of UCNPs allow the acceptors to selectively quench one emission band and leave the others nearly constant, thus making ratiometric detection feasible. Ratiometric detection is

independent of the excitation intensity, which endows the assay with high stability and flexibility [172].

In a typical UC-FRET process, Ln^{3+}-doped UCNPs are first excited upon NIR excitation and then nonradiatively transfer the excitation energy to the spectrally matchable acceptors in close proximity (normally within 10 nm or smaller), leading to the luminescence quenching of UCNPs or the emissions of the acceptors at a given wavelength, subject to the type of acceptors used. The acceptors are commonly those molecules or nanomaterials with large absorption coefficient at the wavelength matchable to the peak emission from UCNPs, such as fluorescent proteins, organic dyes, QDs, Au NPs or nanorods, MnO_2 nanosheets, aromatic polymer nanospheres, carbon NPs or nanotubes, graphenes, and graphene oxides [173–176]. Since the first demonstration of Ln^{3+}-doped UCNPs in UC-FRET assays in 2005 [177], a number of UC-FRET bioassay methods have been developed, typically sandwich assay and inhibition assay distinguished according to the assay format (Fig. 8.15). Typical homogeneous UC-FRET assays by employing Ln^{3+}-doped UCNPs as energy donors are summarized in Table 8.2.

UC-FRET sandwich assays generally utilize a sandwich structure to detect an analyte in which UCNPs and the acceptors are both labeled with the capture molecules that can specifically recognize the analyte (Fig. 8.15a). The UCNPs and the acceptors are initially far apart from each other in the test solution due to the absence of specific recognition; thus, no detectable FRET signal (namely no UCL quenching of the donor or the lack of the acceptor fluorescence) can be resolved. Upon the addition of analyte, the UCNPs and the acceptors are brought into close proximity through specific binding between their surficial capture molecules and the analytes, which forms a FRET pair and gives rise to the binding-modulated signals. As a result, the analyte can be quantified by directly measuring the optical signals of the UCNPs or the luminescent ratios of the acceptors to the UCNPs. A series of UC-FRET sandwich assays have been established by utilizing different donor–acceptor combinations [173, 174, 178–183, 191, 192]. For instance, Li et al. reported an UC-FRET biosensor for the detection of avidin with sub-50 nm $NaYF_4$: Yb,Er UCNPs as the donor and Au NPs as the acceptor, where an LOD as low as 0.5 nM for avidin was achieved under nonoptimized conditions. Xu et al. developed a sandwich-type UC-FRET system comprising human IgG-labeled $NaYF_4$: Yb,Er UCNPs as the donor and rabbit anti-goat IgG-labeled Au NPs as the acceptor, yielding a very low LOD of 0.88 μg/mL for goat antihuman IgG [178]. In their proof-of-concept experiment, Li et al. developed a DNA sensor using streptavidin-functionalized $NaYF_4$:Yb,Er UCNPs as the donor and reporter DNA–TAMRA as the acceptor to detect trace amount of target DNA with a nonoptimized LOD ranging from 10 to 60 nM [174]. For the detection of disease markers, Hao et al. established a sensitive UC-FRET biosensor based on the pair of oligonucleotide-modified $BaGdF_5$:Yb,Er UCNPs and Au NPs for rapid detection of H7 hemagglutinin genes of avian influenza viruses with an LOD down to 7 pM [179]. Simultaneous detection of multiple analytes by using multipeak emission profiles of UC particle donors was accomplished by Rantanen et al. [192]. In a dual-parameter sandwich hybridization assay, two probe oligonucleotides with
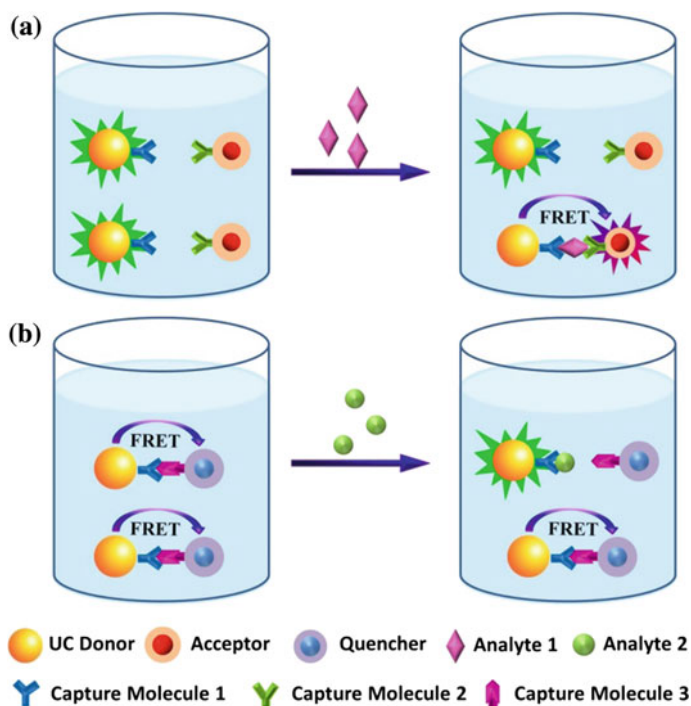
Fig. 8.15 Schematic illustration of typical homogeneous UC-FRET assays based on Ln^{3+}-doped UCNPs: **a** sandwich assay and **b** inhibition assay

sequences complementary to a target sequence of β-actin and HLA-B27 were selectively conjugated to Alexa Fluor 546 (AF546) and Alexa Fluor 700 (AF700), respectively. The oligonucleotide-modified dye molecules and target oligonucleotides were then mixed with $NaYF_4$:Yb,Er UC particles premodified with capture oligonucleotides. Upon formation of the sandwich complex through hybridization, the donor emissions at 540 and 653 nm were quenched by AF546 and AF700, respectively. By measuring the intensities of probe-specific emissions at 600 and 740 nm, two different target oligonucleotide sequences can be detected simultaneously and quantified with a dynamic range of measurement from 0.35 to 5.4 nM.

Besides sandwich-type assays, UC-FRET assays can also be performed in an inhibition way, where the luminescence of UC donors is initially quenched by the energy acceptors linked to the donors through FRET or "inner-filter" effect (Fig. 8.15b). The linkage can be cleaved by the analyte, thus recovering the luminescence of UCNPs. As a result, the optical signal of the UC donors is proportional to the analyte concentration. This method is also known as "quenching/recovery" assay since the detected optical signal experiences a quenching and recovery process. The initial quenching efficiency of the UCNPs is essential for the detection,

Table 8.2 Typical homogeneous UC-FRET assays by employing Ln^{3+}-doped UCNPs as energy donors

Nanoprobes	Size (nm)	Bioconjugation	Energy acceptor (or quencher)	Analyte	LOD (nM)	Assay type	Ref.
NaYF₄:Yb,Er	30–70	IgG	Nano gold	IgG	~6	Sandwich assay	[178]
BaGdF₅:Yb,Er	14	DNA	Nano gold	Gene	7×10^{-3}		[179]
NaYF₄:Yb,Tm	~50	Aptamer	Nano gold	Thrombin	0.118		[180]
NaYF₄:Yb,Er	–	DNA	TAMRA dyes	DNA	1.3		[181]
NaYF₄:Yb,Er	60–100	DNA	TAMRA dyes	DNA	0.6		[182]
NaYF₄:Yb,Er	28	DNA	TAMRA dyes	DNA	0.18		[183]
NaYF₄:Yb,Tm	143	DNA	SG1 dyes	DNA	2.5×10^{-4}		[173]
NaYF₄:Yb,Er	~25	Streptavidin	Cy3 dyes	DNA	3.4×10^{-6}		[184]
NaYF₄:Yb,Er	30–60	ConA	Nano gold	Glucose	43	Inhibition assay	[185]
NaYF₄:Yb,Er	20	Aptmer	TAMRA dyes	ATP	0.2		[186]
NaYF₄:Yb,Er	–	ConA	Graphene oxide	Glucose	25		[176]
NaYF₄:Yb,Er	29	ssDNA	Graphene oxide	ATP	1×10^4		[187]
NaYF₄:Yb,Er	60	Peptide	Graphene oxide	HIV antibody	2		[188]
NaYF₄:Yb,Er	10–20	Aptmer	Graphene	Kanamycin	9×10^{-3}		[189]
NaYF₄:Yb,Er	~50	Aptmer	Carbon NPs	Thrombin	0.18		[190]
NaYF₄:Yb,Tm	30	MnO₂ nanosheets	MnO₂ nanosheets	Glutathione	9×10^2		[175]

which requires the acceptors or quenchers to possess large extinction coefficient at the wavelength matchable to the emissions from UCNPs.

In view of their unique electronic and thermal properties, graphene oxide (GO), carbon nanomaterials like carbon NPs (CNPs), and manganese dioxide (MnO_2) nanosheets are superior quenchers for UC donors [186, 187, 193, 194]. For example, based on the nonradiative energy transfer from UCNPs to GO, Liu and coworkers constructed a novel biosensor for the detection of glucose in human serum samples without any background interference (Fig. 8.16a) [176]. They also designed another type of homogeneous biosensor for the detection of matrix metalloproteinase-2 (MMP-2, a very important biomarker in blood) by employing CNPs as energy acceptors (Fig. 8.16b) [193]. A polypeptide chain containing a specific MMP-2 substrate domain and π-electron-rich region was coupled with PEI-modified $NaYF_4$:Yb,Er UCNPs to serve as energy donors. Upon NIR excitation, the UC-FRET process was initiated via the π–π stacking interaction between the probe peptide and CNPs, thereby leading to the quenching of emissions from UC donors. Upon addition of MMP-2, such a UC-FRET process was inhibited due to the cleavage of the substrate peptide between UCNPs and CNPs. As a consequence, the UC emissions of the donors were recovered, thus providing a straightforward approach to quantify MMP-2 in solution with an LOD as low as 10 pg/mL. Recently, a novel UC-FRET inhibition assay was proposed for the rapid detection of glutathione in aqueous solutions and living cells based on the FRET pair of $NaYF_4$:Yb,Er UCNPs and MnO_2 nanosheets (Fig. 8.16c) [175]. MnO_2 nanosheets coated on the surface of UCNPs served as an efficient quencher for UCL. The luminescence was then turned on by introducing glutathione that reduced MnO_2 into Mn^{2+}. These MnO_2 nanosheets were further explored as a label-free nanoplatform for homogeneous UC-FRET detection of ochratoxin A (OTA) and cathepsin D (Cat D) by using different probes and following different sensing principles [195]. So far, some novel devices (such as UC-μPAD) and signal amplification strategies have been developed for homogeneous UC-FRET assays, with the aim to provide a clinical point-of-care test and improve the detection sensitivity [184, 194].

Besides the detection of biomolecules, the UC-FRET platforms have been exploited to serve as sensitive sensors for the detection of temperature, pH, and other molecules or ions in biological, food, and environmental monitoring, as summarized in some recent reviews [145, 172, 196, 197]. It should be noted that we use the term FRET here following the common convention. In fact, in most cases, the energy transfer from UCNPs to the acceptors might be dominated by the irradiation/reabsorption process instead of the nonradiative process, since the Ln^{3+} emitters on or near the surface of UCNPs that contribute primarily to the distance-dependent FRET process might suffer from serious surface quenching effect. Therefore, the underlying mechanisms in the so-called UC-FRET systems need in-depth study, which is essential for improving their performance in biodetection. It is also highly desirable to develop ultrasmall and highly emissive UCNPs for the distance-dependent homogeneous UC-FRET assays in the future, in order to develop a rapid and ultrasensitive biodetection platform for practical applications.
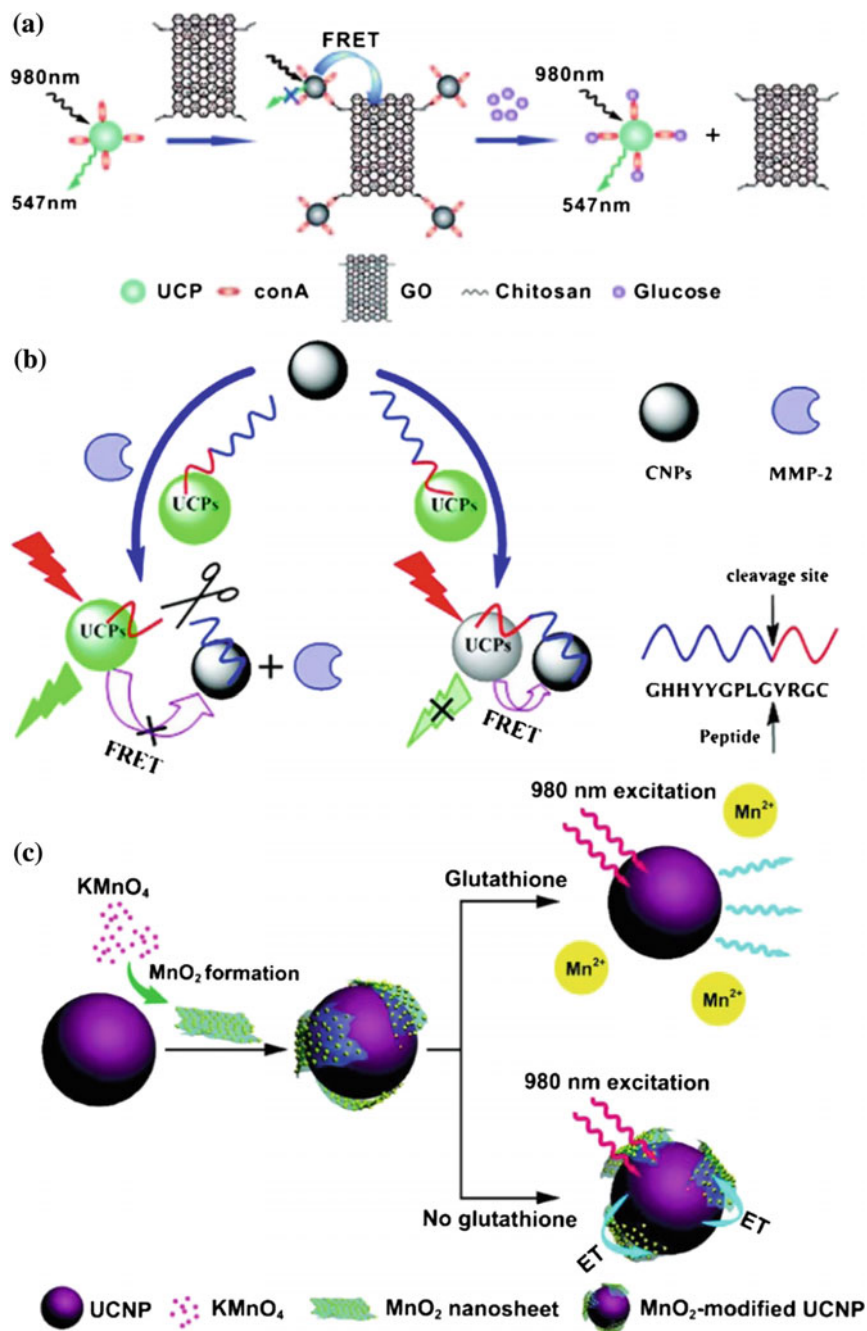
(a)

980nm

547nm

FRET

980nm

547nm

+

○ UCP ⬥ conA ▦ GO 〜 Chitosan ○ Glucose

(b)

CNPs MMP-2

UCPs UCPs

UCPs UCPs

FRET FRET

cleavage site

↓

GHHYYGPLGVRGC

Peptide ↑

(c)

980 nm excitation Mn²⁺

Glutathione

Mn²⁺ Mn²⁺

KMnO₄

MnO₂ formation

980 nm excitation

No glutathione

ET ET

● UCNP ⋰ KMnO₄ ▨ MnO₂ nanosheet ● MnO₂-modified UCNP

8.6 Optical Bioimaging

Fluorescence bioimaging based on Ln^{3+}-doped UCNPs offers a unique approach for visualizing morphological details in tissue with subcellular resolution and thus has recently become a powerful noninvasive tool for visualizing the full range of biospecies from living cells to animals. In comparison with DSL materials, UCL materials by using NIR light as the excitation source have many advantages for bioimaging, such as absence of autofluorescence, low phototoxicity, and improved tissue penetration depth [198, 199]. Due to these attractive merits, Ln^{3+}-doped UCNPs have been developed as a new class of luminescent optical labels [40]. In this section, we will provide a brief overview of the use of Ln^{3+}-doped UCNPs as efficient optical contrast agents for in vitro and in vivo imaging.

8.6.1 In Vitro Imaging

In 1999, Zijlmans et al. [149] firstly utilized submicron-sized Y$_2$O$_2$S:Yb,Tm UCNPs to study the distribution of prostate-specific antigen (PSA) in paraffin-embedded sections of human prostate tissue using standard immunohistological technique. Owing to their inherent high photon conversion efficiency and nonblinking emission behavior, UCNPs even allowed reliable single-molecule imaging, which thus challenged conventional staining agents [200]. After that, the idea of UCL bioimaging was realized by employing some other UCNPs such as oxysulfides or oxide nanomaterials (e.g., Y$_2$O$_3$:Yb/Er [201] and Gd$_2$O$_3$:Yb/Er [202]). An representative work reported by Zako and coworkers conducted cell imaging by employing cyclic arginine-glycine-aspartic acid (RGD) peptide labeled with Y$_2$O$_3$:Er UCNPs [203]. They found that these nanoconjugates can specifically bind to cancer cells with elevated integrin α$_v$β$_3$ expression. The ability to noninvasively visualize the expression level of integrin α$_v$β$_3$ will provide new avenues to detect tumors at early stage, having great potential in cancer imaging in living subjects.

For material selection in practical bioimaging, small size, bright luminescence and biological safety are the necessary requirements [50]. In contrast to the oxysulfide or oxide host materials, fluorides are considered as a better kind of host materials for the doping of Ln^{3+} to achieve intense UC emissions, owning to their low phonon energies and the resulting minimization of the quenching of the excited

state of Ln^{3+} ions [8]. With the development of facile synthetic strategies, many high-quality Ln^{3+}-doped fluoride NPs with controlled crystalline phases, shapes, and sizes have emerged [87, 205, 206]. Among them, $NaYF_4$ and $NaGdF_4$ have been well established as the most efficient UC host materials and thus have been widely used for in vitro cellular imaging; due to their high UC efficiency that offered excellent S/N, these UCNPs even allowed reliable single-molecule imaging [200]. Recently, Wu and coworkers demonstrated that individual $NaYF_4$:Yb/Er NP can emit nonblinking and photostable UCL for single-molecule imaging upon excitation from only a 980-nm continuous-wave (CW) laser source, in contrast to other multiphoton imaging techniques that require high-power pulsed femtosecond laser excitation [50]. Target imaging of tumor cells has also been widely investigated by using surface-functionalized UCNPs. Wang and coworkers demonstrated that $NaYF_4$:Yb,Er NPs conjugated with antibody can be used for highly specific staining and imaging of HeLa cells with antigen expressed on the cell membrane [198]. As observed from the UC fluorescence images (Fig. 8.17), the cells exhibited bright green UC fluorescence, confirming the successful attachment of the NPs to the surface of cells. Their results indicated that labeling by UC particles resulted in superior S/N due to the absence of autofluorescence. More importantly, the UCL was not susceptible to photobleaching, which thus facilitated longtime PL microscopy. In another work, Jiang et al. demonstrated that $NaYF_4$:Yb,Er NPs
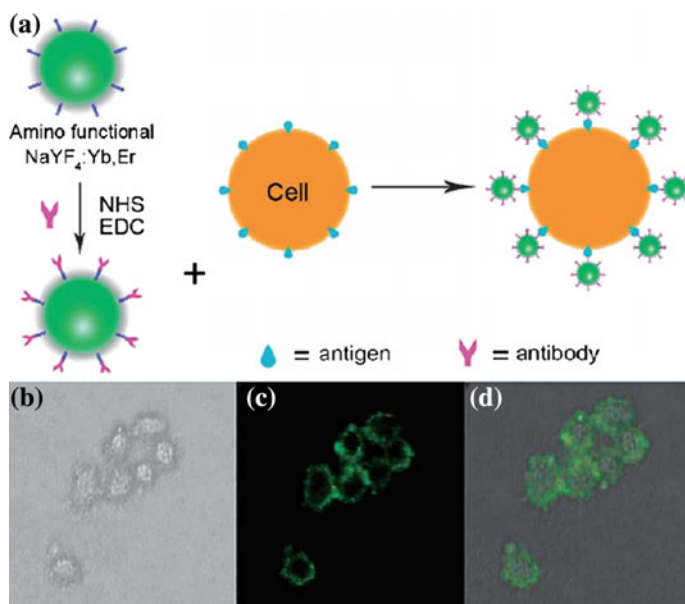
Fig. 8.17 a Schematic diagram of immunolabeling of HeLa cells based on antibody-conjugated $NaYF_4$:Yb,Er UCNPs. The fluorescence imaging of HeLa cells after incubation with antibody-conjugated $NaYF_4$:Yb,Er UCNPs **b** in bright field, **c** in dark field, and **d** overlays of (**b**) and (**c**). (Reprinted with the permission from Ref. [198]. Copyright 2009, American Chemistry Society)

conjugated with antibodies can be used for the delivery and tracking of small interference RNA (siRNA) [204]. To achieve the target delivery, siRNA was attached to anti-Her2 antibody that was further labeled with silica-coated $NaYF_4$: Yb,Er NPs. Intracellular uptake of the NPs was visualized under confocal fluorescence microscope, and the gene-silencing effect of siRNA was evaluated by a luciferase assay.

8.6.2 In Vivo Imaging

In vivo optical imaging, providing more detailed information on drug delivery, biological studies, and clinical application, has already been reported based on fluorescent probes such as organic dyes and QDs, but still confronts with numerous challenges. Firstly, it is difficult to realize deep tissue imaging because of intrinsic tissue signal attenuation. Secondly, the autofluorescence from tissue organic components during signal acquisition often results in poor S/N. As such, the development of in vivo imaging based on highly efficient UC NPs, which display a high S/N and deep tissue penetration, has received increased attention in recent years.

So far, quite a few UC nanoprobes have been employed as novel imaging agents for small animals. Lim and coworkers did the pioneering work on the application of UCNPs in live organism imaging [207]. In their study, Y_2O_3:Er,Yb NPs in the size range of 50–150 nm were inoculated into live nematode *Caenorhabditis elegans* (*C. elegans*) worms and subsequently imaged in the digestive system of the worms. Upon excitation at 980 nm, the statistical distribution of the NPs in the intestines can be clearly visualized (Fig. 8.18). More importantly, the NPs showed good biocompatibility as the worms behaved normally in feeding.
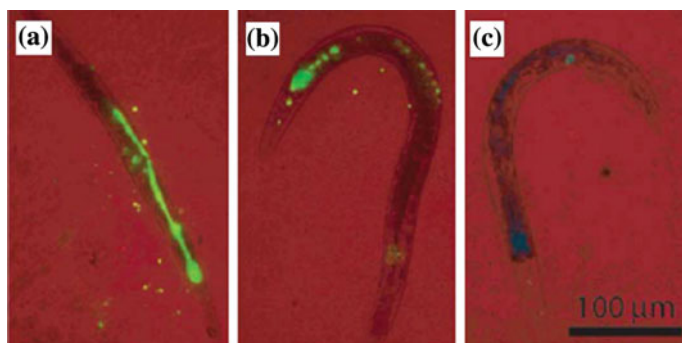
Fig. 8.18 The excretion behavior of *C. elegans* in food abundant medium for **a** 0 h, **b** 1 h, and **c** 2 h. False color images with *red* representing the bright field and *green* standing for the PL emission of Y_2O_3:Yb,Er NPs. (Reprinted with the permission from Ref. [207]. Copyright 2006, American Chemical Society.)

For small animal in vivo imaging, highly sensitive NIR–NIR systems have attracted increasing attention recently, because both the excitation and emission lights are located in the "optical transmission window" of tissues (700–1000 nm) [87]. For this purpose, Tm^{3+} ions are frequently chosen as dopants since they can exhibit strong NIR emission between 750 and 850 nm due to the transition from $^3H_4 \rightarrow {}^3H_6$ under CW laser excitation at 980 nm. So far, in vivo whole-body imaging of small animals has been successfully realized based on Tm^{3+}-doped $NaYF_4$ [208], $NaGdF_4$ [209], $NaLuF_4$ [210], and $NaYbF_4$ [199, 211] NPs. For instance, Li and coworkers conducted whole-body PL imaging of mouse, by employing sub-10 nm citric acid-capped β-$NaLuF_4$:Gd/Yb/Tm NPs [209]. The UC quantum yield (800 nm) for these NPs was measured to be 0.47 ± 0.06 %, and the S/N of the mouse injected subcutaneously with citric acid-modified β-$NaLuF_4$: Gd/Yb/Tm NPs ($\sim$7.8 nm) was 12 times that of citric acid-modified β-$NaYF_4$: Yb/Tm NPs ($\sim$20 nm). These results indicate that by utilizing these β-$NaLuF_4$: Gd/Yb/Tm NPs, high contrast UCL imaging of whole-body mouse with a penetration depth of $\sim$2 cm and an excellent detection limit of 50 cells can be achieved.

In addition, it is anticipated that the combination of the excellent UCL and magnetic properties in one nanocomposite would open up new avenues in the fields of in vivo imaging, since the optical/magnetic multimodal UC bioprobes can easily be guided by the magnetic field. As such, the multimodal NPs can be guided to the site of interest, whereas the UCL from doped Ln^{3+} ions can be used for real-time imaging [212]. Inspired by this concept, Liu et al. realized the in vivo labeling, tracking, and manipulation of mouse mesenchymal stem cells (mMSCs) by employing Au-coated $NaYF_4$:Yb/Er@Fe_3O_4 multifunctional NPs (MFNPs) as probes [213]. Stronger UCL intensity was detected on the site injected with more MFNP-labeled mMSCs. As few as $\sim$10 cells labeled with MFNPs are detected in vivo, indicative of high sensitivity of MFNP-based stem cell tracking. Furthermore, the MFNP-labeled mMSCs intraperitoneally injected in the middle of the abdomen can be guided to wound where a magnet was attached. Bright UCL signals were observed 6 h later from the site with the magnet attached, suggesting that the cells labeled with magnetic NPs can be manipulated by applying a magnetic field.

8.7 Conclusions and Perspectives

Ln^{3+}-doped UCNPs, emerging as a new class of luminescent nanoprobes and as an alternative to conventional DSL molecular probes, have been rapidly developed and pushed forward with unprecedented speed toward diverse biomedical applications in recent years. These nanobioprobes inherit the unique optical properties of Ln^{3+} ions such as long-lived luminescence, large anti-Stokes shifts, narrow emission bands, high resistance to photobleaching and photoblinking, and low toxicity. By taking advantage of these distinct optical features of Ln^{3+} along with the remarkable light penetration depth and the absence of autofluorescence in biological specimens under NIR excitation, a series of efficient analytical methods, such as heterogeneous

UCL and homogeneous UC-FRET assays, UCL bioimaging, NIR-triggered PDT, PTT, and targeted drug delivery techniques, have been established based on these novel Ln^{3+}-doped UC nanoprobes in the past decade.

Although it is still a long way to go for their commercialization, substantial progress has been made on Ln^{3+}-doped UC nanoprobes from their fundamental chemistry and physics to bioapplications, including controlled synthesis, optical spectroscopy, and diverse proof-of-concept bioapplications. Through manipulation over the emissions, excitations, and PL transients of these UC nanoprobes, many novel UC properties, such as multicolor emissions, single-band emissions, polarized emissions, stimulated emission and lasing, excitation wavelength tuning and broadening, and UCL lifetime multiplexing, have been explored very recently, which strikingly stimulate the application of UCNPs in life science. Currently, it is highly demanded to develop ultrasmall (sub 10-nm) biosensors with high UCL efficiency to fulfill the key requirements for in vitro biodetection, especially for UC-FRET bioassays. However, it remains a challenge to synthesize small-sized but highly emissive UC nanoprobes due to the deleterious surface quenching effects in colloidal dispersions. The UC-based bioassay for tumor markers is still in its infancy, and most of the assay LODs and specificity do not satisfy clinical requirements. Therefore, one top priority in the future is to further improve the LOD for various tumor markers and directly analyze human fluid samples (including serum and saliva) to validate their detection accuracy, recovery, and reliability for clinical diagnosis. Particularly, salivary diagnostics of tumor markers, which offers more convenient sampling strategy than common serum-based bioassays to reduce the patient discomfort, are highly promising for versatile cancer screening and monitoring in community medical service. We believe that these goals can be achieved by enhancing the UCL efficiency of nanobioprobes and optimizing current protocols involved in the nanoprobe synthesis or bioassays.

The major problem of current Ln^{3+}-doped UCNPs lies in their low UC QYs, which inevitably limits their commercial bioapplications. Despite a high QY of 7.6 % already achieved in some UCNPs, one should bear in mind that it was obtained upon high-power density excitation that is not acceptable for some in vivo applications. Therefore, one urgent task in the future is to enhance the QY of UC nanoprobes at safe excitation power densities within ANSI standards. This relies on a comprehensive study on the optical properties of UCNPs, which offers a guide to the synthesis and optimization of the materials. In addition, a criterion on the characterization of the absolute UC QY is highly demanded in view of its excitation power density dependency and different laser sources used, in order to make quantitative comparison of the results from worldwide laboratories. This work is now in progress in our laboratory. We look forward to provide a standard protocol for the measurement of absolute UC QY of UCNPs and a criterion for the performance evaluation of various Ln^{3+}-doped UCNPs with certain sizes, structures, and morphologies soon.

On the other hand, some undesirable side effects of Ln^{3+}-doped UC nanobioprobes should be eliminated prior to their use for biosensing. For instance, some key issues such as biocompatibility, stability, and the long-term toxicity of

nanoprobes need to be tackled for in vivo applications, although it may not be a big problem for in vitro biodetection. Moreover, due to the design inadequacy of commercial equipment such as microplate readers for UC biodetection or confocal laser scanning microscopy (CLSM) for UC bioimaging, there is a growing demand for the development of new-generation economic and sensitive detection or imaging systems for UCL. For example, UC-based equipments such as UCL microplate bioassay system or UC-modified CLSM, UCL flow cytometry, and time-gated orthogonal scanning automated microscopy (OSAM) systems integrate with an internal or external NIR (e.g., 980 or 808 nm) diode laser as the excitation source, thereby enabling heterogeneous and homogeneous UCL bioassays and UCL bioimaging for disease diagnosis and high-throughput drug screening.

References

1. Auzel F (2004) Upconversion and anti-stokes processes with f and d ions in solids. Chem Rev 104(1):139-173.
2. Suyver JF, Aebischer A, et al. (2005) Anomalous power dependence of sensitized upconversion luminescence. Phys Rev B 71(12):125123.
3. Liu G, Jacquier B (2005) Spectroscopic Properties of Rare Earths in Optical Materials. Springer: Berlin.
4. Wang YF, Liu GY, et al. (2013) Nd^{3+} Sensitized Upconversion Nanophosphors: Efficient In Vivo Bioimaging Probes with Minimized Heating Effect. ACS Nano 7(8):7200-7206.
5. Tu D, Liu Y, et al. (2013) Optical/Magnetic Multimodal Bioprobes Based on Lanthanide-Doped Inorganic Nanocrystals. Chem-Eur J 19(18):5516-5527.
6. Dong CH, Korinek A, et al. (2012) Cation Exchange: A Facile Method To Make $NaYF_4$:Yb, Tm-$NaGdF_4$ Core-Shell Nanoparticles with a Thin, Tunable, and Uniform Shell. Chem Mater 24(7):1297-1305.
7. van Veggel FCJM, Dong CH, et al. (2012) Ln^{3+} doped nanoparticles for upconversion and magnetic resonance imaging: some critical notes on recent progress and some aspects to be considered. Nanoscale 4(23):7309-7321.
8. Liu YS, Tu DT, et al. (2010) A Strategy to Achieve Efficient Dual-Mode Luminescence of Eu^{3+} in Lanthanides Doped Multifunctional $NaGdF_4$ Nanocrystals. Adv Mater 22 (30):3266-3271.
9. Wang J, Wei T, et al. (2014) Near-infrared-light-mediated imaging of latent fingerprints based on molecular recognition. Angew Chem Int Ed 53(6):1616-1620.
10. Liu Y, Chen M, et al. (2013) A Cyanine-Modified Nanosystem for in Vivo Upconversion Luminescence Bioimaging of Methylmercury. J Am Chem Soc 135(26):9869-9876.

11. Achatz DE, Meier RJ, et al. (2011) Luminescent Sensing of Oxygen Using a Quenchable Probe and Upconverting Nanoparticles. Angew Chem Int Ed 50(1):260-263.
12. Xing HY, Zhang SJ, et al. (2014) Ultrasmall $NaGdF_4$ Nanodots for Efficient MR Angiography and Atherosclerotic Plaque Imaging. Adv Mater 26(23):3867-3872.
13. Chen HY, Qi B, et al. (2014) Synthesis of brightly PEGylated luminescent magnetic upconversion nanophosphors for deep tissue and dual MRI imaging. Small 10(1):160-168.
14. Liu Q, Feng W, et al. (2013) Upconversion luminescence imaging of cells and small animals. Nat Protoc 8(10):2033-2044.
15. Yang YM, Shao Q, et al. (2012) In Vitro and In Vivo Uncaging and Bioluminescence Imaging by Using Photocaged Upconversion Nanoparticles. Angew Chem Int Ed 51 (13):3125-3129.
16. Dong NN, Pedroni M, et al. (2011) NIR-to-NIR Two-Photon Excited CaF_2: Tm^{3+},Yb^{3+} Nanoparticles: Multifunctional Nanoprobes for Highly Penetrating Fluorescence Bio-Imaging. ACS Nano 5(11):8665-8671.
17. Yang YM, Velmurugan B, et al. (2013) NIR photoresponsive crosslinked upconverting nanocarriers toward selective intracellular drug release. Small 9(17):2937-2944.
18. Viger ML, Grossman M, et al. (2013) Low power upconverted near-IR light for efficient polymeric nanoparticle degradation and cargo release. Adv Mater 25(27):3733-3738.
19. Dai YL, Xiao HH, et al. (2013) In Vivo Multimodality Imaging and Cancer Therapy by Near-Infrared Light-Triggered trans-Platinum Pro-Drug-Conjugated Upconverison Nanoparticles. J Am Chem Soc 135(50):18920-18929.
20. Boyer JC, Carling CJ, et al. (2010) Two-Way Photoswitching Using One Type of Near-Infrared Light, Upconverting Nanoparticles, and Changing Only the Light Intensity. J Am Chem Soc 132(44):15766-15772.
21. Gai SL, Yang PP, et al. (2010) Synthesis of Magnetic, Up-Conversion Luminescent, and Mesoporous Core-Shell-Structured Nanocomposites as Drug Carriers. Adv Funct Mater 20 (7):1166-1172.
22. Wang M, Chen Z, et al. (2014) Lanthanide-Doped Upconversion Nanoparticles Electrostatically Coupled with Photosensitizers for Near-Infrared-Triggered Photodynamic Therapy. Nanoscale 6(14):8274-8282.
23. Park YI, Kim HM, et al. (2012) Theranostic Probe Based on Lanthanide-Doped Nanoparticles for Simultaneous In Vivo Dual-Modal Imaging and Photodynamic Therapy. Adv Mater 24(42):5755-5761.
24. Idris NM, Gnanasammandhan MK, et al. (2012) In vivo photodynamic therapy using upconversion nanoparticles as remote-controlled nanotransducers. Nat Med 18 (10):1580-1585.
25. Chen Q, Wang C, et al. (2014) Protein modified upconversion nanoparticles for imaging-guided combined photothermal and photodynamic therapy. Biomaterials 35 (9):2915-2923.
26. Wang YH, Wang HG, et al. (2013) Graphene oxide covalently grafted upconversion nanoparticles for combined NIR mediated imaging and photothermal/photodynamic cancer therapy. Biomaterials 34(31):7715-7724.
27. Cheng L, Yang K, et al. (2011) Facile Preparation of Multifunctional Upconversion Nanoprobes for Multimodal Imaging and Dual-Targeted Photothermal Therapy. Angew Chem Int Ed 50(32):7385-7390.
28. Xiao QF, Zheng XP, et al. (2013) A core/satellite multifunctional nanotheranostic for in vivo imaging and tumor eradication by radiation/photothermal synergistic therapy. J Am Chem Soc 135(35):13041-13048.
29. Fan WP, Shen B, et al. (2013) Rattle-Structured Multifunctional Nanotheranostics for Synergetic Chemo-/Radiotherapy and Simultaneous Magnetic/Luminescent Dual-Mode Imaging. J Am Chem Soc 135(17):6494-6503.
30. Zhang YJ, Zheng F, et al. (2012) Tuning the autophagy-inducing activity of lanthanide-based nanocrystals through specific surface-coating peptides. Nat Mater 11(9):817-826.

31. Chen GY, Qiu HL, et al. (2014) Upconversion Nanoparticles: Design, Nanochemistry, and Applications in Theranostics. Chem Rev 114(10):5161-5214.
32. Wang F, Liu XG (2014) Multicolor tuning of lanthanide-doped nanoparticles by single wavelength excitation. Acc Chem Res 47(4):1378-1385.
33. Sun LD, Wang YF, et al. (2014) Paradigms and challenges for bioapplication of rare Earth upconversion luminescent nanoparticles: small size and tunable emission/excitation spectra. Acc Chem Res 47(4):1001-1009.
34. Gai SL, Li CX, et al. (2014) Recent progress in rare earth micro/nanocrystals: soft chemical synthesis, luminescent properties, and biomedical applications. Chem Rev 114(4):2343-2389.
35. Liu YS, Tu DT, et al. (2013) Lanthanide-doped luminescent nanoprobes: controlled synthesis, optical spectroscopy, and bioapplications. Chem Soc Rev 42(16):6924-6958.
36. Li XM, Zhang F, et al. (2013) Highly efficient lanthanide upconverting nanomaterials: Progresses and challenges. Nano Today 8(6):643-676.
37. Johnson NJJ, Veggel FCJM (2013) Sodium lanthanide fluoride core-shell nanocrystals: A general perspective on epitaxial shell growth. Nano Res 6(8):547-561.
38. Gorris HH, Wolfbeis OS (2013) Photon-Upconverting Nanoparticles for Optical Encoding and Multiplexing of Cells, Biomolecules, and Microspheres. Angew Chem Int Ed 52(13):3584-3600.
39. Feng W, Han CM, et al. (2013) Upconversion-nanophosphor-based functional nanocomposites. Adv Mater 25(37):5287-5303.
40. Zhou J, Liu Z, et al. (2012) Upconversion nanophosphors for small-animal imaging. Chem Soc Rev 41(3):1323-1349.
41. Gnach A, Bednarkiewicz A (2012) Lanthanide-doped up-converting nanoparticles: Merits and challenges. Nano Today 7(6):532-563.
42. Wang GF, Peng Q, et al. (2011) Lanthanide-Doped Nanocrystals: Synthesis, Optical-Magnetic Properties, and Applications. Acc Chem Res 44(5):322-332.
43. Erathodiyil N, Ying JY (2011) Functionalization of Inorganic Nanoparticles for Bioimaging Applications. Acc Chem Res 44(10):925-935.
44. Haase M, Schafer H (2011) Upconverting Nanoparticles. Angew Chem Int Ed 50(26):5808-5829.
45. Eliseeva SV, Bunzli J-CG (2010) Lanthanide luminescence for functional materials and bio-sciences. Chem Soc Rev 39(1):189-227.
46. Wang F, Banerjee D, et al. (2010) Upconversion nanoparticles in biological labeling, imaging, and therapy. Analyst 135(8):1839-1854.
47. Wang F, Liu XG (2009) Recent advances in the chemistry of lanthanide-doped upconversion nanocrystals. Chem Soc Rev 38(4):976-989.
48. Zhao JB, Jin DY, et al. (2013) Single-nanocrystal sensitivity achieved by enhanced upconversion luminescence. Nat Nanotechnol 8(10):729-734.
49. Schietinger S, Aichele T, et al. (2010) Plasmon-enhanced upconversion in single $NaYF_4:Yb^{3+}/Er^{3+}$ codoped nanocrystals. Nano Lett 10(1):134-138.
50. Wu SW, Han G, et al. (2009) Non-blinking and photostable upconverted luminescence from single lanthanide-doped nanocrystals. Proc Natl Acad Sci USA 106(27):10917-10921.
51. Luo WQ, Fu CY, et al. (2011) Er^{3+} Doped Anatase TiO_2 Nanocrystals: Crystal-Field Levels, Excited-State Dynamics, Upconversion, and Defect Luminescence. Small 7(21):3046-3056.
52. Chivian JS, Case WE, et al. (1979) The photon avalanche: A new phenomenon in Pr^{3+} based infrared quantum counters. Appl Phys Lett 35(2):124-125.
53. Joubert M-F (1999) Photon avalanche upconversion in rare earth laser materials. Opt Mater 11(2–3):181-203.
54. Dexter DL (1957) Possibility of luminescent quantum yields greater than unity. Phys Rev 108(3):630-633.
55. Maciel GS, Biswas A, et al. (2000) Blue cooperative upconversion in Yb^{3+} doped multicomponent sol-gel-processed silica glass for three-dimensional display. Appl Phys Lett 76(15):1978-1980.

56. Wang HS, Duan CK, et al. (2008) Visible Upconversion Luminescence from Y_2O_3:Eu^{3+},Yb^{3+}. J Phys Chem C 112(42):16651-16654.

57. Wang F, Deng RR, et al. (2011) Tuning upconversion through energy migration in core-shell nanoparticles. Nat Mater 10(12):968-973.

58. Su QQ, Han SY, et al. (2012) The Effect of Surface Coating on Energy Migration-Mediated Upconversion. J Am Chem Soc 134(51):20849-20857.

59. Sivakumar S, van Veggel FCJM, et al. (2007) Near-infrared (NIR) to red and green up-conversion emission from silica sol-gel thin films made with $La_{0.45}Yb_{0.50}Er_{0.05}F_3$ nanoparticles, hetero-looping-enhanced energy transfer (Hetero-LEET): A new up-conversion process. J Am Chem Soc 129(3):620-625.

60. Wang JW, Tanner PA (2009) Upconversion for White Light Generation by a Single Compound. J Am Chem Soc 132(3):947-949.

61. Rodríguez Burbano DC, Rodríguez EM, et al. (2014) The near-IR photo-stimulated luminescence of CaS:Eu^{2+}/Dy^{3+} nanophosphors. J Mater Chem C 2(2):228-231.

62. Bunzli JCG, Chauvin AS, et al. (2008) Lanthanide bimetallic helicates for in vitro imaging and sensing. In *Fluorescence Methods and Applications: Spectroscopy, Imaging, and Probes*. O. S. Wolfbeis, Ed.; Blackwell Publishing; Oxford pp 97-105.

63. Crosswhite HM, Crosswhite H (1984) Parametric model for f-shell configurations. I. The effective-operator Hamiltonian. J Opt Soc Am B: Opt Phys 1(2):246-254.

64. Wybourne BG (1965) Spectroscopic Properties of Rare Earths. Interscience: New York.

65. Carnall WT, Goodman GL, et al. (1989) A systematic analysis of the spectra of the lanthanides doped into single crystal lanthanum fluoride (LaF_3). J Chem Phys 90 (7):3443-3457.

66. Zheng W, Zhou SY, et al. (2013) Sub-10 nm Lanthanide-Doped CaF_2 Nanoprobes for Time-Resolved Luminescent Biodetection. Angew Chem Int Ed 52(26):6671-6676.

67. Blasse G, Grabmaier BC (1994) Luminescent Materials. Springer-Verlag: Berlin.

68. Renero-Lecuna C, Martín-Rodríguez R, et al. (2011) Origin of the High Upconversion Green Luminescence Efficiency in β-$NaYF_4$:2 %Er^{3+},20 %Yb^{3+}. Chem Mater 23(15):3442-3448.

69. Ju Q, Liu YS, et al. (2009) Optical Spectroscopy of Eu^{3+} Doped BaFCl Nanocrystals. J Phys Chem C 113(6):2309-2315.

70. Tanner PA (2010) Lanthanide Luminescence in Solids. In *Lanthanide Luminescence: Photophysical, Analytical and Biological Aspects, Springer Ser Fluoresc*. P. Hanninen; H. Harma, Eds.; Spinger-Verlag; Berlin Heidelberg.

71. Bunzli J-CG, Piguet C (2005) Taking advantage of luminescent lanthanide ions. Chem Soc Rev 34(12):1048-1077.

72. Liu LQ, Chen XY (2007) Energy levels, fluorescence lifetime and Judd-Ofelt parameters of Eu^{3+} in Gd_2O_3 nanocrystals. Nanotechnology 18(25):255704.

73. Tanner PA (2013) Some misconceptions concerning the electronic spectra of tri-positive europium and cerium. Chem Soc Rev 42(12):5090-5101.

74. Judd BR (1962) Optical absoprtion intensities of rare-earth ions. Phys Rev 127(3):750-761.

75. Ofelt GS (1962) Intensities of Crystal Spectra of Rare-Earth Ions. J Chem Phys 37 (3):511-520.

76. Chen XY, Zhao W, et al. (2004) Anomalous luminescence dynamics of Eu^{3+} in BaFCl microcrystals. Phys Rev B 70(20):205122.

77. Chen XY, Liu GK (2005) The standard and anomalous crystal-field spectra of Eu^{3+}. J Solid State Chem 178(2):419-428.

78. Butler PH (1981) *Point Group Symmetry Application: Method and Tables*. Plenum: New York.

79. Bünzli J-CG (1989) Luminescent probes. In *Lanthanide Probes in Life, Chemical and Eatrh Sciences*. J.-C. G. Bünzli; G. R. Choppin, Eds.; North-Holland: Amsterdam pp 219.

80. Gorller-Walrand C, Binnemans K (1996) Rationalization of crystal-field parameterization. In *Handbook on the Physics and Chemistry of Rare Earth*. K. A. Gschneidner; Jr.; L. Eyring, Eds.; North-Holland: Amsterdam.

81. Tu DT, Liu YS, et al. (2013) Breakdown of Crystallographic Site Symmetry in Lanthanide-Doped $NaYF_4$ Crystals. Angew Chem Int Ed 52(4):1128-1133.
82. Sobolev BP, Mineev DA, et al. (1963) Low-temperature hexagonal modification of $NaYF_4$ having the gagarinite structure Dokl Akad Nauk SSSR 150(4):791-794.
83. Burns JH (1965) Crystal Structure of Hexagonal Sodium Neodymium Fluoride and Related Compounds. Inorg Chem 4(6):881-886.
84. Krämer KW, Biner D, et al. (2004) Hexagonal sodium yttrium fluoride based green and blue emitting upconversion phosphors. Chem Mater 16(7):1244-1251.
85. Aebischer A, Hostettler M, et al. (2006) Structural and spectroscopic characterization of active sites in a family of light-emitting sodium lanthanide tetrafluorides. Angew Chem Int Ed 45(17):2802-2806.
86. Ju Q, Tu DT, et al. (2012) Amine-Functionalized Lanthanide-Doped $KGdF_4$ Nanocrystals as Potential Optical/Magnetic Multimodal Bioprobes. J Am Chem Soc 134(2):1323-1330.
87. Liu R, Tu DT, et al. (2012) Controlled synthesis and optical spectroscopy of lanthanide-doped $KLaF_4$ nanocrystals. Nanoscale 4(15):4485-4491.
88. Chan EM, Gargas DJ, et al. (2012) Concentrating and Recycling Energy in Lanthanide Codopants for Efficient and Spectrally Pure Emission: The Case of $NaYF_4:Er^{3+}/Tm^{3+}$ Upconverting Nanocrystals. J Phys Chem B 116(35):10561-10570.
89. Chan EM, Han G, et al. (2012) Combinatorial Discovery of Lanthanide-Doped Nanocrystals with Spectrally Pure Upconverted Emission. Nano Lett 12(7):3839-3845.
90. Xu CT, Zhan QQ, et al. (2013) Upconverting nanoparticles for pre-clinical diffuse optical imaging, microscopy and sensing: Current trends and future challenges. Laser Photonics Rev 7(5):663-697.
91. van Dijk JMF, Schuurmans MFH (1983) On the nonradiative and radiative decay rates and a modified exponential energy gap law for 4f–4f transitions in rare-earth ions. J Chem Phys 78 (9):5317-5323.
92. Walsh BM, Barnes NP, et al. (1998) Branching ratios, cross sections, and radiative lifetimes of rare earth ions in solids: Application to Tm^{3+} and Ho^{3+} ions in $LiYF_4$. J Appl Phys 83 (5):2772-2787.
93. Librantz AFH, Gomes L, et al. (2009) Population inversion of $^1G_4$ excited state of Tm^{3+} investigated by means of numerical solutions of the rate equations system in Yb:Tm:Nd: $LiYF_4$ crystal. J Appl Phys 105(11):113503
94. Jiang XP, Yang ZM, et al. (2009) Energy transfer between Yb^{3+} and Er^{3+} in barium gallogermanate glass. J Appl Phys 105(10):103113.
95. Tu DT, Liu LQ, et al. (2011) Time-Resolved FRET Biosensor Based on Amine-Functionalized Lanthanide-Doped $NaYF_4$ Nanocrystals. Angew Chem Int Ed 50 (28):6306-6310.
96. Kingsley JD, Fenner GE, et al. (1969) Kinetics and efficience of infrared-to visible conversion in LaF_3:Yb,Er. Appl Phys Lett 15(4):115-117.
97. Kingsley JD (1970) Analysis of Energy Transfer and Infrared-to-Visible Conversion in LaF_3: Yb, Er. J Appl Phys 41(1):175-182.
98. Zhao JB, Lu ZD, et al. (2013) Upconversion luminescence with tunable lifetime in $NaYF_4$: Yb,Er nanocrystals: role of nanocrystal size. Nanoscale 5(3):944-952.
99. Wang F, Wang J, et al. (2010) Direct Evidence of a Surface Quenching Effect on Size-Dependent Luminescence of Upconversion Nanoparticles. Angew Chem Int Ed 49 (41):7456-7460.
100. Pollnau M, Gamelin DR, et al. (2000) Power dependence of upconversion luminescence in lanthanide and transition-metal-ion systems. Phys Rev B 61(5):3337-3346.
101. Reed ED, Moos HW (1973) Multiphonon Relaxation of Excited States of Rare-Earth Ions in YVO_4, $YAsO_4$, and YPO_4. Phys Rev B 8(3):980-986.
102. Layne CB, Weber MJ (1977) Multiphonon relaxation of rare-earth ions in beryllium-fluoride glass. Phys Rev B 16(7):3259-3261.

103. Heer S, Kömpe K, et al. (2004) Highly efficient multicolour upconversion emission in transparent colloids of lanthanide-doped $NaYF_4$ nanocrystals. Adv Mater 16 (23-24):2102-2105.
104. Huang P, Zheng W, et al. (2014) Lanthanide-Doped $LiLuF_4$ Upconversion Nanoprobes for the Detection of Disease Biomarkers. Angew Chem Int Ed 53(5):1252-1257.
105. Zeng SJ, Xiao JJ, et al. (2012) Bi-functional $NaLuF_4$:Gd^{3+}/Yb^{3+}/Tm^{3+} nanocrystals: structure controlled synthesis, near-infrared upconversion emission and tunable magnetic properties. J Mater Chem 22(19):9870-9874.
106. Wang LL, Lan M, et al. (2013) Enhanced deep-ultraviolet upconversion emission of Gd^{3+} sensitized by Yb^{3+} and Ho^{3+} in β-$NaLuF_4$ microcrystals under 980 nm excitation. J Mater Chem C 1(13):2485-2490.
107. Wang J, Deng RR, et al. (2014) Enhancing multiphoton upconversion through energy clustering at sublattice level. Nat Mater 13(2):157-162.
108. Dexter DL, Schulman JH (1954) Theory of Concentration Quenching in Inorganic Phosphors. J Chem Phys 22(6):1063-1070.
109. Blasse G (1967) Concentration Quenching of Eu^{3+} Fluorescence. J Chem Phys 46 (7):2583-2585.
110. Asawa CK, Robinson M (1966) Temperature-Dependent Concentration Quenching of Fluorescence by Cross Relaxation of Nd^{3+} in LaF_3. Phys Rev 141(1):251-258.
111. Suyver JF, Grimm J, et al. (2006) Upconversion Spectroscopy and Properties of $NaYF_4$ Doped with Er^{3+}, Tm^{3+} and/or Yb^{3+}. J Lumin 117(1):1-12.
112. Mahalingam V, Vetrone F, et al. (2009) Colloidal Tm^{3+}/Yb^{3+} Doped $LiYF_4$ Nanocrystals: Multiple Luminescence Spanning the UV to NIR Regions via Low-Energy Excitation. Adv Mater 21(40):4025-4028.
113. Chen GY, Shen J, et al. (2012) (alpha-$NaYbF_4$:Tm^{3+})/CaF_2 Core/Shell Nanoparticles with Efficient Near-Infrared to Near-Infrared Upconversion for High-Contrast Deep Tissue Bioimaging. ACS Nano 6(9):8280-8287.
114. Chen DQ, Wang YS (2013) Impurity doping: a novel strategy for controllable synthesis of functional lanthanide nanomaterials. Nanoscale 5(11):4621-4637.
115. Wang J, Wang F, et al. (2011) Single-band upconversion emission in lanthanide-doped $KMnF_3$ nanocrystals. Angew Chem Int Ed 50(44):10369-10372.
116. Tian G, Gu ZJ, et al. (2012) Mn^{2+} Dopant-Controlled Synthesis of $NaYF_4$:Yb/Er Upconversion Nanoparticles for in vivo Imaging and Drug Delivery. Adv Mater 24 (9):1226-1231.
117. Zhao CZ, Kong XG, et al. (2013) Li^+ ion doping: an approach for improving the crystallinity and upconversion emissions of $NaYF_4$:Yb^{3+}, Tm^{3+} nanoparticles. Nanoscale 5 (17):8084-8089.
118. Dou QQ, Zhang Y (2011) Tuning of the Structure and Emission Spectra of Upconversion Nanocrystals by Alkali Ion Doping. Langmuir 27(21):13236-13241.
119. Ramasamy P, Chandra P, et al. (2013) Enhanced upconversion luminescence in $NaGdF_4$:Yb, Er nanocrystals by Fe^{3+} doping and their application in bioimaging. Nanoscale 5 (18):8711-8717.
120. Niu WB, Wu SL, et al. (2013) Multicolor tunability and upconversion enhancement of fluoride nanoparticles by oxygen dopant. Nanoscale 5(17):8164-8171.
121. Wang F, Han Y, et al. (2010) Simultaneous phase and size control of upconversion nanocrystals through lanthanide doping. Nature 463(7284):1061-1065.
122. Yi GS, Chow GM (2007) Water-soluble $NaYF_4$:Yb,Er(Tm)/$NaYF_4$/polymer core/shell/shell nanoparticles with significant enhancement of upconversion fluorescence. Chem Mater 19 (3):341-343.
123. Schäfer H, Ptacek P, et al. (2008) Synthesis and Optical Properties of KYF_4/Yb, Er Nanocrystals, and their Surface Modification with Undoped KYF_4. Adv Funct Mater 18 (19):2913-2918.
124. Abel KA, Boyer J-C, et al. (2009) Hard Proof of the $NaYF_4$/$NaGdF_4$ Nanocrystal Core/Shell Structure. J Am Chem Soc 131(41):14644-14645.

125. Zhang C, Lee JY (2013) Prevalence of Anisotropic Shell Growth in Rare Earth Core–Shell Upconversion Nanocrystals. ACS Nano 7(5):4393-4402.
126. Wang YF, Sun LD, et al. (2012) Rare-Earth Nanoparticles with Enhanced Upconversion Emission and Suppressed Rare-Earth-Ion Leakage. Chem-Eur J 18(18):5558-5564.
127. Vetrone F, Naccache R, et al. (2009) The Active-Core/Active-Shell Approach: A Strategy to Enhance the Upconversion Luminescence in Lanthanide-Doped Nanoparticles. Adv Funct Mater 19(18):2924-2929.
128. Ghosh P, Oliva J, et al. (2008) Enhancement of Upconversion Emission of $LaPO_4$:Er@Yb Core − Shell Nanoparticles/Nanorods. J Phys Chem 112(26):9650-9658.
129. Yang DM, Li CX, et al. (2011) Colloidal synthesis and remarkable enhancement of the upconversion luminescence of $BaGdF_5$:Yb^{3+}/Er^{3+} nanoparticles by active-shell modification. J Mater Chem 21(16):5923-5927.
130. Chen DQ, Yu YL, et al. (2012) Lanthanide dopant-induced formation of uniform sub-10 nm active-core/active-shell nanocrystals with near-infrared to near-infrared dual-modal luminescence. J Mater Chem 22(6):2632-2640.
131. Zhang F, Che RC, et al. (2012) Direct Imaging the Upconversion Nanocrystal Core/Shell Structure at the Subnanometer Level: Shell Thickness Dependence in Upconverting Optical Properties. Nano Lett 12(6):2852-2858.
132. Johnson NJJ, Korinek A, et al. (2012) Self-Focusing by Ostwald Ripening: A Strategy for Layer-by-Layer Epitaxial Growth on Upconverting Nanocrystals. J Am Chem Soc 134(27):11068-11071.
133. Li XM, Shen DK, et al. (2013) Successive Layer-by-Layer Strategy for Multi-Shell Epitaxial Growth: Shell Thickness and Doping Position Dependence in Upconverting Optical Properties. Chem Mater 25(1):106-112.
134. Jain PK, Huang X, et al. (2008) Noble Metals on the Nanoscale: Optical and Photothermal Properties and Some Applications in Imaging, Sensing, Biology, and Medicine. Acc Chem Res 41(12):1578-1586.
135. Hutter E, Fendler JH (2004) Exploitation of Localized Surface Plasmon Resonance. Adv Mater 16(19):1685-1706.
136. Zhao J, Jensen L, et al. (2007) Interaction of Plasmon and Molecular Resonances for Rhodamine 6G Adsorbed on Silver Nanoparticles. J Am Chem Soc 129(24):7647-7656.
137. Singh MP, Strouse GF (2010) Involvement of the LSPR Spectral Overlap for Energy Transfer between a Dye and Au Nanoparticle. J Am Chem Soc 132(27):9383-9391.
138. Zhang H, Li YJ, et al. (2010) Plasmonic modulation of the upconversion fluorescence in $NaYF_4$:Yb/Tm hexaplate nanocrystals using gold nanoparticles or nanoshells. Angew Chem Int Ed 49(16):2865-2868.
139. Saboktakin M, Ye XC, et al. (2012) Metal-Enhanced Upconversion Luminescence Tunable through Metal Nanoparticle-Nanophosphor Separation. ACS Nano 6(10):8758-8766.
140. Saboktakin M, Ye XC, et al. (2013) Plasmonic Enhancement of Nanophosphor Upconversion Luminescence in Au Nanohole Arrays. ACS Nano 7(8):7186-7192.
141. Sun QC, Mundoor H, et al. (2014) Plasmon-enhanced energy transfer for improved upconversion of infrared radiation in doped-lanthanide nanocrystals. Nano Lett 14(1):101-106.
142. Liu YX, Wang DS, et al. (2013) Magnetic Tuning of Upconversion Luminescence in Lanthanide-Doped Bifunctional Nanocrystals. Angew Chem Int Ed 52(16):4366-4369.
143. Hao JH, Zhang Y, et al. (2011) Electric-Induced Enhancement and Modulation of Upconversion Photoluminescence in Epitaxial $BaTiO_3$:Yb/Er Thin Films. Angew Chem Int Ed 50(30):6876-6880.
144. Bayley H, Cremer PS (2001) Stochastic sensors inspired by biology. Nature 413(6852):226-230.
145. Tu DT, Zheng W, et al. (2014) Luminescent biodetection based on lanthanide-doped inorganic nanoprobes. Coord Chem Rev 273-274:13-29.
146. Weiss A, Abramowski D, et al. (2009) Single-step detection of mutant huntingtin in animal and human tissues: a bioassay for Huntington's disease. Anal Biochem 395(1):8-15.

147. Siitari H, Hemmila I, et al. (1983) Detection of hepatitis B surface antigen using time-resolved fluoroimmunoassay. Nature 301(5897):258-260.

148. Wang XD, Stolwijk JA, et al. (2012) Ultra-small, highly stable, and sensitive dual nanosensors for imaging intracellular oxygen and pH in cytosol. J Am Chem Soc 134 (41):17011-17014.

149. Zijlmans H, Bonnet J, et al. (1999) Detection of cell and tissue surface antigens using up-converting phosphors: A new reporter technology. Anal Biochem 267(1):30-36.

150. van de Rijke F, Zijlmans H, et al. (2001) Up-converting phosphor reporters for nucleic acid microarrays. Nat Biotechnol 19(3):273-276.

151. Zhang F, Shi QH, et al. (2011) Fluorescence Upconversion Microbarcodes for Multiplexed Biological Detection: Nucleic Acid Encoding. Adv Mater 23(33):3775-3779.

152. Zuiderwijk M, Tanke HJ, et al. (2003) An amplification-free hybridization-based DNA assay to detect Streptococcus pneumoniae utilizing the up-converting phosphor technology. Clin Biochem 36(5):401-403.

153. Niedbala RS, Feindt H, et al. (2001) Detection of analytes by immunoassay using up-converting phosphor technology. Anal Biochem 293(1):22-30.

154. Hampl J, Hall M, et al. (2001) Upconverting phosphor reporters in immunochromatographic assays. Anal Biochem 288(2):176-187.

155. Li LP, Zhou L, et al. (2009) Development of up-converting phosphor technology-based lateral-flow assay for rapidly quantitative detection of hepatitis B surface antibody. Diagn Microbiol Infect Dis 63(2):165-172.

156. Zhao P, Wu YY, et al. (2014) Upconversion fluorescent strip sensor for rapid determination of Vibrio anguillarum. Nanoscale 6(7):3804-3809.

157. Yan ZQ, Zhou L, et al. (2006) Rapid quantitative detection of Yersinia pestis by lateral-flow immunoassay and up-converting phosphor technology-based biosensor. Sensor Actuat B-Chem 119(2):656-663.

158. Liang GH, Xiao LF, et al. (2013) Label-free, nucleotide-mediated dispersion of magnetic nanoparticles for "non-sandwich type" MRI-based quantification of enzyme. Biosens Bioelectron 41:78-83.

159. Wu SJ, Duan N, et al. (2012) Simultaneous detection of enterovirus 71 and coxsackievirus A16 using dual-colour upconversion luminescent nanoparticles as labels. Chem Commun 48 (40):4866-4868.

160. Wu SJ, Duan N, et al. (2014) Simultaneous aptasensor for multiplex pathogenic bacteria detection based on multicolor upconversion nanoparticles labels. Anal Chem 86 (6):3100-3107.

161. Ukonaho T, Rantanen T, et al. (2007) Comparison of infrared-excited up-converting phosphors and europium nanoparticles as labels in a two-site immunoassay. Anal Chim Acta 596(1):106-115.

162. Ai Y, Tu DT, et al. (2013) Lanthanide-doped $NaScF_4$ nanoprobes: crystal structure, optical spectroscopy and biodetection. Nanoscale 5(14):6430-6438.

163. Liu Y, Kobayashi T, et al. (2013) Sugar-attached upconversion lanthanide nanoparticles: A novel tool for high-throughput lectin assay. Bioorgan Med Chem 21(11):2832-2842.

164. Achatz DE, Ali R, et al. (2011) Luminescent chemical sensing, biosensing, and screening using upconverting nanoparticles. Top Curr Chem 300:29-50.

165. Corstjens P, Zuiderwijk M, et al. (2001) Use of Up-Converting Phosphor Reporters in Lateral-Flow Assays to Detect Specific Nucleic Acid Sequences: A Rapid, Sensitive DNA Test to Identify Human Papillomavirus Type 16 Infection. Clin Chem 47(10):1885-1893.

166. Li JJ, Ouellette AL, et al. (2008) Optical Scanner for Immunoassays With Up-Converting Phosphorescent Labels. IEEE Trans Biomed Eng 55(5):1560-1571.

167. Mokkapati VK, Sam Niedbala R, et al. (2007) Evaluation of UPlink–RSV. Ann NY Acad Sci 1098(1):476-485.

168. Wang LY, Li YD (2006) Green upconversion nanocrystals for DNA detection. Chem Commun (24):2557-2859.

169. Liu YS, Tu DT, et al. (2013) Lanthanide-doped luminescent nano-bioprobes: from fundamentals to biodetection. Nanoscale 5(4):1369-1384

170. Bunzli JCG (2010) Lanthanide Luminescence for Biomedical Analyses and Imaging. Chem Rev 110(5):2729-2755.

171. Rabouw FT, den Hartog SA, et al. (2014) Photonic effects on the Förster resonance energy transfer efficiency. Nat Commun 5:3610.

172. Yang YM, Zhao Q, et al. (2012) Luminescent Chemodosimeters for Bioimaging. Chem Rev 113(1):192-270.

173. Wang P, Ahmadov TO, et al. (2013) Ligase-assisted signal-amplifiable DNA detection using upconversion nanoparticles. RSC Adv 3(37):16326-16329.

174. Chen ZG, Chen HL, et al. (2008) Versatile synthesis strategy for carboxylic acid-functionalized upconverting nanophosphors as biological labels. J Am Chem Soc 130 (10):3023-3029.

175. Deng RR, Xie XJ, et al. (2011) Intracellular glutathione detection using MnO_2-nanosheet-modified upconversion nanoparticles. J Am Chem Soc 133(50):20168-20171.

176. Zhang CL, Yuan YX, et al. (2011) Biosensing Platform Based on Fluorescence Resonance Energy Transfer from Upconverting Nanocrystals to Graphene Oxide. Angew Chem Int Ed 50(30):6851-6854.

177. Wang LY, Yan RX, et al. (2005) Fluorescence resonant energy transfer biosensor based on upconversion-luminescent nanoparticles. Angew Chem Int Ed 44(37):6054-6057.

178. Wang M, Hou W, et al. (2009) Immunoassay of Goat Antihuman Immunoglobulin G Antibody Based on Luminescence Resonance Energy Transfer between Near-Infrared Responsive $NaYF_4$:Yb, Er Upconversion Fluorescent Nanoparticles and Gold Nanoparticles. Anal Chem 81(21):8783-8789.

179. Ye WW, Tsang MK, et al. (2014) Upconversion Luminescence Resonance Energy Transfer (LRET)-Based Biosensor for Rapid and Ultrasensitive Detection of Avian Influenza Virus H7 Subtype. Small 10(12):2390-2397.

180. Yuan F, Chen HQ, et al. (2014) Aptamer-based luminescence energy transfer from near-infrared-to-near-infrared upconverting nanoparticles to gold nanorods and its application for the detection of thrombin. Chem-Eur J 20(10):2888-2894.

181. Zhang P, Rogelj S, et al. (2006) Design of a highly sensitive and specific nucleotide sensor based on photon upconverting particles. J Am Chem Soc 128(38):12410-12411.

182. Kumar M, Guo YY, et al. (2009) Highly sensitive and selective oligonucleotide sensor for sickle cell disease gene using photon upconverting nanoparticles. Biosens Bioelectron 24 (5):1522-1526.

183. Liu JL, Cheng JT, et al. (2013) Upconversion nanoparticle based LRET system for sensitive detection of MRSA DNA sequence. Biosens Bioelectron 43:252-256.

184. Zhou F, Noor MO, et al. (2014) Luminescence resonance energy transfer-based nucleic acid hybridization assay on cellulose paper with upconverting phosphor as donors. Anal Chem 86 (5):2719-2726.

185. Peng JH, Wang YH, et al. (2011) A new biosensor for glucose determination in serum based on up-converting fluorescence resonance energy transfer. Biosens Bioelectron 28 (1):414-420.

186. Song K, Kong XG, et al. (2012) Aptamer optical biosensor without bio-breakage using upconversion nanoparticles as donors. Chem Commun 48(8):1156-1158.

187. Liu CH, Wang Z, et al. (2011) Efficient fluorescence resonance energy transfer between upconversion nanophosphors and graphene oxide: a highly sensitive biosensing platform. Chem Commun 47(16):4661-4663.

188. Wu Y-M, Cen Y, et al. (2014) Upconversion fluorescence resonance energy transfer biosensor for sensitive detection of human immunodeficiency virus antibodies in human serum. Chem Commun 50(36):4759-4762.

189. Li H, Sun D-e, et al. (2014) An ultrasensitive homogeneous aptasensor for kanamycin based on upconversion fluorescence resonance energy transfer. Biosens Bioelectron 55:149-156.

190. Wang YH, Bao L, et al. (2011) Aptamer biosensor based on fluorescence resonance energy transfer from upconverting phosphors to carbon nanoparticles for thrombin detection in human plasma. Anal Chem 83(21):8130-8137.

191. Zhang JP, Mi CC, et al. (2012) Synthesis of NaYF$_4$:Yb/Er/Gd up-conversion luminescent nanoparticles and luminescence resonance energy transfer-based protein detection. Anal Biochem 421(2):673-679.

192. Rantanen T, Jarvenpaa ML, et al. (2009) Upconverting phosphors in a dual-parameter LRET-based hybridization assay. Analyst 134(8):1713-1716.

193. Wang YH, Shen P, et al. (2012) Upconversion Fluorescence Resonance Energy Transfer Based Biosensor for Ultrasensitive Detection of Matrix Metalloproteinase-2 in Blood. Anal Chem 84(3):1466-1473.

194. He MY, Liu ZH (2013) Paper-based microfluidic device with upconversion fluorescence assay. Anal Chem 85(24):11691-11694.

195. Yuan YX, Wu SF, et al. (2014) An MnO$_2$ nanosheet as a label-free nanoplatform for homogeneous biosensing. Chem Commun 50(9):1095-1097.

196. Wang XD, Wolfbeis OS, et al. (2013) Luminescent probes and sensors for temperature. Chem Soc Rev 42(19):7834-7869.

197. Jung JH, Lee JH, et al. (2011) Functionalized magnetic nanoparticles as chemosensors and adsorbents for toxic metal ions in environmental and biological fields. Chem Soc Rev 40 (9):4464-4474.

198. Wang M, Mi CC, et al. (2009) Immunolabeling and NIR-Excited Fluorescent Imaging of HeLa Cells by Using NaYF$_4$:Yb,Er Upconversion Nanoparticles. ACS Nano 3 (6):1580-1586.

199. Zhan QQ, Qian J, et al. (2011) Using 915 nm Laser Excited Tm^{3+}/Er^{3+}/Ho^{3+} Doped NaYbF$_4$ Upconversion Nanoparticles for in Vitro and Deeper in Vivo Bioimaging without Overheating Irradiation. ACS Nano 5(5):3744-3757.

200. Yu MX, Li FY, et al. (2009) Laser Scanning Up-Conversion Luminescence Microscopy for Imaging Cells Labeled with Rare-Earth Nanophosphors. Anal Chem 81(3):930-935.

201. Hilderbrand SA, Shao FW, et al. (2009) Upconverting luminescent nanomaterials: application to in vivo bioimaging. Chem Commun (28):4188-4190.

202. Zhou LJ, Gu ZJ, et al. (2012) Size-tunable synthesis of lanthanide-doped Gd$_2$O$_3$ nanoparticles and their applications for optical and magnetic resonance imaging. J Mater Chem 22(3):966-974.

203. Zako T, Nagata H, et al. (2009) Cyclic RGD peptide-labeled upconversion nanophosphors for tumor cell-targeted imaging. Biochem Bioph Res Co 381(1):54-58.

204. Jiang S, Zhang Y, et al. (2009) NIR-to-visible upconversion nanoparticles for fluorescent labeling and targeted delivery of siRNA. Nanotechnology 20(15):155101.

205. Zeng JH, Su J, et al. (2005) Synthesis and upconversion luminescence of hexagonal-phase NaYF$_4$:Yb^{3+}, Er^{3+}, phosphors of controlled size and morphology. Adv Mater 17 (17):2119-2123.

206. Ye XC, Collins JE, et al. (2010) Morphologically controlled synthesis of colloidal upconversion nanophosphors and their shape-directed self-assembly. Proc Natl Acad Sci USA 107(52):22430-22435.

207. Lim SF, Riehn R, et al. (2006) In vivo and scanning electron microscopy imaging of upconverting nanophosphors in Caenorhabditis elegans. Nano Lett 6(2):169-174.

208. Xia A, Gao Y, et al. (2011) Core-shell NaYF$_4$:Yb^{3+},Tm^{3+}@Fe$_x$O$_y$ nanocrystals for dual-modality T$_2$-enhanced magnetic resonance and NIR-to-NIR upconversion luminescent imaging of small-animal lymphatic node. Biomaterials 32(29):7200-7208.

209. Liu Q, Sun Y, et al. (2011) Sub-10 nm Hexagonal Lanthanide-Doped NaLuF$_4$ Upconversion Nanocrystals for Sensitive Bioimaging in Vivo. J Am Chem Soc 133(43):17122-17125.

210. Xia A, Chen M, et al. (2012) Gd^{3+} complex-modified NaLuF$_4$-based upconversion nanophosphors for trimodality imaging of NIR-to-NIR upconversion luminescence, X-Ray computed tomography and magnetic resonance. Biomaterials 33(21):5394-5405.

211. Xing HY, Bu WB, et al. (2012) A NaYbF$_4$: Tm^{3+} nanoprobe for CT and NIR-to-NIR fluorescent bimodal imaging. Biomaterials 33(21):5384-5393.
212. Cheng L, Yang K, et al. (2012) Multifunctional nanoparticles for upconversion luminescence/MR multimodal imaging and magnetically targeted photothermal therapy. Biomaterials 33(7):2215-2222.
213. Cheng L, Wang C, et al. (2012) Multifunctional Upconversion Nanoparticles for Dual-Modal Imaging-Guided Stem Cell Therapy under Remote Magnetic Control. Adv Funct Mater 23 (3):272-280.

Chapter 9
Lanthanide-Doped Core–Shell Upconversion Nanophosphors

Tianying Sun and Feng Wang

Abstract A core–shell upconversion (UC) nanoparticle is typically composed of an upconversion core coated with one or more shell layers, which essentially preserve the properties of core-only nanoparticle. However, when compared with the core-only nanoparticle, core–shell structure provides more rooms for UC studies due to the increased flexibility in nanoparticle design. The core–shell structure can boost the UC efficiency by passivating the surface lattice defects and shielding the core nanoparticles from the surrounding environment. In addition, core–shell structures greatly expand the optical tunability and enable functional integration at single nanoparticle levels. In this chapter, we highlight recent advances in general synthetic strategies and possibility for composing core–shell upconversion nanoparticles. We also bring to the forefront several challenges for future study.

9.1 Introduction

Phonon upconversion (UC) refers to nonlinear anti-Stokes process in which two or more near-infrared photons are sequentially absorbed via physically existing intermediate energy states. UC phenomenon was first discovered in the 1960s by Auzel, Ovsyakin, and Feofilov independently [1–3]. But for a long time, the studies on upconversion were largely limited in bulk materials, because of the lag of nanomaterials fabrication at that time. Not until the 1990s, promoted by the prevalence of nanofabrication, did the UC nanomaterials attract a numerous research interests.

There are several types of UC nanomaterials. (i) Lanthanide-doped nanomaterials [4]: The luminescent center is provided by the lanthanide dopants in inorganic host that usually do not exhibit UC luminescence itself. (ii) Transition metal-doped nanomaterials [5]: spectroscopically active d orbitals of transition metals are

T. Sun · F. Wang (✉)
Department of Physics and Materials Science, City University of Hong Kong,
83 Tat Chee Avenue, Hong Kong SAR, China
e-mail: fwang24@cityu.edu.hk

strongly influenced by the local crystal field, making multi-photon excitation possible. (iii) Triplet-triplet annihilation (TTA) UC in a pair of sensitizer-annihilator dyes [6]: One excitation photon excites the sensitizer to populate the singlet excited states along with the intersystem crossing process to populate its triplet excited state. Then, energy transfers from a triplet sensitizer to a nearby triplet acceptor. Successive interaction of two acceptors yields TTA, which combines two triplet excitons to create one higher energy singlet state and gives rise to UC luminescence. Apart from these three types of materials, compositional and morphological engineering in semiconductor nanomaterials have also lead to UC emissions [7, 8].

Lanthanide-doped core–shell UC nanoparticles are among the most widely investigated UC nanomaterials. When compared to the core-only nanoparticles that principally inherit the optical properties from the corresponding bulk counterparts, core–shell nanostructure provides more rooms for UC studies due to the increased flexibility in nanoparticle design. The core–shell structure can boost the UC efficiency by passivating the surface lattice defects and shielding the core nanoparticles from the surrounding environment. In addition, core–shell structures also greatly expand the optical tunable ability as well as combining functionality at single nanoparticle levels.

In this chapter, we discuss several current research interests regarding lanthanide-doped core–shell UC nanophosphor. In Sect. 9.2, we give a brief introduction of UC processes that are involved in lanthanide-doped core–shell UC nanophosphor. The general synthetic protocols to high-quality lanthanide-doped core–shell UC nanoparticles with tunable composition and controlled shell thickness are described in Sect. 9.3. In Sect. 9.4, we attempt to highlight the effect of core–shell structure on properties of the nanophosphors.

9.2 UC Process Involved in Lanthanide-Doped core–shell Nanostructure

Energy transfer upconversion (ETU) and energy migration-mediated upconversion (EMU) are dominated processes in core–shell UC nanoparticles. In a typical UC procedure, several basic steps are involved. A light harvesting agent (sensitizer) is firstly excited by a NIR light, followed by energy transfer to a neighborhood activator via a short-range energy transfer UC process, resulting in emission (Scheme 9.1a). If activators are located far apart from the sensitizers, the energy transfer should be under the assistance of migrator ions via a long-range energy migration-mediated UC process (Scheme 9.1b). In the meantime, some other processes such as cross-relaxation process and energy interaction between rare earth dopants and surface-related deactivators cannot be neglect. Typical upconversion process in core–shell structures containing NIR excitation, nonradiative energy transfer, cross-relaxation, UC emission, and energy interaction is demonstrated in Fig. 9.1.

Scheme 9.1 Schematic representation of energy-level diagram depicting two typical energy transfer upconversion process. **a** Energy transfer upconversion (ETU). **b** Energy migration-mediated upconversion
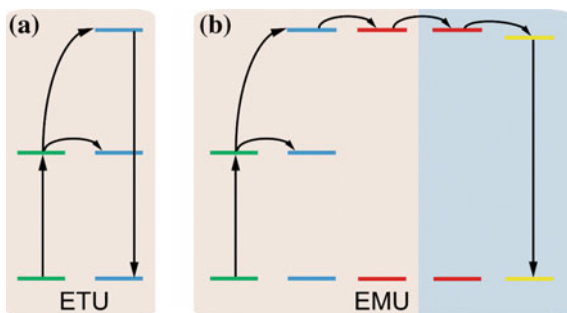
Fig. 9.1 Schematic illustration of main optical processes in lanthanide-doped core–shell UC nanoparticles. Typical processes include energy excitation, nonradiative energy transfer between lanthanide dopants, cross-relaxation between lanthanide dopants, energy excitation with surface quenchers, and light emission from lanthanide emitters
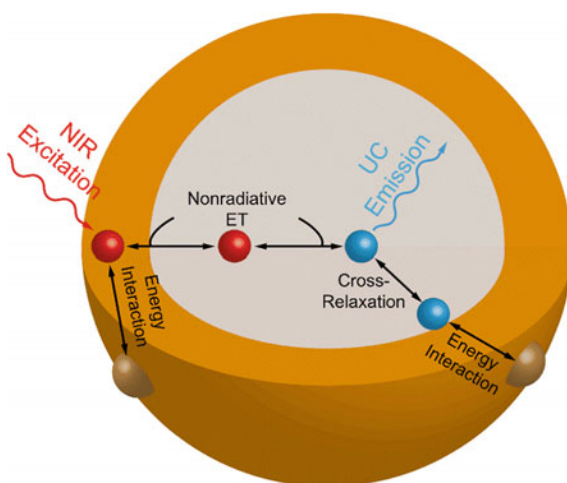
9.2.1   NIR Excitation

UC emissions start with the absorption of NIR light. For a given excitation wavelength, the excitation rate (R) of state i can be described as:

$$R_i \propto I_{\text{exc}} \sigma_i N_i$$

σ_i represents for the absorption cross section of states i at a given excitation wavelength. N_i and I_{exc} stand for the population and excitation density, respectively.

From this point, we can easily deduce that the larger the absorption cross section, the larger the excitation rate.

To promote the excitation process, sensitizer ions possessing relatively large absorption cross sections are typically included in UC nanoparticles. Yb^{3+} featuring an extremely simple energy-level structure with only one excited state $^2F_{5/2}$ is frequently used to sensitize UC emissions. Nd^{3+}–Yb^{3+}-cosensitized process has also received widely attention in these days. The single absorption band of Yb^{3+}

lies in around 980 nm, which coincides with the strong water absorption band and leads to overheating in biological applications. With the assistance of Nd^{3+} featuring multiple excitation bands at around 730, 808, and 865 nm, the excitation wavelength can be blueshifted, thus largely reducing the heating effect. In particular, the cross-relaxation of Nd^{3+} at 808 nm (1.2×10^{-19} cm^2) is even larger than that of Yb^{3+} at 980 nm (1.2×10^{-20} cm^2).

For an unsaturated process, the intensity of UC luminescence I_{UC} will be proportional to n orders of the pump power (P) according to the following equation:

$$I_{uc} \propto P^n$$

In order to obtain intense UC luminescence, the excitation power must be sufficiently high. However, at significantly higher excitation powers, a smaller "n" value may be derived due to saturation effects. Note that saturation usually occurs at widely different excitation powers for different UC nanoparticles. Due to the nonlinear response to NIR excitations, the spectral profile of UC emission and "n" value for a particular UC process are only meaningful when excitation power density is provided.

9.2.2 Nonradiative Energy Transfer Within Core–Shell Structure

After photon excitation, the sensitizers need to successively transfer their energies to the activators where these energies are amassed to produce the higher energy emission photons.

Activators should meet stringent requirements. For instance, they should possess intermediate states with energy differences match that of the sensitizer. In addition, the lifetime of the intermediate state should be sufficiently long so that further excitation to a higher-lying state is possible. A large energy gap typically leads to long-lived energy state by decreasing the probability of nonradiative relaxation according to the energy gap law:

$$W_{NR} = W_0 \exp(-\alpha \Delta E)$$

where W_{NR} represents for the nonradiative relaxation probability. W_0 and α are parameters related to the host. ΔE is the energy gap between a populated state and the next low-lying state. According to the energy gap law, the larger the energy gap, the lower the nonradiative relaxation probability.

In line with the criteria, Er^{3+}, Tm^{3+}, and Ho^{3+} with ladder-like arrangement of energy level are three commonly used activators in UC process. These ions can directly receive the excitation energy of Yb^{3+} to generate UC emission through short-range energy transfer UC (ETU).

Large energy gaps are also found in lanthanide activators such as Tb^{3+}, Eu^{3+}, Dy^{3+}, and Sm^{3+}. However, the absence of effective intermediate states disqualifies the use of these ions as UC activators. Wang and Liu [9] devised a new scheme named energy migration-mediated upconversion (EMU) to realize UC emission in these ions. The method is based on the combination of core–shell structural engineering and energy migration to create well-defined energy exchange interaction between multiple lanthanide ions. EMU can be considered as an extension of ETU because the accumulator ion receives the excitation energy from the sensitizer via the ETU process. The energy is then captured by the migrator ions and randomly hops among the migrator sublattice through the core–shell interface before being trapped by the activator ions.

Energy transfer in UC nanoparticles is typically dominated by nonradiative energy transfer via exchange interactions or multi-polar interactions. With the development core–shell techniques, however, guest optical entities, such as organic dye or semiconductor materials, are involved in composing UC nanoparticles. In these nanocomposites, radiative energy transfer become significant (vide infra).

9.2.3 Cross-relaxation Between Lanthanide Dopants

Cross-relaxation means an energy donor partially transfers its energy to an energy acceptor. These two ions can either be of the same type or different. For instance, efficient cross-relaxations can take place between Er^{3+}–Tm^{3+} [10], Ho^{3+}–Ce^{3+} [11], Nd^{3+}–Nd^{3+} [12], and Tm^{3+}–Tm^{3+} [13]. Cross-relaxation is strongly dependent on the dopant concentrations that dictate average separation between adjacent ions. A high doping concentration typically elevates the probability of cross-relaxation and may lead to concentration quenching of a luminescence process. Although, in most cases, cross-relaxation is deleterious to efficient UC processes, the effect can be harness to tune emission colors by selectively enhancing the population in a particular excited state.

9.2.4 Energy Interaction Between Lanthanide Dopants with Surface Quenchers

Energy exchange interactions between rare earth dopants and surface quenchers can be categorized into two types. Dopants located on or near the surface can be directly deactivated by surface quenchers through nonradiative relaxation. For another type, energy carried by dopants in the interior lattice can migrate over a long distance to the surface quenchers and dissipates nonradiatively. Both direct surface quenching and indirect quenching due to energy migration can be largely suppressed by applying an inert shell coating (vide infra).

9.3   General Chemical Approaches to Preparing Core–Shell UC Nanoparticles

The synthesis strategies for core-only UC nanoparticles will not discuss in this chapter. For readers who are interested, a dedicated review article on this topic is recommended [14]. In this section, we will focus on commonly used strategies for synthetizing epitaxial core–shell UC nanoparticles and general fabrication strategies for UC nanoparticles-based nanocomposites.

9.3.1   Epitaxial Fabrication of Core–Shell Structure

It is very important to synthesize uniform core–shell structure because the homogeneity of their chemical and physical properties is directly related to their size uniformity. Numerous reports on uniform epitaxial shell coating have popularized two control syntheses, namely the "heat-up strategy" and the "hot-injection strategy." In addition, cation exchange strategy has also been proposed as a convenient route for preparing core–shell structures.

In a typical heat-up method for synthetizing core–shell structures, core nanoparticles was first synthesized by an appropriate method and extracted. The shell layer was then grown epitaxially around the core lattice in a new synthesis. This idea was first proposed by Mai and Yan in 2007 [15]. The as-prepared $NaYF_4$: Yb/Er core structures were first purified and transferred to a three-necked flask containing metal trifluoroacetate shell precursors, high-boiling solvent ODE, and surfactant OA, followed by an identical protocol for the core synthesis. This protocol was then refined by Qian and Zhang in 2008 [16]. In both studies, the essence for heat-up strategy to synthesizing uniform core–shell structure is the same, i.e., addition of preformed core nanoparticles into the shell precursor before initiating the nucleation and growth by heating.

For heat-up method, the shell composition can be adjusted, catering for the needs of homogeneous or heterogeneous core–shell nanoparticles. However, the shell layer should exhibit a low lattice mismatch with the core materials to satisfy an epitaxial growth and to create a coherent interface between the core and the shell. The shell thickness can be well-controlled by the concentration of served shell precursor. In Zhang and Zhao's work [17], by using spherical concentric shell model for calculation, the shell thickness of each shell can even reach one atomic layer. Also in their work, they compared 6 monolayer thickness shell synthesized by successive ion layer adsorption and reaction (SILAR) [17] and one-step coating procedure. The SILAR method can yield more uniform homogenous core–shell structure than one-step method.

The most prominent advantage of heat-up strategy is that the shell coating process can be carried out by repeating a concise synthetic protocol except for the inclusion of core nanoparticles in the precursor solution. Furthermore, the

preformed core nanoparticles can be used as starting materials, serving for parallel heat-up shell coatings of varying shell composition and thickness, providing an accurate solution to correlating the effect of shell characteristics with the properties of the nanoparticles.

Despite the advantages, heat-up strategy suffers from several limitations. On the basis of cryo-transmission electron microscopy together with other tools for characterization, the groups of Veggel [18] and Zhao [17] found that the shell coatings are usually anisotropic. Also, the heat-up method is considered to be laborious and must undergo lengthy cooling, volatile solvent removing, and product purification processes. The drawback is more problematic for preparing multi-shelled nanoparticles.

The hot-injection method was first introduced by Murray and Bawendi [19] in 1993 for synthesizing semiconductor nanocrystallites. The synthesis is based on the pyrolysis of organometallic reagents by injection into hot coordinating solvent. Hot-injection method for synthesizing core–shell UC nanoparticles follows the same idea. Typically, a solution containing shell precursors is rapidly injected into a hot solution containing as-prepared core particles (without preseparation), high-boiling solvent, and surfactants. One of the most important characteristics of the hot-injection is the high flexibility. This method has been extended to the synthesis of various core–shell structures. In one pioneering work for synthetizing core–shell lanthanide-doped UC nanoparticles, Yi and Chow prepared monodispersed $NaYF_4$:Yb/Er(Tm)@$NaYF_4$ core–shell nanoparticles with an average diameter of ∼11.1 nm [20]. In their thermal decomposition synthesis, metal trifluoacetate precursors dissolved in OM were first heated in 340 °C for 30 min for the formation of the core product. For epitaxial shell coating, without cooling down the reaction, solution containing shell precursors in OM were then injected into the hot solution and heated for another 30 min.

One of the most important advantages of hot-injection strategy is that it allows one-pot successive layer-by-layer (SLBL) synthesis of multi-shelled nanostructures. In a reprehensive study conducted by Zhang and Zhao (Fig. 9.2) [21], a reaction solution containing preformed core particles was stabilized at 280 °C, to which RE-OA and Na-TFA-OA shell precursor were alternatively injected drop by drop. Each injection was kept for 15 min for ripening before another injection. The key point for the formation of uniform shell is that the monomer concentration is always kept below the critical nucleation concentration during the whole process, thus preventing homogeneous nucleation of shell precursor. Several distinguished features of this SLBL method are that the shell coating is quite uniform and complete (unlike partially shell covered structure prepared by heating-up strategy). Also, this method can avoid lengthy multi-cycle operation, especially when multiple shell layers are to be coated.

However, for hot-injection process, stringent control over the introduction of shell component (injection concentration and rate) is often needed for the elimination of homogeneous shell nucleation. To circumvent this limitation, Johnson and Veggel and coworkers exploited a novel and versatile hot-injection epitaxial shell growth strategy which was driven by Ostwald ripening phenomenon (Fig. 9.3) [22].
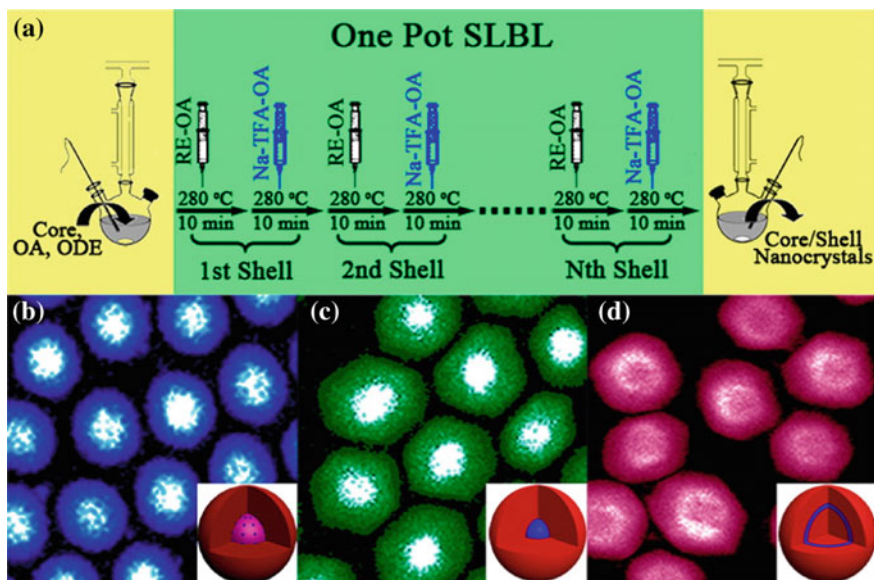
Fig. 9.2 One-pot SLBL heat-up synthesis of core–shell UC nanoparticles. **a** Schematic illustration of the grow process. **b–d** HAADF-STEM images of the **b** β-NaGdF$_4$:Yb/Er@NaYF$_4$ core–shell nanoparticles, **c** α-NaYbF$_4$:Er@NaYF$_4$ core–shell nanoparticles, **d** α-NaYF$_4$@NaYbF$_4$: Er@NaYF$_4$ core–shell-shell nanoparticles obtained by SLBL method. Reprinted with the permission from Ref. [21]. Copyright 2013 American Chemical Society
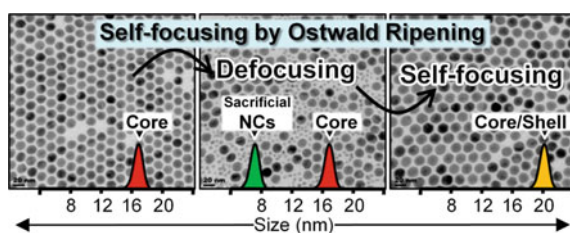
Fig. 9.3 Schematic illustration of hot-injection shell growth strategy driven by self-focusing Ostwald ripening. The *left panel* refers to initial core nanoparticles at $t = 0$ s. The *middle panel* indicates $t = 15$ s after injecting of sacrificial nanoparticles. The *right panel* stands for self-focusing process of core–shell nanoparticles at $t = 10$ min. Reprinted with the permission from Ref. [22]. Copyright 2012 American Chemical Society

Ostwald ripening refers to the process that energetically more stable larger particles grow at the expense of less stable smaller ones. In their work, small alpha-phase NaYF$_4$ nanoparticles was firstly synthesized and used as shell precursor. Once being injected into hot core solution, the small alpha-nanoparticles dissolved and deposited on the larger core nanoparticles. The resulting particle shows narrow size

distribution and the shell thickness can be precisely controlled by the amount of sacrificial nanoparticles involved.

Another method to synthesize core–shell structure is based on the cation exchange. Ionic exchange reaction was originally developed to synthesize semiconductor nanoparticles by Alivisatos [23] and was first adapted to synthesize lanthanide fluoride core–shell nanoparticles in 2008 by Dong and Veggel [24]. In their study, GdF_3 nanoparticles was exposed to excess amount of La^{3+} in the presence of extra citrate in an aqueous solution. The surface cation Gd^{3+} can be partially replaced by the added La^{3+}, thus forming a new LaF_3 layer outside the core nanoparticles. By refining this route, they prepared $NaYF_4$:Yb/Tm@$NaYF_4$ core–shell structure with a thin (up to ca. 1 nm), tunable thickness shell. This cation exchange strategy was also utilized by other groups. Liu and Li synthesized UC nanoparticles modified by Gd^{3+} based on rare earth cation-assisted ligand assembly [25]. The Gd-modified $NaYF_4$:Yb/Er nanoparticles can be used as multimodal bioprobes. In their study, three steps were involved for surface modification. Firstly, the original ligands were cleaved from the nanoparticle surface by treating with chloroform under sonication. Secondly, Gd^{3+} ions were introduced into the $NaYF_4$: Yb/Er nanoparticles via cation exchange with Y^{3+}. Thirdly, assemble of Gd^{3+} toward a new ligand containing –COOH which possess strong coordination ability with rare earth ions, resulting in a Gd^{3+}-rich shell layer.

9.3.2 Fabrication of UC Nanoparticles-Based Nanocomposites

Besides epitaxial growth of UC nanoparticles-based core–shell structure, some guest optical entities exhibit large lattice mismatch with UC nanoparticles can also be used to compose UC nanoparticles-based core–shell nanocomposites. Many alien entities, such as SiO_2, noble metals, semiconductor quantum dots as well as organic molecules, have been coated around UC core nanoparticles.

Silica coating is a popular technique for building core–shell nanostructure. Silica shells are porous and optically transparent. Modified Stöber method is usually employed for coating SiO_2 to hydrophobic UC nanoparticles and hydrophilic UC nanoparticles.

Since the most efficient synthesis method yields UC nanoparticles with hydrophobic surface, modified Stöber method with the assistance of reverse microemulsion is the most widely used method to grow a silica shell. Reverse microemulsion usually involves the dispersion of the hydrophobic UC nanoparticles in cyclohexane solution containing ammonia and surfactant. Those homogeneous mixture of reactant can generate numerous small aqueous compartment surrounded by the surfactant layer while dispersed in the oil phase. This surfactant-stabilized aqueous compartment was called a water-in-oil type of reverse microemulsion. During the hydrolysis of tetraethyl orthosilicate (TEOS), these

reverse microemulsion acted as nanoreactor for silica shell coating. In this reaction, the surfactant not only helped to form the adequately stable reverse microemulsion, but also acted as stabilizer to inhibit the aggregation during the reaction. TEOS served as silica precursor, and ammonia was added as a catalyst for initiating the shell coating. Various silica shell thickness can be adjusted by the amount of TEOS added. In a representative example, Jalil and Zhang reported the use of reverse microemulsion method (using CO-520 as the surfactant) to synthetize uniform silica-coated UC nanoparticles with excellent solubility in water as well as high biocompatibility [26]. In the Stöber method for coating hydrophilic UC nanoparticles, the reaction can be conveniently conducted in a water/alcohol/ammonia mixture without the use of surfactants. Various amounts of TEOS can lead to tunable silica shell thickness [27].

Mesoporous silica ($mSiO_2$) can induce new therapeutic functionalities because $mSiO_2$ can entrap therapeutic agents and deliver them to the disease site. Liu and Shi [28] demonstrated an organic template method synthesis of $mSiO_2$-coated UC nanoparticles for light-triggered release of anticancer drug. They use CTAC as the structure-directing agent and template. CTAC has another function that is the stabilizing surfactant for transferring hydrophobic nanoparticles to hydrophilic ones. First, the hydrophilic complex of CTAC with UC nanoparticles was produced, followed by a template-directed silica coating process. Finally, the core–shell product was extracted and the CTAC template was removed with sodium chloride. Qian and Zhang [29] prepared UC nanoparticles@$mSiO_2$ core–shell structure for synergistic imaging and PDT of cancer cell. The first step is the use of the modified Stöber process with TEOS as silica precursor and octadecyltrimethoxysilane (C18TMs) as a surfactant for coating a thin and dense silica shell, followed by calcination at high temperature (Fig. 9.4a, b). Fan and Shi [30] reported the etching method for $mSiO_2$ coating. They first coated the UC nanoparticles with two dense SiO_2 shells. Finally, UC nanoparticles@$mSiO_2$ core–shell structure was synthesized by a "surface-protected hot water etching process," by using PVP as the surface protector. This etching method etches away the first layer of dense silica shell to create a hollow cavity while etches the outer layer of silica shell into porous one. The cisplatin (CDDP)-loaded UC@$mSiO_2$ core–shell nanoparticles can be used as radio sensitizer for dual-mode imaging.

Organic molecules can be either bound covalently between reactive groups of the particle surface and the organic molecules or noncovalently through absorption of organic molecule in a hydrophobic–hydrophobic intermediate layer. Zhou and Yan [31] demonstrated aldehyde group-functionalized UC nanoparticles that can be covalently conjugated with amino-containing organic molecules MOTEA. The organic molecule-functionalized UC nanoparticles afforded a novel detection capability for Ce^{4+} ions based on the dual emission from UC nanoparticles and organic molecule, respectively. Cheng and Liu [32] reported an amphiphilic polymer PEG-PMHC$_{18}$-functionalized UC nanoparticle via a hydrophobic–hydrophobic interaction between OA layer and hydrocarbon chains of the polymer. Additionally, hydrophobic organic dyes can be noncovalently absorbed to the hydrophobic intermediate layer composed of OA and carbon chains of polymer.
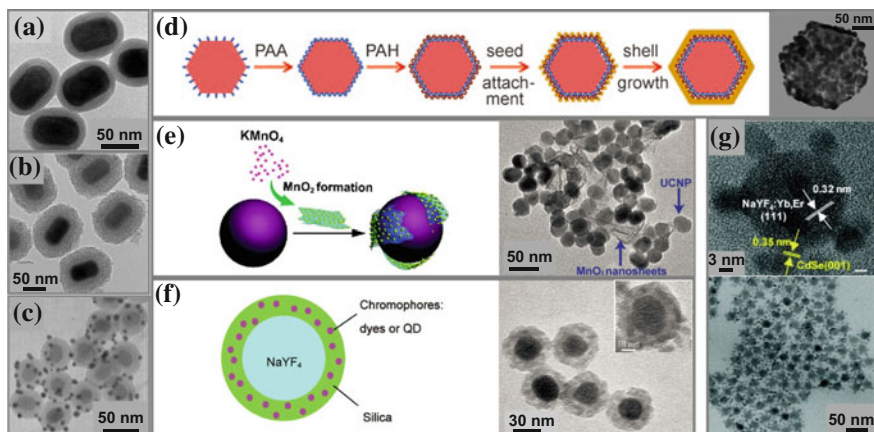
Fig. 9.4 Schematic illustration and TEM image of various UC nanoparticles-based nanocomposites. **a** TEM image of $NaYF_4$:Yb/Er@SiO_2 nanoparticles and **b** TEM image of mesoporous $NaYF_4$:Yb/Er@$mSiO_2$ nanoparticles synthesized by calcination method. Adapted from Ref. [29] by permission of John Wiley & Sons Ltd. **c** TEM image of $NaYF_4$:Yb/Er@SiO_2@Au nanoparticles. Adapted with the permission from Ref. [36]. Copyright 2011 American Chemical Society. **d** Schematic illustration and TEM image of surface functionalization processes for coating a gold nanoshell on the surface of UC nanoparticles. Adapted from Ref. [33] by permission of John Wiley & Sons Ltd. **e** Experimental design and TEM image of MnO_2-nanosheet-modified UC nanoparticles. **g** TEM image of CdSe-NaYF4 core–shell nanocomposites. Adapted with the permission from Ref. 36. Copyright 2010 American Chemical Society

The resultant UC nanoparticles–dye nanocomposites were used for in vivo multi-color UC luminescence imaging based on energy transfer.

The assembly of inorganic optical nanoparticle entities to the UC nanoparticles may lead to even more favorable effect on the UC luminescence. Zhang and Duan [33] reported a four-step synthesis of gold nanoshell-coated UC nanoparticles (Fig. 9.4d). Prior to gold seed attachment and gold seed growth, the UC nanoparticles were first subjected to surface modification with PAA and PAH. First, negative-charged PAA displaces the hydrophobic OA ligand on the surface of UC nanoparticles, followed by another positive-charged PAH layer coating which faciles the electrostatic attraction of Au. After the gold shell coating, the UC emission can be enhanced by twofold. The enhancement can be partly contributed to surface plasmon-coupled emission. Yan and Perepichka [34] developed the synthesis of CdSe QDs-decorated $NaYF_4$ UC nanoparticles by a seeded-growth method (Fig. 9.4g). UC nanoparticles were added as the seed for the direct growth of CdSe QDs. CdSe and UC nanoparticles were capped with positive-charged OM and negative-charged OA ligand, respectively. The linking of two nanoparticles was based on the electrostatic attraction between negative-charged OA ligand of UC nanoparticles and positive-charged OM ligand of CdSe. The combination of UC and semiconduction properties of CdSe-$NaYF_4$ core–shell nanocomposites appeared sub-band-gap photoconductivity. MnO_2 nanosheets were grown by Deng and Liu (Fig. 9.4e) [35]. First, surface modification of UC nanoparticles was

needed to oxidize the OA ligand to afford azelaic acid. Then, $KMnO_4$ was reduced to form amorphous MnO_2 nanosheet. The linkage between UC nanoparticles and MnO_2 was dominantly due to an electrostatic interaction. The MnO_2-nanosheet-modified UC nanoparticles can be used for glutathione quantification detection.

The dense or mesoporous silica shell is a universal inorganic layer that can act as a substrate or media for encapsulating and/or attaching other guest optical entities. Li and Xiong [36] reported a silica shell-assisted $NaYF_4$:Yb/Er@SiO_2@Au core–shell nanostructure (Fig. 9.4c). Reverse microemulsion method was first applied to coat a silica shell on the hydrophobic surface of UC nanoparticles. And then, silica-coated nanoparticles were further functionalized with amino groups. Au nanoparticles are attached to the surface of silica-coated UC nanoparticles via a strong coordination among the amino groups and Au nanoparticles. Li and Zhang [37] encapsulated two kinds of dyes (FITC and TRITC) as well as quantum dots (QD560) into the silica shell (Fig. 9.4f). First, the stability of the dye was improved by grafting the dye with (3-aminopropyl) triethoxysilane (APS) to form FITC-APS and TRITC-APS. And then, the dye or the QDs were cohydrolyzed with TEOS. Entrapment of dye molecules or QDs was achieved concomitantly with the formation of silica layer around the UC nanoparticles. The same group also incorporated a photosensitizer dye zinc phthalocyanine (ZnPc) into the mesoporous silica layer by simply soaking the silica-coated UC nanoparticles in the solution containing dye [31]. The ZnPc in the mesoporous silica shell can generate active oxygen species to kill cancer cells.

9.4 Expanding the Scope of UC with Core–Shell Structure

Core–shell structure offers high flexibility in doping the lanthanide ions (Fig. 9.5), which has been proven useful to eliminate unwanted quenching effect for efficient emission processes [38–46]. Most importantly, core–shell structure can be harnessed to integrate multiple functionalities at single particle levels and to modulate energy exchange interactions for unprecedented optical tuning.

9.4.1 Integrating Functionality

For bioanalytical applications such as multiplexed biodetection and multi-color imaging, a set of nanoparticles with well-resolved emissions are needed. Doping multiple lanthanide ions homogenously in a nanoparticle can produce multi-color emissions. However, deleterious cross-relaxation between dopant ions typically attenuates the emission intensities. Qian and Zhang [16] first reported the idea of using core–shell structure to separate incompatible lanthanide ions in different layers. They found that the luminescence from Tm^{3+} is quenched by Er^{3+} in

Fig. 9.5 Schematic illustration of different strategies for designing core–shell structures. **a** Active core covered by an undoped inert shell. **b** Active core covered by a doped active shell. **c** Multilayer design of sandwiched structure with a spacing layer between two active layers. **d** Multilayer design of δ-doped structure comprising a doped layer wrapped in two undoped layers
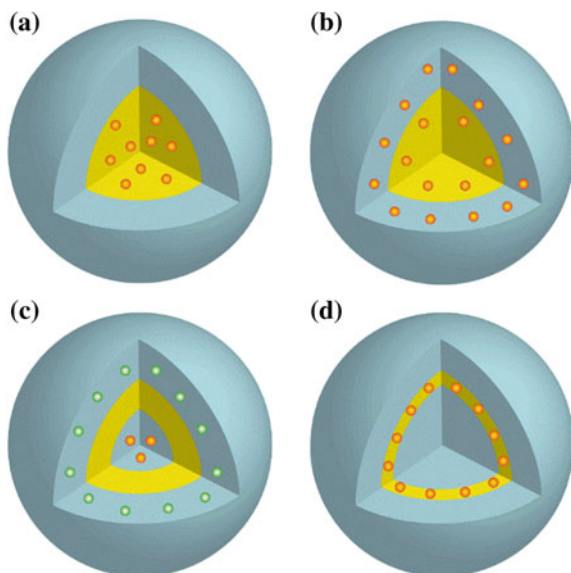
homogenously doped $NaYF_4$ nanoparticles. A marked enhancement in UC emission was observed when Tm^{3+} and Er^{3+} dopants were confined in different layers of a $NaYF_4:Yb/Tm@NaYF_4:Yb/Er$ core–shell structure. The suppression of deleterious cross-relaxation in core–shell structures has enabled researcher to rationally achieve dual-mode luminescence. For example, the group of Chen [49] designed $NaGdF_4:Yb/Tm@NaGdF_4:Eu$ core–shell structure in order to achieve dual-mode luminescence from Eu^{3+} ions by UV and NIR excitation, respectively (Fig. 9.6a). The emission of Eu^{3+} in the core–shell nanoparticles is much stronger than that in $Yb^{3+}/Tm^{3+}/Eu^{3+}$ triply doped core-only $NaGdF_4$ nanoparticles, owing to elimination of cross-relaxation between these ions. Wen and Wang [47] synthesized $NaGdF_4:Yb/Tm@NaGdF_4@NaYbF_4:Nd@Na(Yb,Gd)F_4:Ho@NaGdF_4$ nanoparticles with four shells for distinct upconversion emissions by excitation of 976 and 808 nm, respectively (Fig. 9.6b). Li and Zhao [48] demonstrated a Nd^{3+} sensitized dual-mode emission process under a single 808-nm excitation (Fig. 9.6c, d). They prepared $NaGdF_4:Nd@NaYF_4@NaGdF_4:Nd/Yb/Er@NaYF_4$ core–shell nanoparticles. The core layer contributes to a downshifting process and the second shell layer was responsible for UC.

Ionic dopants presenting various functionalities can be doped in core–shell UC nanoparticles to create multimodal bioprobes. Owing to the seven unpaired 4f electrons, Gd^{3+} ions can efficiently alter the relaxation time of surrounding water protons, rendering gadolinium compounds popular contrast agents for magnetic resonance imaging (MRI). Guo and Muhammad [38] reported a core–shell nanoparticle comprised a $NaYF_4:Yb/Er$ UC core covered with $NaGdF_4$ shell, which plays dual role to protect the UC process and to interact with surrounding water protons. This core–shell structure has been demonstrated to provide improved
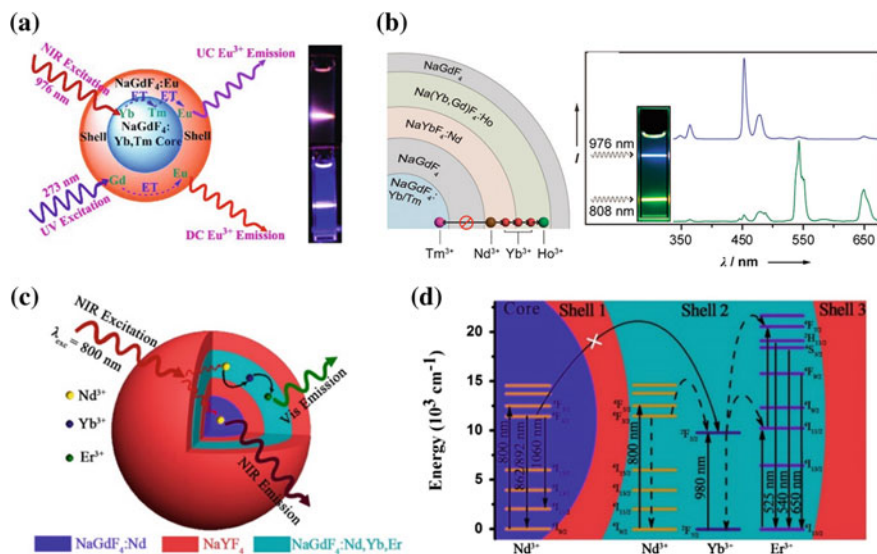
Fig. 9.6 **a** Schematic illustration of dual-mode NaGdF$_4$:Yb/Tm@NaGdF$_4$:Eu nanoparticles and the corresponding luminescence photographs under the excitation of 273 nm (*top*) and 976 nm (*bottom*), respectively. Adapted from Ref. [49] by permission of John Wiley & Sons Ltd. **b** Schematic illustration and spectra of multi-shelled nanoparticles under dual excitation of 976 and 808 nm. Adapted from Ref. [47] by permission of John Wiley & Sons Ltd. **c, d** Schematic illustration and proposed energy transfer mechanisms for dual-mode luminescence under single 808-nm excitation. Adapted by permission from Macmillan Publishers Ltd: Ref. [48], copyright 2013

UC luminescence as well as enhanced MR relaxivity. With core–shell structure, researchers have also combined T$_2$-weight contrast agent with T$_1$-weight Gd-doped UC nanoparticles. Chen et al. [50] demonstrated a Fe$_3$O$_4$@NaGdF$_4$:Yb/Tm core–shell structure. The magnetic nanoparticles with iron oxide core and gadolinium shell showed good potential as both T$_1$- and T$_2$-weighted MRI contrast agent as well as cell labeling reagents for luminescence bioimaging. Apart from iron oxide nanoparticles as T$_2$-weighted contrast agent, Ho^{3+} as well as Dy^{3+} can also result in efficient T$_2$ relaxation among lanthanide ions [51, 52]. Zhang and Tan [51] reported a rational design of NaDyF$_4$:Yb@NaGdF$_4$:Yb/Er core–shell structure with the ability to show tunable negative/positive T$_1$ contrast and negative T$_2$ contrast. The emitter (Er^{3+}) ions are located in the shell layer and physically separated from the quencher (Dy^{3+}) ions. The shell layer-contained Gd^{3+} ions facilitate interaction with surrounding water protons while the core-contained Dy^{3+} ions produce T$_2$ contrast.

It is highly desirable to develop single particle-based bioprobes for multimodal imaging, which would greatly reduce the laborious testing step and time for diagnose and can provide complementary and accurate information such as optical, MRI, positron emission tomography (PET), single-photon emission computed
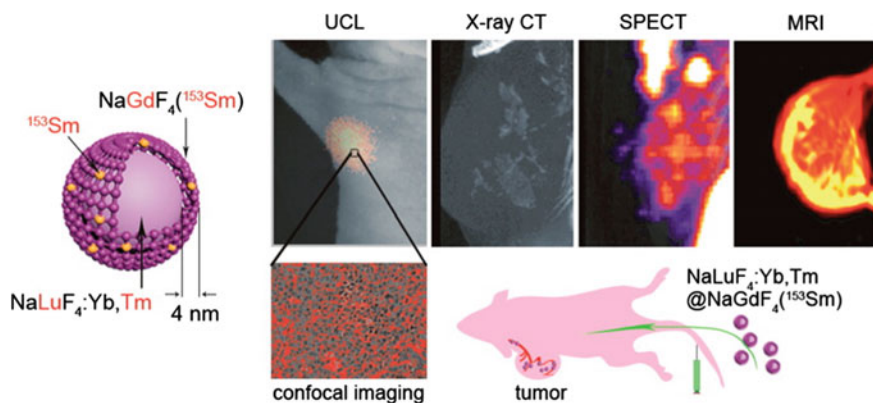
Fig. 9.7 Schematic illustration of $NaLuF_4:Yb/Tm@NaGdF_4:^{153}Sm$ core–shell structure as well as its use for four-modal (UCL, X-ray CT, SPECT, MR) tumor angiogenesis imaging. Reprinted with the permission from Ref. [53]. Copyright 2013 American Chemical Society

tomography (SPECT) and X-ray computed tomography (CT). To this end, the synergic combination of lanthanide ions that possess rich properties in core–shell structure has been harnessed for multimodal imaging. An excellent example was reported by Sun and Li [53], who prepared $NaLuF_4:Yb/Tm@NaGdF_4:^{153}Sm$ core–shell structure as a four-modal imaging agent (Fig. 9.7). Gd^{3+} contributed to the T_1-weighted MR imaging and located in the outer shell. Positioning the gamma photons emitter ^{153}Sm in the outmost $NaGdF_4$ shell layer allows for SPECT imaging. Lu-based nanoparticles with strong X-ray absorption contributed to X-ray CT imaging. Yb/Er codoped in the $NaLuF_4$ host was for UC luminescence imaging.

9.4.2 Enhancing Spectral Tunability

One outstanding feature of core–shell structure is for manipulating energy exchange interaction within the nanoparticles. The epitaxial core–shell structure explores different combinations of lanthanide dopants in one nanoparticle, while spatially isolates them in separate layers. The optical property can be rationally designed and tuned through control over the energy transfer or migration through the core–shell interfaces. When compared to conventional method for optical tuning in core-only nanoparticles, this approach adds an additional dimension of core–shell combination that enhances the spectral tunability.

Energy transfer between lanthanide ions usually requires a short separation between the donor and acceptor ions, which precludes efficient energy exchange between lanthanide ions embedded in separate layers of a core–shell structure. This problem has been solved by Wang and Liu [9], who devised a method based on gadolinium (Gd) sublattice-mediated energy migration to realize energy delivery

Fig. 9.8 **a** Schematic illustration of $NaGdF_4$:Yb/Tm@$NaGdF_4$:X core–shell structure. **b** Proposed energy transfer mechanism between lanthanide dopants. **c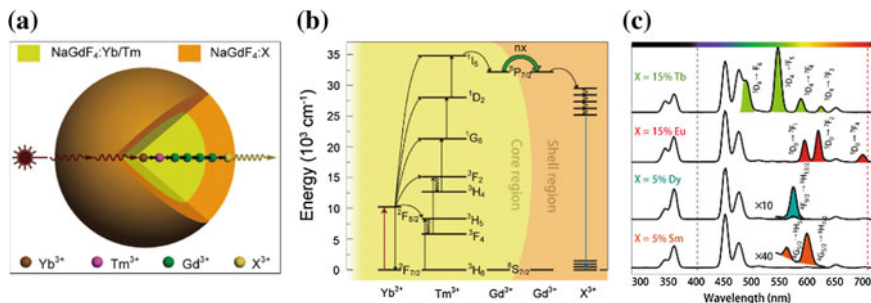** Emission spectra of X = Tb, Eu, Dy, Sm, respectively. Reprinted by permission from Macmillan Publishers Ltd: Ref. [9], copyright 2011

over long distance. In their study, an energy migration-mediated UC (EMU) process was demonstrated in $NaGdF_4$:Yb/Tm@$NaGdF_4$:X (X: activator ion) nanoparticles (Fig. 9.8). A key element in this study is the Gd-sublattice through the core–shell interface that extracts the excitation energy of Tm^{3+} in the core layer. Subsequent energy hopping through the Gd-sublattice delivers the energy to the activators embedded in the shell layer with high efficiency. The combination of core–shell structural engineering and energy migration offers an elegant solution to regulating complex lanthanide interactions, which has resulted in unprecedented upconversion emission in a wide collection of lanthanide ions including Tb^{3+}, Eu^{3+}, Dy^{3+}, and Sm^{3+}. The same group later refined the EMU process by surface coating of an inner shell $NaYF_4$ to prevent dissipating of excitation energy stored in the migrator sublattice, which promotes maximal energy capture by the activators [54].

Apart from Gd^{3+} that act as a migrator, some other optical active lanthanide ions like Yb^{3+} have the similar functionality. The criteria for selecting migrator ions are quite stringent. At almost the same time, the groups of Wang [47], Liu [55], and Yan [56] reported Nd^{3+}-sensitized UC in core–shell structure with Yb^{3+} acting as migrator ion. In these studies, Yb^{3+} ions are responsible to extract the excitation energies harvested by Nd^{3+} sensitizers and to initiate an energy migration process to deliver the energy to upconverting ions such as Tm^{3+}, Er^{3+}, and Ho^{3+}. These studies successfully shift the conventional excited 980 nm wavelength to 808 nm, thus greatly minimizing the tissue overheating effect. In the study by Wen and Wang [47], a $NaYbF_4$:Nd@Na(Yb,Gd)F_4:Tm@$NaGdF_4$:Tb (Eu, Dy) core–shell structure was used to cascade energy migration through the Yb- and Gd-sublattices, which has led to UC emission in common lanthanide ions such as Tb^{3+} and Eu^{3+} by 808-nm excitation.

Lanthanide-doped UC nanoparticles can act as a platform to assemble various building blocks to form composite core–shell structure. Various components that interact with lanthanide-doped nanoparticles substrate in a single particle may lead

to fascinating new optical phenomenon. In most nanocomposites, UC nanoparticles donate their excitation energy to optical entities such as organic dye, semiconductor materials, manganese dioxide, leading to modulated UC emissions. Gorris and Wolfbeis [57] constructed an organic dye-decorated core–shell UC nanoparticle. The organic dye (rhodamine B, S-0378, fluorescein, NIR-797) shell served as a screen layer that selectively absorbs the green and red emission bands of UC nanoparticles, which provides a new strategy for spectral encoding toward multi-plexed biodetection. Cheng and Liu [32] developed a similar composite UC nanoparticles system for modulating UC emissions. The nanocomposites were further applied to in vivo multi-color UC luminescence imaging studies. In another study, Yan and Perepichka [34] reported a novel $NaYF_4$:Yb/Er@CdSe core–shell structure that uses the NIR photon to create charge carriers in CdSe-based films, leading to a reversible and stable NIR photoconductivity switch. A new hetero-nanostructured photoanodes with the ability to enhance near-infrared light harvesting was reported by Su and Tok [58]. This heterogeneous core multi-shelled structure is composed of $NaYF_4$:Yb/Er@$NaYF_4$ UC core coated with a thin layer of TiO_2 matrix that suitable for subsequent attachment of QDs. When the photoanode was excited by near-infrared light, energy transferred from UC nanoparticles to QDs will occur and inject electrons into TiO_2.

Optical entity attached to UC nanoparticles can also transfer their energy to lanthanide ions embedded in the crystalline lattice, which enhances UC emissions via an antenna effect. Due to the parity-forbidden intra-4f transitions, the absorption coefficient of Ln^{3+} is typically low. Organic chromophores displaying much larger absorption coefficient can largely enhance the light absorption process. The antenna effect for sensitizing lanthanide emission was first exploited by Zhang and Petoud [59], who constructed a Tropolonate ligand-capped $NaYF_4$:Yb(Nd) nanoparticles. These novel systems use the inorganic $NaYF_4$ matrix to protect Ln^{3+} from surface quenching, while the chromophoric coating sensitizes near-infrared luminescence. When compared to chelated structures that are composed of lanthanide ions directly bound to organic chromophores, a more than five- and 11-fold longer luminescence lifetime was observed for Yb^{3+} and Nd^{3+}, respectively. A fascinating example was reported by Zou and Hummelen [60], who proposed a dye-sensitized UC nanoparticles. A commercially available cyanine dye, IR-780, was selected as the antenna to harvest photon excitation in the NIR region of spectrum. The strategy dramatically enhanced the spectral response of UC nanoparticles in the 720–1000 nm range by over 3000 times (Fig. 9.9).

9.5   Conclusion

The core–shell design leads to largely enhanced UC efficiency and integrity by spatial confinement of lanthanide dopants, in addition to providing unprecedentedly high designability and tunability. However, there remain several challenges for the future studies. (i) Intra-4f transitions result in low absorption coefficient of Ln^{3+}
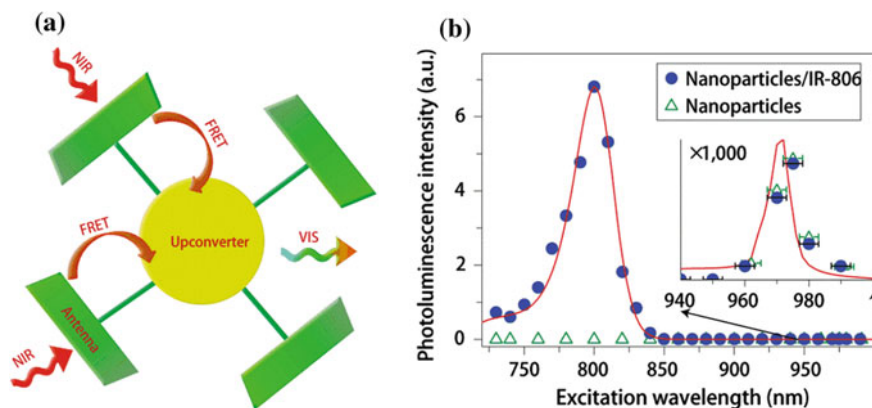
Fig. 9.9 **a** Schematic design of dye-sensitized UC nanoparticles. **b** UC emission spectra of β-NaYF$_4$:Yb/Er nanoparticles and β-NaYF$_4$:Yb/Er@IR-806 nanocomposites, respectively. Reprinted by permission from Macmillan Publishers Ltd: Ref. [60], copyright 2012

ions. More studies need to focus on antenna effect to develop effective sensitizing shells, which may be of great help for enhancing absorptivity as well as UC emission intensity. (ii) It is an arduous task to synthesize core–shell UC nanoparticles with ultrasmall size (<10 nm) and high quantum efficiency, which are critical prerequisites for important bioapplications such as labeling cell nucleus. (iii) Effective new techniques are to be established for discerning the core–shell structure with high resolution and precision.

References

1. Auzel F (1966) Compteur quantique par transfert d'énergie entre deux ions de terres rares dans un tungstate mixte et dans un verre germinate. C. R. Acad. Sci. 262: 1016.
2. Ovsyankin VV, Feofilov PP (1966) On the mechanism of adding of electronic excitations in doped crystals. Sov. Phys. JETP Lett. 3: 322.
3. Ovsyankin VV, Feofilov PP (1966) Cooperative sensitization of luminescence in crystals activated with rare earth ions. Sov. Phys. JETP Lett. 4: 317.
4. Chen X, Peng DF, Ju Q, Wang F (2015) Photon upconversion in core–shell nanoparticles. Chem. Soc. Rev. 44: 1318.
5. Gamelin DR, Güdel HU (2000) Design of luminescent inorganic materials: new photophysical processes studied by optical spectroscopy. Acc. Chem. Res. 33: 235.
6. Singh-Rachford TN, Castellano FN (2010) Photon upconversion based on sensitized triplet–triplet annihilation. Coord. Chem. Rev, 254: 2560.
7. Stehr JE, Chen SL, Reddy NK, Tu CW, Chen WM, Buyanova IA (2014) Turning ZnO into an efficient energy upconversion material by defect engineering. Adv. Funct. Mater. 24: 3760.

8. Deutsch Z, Neeman L, Oron, D (2013) Luminescence upconversion in colloidal double quantum dots. Nat. Nanotechnol. 8: 649.

9. Wang F, Deng RR, Wang J, Wang QX, Han Y, Zhu HM, Chen XY, Liu XG (2011) Tuning upconversion through energy migration in core–shell nanoparticles. Nat. Mater. 10: 968.

10. Huang LJ, Wang LL, Xue XJ, Zhao D, Qin GS, Qin WP (2011) Enhanced red upconversion luminescence in Er-Tm codoped NaYF$_4$ phosphor. J. Nanosci. Nanotechnol. 11: 9498.

11. Wang GF, Peng Q, Li YD (2010) Luminescence tuning of upconversion nanocrystals. Chem. Eur. J. 16: 4923.

12. Bednarkiewicz A, Wawrzynczyk D, Nyk M, Strek W (2011) Synthesis and spectral properties of colloidal Nd^{3+} doped NaYF$_4$ nanocrystals. Optical Materials 33: 1481.

13. Wang F, Liu XG (2008) Upconversion multicolor fine-tuning: visible to near-infrared emission from lanthanide-doped NaYF$_4$ nanoparticles. J. Am. Chem. Soc. 130: 5642.

14. Gai SL, Li CX, Yang PP, Lin J (2014) Recent progress in rare earth micro/nanocrystals: soft chemical synthesis, luminescent properties, and biomedical applications. Chem. Rev. 114: 23430.

15. Mai HX, Zhang YW, Sun LD, Yan CH (2007) Highly efficient multicolor up-conversion emissions and their mechanisms of monodisperse NaYF$_4$:Yb,Er core and core/shell-structured nanocrystals. J. Phys. Chem. C 111: 13721.

16. Qian HS, Zhang Y (2008) Synthesis of hexagonal-phase core–shell NaYF$_4$ nanocrystals with tunable upconversion fluorescence. Langmuir 24: 12123.

17. Zhang F, Che RC, Li XM, Yao C, Yang JP, Shen DK, Hu P, Li W, Zhao DY (2012) Direct imaging the upconversion nanocrystal core/shell structure at the subnanometer level: shell thickness dependence in upconverting optical properties. Nano Lett. 12: 2852.

18. Abel KA, Boyer JC, Andrei CM, van Veggel FCJM (2011) Analysis of the shell thickness distribution on NaYF$_4$/NaGdF$_4$ core/shell nanocrystals by EELS and EDS. J. Phys. Chem. Lett. 2: 185.

19. Murry CB, Norris DJ, Bawendi MG (1993) Synthesis and characterization of nearly monodisperse CdE (E = sulfur, selenium, tellurium) semiconductor nanocrystallites. J. Am. Chem. Soc. 115: 8706.

20. Yi GH, Chow GM (2007) Water-soluble NaYF$_4$:Yb,Er(Tm)/NaYF$_4$/polymer core/shell/shell nanoparticles with significant enhancement of upconversion fluorescence. Chem. Mater. 19: 341.

21. Li XM, Shen DK, Yang JP, Yao C, Che RC, Zhang F, Zhao DY (2013) Successive layer-by-layer strategy for multi-shell epitaxial growth: Shell thickness and doping position dependence in upconverting optical properties. Chem. Mater. 25: 106.

22. Johnson NJJ, Korinek A, Dong CH, van Veggel FCJM (2012) Self-focusing by ostwald ripening: a strategy for layer-by-layer epitaxial growth on upconverting nanocrystals. J. Am. Chem. Soc. 134: 11068.

23. Son DH, Hughes SM, Yin YD, Alivisatos AP (2004) Cation exchange reactions in ionic nanocrystals. Science, 306: 1009.

24. Dong CH, van Veggel FCJM (2008) Cation exchange in lanthanide fluoride nanoparticles. ACS Nano 3: 123.

25. Liu Q, Sun Y, Li CG, Zhou J, Li CY, Yang TS, Zhang XZ, Yi T, Wu DM, Li FY (2011) ^{18}F-labeled magnetic-upconversion nanophosphors via rare-earth cation-assisted ligand assembly. ACS Nano 5: 3146.

26. Jalil RA, Zhang Y (2008) Biocompatibility of silica coated NaYF$_4$ upconversion fluorescent nanocrystals. Biomaterials 29: 4122.

27. Mader HS, Link M, Achatz DE, Uhlmann K, Li XH, Wolfbeis OS (2010) Surface-modified upconverting microparticles and nanoparticles for use in click chemistries. Chem. Eur. J. 16: 5416.

28. Liu JN, Bu WB, Pan LM, Shi JL (2013) NIR-triggered anticancer drug delivery by upconverting nanoparticles with integrated azobenzene-modified mesoporous silica. Angew. Chem. Int. Ed. 52: 4375.

29. Qian HS, Guo HC, Ho PCL, Mahendran R, Zhang Y (2009) Mesoporous-silica-coated up-conversion fluorescent nanoparticles for photodynamic therapy. Small 5: 2285.

30. Fan WP, Shen B, Bu WB, Chen F, Zhao KL, Zhang SJ, Zhou LP, Peng WJ, Xiao QF, Xing HY, Liu JN, Ni DL, He QJ, Shi JL (2013) Rattle-structured multifunctional nanotheranostics for synergetic chemo-/radiotherapy and simultaneous magnetic/luminescent dual-mode imaging. J. Am. Chem. Soc. 135: 6494.

31. Zhou HP, Xu CH, Sun W, Yan CH (2009) Clean and flexible modification strategy for carboxyl/aldehyde-functionalized upconversion nanoparticles and their optical applications. Adv. Funct. Mater. 19: 3892.

32. Cheng L, Yang K, Shao MW, Lee ST, Liu Z (2011) Multicolor in vivo imaging of upconversion nanoparticles with emissions tuned by luminescence resonance energy transfer. J. Phys. Chem. C 115: 2686.

33. Zhang H, Li YJ, Ivanov IA, Qu YQ, Huang Y, Duan XF (2010) Plasmonic modulation of the upconversion fluorescence in $NaYF_4$:Yb/Tm hexaplate nanocrystals using gold nanoparticles or nanoshells. Angew. Chem. Int. Ed. 49: 2865.

34. Yan CL, Dadvand A, Rosei F, Perepichka DF (2010) Near-IR photoresponse in new up-converting CdSe/$NaYF_4$:Yb,Er nanoheterostructures. J. Am. Chem. Soc. 132: 8868.

35. Deng RR, Xie XJ, Vendrell M, Chang YT, Liu XG (2011) Intracellular glutathione detection using MnO_2-nanosheet-modified upconversion nanoparticles. J. Am. Chem. Soc. 133: 20168.

36. Li ZQ, Wang LM, Wang ZY, Liu XH, Xiong YJ (2011) Modification of $NaYF_4$:Yb,Er@SiO_2 nanoparticles with gold nanocrystals for tunable green-to-red upconversion emissions. J. Phys. Chem. C 115: 3291.

37. Li ZQ, Zhang Y, Jiang S (2008) Multicolor core/shell-structured upconversion fluorescent nanoparticles. Adv. Mater. 20: 4765.

38. Guo HS, Li ZQ, Qian HS, Hu, Y, Muhammad IN (2010) Seed-mediated synthesis of $NaYF_4$: Yb, Er/$NaGdF_4$ nanocrystals with improved upconversion fluorescence and MR relaxivity. Nanotechnology 21: 125602.

39. Chen GY, Shen J, Ohulchanskyy TY, Patel NJ, Kutikov A, Li ZP, Song J, Pandey RK, Ågren H, Prasad PN, Han, G (2012) (α-$NaYbF_4$:Tm^{3+})/CaF_2 core/shell nanoparticles with efficient near-infrared to near-infrared upconversion for high-contrast deep tissue bioimaging. ACS Nano 6: 8280.

40. Vetrone F, Naccache R, Mahalingam V, Morgan CG, Capobianco J A (2009) The active-core/active-shell approach: a strategy to enhance the upconversion luminescence in lanthanide-doped nanoparticles. Adv. Funct. Mater. 19: 2924.

41. Ghosh P, Oliva J, Rosa EDL, Haldar KK, Solis D, Patra A (2008) Enhancement of upconversion emission of $LaPO_4$:Er@Yb core − shell nanoparticles/nanorods. J. Phys. Chem. C 112: 9650.

42. Yang DM, Li CX, Li GG, Shang MM, Kang XJ, Lin J (2011) Colloidal synthesis and remarkable enhancement of the upconversion luminescence of $BaGdF_5$:Yb^{3+}/Er^{3+} nanoparticles by active-shell modification. J. Mater. Chem. 21: 5923.

43. Chen DQ, Yu YL, Huang F, Lin H, Huang P, Yang AP, Wang ZX, Wang YS (2012) Lanthanide dopant-induced formation of uniform sub-10 nm active-core/active-shell nanocrystals with near-infrared to near-infrared dual-modal luminescence. J. Mater. Chem. 22: 2632.

44. Zhong YT, Tian G, Gu ZJ, Yang YJ, Gu L, Zhao YL, Ma Y, Yao JN (2014) Elimination of photon quenching by a transition layer to fabricate a quenching-shield sandwich structure for 800 nm excited upconversion luminescence of Nd^{3+}-sensitized nanoparticles. Adv. Mater. 26: 2831.

45. Liu XM, Kong XG, Zhang YL, Tu LP, Wang Y, Zeng QH, Li CG, Shi Z, Zhang H (2011) Breakthrough in concentration quenching threshold of upconversion luminescence via spatial separation of the emitter doping area for bio-applications. Chem. Commun. 47: 11957–11959.

46. Li ZH, Park W, Zorzetto G, Lemaire JS, Summers CJ (2014) Synthesis protocols for δ-doped $NaYF_4$: Yb, Er. Chem. Mater. 26: 1770.

47. Wen HL, Zhu H, Chen X, Hung TF, Wang BL, Zhu GY, Yu SF, Wang F (2013) Upconverting near-infrared light through energy management in core–shell-shell nanoparticles. Angew. Chem. Int. Ed. 52: 13419.
48. Li XM, Wang R, Zhang F, Zhou L, Shen DK, Yao C, Zhao DY (2013) Nd^{3+} sensitized up/down converting dual-mode nanomaterials for efficient in-vitro and in-vivo bioimaging excited at 800 nm. Sci. Rep. 3: 3536.
49. Liu YS, Tu DT, Zhu HM, Li RF, Luo WQ, Chen XY (2010) A strategy to achieve efficient dual-mode luminescence of Eu^{3+} in lanthanides doped multifunctional $NaGdF_4$ nanocrystals. Adv. Mater. 22, 3266.
50. Chen HY, Qi B, Moore T, Colvin DC, Crawford T, Gore JC, Frank A, Mefford T, Anker JN (2014) Synthesis of brightly PEGylated luminescent magnetic upconversion nanophosphors for deep tissue and dual MRI imaging. Small, 10: 160.
51. Zhang Y, Das GK, Vijayaragavan V, Xu QC, Padmanabhan P, Bhakoo KK, Selvan ST, Tan TTY (2014) "Smart" theranostic lanthanide nanoprobes with simultaneous up-conversion fluorescence and tunable T_1-T_2 magnetic resonance imaging contrast and near-infrared activated photodynamic therapy. Nanoscale 6: 12609.
52. Das GK, Johnson NJJ, Cramen J, Blasiak B, Latta P, Tomanek B, van Veggel FCJM (2012) $NaDyF_4$ nanoparticles as T_2 contrast agents for ultrahigh field magnetic resonance imaging. J. Phys. Chem. Lett. 3: 524.
53. Sun Y, Zhu XJ, Peng JJ, Li FY (2013) Core–shell lanthanide upconversion nanophosphors as four-modal probes for tumor angiogenesis imaging. ACS Nano 7: 11290.
54. Su QQ, Han SY, Xie XJ, Zhu HM, Chen HY, Chen CK, Liu RS, Chen XY, Wang F, Liu XG (2012) The effect of surface coating on energy migration-mediated upconversion. J. Am. Chem. Soc. 134: 20849.
55. Xie XJ, Gao NY, Deng RR, Sun Q, Xu QH, Liu XG (2013) Mechanistic investigation of photon upconversion in Nd^{3+}-sensitized core–shell nanoparticles. J. Am. Chem. Soc. 135: 12608.
56. Wang, YF, Liu GY, Sun LD, Xiao JW, Zhou JC, Yan CH (2013) Nd^{3+}-sensitized upconversion nanophosphors: efficient in vivo bioimaging probes with minimized heating effect. ACS Nano 7: 7200.
57. Gorris HH, Ali R, Saleh SM, Wolfbeis OS (2011) Tuning the dual emission of photon-upconverting nanoparticles for ratiometric multiplexed encoding. Adv. Mater. 23: 1652.
58. Su LT, Karuturi SK, Luo JS, Liu LJ, Liu XF, Guo J, Sum TC, Deng RR, Fan HJ, Liu XG, Tok AIY (2013) Photon upconversion in hetero-nanostructured photoanodes for enhanced near-infrared light harvesting. Adv. Mater. 25: 1603.
59. Zhang J, Shade CM, Chengelis DA, Petoud S (2007) A strategy to protect and sensitize near-infrared luminescent Nd^{3+} and Yb^{3+}: organic tropolonate ligands for the sensitization of Ln^{3+}-doped $NaYF_4$ nanocrystals. J. Am. Chem. Soc. 129: 14834.
60. Zou WQ, Visser C, Maduro JA, Pshenichnikov MS, Hummelen JC (2012) Broadband dye-sensitized upconversion of near-infrared light. Nat. Photon. 6: 560.

Chapter 10
Upconversion Luminescence Behavior of Single Nanoparticles

Jiajia Zhou and Jianrong Qiu

Abstract Upconversion nanoparticles (UCNPs) have made a significant and valuable contribution to materials science, photophysics, and biomedicine, which benefit from their specific spectroscopic characters. However, the ensemble spectroscopy of UCNPs is limited for the electronic behavior in average effect, which ignores the fact that the nanoparticles are heterogeneous. Toward the research focus of heterogeneous intrinsic structure, unique photophysical phenomena, and advanced applications, the optical characterization of single UCNPs is promoted to a frontier breakthrough of UCNPs community. In this chapter, we overview the importance of the single UCNPs characterization, the typical principles of upconversion, and the single particle detection approaches. A considerable emphasis is placed on the specific spectroscopic study of single UCNPs, which shows us fantastic photophysical phenomena beyond ensemble measurement. Parallel efforts are devoted to the currently applications of single UCNPs.

10.1 Introduction

Upconversion (UC) luminescence from lanthanide-doped nanoparticles with unique spectroscopic conversion ability has become a fast-developing research field in recent years, which exhibits kinds of promising applications in biomedicine, photovoltaic, 3D display, sensing, etc. This photon management in nanoscale owns a

J. Zhou · J. Qiu (✉)
College of Optical Science and Engineering,
State Key Laboratory of Modern Optical Instrumentation,
Zhejiang University, Hangzhou 310027, China
e-mail: qjr@zju.edu.cn

J. Zhou
e-mail: zhzz85@zju.edu.cn

superiority in optical tunability including the aspects of excited-state dynamics, emission spectra, quantum efficiency, etc. For instance, near-infrared (NIR) excited multicolor UC could be applied in multiplexed labeling through the control of dopant species, concentration, and their spatial distribution [1–5]; Single-band red or NIR UC emission with high productivity is very promising for deep in vivo imaging and cell tracking [6–9]; Composite composed of UC nanoparticles and semiconductors (TiO_2, ZnO, etc.) has spectral conversion characteristic from NIR to ultraviolet for solar energy harvest in photovoltaic or photocatalysis [10–12]. One will easily find that all of these prevalent researches on UC nanoparticles (UCNPs) are focusing on their optical performance by ensemble spectroscopy techniques. Little efforts have been donated to the single nanoparticle UC luminescence behavior, though it is well known that with the knowledge gained through single particle spectroscopy, the performance of the UC particles will be optimized.

Why single nanoparticle? UCNPs, e.g. $NaYF_4$, which is considered a typical representative, have an average size ranging from sub-20–100 nm. Most of the UCNPs are synthesized by wet chemical methods and are expected to disperse in kinds of solvents to form a colloid. What's more, the surface functionalization of UCNPs is an extremely important process for their bio-applications [13–19]. For instance, the significant proportion of the atoms lying at or near the surface, combined with the enriched surface defects and organic ligands, can significantly complicate the photophysical behaviors of the doped lanthanides. The electronic behavior detection aiming at a single nanoparticle will show signals from the microstructure of nanoparticles. And also the single nanoparticle spectroscopy offers clear insight into the interplay between intrinsic and extrinsic influences without annoying noise and subsequently gives instructions for the high quality preparation of UCNPs.

On the other hand, single nanoparticle optical characterization possesses the powerful capacity to explore the crystalline structure anisotropy-related optical differences or some unexpected unique optical phenomena at sub-micron and even nanoscale. As the earlier developed artificial nanomaterials, quantum dots and metal nanoparticles have been widely investigated in single nanoparticle photophysics [20–22]. For example, the first reports of the detection of single CdSe nanocrystals revealed a number of novel photophysical phenomena that had not been expected [23–26]. $NaYF_4$, or any other UCNPs with isolated activators, which are different from the conductor or semiconductor, are expected to be discovered new photophysical phenomena. From photophysical theoretical investigations to single nanoparticle technical applications, single UCNPs-focused optical characterization plays an important role in optical super-resolution imaging, local field enhanced luminescence, etc.

In this chapter, we present the first short review on the UC behaviors of single UCNPs spanning from the typical UC principles, single particle spectroscopic detection technology, to the recent developed new photophysical phenomena and applications in single particle level.

10.2   Principles of Upconversion Luminescence

Upconversion is an anti-Stokes process, which converts two or more low-energy photons into one high-energy photon [13, 17]. The occurrence of this fantastic phenomenon is benefited from the relative long lifetime of most of the excited states in trivalent lanthanides. UC luminescence has been attracted unprecedented attention referring to various promising applications including photovoltaic, bioimaging, solid-state laser diode, temperature sensor, lighting, etc., since the UC has been firstly focused by Auzel in 1960s [4, 6, 28–64].

The higher prevalence and practicability of UC compared to multiphoton absorption and second/third harmonic generation are contributed by the relatively low excitation energy and high quantum efficiency. In generally, the UC approaches contain the following four ways, which are shown in Fig. 10.1. Figure 10.1a is the excited-state absorption (ESA), which means sequential absorption of two photons to pump the ion into higher excited state via a real intermediary state intra single ion. Figure 10.1b shows the energy transfer UC (ETU), which means two neighboring ions are excited to the intermediary states by ground-state absorption followed by non-radiative energy transfer between the two ions, and finally one ion reaches to the excited state and the other one is back to the ground state. Figure 10.1c presents the photon avalanche (PA). This is an unconventional process, where the strong UC luminescence occurs without the resonance ground-state absorption when the excitation power exceeds a certain threshold. The pump wavelength is only resonant between a metastable state and a higher energy state. The energy migration-mediated UC (EMU) in Fig. 10.1d is recently proposed by Wang et al. [32], involving the use of four types of lanthanide ions and a core-shell
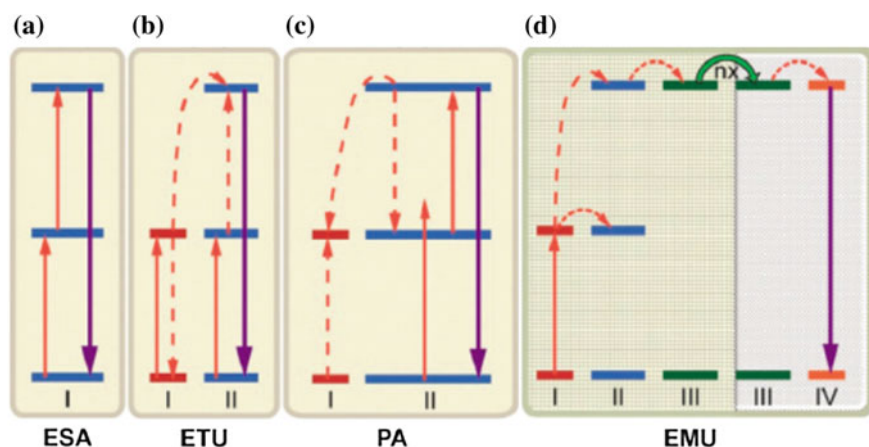

Fig. 10.1   Proposed typical UC processes: **a** excited-state absorption (*ESA*); **b** energy transfer UC (*ETU*); **c** photon avalanche (*PA*). **d** energy migration-mediated UC (*EMU*) involving the use of four types of lanthanide ions and a core-shell design. Reproduced from Ref. [27] by permission of The Royal Society of Chemistry

structure. The ions without long-lived intermediary energy states ($Ln^{3+} = Eu^{3+}$, Tb^{3+}, Dy^{3+}, Sm^{3+}) become activators to generate efficient UC luminescence in $NaGdF_4$:Tm^{3+}/Yb^{3+}@$NaGdF_4$:Ln^{3+} core-shell nanoparticles benefiting from the energy migration effect of Gd^{3+} located in the host lattice.

10.3   Detection Approaches for Single Particle Spectroscopy

Detection of single UCNPs is an advanced technique with the requirement of background knowledge in material science and optical engineering. In all the detection approaches, high-resolution microscopes overcoming the light diffraction limit composes the key component, which can be learned from the detection of other materials system. Except for the difference that the anti-Stokes transitions of UCNPs are the target, the 980-nm laser source is employed to excitation and selected ultraviolet, visible or NIR wavelength regions are detected. So far, two mainstream approaches for single UCNPs' optical characterization called confocal scanning microscopy and fiber-loaded measurement stand out from the rest ways, e.g. photonic force microscopy, fiber tapper measurement [65, 66]. In this part, we will give a brief introduction of the key techniques in these two approaches.

10.3.1   Confocal Scanning Microscopy

Confocal scanning microscopy possesses the superiority of high signal-to-noise ratio with the spatial filtering effect by focusing the illuminating light source and placing a pinhole in front of the photodetector compared to wide-field microscopy [67, 68]. In this scheme, the out-of-focus signals do not pass the hole and are not detected by the detector, as is shown by the gray dot lines in Fig. 10.2. In a typical
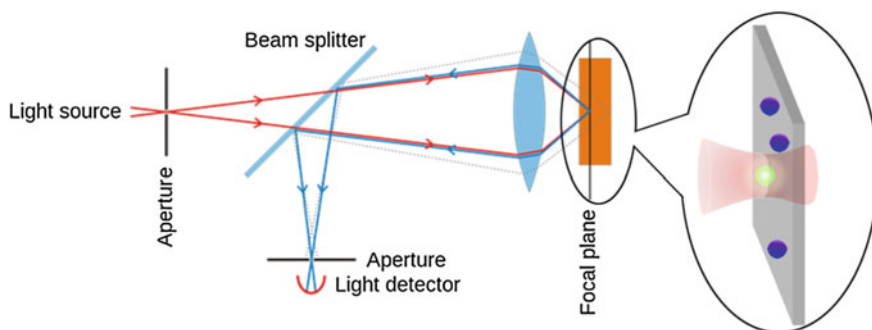

Fig. 10.2 Schematic diagram of confocal scanning microscopy

single nanoparticle upconversion measurement [69–75], a 980-nm diode laser is tightly focused on the sample through an objective. The sample is raster-scanned by a piezo-actuated three-dimensional nanopositioning stage. At each pixel, the UC luminescence is collected through the same objective and passed through a dichroic beam splitter and short-pass filters, while the 980-nm excitation light was completely filtered out. After passing through a confocal pinhole, the upconversion luminescence is either detected by a spectrometer for spectrum collection or an avalanche photo diode (APD) for luminescence image acquisition.

In the confocal scanning microscopy, single nanoparticle hunting is time consuming, which makes the sample preparation to be a skillful work though the atomic force microscope (AFM) is in situ exploited combined to the optical detection [70, 71]. Empirical methods contain the TEM grids loading and coverslip loading through dropping process of diluted nanoparticle solution with reported concentration of ~ 0.1 nM. Using the TEM grids, the single particles could be further confirmed by the TEM or SEM imaging. Note that this should be carried out after all optical characterization to avoid perturbing the optical properties caused by high-energy electrons. For the coverslip approach, it is indeed a tricky thing to obtain the monodispersed particles in appropriate distribution for single detection, where the employment of surface treatment agent on top of the coverslip may be helpful. Besides, to avoid agglomeration of the nanoparticles during evaporation of the solvent, the coverslip itself could be stored on a support mount on a beaker in an ultrasonic bath.

10.3.2   Fiber-Loaded Measurement

Luminescence detection using liquid-immersed exposed-core microstructured optical fibers (MOF) has been frequently reported by Monro's group [77–79]. Recently, the single nanocrystal sensitivity achieved by enhanced UC luminescence, which results from the cooperation of Jin's group and Monro's group, drives this fiber-loaded technology to be a powerful approach for single UCNPs detection [76, 80–82]. The schematic of the experimental configuration for capturing UC luminescence of nanoparticles using a suspended core microstructured optical fiber dip sensor is shown in Fig. 10.3. A 980-nm fiber-coupled diode laser source is used for excitation. It is coupled into the MOF using a dichroic mirror and a microscope objective. The UC emission is collected by the fiber core and measured for light propagating in the backwards direction (i.e. light traveling toward the launch/input end of the fiber), with the dichroic filter passing visible-NIR emission. A broad band-pass filter is used to further suppress residual pump light, and the particle luminescence is detected by a spectrometer. The experimental procedure involved first optimizing and recording the amount of power coupled into the suspended core of the fiber by varying the fiber position using XYZ stages. The lens is then removed from the output coupling stage, and the tip of the fiber immersed in the nanoparticle solution and allowed to fill using capillary forces. The fiber is then
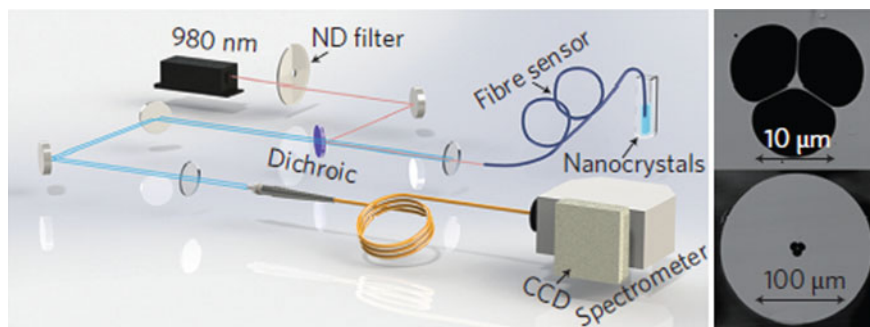
Fig. 10.3 Schematic of the experimental configuration for capturing UC luminescence of nanoparticles using a suspended-core microstructured optical fiber dip sensor. Reprinted by permission from Macmillan Publishers Ltd: Ref. [76], copyright 2013

removed from the solution and the measurement is performed. Here, the nanoparticle solution is diluted UCNPs dispersed in a nonpolar solvent, e.g. toluene, cyclohexane, with a concentration ranging between dozens of nM and dozens of fM.

10.4 Specific Spectroscopic Study of Single UCNPs Beyond Ensemble Spectroscopy

Single particle characterization is a powerful technical approach to exploit the microstructural-dependent spectroscopic characters, which is always compromised in ensemble spectroscopy. For instance, both of the "bright" and "dark" spots representing the UC efficiency of different hexagonal $NaYF_4$ may coexist in an imaging field. It is a clear signal that some unknown defects may be induced in the synthesis to generate inconsistent crystalline symmetries between particles though they have similar morphologies, or the different particles lying with different lattice planes on surface, which may have specific atomic density and orientation effects with polarized laser beam. This kind of precise spectroscopic study is of great importance to improve the quality of UCNPs, but it is ignored in ensemble measurements. Here, we would like to introduce some important fundamental developments devoted to the upconversion luminescence behaviors of single nanoparticles.

10.4.1 Nonblinking and Nonbleaching Luminescence

Photoluminescence blinking—random switching between states of high (ON) and low (OFF) emissivities—is a universal property of molecular emitters found in single quantum dots and fluorophores [25, 83, 84]. Also, the blink on a variable time
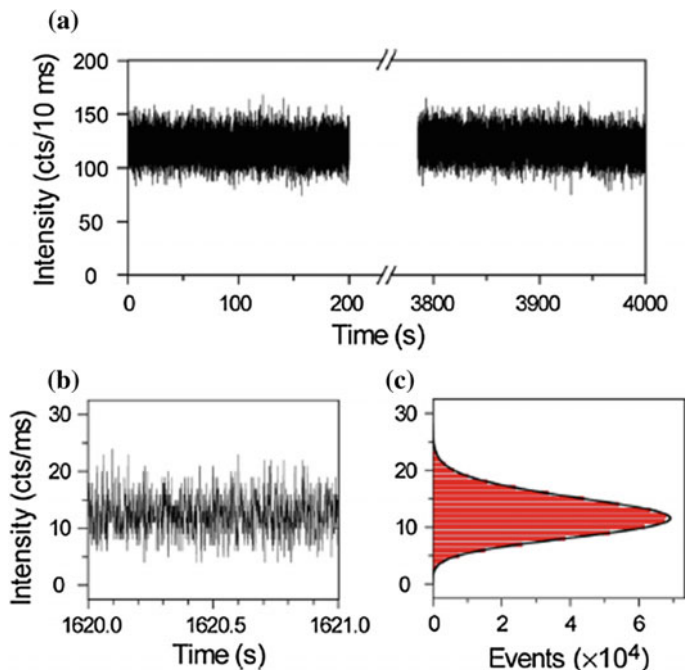
Fig. 10.4 Photostability and non-blinking behavior of a single UC nanoparticle. **a** The time trace of emission intensity from a single UC nanoparticle under continuous laser illumination for more than 1 h. **b, c** The zoom-in time trace and histogram of emission intensity, showing no on/off behavior—non-blinking. Reprinted with permission from Ref. [69]

scale ranging from several hundred milliseconds to several seconds of single Eu^{3+} ions incorporated in Y_2O_3 nanoparticles has been observed [85]. However, such behavior is absent in single nanoparticles with abundant lanthanides. For the lanthanide-activated UCNPs, the question—blink or not—has been confirmed by single particle characterization using confocal or wide-field microscopy [68, 69, 75]. As shown in Fig. 10.4, the first graphical demonstration of nonblinking behavior and no photobleaching or photodamage after 1 h of continuous laser illumination was reported by Cohen et al. in single (β-$NaYF_4$) nanoparticle doped with 20 % Yb^{3+} and 2 % Er^{3+}, which subsequently be considered to be ideally suited for single molecule imaging.

10.4.2 Polarization Anisotropic Upconversion

Micropolarized spectroscopy that focuses on the single particle luminescence has attracted great attention in semiconductor system. In contrast to single emission bands observed for semiconductor system, the lanthanide-doped UCNPs generally

show a distinct set of sharp emission peaks arising from f–f orbital electronic transitions. The multiple-peak patterns should provide spectroscopic fingerprints, which are particularly useful for accurate interpretation in the event of overlapping emission spectra, thus possibly lending themselves to detailed theoretical analysis. What's more, UC with the requirement of laser excitation will be affected by the polarization state spontaneously. However, it is still an open question that whether the nanoparticles with abundant activators should exhibit polarization anisotropy under linearly polarized laser excitation though the single lanthanide ion transitions has orientation polarization. Therefore, we tried to demonstrate micropolarized optical detection of UC based on lanthanide-doped inorganic dielectric system, namely Tm^{3+}–Yb^{3+} ion couple activated β-$NaYF_4$ single microrod for the first time [72]. During this single particle detection, unique luminescent phenomena, e.g. sharp energy-level split and singlet-to-triplet transitions at room temperature, multiple discrete fluorescence intensity periodic variation with polarized direction have been observed upon excitation with 980-nm linearly polarized laser. The comparative experiments suggested that intra-ions transition orientation and crystal local symmetry dominate the polarization anisotropy. In purpose of the origin exploration with convincing experimental design, we further employed the excitation polarization detection considering of the interplay between the laser polarized direction and the crystallography axis [86]. As shown in Fig. 10.5i, k, the linearly polarized laser was focused to two nanodisks with face up (i) and side up (k), and the excitation polarization angle was defined to be 0° when the laser polarized direction parallel to the a-axis or c-axis, respectively. For the side up particle, it is
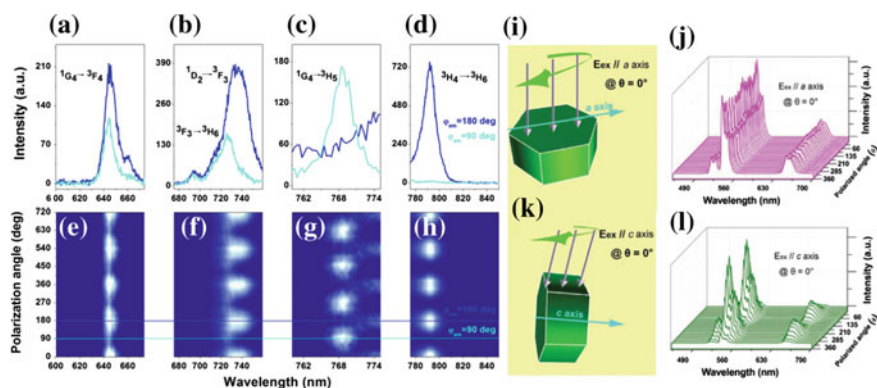
Fig. 10.5 **a–d** Emission spectra of UC from β-$NaYF_4$: Tm^{3+}–Yb^{3+} single microrod in the transitions of Tm^{3+}: **a** $^1G_4 \rightarrow {}^3F_4$, **b** $^3F_3 \rightarrow {}^3H_6$, $^1D_2 \rightarrow {}^3F_3$, **c** $^1G_4 \rightarrow {}^3H_5$, **d** $^3H_4 \rightarrow {}^3H_6$, respectively. **e–h** show the dependence of the corresponding spectra on the emission polarization angle (φ_{em}). **i**, **k** Schematic representation of the $NaYF_4$ nanodisk with its a-axis (**i**) or c-axis (**k**) parallel to the horizontal plane (HP). **j**, **l** UC luminescence spectra of a single nanodisk, whose a-axis (**j**) or c-axis (**l**) is parallel to HP, recorded at excitation polarization angles varying from 0° to 360°, with no polarizer placed in the detection part. **a–h** Adapted with the permission from Ref. [72]. Copyright 2011 American Chemical Society. **i–l** Adapted from Ref. [86] by permission of The Royal Society of Chemistry

observed that the UC luminescence intensity changes periodically when the polarization angle of excitation light is changed from 0° to 360°. And the polarization degree is as large as 0.78, 0.79, and 0.74 for the $^2H_{11/2} \rightarrow \,^4I_{15/2}$, $^4S_{3/2} \rightarrow \,^4I_{15/2}$, and $^4F_{9/2} \rightarrow \,^4I_{15/2}$ transitions of Er^{3+}. However, this excitation polarization dependence of the UC luminescence could be ignored in the case of the face up particles. This measurement proved that the polarization of UC luminescence depends upon the orientation of the nanodisk with respect to the polarization angle of the excitation light or the detection.

10.4.3   Concentration Quenching Abatement

Dopant concentration is a crucial factor to determine the UC brightness and color display [5, 87]. Strong absorption, critical distance between donor and acceptor, and radiative efficiency are concentration-dependent. High dopant concentrations have been found to result in quenching of the luminescence due to cross-relaxation. Therefore, optimum dopant concentration to avoid quenching is frequently emphasized in most studies, e.g. the optimal Tm^{3+} concentration in the upconverted $NaYF_4$ host lattices has been found in the range of ~ 0.2–0.5 mol% at excitation irradiance below 100 W cm^{-2} (with ~ 20–40 mol% Yb^{3+}) [88–92]. Recently, Zhao et al. [76] presented evidence that UC luminescence can be significantly enhanced by using much higher activator concentrations under relatively high-irradiance excitation. In other words, the concentration quenching or UC saturation threshold value could be greatly improved in single nanoparticle with high power excitation. As shown in Fig. 10.6a, increasing the excitation irradiance from 1.6×10^4 to 2.5×10^6 W cm^{-2} enhances the overall UC luminescence intensity by factors of 5.6, 71, and 1105 for 0.5, 4, and 8 mol% Tm^{3+}, respectively. Importantly, at high excitation and high Tm^{3+} doping level, the fraction of excitation energy producing UC emission is increased. This shows that UC is more efficient at high excitation and for high Tm^{3+} doping. Similarly, Gargas et al. [73] also reported that the extra UC yield could be produced with high concentration and high excitation irradiance in the case of 20 mol% Yb^{3+}–20 mol% Er^{3+} couple. And the fascinating single particle luminescence images with low, medial, and high laser intensity give a clear evidence of this concentration quenching abatement effect of single nanoparticles with high doping (Fig. 10.6b).

10.4.4   Intense Multiphoton Upconversion

Multiphoton UC with large anti-Stokes shift is produced to potential applications including photocatalysis, super-resolution imaging. Tm^{3+}, as the most popular activator to generate multiphoton UC, has perfect ladder-type electron configuration with fairly small mismatch in relation to the energy feeding from Yb^{3+} step-by-step.
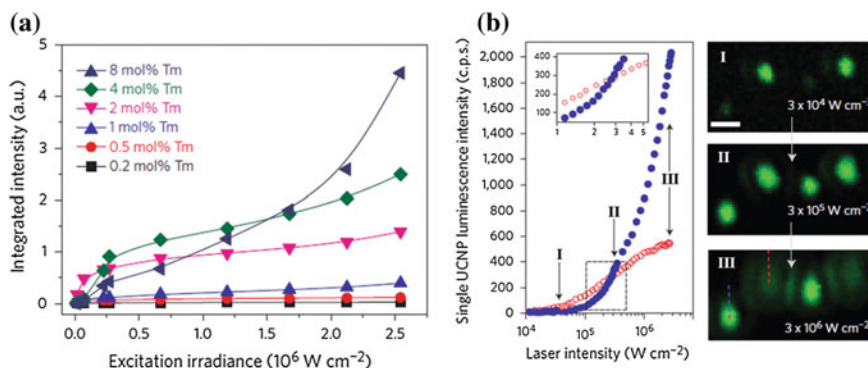
Fig. 10.6 Luminescence intensity of single UCNPs as a function of doping concentration and laser intensity. **a** Integrated UC luminescence intensity ($\sim$400–850 nm) as a function of excitation irradiance for a series of Tm^{3+}-doped nanoparticles. Adapted by permission from Macmillan Publishers Ltd.: Ref. [76], copyright 2013. **b** Luminescence intensity of single 8-nm UCNPs with 20 % (*blue circles*) and 2 % (*red circles*) Er^{3+}, each with 20 %Yb^{3+}, plotted as a function of excitation intensity. Confocal luminescence images taken at points shown in (**b**) of single UCNPs containing a mixture of 2 and 20 % Er^{3+} Adapted by permission from Macmillan Publishers Ltd.: Ref. [73], copyright 2014

The concentration of the classic combination for Tm^{3+}–Yb^{3+} couple is about 2–20 mol% in hexagonal $NaYF_4$ host, which is found for the utilization of the strong 2-photon near-infrared (NIR) emission [94]. Actually, the lower the concentration of Tm^{3+}, the higher the multiphoton UC percentage will be obtained on account of the avoidance of cross-relaxation quenching. However, one should note that this energy distribution status of multi- and 2-photons populations shown in the spectrum is at the cost of the overall quantum efficiency of UC due to the small activator number. Benefiting from the saturation excitation effect in single nanoparticle mode, we successfully observed the luminescent switching between the emissions from 2-photon UC and multiphoton UC at 2 mol% Tm^{3+}–20 mol% Yb^{3+} with the increase in laser power (Fig. 10.7a, b). The achievement of the super-intense multiphoton UC of Tm^{3+}—specifically, the emission intensity of blue 4-photon UC exhibits an increase by a factor of $\sim$70 in comparison with the NIR 2-photon UC under 980-nm excitation (Fig. 10.7c), may promote the Yb^{3+}–Tm^{3+} ion couple to be a good candidate of lanthanide activator for NIR-excited super-resolution UC imaging .

10.4.5   Heterogeneous Emission Profile

Nanoparticles, which are synthesized by wet chemical methods with kinds of surfactants, are usually capped with corresponding surface chemical bonding. For example, all of the three conventional ways (coprecipitation, thermal decomposition,
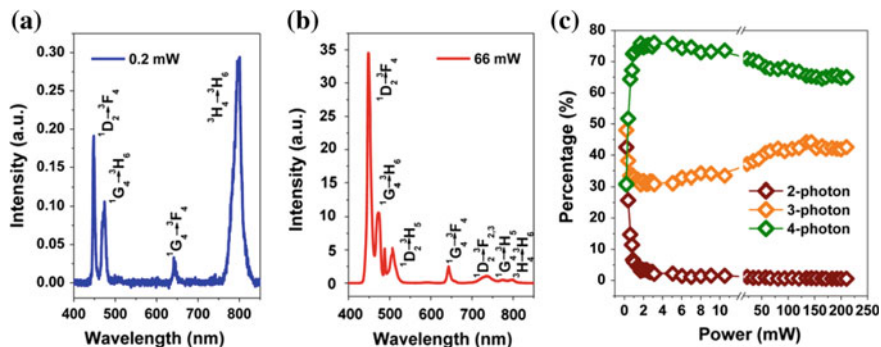
Fig. 10.7 a, **b** Emission spectra of single β-NaYF$_4$: 20 Yb^{3+}–2 Tm^{3+} nanoparticle excited with 980-nm laser illumination at the power of 0.2 mW ($\sim 3.5 \times 10^4$ W/cm^2) and 66 mW ($\sim 1.1 \times 10^7$ W/cm^2), respectively. **c** Laser power dependent multiphoton UC radiative percentages in the wavelength range from 400 to 850 nm of single β-NaYF$_4$: 20 Yb^{3+}–2 Tm^{3+} nanoparticle. Reproduced from Ref. [93] by permission of The Royal Society of Chemistry

and solvothermal ways) used to synthesize NaYF$_4$UCNPs cause the introduction of oleic acid molecules or oleic acid ions ligands attaching to the surface of the particles [32]. These surface ligands accompanying with the crystal defects will affect the precision spectroscopy of each nanoparticles. From the precision spectral investigation particle-by-particle, the microscopic electron behavior and energy transfer mechanism exploration would be certainly improved; more importantly, it makes sense to obtain high-efficient UCNPs by intrinsic improvement. A pioneering discovery has been reported by Gargas et al, typical heterogeneous high-resolution spectra are shown in Fig. 10.8, with particle-to-particle variations in peak intensities at 541 and 557 nm. The addition of undoped NaYF$_4$ shells to these nanoparticles eliminates this heterogeneity (Fig. 10.8, bottom trace), suggesting a region within the nanoparticles in which the lanthanides may be emissive but are energetically coupled to the surface. The observed spectral differences may arise from either variation in lanthanide distributions between nanoparticles or from subtle variations in surface defects, surface reconstruction, or faceting. This identification of losses from energy transfer to the surface suggests one means for improving emission from nanoparticles (Fig. 10.8).

10.5   Applications in Single UCNPs Level

10.5.1   Super-Resolution Upconversion Imaging

Upconversion is of high interest for microscopy because of the excellent imaging quality without luminescence background. The combination of the advantages of super-resolution optical microscopy techniques and the UCNPs is an advanced

Fig. 10.8 Fine spectra of the *green* emission bands collected from four single 8-nm UCNPs (*curves 1–4*) and their averaged spectra (*curve Σ*). *Vertical dotted lines* highlight peaks exhibiting heterogeneity between individual UCNPs. The *green* emission spectrum of an 8-nm UC nanoparticle with epitaxial 1.8-nm undoped shell is shown below the *horizontal dashed line*. Reprinted with permission from Macmilan Publishers Ltd Ref. [73], copyright 2014
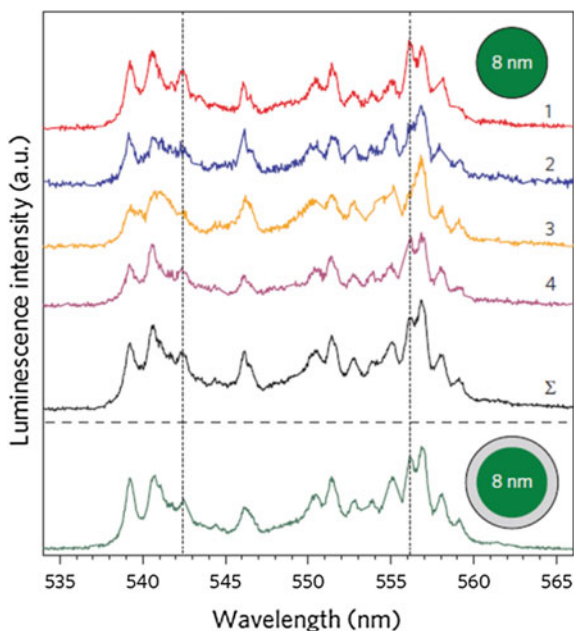
exploration with significant importance. In terms of the fluorescent species-dependent super-resolution technique, a breakthrough of optical resolution could be achieved by using UCNPs. Simultaneously, for the widespread research on lanthanide-doped UCNPs spanning from chemosynthesis, dynamical model, spectroscopic analysis, and ensemble application, it is a frontier development in single particle level to realize super-resolution UC imaging. Up to now, the reported feasible solution is a method resembles stimulated emission depletion microscopy (STED) involving stimulated absorption rather than stimulated emission. In this method, a three-level system and long-lived intermediary state are necessary, e.g. Pr^{3+}: $^3H_4$–$^1D_2$-4f5d system with long lifetime of $^1D_2$ (150–200 μs) was used by Kolesov et al. [95]. As shown in Fig. 10.9a, the $^1D_2$ level is excited by an orange 609-nm laser, and a donut-shaped 532-nm beam is exploited as a second excitation step. In that situation, the population of $^1D_2$ level will be depleted by the donut green beam unless the particle is not in the very center of the donut. After that, the remaining population of $^1D_2$ state can be read out by a short 532-nm pulse. Finally, comparing with the confocal images (Fig. 10.9b) and the super-resolution images (Fig. 10.9c), the optical resolution value can be improved by at least an order of magnitude. This best resolution obtained so far was ∼50 nm and is limited by the nanoparticle size. Further improvement is expected to be realized using $NaYF_4$: Yb^{3+}–Tm^{3+} UC system with smaller particle size.
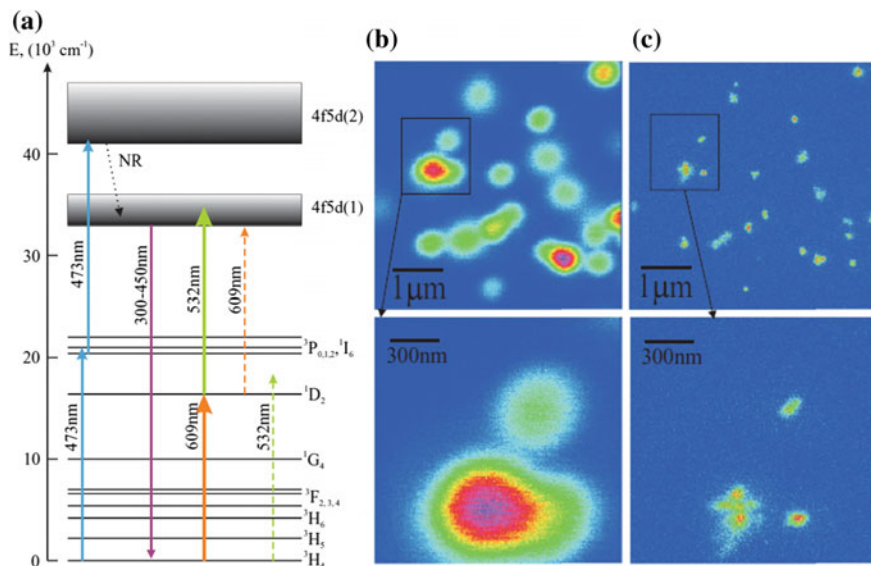
Fig. 10.9 **a** Energy-level diagram of Pr^{3+} electronic states in YAG crystal. **b** Confocal image of Pr^{3+}: YAG nanoparticles. **c** Super-resolution image of the same area. Reproduced from Ref. [95] by permission of American Physical Society

10.5.2   Location Control Investigation of Luminescence Enhancement

Plasmonic local field effect on luminescence is a controversial topic because of the vague theoretical origin of enhancement and the random occurrence of enhancement or quenching [97–99]. One recognized experience from the previous research is that the positional relation between emitters and the metallic surfaces or particles possesses a critical importance on the field effect [100]. The investigation to this point has been successfully performed with controllable nanoassembly of UCNPs and gold nanospheres in single particle mode, and even with the consideration of the laser polarization effect [71]. As shown in Fig. 10.10a, the gold sphere was brought in the vicinity of the UC nanoparticle with their central axis along the laser polarization axis. The non-equative rates of increase between green and red emission by a factor of 4.8 and 2.7 have been observed from the UC spectra in Fig. 10.10b. The plasmonic enhancement effect on the emission of the nanoparticle was also reflected in a reduction of the rise and decay times (see Fig. 10.10c). This controlled study of UC using single nanoparticle accurate characterization will provide important input for the optimum design of future hybrid UCNPs and metal nanostructures.

Similarly, tip-enhanced luminescence is an effect that the locally enhanced electric fields in the vicinity of a sharp metal tip to amplify the excitation and
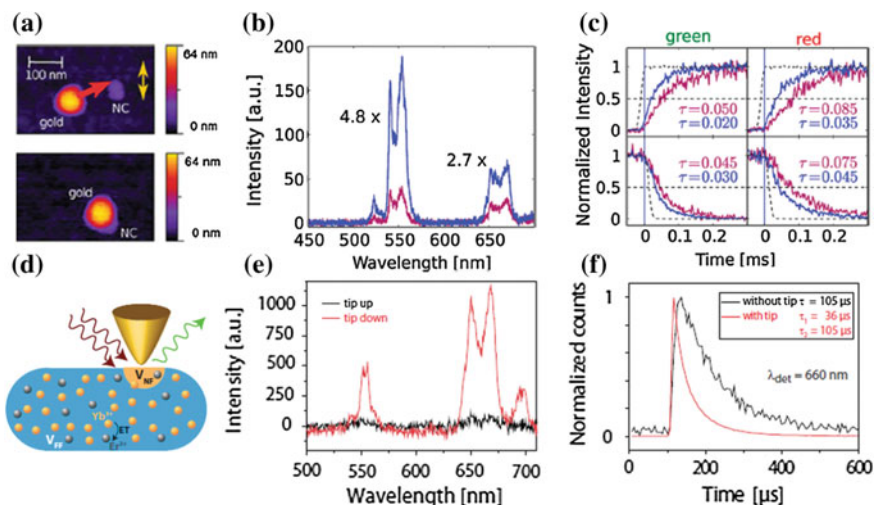
Fig. 10.10 **a** AFM image showing the nanoassembly approach: The 60-nm gold nanosphere is attached to the NC with the help of the AFMtip. The *yellow arrow* indicates the polarization axis of the excitation light. **b** UC emission spectra of the nanoparticle without (*violet curve*) and with (*blue curve*) the gold nanosphere in close vicinity. **c** Rise (*upper*) and decay times (*lower*) of the *green* (*left*) and *red* (*right*) emission with the color code as in part (**b**). **d** Schematic of the tip enhancement of a single UC nanoparticle. **e** UC emission spectra with retracted and approached tip, respectively. **f** Decay curves for *red* emission detected with and without tip at 660 nm [71, 96]. **a**–**c** Reprinted with the permission from Ref. [71]. Copyright 2011 American Chemical Society, **d**–**f** Reprinted with the permission from Ref. [96]. Copyright 2015 American Chemical Society

emission rates in a nearby sample object. Very recently, Mauser et al. [96] presented the first near-field study of a single NaYF$_4$ nanoparticle doped with Yb^{3+}–Er^{3+} using an AFM scanning tip. The strong UC luminescence amplification (Fig. 10.10e) indicated the tip-enhanced near-field effect, and the enhancement factor was in general agreement with the near-field-to-far-field ratios calculated according to the experimental configuration (Fig. 10.10d). The significantly faster decay of the lifetime in the presence of the tip (Fig. 10.10g) and tip-sample distance curves confirmed the contribution of radiative rate enhancement. This study indicates the penitential of this single nanoparticle technique for the characterization of more complex upconverting structures with subtle target, e.g. to demonstrate the lattice plane sensitive enhancement in a single hexagonal particle.

10.5.3 Single Particle Multicolor Barcoding

Optical microbarcodes are emerging as an attractive media for multiplexed analyte detection or anticounterfeiting applications [102–108]. Here, the lanthanide-doped UC system with multicolor anti-Stokes emissions using single-wavelength NIR
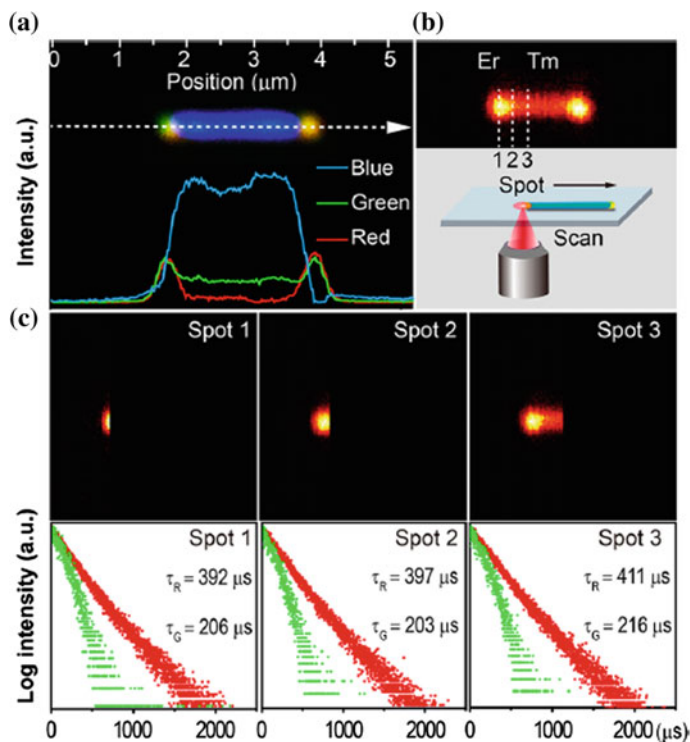
Fig. 10.11 **a** Wide-field luminescence image of a single microrod exhibiting YBY dual-color UC emission. **b** Confocal microscope image of a different dual-color microrod. **c** The corresponding *green* ($^4S_{3/2}$) and *red* ($^4F_{9/2}$) emission lifetimes in three different areas (marked with *spot 1, 2, 3* shown in **b**) of the microrod. Reprinted with the permission from Ref. [101]. Copyright 2014 American Chemical Society

laser excitation provides a feasible strategy to generate a large, diverse library of optical barcodes. However, it is still a challenge to display an optical barcode in single particle level because of the optical resolution limitation of the common designed core-shell UC nanoparticles. Therefore, it is critical to design a multicolor structure with the monochromaticity of spatial separation. Recently, Liu et al. reported a design that one-dimensional epitaxial growth on the tips of a parent rod structure, where different activators exhibiting RGB colors were doped in the epitaxial material and parent rods, respectively (Fig. 10.11a) [101]. Using the confocal single particle optical characterization, the energy transfer at the tip junction was investigated by lifetime comparison. The unaltered lifetimes of Er^{3+} recorded at three different spots obtained with focus moving indicated that there is no apparent crosstalk between Tm^{3+} and Er^{3+} activators even at the tip junction.

10.6 Conclusion and Perspective

Significant achievements in the fields of UCNPs have been made in the past few years promptly, spanning from nanofabrication, photophysical theory, to application. Toward the further enormous progress, the advanced technical promotion in regard of the crystal growth kinetic-related intrinsic structure combing with the size effect, surface effect, and local field effect is urgently necessary. In this regard, the characterization of single nanoparticle UC behaviors is extremely effective to offer breakthrough insight of the UC investigations. Beyond the universality of ensemble spectroscopy, single particle optical characterization exhibits its superiority in inhomogeneous or anisotropic spectra, unique photophysical phenomena, and tailored applications.

Despite the growing efforts have been devoted to the single particle behavior of UC luminescence, further thinking to push the research to a remarkable depth and breadth is necessary. Firstly, optical detection technique that has high-speed nanopositioning method aiming at single particles with size of 1–100 nm is pursued to fast lead the progress on materials science. Taking the confocal scanning technique as an example, the specimen treatment and point-by-point scanning way is time consuming. And it should be noticed that the less optical components employed in the detection part, the high credibility of the data collected and high signal-to-noise ratio will be achieved. Secondly, systematic researches with precise controllability of optical function in single nanoparticle level are expected to be carried out beyond the limits of currently phenomenological exploration. For example, the accession of external fields on single UCNPs, e.g. cryogenics, strain, pressure, and magnetic or electronic fields, is expected to show fantastic modulation capability of UC luminescence. Up to now, we consider that the most promising applicable way out of UC luminescence from single nanoparticles lies in the optical super-resolution imaging and the dynamic detection of diagnosis and therapy in biomedical fields.

References

1. Heer S, Kömpe K, Güdel HU, Haase M (2004) Highly efficient multicolour upconversion emission in transparent colloids of lanthanide-doped $NaYF_4$ nanocrystals. Adv Mater 16: 2102.
2. Mai H-X, Zhang Y-W, Sun L-D, Yan C-H (2007) Highly efficient multicolor up-conversion emissions and their mechanisms of monodisperse $NaYF_4$: Yb, Er core and core/shell-structured nanocrystals. J Phys Chem C 111: 13721.
3. Wang L, Li Y (2006) $Na(Y_{1.5}Na_{0.5})F_6$ single-crystal nanorods as multicolor luminescent materials. Nano Lett 6: 1645.

4. Ehlert O, Thomann R, Darbandi M, Nann T (2008) A four-color colloidal multiplexing nanoparticle system. ACS nano 2: 120.

5. Wang F, Liu XG (2008) Upconversion multicolor fine-tuning: Visible to near-infrared emission from lanthanide-doped $NaYF_4$ nanoparticles. J Am Chem Soc 130: 5642.

6. Wang J, Wang F, Wang C, Liu Z, Liu XG (2011) Single-band upconversion emission in lanthanide-doped $KMnF_3$ nanocrystals. Angew Chem Int Ed 50: 10369.

7. Chan EM, Han G, Goldberg JD, et al. (2012) Combinatorial discovery of lanthanide-doped nanocrystals with spectrally pure upconverted emission. Nano Lett 12: 3839.

8. Chen D, Lei L, Zhang R, Yang A, Xu J, Wang Y (2012) Intrinsic single-band upconversion emission in colloidal Yb/Er(Tm):$Na_3Zr(Hf)F_7$ nanocrystals. Chem Commun 48: 10630.

9. Tian G, Gu Z, Zhou L, et al. (2012) Mn^{2+} dopant-controlled synthesis of $NaYF_4$:Yb/Er upconversion nanoparticles for in vivo imaging and drug delivery. Adv Mater 24: 1226.

10. Shan GB, Demopoulos GP (2010) Near-infrared sunlight harvesting in dye-sensitized solar cells via the insertion of an upconverter-TiO_2 nanocomposite layer. Adv Mater 22: 4373.

11. Liang L, Liu Y, Bu C, et al. (2013) Highly uniform, bifunctional core/double-shell-structured beta-$NaYF_4$:Er^{3+},Yb^{3+}@SiO_2@TiO_2 hexagonal sub-microprisms for high-performance dye sensitized solar cells. Adv Mater 25: 2174.

12. Chang J, Ning YH, Wu SL, Niu WB, Zhang SF (2013) Effectively utilizing NIR light using direct electron injection from up-conversion nanoparticles to the TiO_2 photoanode in dye-sensitized solar cells. Adv Funct Mater 23: 5910.

13. Wang F, Liu XG (2009) Recent advances in the chemistry of lanthanide-doped upconversion nanocrystals. Chem Soc Rev 38: 976.

14. Zhou J, Liu Z, Li FY (2012) Upconversion nanophosphors for small-animal imaging. Chem Soc Rev 41: 1323.

15. Cheng L, Wang C, Liu Z (2013) Upconversion nanoparticles and their composite nanostructures for biomedical imaging and cancer therapy. Nanoscale 5: 23.

16. Chatterjee DK, Gnanasammandhan MK, Zhang Y (2010) Small upconverting fluorescent nanoparticles for biomedical applications. Small 6: 2781.

17. Wang F, Banerjee D, Liu YS, Chen XY, Liu XG (2010) Upconversion nanoparticles in biological labeling, imaging, and therapy. Analyst 135: 1839.

18. Gorris HH, Wolfbeis OS (2013) Photon-upconverting nanoparticles for optical encoding and multiplexing of cells, biomolecules, and microspheres. Angew Chem Int Ed 52: 3584.

19. Haase M, Schafer H (2011) Upconverting nanoparticles. Angew Chem Int Ed 50: 5808.

20. Fernee MJ, Tamarat P, Lounis B (2014) Spectroscopy of single nanocrystals. Chem Soc Rev 43: 1311.

21. Sonntag MD, Klingsporn JM, Zrimsek AB, Sharma B, Ruvuna LK, Van Duyne RP (2014) Molecular plasmonics for nanoscale spectroscopy. Chem Soc Rev 43: 1230.

22. Cui J, Beyler AP, Bischof TS, Wilson MW, Bawendi MG (2014) Deconstructing the photon stream from single nanocrystals: From binning to correlation. Chem Soc Rev 43: 1287.

23. Empedocles SA, Neuhauser R, Shimizu K, Bawendi MG (1999) Photoluminescence from single semiconductor nanostructures. Adv Mater 11: 1243.

24. Blanton SA, Hines MA, Guyot-Sionnest P (1996) Photoluminescence wandering in single CdSe nanocrystals. Appl Phys Lett 69: 3905.

25. Nirmal M, Dabbousi B, Bawendi M, et al. (1996) Fluorescence intermittency in single cadmium selenide nanocrystals. Nature 383: 802.

26. Empedocles S, Bawendi M (1997) Quantum-confined stark effect in single CdSe nanocrystallite quantum dots. Science 278: 2114.

27. Huang X, Han S, Huang W, Liu X (2013) Enhancing solar cell efficiency: the search for luminescent materials as spectral converters. Chem Soc Rev 42: 173.

28. Auzel F (2004) Upconversion and anti-Stokes processes with f and d ions in solids. Chem Rev 104: 139.

29. Wang HQ, Batentschuk M, Osvet A, Pinna L, Brabec CJ (2011) Rare-earth ion doped up-conversion materials for photovoltaic applications. Adv Mater 23: 2675.

30. Trupke T, Green M, Würfel P (2002) Improving solar cell efficiencies by up-conversion of sub-band-gap light. J Appl Phys 92: 4117.

31. de Wild J, Meijerink A, Rath JK, van Sark WGJHM, Schropp REI (2011) Upconverter solar cells: materials and applications. Energ Environ Sci 4: 4835.

32. Wang F, Deng RR, Wang J, et al. (2011) Tuning upconversion through energy migration in core-shell nanoparticles. Nat Mater 10: 968.

33. Vetrone F, Naccache R, Zamarron A, et al. (2010) Temperature sensing using fluorescent nanothermometers. ACS nano 4: 3254.

34. Wang F, Han Y, Lim CS, et al. (2010) Simultaneous phase and size control of upconversion nanocrystals through lanthanide doping. Nature 463: 1061.

35. Wang F, Wang JA, Liu XG (2010) Direct evidence of a surface quenching effect on size-dependent luminescence of upconversion nanoparticles. Angew Chem Int Ed 49: 7456.

36. Yang YM, Shao Q, Deng RR, et al. (2012) In vitro and in vivo uncaging and bioluminescence imaging by using photocaged upconversion nanoparticles. Angew Chem Int Ed 51: 3125.

37. Deng RR, Xie XJ, Vendrell M, Chang YT, Liu XG (2011) Intracellular glutathione detection using MnO_2-nanosheet-modified upconversion nanoparticles. J Am Chem Soc 133: 20168.

38. Xue XJ, Wang F, Liu XG (2011) Emerging functional nanomaterials for therapeutics. J Mater Chem 21: 13107.

39. Downing E, Hesselink L, Ralston J, Macfarlane R (1996) A three-color, solid-state, three-dimensional display. Science 273: 1185.

40. Wang G, Peng Q, Li Y (2011) Lanthanide-doped nanocrystals: synthesis, optical-magnetic properties, and applications. Acc Chem Res 44: 322.

41. Fischer LH, Harms GS, Wolfbeis OS (2011) Upconverting nanoparticles for nanoscale thermometry. Angew Chem Int Ed 50: 4546.

42. Zhou J, Liu Z, Li F (2012) Upconversion nanophosphors for small-animal imaging. Chem Soc Rev 41: 1323.

43. Li C, Lin J (2010) Rare earth fluoride nano-/microcrystals: synthesis, surface modification and application. J Mater Chem 20: 6831.

44. Haase M, Schäfer H (2011) Upconverting nanoparticles. Angew Chem Int Ed 50: 5808.

45. Ju Q, Tu D, Liu Y, et al. (2011) Amine-functionalized lanthanide-doped $KGdF_4$ nanocrystals as potential optical/magnetic multimodal bioprobes. J Am Chem Soc 134: 1323.

46. Tu D, Liu L, Ju Q, et al. (2011) Time-resolved FRET biosensor based on amine-functionalized lanthanide-doped $NaYF_4$ nanocrystals. Angew Chem Int Ed 50: 6306.

47. Mader HS, Kele P, Saleh SM, Wolfbeis OS (2010) Upconverting luminescent nanoparticles for use in bioconjugation and bioimaging. Curr Opin Chem Biol 14: 582.

48. Yan C, Dadvand A, Rosei F, Perepichka DF (2010) Near-IR photoresponse in new up-converting $CdSe/NaYF_4$: Yb, Er nanoheterostructures. J Am Chem Soc 132: 8868.

49. Bogdan N, Vetrone F, Ozin GA, Capobianco JA (2011) Synthesis of ligand-free colloidally stable water dispersible brightly luminescent lanthanide-doped upconverting nanoparticles. Nano Lett 11: 835.

50. Ye X, Collins JE, Kang Y, et al. (2010) Morphologically controlled synthesis of colloidal upconversion nanophosphors and their shape-directed self-assembly. Proc Natl Acad Sci USA 107: 22430.

51. Chen F, Bu W, Zhang S, et al. (2011) Positive and negative lattice shielding effects co-existing in Gd (III) ion doped bifunctional upconversion nanoprobes. Adv Funct Mater 21: 4285.

52. Zhang F, Braun GB, Pallaoro A, et al. (2011) Mesoporous multifunctional upconversion luminescent and magnetic "nanorattle" materials for targeted chemotherapy. Nano Lett 12: 61.

53. Cheng L, Yang K, Li Y, et al. (2012) Multifunctional nanoparticles for upconversion luminescence/MR multimodal imaging and magnetically targeted photothermal therapy. Biomaterials 33: 2215.

54. Bouzigues C, Gacoin T, Alexandrou A (2011) Biological applications of rare-earth based nanoparticles. ACS nano 5: 8488.
55. Jayakumar MKG, Idris NM, Zhang Y (2012) Remote activation of biomolecules in deep tissues using near-infrared-to-UV upconversion nanotransducers. Proc Natl Acad Sci USA 109: 8483.
56. Zhou J-C, Yang Z-L, Dong W, Tang R-J, Sun L-D, Yan C-H (2011) Bioimaging and toxicity assessments of near-infrared upconversion luminescent $NaYF_4$: Yb, Tm nanocrystals. Biomaterials 32: 9059.
57. Zeng S, Xiao J, Yang Q, Hao J (2012) Bi-functional $NaLuF_4$: Gd^{3+}/Yb^{3+}/Tm^{3+} nanocrystals: structure controlled synthesis, near-infrared upconversion emission and tunable magnetic properties. J Mater Chem 22: 9870.
58. Ren W, Tian G, Zhou L, et al. (2012) Lanthanide ion-doped $GdPO_4$ nanorods with dual-modal bio-optical and magnetic resonance imaging properties. Nanoscale 4: 3754.
59. Chen F, Zhang S, Bu W, et al. (2012) A uniform sub-50 nm-sized magnetic/upconversion fluorescent bimodal imaging agent capable of generating singlet oxygen by using a 980 nm laser. Chem-Eur J 18: 7082.
60. Wei Y, Chen Q, Wu B, Zhou A, Xing D (2012) High-sensitivity in vivo imaging for tumors using a spectral up-conversion nanoparticle $NaYF_4$: Yb^{3+}, Er^{3+} in cooperation with a microtubulin inhibitor. Nanoscale 4: 3901.
61. Wu S, Duan N, Ma X, et al. (2012) Simultaneous detection of enterovirus 71 and coxsackievirus A16 using dual-colour upconversion luminescent nanoparticles as labels. Chem. Commun. 48: 4866.
62. Li LL, Zhang R, Yin L, et al. (2012) Biomimetic surface engineering of lanthanide-doped upconversion nanoparticles as versatile bioprobes. Angew Chem Int Ed 124: 6225.
63. Wei W, He T, Teng X, et al. (2012) Nanocomposites of graphene oxide and upconversion rare-earth nanocrystals with superior optical limiting performance. Small 8: 2271.
64. Liu Q, Sun Y, Yang T, Feng W, Li C, Li F (2011) Sub-10 nm hexagonal lanthanide-doped $NaLuF_4$ upconversion nanocrystals for sensitive bioimaging in vivo. J Am Chem Soc 133: 17122.
65. Mor FM, Sienkiewicz A, Forro L, Jeney S (2014) Upconversion particle as a local luminescent brownian probe: a photonic force microscopy study. Acs Photonics 1: 1251.
66. Gu FX, Zeng HP, Zhu YB, Yang Q, Ang LK, Zhuang SL (2014) Single-crystal Pd and its alloy nanowires for plasmon propagation and highly sensitive hydrogen detection. Adv Opt Mater 2: 189.
67. Park YI, Lee KT, Suh YD, Hyeon T (2014) Upconverting nanoparticles: a versatile platform for wide-field two-photon microscopy and multi-modal in vivo imaging. Chem Soc Rev 44: 1302.
68. Park YI, Kim JH, Lee KT, et al. (2009) Nonblinking and nonbleaching upconverting nanoparticles as an optical imaging nanoprobe and T1 magnetic resonance imaging contrast agent. Adv Mater 21: 4467.
69. Wu SW, Han G, Milliron DJ, et al. (2009) Non-blinking and photostable upconverted luminescence from single lanthanide-doped nanocrystals. Proc Natl Acad Sci USA 106: 10917.
70. Schietinger S, Menezes LD, Lauritzen B, Benson O (2009) Observation of size dependence in multicolor upconversion in single Yb^{3+}, Er^{3+} codoped $NaYF_4$ nanocrystals. Nano Lett 9: 2477.
71. Schietinger S, Aichele T, Wang HQ, Nann T, Benson O (2010) Plasmon-enhanced upconversion in single $NaYF_4$:Yb^{3+}/Er^{3+} codoped nanocrystals. Nano Lett 10: 134.
72. Zhou JJ, Chen GX, Wu E, et al. (2013) Ultrasensitive polarized up-conversion of Tm^{3+}-Yb^{3+} doped beta-$NaYF_4$ Single nanorod. Nano Lett 13: 2241.
73. Gargas DJ, Chan EM, Ostrowski AD, et al. (2014) Engineering bright sub-10-nm upconverting nanocrystals for single-molecule imaging. Nat Nanotechnol 9: 300.
74. Kolesov R, Xia K, Reuter R, et al. (2012) Optical detection of a single rare-earth ion in a crystal. Nat Commun 3: 1029.

75. Ostrowski AD, Chan EM, Gargas DJ, et al. (2012) Controlled synthesis and single-particle imaging of bright, sub-10 nm lanthanide-doped upconverting nanocrystals. ACS nano 6: 2686.

76. Zhao JB, Jin DY, Schartner EP, et al. (2013) Single-nanocrystal sensitivity achieved by enhanced upconversion luminescence. Nat Nanotechnol 8: 729.

77. Warren-Smith SC, Afshar S, Monro TM (2008) Theoretical study of liquid-immersed exposed-core microstructured optical fibers for sensing. Opt Express 16: 9034.

78. Afshar SV, Ruan YL, Warren-Smith SC, Monro TM (2008) Enhanced fluorescence sensing using microstructured optical fibers: a comparison of forward and backward collection modes. Opt Lett 33: 1473.

79. Ruan Y, Schartner EP, Ebendorff-Heidepriem H, Hoffmann P, Monro TM (2007) Detection of quantum-dot labelled proteins using soft glass microstructured optical fibers. Opt Express 15: 17819.

80. Schartner EP, Jin DY, Ebendorff-Heidepriem H, Piper JA, Lu ZD, Monro TM (2012) Lanthanide upconversion within microstructured optical fibers: improved detection limits for sensing and the demonstration of a new tool for nanocrystal characterization. Nanoscale 4: 7448.

81. Schartner EP, Jin D, Ebendorff-Heidepriem H, Piper JA, Monro TM (2012) Lanthanide upconversion nanocrystals within microstructured optical fibres; a sensitive platform for biosensing and a new tool for nanocrystal characterisation. Third Asia Pacific Optical Sensors Conference 8351.

82. Schartner EP, Jin DY, Zhao JB, Monro TM (2013) Sensitive detection of $NaYF_4$: Yb/Tm nanoparticles using suspended core microstructured optical fibers. Colloidal Nanocrystals for Biomedical Applications Viii 8595.

83. Dickson RM, Cubitt AB, Tsien RY, Moerner WE (1997) On/off blinking and switching behaviour of single molecules of green fluorescent protein. Nature 388: 355.

84. Galland C, Ghosh Y, Steinbruck A, et al. (2011) Two types of luminescence blinking revealed by spectroelectrochemistry of single quantum dots. Nature 479: 203.

85. Barnes M, Mehta A, Thundat T, Bhargava R, Chhabra V, Kulkarni B (2000) On-off blinking and multiple bright states of single europium ions in Eu^{3+}: Y_2O_3 nanocrystals. J Phys Chem B 104: 6099.

86. Chen P, Song M, Wu E, et al. (2015) Polarization modulated upconversion luminescence: single particle vs. few-particle aggregates. Nanoscale.

87. Wang J, Deng R, MacDonald MA, et al. (2014) Enhancing multiphoton upconversion through energy clustering at sublattice level. Nat Mater 13: 157.

88. Zhang H, Li Y, Lin Y, Huang Y, Duan X (2011) Composition tuning the upconversion emission in $NaYF_4$:Yb/Tm hexaplate nanocrystals. Nanoscale 3: 963.

89. Yin A, Zhang Y, Sun L, Yan C (2010) Colloidal synthesis and blue based multicolor upconversion emissions of size and composition controlled monodisperse hexagonal $NaYF_4$: Yb,Tm nanocrystals. Nanoscale 2: 953.

90. Mahalingam V, Vetrone F, Naccache R, Speghini A, Capobianco JA (2009) Colloidal Tm^{3+}/Yb^{3+}-doped $LiYF_4$ nanocrystals: multiple luminescence spanning the UV to NIR regions via low-energy excitation. Adv Mater 21: 4025.

91. Krämer KW, Biner D, Frei G, Güdel HU, Hehlen MP, Lüthi SR (2004) Hexagonal sodium yttrium fluoride based green and blue emitting upconversion phosphors. Chem Mater 16: 1244.

92. Liang L, Wu H, Hu H, Wu M, Su Q (2004) Enhanced blue and green upconversion in hydrothermally synthesized hexagonal $NaY_{1-x}Yb_xF_4$: $Ln^{3+}(Ln^{3+}=Er^{3+}$ or $Tm^{3+})$. J Alloy Compd 368: 94.

93. Zhou JJ, Chen GX, Zhu YB, et al. (2015) Intense multiphoton upconversion of Yb^{3+}-Tm^{3+} doped beta-$NaYF_4$ individual nanocrystals by saturation excitation. J Mater Chem C 3: 364.

94. Nyk M, Kumar R, Ohulchanskyy TY, Bergey EJ, Prasad PN (2008) High contrast in vitro and in vivo photoluminescence bioimaging using near infrared to near infrared up-conversion in Tm^{3+} and Yb^{3+} doped fluoride nanophosphors. Nano Lett 8: 3834.

95. Kolesov R, Reuter R, Xia KW, Stohr R, Zappe A, Wrachtrup J (2011) Super-resolution upconversion microscopy of praseodymium-doped yttrium aluminum garnet nanoparticles. Phys Rev B 84.
96. Mauser N, Piatkowski D, Mancabelli T, Nyk M, Mackowski S, Hartschuh A (2015) Tip-enhancement of up-conversion photoluminescence from rare-earth ion doped nanocrystals. ACS nano.
97. Glass AM, Liao PF, Bergman JG, Olson DH (1980) Interaction of metal particles with adsorbed dye molecules: absorption and luminescence. Opt Lett 5: 368.
98. Lakowicz JR (2001) Radiative decay engineering: biophysical and biomedical applications. Analytical biochemistry 298: 1.
99. Dulkeith E, Morteani AC, Niedereichholz T, et al. (2002) Fluorescence quenching of dye molecules near gold nanoparticles: radiative and nonradiative effects. Phys Rev Lett 89: 203002.
100. Saboktakin M, Ye X, Oh SJ, et al. (2012) Metal-enhanced upconversion luminescence tunable through metal nanoparticle-nanophosphor separation. ACS nano 6: 8758.
101. Zhang YH, Zhang LX, Deng RR, et al. (2014) Multicolor barcoding in a single upconversion crystal. J Am Chem Soc 136: 4893.
102. Nam JM, Thaxton CS, Mirkin CA (2003) Nanoparticle-based bio-bar codes for the ultrasensitive detection of proteins. Science 301: 1884.
103. Agasti SS, Liong M, Peterson VM, Lee H, Weissleder R (2012) Photocleavable DNA barcode-antibody conjugates allow sensitive and multiplexed protein analysis in single cells. J Am Chem Soc 134: 18499.
104. Kim SH, Shim JW, Yang SM (2011) Microfluidic multicolor encoding of microspheres with nanoscopic surface complexity for multiplex immunoassays. Angew Chem Int Ed 50: 1171.
105. Pregibon DC, Toner M, Doyle PS (2007) Multifunctional encoded particles for high-throughput biomolecule analysis. Science 315: 1393.
106. Creran B, Yan B, Moyano DF, Gilbert MM, Vachet RW, Rotello VM (2012) Laser desorption ionization mass spectrometric imaging of mass barcoded gold nanoparticles for security applications. Chem Commun 48: 4543.
107. Dejneka MJ, Streltsov A, Pal S, et al. (2003) Rare earth-doped glass microbarcodes. Proc Natl Acad Sci USA 100: 389.
108. Gorris HH, Wolfbeis OS (2013) Photon-upconverting nanoparticles for optical encoding and multiplexing of cells, biomolecules, and microspheres. Angew Chem Int Ed 52: 3584.

Chapter 11
Persistent Luminescence Nanomaterials for Biomedical Applications: A Quick Grasp of the Trend

Wai-Lun Chan, ZhenYu Liu and Ka-Leung Wong

Abstract Persistent luminescence nanomaterials (PLNMs) have recently come into limelight due to their remarkably long emission lifetime that is excitable ex vivo/in vivo and emissive in biological windows. All this potentiates themselves for better biodistribution mapping, pharmacokinetic evaluation, as well as longitudinal measurement than any other imaging counterparts. Upon combination with other modalities, multifunctional PLNMs have also been reported, such as photodynamic therapy, drug delivery, and bioanalytical sensing. In this chapter, we attempt to introduce readers from a newcomer perspective to the historical development, design and optimization principles, and potential bioapplications of PLNMs, hoping that you can appreciate the long afterglow and, as the chapter title, quickly grasp the trend.

11.1 Introduction—Present Brightness from Past Afterglow

Throughout the human history, light plays an essential role in our lives. It is a long-standing subject in humanity and in science not only because William Shakespeare said that "light, seeking light, doth light of light beguile," but also the scientific fact is that "seeing is believing"—both involving our complex visual sensation that simply entails light. Since then, human beings along with the civilization learn how to harness natural sunlight and even manipulate light from artificial sources, exploring thereby the universe and communicating around the world. The last century has seen a significant and fruitful development of luminescence research [1, 2], ranging from intricate optical theories (e.g., laser [3], fluorescence resonance energy transfer [4], photon upconversion [5], and aggregation-induced emission [6]) to advanced photonic materials (e.g., semiconductor/graphene quantum dots [7, 8],

W.-L. Chan · Z. Liu · K.-L. Wong (✉)
Department of Chemistry, Hong Kong Baptist University, Kowloon Tong, Hong Kong SAR
e-mail: klwong@hkbu.edu.hk

nanodiamonds [9], gold nanoclusters [10], lanthanide metal-organic frameworks [11], fluorescent proteins [12], and metamaterials [13]). Milestones, in particular, lie in multifaceted bioapplications of light that fluorescence bioimaging [14] and photodynamic therapy [15] emerge with state-of-the-art instruments (e.g., time-resolved fluorescence spectroscopy and two-photon confocal microscopy [16]) and multifunctional biomaterials (e.g., near-infrared (NIR) fluorescent bioprobes [17, 18], functionalized bioconjugates [19], and theranostic bioagents [20]).

In recent decades, optical imaging with high sensitivity and cost-effectiveness has become a research hot spot for in vitro/in vivo studies [21]. Among the novel noninvasive imaging tools developed (Fig. 11.1), luminescent lanthanide upconversion nanomaterials (UCNMs) have become a buzzword in the field [22–24]. They demonstrate not merely NIR excitation availability yet also long emission lifetime within the biological windows that make deep light penetration and autofluorescence elimination for high-resolution optical imaging come true [21]. Comprehensive assessments and reviews of UCNMs' virtues and potentials, design and engineering principles, and synthetic and characterization methods have all been well articulated in the previous chapters as well as in the literature. That said UCNMs are not without their limitations. Apart from the low quantum efficiency, it is harshly difficult for them to operate without sophisticated laser equipment and undergo biodistribution and pharmacokinetic studies without ex vivo experimentation that might reflect not the whole true in vivo picture, not to mention any sought-after real-time, long-term in vivo visualization for in-depth, longitudinal physiological and pathological tracing in animal models [26].

To address such critical issues, scientists have very recently poured the old wine into new bottles and successfully foregrounded NIR-emitting persistent luminescence nanomaterials (PLNMs) for various biomedical applications [27]. Therein lies the very scope of this chapter for us to introduce promising them. What is persistent luminescence? How does it work? What materials can generate it? How can PL be optimized for potential bioapplications at the nanoscale? What is the current challenges and will be the future direction of persistent luminescence (PL) research? We would try to answer all these questions here from a newcomer chemist's perspective one by one, with indicative but not exhaustive chapter contents being also selected and organized.

11.2 Persistent Luminescence: Definition and Mechanism

11.2.1 Definition and Mechanism

Persistent luminescence (PL), otherwise known as long-lasting phosphorescence (LLP) or thermally stimulated luminescence (TSL), is an optical phenomenon by which particular materials exhibit hour/daylong afterglow or delayed emission in
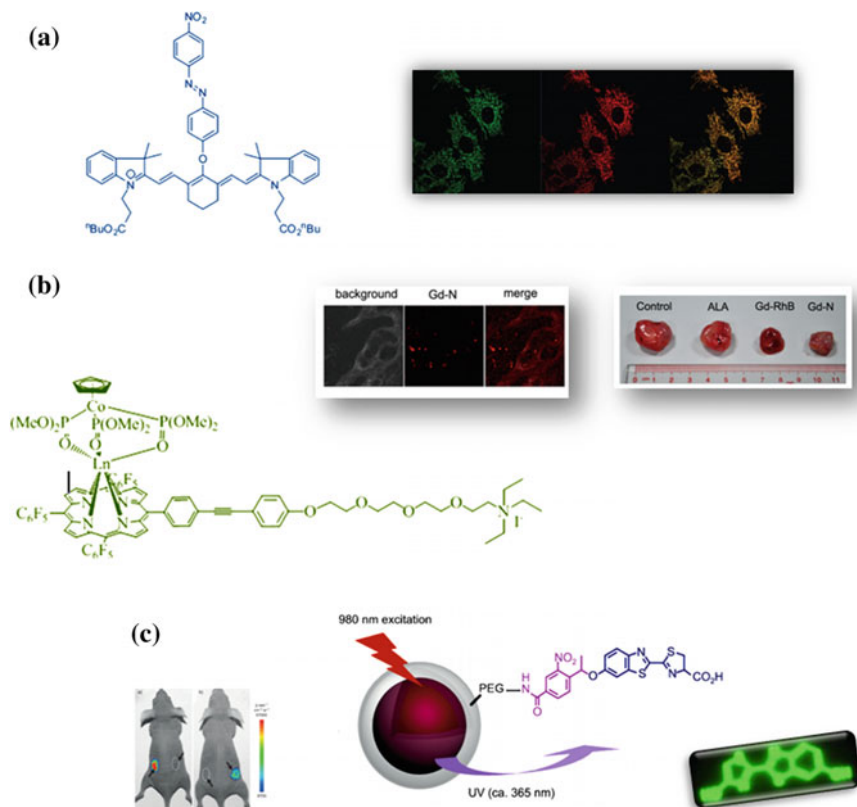
Fig. 11.1 a An NIR-emitting mitochondrion-targeting reaction-based organic heptamethine-azo fluorescent bioprobe (MitroGP) for selective GSH detection in vitro (Reprinted with the permission from Ref. [17], Copyright © 2014, American Chemical Society). **b** A dual-functional —photodynamic therapy and NIR imaging—theranostic gadolinium–porphyrin bioagent (Gd–N) which can target cancer cells specifically in vivo (Reprinted with the permission from Ref. [20]). **c** A D-luciferin-conjugated core–shell upconversion nanoparticle for bioluminescence imaging via NIR photolysis (Reprinted with the permission from Ref. [25]. Copyright © 2012, John Wiley & Sons)

the visible or NIR regions much after the removal of an excitation source (e.g., UV, Vis, X-ray or γ-ray) [27, 28]. It is far well-documented in the literature, from the serendipitous discovery of the Bologna stone (impure BaSO$_4$) in 1602 for alchemy to the perennial pursuit of luminous pearls as noble gemstones [1]; due to the inherent constraints in deficient brightness and lifetime, modern common utilizations of PL phosphors/paints (e.g., copper/cobalt-doped ZnS [29]) are interestingly found only in emergency signs, watch dials, and glow-in-the-dark toys. Still, lesser understood has PL been in terms of the underlying mechanism until the last decade.

By rigorous definition, persistent luminescence is not a form of phosphorescence but thermoluminescence [2, 30] (Table 11.1). Phosphorescence arises from a

Table 11.1 Simple comparison and contrast of phosphorescence and persistent luminescence

	Phosphorescence	Persistent luminescence
(1) Excitation source	Photoirradiation	
(2) Levels of metastable states	Higher singlet states (orbitally unpaired but spin paired) and lower triplet states (both orbitally and spin unpaired) ∵ spin correlation effect of magnetic repulsion	Shallow and deep locations with respect to the bandgap of the host materials ∵ (i) intrinsic properties of the dopant species, (ii) material surface, (iii) crystal structure, codoping, and synthetic methods
(3) Time dependence	Yes (usually exponentially)	
(4) Temperature dependence	Yes (−) ∵ thermal quenching	Yes (0 when $E > kT$; slightly + when $kT > E$; − when $kT \gg E$)
(5) Luminescence dynamics	Single-system (rigidity and heavy atom effect)	Traps and emitters (dopant and host effects)
(6) Decay lifetime	Long ($\sim$ms) ∵ spin-forbidden transitions	Long ($\sim$hr) ∵ piecemeal release of stored excitation energy

spin-forbidden radiative transition of a photoexcited electron between states of different multiplicity (i.e., quasistable triplet excited state and the stable singlet ground state) from which its long decay lifetime stems (Fig. 11.2). It is a transient luminescence phenomenon (i.e., time-dependent) [31]. The decay of it exhibits strong inverse temperature dependence (due to thermal quenching, a process that impairs the luminescence efficiency by increased probability of nonradiative transitions under increased temperature) and falls on the order of milliseconds (Fig. 11.3).

Figure 11.3 shows how configurational coordinate diagram is used to elaborate the temperature influence on the general process of absorption and emission via nonradiative routes [31, 32]. At room temperature, after photoexcitation, promoted electrons (with holes generated) occupying an upper vibrational level of an excited state (the upper energy surface) will first lose energy via phonon releasing and relax to the lowest vibrational level of that state (i.e., the emissive state). Following radiative emission, the electrons will fall back to the ground state (the lower energy surface) of higher vibrational level and dissipate further the rest of additional energy via the release of phonons on their return to their ground state equilibrium. A Stokes' shift can therefore be resulted and detected. However, at higher temperatures that $kT > \Delta E$ (the thermal activation energy), nonradiative transitions become overwhelming as electrons in the excited state can relax to the ground state directly by means of vibrational relaxation via thermal quenching (i.e., the intersection curves).

When it comes to the luminescence in phosphors, we should consider in fact the situations (i.e., Figs. 11.2 and 11.3) of the luminescent center (i.e., dopants or impurities, exotic elements incorporated into the lattice) in a solid host system using
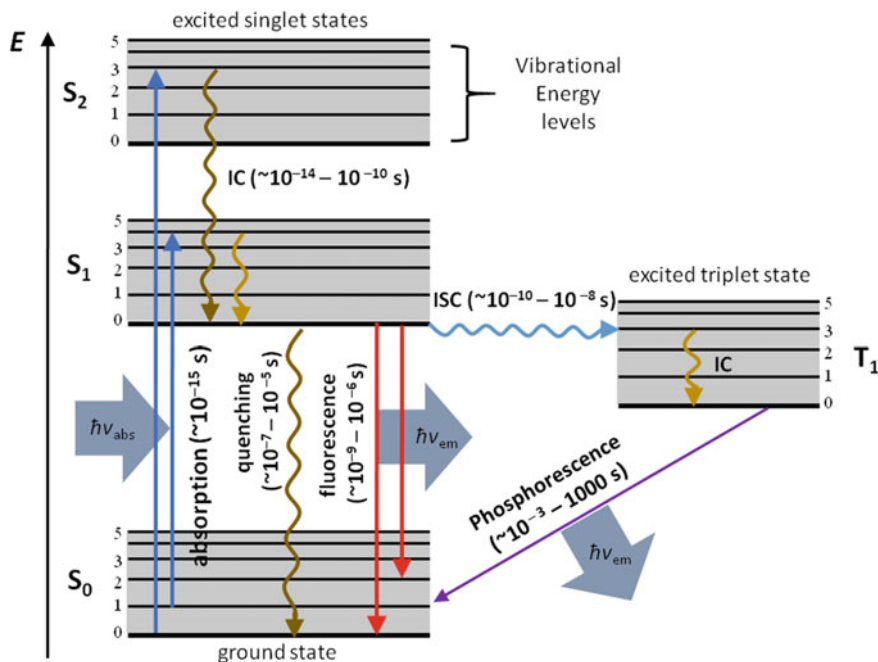
Fig. 11.2 Jablonski diagram of fluorescence and phosphorescence, where *IC* and *ISC* stand for nonradiative internal conversion and intersystem crossing, respectively

a characteristic bandgap energy model (Fig. 11.4). The absorption of the excitation energy takes place now by the host lattice or the doped impurities (i.e., the sensitizer), while the emission proceeds on the emissive impurity ions (i.e., the activator/emitter) [33]. As the intrinsic property, several dense ladder energy levels of the activator ions (n.b. mostly transition metals and lanthanides for our topic) exist within the bandgap, E_g, near either the conduction band or the valence band, serving as the electron donors or electron acceptors, respectively, which can be populated by direct excitation. The underlying optical transitions can account for (1) the emission of the emitter itself (e.g., *d–d*, *d–f*, and *f–f* transitions), (2) the charge-transfer emission (i.e., transitions between different electronic states of different ions in the surrounding lattice, and (3) the emission due to the donor–acceptor pair (n.b. distance-dependent in lattice and stabilized by electrostatic neutralization) [34]. More energy transfer mechanisms as well as their mathematical expressions can be referred to the assigned reference.

Impurities and defects can, in addition to facilitating the luminescence process (by providing desirable mid-level pathways for electron transfer instead of direct electronic transition), also hamper the luminescence efficiency of a host matrix. Be inherent or incidental, unwanted they in different sorts and quantities can be referred to as quenching traps in normal cases that undergo two proposed mechanisms: (1) The traps that are deep in the forbidden band act as the nonradiative
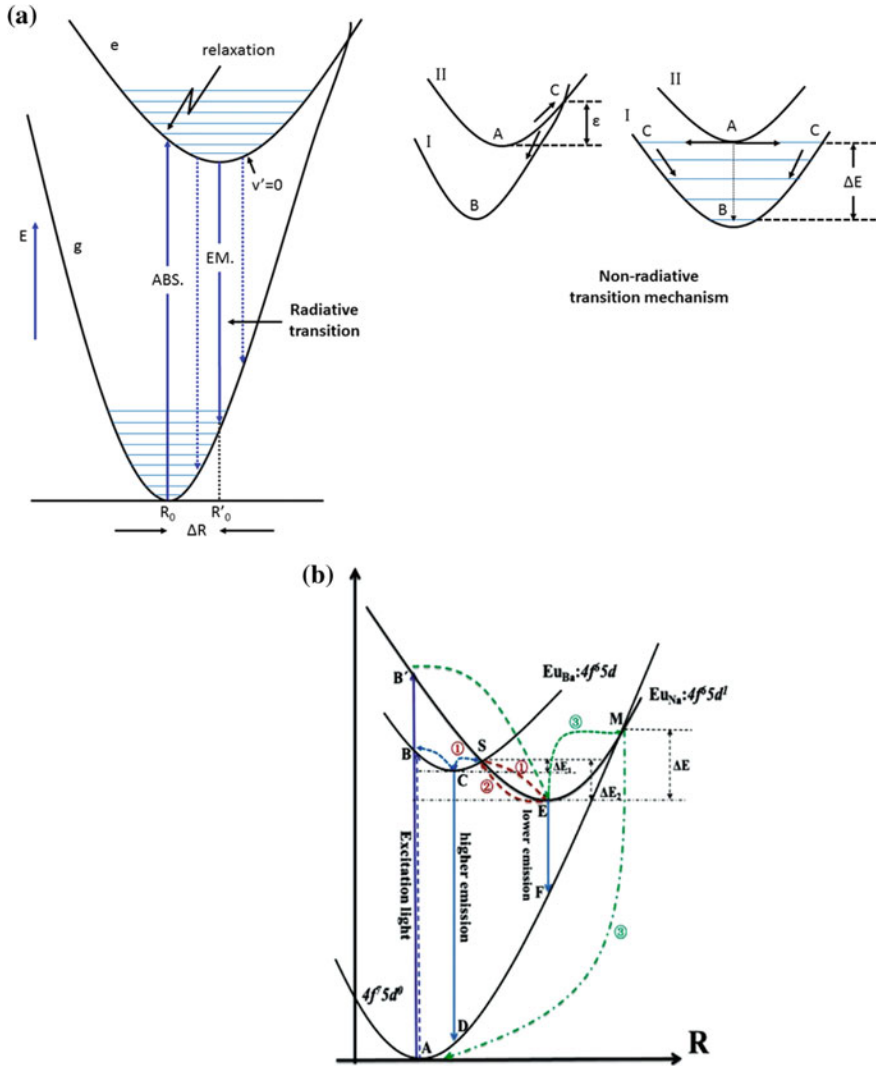
recombination centers for electrons in the conduction band and holes in the valence band, and (2) nonradiative quenching pathways are available and more preferable once the electron from the luminescence center is excited. Quenching traps are, therefore, what scientists and engineers try hard to avoid in most phosphor manufacturing, becoming a key topic in defect engineering except for the exceptional case of our topic—persistent and storage phosphors that a kind of special traps caused by defects are reversely highly essential and appreciated.

◀ **Fig. 11.3** **a** Simple configurational coordinate models (CCM) of radiative transitions and, the *inset*, nonradiative relaxation processes—(*left*) thermal quenching and (*right*) multiphonon relaxation. The symbol *e* denotes an excited state, and *g* represents a ground state. For the thermal case, the center is thermally activated from the point *A*, the lowest energy of the excited state *II*, to the crossing point *C* where the electronic states of the excited and ground states are overlapped and then thermally released from the point *C* to *B* of the ground state *I*. **b** A selected real-case example of CCM and the thermal degradation of doped Eu^{2+} in $NaBaScSi_2O_7$ at two different accommodation sites Eu_{Na} and Eu_{Ba}. The thermal degradation of the phosphor system can be attributed to the nonradiative transition from the excited state ($4f^65d^1$) to the ground state ($4f^75d^0$). At room temperature, upon excitation of AB, radiative transitions CD and EF (through process ①) can be normally observed without temperature dependence being shown. But when the temperature rises, extra thermal energy allows the electron in the excited state to overcome the thermal activation energy barrier, ΔE, and crossover to the ground state nonradiatively (through process ③) predominantly, weakening the luminescence intensity as a result. The bond lengths between the luminescent center Eu^{2+} and its coordination ions O^{2-} increase also, resulting in the decreased crystal field strength and distorted site symmetry by the pronounced Jahn–Teller effect. These two factors engender the two nondegenerate excited states. However, in this reported system, a blueshift is observed with increased temperatures. An explanation is provided that thermal back-transfer activation and thermally active phonon-assisted tunneling, the exactly reverse processes of thermal quenching and multiphonon relaxation, come into effect (through process ②). (Reprinted with the permission from Ref. [32]. Copyright © 2014, Royal Society of Chemistry)

Persistent luminescence, in contrast to the aforementioned, occurs when a photoexcited electron is trapped by nonemissive metastable states (due to the presence of localized defects or impurities in lattice, more solid-state details can refer to [35]) and subsequently stimulated and released gradually the stored excitation energy in the form of delayed radiation upon thermal activation (at even room temperature). It can last for several hours or even days. Given a perturbation of the electronic system of an insulating/semiconducting material, an electron–hole pair is meanwhile generated and held by respective trapping levels separately but not both simultaneously. Heat serves in the PL case as the stimulant for popularizing phonon interactions and catalyzing the electron trapping–detrapping dynamics into and out of the traps so that excited electrons, under such a thermodynamic nonequilibrium, can go back toward the conduction band and reach finally an emitter's luminescence states for the ultimate electron–hole recombination (Fig. 11.5).

If the electronic transition into the trapping levels takes place at a temperature T, where the energy difference, E_t, between the trap and the conduction band/emitting excited state is such that $E_t > kT$, the electron would have a strong preference to remain trapped for a considerable period before the thermal stimulation ($kT > E_t$), electron discharge, final relaxation, and associated luminescence (by the probability of trap escaping assuming a Maxwell distribution of energies). A substantial lifetime of the whole process can therefore be resulted—that is why we call it persistent luminescence. From the mechanistic perspective, various conceptual and empirical models of PL mechanism have been suggested in the development of PL research
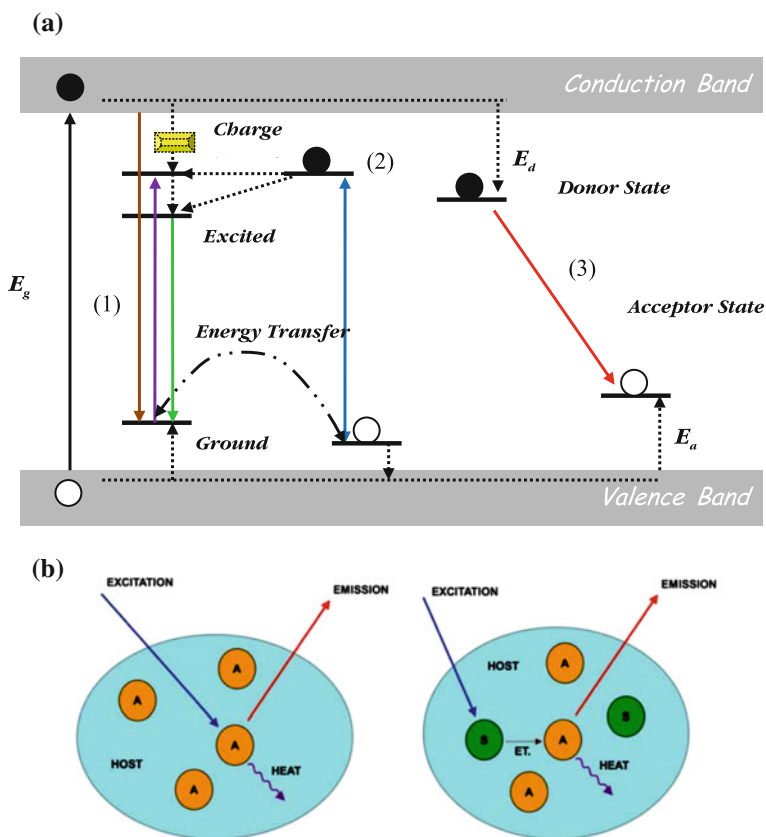
Fig. 11.4 **a** Schematic diagram of the conduction band and valence band in the vicinity of the gap in metal-doped solid system. The theoretical energy difference between them (i.e., the bandgap) is labeled as E_g. The lowest emissive state and ground state of the emitter are located at the in-between. For host sensitized (*1*) pathway, as-produced (originated from the conduction band) and annealed (relaxed from the emitter's excited state) emissions are resulted from direct excitation and defect-assisted charge recombination (the *yellow box*). Through energy transfer, charge-transfer luminescence (*2*) and donor–acceptor pair luminescence (*3*) are also engendered. The donor levels are placed shortly below the conduction band edge (E_d). Ionization of a donor equates with the transfer of the electron into the conduction band to delocalize. The acceptor levels are placed just above the valence band (E_a). Ionization of an acceptor corresponds to accepting an electron from the valence band and thereby generating a mobile hole. **b** Schematic drawing demonstrates the luminescence process of a doped activator (A) via (*left*) direct excitation and (*right*) sensitization by a neighbor sensitizer (S) involving energy transfer (ET). (Reprinted with the permission from Ref. [33]. Copyright © 2013, Royal Society of Chemistry)
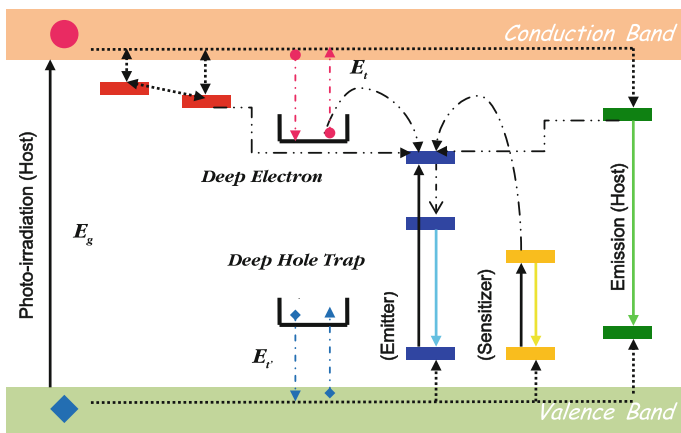
Fig. 11.5 Schematic representations of persistent luminescence—Step 1: Photoirradiation of the host, the sensitizer or even the emitter itself, triggers electron promotion, charge separation, and electron–hole pair formation; Step 2: Energy carriers (i.e., the electron and hole) go through various radiative and nonradiative pathways in an attempt to recombine each other again; Step 3: Localized defects give rise to metastable energy trapping levels that retard the whole electron/hole transfer process and capture part of the electron and hole carriers; Step 4: The stored or trapped electrons and holes are thermally stimulated to slowly release and circulate back into the pathways again; Step 5: Delayed emission is observed when it comes to final electronic relaxation and charge recombination. The *boxes* represent the energy levels due to (*red*) solid defects and surface disorders, (*blue*) the excited state, the emissive state, and the ground state of the emitter, (*yellow*) the excited state and ground state of the sensitizer, (*green*) the emissive state and the upper vibrational ground state of the host matrix. The *pink circle* and the *blue square* denote the electron carrier and the hole carrier, respectively, which are subjected to seizure by the deep electron/hole traps

for various PL phosphor systems since 1996 [36]. Many in-depth experimental and theoretical studies are still ongoing.

11.2.2 The Matsuzawa Model

After the discovery of their $SrAl_2O_4:Eu^{2+}$, Dy^{3+} system with extraordinary persistent luminescence in 1996 [37], Matsuzawa et al. had also provided a description pertaining to the mechanism, assuming that holes are the main charge carriers. When a doped Eu^{2+} is photoexcited, it is very likely for it to become Eu^{+} and a hole is favorably generated and transferred via the valence band that will finally be captured by Dy^{3+} to be further oxidized to Dy^{4+}. Then, slow liberation of the hole back to the valence band is activated thermally from time to time, and the hole will return to the Eu^{2+} ground state, triggering the emission persistently (Fig. 11.6).
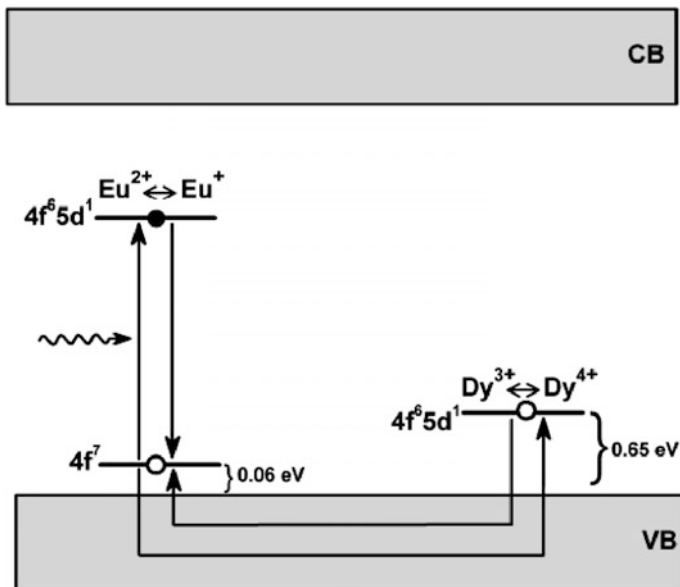
Fig. 11.6 Persistent luminescence mechanism proposed by Matsuzawa et al. for $SrAl_2O_4:Eu^{2+}$, Dy^{3+} phosphor. Reprinted with the permission from Ref. [36], an open-access article distributed under the terms and conditions of the Creative Commons Attribution license (http://creativecommons.org/licenses/by/3.0/)

11.2.3 The Aitasalo Model

In the model developed by Aitasalo et al. in 2003 [38] for the $CaAl_2O_4:Eu^{2+}$, Dy^{3+} system, a quite distinctly different mechanism had been proposed, compared with the Matsuzawa model, that (Fig. 11.7) electrons can be directly excited from the valence band into a certain traps of unspecified origin, while holes created subsequently can migrate toward a calcium vacancy where they are entrapped. Upon thermal stimulation and tunneling, freed electrons will finally reach an oxygen vacancy and relax to the calcium vacancy, thereby at the same time transferring energy (e.g., föster resonance energy transfer or excited state absorption) to the nearby europium ions for persistent luminescence. This model helps address the loophole of Matsuzawa because it can elucidate why it is possible sometime for the occurrence of persistent luminescence excited by lower energy photons.

11.2.4 The Dorenbos Model

Dorenbos who was not gratified with the above model had presented another model in 2005 by calculating the energy level of Dy^{2+} (reduced form of Dy^{3+}) in $SrAl_2O_4$
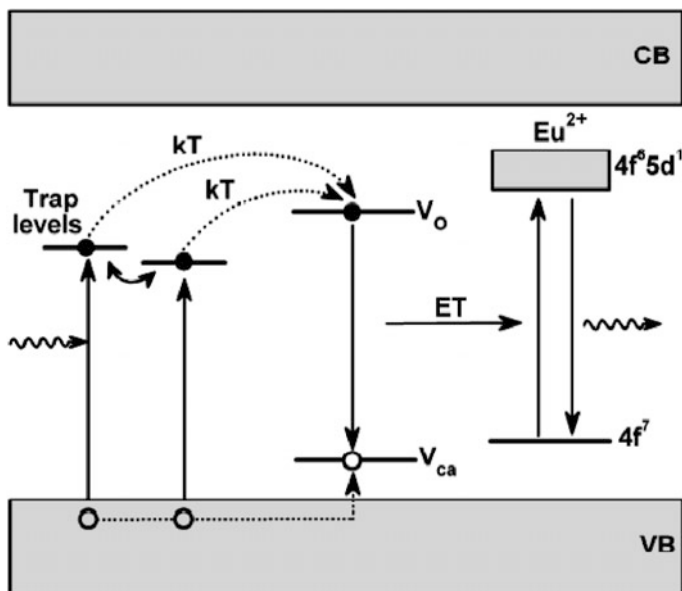
Fig. 11.7 Persistent luminescence mechanism proposed by Aitasalo et al. for $CaAl_2O_4:Eu^{2+}$, Dy^{3+} phosphor. Reprinted with the permission from Ref. [36], an open-access article distributed under the terms and conditions of the Creative Commons Attribution license (http://creativecommons.org/licenses/by/3.0/)

structure to be approximately 0.9 V below the conduction band [39] (Fig. 11.8). Such findings are important because this offers a reasonable explanation for the quenching effect of doping Sm^{3+} or Yb^{3+} toward afterglow given that their relevant levels are far lower (i.e., deeper) than Dy^{2+}.

11.2.5 The Clabau Model

With the EPR experimental results revealing that the concentration of Eu^{2+} diminishes upon photoirradiation of $SrAl_2O_4:Eu^{2+}$, Dy^{3+}, Clabau et al. [40] also suggested a modified version of PL mechanism that is based on the photoconductivity of the system, and in this model, electrons can be transferred directly between dopants at close proximity. That is, there is no any electron migration through the conduction band, and direct trap–trap interactions are feasible (Fig. 11.9). What is more, by close and careful analysis of the glow curve that relevant peaks exhibit different sizes and locations but the same shape, the authors then pointed out that the chemical nature of the trap is affected more by lattice defects (e.g., oxygen vacancies in the system) to what extent they are stabilized rather than intrinsic energy levels of codopants [41].
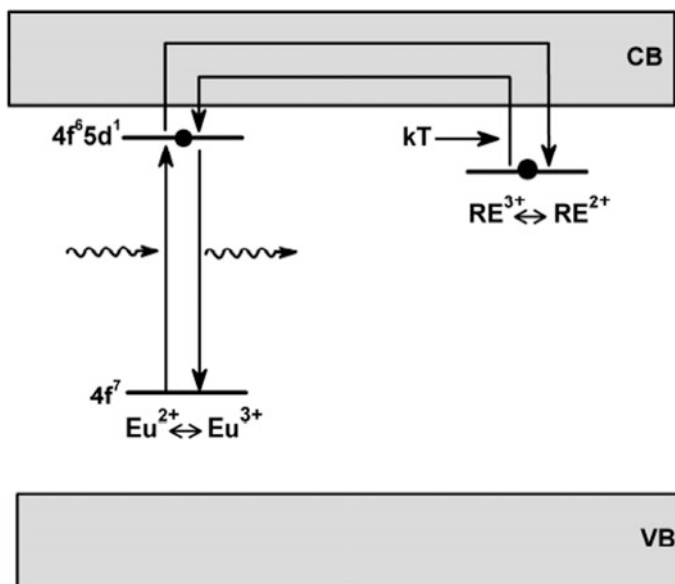
Fig. 11.8 Persistent luminescence mechanism proposed by Dorenbos et al. for aluminate and silicate. Reprinted with the permission from Ref. [36], an open-access article distributed under the terms and conditions of the Creative Commons Attribution license (http://creativecommons.org/licenses/by/3.0/)

Fig. 11.9 Persistent luminescence mechanism proposed by Clabau et al. for $SrAl_2O_4:Eu^{2+}$, Dy^{3+} system. Reprinted with the permission from Ref. [36], an open-access article distributed under the terms and conditions of the Creative Commons Attribution license (http://creativecommons.org/licenses/by/3.0/)
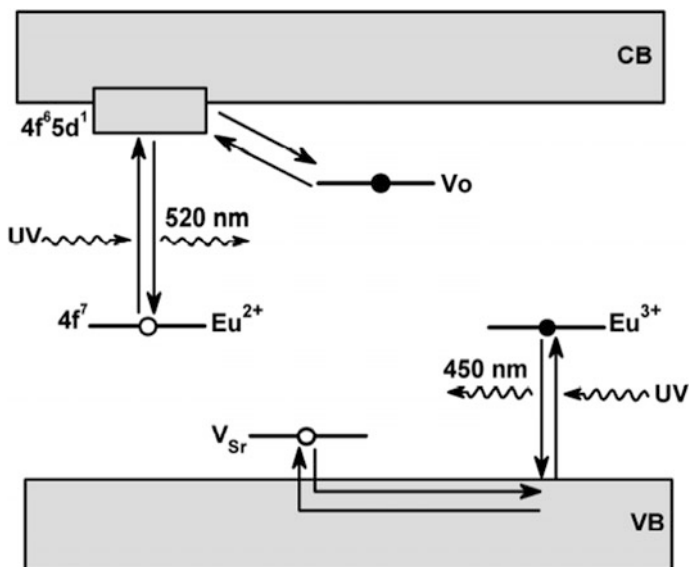
Based on the results and efforts of the above, Aitasalo et al. redraw a combined mechanism in 2006 that looks more or less like Fig. 11.5. Very recently, various phenomenological kinetic models have also been developed to analyze the decay process and electron thermalization length of long PL [42, 43], and different material systems have been discovered and engineered to show this spectacular phenomenon for in vitro/in vivo imaging and bioanalytical assays. (vida infra) In the next section, we would try to provide some useful guidelines on what criteria should be considered when designing or engineering PL materials, citing, and dissecting the latest trendsetting literature for some practical insights.

11.3 Persistent Luminescence Nanomaterials: Design and Optimization

Whatever the proposed mechanisms of persistent luminescence mentioned previously, we have no difficulties finding that (1) the structure and the bandgap of host materials; (2) the type, number, and depth of the electron/hole energy traps; (3) the presence, nature, and concentration of dopants; and (4) the surrounding temperature is critical parameters for the occurrence and modulation of PL [44–46]. To exploit its merits and potentials for biomedical research, many strategies for designing, preparing, and modifying new nanoscale surface-functionalized PL materials have been proposed and practised [47, 48]. Conventional syntheses of PL phosphors encompass (1) solid-state reactions, (2) combustion methods, (3) sol-gel approach, and (4) hydrothermal techniques. We would discuss here mainly about the trial-and-error planning for material design and optimization more systematically in detail in the following.

11.3.1 The Host Factor

Over the past few decades, many persistent phosphor hosts have been developed, such as silicates (e.g., $Sr_2MgSi_2O_7:Eu^{2+}$, Dy^{3+} [51]), aluminates (e.g., $CaAl_2O_4:Eu^{2+}$, Dy^{3+} [38]), germinates (e.g., $MgGeO_3:Mn^{2+}$ [49]), and phosphates (e.g., $YPO_4:Pr^{3+}$, Ln^{3+} [50]). The selection criteria for a PL suitable host can be as follows: (1) single-phase crystal structure that offers different sites and symmetries for substituting dopants and (2) high thermal and chemical stability, for example, in $Sr_2MgSi_2O_7$ (space group: $P42_1m$, no. 113, Z: 2, a: 7.9957, c: 5.1521 Å) [51]. Surprisingly, introducing foreign Eu^{2+} and Dy^{3+} impurity can favor purer and desired phase without significant distortions. The density functional calculation (DFT) can be used to study the modification of the crystal lattice upon doing and thus the creations of isolated defects and defect aggregates, as well as the changes in dopant–ligand ion distances, in terms of total energy. Recently, an oxycarbonate, $Gd_{2-x}RE_xO_2CO_3$, has

also been reported [44]. Table 11.2 enumerates several PL host systems [52]. Hosts play an important role in providing the means to store excitation energy and determining the efficiency of energy transfer toward the luminescence center.

Table 11.2 Detail of host matrix, dopant ion(s), emission colour/wavelength, and duration of persistent luminescence of different types of red-emitting persistent materials

Host (References)	Dopant ion(s)	$\lambda_{emission}$ (nm)	Persistent time	Remarks
CaS (Ref. [64])	Eu^{2+}, Tm^{3+}/Bi^{3+}	650	1 h	Effect of Na^+ codoping
CaS (Ref. [65])	Eu^{2+}	655/670	–	Effect of Cl^- codoping
CaS (Ref. [66])	Bi^{3+}	650	1 h	Effect of Cl^- codoping
CaS (Ref. [67])	Ce^{3+}, Pr^{3+}	Green/red	1 h	Effect of Li^+ codoping
$Ca_{1-x}Sr_xS$ (Ref. [68])	Eu^{2+}	650	1 h	White light emission
SrS (Ref. [69])	Eu^{2+}, Dy^{3+}	616	–	Nanosize particle
CaS (Ref. [70])	Eu^{2+}, Pr^{3+}	–	–	Effect of Li^+ codoping
$Ca_{1-x}Sr_xS$ (Ref. [71])	Eu^{2+}, Pr^{3+}	650	–	Effect of Li^+ codoping
SrS (Ref. [72])	Pr^{3+}	Blue/green/red	–	–
SrS (Ref. [73])	Eu^{2+}	615	–	Lanthanide(3+)codoping
CaS (Ref. [74])	Eu^{2+}, Dy^{3+}	650	–	Nano, photostimulated
Y_2O_2S (Ref. [75])	Eu^{3+}, Mg^{2+}, Ti^{4+}	611	1 h	Nanorods
Y_2O_2S (Ref. [76])	Eu^{3+}, Mg^{2+}, Ti^{4+}	611	1 h	Solid-state reaction
Y_2O_2S (Ref. [77])	Ti^{4+}/Ti^{2+}	565	5 h	High sintering temp
Y_2O_2S (Ref. [78])	Sm^{3+}	610	1 h	–
Y_2O_2S (Ref. [79])	Mg^{2+}, Ti^{4+}	594, broad	–	High temperature
Gd_2O_2S (Ref. [80])	Er^{3+}/Ti^{4+}	555, 675	1.2 h	–
$MgSiO_3$ (Refs. [81, 82])	Mn^{2+}, Eu^{2+}, Dy^{3+}	660	4 h	High sintering temp
$CdSiO_3$ (Ref. [83])	Mn, Ni, Cr	550–720	<1 h	Solid-state reaction
$CaMgSi_2O_6$ (Refs. [84, 85])	Mn	550–800	<1 h	Sol-gel route
$CaMgSi_2O_6$ (Ref. [86])	Mn^{2+}, Dy^{3+}	550–800	<1 h	Nanoparticle synthesis
$SrMg(SiO_3)_2$ (Ref. [87])	Mn^{2+}, Dy^{3+}	500–800	<1 h	Solid-state reaction
$Sr_3MgSi_2O_8$ (Ref. [88])	Eu^{2+}, Mn^{2+}, Dy^{3+}	670	2 h	Solid-state reaction

Table 11.2 (continued)

Host (References)	Dopant ion(s)	$\lambda_{emission}$ (nm)	Persistent time	Remarks
$BaMg_2Si_2O_7$ (Ref. [89])	Mn^{2+}, Ce^{3+}	620/670	2 h	Solid-phase reaction
$Ca_3MgSi_2O_8$ (Ref. [90])	Eu^{2+}, Dy^{3+}	Green/red	5 h	–
$MgGeO_3$ (Refs. [91, 92])	Yb^{3+}/Bi_2O_3	600–720	–	–
$M_2Si_5N_8$ (Ref. [93])	Eu(M = Ca, Sr, Ba)	580–620	–	–
$Ca_2Sn_2O_4$ (Ref. [94])	Sm^{3+}	Orange-red	–	–
β-$Zn_3(PO_4)_2$ (Ref. [95])	Mn^{2+}	616	2 h	Role of excess Zn^{2+}
β-$Zn_3(PO_4)_2$ (Refs. [96, 97])	Mn^{2+}, Al^{3+}, Ga^{3+}	570–700	–	Solid-state reaction
β-$Zn_3(PO_4)_2$ (Ref. [98])	Sm^{3+}, Mn^{2+}	616	2 h	Solid-state reaction
YPO_4 (Ref. [99])	Pr^{3+}, Ln^{3+}	Red	–	High temperature
$Ca_3(PO_4)_2$ (Refs. [100, 101])	$Mn^{2+}/Tb/Dy$	660	–	Biocompatible host
$Ca_9Ln(PO_4)_7$ (Ref. [102])	Lanthanides, Mn	Red	–	–
CaO-Al_2O_3 (Ref. [103])	Tb^{3+}	Green/red	–	Glass
$CaTiO_3$ (Ref. [104])	Pr^{3+}	612	0.1 h	–
$CaTiO_3$ (Ref. [104])	Al^{3+}	612	0.2 h	–
$Ca_2Zn_4Ti_{16}O_{38}$ (Ref. [105])	Pr^{3+}	614, 644	–	Dual phosphorescence
MO (Ref. [106])	Eu(M = Ca, Sr, Ba)	Orange-red	2 h	Solid-state reaction
Lu_2O_3 (Ref. [107])	Pr, Hf	610, 632	–	Thermal/photostimulation
CaF_2 (Ref. [108])	Tm/Dy/Mn	Miscellaneous	–	–
$Ca_2Si_5N_8$ (Ref. [109])	Eu^{2+}, Tm^{3+}	610	–	Bioimaging application

11.3.2 The Dopant Factor

The intrinsic properties of alien ions doped give rise to persistent luminescence in certain phosphor systems. Dopants cannot only distort the host lattice, but also provide additional energy levels in the bandgap for charge carrier capture (see the previous section). Most importantly, they are added for multicolor tuning for PL

phosphors. To probe the trap depth distribution, thermoluminescence experiments and synchrotron radiation (SR) studies become routine procedures which are both powerful and versatile tools to investigate the location of the traps in persistent phosphors [53]. For instance, in [54], synchrotron radiation is widely used to study the spectroscopic properties of $CdSiO_3$ and the position of the dopants' energy levels with respect to the host's band structure (Fig. 11.10). The traps in the authors' materials are found from two origins: intrinsic and charge compensation defects.
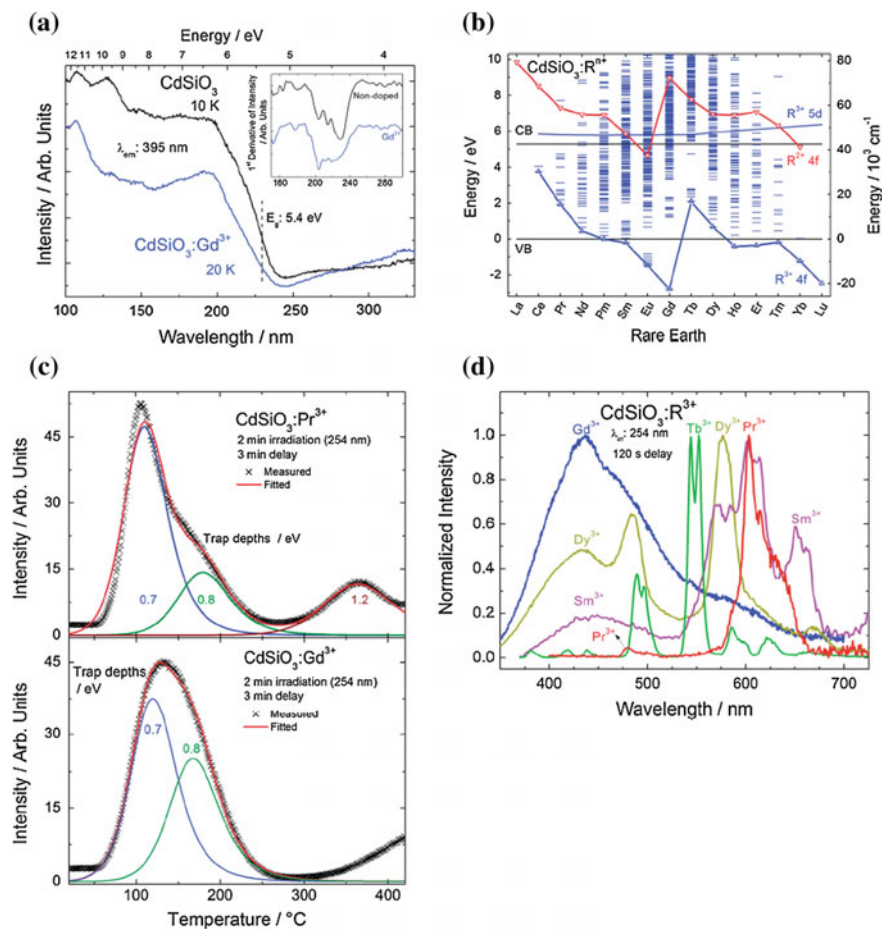
Fig. 11.10 **a** The low temperature SR VUV-UV excitation spectra of nondoped and Gd^{3+}-doped $CdSiO_3$. **b** The $R^{2+/3+}$ energy level diagrams in the $CdSiO_3$ host. **c** The deconvolution of the thermoluminescence glow curves of Pr^{3+} (*top*)- and Gd^{3+} (*bottom*)-doped $CdSiO_3$ from 20 to 420 °C. **d** The room temperature persistent luminescence spectra of selected $CdSiO_4:R^{3+}$ (Reprinted with the permission from Ref. [54]. Copyright © 2014, Royal Society of Chemistry)

By reasoning whether the Mn^{2+} dopant acts as both the recombination center and hole trap in the solid system of $CaMgSi_2O_6$:Mn^{2+}, Ln^{3+}, authors in [55] strategically control the electron trap depth by taking into account the electron affinity and the ionization energy along the lanthanide series to choose and optimize the most best-fit lanthanide-based electron traps for finally in vivo imaging (Fig. 11.11).

In essence, with reference to the literature, lanthanide ions such as Eu^{2+} and Dy^{3+} and transition metal ions such as Mn^{2+} and Cr^{3+} are the most favorable dopants for PL. A comprehensive review article has recently published [52] so herein we try not to repeat again. Readers are encouraged to go through it or elsewhere for more specific and detailed information. However, it should be reminded that only little dopants have to be incorporated due to the reasons of concentration-dependent cross-relaxation quenching among nearby dopants of similar orbital ladders as well as extensive host's structural distortion.
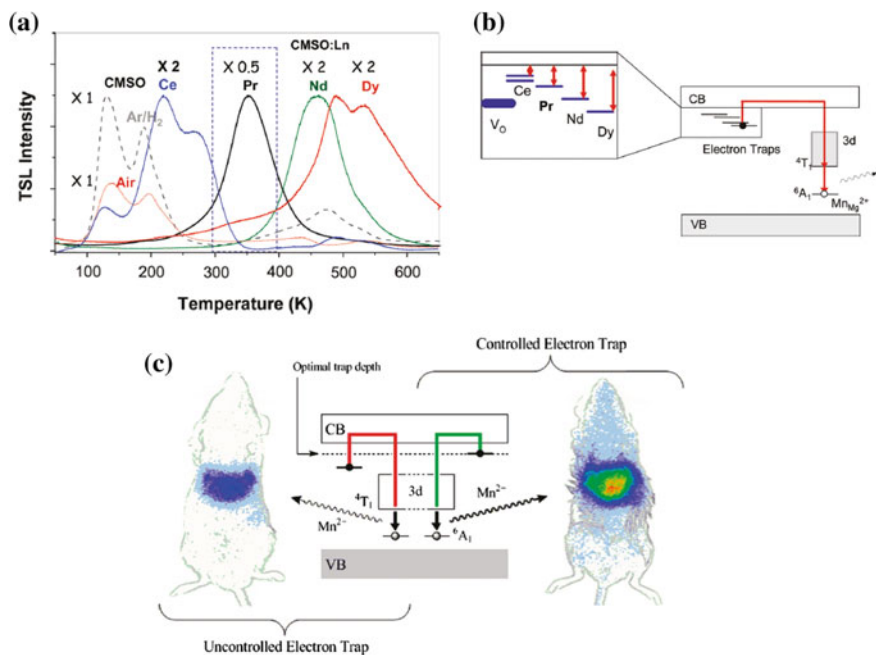

Fig. 11.11 **a** Mn^{2+} TSL intensity at 685 nm of Mn^{2+}/Ln^{3+}doped and pure $CaMgSi_2O_6$ (CMSO) materials, recorded after 10-min X-ray irradiation. The approximate temperature range of interest for room temperature persistent luminescence is delimited by a *dotted rectangle*. The *dotted curve* (in *red*) and the interrupted *curve* (in *black*) represent TSL of CMSO treated at 1100 °C in air and in Ar/H2 atmosphere, respectively. The other curves represent TSL of CMSO:Ln, with 1 % doping with Ln = Ce^{3+}, Nd^{3+}, Dy^{3+}, and Pr^{3+}. **b** Schematic energy level diagram of Mn^{2+} and Ln^{3+} in CMSO. The main hole traps are Mn^{2+} ions in the Mg^{2+} site, while electrons are trapped by oxygen vacancies (VO) and Ln^{3+} ions. The *insert* shows the relative positions of electron trap levels with respect to the conduction band edge. **c** Comparative in vivo imaging of the persistent luminescence performance of CMSO materials of controlled and uncontrolled electron trap depth. (Reprinted with the permission from Ref. [55]. Copyright © 2011, American Chemical Society)

11.3.3 The Temperature Factor and Surface Factor

In the course of chemical synthesis, the higher sintering temperature is applied, the higher degree of thermal lattice distortions and surface disorders is resulted due to thermodynamic considerations that, for example, the enthalpy of formation of the cation 266 antisite vacancies entails very low energy input [47]. Indeed, changing the surrounding atmosphere (e.g., oxidizing and reducing, under air or nitrogen or argon) and pressure during calcinations does all affect the product's structural outcome and so does its persistent luminescence properties [46].

Surface functionalization with biomolecules furnishes a promising and effective means to improve the biocompatibility and biofunctionality of organic–inorganic hybrid PLNMs [48]. Like UCNMs, water-soluble PEG chains and target-binding/ cancer-selective vectors can be coated on the PLNMs' surface [58] (Fig. 11.12).

11.4 Persistent Luminescence Nanomaterials: Potential Bioapplications

After summarizing the literature up to this moment, biomedical applications, either in vitro or in vivo, of persistent luminescence nanomaterials embrace mainly two directions: (1) bioimaging and (2) bioanalysis. Several therapeutic PLNMs as well as drug delivery do also have been reported. We would here try to briefly outline
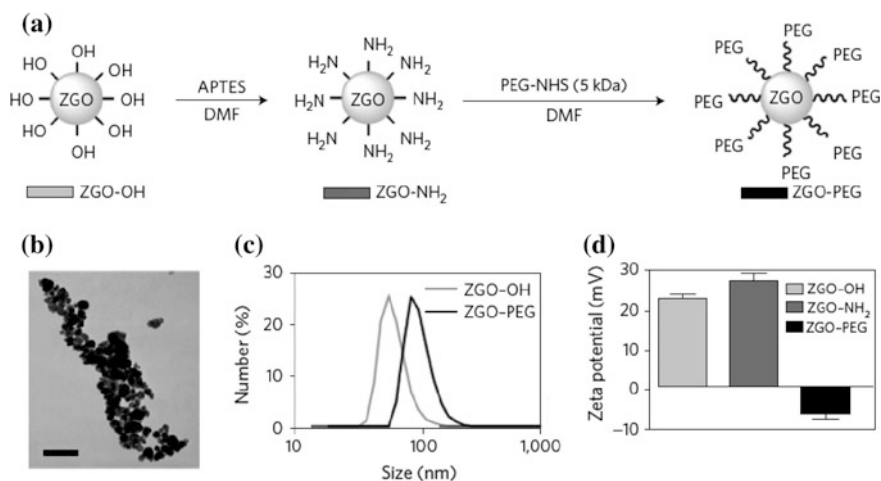

Fig. 11.12 The surface functionalization and characterization of red-excitable PLNPs. **a** A schematic representation of ZGO–OH surface functionalization. **b** A transmission electron micrograph of ZGO–OH nanoparticles. Scale bar, 100 nm. **c** The hydrodynamic diameter measured by dynamic light scattering in 5 % glucose before and after PEG coverage. **d** The evolution of zeta potential as a function of surface coverage. (Reprinted with the permission from Ref. [57]. Copyright © 2014, Macmillan Publishers Limited)

the most salient them with a categorized checklist for all readers so that they can consult the papers quickly on their own despite information overload in the literature.

11.4.1 Persistent Luminescence and In Vitro/In Vivo Imaging

11.4.1.1 Lanthanide-Based NIR Emission via Ex Vivo Excitation

In 2007, le Masne de Chermont et al. [56] published the first research article on NIR-emitting persistent luminescence nanoprobes, $MgSiO_3:Eu^{2+}$, Dy^{3+}, Mn^{2+} (MSOEDM), for in vivo imaging. Experiment-wise, ex vivo excitation is adopted prior to administration of the PLNMs into the genuine pig as depicted in Fig. 11.13.
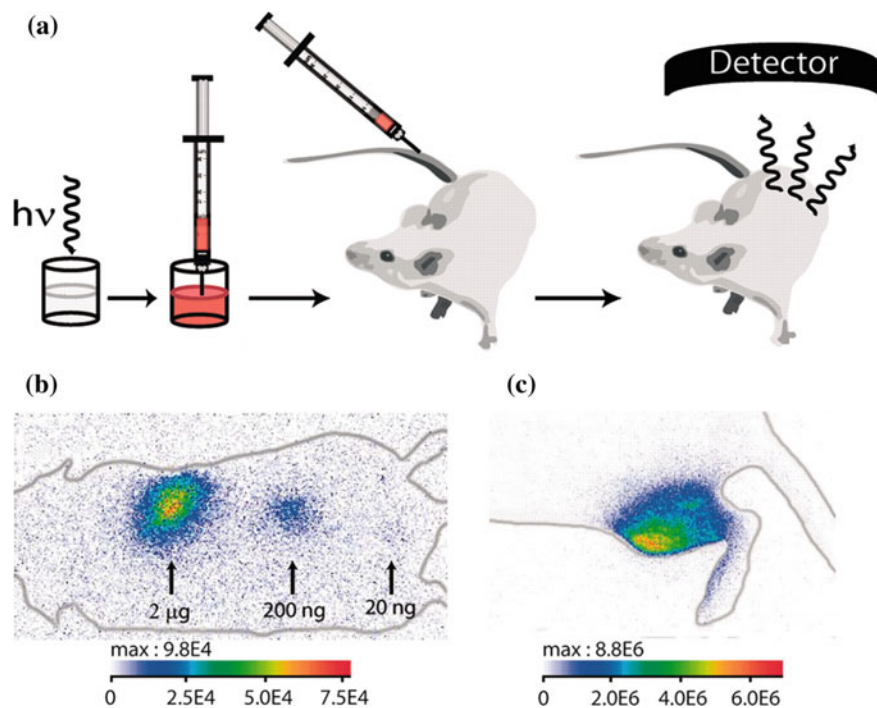

Fig. 11.13 Principles of in vivo experiment and first in in vivo images using PLNMs. **a** A suspension containing MSOEDM is externally excited with UV lamp and then directly injected into an anesthetized mouse. **b** and **c** in vivo images via s. c. and intramuscular injections, respectively. (Reprinted with the permission from Ref. [56]. Copyright © 2007, National Academy of Science, USA)
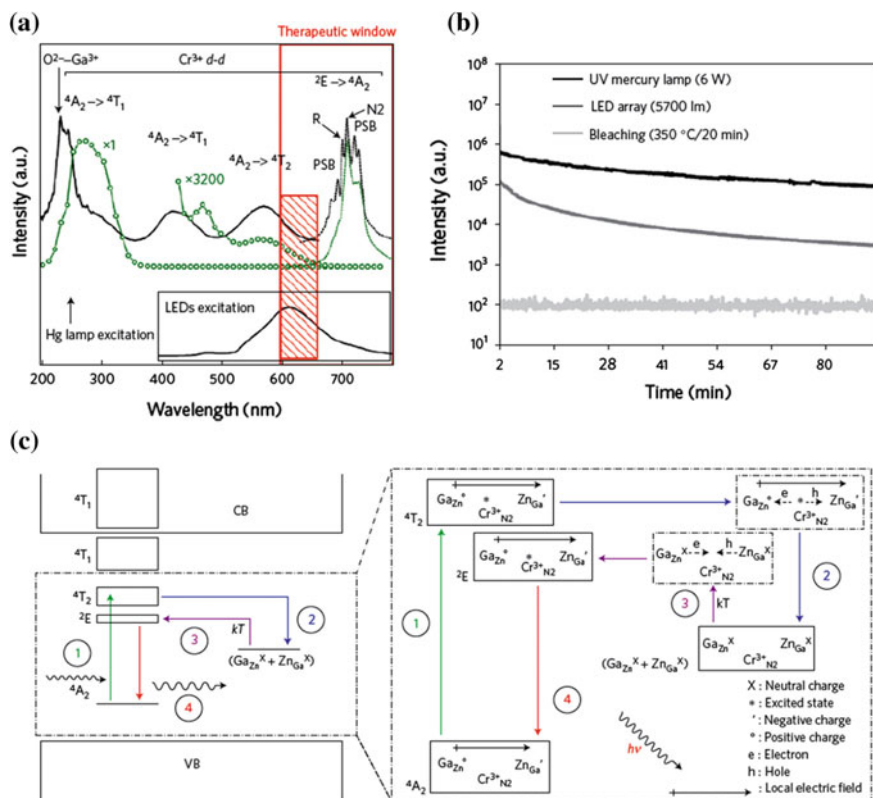
Fig. 11.14 **a** PL excitation (*black solid line*) and emission (*black dotted line*) spectra, compared with TSL excitation (*green open points*), and emission (*green dotted lines*) spectra of Cr^{3+} doped n-ZGO. The hatched *red rectangle* represents the region where the $^4A_2$ (^4F) → $^4T_2$ (^4F) excitation band of Cr^{3+} partly corresponds to the tissue transparency window (*open red rectangle*). **b** Room temperature persistent luminescence decay *curves* of bleached n-ZGO obtained with two different excitations for 2 min under either ultraviolet light or a LED array source, as compared with the background signal obtained after proper bleaching of the nanoparticles. **c** Schematic illustration of the proposed PL mechanism. A detailed approach of the mechanism is presented on the right. *Step 1* Cr^{3+} excitation. *Step 2* charge separation and trapping. *Step 3* thermal detrapping of electron–hole pair and capture by Cr^{3+}. *Step 4* Cr^{3+} emission, where PSB means phonon side band; *k*, Boltzmann's constant; *T*, temperature. (Reprinted with the permission from Ref. [57]. Copyright © 2014, Macmillan Publishers Limited)

11.4.1.2 Transition Metal-Based NIR Emission via In Vivo Excitation

In 2014, Maldiney et al. [57] had pioneered and prepared an well-optimized new PLNMs $ZnGa_{1.995}Cr_{0.005}O_4$ (ZGO:Cr^{3+}) for NIR imaging vascularization, tumors, and grafted cells in vivo. In this paper, the authors can excite the nanosystem in vivo with LED light source, thereby potentiating the real-time biodistribution and

longitudinal studies. The underlying PL mechanism of the new nanosystems had also been well spelt out (Fig. 11.14).

11.4.1.3 Specific Reaction-Based Detection and Imaging

Li et al. [58] have published their work of specific sensing and imaging of the ascorbic acid (AA) in vitro and in vivo through a specific reaction-based strategy between cobalt oxyhydroxide nanoflakes (CoOOHNFs) modified on $Sr_2MgSi_2O_7$: Eu (PLNPs) and the cellular AA (Fig. 11.15).

11.4.2 Persistent Luminescence and Bioanalytical Assays

11.4.2.1 FRET Inhibition Assays

Wu et al. [59] have reported their first example of fluorescence resonance energy transfer (FRET) inhibition assay highly selective and sensitive for α-fetoprotein (AFP) excreted during cancer cell growth using water-soluble polyethyleneimine-coated $Ca_{1.86}Mg_{0.14}ZnSi_2O_7:Eu^{2+}$, Dy^{3+} (PEI-PLNPs) conjugated with AFP-antibody-coated gold nanoparticle (Ab-AuNPs). The modulation of FRET is based on the maximum overlapping of the emission spectrum of PEL-PLNPs and the absorption spectrum of AFP-AuNPs in close proximity, giving rise to maximum FRET efficiency. The inhibition effect is accomplished by the keen competition between AFP and PEI-PLNPs to vie for Ab-AuNPs, where the former has the strong and specific affinity between AFP and the AFP antibodies (Fig. 11.16).

11.4.2.2 Lateral Flow Assay

Paterson et al. [60] have displayed their successful application of persistent luminescence nanoparticles $SrAl_2O_4:Eu^{2+}$, Dy^{3+} upon silica encapsulation and NeutrAvidin bioconjugation (NeutrAvidin-PLNPs) as reporters in lateral flow assay (LFA) for biotinylated hen egg lysozymes (bHEL). The detection limit of this nanosystem has also been revealed below 100 pg/mL, which is as approximately an order of magnitude more sensitive than colloidal gold nanoparticles. Saliently, the preparation of the PLNPs is done by direct wet milling and differential isolation of commercially available lanthanide-doped strontium aluminates of larger size (Fig. 11.17).
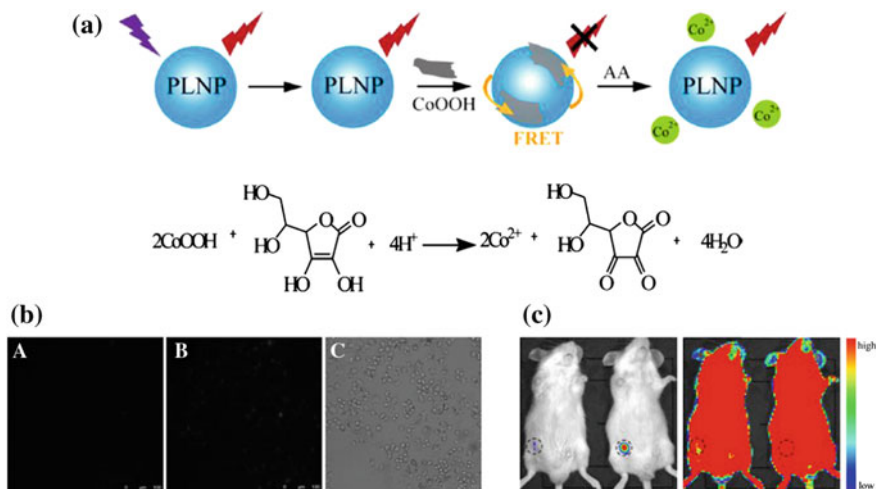
Fig. 11.15 a Schematic illustration of the reaction-based design for AA detection using CoOOH-modified PLNPs. **b** PL imaging of AA in living cells. (*A*) PL image of the nanoprobe in RAW 264.7 macrophages. (*B*) PL image of the same sample after the addition of AA (100 μM). (*C*) bright-field image of the samples in (*A*) and (*B*). Scale bars are 100 μm. **c** PL imaging of AA in vivo. (*left*) PL image of the mouse treated with 0.1 mL of normal saline and the nanoprobe and the mouse treated with 0.1 mL of AA (0.1 mol/L) and the nanoprobe (*right*) without excitation. (Reprinted with the permission from Ref. [58]. Copyright © 2014, American Chemical Society)
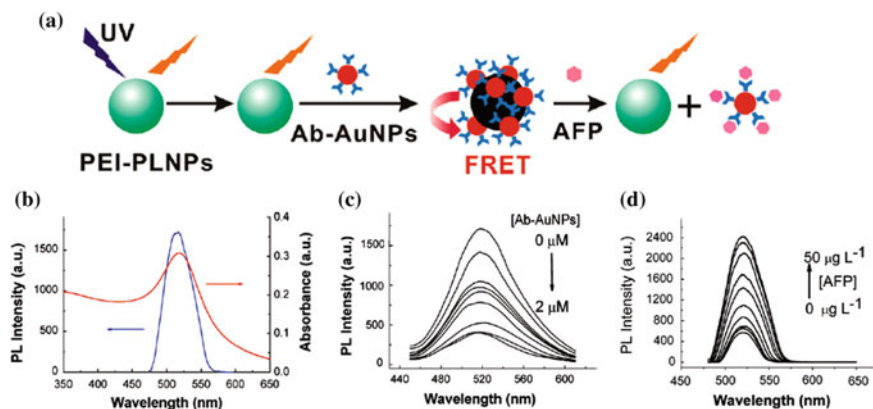

Fig. 11.16 a Schematic illustration of the working principle of turn-on FRET inhibition assay for AFP due to the photoluminescence quenching of PEI-PLNPs by Ab-AuNPs and the competitive recognition of AFP and Ab-AuNPs. **b** Photoluminescence emission spectrum of PEI-PLNPs (*blue curve*) and absorption spectrum of Ab-AuNPs (*red curve*). **c** Quenching effect of Ab-AuNPs on the photoluminescence emission of PEI-PLNPs. **d** Effect of AFP concentration on the photoluminescence emission of PEI-PLNPs/Ab-AuNPs. (Reprinted with the permission from Ref. [59]. Copyright © 2011, American Chemical Society)
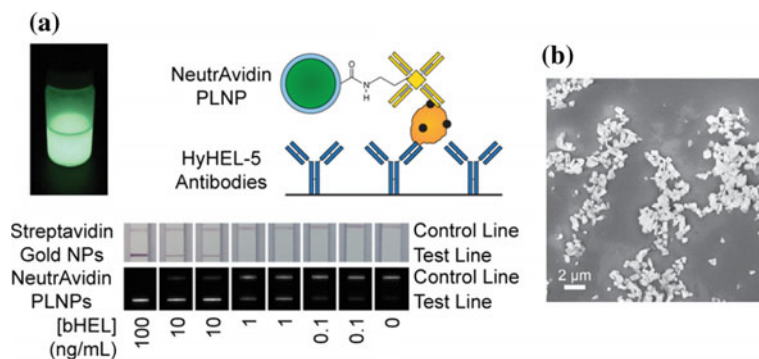
Fig. 11.17 **a** Schematic diagram of the working principle of NeutrAvidin-PLNPs sensing toward bHEL by anti-HEL antibodies on LFA strips, with the detection limit compared with Streptavidin gold nanoparticles and PL emission recorded after 30 s of 370-nm excitation. **b** SEM micrographs of the phosphors of 248 nm mean size after 9 days of wet milling. (Reprinted with the permission from Ref. [60]. Copyright © 2014, American Chemical Society)

11.4.3 Persistent Luminescence and Theranostics

11.4.3.1 Drug Delivery

Maldiney et al. [61] have also recently developed a multifunctional nanoplatform based on their hybrid persistent luminescence $Zn_{1.995}Cr_{0.005}O_4$ core/mesoporous silica shell architecture loaded with a drug model doxorubicin (ZGO@SiO$_2$-DOX) that can be used as an efficient cytotoxic doxorubicin-delivery vehicle against U87MG cells and a highly sensitive persistent nanobioprobe that can be excited in situ via simple orange-red LED and can indicate its own real-time biodistribution in vivo without any autofluorescence. In particular, neither acute nor long-term in vivo nanotoxicity of their nanoplatform is observed through the histopathological tissue analysis of the main reticuloendothelial system organs (Fig. 11.18).

11.4.3.2 Photodynamic Therapy

Chen and Zhang [62] have pioneered the use of a new photodynamic therapy (PDT) system based on X-ray-stimulated persistent luminescence nanoparticle–photosensitizer porphyrin (PLNP-Por) conjugates that can assault tumors via the porphyrin's cytotoxic singlet oxygen generation activated by the PLNPs, thereby affording dual-functional radiation and PDT simultaneously.
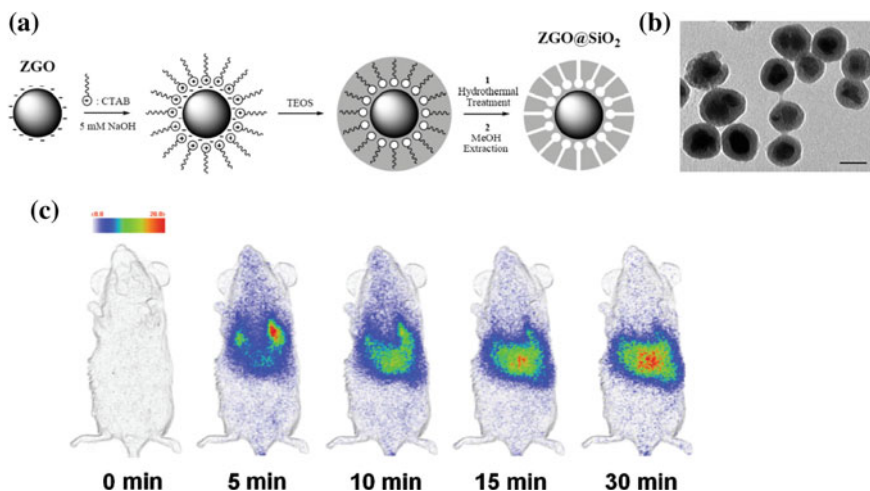
Fig. 11.18 a Schematic representation of ZGO@SiO$_2$ synthesis. **b** Transmission electron micrograph (TEM) of ZGO@SiO$_2$. **c** Persistent luminescence images up to 30 min after systematic intravenous injection in a mouse that show in vivo biodistribution of ZGO@SiO$_2$-DOX nanoparticles. (Reprinted with the permission from [61]. Copyright © 2014, Royal Society of Chemistry)

## 11.5 Persistent Luminescence Nanomaterials: Challenges and Opportunities

11.5.1 Remaining Challenges

11.5.1.1 Photophysical–Mechanistic Aspects

To discover or develop new PL phosphor materials, scientists have to unravel the ambiguity and mystery of detailed mechanisms of persistent luminescence. As the authors Chen et al. (2014) in [63] said, for their promising NIR-emitting PL oxy-carbonate, they cannot even base on the time decay profile to rule out whether their system Cr/Yb/Tm:Ca$_3$Ga$_2$Ge$_3$O$_{12}$ (Cr/Yb/Tm:CGGG) undergoes the continuous trap depth distribution mechanism, the athermal tunneling luminescence mechanism, or the direct tunneling recombination mechanism. Further comprehensive studies are necessary in order to better understand the PL process and to discriminate among various proposed hypotheses (Fig. 11.19).

11.5.1.2 Biodistribution-Nanotoxicological Aspects

Nanotoxicity has long been great concern for scientists as well as government officials whether or not to approve nanomaterials as drugs compared to their
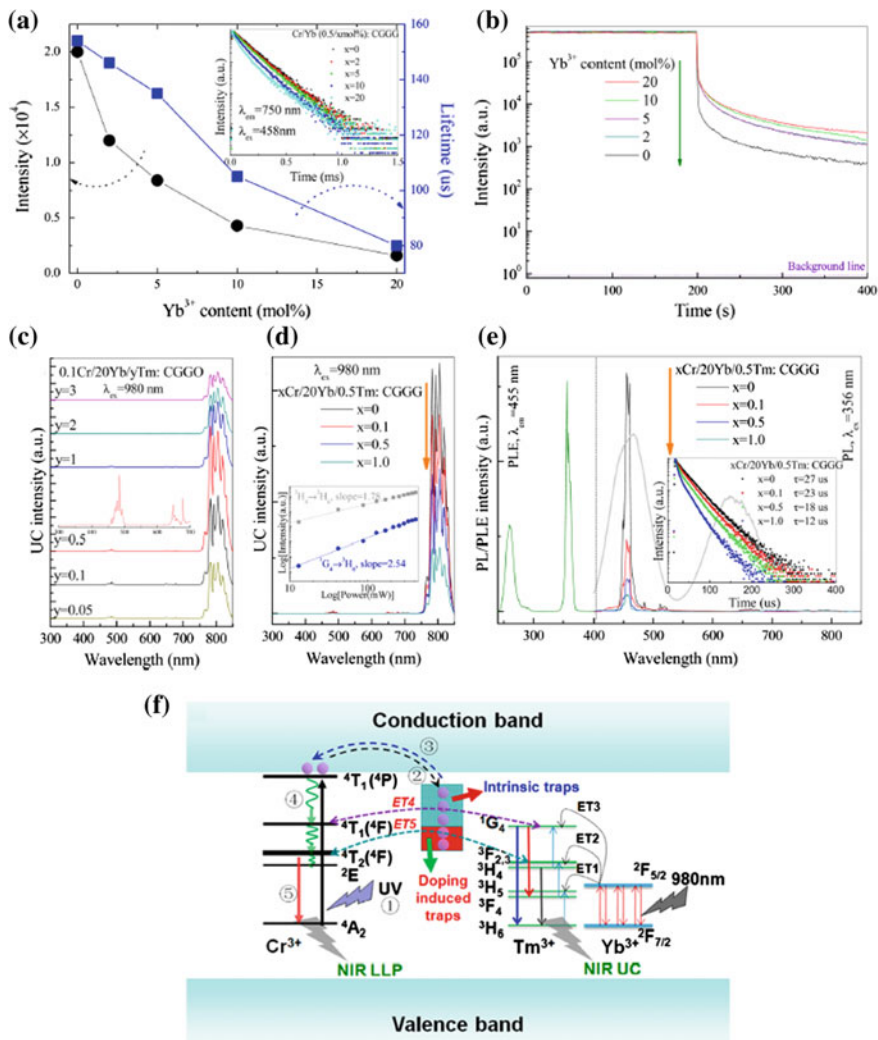
molecular counterparts [64]. Further various relevant in vivo investigations, in particular, e.g., biodistribution and pharmacokinetic studies, have to be carried out. Experts in the field are all in the right track to contribute to address the issues via surface functionalization, size/morphology modification, and nanomaterials' biodegraded/metabolized product of tracing.

◄ **Fig. 11.19** **a** The dependence of emission intensity and lifetime (corresponding to the Cr^{3+} $^4T_2 \rightarrow {}^4A_2$ transition) in Cr/Yb:CGGG on Yb^{3+} doping content; inset shows PL decay curves of 0.5Cr/xYb:CGGG ($x = 0, 2, 5, 10,$ and 20 mol%) samples. **b** LLP decay curves of 0.5Cr/xYb: CGGG phosphors after 286-nm light illumination for 200 s. **c** UC emission spectra of xCr/20Yb/0.5Tm ($x = 0, 0.1, 0.5,$ and 1.0 mol%) and **d** 0.1Cr/20Yb/yTm ($y = 0.05, 0.1, 0.5, 1,$ 2, and 3 mol%) triply doped CGGG samples. *Inset* of panel (**d**) is the enlarged spectrum in the wavelength range of 300–700 nm, and *inset* of panel d is the log–log plots of UC emission intensity versus NIR excitation power. **e** PLE and PL spectra of xCr/20Yb/0.5Tm:CGGG samples (PLE spectrum for Cr^{3+} 750-nm emission is also provided as a comparison); *inset* shows PL decay *curves* of the corresponding samples in panel **e**. **f** Schematic illustration of the NIR LLP and NIR-to-NIR upconversion luminescence mechanisms in Cr/Yb/Tm:CGGG; the *straight-line* and *dotted-line arrows* represent optical transition and electron transfer processes, respectively, and the *wave arrows* represent nonradiative relaxation. (Reprinted with the permission from Ref. [63]. Copyright © 2014, American Chemical Society)

11.5.2 Forthcoming Opportunities

11.5.2.1 Development of New Systems for Super-Long Afterglow

As Yan et al. have achieved in [64], more new systems such as LPLNMs, Cr^{3+}/Pr^{3+} codoped $Zn_{2.94}Ga_{1.96}Ge_2O_{10}$ (ZGGO), can be developed to fine-tune the persistent luminescence lifetime that is more suitable and applicable for bioimaging (Fig. 11.20).

11.5.2.2 Multimodal Neuroimaging

Persistent luminescence nanomaterials with metal dopants can demonstrate several magnetic properties. This can also pave the road in future for potential applications in dual-functional longitudinal persistent luminescence and magnetic resonance imaging for neurodegenerative diseases [65, 66].

11.6 Conclusion

Persistent luminescence nanomaterials hold tremendous promises in biomedical research due to their intrinsic long-lived emission that makes autofluorescence-free, time-resolved longitudinal measurements with higher signal-to-noise excited ratios either by ex vivo or by in vivo feasible. Sophisticated and expensive optical hardware can be also no longer indispensable. In essence, various investigations of PLNMs for discovery of new PL crystalline nanosystems, theoretical modeling of PL decays and energy trap mechanisms, multimodal theranostics, and chemical optimization of quality synthetic methods and facile bioconjugation strategies are
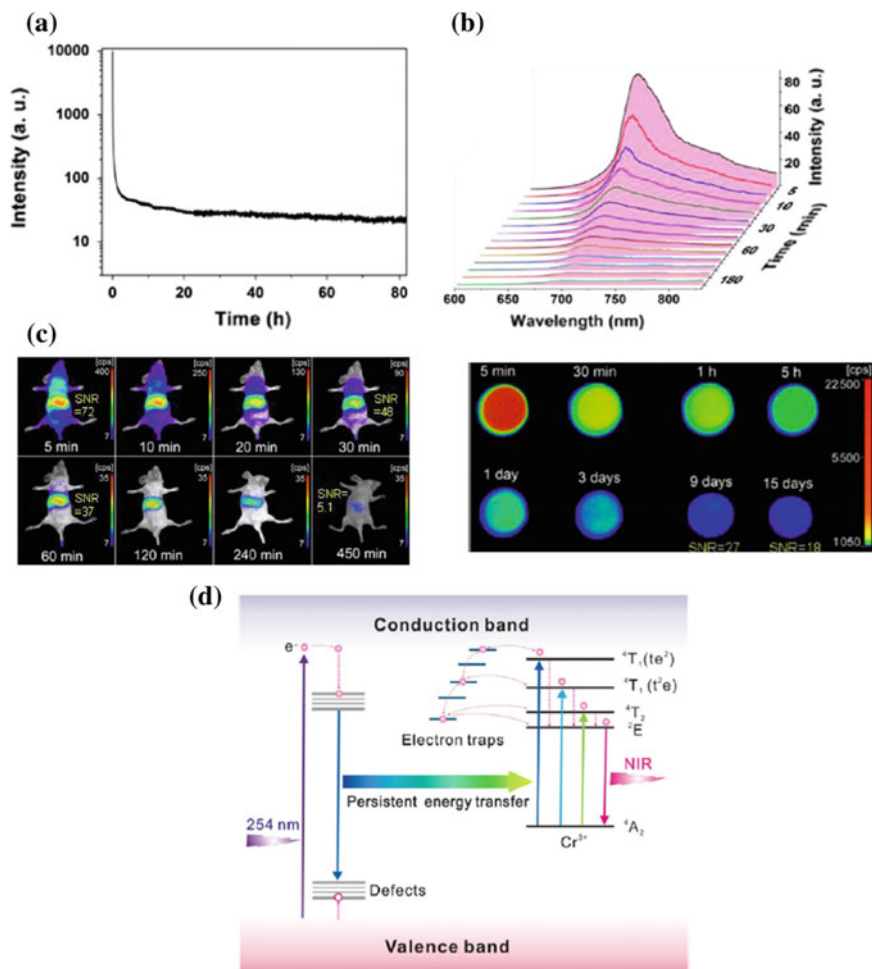
Fig. 11.20 NIR afterglow decay of LPLNPs powder after 5-min irradiation with a 254-nm UV lamp. **a** Persistent luminescence intensity monitored at 695 nm. **b** Time-dependent persistent luminescence spectra. **c** (*left*) In vivo NIR images of a normal mouse after intravenous injection of PEG-LPLNPs and (*right*) NIR afterglow decay images (n.b. 10 min irradiation). **d** Schematic illustration of the persistent energy transfer mechanism between ZGGO host and Cr^{3+} ion. *Dotted-line arrows* represent nonradiative electron (or hole) transfer processes. (Reprinted with the permission from Ref. [64]. Copyright © 2013, American Chemical Society)

all in heated progress. With their superior photostability, chemical stability, and thermal stability relative to organic fluorophores, as well as versatile bioapplications discovered or still under development, we can foresee that PLNMs in the nanobiomedical field are going to be flourishing, or we should say that, apart from photon upconversion, we do now start to enter the era of persistent luminescence.

References

1. Harvey EN (1957) History of Luminescence. The American Philosophical Society, Philadelphia
2. Valeur B, Berberan-Santos MN (2013) Molecular Fluorescence: Principles and Application, 2 edn. Wiley-VCH, Weinheim
3. Demtröder W (2008) Laser Spectroscopy Volume 1 Basic Principles. Springer, Berlin Heidelberg New York
4. Medintz I, Hildebrandt N (2013) FRET – Förster Resonance Energy Transfer: From Theory to Applications. Wiley-VCH, Weinheim
5. Zhang F (2015) Photon Upconversion Nanomaterials. Springer, Berlin Heidelberg New York
6. Qin A, Tang BZ (2013) Aggregation-Induced Emission: Fundamentals and Applications, Volume 1 and 2. Wiley, Chichester
7. Tartakovskii AG (2012) Quantum Dots: Optics, Electron Transport, and Future Applications. Cambridge University Press, Cambridge
8. Güçlü AD, Potasz P, Korkusinski M, Hawrylak P (2014) Graphene Quantum Dots. Springer, Berlin Heidelberg New York
9. Williams OA (2014) Nanodiamond. Royal Society of Chemistry, Cambridge
10. Louis C, Pluchery O (2012) Gold Nanoparticles for Physics, Chemistry and Biology. Imperial College Press, London
11. Cheng P (2015) Lanthanide Metal-Organic Frameworks. Springer, Berlin Heidelberg New York
12. Jung G (2012) Fluorescent Proteins I From Understanding to Design, Volume 11. Springer, Berlin Heidelberg New York
13. Cai W, Shalaev V (2010) Optical Metamaterials: Fundamentals and Applications. Springer, Berlin Heidelberg New York
14. Long N, Wong WT (2014) The Chemistry of Molecular Imaging. Wiley, Chichester
15. Abdel-Kader MH (2014) Photodynamic Therapy: From Theory to Application. Springer, Berlin Heidelberg New York
16. Gauglitz G, Moore DS (2014) Handbook of Spectroscopy, 4 Volume Set, 2 edn. Wiley-VCH, Weinheim
17. Lim SY, Hong KH, Kim DI, Kwon H, Kim HJ (2014) Tunable Heptamethine-Azo Dye Conjugate as an NIR Fluorescent Probe for the Selective Detection of Mitochondria Glutathione over Cysteine and Homocysteine. J Am Chem Soc 136:7018–7025
18. Lukinavičius G, Umezawa K, Olivier N, Honigmann A, Yang G, Plass T, Mueller V, Reymond L, Corrêa Jr IR, Luo ZG, Schultz C, Lemke E, Heppenstall P, Eggeling C, Manley S, Johnsson K (2013) A Near-Infrared Fluorophore for Live-Cell Super-Resolution Microscopy of Cellular Proteins. Nat Chem 5:132–139
19. Narain R (2014) Chemistry of Bioconjugates: Synthesis, Characterization, and Biomedical Applications. John Wiley and Sons Ltd, Hoboken, New Jersey
20. Zhang T, Lan R, Chan CF, Law GL, Wong WK, Wong KL (2014) In vivo Selective Cancer-Tracking Gadolinium Eradicator as New-Generation Photodynamic Therapy Agent. Proc Natl Acad Sci U S A 111:E5492–E5497
21. Ntziachristos V (2006) Fluorescence molecular imaging. Annu Rev Biomed Eng 8:1–33
22. Hälmninen P, Härmä H (2011) Lanthanide Luminescence Photophysical, Analytical and Biological Aspects. Springer, Berlin Heidelberg New York
23. Zheng W, Huang P, Tu D, Ma E, Zhu H, Chen X (2015) Lanthanide-Doped Upconversion Nano-Bioprobes: Electronic Structures, Optical Properties, and Biodetection. Chem Soc Rev 44:1379–1415
24. Zhou J, Liu Q, Feng W, Sun Y, Li F (2015) Upconversion Luminescent Materials: Advances and Applications. Chem Rev 115:395–465

25. Yang Y, Shao Q, Deng R, Teng X, Wang C, Cheng K, Cheng Z, Huang L, Liu Z, Liu X, Xing B (2012) In Vitro and In Vivo Uncaging and Bioluminescence Imaging through Photocaged Upconversion Nanoparticles. Angew Chem Int Ed 51:3125–3129
26. Helmchen F, Denk W (2005) Deep Tissue Two-Photon Microscopy. Nat Methods 2:932–940
27. Maldiney T, Scherman D, Richard C (2012) Persistent Luminescence Nanoparticles for Diagnostics and Imaging, Ch 1. In Functional Nanoparticles for Bioanalysis, Nanomedicine, and Bioelectronic Devices Volume 2. January 1, 1–25
28. Hölsä J (2009) Persistent Luminescence Beats the Afterglow: 400 Years of Persistent Luminescence. The Electrochem Soc Interface, Winter
29. Yen WM, Shionoya S, Yamamoto H (2007) Phosphor Handbook, 2 edn. CRC Press/Taylor and Francis: Boca Raton
30. Furetta C (2009) Handbook of Thermoluminescence, 2 edn. World Scientific Co Pte Ltd, Singapore
31. Jaffe HH, Miller AL (1966) The fates of electronic excitation energy. J. Chem. Educ. 43:469-473
32. Zhu G, Shi Y, Mikami M, Shimomura Y, Wang Y (2014) Electronic structure and photo/cathodoluminescence properties investigation of green emission phosphor $NaBaScSi_2O_7$:Eu^{2+} with high thermal stability. CrystEngComm 16:6089–6097
33. Zhang Y, Hao J (2013) Metal-ion doped luminescent thin films for optoelectronic applications. J. Mater. Chem C 1:5607–5618
34. Ronda C (2008) Luminescence: From Theory to Applications. Wiley-VCH, Weinheim
35. West AR (2014) Solid State Chemistry and Its Applications, 2 edn, student edn. Wiley, Chichester
36. Van den Eeckhout K, Smet PF, Poelman D (2010) Persistent Luminescence in Eu^{2+}-Doped Compounds: A Review. Materials 4:2526–2566
37. Matsuzawa T, Aoki Y, Takeuchi N, Murayama Y (1996) A new long phosphorescent phosphor with high brightness, $SrAl_2O_4$: Eu^{2+}, Dy^{3+}. *J Electrochem Soc* 143:2670–2673
38. Aitasalo T, Deren P, Hölsä J, Jungner H, Krupa JC, Lastusaari M, Legendziewicz J, Niittykoski J, Strek W (2003) Persistent luminescence phenomena in materials doped with rare earth ions. J Solid State Chem 171:114–122
39. Dorenbos P (2005) Mechanism of persistent luminescence in Eu2+ and Dy3+ codoped aluminate and silicate compounds. J Electrochem Soc 152:H107–H110.
40. Clabau F, Rocquefelte X, Jobic S, Deniard P, Whangbo MH, Garcia A, Le Mercier T (2005) Mechanism of phosphorescence appropriate for the long-lasting phosphors Eu2+-doped SrAl2O4 with codopants Dy3+ and B3+. Chem. Mat. 17:3904–3912
41. Clabau F, Rocquefelte X, Jobic S, Deniard P, Whangbo MH, Garcia A, Le Mercier T (2007) On the phosphorescence mechanism in SrAl2O4:Eu2+ and its codoped derivatives. Solid State Sci 9:608–612
42. Chen B, Hao HC, Zhu J, Lu M (2011) A Phenomenological Model for Decay Process of Long Persistent Phosphorescence. Chin Phys Lett 28(5):053201
43. Belsky A, Ivanovskikh K, Vasil'ev A, Joubert MF, Dujardin C (2013) Estimation of the Electron Thermalization Length in Ionic Materials. J Phys Chem Lett 4:3534–3538
44. Caratto V, Locardi F, Costa GA, Masini R, Fasoli M, Panzeri L, Martini M, Bottinelli E, Gianotti E, Miletto I (2014) NIR Persistent Luminescence of Lanthanide Ion-Doped Rare Earth Oxycarbonates: The Effect of Dopants. ACS Appl Mater Interfaces 6:17346–17351
45. Van den Eeckhout K, Poelman D, Smet PF (2013) Persistent Luminescence in Non-Eu^{2+}-Doped Compounds: A Review. Materials 6:2789–2818
46. Li Y, Zhou S, Li Y, Sharafudeen K, Ma Z, Dong G, Peng M, Qiu J (2014) Long Persistent and Photo-Stimulated Luminescence in Cr^{3+}-Doped Zn-Ga-Sn-O Phosphors for Deep and Reproducible Tissue Imaging. J Mater Chem C 2:2657–2663
47. Pan Z, Lu YY, Liu F (2012) Sunlight-Activated Long-Persistent Luminescence in the Near-Infrared from Cr^{3+}-doped Zinc. Nat Mater 11(1):58–63

48. Maldiney T, Richard C, Seguin J, Wattier N, Bessodes M, Scherman D (2011) Effect of core diameter, surface coating, and PEG chain length on the biodistribution of persistent luminescence nanoparticles in mice. ACS Nano 5(2):854–862

49. Katayama Y, Ueda J, Tanabe S (2014) Effect of Bi_2O_3 doping on persistent luminescence of $MgGeO_3$: Mn^{2+} phosphor. Opt Mater Express 4:613–623

50. Lecointre A, Bessière A, Bos AJJ, Dorenbos P, Viana B, Jacquart S (2011) Designing a red persistent luminescence phosphor: the example of YPO_4:Pr^{3+}, Ln^{3+} (Ln=Nd, Ho, Dy). J Phy Chem C 115:4217–4227

51. Kimata M (1983) The structural properties of synthetic Sr-akermanite, $Sr_2MgSi_2O_7$. Z. Kristallogr. 163:295–304

52. Singh SK (2014) Red and near infrared persistent luminescence nano-probes for bioimaging and targeting. RSC Adv 4:58674–58698.

53. Van den Eechkout K, Bos AJJ, Poelman D, Smet PF (2013) Revealing trap depth distributions in persistent phosphors. Phys Rev B 87:045126

54. Rodrigues LCV, Hölsä J, Lastusaari M, Felinto MCFC, Brito HF (2014) Defect to R^{3+} energy transfer colour tuning of persistent luminescence in $CdSiO_3$. J Mater Chem C 2:1612–1618

55. Maldiney T, Lecointre A, Viana B, Bessière M, Courier D, Ricard C, Scherman D (2011) Controlling electron trap depth to enhance optical properties of persistent luminescence nanoparticles for in vivo imaging. J Am Chem Soc 133:11810–11815

56. le Masne de Chermont Q, Chanéac C, Seguin J, Pellé F, Maîtrejean S, Jolivet J-P, Gourier D, Bessodes M, Scherman D (2007) Nanoprobes with near-infrared persistent luminescence for in vivo imaging. Proc Natl Acad Sci U S A 104:9266–9271

57. Maldiney T, Bessière A, Seguin J, Teston E, Sharma SK, Viana B, Bos AJJ, Dorenbos P, Bessodes M, Gourier D, Scherman D, Richard C (2014) The in vivo activation of persistent nanophosphors for optical imaging of vascularization, tumors and grafted cells. Nat Mater 13:418–426

58. Li X, Li Y, Han Y, Pan W, Zhang T, Tang B (2014) A Highly Selective and Instantaneous Nanoprobe for Detection and Imaging of Ascorbic Acid in Living Cells and In Vivo. Anal Chem 86:3924–3930

59. Wu BY, Wang HF, Chen JT, Yan XP (2011) Fluorescence Resonance Energy Transfer Inhibition Assay for α-Fetoprotein Excreted during Cancer Cell Growth Using Functionalized Persistent Luminescence Nanoparticles. J Am Chem Soc 133:686–688

60. Paterson AS, Raja B, Garvey G, Kolhatkar A, Hagström AEV, Kourentzi K, Lee TR, Willson RC (2014) Persistent Luminescence Strontium Aluminate Nanoparticles as Reporters in Lateral Flow Assays. Anal Chem 86:9481–9488

61. Maldiney T, Ballet B, Bessodes M, Scherman D, Richard D (2014) Mesoporous persistent nanophosphors for in vivo optical bioimaging and drug-delivery. Nanoscale 6:13970–13976

62. Chen W, Zhang J (2006) Using Nanoparticles to Enable Simultaneous Radiation and Photodynamic Therapies for Cancer Treatment. J Nanotec Nanosci 8:1159–1166

63. Chen DQ, Chen Y, Lu HW, Ji ZG (2014) A bifunctional Cr/Yb/Tm:$Ca_3Ga_2Ge_3O_{12}$ phosphor with near-infrared long-lasting phosphorescence and upconversion luminescence. Inorg Chem 53:8638–8645

64. Abdukayum A. Chen JT, Zhao Q, Yan XP (2013) Functional near infrared-emitting Cr^{3+}/Pr^{3+} co-doped zince gallogermanate persistent luminescent nanoparticles with superlong afterglow for in vivo targeted bioimaging. J Am Chem Soc 135:14125–14133

65. Li G, Wang Y, Zeng W, Chen W, Han S, Guo H (2015) Luminescent and magnetic properties of the afterglow phosphors GdSr2AlO5:RE3+ (RE3+ = Eu3+, Pr3+ and Dy3+). RSC Adv 5:20884–20889

66. Domínguez JF, Egan GF, Gray MA, Poudel GR, Churchyard A, Chua P, Stout JC, Georgiou-Karistianis N (2013) Multi-modal neuroimaging in premanifest and early Huntington's deases: 18 month longitudinal data from the IMAGE-HD study. PLOS one 8 (9):e74131

Chapter 12
Upconversion Nanoparticles
for Bioimaging

Xiangzhao Ai, Junxin Aw and Bengang Xing

Abstract Rare earth lanthanide-doped upconversion nanoparticles (UCNPs), which can nonlinearly convert long wavelength near-infrared (NIR) light illumination into multiplex emissions, have been widely used in biomedical applications for in vitro and in vivo biolabeling and optical data storage based on their controllable multicolor emission properties. Compared to the traditional used downconversion fluorescence imaging strategies, such NIR light-excited luminescence of UCNPs displays low cytotoxicity and high photostability with little background auto-fluorescence. In this way, it therefore allows for deep tissue penetration, making them attractive as promising contrast agents for biological sensing, biomedical imaging, and diseases theranostics. In this chapter, we mainly place our attention on the recent development of new type of lanthanide-doped UCNP nanomaterials for their in vitro and in vivo bioimaging applications and we also highlight some key challenges for future biomedical studies.

12.1 Introduction

In recent years, there is a new breakthrough in molecular imaging technology that enables various people coming from different fields to perform in vivo study in living animal through a noninvasive manner by monitoring its biological process and cellular functions. Generally, the application of this new method will help in deducing numerous important insights within an organism under physiological events under single cell and/or molecular levels. This enables the diagnosis of various diseases which include cancers, neurological disorders, and heart disease [1–8]. Hence, molecular imaging provides as a very useful tool for many biomedical applications toward the monitoring of therapy intervention and the

X. Ai · J. Aw · B. Xing (✉)
Division of Chemistry and Biological Chemistry, School of Physical
and Mathematical Sciences, Nanyang Technological University,
21 Nanyang Link, Singapore 637371, Singapore
e-mail: Bengang@ntu.edu.sg

early-stage disease diagnosis [1–5]. Generally, it can be further classified into different specialities based on their imaging mechanism, applied imaging contrast agents, and detection instrumentation. These imaging methods include computed tomography (CT), optical imaging, magnetic resonance imaging (MRI), single photon emission tomography (SPECT), ultrasound imaging, and positron emission tomography (PET) [1–8].

Among these different groups of imaging modalities, optical imaging is one of the most commonly applied techniques for in vitro and in vivo studies as they allow a simple and direct method for specific molecular target observations through using fluorescent and bioluminescence imaging. Fluorescent imaging relies mainly on the emission of light from various fluorochromes by using appropriate irradiation of light sources at a suitable wavelength. On the other hand, bioluminescence imaging depends mainly on the endogenous light emission from a group of different living organisms and these include bacteria luciferases, eukaryotic firefly luciferases, and Renilla (sea pansy) luciferases [9, 10].

Lately, there has been an increasing amount of biomedical research that used common fluorochromes such as fluorescein, coumarin, boron-dipyrromethene (BODIPY), rhodamine, and their respective analogs for in vitro biosensing and imaging purposes [11–21]. Furthermore, organic fluorophores that emit wavelength in the near-infrared (NIR) region have also been used in this purpose, in which squaraine dyes, phthalocyanines derivatives, and cyanine dyes have been extensively employed for in vivo cell trafficking [12], noninvasive gene expression [11] enzyme activities identifications [13–21], early stage of disease diagnosis [22, 23], and new therapeutic development in living system, owing to the reduced light-scattering effect, minimal auto-fluorescence, and relatively high tissue penetration. Despite being a widely studied and applied strategy, the use of NIR organic dye often contains certain issues which consist of limited quantum yield, short lifetime, a short stoke shift, and poor photostability [17–21]. Hence, there is a need for the development of alternative long-emission materials which would improve the current photophysical properties.

In the past decades, there has been a rising interest in biomedical research toward using nanomedicine and diagnostic imaging as a valuable platform for the investigation of different aspects of pharmacokinetics profiles, biodistribution, and various therapeutic effects of nanoconjugates [15] through real-time imaging. Quantum dots (QDs) have been widely studied as an important nanomaterial for many optical imaging purposes [24–31]. In general, QDs are known to be mono-dispersing inorganic fluorescent nanocrystals that displayed superior optical properties than most organic fluorophores mainly owing to its semiconductor material components [11–21]. The improved optical property obtained from QDs includes higher quantum yields, a longer fluorescent half-life (>10 ns), higher molar extinction coefficients, continuous absorption spectra ranging from UV to NIR, narrow emission spectra, and a longer effective stoke shifts. Till to date, the development of QDs has been widely expanded in the biomedical fields and bio-nanotechnology as an effective multiplexed biosensor and labeling, selective gene or drug delivery, and in vitro or in vivo biological imaging [24–31]. Despite the promising features and

initial success in using QDs as an effective biosensing tool, the application of this nanotechnology into living study is often limited by the toxicity of Cd^{2+} present in QDs [27–31]. Thus, the request to search for a stable, non-toxic and a longer wave irradiation for better tissue penetration in replacement for a high quantum yield is highly desired but remains as a big arduous goal.

Recently, there has been a rise in interest in the area of using rare earth lanthanide-doped upconversion nanoparticles (UCNPs) to perform molecular imaging as it displays good biocompatibility and serves as a promising vector for biosensing and imaging due to their unique photon-upconverted properties. Upon NIR irradiation (e.g., at 980 nm) to UCNPs, the nanostructure will convert it into a broad range of spectrum ranging from UV to NIR region [32, 33]. This resulted in a nonlinear optical upconversion process (Fig. 12.1), which is vastly
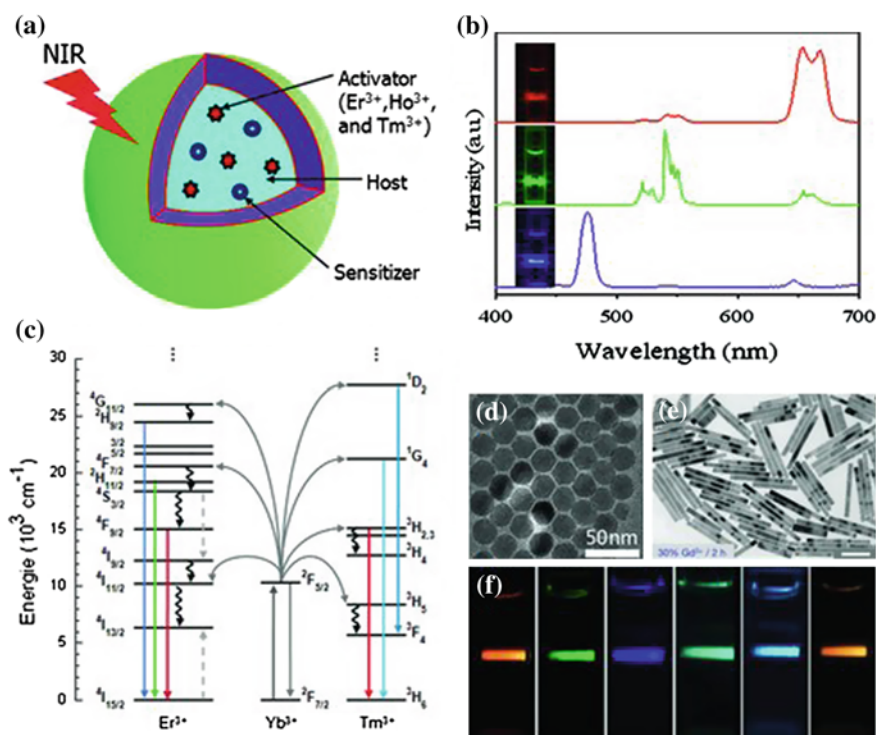

Fig. 12.1 Structure and optical properties of UCNPs: **a** Scheme illustration of the structure and components of the UCNPs. **b** Typical emission spectra of Yb/Er(Tm) co-doped $NaYF_4$ UCNPs. *Inset* Their corresponding luminescent photographs under 980-nm NIR excitation. **c** Proposed energy transfer mechanisms exhibiting the upconversion processes in Er^{3+}, Tm^{3+}, and Yb^{3+}-doped crystals under 980-nm excitation. TEM images of monodisperse **d** $NaYF_4$:Yb/Er nanoplates and **e** Gd^{3+}-doped $NaYF_4$:Yb/Er nanorods. **f** Multicolor fine-tuning through the use of $GdVO_4$ UCNPs with different dopant ions or varying dopant ratios. Reproduced from Ref. [39] with the permission of John Wiley & Sons Ltd

different from the downconversion forms of QDs and traditional organic fluorescent dye [34–37]. The numerous benefits using UCNPs include narrow bandwidth emission, high photostability, a long fluorescence lifetime, and high resistance to photobleaching [38–42]. In addition, it displays lesser auto-fluorescence with minimum light scattering, which allows a deep tissue penetration and thus makes UCNPs function as an attractive optical contrast agent for numerous biosensing and imaging applications both in vitro and in vivo. By doping the UCNPs with different elements such as Gd^{3+} and Sm^{3+}, it will enable the nanostructures to display multimodality imaging characteristic and these include CT, SPECT, MRI, PET, and photoacoustic imaging (PAI) [43].

There have been numerous review articles that emphasize the synthesis [34, 35], bioapplications [38, 43], and photophysical properties of the UCNPs [13–31]. In this chapter, we aim to summarize some of the latest breakthroughs in UCNPs for molecular imaging, their possible future challenges, and some of the perspectives that UCNPs can bring in biosensing and biomedical imaging in vitro and in vivo.

12.2 Synthesis, Characterization, Surface Modification, and Biocompatibility of Lanthanide UNCPs

The general components of UCNPs are basically composed of a host matrix doped with a sensitizer (light absorbers) together with an activator (light-emitting ions) [34, 35] (Fig. 12.2). The rare earth ion especially Ln^{3+} is commonly used as an activator due to their ladder-like arranged energy level that enables the promotion of

Fig. 12.2 Examples of nanomaterials and their functional groups modified on surfaces for biological applications. Reproduced from Ref. [27] with the permission of The Royal Society of Chemistry
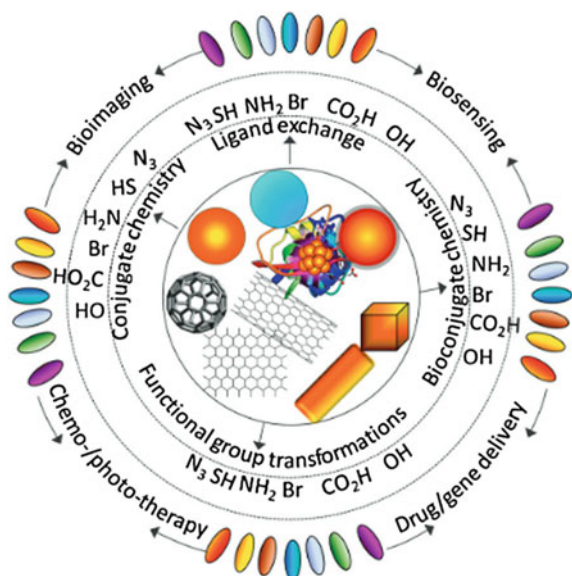
energy (upconversion) caused by the absorption of multiple photons. In most synthesis, the host materials normally comprise close lattice which matches to low phonon energies of dopant ions. Due to this reason, rare earth fluorides such as binary REF_3 and complex $AREF_4$ (RE = rare earth, A = alkali), including $NaGdF_4$, $NaYF_4$, KYF_4, $NaLuF_4$, LaF_3, $NaYbF_4$, $KMnF_3$, CaF_2, $KGdF_4$, and YF_3, is one of the most commonly used host components for UCNP preparation [34, 35, 38].

The size distribution and morphology of UCNPs will be the key factors responsible for the effective bioimaging applications. Currently, some existing methods have been well documented for the preparation of UCNPs with uniform shape (nanorods, nanospheres, nanoplates, nanotubes, etc.) and suitable size distribution (ranging from sub-10 nm to submicrometer). Most of the UCNPs have been well prepared on the basis of the methods including thermal decomposition [33, 44–49], hydrothermal synthesis [50–54], co-precipitation [55], sol-gel processing, etc. [56–60]. Among these methods that have been used, hydrothermal synthesis and thermal decomposition are among the most popular strategies toward the fabrication of UCNPs [34, 35, 40–43].

Besides the suitable size distribution and uniform morphology of UCNPs which are crucial factors for their promising biological applications, the surface properties will be another key important factor that must not be overlooked. Among all the efforts that have been made to fabricate UCNPs, one will realize that most of their surfaces are coated mainly with hydrophobic ligands which include oleic acid (OA), adamantine-acetic acid (Ad), and oleylamine (OM). These types of coating generally decrease the overall solubility of the biological buffer or aqueous solution. Therefore, it is essential to perform further surface modification in order to improve the solubility, hence biocompatibility of UCNPs for potential biomedical applications. To this end, a variety of strategies have been reported that mostly employ functional polymers (e.g., in particular polyethylene glycol (PEG)) [61], silica [62], peptide sequences [63], and other biomolecules [64], to functionalize UCNPs with methods of ligand exchange [65, 66], ligand removal [67, 68], ligand oxidation [69, 70], layer-by-layer assembly [71, 72], silica coating [62, 73, 74], or amphiphilic polymer coating, etc. [34, 35, 38, 75, 76]. These strategies have been successfully applied in improving the solubility, chemical stability, and biocompatibility and importantly to provide optimal reaction sites for further bioconjugation. And as shown in Fig. 12.2, most of surface modifications of UCNPs will be based on $-N_3$, $-NH_2$, $-SH$, and $-COOH$ groups, which can easily achieve more effective and convenient bioconjugation on the surface of UCNPs to improve its biocompatibility for more biomedical applications.

The importance of biocompatibility for UCNPs could not be further emphasized as it is a critical factor that determines the extents of its biological applications [77]. Hence, there is a need to address the biocompatibility and potential toxicity in using both in vitro and in vivo studies. To this point, there has been a considerable amount of efforts performed for in vitro and in vivo experiments toward the evaluation of the cytotoxicity of UCNPs by using the MTT (methyl thiazolyl tetrazolium) assay, CKK-8 assays (Cell Counting Kit-8 mitochondrial metabolic activity assays), and MTS assay [3-(4,5-dimethylthiazol-2-yl)-5-(3-carboxymethoxyphenyl)-2-(4-sulfophenyl)-

2H-tetrazolium, sodium salts] [64, 78, 79]. Most of these results suggested a negligible cytotoxicity effect from the surface-modified UCNPs with different types of ligands or the biocompatible-coating molecules at the cellular levels. Moreover, extensive efforts have been performed for in vivo studies so as to evaluate the long-term effects and toxicity of UCNPs in different living systems such as *Caenorhabditis elegans* (*C. elegans*) worms [80], zebrafish embryos [81], and mice [64]. For instance, in vivo results on *C. elegans* has demonstrated that the UCNPs prepared by homogenous precipitation in aqueous solution of $Y(NO_3)_3 \cdot 6H_2O$ (50 mM), $Yb(NO_3)_3 \cdot 5H_2O$ (1 mM), $Er(NO_3)_3 \cdot 5H_2O$ (0.5 mM), and urea (15 mM) did not reveal any significant toxicity when the concentration is up to 10 mg/mL [80]. Further toxicity evaluation in mice was also conducted through body measurement, behavior observation, hematology analysis, histology, and serum biochemistry assay. Similarly, the toxicity studies have also been performed based on polyacrylic acid (PAA)-coated $NaYF_4$: Yb/Tm, which confirmed that there was no obvious toxicity with a dose administration up to 15 mg/kg in living mice for approximately 3 months [64]. Latest studies also demonstrated a good biocompatibility and very low toxicity of Gd/Mn-doped $NaYF_4$: Yb/Er in mice. The survival rates for the mice were found to be 100 % for thirty days after injection. The inductively coupled plasma mass spectrometry (ICP-MS) analysis further revealed the Gd^{3+}/Mn^{2+} ions confined in a rigid matrix of host UCNPs nanocrystals, which could not be easily released into the living environments that help in minimizing their potential cytotoxicity [54].

12.3   Lanthanide UCNPs for Optical Imaging

Upon the surface modification for superior biocompatibility and less cytotoxicity, UCNPs demonstrated great potentials for their promising applications in biomedical imaging, mainly attributed to their unique optical properties, which can be excited with long wavelength NIR light from 795 to 980 nm. This long wavelength light illumination can be converted into multiplexed emissions with a broad range from the UV to NIR region [32–35]. Such unique optical properties offer an ideal opportunity for noninvasively visualizing biological distribution and real-time imaging of biological processes in deep tissue. As promising contrast agents for molecular imaging in vitro and in vivo, UCNPs demonstrated more intrinsic advantages compared to those conventionally used organic dyes such as narrow-bandwidth emission, a long lifetime, tunable emission, high photostability, and high resistance to photobleaching. With the excitation of NIR light, the emitted light from the UV to NIR region can be applied for multicolor imaging [38, 39]. Among the various converted emissions, NIR-to-NIR (using NIR excited light to emit NIR light)-based UCNP luminescence imaging has gained increasing attention, as both the excitation and the emission NIR light can penetrate the "optical transmission window" of tissues (700–1000 nm) [82], thus providing a direct powerful tool for visualizing the biodistribution of UCNPs in vivo.

Basically, in the process of biological imaging on the basis of lanthanide-doped UCNP nanomaterials, three main aspects have been classified which include non-specific targeting imaging, active targeting imaging, and activatable imaging, mostly based on the reaction mechanism of the UCNP-based imaging probes and their related biological targets in vitro and in vivo. For example, nonspecific targeting imaging studies based on UCNPs clearly demonstrated that 50 nm of NaYF$_4$:Yb/Er UCNPs could be employed for in vivo imaging in anesthetized Wistar rats (Fig. 12.3) after the rats were subjected to direct injection of nanoparticles under the skin in the groin and upper leg regions [83]. Upon 980 nm NIR laser irradiation, the nanoparticles could be detected up to 10 mm beneath the skin, far deeper than depth through the use of QDs. These results provided promising examples for in vivo optical imaging at a deeper tissue level for performing minimal invasive imaging in real time. With the superiority of the deep penetration of their emitted light, the NaYF$_4$:Yb/Er UCNPs doped with 30 mol% Mn^{2+} ions and KMnF$_3$ UCNPs doped with Yb/Er, Yb/Ho or Yb/Tm have also been applied for NIR-to-NIR single-band luminescence imaging [54]. So far, Tm^{3+}-doped NaYF$_4$,
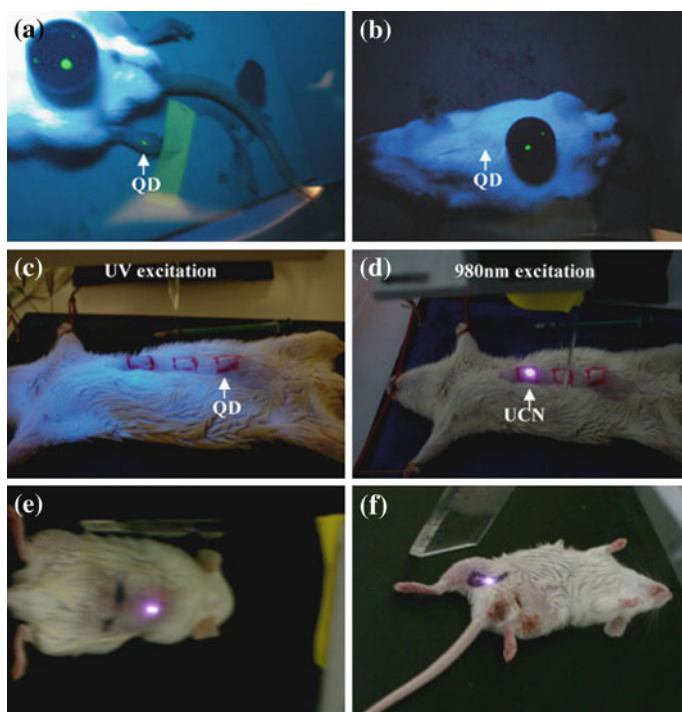

Fig. 12.3 In vivo imaging of rat: Quantum dots (QDs) injected into translucent skin of foot (**a**) show fluorescence, but not through thicker skin of back (**b**) or abdomen (**c**); PEI/NaYF$_4$:Yb/Er nanoparticles injected below abdominal skin (**d**), thigh muscles (**e**), or below skin of back (**f**) show luminescence. QDs on a black disk in (**a**, **b**) are used as the control. Reprinted from Ref. [83]. Copyright 2008, with the permission from Elsevier
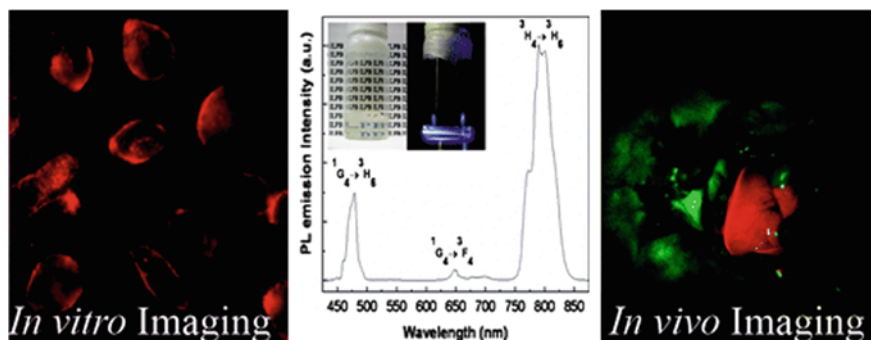
Fig. 12.4 In vitro (*left*) and in vivo (*right*) imaging with UCNPs. The *red* color indicates emission from UCNPs; *green* and *black* show the background. Reprinted with the permission from Ref. [78]. Copyright 2008 American Chemical Society

NaGdF$_4$, NaLuF$_4$, and NaYbF$_4$ UCNPs have been widely applied for nonspecific imaging in living animals [84–86]. Recently, Prasad et al. [78] also reported a new approach for in vivo imaging by using NaYF$_4$:Yb/Tm—UCNPs as photoluminescence imaging probes, with their promising light penetration depth up to ~20 mm in mouse (Fig. 12.4).

By employing sub-10-nm citric acid-capped NaLuF$_4$-based particles co-doped with Gd^{3+}, Yb^{3+} and Er^{3+} (or Tm^{3+}), the high-contrast imaging in living mouse would allow an excellent detection limit down to 50 and 1000 UCNPs-labeled cells after the subcutaneous and intravenous injections of these probes [87] (Fig. 12.5). Moreover, the nonspecific whole-body imaging based on polyacrylic acid (PAA)-coated NaYF$_4$:Yb/Tm (PAA-UCNPs) as luminescence probes for long-term in vivo distribution also showed that most of the PAA-UCNPs in the liver and the spleen would be cleared very slowly from the body through hepatobiliary excretion. Similarly, PAA-NaLuF$_4$:Yb/Tm UCNPs as optical contrast probes have also been used noninvasively imaging of black mouse and living rabbit with an excellent signal-to-noise ratio [88]. More recently, UCNP systems with surface-modified oligo-arginine sequences have also been applied for whole-body imaging at the single-cell level through ultra-sensitive stem cell labeling for long-term stem cell tracking. It was reported that as few as ~10 cells in a mouse could be detected with an ultra-high sensitivity when compared to the currently used exogenous stem cell-labeling nanoagents, such as QDs [89].

Although UCNPs display initial successful applications in living animal imaging, the nonspecific and biocompatible UCNPs lack reactive groups for selective recognition and further effective conjugation, which would be great barriers to hamper their extensive applications in biological imaging. To this direction, one simple and effective strategy to overcome the nonspecific targeting and to improve their selectivity for the target site in a living system is to connect the bioactive ligand moieties with the UCNPs, which would exhibit strong affinity to specific molecular targets. Thus, the ligand-mediated UCNP conjugates will be able to
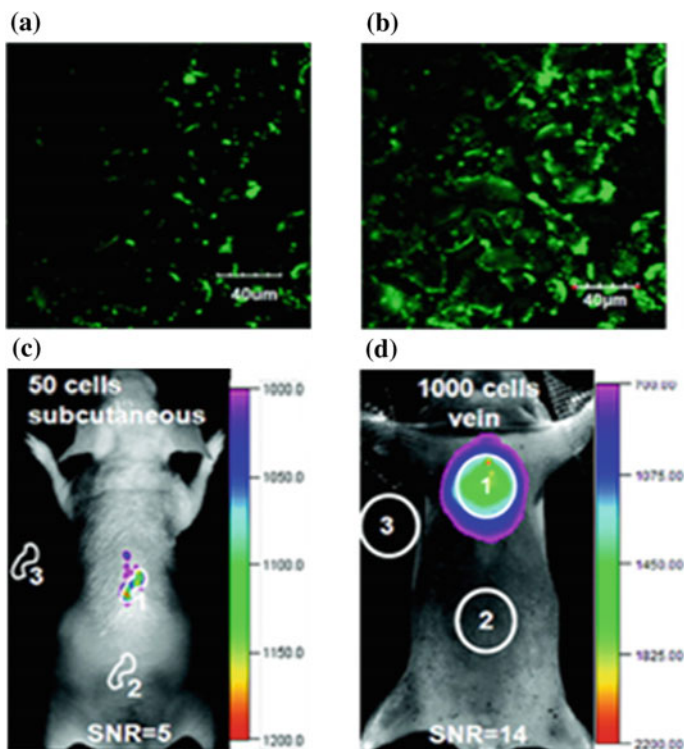
Fig. 12.5 **a** Confocal UCL image and **b** its overlay with a bright-field image of cells stained with 200 μg mL^{-1} cit-Lu6-Tm for 2 h at 37 °C (λex = 980 nm, λem = 450–490 nm). **c**, **d** In vivo UCL imaging of athymic nude mice after (**a**) subcutaneous injection of 50 KB cells and **d** vein injection of 1000 cells. The KB cells were incubated with 200 μg mL^{-1} cit-Lu6-Tm for 2 h. SNR = [(mean luminescence intensity of 1) − (mean luminescence intensity of 3)]/[(mean luminescence intensity of 2) − (mean luminescence intensity of 3)]. Reprinted with the permission from Ref. [87]. Copyright 2011 American Chemical Society

recognize the targets and can be easily trapped at the targeting region for a prolonged time. As control, the unbound UCNPs lack affinity within the specific region and will thereby result in limited accumulation during the circulation process. In general, most of the applied high-affinity ligand moieties include small organic molecules, peptides, proteins, antibodies, or their fragments [90]. Following are some representative examples for using the strategy of active targeting optical imaging via of ligand-modified UCNPs.

As a proof of concept, arginine-glycine-aspartic (RGD) peptide and folic acid-modified UCNPs are typical examples which have been used as affinity ligands for in vitro and in vivo tumor targeting [91, 92]. As demonstrated in Fig. 12.6, after tail vein injection of folic acid functionalized UCNPs into xenograft living mouse in which tumors have been implanted by subcutaneous injection of Hela cells (folate receptor overexpressed cell line), the obvious luminescence signal at 600–700 nm
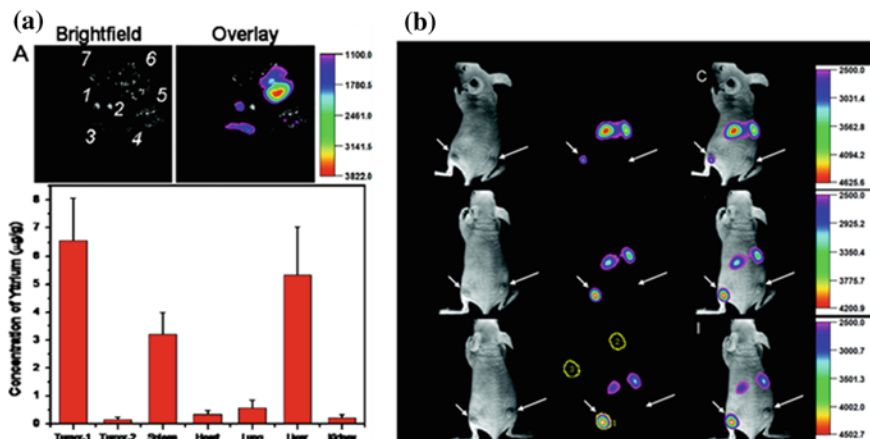
Fig. 12.6 a Representative images of dissected organs and particles biodistribution of a tumor-bearing mouse killed at the 24 h time point after intravenous injection of UCNP-RGD (power ≈ 50 mW/cm^2 and temperature ≈ 21.5 °C on the surface of the mouse). *1* U87MG tumor; *2* MCF-7 tumor; *3* spleen; *4* heart; *5* lung; *6* liver; *7* kidney. **b** Time-dependent in vivo upconversion luminescence imaging of subcutaneous U87 MG (left hind leg, indicated by *short arrows*) and MCF-7 (Michigan Cancer Foundation-7) tumor (right hind leg, indicated by *long arrows*) borne by athymic nude mice after intravenous injection of UCNP-RGD over a 24-h period. UCNP-RGD conjugate was prepared from UCNP-OA complex (OA: oleylamine). All images were acquired under the same instrumental conditions (power ≈ 80 mW/cm^2 and temperature ≈ 21.5 °C on the surface of the mouse). Reprinted with the permission from Ref. [92]. Copyright 2009 American Chemical Society

was clearly detected in the tumor, whereas no significant luminescence signals could be observed in the control group. In addition, similar RGD peptide-conjugated UCNPs could also effectively target the U87 Malignant Glioma (MG) human glioblastoma tumor with in vivo imaging in living animals. It has been well known that U87 MG human glioblastoma tumors could overexpress $\alpha_v\beta_3$ integrin receptors, which plays an important role in tumor angiogenesis and could be easily recognized by RGD sequences with high affinity [93–96]. The further in vivo imaging results also demonstrated that the neurotoxin-mediated upconversion nanoprobes for tumor targeting and visualization in living mice could produce a high-contrast image through their highly specific binding activity to tumors [97].

Furthermore, our recent studies demonstrated that UCNPs could be also applied for site-specific imaging of the targeted drug release in the folic acid receptor expressed HeLa cells upon particle surface modification with folic acid moiety [73] (Fig. 12.7). Basically, by capping the mesoporous silica-UCNPs with the cross-linked *o*-nitrobenzyl photoactivatable linker, the functionalized silica-coated core-shell UCNPs could act as photocaged nanocarriers to encapsulate the drug molecules within the mesopores silica structure. After loading with the antitumor drug, doxorubicin (Dox) and followed by a 980 nm NIR light irradiation, the
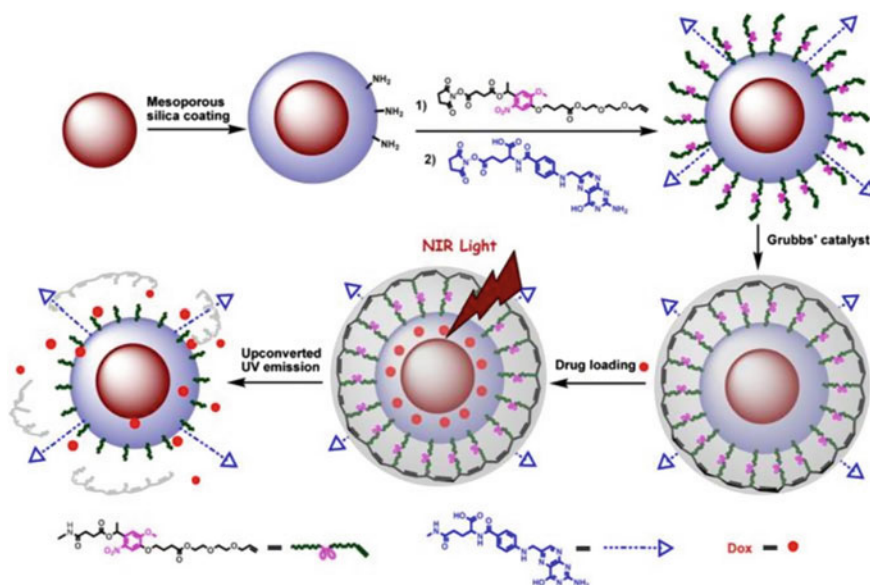
Fig. 12.7 Design for photocontrolled dox delivery through mesoporous silica-coated UCNPs conjugated with folic acid. Reproduced from Ref. [73] with the permission of John Wiley & Sons Ltd

cross-linked *o*-nitrobenzyl photoactive linker could be efficiently cleaved by the converted UV light from UCNPs, which therefore effectively triggered the photo-controlled drug release into the living cells.

Moreover, upon the functionalization of the photocaged nanocarriers with folic acid units, selective drug delivery can be easily achieved in the targeted tumor cells in which the folate receptor has been highly expressed. This novel and effective drug-loaded photocaged nanocarriers may demonstrate a new possibility for selective cell imaging and controlled drug release in living system with less pho-todamage and deeper light penetration. Similarly, in order to further improve the targeting selectivity, Yeh's group recently constructed an interesting NIR photo-controlled and folic acid caged strategy with UCNPs platform for targeted bioimaging and chemotherapy of cancer [98] (Fig. 12.8). Upon irradiation of 980-nm laser, the emitted UV light (360 nm) of UCNPs photocleaved the o-nitrobenzyl (ONB) photolabile cap, releasing cage molecules that allowed FA to target cancer cells subsequently. Moreover, DOX was thiolated on the surface of UCNPs to provide chemotherapeutic function in the cancer cells. The evidence of in vitro and in vivo imaging and chemotherapeutic efficacy supported that the caged UCNPs can serve as a unique platform for the improvement of selective targeting and reduction of adverse side effects from chemotherapy.

In terms of the selective recognition to the biological imaging targets in living system, a promising alternative strategy to effectively activate imaging specificity is
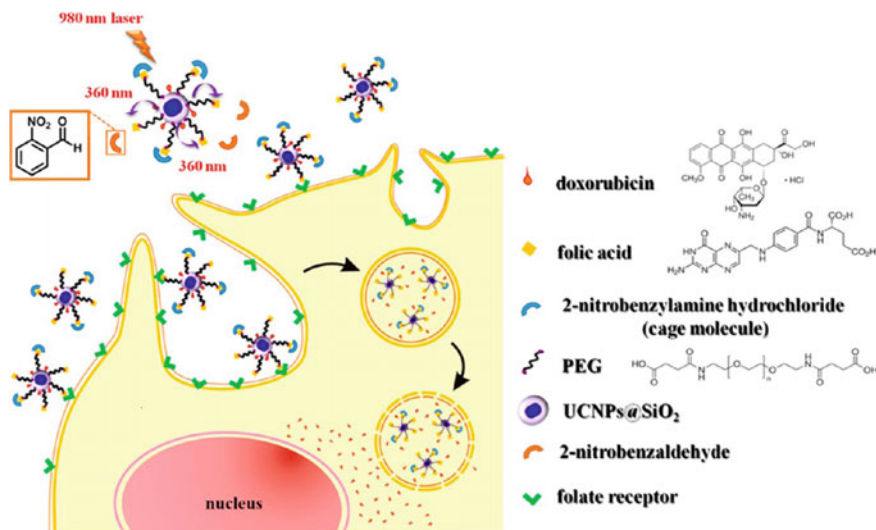
Fig. 12.8 Illustration of photocaged UCNPs following NIR laser activation to remove cage molecules and subsequent targeting of cancer cells. Upon irradiation of a 980-nm laser diode on UCNPs, the emitted UV light (360 nm) photocleaved the o-nitrobenzyl (ONB) photolabile group, releasing cage molecules that allowed FA to target FR. To provide chemotherapeutic function, doxorubicin (DOX) was thiolated on the surface of UCNPs, forming a disulfide bond that can be cleaved by lysosomal enzymes within the cells. Reprinted with the permission from Ref. [98]. Copyright 2013 American Chemical Society

to develop environmentally responsive targeting probes, which would rely on the controlled manipulation of the fluorescent output of UCNP platforms by changing their local chemical environments or structural conformations. On the basis of this process, the fluorescent signals could be generated or significantly amplified only after the particle-based nanoprobes have been specifically activated by an environmental stimulation.

Among the various strategies to respond to environmental stimulation, photolysis of photoactivatable or "caged" molecules has been well proven to be one effective strategy for the noninvasive regulation of biological activities and processes in living systems [99–102]. The activation process could be easily modulated by a beam of light with high spatial and temporal precision. In general, the active sites in targeted biological molecules were covalently modified with photolabile protecting groups (e.g., 2-nitrobenzyl derivatives, spiropyran, or diazobenzene moieties), which would keep these molecules at inactive stages before photolysis. Upon brief light irradiation, these photoactive protecting groups could be cleaved and the photocaged biological molecules would be released, thus recovering the intrinsic bioactivity [99–102]. So far, the photocaged activation strategies have been successfully applied as powerful tools to monitor biological processes and study their native functions in well-resolved space and time resolutions. However, most of photoactivatable compounds have been so far designed to mainly respond to UV

light irradiation and they could not be activated by visible or NIR light. In general, significant shortcomings have been found to associate with the utilities of the short wavelength of UV or visible light for photoactivation. For example, significant cellular damage in nucleic acids or proteins will present after excessive exposure to UV light. Meanwhile, the low penetration depth of short-wavelength UV or visible light could greatly limit their extensive applications for living animal imaging and the activation of the photocaged biomolecules in vivo. Therefore, the rational design of new photocaged strategies or alternative materials with higher tissue penetration depth but with limited biological damage would be highly significant. Considering the advantage of the promising properties of UCNPs which can transmit NIR to UV or visible light emission, lanthanide-doped nanoparticle systems have received significant attention which could work as suitable functional materials toward photoactivatable imaging in vitro and in vivo without worrying about the issues caused by direct UV or visible light irradiation.

As a proof-of-concept, we [62] have recently reported a simple and effective method for the controlled uncaging of D-luciferin and bioluminescence imaging on the basis of photocaged UCNPs, which takes advantage of the photon upconversion of NIR light to UV light to trigger the uncaging of D-luciferin from D-luciferin-conjugated UCNPs (Fig. 12.9). As the first example of photocaged imaging through UCNPs, the released D-luciferin effectively conferred enhanced fluorescence and bioluminescence signals in vitro and in vivo with deep light penetration and low cellular damage.
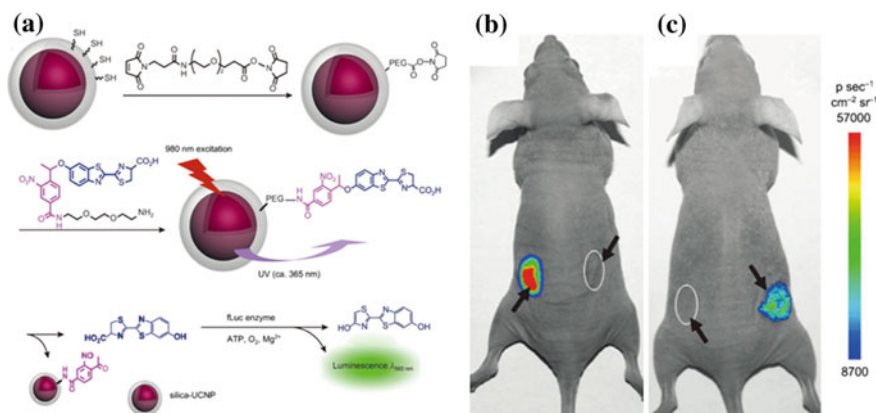

Fig. 12.9 Bioluminescent images of firefly luciferase (fLuc) activity in living mice that were treated with D-luciferin. **a** Experimental design for uncaging D-luciferin and subsequent bioluminescence through the use of photocaged core-shell upconversion nanoparticles. **b** *Left* injection with D-luciferin (20 μM, 20 μL); *right* injection with photocaged nanoparticles without NIR light irradiation. **c** *Left* injection with photocaged nanoparticles and irradiation with UV light for 10 min; *right* injection with photocaged nanoparticles and irradiation with NIR light for 1 h. Reproduced from Ref. [62] with the permission of John Wiley & Sons Ltd

Recently, we also demonstrated a novel and personalized near-infrared (NIR) light-activated prodrug nanoplatform through the combination of photoactivatable platinum(IV) prodrug and caspase-imaging peptide conjugated with silica-coated UCNPs for the remote control of antitumor platinum prodrug activation and real-time imaging of apoptosis induced by the activated cytotoxicity subsequently [103] (Fig. 12.10). After NIR light irradiation, the Pt(IV) prodrug complex could be activated from the surface of UCNPs and the selective release of active components could exhibit potent cytotoxicities against human ovarian carcinoma A2780 cells and their cisplatin-resistant variant A2780cis cells. More importantly, the systematic programmed cell death was also found to be involved in the NIR responsive tumor inactivation, and the triggered caspase enzymes would effectively cleave the recognition peptide sequence with a flanking fluorescent resonance energy transfer (FRET) pair consisting of NIR fluorophore, Cy5, and relevant quencher Qsy21, thereby allowing the direct imaging of apoptosis by separating Cy5 from Qsy21 quencher in vitro and in living cells. Such specific and
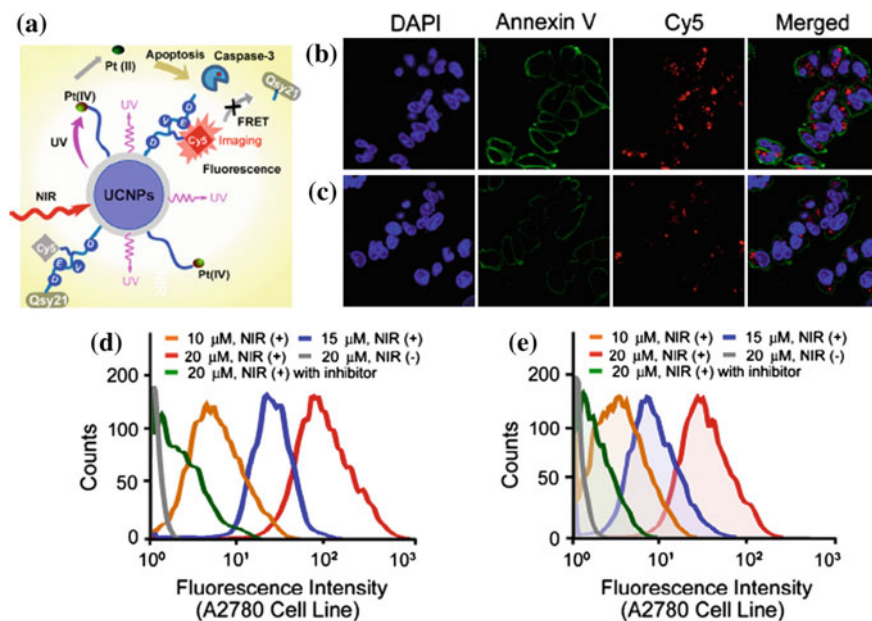

Fig. 12.10 Live cell apoptosis imaging for NIR irradiation of Pt(IV)-probe UCNPs@SiO$_2$ (15 μM) incubated cells: **a** schematic illustration of NIR light activation of platinum(IV) prodrug and intracellular apoptosis imaging through upconversion nanoparticles; **b** A2780 cells; and **c** cisplatin-resistant A2780cis cells. (*Blue*: DAPI (4,6-Diamidino-2-phenylindole); *green*: Annexin V; *red*: Cy5.) Quantitative flow cytometric analysis of **d** A2780 and **e** A2780cis cells treated with different concentrations of Pt(IV)-probe UCNPs@SiO$_2$ (10, 15, and 20 μM, respectively) and 1 h NIR irradiation. Cells treated with Ac-DEVD (aspartic acid–glutamic acid–valine-aspartic acid)–CHO (20 μM) inhibitor and NIR irradiation of cells without Pt(IV)-probe UCNP incubation were used as controls. Reproduced from Ref. [103] with the permission of John Wiley & Sons Ltd

novel rational design exhibited the promising opportunity to remotely control the activation of platinum drug in the targeted tumors. More importantly, it could also evaluate in real time the antitumor activities by imaging of apoptosis triggered from the photoactivated drug release, thus providing great potentials for personalized tumor therapeutic and diagnostic applications in the future.

Another strategy for the development of tumor environmentally responsive targeting probes would rely on the inner stimulation from cancer microenvironment moieties, such as relative oxygen species (ROS), pH, and temperature [104–106]. Among these moieties, overgeneration of ROS has been well known as an effective biomarker associated with the biological process of human disease. Recently, Qu et al. [104] developed a novel upconversion nanoprobe that utilizes polyvalent hyaluronic acid (HA) as a versatile ligand to engineer UCNPs (HA-UCNPs) for high sensitively sensing and bioimaging ROS in vitro and efficiently diagnosing rheumatoid arthritis (RA) in vivo (Fig. 12.11). The HA backbone labeled with
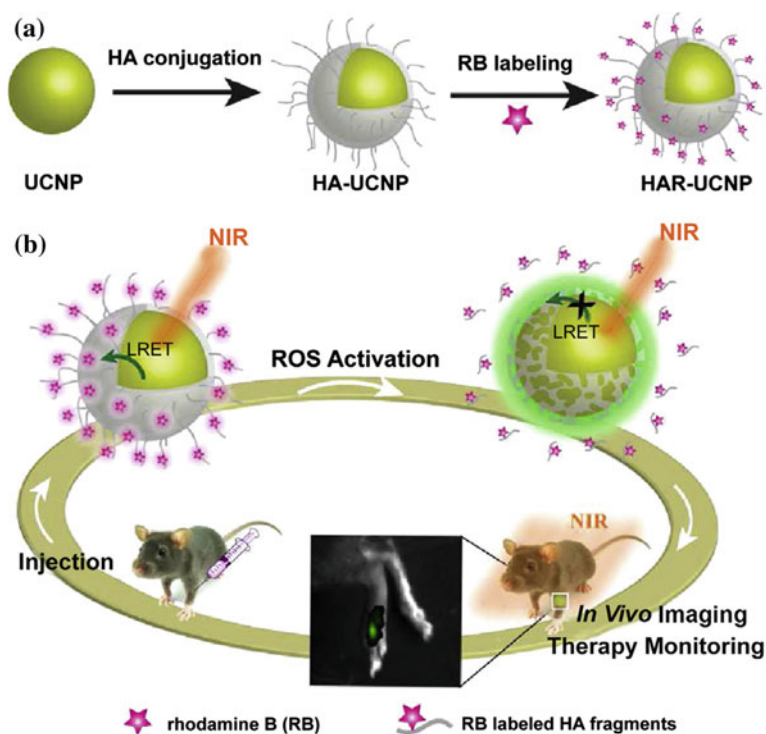

Fig. 12.11 Schematic illustration of HAR-UCNP nanoprobes for ROS imaging and rheumatoid arthritis diagnosing. **a** The conjugation of HA confers UCNPs not only water solubility but also biocompatibility and ROS recognizing properties. The functional groups on HA backbone are available for conjugation of upconversion luminescence acceptor chromophores. **b** The LRET process of HAR-UCNPs toward ROS for rheumatoid arthritis diagnosing and therapy monitoring. Reprinted from Ref. [104]. Copyright 2015, with the permission from Elsevier

rhodamine B can effectively cleaved and detached from UCNPs surface induced by ROS, which can inhibited the LRET and allow rational metric upconversion luminescence (UCL) emission as the detection imaging signal. Importantly, the upconversion nanoprobe showed high effectiveness for early evaluates the treatment response of arthritic animals to an antiarthritic drug methotrexate (MTX), which can work as a robust approach to provide pathological and medical intervention information for ROS involved disease diagnosis.

12.4 Doped Lanthanide UCNPs for Multimodality Imaging

In addition to applied optical imaging, UCNPs could be further developed as incorporate multiple modality imaging moieties for the integrated identification of specific biological pathways and anatomic structures under high-resolution properties, as well as real-time monitoring of physiological functions in living tissues. Upon doping or labeling biomedical elements, such as Gd^{3+}, ^{18}F, UCNPs could be extensively applied in multifunctional imaging not only through individual MRI, PET (photoinduced electron transfer), CT, SPECT, and photoacoustic (PA) imaging but also dual-modal or multi-modal techniques processes. For example, Li et al. [84] reported Gd^{3+}-doped UCNPs that could offer both T_1-weighted MRI contrast and optical imaging for in vivo dual-modal imaging in living mice. Dual-modal T_2-weighted MRI and fluorescent imaging through one unified platform was constructed by integrate UCNPs and super-paramagnetic iron oxide nanoparticles (IONP) as hetero-structures. In addition, Liu et al. [107] also developed a novel type of multifunctional nanoparticles based on UCNP@IONP@Au with combined optical and magnetic properties useful in dual-modal imaging and targeted photothermal tumor therapy in living subjects.

Dual-modal CT/optical imaging in vivo was also reported using lanthanide-doped $NaGdF_4$ UCNPs as effective contrast agents with both of the signals co-located well in the subcutaneous injection site in living mice [108]. PET and luminescent imaging of sentinel lymph node in different living animals was reported with ^{18}F-labeled $NaYF_4$:Yb/Tm UCNPs by Li et al. [109]. In this study, the UCNPs could be tracked in real time with high sensitivity based on the designed dual modality strategies in vivo from mice to large animals. Moreover, considering the potential issue of the short half-life of ^{18}F, another novel ^{153}Sm-labeled $NaLuF_4$:Yb/Tm UCNP through the hydrothermal synthesis strategy was developed in the same group for improved SPECT and fluorescent imaging of living animals. The half-life of ^{153}Sm (46.3 h) was found to be greatly enhanced [110], and the biological distribution of the ^{153}Sm-labeled $NaLuF_4$:Yb/Tm UCNPs had been well quantified in vivo by using the SPECT imaging technique which was consistent with the method done by fluorescent imaging (Fig. 12.12).
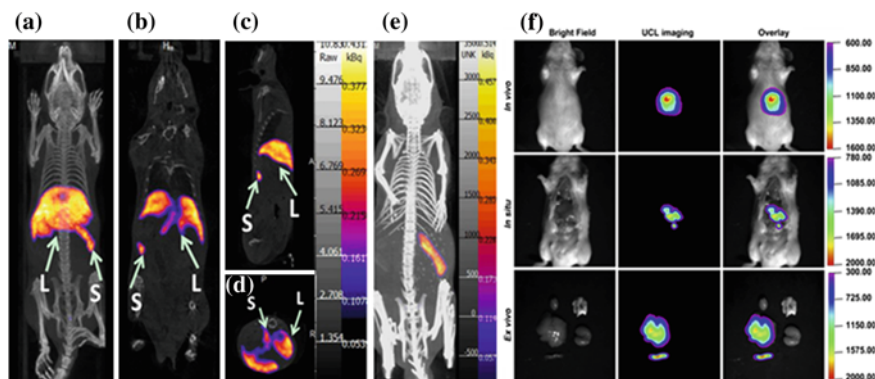
Fig. 12.12 In vivo single photon emission tomography (SPECT)/optical imaging study after intravenous injection of 153Sm-UCNPs. **a** Whole-body three-dimensional projection, **b** coronal, **c** sagittal, and **d** transversal images acquired at 1 h and **e** whole-body three-dimensional projection images acquired at 24 h are shown, respectively. The *arrows* in the *inset* point to the liver (L) and spleen (S). **f** In vivo upconversion luminescence imaging of the Kunming mouse 1 h after tail vein injection of the 153Sm-UCNPs (20 mg/kg). Reprinted from Ref. [110]. Copyright 2013, with the permission from Elsevier

Furthermore, multimodal imaging with doping different elements into lanthanide-based UCNPs structures could also be developed in recent years. For example, it is reported that the fabrication of ^{18}F-labeled NaGdF$_4$:Yb/Er UCNPs has been further used for PET/MRI/optical triple-modal imaging in vitro and in vivo [111]. Similarly, CT, MRI, and fluorescent imaging platform were proved by combination of Gd^{3+}-doped UCNPs with gold nanoparticles as multifunctional nanostructure in living mice. Moreover, a similar triple-modal imaging application was also reported on the basis of Gd^{3+} complex-modified NaLuF$_4$ core-shelled upconversion nanophosphors for CT, T$_1$-enhanced MRI, and NIR-to-NIR fluorescent imaging of tumor status in living subjects [85] (Fig. 12.13). The cell viability assay and histological analysis of viscera sections further confirmed the good biocompatibility and minimum biological toxicity of mixed UCNPs@SiO$_2$–Gd–DTPA (Diethylenetriaminepentaacetic acid) nanoparticle components in vitro and in vivo studies. Very recently, a promising hexamodal imaging strategy was reported based on porphyrin–phospholipid-coated UCNP platforms [112]. In this system, fluorescence and PA provided unique information on the self-assembly status of the particles, PET and CT provided the deepest imaging capabilities, and Cerenkov luminescence (CL) and upconversion imaging were effective for less invasive signal detection at intermediate depths substantially deeper than FL (Fig. 12.14). The contrast enhancement conferred to these diverse imaging methods shows that engineering simple yet higher-order multimodal imaging agents is feasible and potential useful for the development of hyper-integrated imaging systems.
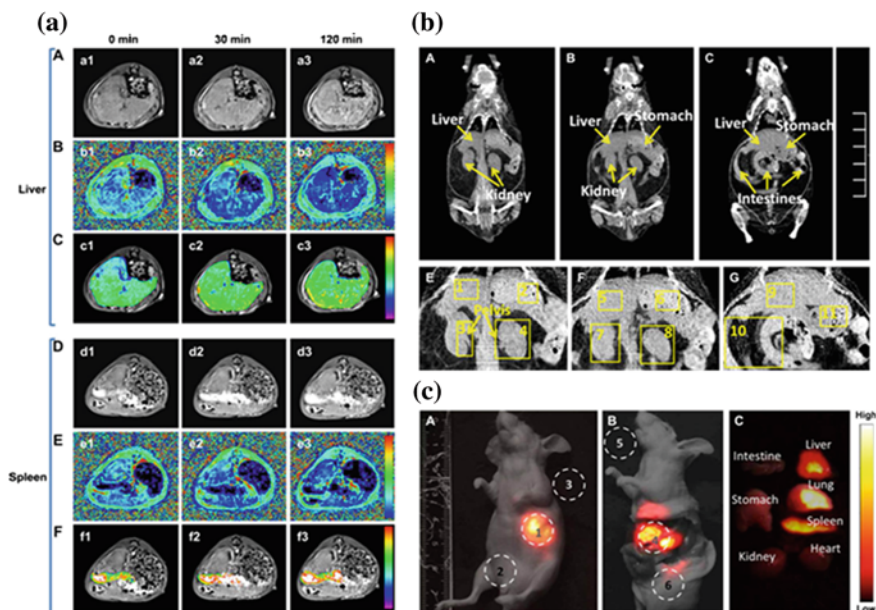
Fig. 12.13 (**a**) The application of in vivo MRI imaging of the Kunming mice. (**a**-*A*) T_1-weighted MR images of liver after injection with UCNPs@SiO$_2$–GdDTPA for 0, 30, and 120 mins. (**a**-*B*) T_1 distribution images of liver after injection with UCNPs@SiO$_2$–GdDTPA for 0, 30, and 120 min. (**a**-*C*) Local *colorized* T_1-weighted MR images of liver after injection with UCNPs@SiO$_2$–GdDTPA for 0, 30, and 120 mins. (**a**-*D*) T_1-weighted MR images of spleen after injection with UCNPs@SiO$_2$–GdDTPA for 0, 30, and 120 min. (**a**-*E*) T_1 distribution images of spleen after injection with UCNPs@SiO$_2$–GdDTPA for 0, 30, and 120 mins. (**a**-*F*) Local colorized T_1-weighted MR images of spleen after injection with UCNPs@SiO$_2$–GdDTPA for 0, 30, and 120 mins. **b** The application of in vivo CT imaging in Kunming mice. (**b**-*A*, *B*, and *C*) Serial coronal CT images of Kunming mouse at different layers after injection with UCNPs@SiO$_2$–GdDTPA. (**b**-*E*, *F*, and *G*) Partial enlarged CT view of abdomen. **c** A whole-body imaging of UCNPs@SiO$_2$–GdDTPA (diethylenetriaminepentaacetic acid) for 10 mins. (**c**-*A*) In vivo imaging of the killed nude mouse after injection with UCNPs@SiO$_2$–GdDTPA for 10 mins. (**c**-*B*) Ex vivo imaging of nude mouse. (**c**-*C*) Ex vivo imaging of viscera. All images were acquired under the same instrumental conditions, and the power density of the 980-nm laser is 150 mW/cm^2. Reprinted from Ref. [85]. Copyright 2012, with the permission from Elsevier

12.5 Summary

To sum up, this chapter highlighted some of the key developments of lanthanide-doped UCNPs for the past few years with the focus in the area of molecular imaging both in vitro and in vivo. By integrating the use of 980- or 808-nm-long wavelengths through the proper modification on the surface of the nanoparticles, the UCNPs have been proven to be beneficial for real-time imaging of biological processes with deep penetration depth with minimum cytotoxicity. The unique chemical properties and luminescent features of UCNPs offer promising
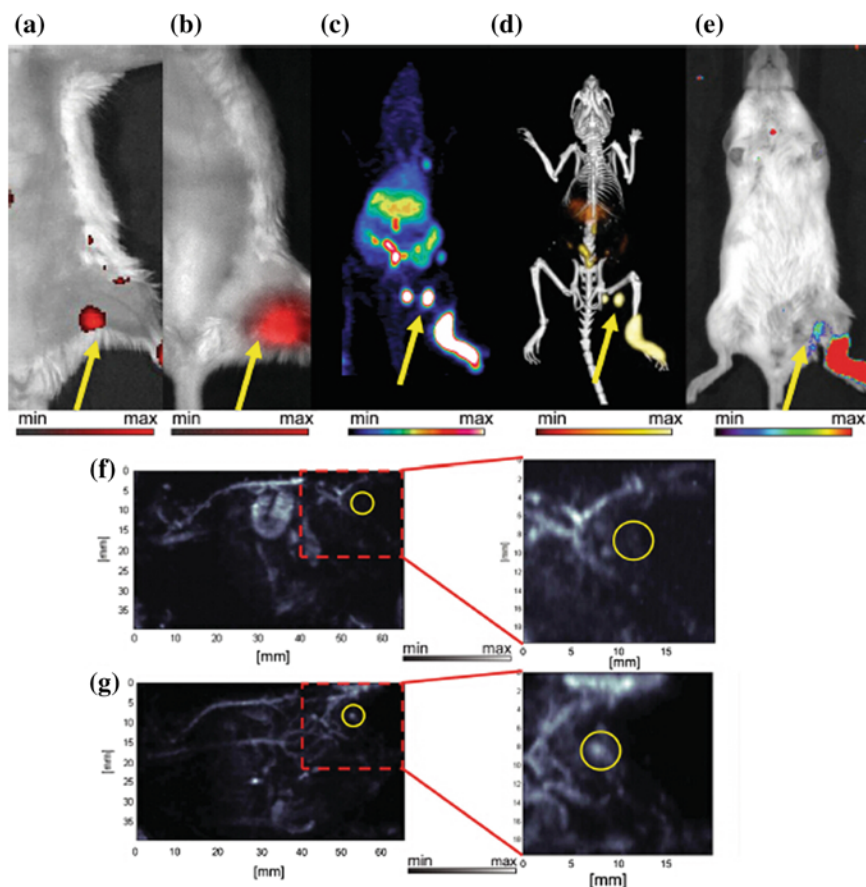
Fig. 12.14 In vivo lymphatic imaging using PoP-UCNPs in mice. PoP-UCNPs were injected in the rear left footpad and imaged in six modalities 1-h post-injection. Accumulation of PoP-UCNPs in the first draining lymph node is indicated by *yellow arrows*. **a** Traditional FL and **b** UC images with the injection site cropped out of frame. **c** Full anatomy PET, **d** merged PET/CT, and **e** CL images. **f** PA images before and **g** after injection show endogenous PA blood signal compared to the contrast enhancement that allowed visualization of the previously undetected lymph node. Reproduced from Ref. [112] with the permission of John Wiley & Sons Ltd

future applications in various biomedical researches which include bioimaging, medical diagnostic, targeted drug and gene delivery, and light-controlled therapy in the near future. With the rise of multimodality nanostructures based on UCNPs, it offers as a new form of theranostic tool for more accurate diagnostic and proper treatments via multimodal imaging moieties toward PET, SPECT, CT, MRI, and PAI [84, 107–113]. At the same time, the use of novel multifunctional materials by integrating the use of photoactivated therapeutic agents with UCNPs for the possibility of improving in vivo therapeutics through several strategies consists of siRNA treatment, photothermal therapy (PDT), photodynamic therapy (PDT), etc.

[32, 42, 114–117]. Through these series of efforts contributed in the development of functional UCNPs, it has enabled a significant breakthrough which benefited scientists from various diverse fields. Despite the initial success that has been obtained in the development of using UCNPs toward biomedical applications, there are still many challenges remain unresolved and remain urgently to be addressed.

One of the key challenges that require to be addressed is the development of new functional UCNPs that is able to display higher stability and more efficient converting optical properties under shorter wavelength. Currently, most of the irradiation wavelength relies mainly on NIR laser at 980 nm which directly overlaps the absorption wavelength of water [82]. This could pose a series of problem which include overheating and potentially damaged biological tissues by its unavoidable heat effects (Fig. 12.15) which limit the application of using UCNPs for treatments or in vivo studies [74, 118]. Hence, the need for new functionalized UCNPs that could be irradiated at shorter wavelength is highly desirable [119, 120]. Moving forward in this direction, Hummelen et al. recently reported a new dye-sensitized UCNPs could be excited under a shorter wavelength of 800 nm light irradiation when the UCNPs materials were doped with Nd^{3+} [120]. In addition, Han et al. also proposed the use of a new generation of $Nd^{3+}/Yb^{3+}/Er^{3+}$ (Tm^{3+}) cascade sensitized tri-doped core/shell β-$NaYF_4$ colloidal UCNPs with a constitutional excitation peak at 800 nm [121]. By using a similar design, it was found that the core shell of UCNPs doped with Nd^{3+} was found also to be effectively excited at 795 nm [122]. The cellular experiments were conducted using this new series of UCNPs, and it
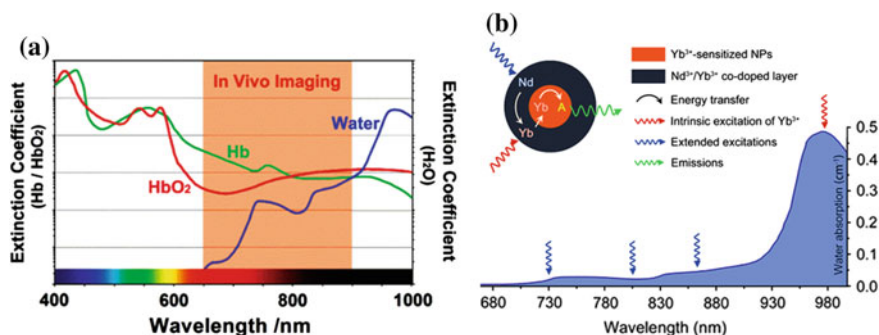

Fig. 12.15 a Spectra profiles of tissue optical window. The extinction coefficient of water at 800 nm is about 20 times lower than that at 980 nm (Hb: hemoglobin; HbO_2: oxyhemoglobin). Reproduced from Ref. [121] with the permission of John Wiley & Sons Ltd. **b** Absorption of water in the NIR and the integration scheme of the $Nd^{3+} \rightarrow Yb^{3+}$ energy transfer (ET) process by introducing the Nd^{3+}/Yb^{3+} co-doped shell. The resulting $Nd^{3+} \rightarrow Yb^{3+} \rightarrow$ activator ET could extend the effective excitation bands for conventional Yb^{3+}-sensitized UCNPs. Featuring lower water absorptions, these alternative excitation bands are expected to minimize the tissue overheating effect caused by NIR laser exposure (the *blue line* represents the absorption spectrum of water). Reprinted with the permission from Ref. [119]. Copyright 2013 American Chemical Society
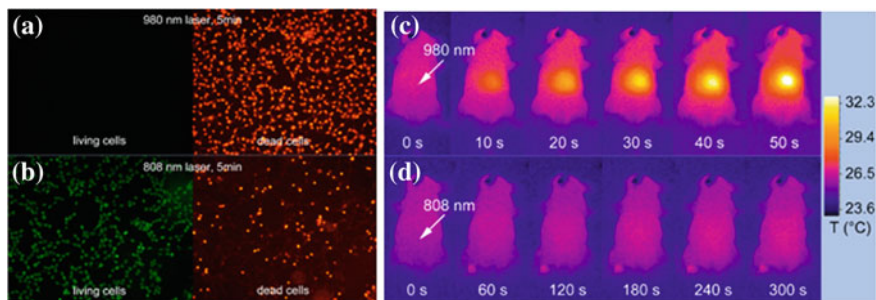
Fig. 12.16 In vitro and in vivo heating effect induced by laser irradiation. (**a**, **b**) HEK (human embryonic kidney) 293T cells after 5 min irradiation of 980 nm (**a**) and a 808 nm laser (**b**). Living cells and dead cells were stained with calcein AM (acetomethoxy) and propidium iodide, respectively. (**c**, **d**) Infrared thermal image of a nude mouse during continuous (**c**) 980 nm laser irradiation for 50 s and (**d**) 808 nm laser irradiation for 300 s. Irradiation spots are denoted with the *white arrows*. Reprinted with the permission from Ref. [119]. Copyright 2013 American Chemical Society

was found that the Nd^{3+}-doped UCNPs with 795 nm irradiation wavelength demonstrated a better biocompatibility compared with the conventional UCNPs which irradiated at 980 nm. At the same period of time, Yan et al. reported a new class of Nd^{3+}-sensitized upconversion nanophosphors by introducing Nd^{3+} as the sensitizer to build up the shell/core nanostructure so as to ensure successive $Nd^{3+} \rightarrow Yb^{3+} \rightarrow$ activator energy transfer [119]. The results that have been obtained thus far for 808 nm laser excitation show that this form of irradiation is suitable for in vivo imaging applications. In addition, the established Tm@Nd UCNPs and Er@Nd UCNPs demonstrated an effective multiplex imaging effects upon laser irradiation at a short wavelength of 808 nm. By introducing the use of a 808 nm laser irradiation, it has been demonstrated that it could be used to greatly reduce the overheating effect caused by 980 nm laser irradiation for living animal studies (Fig. 12.16).

Although overheating effect is an important factor to consider when comes to applying UCNPs for in vivo studies, another crucial factor for us to look at is its biocompatibility and its long-term toxicity. Despite the negligible toxicity for in vitro and in vivo in a short-term study after modifying the surface of the particles with biocompatible ligand moieties, its long-term immune effect is still a task that requires further investigation. Moreover, another key aspect that we need to consider is its reiculoendothelial system (RES) uptake in regions of the living system such as the liver, spleen, etc., and these are some of the key factors to consider that would greatly influence its application toward biomedical regions. Therefore, efforts toward functionalization of UCNPs, shape, size, etc., are important to understand this key aspect cellular uptake.

Lastly, even though UCNPs have functioned as an excellent candidate for numerous imaging processes in various biological systems, its application is still limited owing that most UCNPs still rely on $NaYF_4$ as the main host materials

which make the upconversion luminescence (UCL) efficiency to have any major improvement. Therefore, there is still a need in the development of novel methods or new functionalization of UCNPs with better converting efficacy, improved quantum yield, and better photostability. To circumvent this issue, some NIR dye molecules have been employed recently as antennas to enhance and broaden the excitation of UCNPs which help in improving the conversion efficacy (e.g., 3000 times) [120]. This improvement in efficacy is a result of the increased absorptivity of the nanostructure complexes. On the other hand, a new host material as a replacement for $NaYF_4$ is still highly desirable to enhance the UCL intensity. To improve the efficiency of the upconversion luminescence, another crucial factor that we need to look at it is the size distribution of the UCNPs as it has been known that smaller size nanostructures improve the overall cellular uptake, while at the same time it generally induces a lower luminescence emission. This dilemma consideration gave us an important insight if a well-defined sub-10 nm UCNPs with high luminescence emission could be synthesised in the near future. Therefore, there is still a need to develop new strategies or alternative functionalized UCNPs with more and improved optical properties such as higher quantum yield, a variable irradiation wavelength, improved efficiency, and better biocompatibility to address some of the potential issues observed in most current lanthanide-based UCNPs. The continuous innovations and new discoveries make in the area of material chemistry, biology, and photophysics will enable these functionalized nanocrystal structures to expand its applicability. In this way, it will be able to provide new insights for biosensing, more effective theranostic, targeted gene or drug delivery, a better non-invasive molecular imaging, and light controlled personal diseases treatments.

References

1. Achilefu S (2010) Introduction to concepts and strategies for molecular imaging. Chem Rev 110: 2575.
2. He X, Gao J, Gambhir SS, Cheng Z (2010) Near-infrared fluorescent nanoprobes for cancer molecular imaging: Status and challenges. Trends Mol Med 12: 574.
3. Hildebrandt IJ, Gambhir SS (2008) Molecular imaging applications for immunology. Clin Immunol 2: 210.
4. Weissleder R, Pittet MJ (2008) Imaging in the era of molecular oncology. Nature 452: 580.
5. Jiang TT, Xing BG, Rao JH (2008) Recent development of biological reporter technology for detecting gene expression. Biotech Genet Eng Rev 25: 41.
6. Massoud TF, Gambhir SS (2003) Molecular imaging in living subjects: Seeing fundamental biological processes in a new light. Genes Dev 17:545.
7. Willmann JK, Van Bruggen N, Dinkelborg LM, Gambhir SS (2008) Molecular imaging in drug development. Nat Rev Drug Discov 7:591.
8. Mullard A (2013) Molecular imaging as a de-risking tool: Coming into focus? Nat Rev Drug Discov 12: 251.
9. Hastings JW (1996) Chemistries and colors of bioluminescent reactions: A review. Gene 173:5.
10. Leoning AM, Wu AM, Gambhir SS (2007) Red-shifted Renilla reniformis luciferase variants for imaging in living subjects. Nat Methods 4:641.

11. Contag CH, Bachmann MH (2002) Advances in vivo bioluminescence imaging of gene expression. Annu Rev Biomed Eng 4:235.
12. Ray P, Gambhir SS (2007) Noninvasive imaging of molecular events with bioluminescent reporter genes in living subjects. Methods Mol Biol 411: 131.
13. Wehrman TS, von Degenfeld G, Krutzik PO, Nolan GP, Blau HM (2006) Luminescent imaging of beta-galactosidase activity in living subjects using sequential reporter-enzyme luminescence. Nat methods 3:295.
14. Tung CH, Zeng Q, Shah K, Kim DE, Schellingerhout D, Weissleder R (2004) In vivo imaging of beta-galactosidase activity using far red fluorescent switch. Cancer Res 6:1579.
15. Shah K, Tung CH, Breakefield XO, Weissleder R (2005) In vivo imaging of S-TRAIL-mediated tumor regression and apoptosis. Mol Ther 11: 926.
16. Zhou W, Valley MP, Shultz J, Hawkins EM, Bernad L, Good T, Good D, Riss TL, Klaubert DH, Wood KV (2006) New bioluminogenic substrates for monoamine oxidase assays. J Am Chem Soc 128:3122.
17. Rao J, Dragulescu-Andrasi A, Yao H (2007) Fluorescent imaging in vivo: Recent advances. Curr Opin Biotech 18:17.
18. Licha, K, Olbrich, C (2005) Optical imaging in drug discovery and diagnostic applications. Adv Drug Deliv Rev 57:1087.
19. Stefflova K, Chen J, Zheng G (2007) Using molecular beacons for cancer imaging and treatment. Front Biosci 12:4709.
20. Escobedo JO, Rusin O, Lim S, Strongin RM (2010) NIR dyes for bioimaging applications. Curr Opin Chem Biol 184:64.
21. Shao Q, Yang YM, Xing BG (2010) Chemistry of optical imaging probes. In molecular imaging probes for cancer research, world science: British Columbia, Canada, 2010.
22. Rothman DM, Shults MD, Imperiali B (2005) Chemical approaches for investigating phosphorylation in signal transduction networks. Trends Cell Biol 15:502.
23. Lawrence DS (2005) The preparation and in vivo applications of caged peptides and proteins. Curr Opin Chem Biol 9:570.
24. Erathodiyil N, Ying JY (2011) Functionalization of inorganic nanoparticles for bioimaging applications. Acc Chem Res 44:925.
25. Gao JH, Chen XY, Cheng Z (2010) Near-infrared quantum dots as optical probes for tumor imaging. Curr Top Med Chem 10:1147.
26. Cai WB, Chen XY (2007) Nanoplatforms for targeted molecular imaging in living subjects. Small 3:1840.
27. Biju V (2014) Chemical modifications and bioconjugate reactions of nanomaterials for sensing, imaging, drug delivery and therapy. Chem Soc Rev 43:744.
28. Michalet X, Pinaud FF, Bentolila LA, Tsay JM, Doose S, Li J, Sundaresan G, Wu A, Gambhir S.S, Weiss S (2005) Quantum dots for live cells, in vivo imaging, and diagnostics. Science 307:538.
29. Probst CE, Zrazhevskiy P, Bagalkot V, Gao XH (2013) Quantum dots as a platform for nanoparticle drug delivery vehicle design. Adv Drug Deliv Rev 65: 703.
30. Biju V, Itoh T, Ishikawa M (2010) Delivering quantum dots to cells: Bioconjugated quantum dots for targeted and nonspecific extracellular and intracellular imaging. Chem Soc Rev 39:3031.
31. Chi X, Huang D, Zhao Z, Zhou Z, Yin Z, Gao J (2012) Nanoprobes for in vitro diagnostics of cancer and infectious diseases. Biomaterials 33:189.
32. Jayakumar MK, Idris NM, Zhang Y (2012) Remote activation of biomolecules in deep tissues using near-infrared-to-UV upconversion nanotransducers. Proc Natl Acad Sci USA 109:8483.
33. Wang F, Liu X (2008) Upconversion multicolor fine-tuning: Visible to near-infrared emission from lanthanide-doped NaYF4 nanoparticles. J Am Chem Soc 130:5642.
34. Wang F, Liu X (2009) Recent advances in the chemistry of lanthanide-doped upconversion nanocrystals. Chem Soc Rev 38:976.
35. Haase H, Schafer H (2011) Upconverting nanoparticles. Angew Chem Int Ed 50:5808.

36. Mader HS, Kele P, Saleh SM, Wolfbeis OS (2010) Upconverting luminescent nanoparticles for use in bioconjugation and bioimaging Curr Opin Chem Biol 14:582.
37. Feng W, Sun LD, Zhang YW, Yan CH (2010) Synthesis and assembly of rare earth nanostructures directed by the principle of coordination chemistry in solution-based process. Coordin Chem Rev 254:1038.
38. Cheng L, Wang C, Liu Z (2013) Upconversion nanoparticles and their composite nanostructures for biomedical imaging and cancer therapy. Nanoscale 5:23.
39. Gu Z, Yan L, Tian G, Li S, Chai Z, Zhao Y (2013) Recent advances in design and fabrication of upconversion nanoparticles and their safe theranostic applications. Adv Mater 25:3758.
40. Liu Y, Tu D, Zhu H, Chen X (2013) Lanthanide-doped luminescent nanoprobes: Controlled synthesis, optical spectroscopy, and bioapplications. Chem Soc Rev 42:6924.
41. Wang F, Banerjee D, Liu Y, Chen X, Liu X (2010) Upconversion nanoparticles in biological labeling, imaging, and therapy. Analyst 135:1839.
42. Cheng L, Yang K, Li Y, Chen J, Wang C, Shao M, Lee ST, Liu Z (2011) Facile preparation of multifunctional upconversion nanoprobes for multimodal imaging and dual-targeted photothermal therapy. Angew Chem Int Ed 50:7385.
43. Zhou J, Liu Z, Li F (2012) Upconversion nanophosphors for small-animal imaging. Chem Soc Rev 41:1323.
44. Yi GS, Chow GM (2006) Synthesis of hexagonal-phase $NaYF_4$:Yb,Er and $NaYF_4$:Yb,Tm nanocrystals with efficient up-conversion fluorescence. Adv Funct Mater 16: 2324.
45. Wang F, Han Y, Lim CS, Lu Y, Wang J, Xu J, Chen H, Zhang C, Hong M, Liu X (2010) Simultaneous phase and size control of upconversion nanocrystals through lanthanide doping. Nature 463:1061.
46. Mai HX, Zhang YW, Si R, Yan ZG, Sun LD, You LP, Yan CH (2006) High-quality sodium rare-earth fluoride nanocrystals: Controlled synthesis and optical properties. J Am Chem Soc 128:6426.
47. Zhang YW, Sun X, Si R, You LP, Yan CH (2005) Single-crystalline and monodisperse LaF_3 triangular nanoplates from a single-source precursor. J Am Chem Soc 127:3260.
48. Mai HX, Zhang YW, Sun LD, Yan CH (2007) Highly efficient multicolor up-conversion emissions and their mechanisms of monodisperse $NaYF_4$:Yb,Er core and core/shell-structured nanocrystals. J Phys Chem C 111:13721.
49. Mai HX, Zhang YW, Sun LD, Yan CR (2007) Size- and phase-controlled synthesis of monodisperse $NaYF_4$:Yb,Er nanocrystals from a unique delayed nucleation pathway monitored with upconversion spectroscopy. J Phys Chem C 111:13730.
50. Wang X, Zhuang J, Peng Q, Li Y (2005) A general strategy for nanocrystal synthesis. Nature 437:121.
51. Wang L, Li P, Zhuang J, Bai F, Feng J, Yan X, Li Y (2008) Carboxylic acid enriched nanospheres of semiconductor nanorods for cell imaging. Angew Chem Int Ed 47:1054.
52. Wang M, Liu JL, Zhang YX, Hou W, Wu XL, Xu SK (2009) Two-phase solvothermal synthesis of rare-earth doped $NaYF_4$ upconversion fluorescent nanocrystals. Mater Lett, 63:325.
53. Sun YJ, Chen Y, Tian LJ, Yu Y, Kong XG, Zhao JW, Zhang H (2007) Controlled synthesis and morphology dependent upconversion luminescence of $NaYF_4$:Yb,Er nanocrystals. Nanotechnology 18:275609.
54. Tian G, Gu Z, Zhou L, Yin W, Liu X, Yan L, Jin S, Ren W, Xing G, Li S, Zhao Y (2012) Mn^{2+} Dopant-controlled synthesis of $NaYF_4$:Yb/Er upconversion nanoparticles for in vivo imaging and drug delivery. Adv Mater 24:1226.
55. Stouwdam JW, van Veggel FCJM (2002) Near-infrared emission of redispersible Er^{3+}, Nd^{3+}, and Ho^{3+} doped LaF_3 nanoparticles. Nano Lett 2:733.
56. Patra A, Friend CS, Kapoor R, Prasad PN (2002) Upconversion in Er^{3+}:ZrO_2 nanocrystals. J Phys Chem B 106:1909.
57. Vetrone F, Boyer JC, Capobianco JA, Speghini A, Bettinelli M (2004) Significance of Yb^{3+} concentration on the upconversion mechanisms in codoped Y_2O_3:Er^{3+}, Yb^{3+} nanocrystals. J Appl Phys 96:661.

58. Xu LL, Yu YN, Li XG, Somesfalean G, Zhang YG, Gao H, Zhang ZG (2008) Synthesis and upconversion properties of monoclinic Gd_2O_3:Er^{3+} nanocrystals. Opt Mater 30: 1284.

59. Kong WJ, Shan J, Ju YG (2010) Flame synthesis and effects of host materials on Yb^{3+}/ Er^{3+} co-doped upconversion nanophosphors. Mater Lett 64: 688.

60. Qin X, Yokomori T, Ju YG (2007) Flame synthesis and characterization of rare-earth (Er^{3+}, Ho^{3+}, and Tm^{3+}) doped upconversion nanophosphors. Appl Phys Lett 90:073104.

61. Ma P, Xiao H, Li X, Li C, Dai Y, Cheng Z, Jing X, Lin J (2013) Rational design of multifunctional upconversion nanocrystals/polymer nanocomposites for cisplatin(IV) delivery and biomedical imaging. Adv Mater 25:4898.

62. Yang Y, Shao Q, Deng R, Wang C, Teng X, Cheng K, Chen Z, Huang L, Liu Z, Liu X, Xing B (2012) In vitro and in vivo uncaging and bioluminescence imaging by using photocaged upconversion nanoparticles. Angew Chem Int Ed 51:3125.

63. Liu JN, Bu W, Pan LM, Zhang S, Chen F, Zhou L, Zhao KL, Peng W, Shi J (2012) Simultaneous nuclear imaging and intranuclear drug delivery by nuclear-targeted multifunctional upconversion nanoprobes. Biomaterials 33:7282.

64. Xiong L, Yang T, Yang Y, Xu C, Li F (2010) Long-term in vivo biodistribution imaging and toxicity of polyacrylic acid-coated upconversion nanophosphors. Biomaterials 31:7078.

65. Rantanen T, Jarvenpaa ML, Vuojola J, Kuningas K, Soukka T (2008) Fluorescence-quenching-based enzyme-activity assay by using photon upconversion. Angew Chem Int Ed 47:3811.

66. Naccache R, Vetrone F, Mahalingam V, Cuccia LA, Capobianco JA (2009) Controlled synthesis and water dispersibility of hexagonal phase $NaGdF4$:Ho^{3+}/Yb^{3+} nanoparticles. Chem Mater 21:717.

67. Bogdan N, Vetrone F, Ozin GA, Capobianco JA (2011) Synthesis of ligand-free colloidally stable water dispersible brightly luminescent lanthanide-doped upconverting nanoparticles. Nano Lett 11:835.

68. Chen, J, Guo C, Wang M, Huang L, Wang L, Mi C, Li J, Fang X, Mao C, Xu S (2011) Controllable synthesis of $NaYF_4$:Yb,Er upconversion nanophosphors and their application to in vivo imaging of Caenorhabditis elegans. J Mater Chem 21:2632.

69. Zhou HP, Xu CH, Sun W, Yan CH (2009) Clean and flexible modification strategy for carboxyl/aldehyde-functionalized upconversion nanoparticles and their optical applications. Adv Funct Mater 19:3892.

70. Chen Z, Chen H, Hu H, Yu M, Li F, Zhang Q, Zhou Z, Yi T, Huang C (2008) Versatile synthesis strategy for carboxylic acid-functionalized upconverting nanophosphors as biological labels. J Am Chem Soc 130:3023.

71. Wang LY, Yan RX, Hao ZY, Wang L, Zeng JH, Bao J, Wang X, Peng Q, Li YD (2005) Fluorescence resonant energy transfer biosensor based on upconversion-luminescent nanoparticles. Angew Chem Int Ed 44:6054.

72. Bao Y, Luu QAN, Lin CK, Schloss JM, May PS, Jiang CY (2010) Layer-by-layer assembly of freestanding thin films with homogeneously distributed upconversion nanocrystals. J Mater Chem, 20:8356.

73. Yang YM, Velmurugan B Liu, Xing BG (2013) NIR photoresponsive crosslinked upconverting nanocarriers toward selective intracellular drug release. Small 9:2937.

74. Yang YM, Liu F, Liu XG, Xing BG (2013) NIR light controlled photorelease of siRNA and its targeted intracellular delivery based on upconversion nanoparticles. Nanoscale 5:231.

75. Cao T, Yang Y, Gao Y, Zhou J, Li Z, Li F (2011) High-quality water-soluble and surface-functionalized upconversion nanocrystals as luminescent probes for bioimaging. Biomaterials 32: 2959.

76. Nichkova M, Dosev D, Gee SJ, Hammock BD, Kennedy IM (2005) Microarray immunoassay for phenoxybenzoic acid using polymer encapsulated Eu:Gd_2O_3 nanoparticles as fluorescent labels. Anal Chem 77: 6864.

77. Peer D, Karp JM, Hong, S, FaroKHzad OC, Margalit R, Langer R (2007) Nanocarriers as an emerging platform for cancer therapy. Nat Nanotechnol 2:751.

78. Nyk M, Kumar R, Ohulchanskyy TY, Bergey EJ, Prasad, PN (2008) High contrast in vitro and in vivo photoluminescence bioimaging using near infrared to near infrared up-conversion in Tm^{3+} and Yb^{3+} doped fluoride nanophosphors. Nano Lett 8:3834.

79. Xing H, Zheng X, Ren Q, Bu W, Ge W, Xiao Q, Zhang S, Wei C, Qu H, Wang Z, Hua Y, Zhou L, Peng W, Zhao K, Shi J (2013) Computed tomography imaging-guided radiotherapy by targeting upconversion nanocubes with significant imaging and radiosensitization enhancements. Sci Rep UK 3:1.

80. Lim SF, Riehn R, Ryu WS, Khanarian N, Tung CK, Tank D, Austin RH (2006) In vivo and scanning electron microscopy imaging of up-converting nanophosphors in Caenorhabditis elegans. Nano Lett 6:169.

81. Wang K, Ma JB, He M, Gao G, Xu H, Sang J, Wang YX, Zhao BQ, Cui DX (2013) Toxicity assessments of near-infrared upconversion luminescent LaF_3:Yb,Er in early development of zebrafish embryos. Theranostics 3:258.

82. Mitsunaga M, Ogawa M, Kosaka N, Rosenblum LT, Choyke PL, Kobayashi H (2011) Cancer cell-selective in vivo near infrared photoimmunotherapy targeting specific membrane molecules. Nat Med 17:1685.

83. Chatterjee DK, Rufaihah AJ, Zhang Y (2008) Upconversion fluorescence imaging of cells and small animals using lanthanide doped nanocrystals. Biomaterials 29:937.

84. Zhou J, Sun Y, Du X, Xiong L, Hu H, Li F (2010) Dual-modality in vivo imaging using rare-earth nanocrystals with near-infrared to near-infrared (NIR-to-NIR) upconversion luminescence and magnetic resonance properties. Biomaterials 31:3287.

85. Xia A, Chen M, Gao Y, Wu, D Feng, W, Li F (2012) Gd^{3+} complex-modified $NaLuF_4$-based upconversion nanophosphors for trimodality imaging of NIR-to-NIR upconversion luminescence, X-ray computed tomography and magnetic resonance. Biomaterials 33:5394.

86. Xing H, Bu W, Ren Q, Zheng X, Li M, Zhang S, Qu H, Wang Z, Hua Y, Zhao K, Zhou L, Peng W, Shi J (2012) A $NaYbF_4$:Tm^{3+} nanoprobe for CT and NIR-to-NIR fluorescent bimodal imaging. Biomaterials 33:5384.

87. Liu Q, Sun Y, Yang T, Feng W, Li C, Li F (2011) Sub-10 nm hexagonal lanthanide-doped NaLuF4 upconversion nanocrystals for sensitive bioimaging in vivo. J Am Chem Soc 133:17122.

88. Yang T, Sun Y, Liu Q, Feng W, Yang P, Li F (2012) Cubic sub-20 nm $NaLuF_4$-based upconversion nanophosphors for high-contrast bioimaging in different animal species. Biomaterials 33:3733.

89. Wang C, Cheng L, Xu H, Liu Z (2012) Towards whole-body imaging at the single cell level using ultra-sensitive stem cell labeling with oligo-arginine modified upconversion nanoparticles. Biomaterials 33:4872.

90. Chari RV (2008) Targeted cancer therapy: Conferring specificity to cytotoxic drugs. Acc Chem Res 41:98.

91. Xiong L, Chen Z, Yu M, Li F, Liu C, Huang C (2009) Synthesis, characterization, and in vivo targeted imaging of amine-functionalized rare-earth up-converting nanophosphors. Biomaterials 30:5592.

92. Xiong L, Chen Z, Tian Q, Cao T, Xu C, Li F (2009) High contrast upconversion luminescence targeted imaging in vivo using peptide-labeled nanophosphors. Anal Chem 81:8687.

93. Danhier F, Le Breton, A Préat V (2012) RGD-based strategies to target alpha(v) beta(3) integrin in cancer therapy and diagnosis. Mol. Pharm. 9:2961.

94. Li Y, Jing C, Zhang L, Long Y (2012) Resonance scattering particles as biological nanosensors in vitro and in vivo. Chem Soc Rev 41:632.

95. Cai W, Chen X (2006) Anti-angiogenic cancer therapy based on integrin alphavbeta3 antagonism. Anticancer Agents Med Chem 6:407.

96. Meyer A, Auernheimer J, Modlinger A, Kessler H (2006) Targeting RGD recognizing integrins: Drug development, biomaterial research, tumor imaging and targeting. Curr Pharm Des 12: 2723.

97. Yu XF, Sun Z, Li M, Xiang Y, Wang QQ, Tang F, Wu Y, Cao Z, Li W (2010) Neurotoxin-conjugated upconversion nanoprobes for direct visualization of tumors under near-infrared irradiation. Biomaterials 31:8724.

98. Chien Y, Chou Y, Wang S, Hung S, Liau M, Chao Y, Su C, Yeh C (2013) Near-infrared light photocontrolled targeting, bioimaging, and chemotherapy with caged upconversion nanoparticles in vitro and *in vivo*. ACS Nano 7:8516.

99. Shao Q, Xing B (2010) Photoactive molecules for applications in molecular imaging and cell biology. Chem Soc Rev 39: 2835.

100. Mayer G, Heckel A (2006) Biologically active molecules with a "light switch". Angew Chem Int Ed 45:4900.

101. Lee H, Larson DR, Lawrence DS (2009) Illuminating the chemistry of life: Design, synthesis, and applications of "caged" and related photoresponsive compounds. ACS Chem Biol 4:409.

102. Young DD, Deiters A (2007) Photochemical control of biological processes. Org Biomol Chem 5: 999.

103. Min Y, Li J, Liu F, Yeow EK, Xing B (2014) Near-infrared light-mediated photoactivation of a platinum antitumor prodrug and simultaneous cellular apoptosis imaging by upconversion-luminescent nanoparticles. Angew Chem Int Ed 53:1012.

104. Chen Z, Liu Z, Li Z, Ju E, Gao N, Zhou L, Ren J, Qu X (2015) Upconversion nanoprobes for efficiently in vitro imaging reactive oxygen species and in vivo diagnosing rheumatoid arthritis. Biomaterials 39:15.

105. Yang D, Dai Y, Liu J, Zhou Y, Chen Y, Li C, Ma P, Lin J (2014) Ultra-small $BaGdF_5$-based upconversion nanoparticles as drug carriers and multimodal imaging probes. Biomaterials 35:2011.

106. Yang Y, Mijalis AJ, Fu, H, Agosto C, Tan KJ, Batteas JD, Bergbreiter DE (2012) Reversible Changes in Solution pH Resulting from Changes in Thermoresponsive Polymer Solubility. *J Am Chem Soc* 134:7378.

107. Cheng L, Yang K, Li Y, Zeng X, Shao M, Lee ST, Liu Z (2012) Multifunctional nanoparticles for upconversion luminescence/MR multimodal imaging and magnetically targeted photothermal therapy. Biomaterials 33:2215.

108. He M, Huang P, Zhang C, Hu H, Bao C, Gao G, He R, Cui D (2011) Dual phase-controlled synthesis of uniform lanthanide-doped NaGdF4 upconversion nanocrystals via an OA/ionic liquid two-phase system for in vivo dual-modality imaging. Adv Funct Mater 21:4470.

109. Sun Y, Yu M, Liang S, Zhang Y, Li C, Mou T, Yang W, Zhang X, Li B, Huang C, Li F (2011) Fluorine-18 labeled rare-earth nanoparticles for positron emission tomography (PET) imaging of sentinel lymph node. Biomaterials 32:2999.

110. Yang Y, Sun Y, Cao T, Peng J, Liu Y, Wu Y, Feng W, Zhang Y, Li F (2013) Hydrothermal synthesis of $NaLuF_4$ Sm,Yb,Tm nanoparticles and their application in dual-modality upconversion luminescence and SPECT bioimaging. Biomaterials 34:774.

111. Zhou J, Yu M, Sun Y, Zhang X, Zhu X, Wu Z, Wu D, Li F (2011) Fluorine-18-labeled Gd^{3+}/ Yb^{3+}/Er^{3+} co-doped $NaYF_4$ nanophosphors for multimodality PET/MR/UCL imaging. Biomaterials 32:1148.

112. Rieffel J, Chen F, Kim J, Chen G, Shao W, Shao S, Chitgupi U, Hernandez R, Graves SA, Nickles RJ, Prasad P N, Kim C, Cai W, Lovell JF (2015) Hexamodal imaging with porphyrin-phospholipid-coated upconversion nanoparticles. Adv Mater 27: 1785.

113. Xing H, Bu W, Zhang S, Zheng X, Li M, Chen F, He Q, Zhou L, Peng W, Hua Y, Shi J (2012) Multifunctional nanoprobes for upconversion fluorescence, MR and CT trimodal imaging. Biomaterials 33:1079.

114. Chen G, Ohulchanskyy TY, Kachynski A, Agren H, Prasad PN (2011) Intense visible and near-infrared upconversion photoluminescence in colloidal $LiYF_4$:Er^{3+} nanocrystals under excitation at 1490 nm. ACS Nano 5:4981.

115. Idris NM, Gnanasammandhan MK, Zhang J, Ho PC, Mahendran R, Zhang Y (2012) In vivo photodynamic therapy using upconversion nanoparticles as remote-controlled nanotransducers. Nat Med 18:1580.

116. Wang C, Tao HQ, Cheng L, Liu Z (2011) Near-infrared light induced in vivo photodynamic therapy of cancer based on upconversion nanoparticles. Biomaterials 32: 6145.
117. Cui S, Yin D, Chen Y, Di Y, Chen H, Ma Y, Achilefu S, Gu Y (2013) In vivo targeted deep-tissue photodynamic therapy based on near-infrared light triggered upconversion nanoconstructure. ACS Nano7: 676.
118. Zhan Q, Qian J, Liang H, Somesfalean G, Wang D, He S, Zhang Z, Andersson-Engels S (2011) Using 915 nm laser excited $Tm^{3+}/Er^{3+}/Ho^{3+}$ doped $NaYbF_4$ upconversion nanoparticles for in vitro and deeper in vivo bioimaging without overheating irradiation. ACS Nano 5:3744.
119. Wang YF, Liu GY, Sun LD, Xiao JW, Zhou JC, Yan CH (2013) Nd^{3+}-sensitized upconversion nanophosphors: Efficient in vivo bioimaging probes with minimized heating effect. ACS Nano 7:7200.
120. Zou W, Visser C, Maduro JA, Pshenichnikov MS, Hummelen JC (2012) Broadband dye-sensitized upconversion of near-infrared light. Nat Photon 6:560.
121. Shen J, Chen G, Vu AM, Fan W, Bilsel OS, Chang CC, Han G (2013) Engineering the upconversion nanoparticle excitation wavelength: Cascade sensitization of tri-doped upconversion colloidal nanoparticles at 800 nm. Adv Opt Mater 1:644.
122. Xie X, Gao N, Deng R, Sun Q, Xu QH, Liu X (2013) Mechanistic investigation of photon upconversion in Nd^{3+}-sensitized core-shell nanoparticles. J Am Chem Soc 135:12608.

Chapter 13
Upconversion Nanoparticle as a Platform for Photoactivation

Pounraj Thanasekaran, Hua-De Gao and Hsien-Ming Lee

Abstract Photoactivation technology is a very powerful tool in chemical biology, as light is a remote, bio-orthogonal, fast-acting stimulus to activate effectors (such as chemically caged drugs, hormones, peptides, proteins, or genetic materials already deposited in a living subject being studied) with high spatiotemporal resolution and minimal invasion. However, most of the photoactivable compounds only respond to ultraviolet (UV), which has phototoxicity in the living organism and very poor penetration depth in biological tissue. Photoactivation technology based on lanthanide-doped upconversion nanoparticle (UCNP), which can upconvert NIR to visible or even UV band, provides a mean to overcome the shortcomings of traditional UV photoactivation techniques. The upconverted UV provides spatiotemporally restricted photochemical reactions near the particle surface in nanometer regime and hence results in minimal photodamage in the subject being studied. NIR light source also enhanced the penetration depth when applied to the uncaging technique in deep biological tissue. Unlike two-photon technology, UCNP-assisted photoactivation does not require an expensive light source or redeveloping the large cross-sectional photoprotecting groups. The aim of this chapter is to address the recent developments in photoactivation technology with an emphasis on upconversion luminescence-assisted photolysis.

13.1 Introduction

Tremendous interest has been witnessed in recent years in the field of photoactivation technology since light represents an optimal remote-control tool with very high spatial and temporal resolutions to create active patterns of biomolecules and is relatively compatible with cells, tissues, and live animals. Other spatiotemporal stimuli, especially "in vivo triggers" such as temperature, pH, redox, and enzyme

P. Thanasekaran · H.-D. Gao · H.-M. Lee (✉)
Institute of Chemistry, Academia Sinica, 128 Academia Road,
Section 2, Nankang, Taipei 11529, Taiwan
e-mail: leehm@chem.sinica.edu.tw

provide no remote control while remotely controllable *"ex vivo triggers"* such as electric and magnetic fields are not very well developed [1–3]. Photoactivation techniques, generationally speaking, including photolysis (photo-triggered release), sensitizer-assisted light-induced redox, and photoisomerization, have proved attractive in various fields of chemistry and biology [4]. Since the term "caged" was coined by Kaplan, Forbush, and Hoffman in 1978 [5], this strategy has been successfully developed and used to mask the activities of various biomolecules, including peptides, proteins, nucleic acids, and many other bio-effectors [2, 6, 7]. The use of UV photo-irradiation (normally within power density 10^{-1} to 10^{-3} W/cm^2) to manipulate the functions of biomolecules or mediate on-demand drug release (mostly via photolysis) in live systems via effective photoactivation with very high spatial and temporal regulations is a remarkable and well-developed technique [8–10]. However, excessive ultraviolet A (UVA 315–400 nm) light may induce damages in proteins, lipids, and nucleic acid (so-called UV phototoxicity). Moreover, the penetration depth for UVA is less than millimeter in biological tissue, which only works in cell level and is too short for a remote-control trigger in tissue level, hence make it unpleasing for in vivo and clinical use [11, 12].

The challenge to redshift the wavelengths for photolysis in biological application is to overcome the dilemma that only high energy light can induce photochemical reactions, which cause damages to the biological tissue along the light path in the meantime. One strategy to lower phototoxicity within the domain of one-photon excitation process is to tailor the caging groups with extended π-conjugation and introduce heteroatom and functional groups in the ring system so that larger dipole change can be generated when being excited. Literatures have suggested that the coumarin-based caging platform exhibits pronounced redshift [4, 13–17]. Another strategy is to use two-photon photolysis, which requires long wavelength pulsed laser (2 λ_{ex} of caging group) for enabling photoactivation. Coumarin derivatives also play an important role in two-photon caging groups for their large two-photon Goeppert-Mayer cross section, where 1 GM is 10^{-50} cm^4 s photon^{-1} [18, 19]. However, this technique not only requires new developments of photocaging group with a larger molecular two-photon cross section (which may inevitably result in higher hydrophobicity and low solubility), but also needs complex light source (pulsed laser with high-peak power $\sim 10^8$ W cm^{-2}) to induce two-photon photoreactions [20]. These features have stimulated the needs of in situ nanotransducer that can generate UV light with a biofriendly low-energy NIR excitation. And also, these nanoparticles can provide spatial-restricted photochemical reactions in nanometer regime around the particle surface, resulted in minimal photodamage while enhancing the penetration depth of excitation light in biological tissues.

In recent years, lanthanide-doped upconversion nanoparticles (UCNPs) have emerged as an appealing candidate to function as a NIR-induced mediator due to their intrinsic upconversion-luminescent properties, which requires only up to 10^2 to 10^1 W/cm^2 irradiation ($\sim 10^6$ folds less in power density than two-photon process). They provide several advantages in biomedical applications including biosensing [21], chemical sensing [22], biological imaging [23], and photo-induced chemical reaction types including photoactivation [3], drug delivery [24], and

photodynamic therapy [25]. The general principle of conventional, upconversion, and two-photon luminescence processes is depicted in Scheme 13.1a. Because of the unique ladder-like hierarchical excited states (*f*-block energy levels) with long lifetimes of lanthanide ions (such as Tm^{3+}, Er^{3+}, and Ho^{3+}), UCNPs are able to absorb NIR photons and convert it into visible/UV light efficiently through an upconversion process (Scheme 13.1b).

These properties make them a conveniently versatile, powerful tool for biological applications. To utilize the upconversion luminescence for photoactivation, the intensity has to be strong enough for fast photoactivation kinetics (for temporal resolution) compared with conventional UV irradiation [4, 26, 27]. Nanocrystals made of sodium yttrium fluoride ($NaYF_4$) co-doped with ytterbium (Yb^{3+}) and thulium (Tm^{3+}) can emit in the UV-visible region (especially emission from $^1I_6 \rightarrow {}^3F_4$ and $^1D_2 \rightarrow {}^3H_6$, transitions of Tm^{3+}, Fig. 13.1) and are commonly used for photoactivation (photolysis) study. Several synthetic routes including co-precipitation through the liquid–solid–solution (LSS) or the oleate route have been employed to prepare β-$NaYF_4$-based UCNPs [28]. They are then coated with (mesoporous) silica layer, which makes them dispersible in water, biocompatible, and renders the introduction of reactive groups and subsequent bioconjugation [29]. The photosensitive compounds then can be decorated on to the surface of core–shell UCNPs through covalent bonding or physical adsorption for photoactivation in biological studies. In addition, studies have proved that lanthanide-doped UCNPs show attractive merits including excellent photostability and low cytotoxicity [30, 31]. UCNPs have moved into the spotlight as an efficient platform for the construction of multifunctional nanoprobes [32, 33]. Various photochemical reactions have been performed using the UV emission of UCNPs for photoactivation of caged molecules and photo-triggered release of molecules depending upon the end application. In this chapter, we describe the use of UCL emitted from the
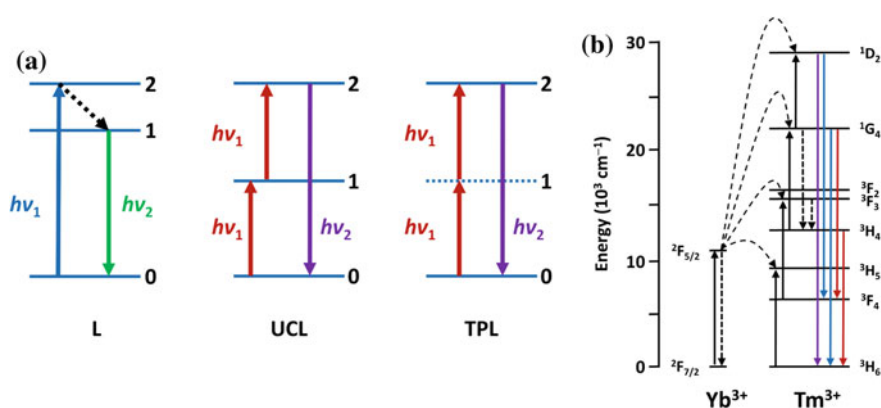
Scheme 13.1 **a** Schematic illustration of conventional luminescence (L), upconversion luminescence (UCL), and two-photon luminescence (TPL) processes. **b** Upconversion mechanism of the lanthanide UCNPs co-doped with Yb^{3+} and Tm^{3+}
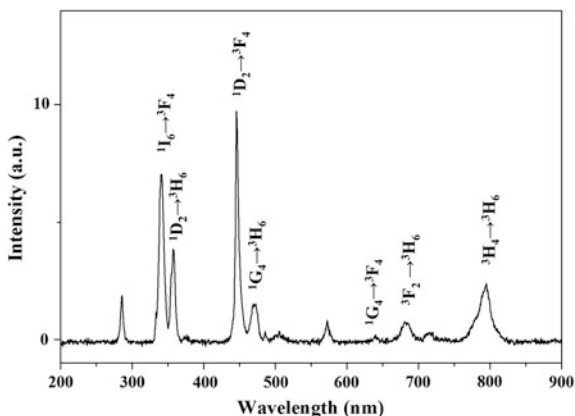
NIR-irradiated UCNP, which acts as a switch to photoactivate the caged molecules, thereby rendering them fully functional. In addition, their applications toward photo-triggered release, photoactivation of targeting ligands, photoactivation of bioluminescence, and photo-triggered prodrug activation are also discussed.

13.2 Significance of Photouncaging Technique

In chemical biology, photouncaging technology allows scientists to remotely trigger on/off biochemical pathways at a molecular level and generate significant differences in a living organism, where one want to have minimal chemical perturbations, such as living cellular or tissue, at a desired timing and location with a pulse of light [2, 34]. In this method, photolabile groups masked biomolecules that remain inactive before photolysis. Upon light irradiation, the protecting groups are photolytically cleaved and the biomolecules are restored irreversibly (Scheme 13.2),
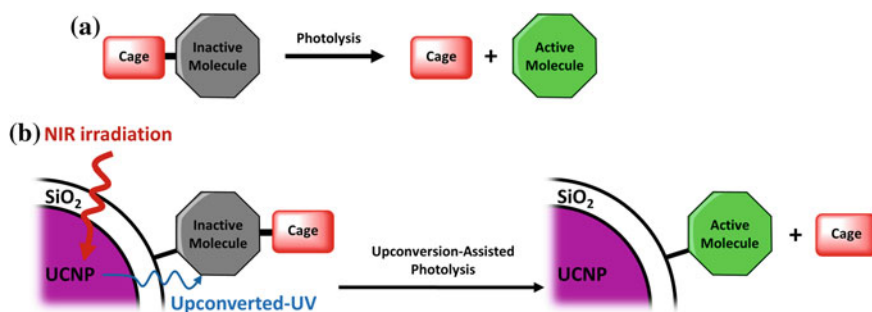
Scheme 13.2 Schematic diagram showing the principle of the **a** traditional conventional caged compounds and **b** upconversion-assisted photolysis of caged compounds
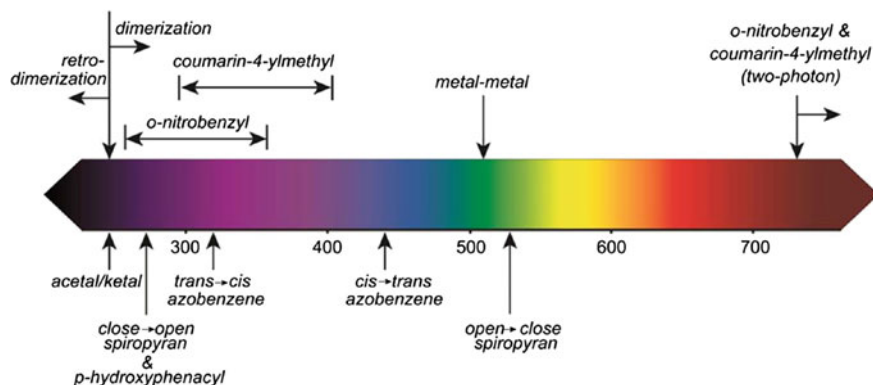
Fig. 13.2 Typical absorption wavelengths in nanometers for assorted functional groups that are commonly employed in photocaged systems. Reprinted with the permission from Ref. [35]. Copyright 2014 American Chemical Society

thereby recovering the intrinsic activity of the biomolecules in the specific irradiated area. *O*-nitrobenzyl group derivatives relying on both one- and two-photon excitation have been the most commonly used photolabile groups to cage amine, thiol, phosphate, amino hydroxyl and carboxyl groups. Apart from this, photoprotecting species responsive to specific wavelengths from UV through visible to the near IR have been emerged (Fig. 13.2). Uncaging is usually straightforward to achieve excellent ON/OFF ratios, showing the fact that uncaging usually yields the recovered (native), active parent compound, but normally is a one-way process. This method takes advantage of the unique properties of photon as stimuli including high spatiotemporal control, bio-orthogonality, tolerable cellular toxicity, and the possibility to tune both intensity and wavelength over its delivery. Further developments would show the applicability of photouncaging concepts to the investigation of important biological questions.

13.3 Photolysis Using Upconversion Nanoparticle Platform

Effectors involved in biochemical process can be chemically caged, and, in response to UV irradiation, generate a concentration burst of a specific species, without disrupting other aspects of the system. With the cooperation of the UCNPs in the photouncaging system, the recovery of bio-effectors in the nanocomposite could be controlled by NIR light directly. Herein, we describe the latest developments in photoactivation technology with an emphasis on upconversion luminescence-assisted photolysis.

### 13.3.1 Release of Small Molecules and Drugs by Upconverted Light

UCNPs with light-induced release functionality offer potential for the development of platforms from which to build delivery systems for the NIR-induced release of toxic reagent to a specific site. Reports in the literature have shown many upconversion-triggered applications to release the payload upon NIR excitation in both in vitro and in vivo experiments.

Branda's group is the first group demonstrated that upconverted UV light emitted from UCNPs is effective to trigger the uncaging (or photo-triggered releasing) in a remote-control process [36]. 3′,5′-di(carboxymethoxy)benzoin acetate (**1**) was found to be suited as a photocaged molecule, which released carboxylic acid upon UV photolysis (Scheme 13.3). Surface modification of $NaYF_4$: Yb,Tm@$NaYF_4$ UCNPs with 3′,5′-di(carboxymethoxy) benzoin acetate (**1**[$NaYF_4$: TmYb]) through physical adsorption was achieved. Upon the exposure of NIR light (power density = 550 W/cm^{-2}), the UCNPs generated upconverted UV light, and consequently caused the photocleavage of caged molecule and **2**[$NaYF_4$:TmYb] similar to the conventional UV photolysis, as evidenced by UV–Vis spectral analysis. The authors believe that this strategy is able to perform equally well in the release of other caged benzoin compounds. This very experiment, in principle, proves the possibility to trigger the conventional photolysis using upconversion technology.

Ford, Zhang, and co-workers demonstrated the use of upconversion nanoparticles (UCNPs) to trigger photochemical NO release from an iron-nitrosyl complex by a 980 nm irradiation [37]. Positive UCNPs@SiO_2 nanocarriers was synthesized by coating (3-aminopropyl)triethoxysilane to silica-coated hexagonal $NaYF_4$:Yb, Er@$NaYF_4$ core–shell–shell UCNPs to obtain cationic –NH^{3+} groups on the surface of silica layer (Scheme 13.4). The iron/sulfur/nitrosyl cluster Roussin's black salt anion $Fe_4S_3(NO)^{7-}$ (RBS, Na^+ salt) as the NO precursor was used to coat on the positively charged UCNP. When the UCNPs@SiO_2 were mixed with an RBS solution in aqueous medium and subjected to 980 nm photolysis operating at 1 W
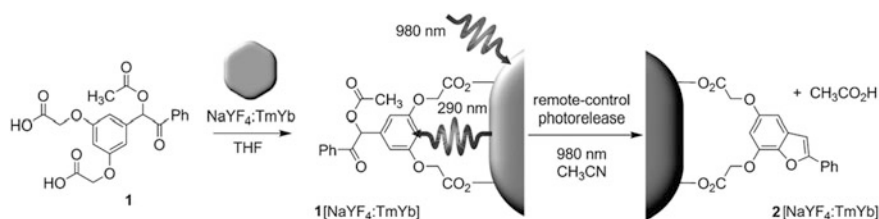
Scheme 13.3 Decoration of upconversion nanoparticles with 3′,5′-di(carboxymethoxy)benzoin cage **1** produces the remote-control release system (**1**[$NaYF_4$:TmYb]), which can be triggered by indirect irradiation with NIR light to generate **2**[$NaYF_4$:TmYb] and release a carboxylic acid. Reproduced from Ref. [36] by permission of John Wiley & Sons Ltd
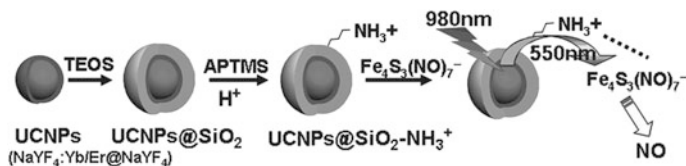
Scheme 13.4 Scheme for the synthesis of the UPNCs@SiO$_2$ nanostructures and for NIR light-triggered photochemical nitric oxide release. Reproduced from Ref. [37] by permission of John Wiley & Sons Ltd

(power density = 5–30 W/cm^{-2}), bio-effector nitric oxide was released with a quantum yield (Φ_{NO}) of ~0.001. In order to understand the premise for future applications, the NaYF$_4$:Yb/Er@NaYF$_4$@SiO$_2$ UCNPs were coated with a layer of mesoporous silica and then encapsulated with RBS into the pores. These UCNPs were further coated with poly(allylamine hydrochloride) (PAH) to inhibit diffusion of the NO precursor back into the solution. The resulting composites were then irradiated with a 4.0 W of 980 nm light to release nitric oxide, which displayed a linear response to the irradiation time but not to the laser power.

The same group also has shown in another study that UCNP-RBS-PD device is capable of releasing biologically relevant amounts of NO under NIR irradiation [38]. They formulated this novel device, in which poly(dimethylsiloxane) (PDMS) composites were mixed with upconversion nanoparticles (three compositions of Na(Y/Gd)F$_4$@NaYF$_4$) UCNPs (20 % Gd, 20 % Yb, and 2 % Er), (20 % Gd, 30 % Yb, and 2 % Er), and (20 % Gd, 20 % Yb, and 0.2 % Tm), and RBS to obtain a biocompatible polymer disk (PD) device (Fig. 13.3). PDMS has the property of moldable, transparent to visible and NIR right and hydrophobic. Dramatic enhancements of NO production were observed upon the NIR laser (power
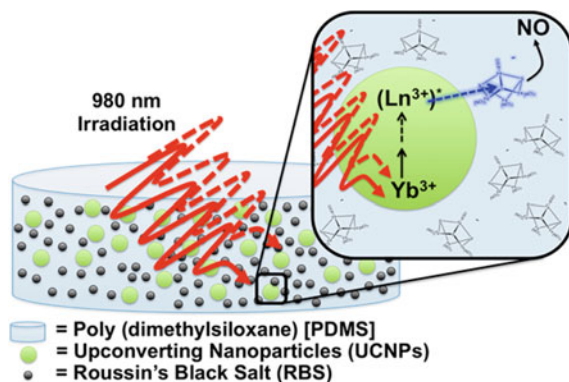
Fig. 13.3 Cartoon depicting how the photochemically active NO releasing polymer disks (PDs) are proposed to function. NIR light excitation of the UCNPs results in visible emission that is absorbed by the photochemical precursor (RBS in this case) triggering the release of NO. Reprinted with the permission from Ref. [38]. Copyright 2013 American Chemical Society

density = 400 W/cm^{-2}) irradiation of UCNPs–RBS solution. UV–Vis spectral analysis revealed that the infused PDs exhibited 50 nmols of RBS corresponds to ∼350 nmols of available NO per PD device. The release of NO and the effectiveness of NIR irradiation were also proven by using "filters" composed of porcine muscle, skin, and fat tissues (to mimic the tissue along the light path). This composite device is proven to be a stable, NIR active, photochemical NO delivery system that could be triggered on demands using tissue-penetrating NIR light in a desired location.

Krull et al. [39] designed experiments to show the possibility of using UCNPs for NIR light-triggered releasing of chemotherapeutic 5-fluorouracil (5-FU). Core–shell NaYF$_4$:Yb,Tm@NaYF$_4$ UCNPs were coated with *o*-phosphorylethanolamine using ligand exchange to replace oleic acid and then coupled to an *o*-nitrobenzyl (ONB) acid derivative of 5-FU (Scheme 13.5). When the particle complex were exposed to NIR irradiation (power density = 7.9–63.2 mW/cm^{-2}), the UCNPs produced emission bands centered at 365, 455, and 485 nm; the 365 nm emission resulted in photocleavage and subsequently released the 5-FU drug from the UCNPs in in vitro studies. It was shown that the rate of 5-FU release could be controlled and tuned by varying the intensity of incident NIR light. For example, when a NIR laser source was operated at a power of 80 mW, the initial kinetics constant (k_0) for 5-FU release was 130 μM min^{-1}. However, when NIR reduced to 10 mW, the initial release kinetics constant decreased to 18 μM min^{-1}. The reaction completion of drug release from the UCNPs upon NIR excitation was high as 77 % in comparison with direct UV illumination to trigger photolysis.

Another interesting application in which UCNPs are used is photoisomerization reactions. Branda et al. focused their studies on how dithienylethene (DTE) photoswitches undergo their ring-closing and ring-opening reactions using NIR light (power density = 150 W/cm^{-2}) in the presence of two types of UCNPs, (NaYF$_4$:TmYb), and (NaYF$_4$:ErYb) [40]. They demonstrated that these dithienylethene (DTE) isomers can be interconverted where the highest emission energy (UV) from NaYF$_4$:TmYb was appropriate for ring closing and the green emission
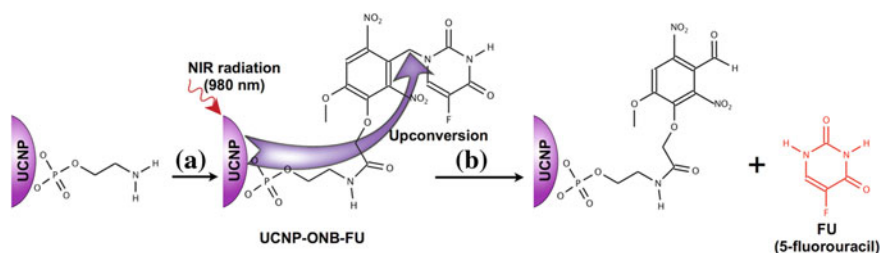
Scheme 13.5 **a** Modification of water-soluble β-NaYF$_4$:4.95 % Yb, 0.08 % Tm/β-NaYF$_4$-doped core–shell *o*-phosphorylethanolamine-capped UCNPs with ONB-FU. **b** NIR excitation (980 nm) of the UCNPs resulted in upconverted PL emission at 364 nm used for photocleavage of the ONB–FU bond and subsequent release of 5-fluorouracil from the UCNP surface. Reprinted with the permission from Ref. [39]. Copyright 2014 American Chemical Society
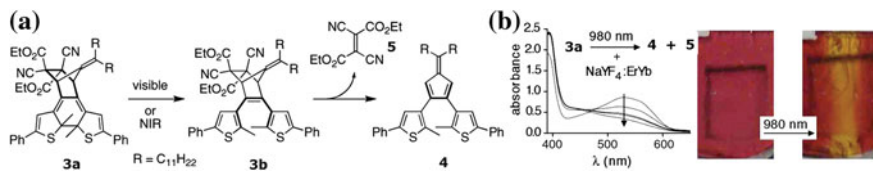
Fig. 13.4 **a** Scheme illustrating the ring opening and release reactions of bicyclic compound **3a** as it is irradiated with visible or NIR light. **b** Changes in the UV–vis absorption spectra (*left*) and cropped photographs (*right*) of an acrylate film containing **3a**+ NaYF$_4$:ErYb as it is irradiated with 980 nm light. The stripe observed in the right panel corresponds to the direction of the beam of the 980 nm laser. Reprinted with the permission from Ref. [40]. Copyright 2009 American Chemical Society

intensity of NaYF$_4$:ErYb induced ring opening, as shown in Fig. 13.4. Remote control photoswitching was also done by casting ring-closing DTE with NaYF$_4$: TmYb or ring-opening DTE with NaYF$_4$:ErYb in a cross-linked poly(ethyleneg-lycol)-dimethacrylate composite material, which provided a flexible environment for the photoreactions of DTE. In addition, the authors demonstrated the use of visible light to trigger the release of a small molecule from a DTE derivative by inducing the ring-opening reaction of a ring-closed species. They developed a photoresponsive ring-closed Diels-Alder product (**3a**), which was synthesized by the reaction of dithienylfulvene (**4**) with diethyl dicyanofumarate (**5**) followed by exposing the unstable intermediate (**3b**) to UV light. NIR illumination of an acrylate film containing **3a** and NaYF$_4$:ErYb led to formation of similar color changes, confirming that "remote control" switching also operated in this system.

13.3.2 Profluorophore Activation in Bioimaging by Upconverted Light

Xing and his team successfully designed a method for uncaging photocaged D-luciferin in both in vitro and in vivo systems using NaYF$_4$:Yb,Tm@NaYF$_4$ core–shell UCNPs as a platform, in which the inert shell NaYF$_4$ possess a reduced surface quenching effect [41]. These UCNPs were first silica coated and func-tionalized with thiolated silane, followed by conjugated with D-luciferin that was caged with a 1-(2-nitrophenyl)ethyl group. NIR illumination of the particle complex resulted in the recovery of D-luciferin, which was monitored either by tracking the fluorescence intensity of D-luciferin or using an fLuc enzyme reporter for biolu-minescence (Scheme 13.6). The photolysis of UCNPs conjugated caged D-luciferin, upon irradiation with NIR light (power density = 500 W/cm^{-2}), showed success photouncaging whereas plain caged D-luciferin (without UCNP conjugated) with NIR irradiation had no significant effect. In order to understand cellular uptake and NIR-activated uncaging of the D-luciferin/nanoparticle conjugate in living cells, they were tested in C6 glioma cells and MCF-7 cells (in vitro) and in nude mice
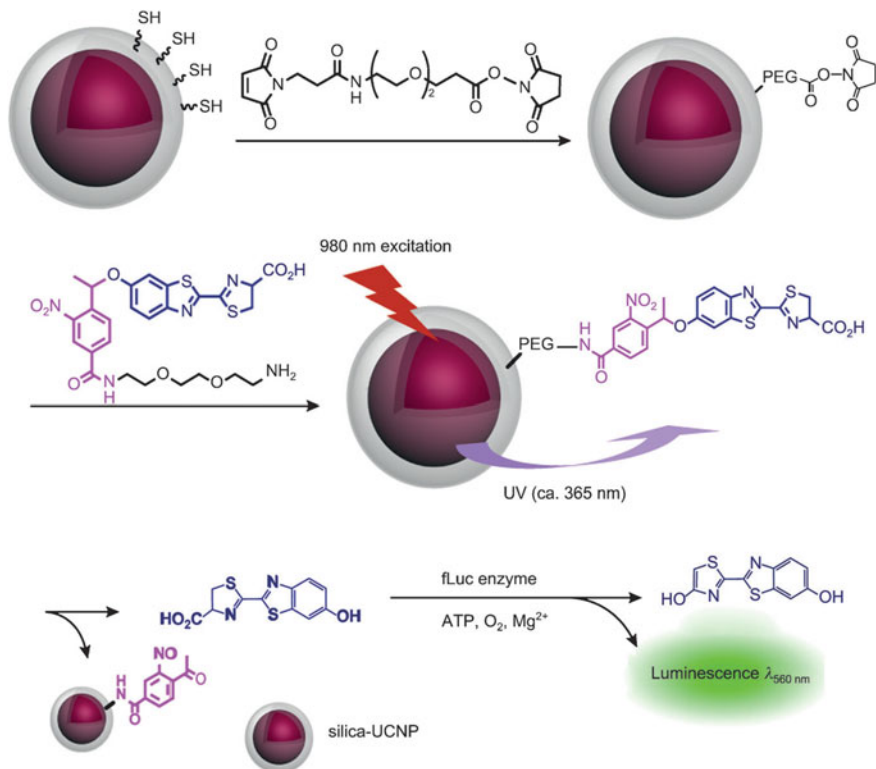
Scheme 13.6 Experimental design for uncaging D-luciferin and subsequent bioluminescence through the use of upconverted UV. Reproduced from Ref. [41] by permission of John Wiley & Sons Ltd

(in vivo). In vivo studies showed the versatility of using NIR photoactivation of the D-luciferin/nanoparticle conjugate for bioluminescence studies at substantial tissue depths.

In another study, Han's group developed a biocompatible core–shell CaF_2-coated α-NaYF$_4$:Yb,Tm core/shell UCNPs to generate efficient upconverted UV emission [42]. These UCNPs afforded to minimize the surface quenching effect as well as improved resistance to aqueous quenchers to preserve the upconverting UV emissions. In addition, doping the high concentration of Yb^{3+} on to the core surface induced tunable enhancement of NIR-to-UV emission with a high quantum yield (0.1 %) and 9 times higher emitting counts than that of β-NaYF$_4$ core–shell UCNPs. Improving NIR-to-UV upconversion, efficiency could enhance photolysis rate and reduce NIR-induced heating effects, as aqueous environment has high water molar concentration (~ 55 M). Although water has very low excitation at 980 nm ($\varepsilon = 0.3$ cm^{-1} M^{-1}), it still makes heating a worrisome problem during upconversion-assisted photolysis, especially for practical photolysis rate when
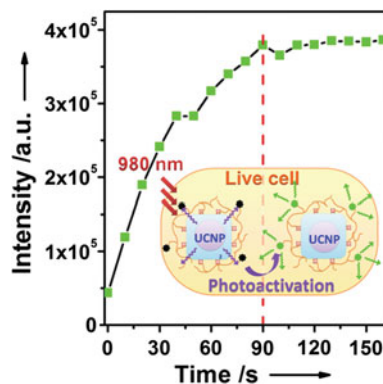
higher NIR photon density is needed. These UCNPs were further conjugated with branched polyethylenimine (PEI) followed by linked to succinimidyl ester-derivatized caged fluorescein and delivered to HeLa cells. Upon uncaging, the fluorescence signal from fluorescein was monitored and recorded in real time using fluorescence microscopy. The photoactivation was completed within 90 s upon irradiation with a NIR (975 nm) CW laser (power density = 2.6 W/cm^{-2}) (Fig. 13.5).

13.3.3   Prodrug Activation in Therapeutics by Upconverted Light

Of the various applications involved in the upconversion process, photochemical activation of an anticancer prodrug is interesting and potentially useful, since drug activity could be triggered by NIR irradiation directly at the tumor site, even in deep tissue. Cisplatin and its second-generation derivatives (carboplatin and oxaliplatin) have been the first-line drugs available for treating varieties of cancers for many years. Pt(IV) compounds are kinetically inert but typically operate as prodrugs that can be reduced in the hypoxic environment of cancer cells, losing two axial ligands in the process to form active planar Pt(II) species. Despite the increasing clinical use of photoactive Pt(IV) prodrugs, the activation of Pt(IV) prodrugs to specific tumor cells is either slow (via intracellular reduction) or phototoxic (via UV activation). NIR-to-visible upconversion property of UCNP can be used to precisely photoactivate the Pt(IV) prodrug complexes around the tumor region with a minimum damage to normal tissue.

UCNPS were used as multimodality bioimaging agents and transducers by converting NIR light into UV for control of drug activity in cancer therapy [43]. Lin, Yang, Ma, and their collaborators first coated the core NaYF$_4$:Yb^{3+}/Tm^{3+} with Yb^{3+}-doped NaGdF$_4$ active shell to enhance the upconverting luminescent intensity. After synthesizing the core–shell structured UCNPs, NaYF$_4$:Yb,
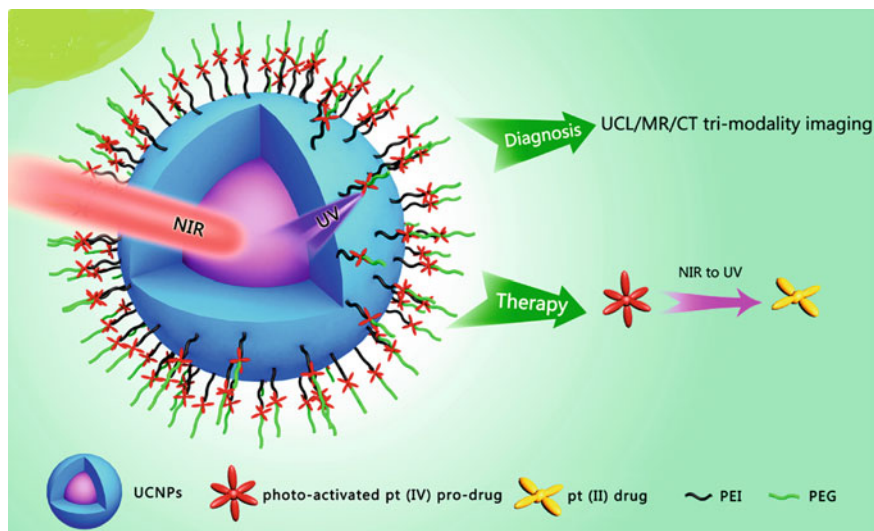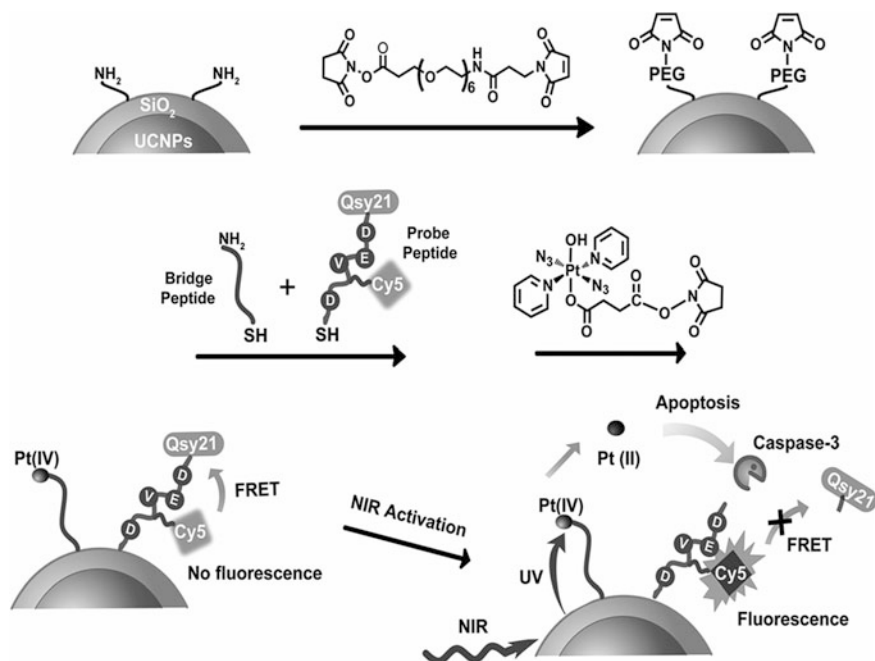
Fig. 13.6 Schematic illustration of UCNP-Pt(IV) prodrug nanoparticles. Reprinted with the permission from Ref. [43]. Copyright 2013 American Chemical Society

Tm@NaGdF$_4$, the surface of the UCNPs were conjugated with light-activatable prodrugs DPP (*trans,trans,trans*-[Pt(N$_3$)$_2$(NH$_3$)(py)(O$_2$CCH$_2$CH$_2$COOH)$_2$]) as drug carrier (Fig. 13.6). In order to improve circulation and reduce the immunogenicity of the UCNPs, they were grafted with polyethylene glycol (PEG). When UCNPS were exposed to 980 nm NIR light (power density = 2.5 W/cm^{-2}) (or direct 365 nm UV irradiation) for 30 min, a 48.4 % (57.3 % under UV) of the prodrug was activated. UV–Vis spectral studies revealed that single UCNP released around 3000 and 10,000 molecules of DPP within 1 h of 980 nm laser (power density = 2.5 W/cm^{-2}) and 365 nm UV light irradiation, respectively. In vitro cytotoxicity effect of the activated drug was evaluated in HeLa cells. The UCNP-DPP-PEG displayed a low cytotoxicity in the dark but exerted a destructive effect on HeLa cells upon exposure to UV or 980 nm light due to prodrug activation. The best cell growth inhibition efficacy was observed when the cells were pre-incubated with UCNPs and photoactivated using a NIR laser for 40 min. Furthermore, these UCNPs were also tested on liver cancer cell line H22 xenografted nude mice. Compared with UV irradiation, NIR light treatment had a better inhibition of tumor growth due to the higher tissue penetration depth. In these studies, direct irradiation with a NIR laser alone did not cause any significant change in cell viability (in vitro) or in the tumor size (in vivo). Apart from these studies, the authors also have shown that UCNPs can be used as trimodality imaging contrast agents for upconversion luminescence (UCL)/magnetic resonance (MR)/computer tomography (CT), which provide useful information to guide the efficiency and accuracy for diagnosis. The 800 nm emission from the core–shell NaYF$_4$:Yb,Tm@NaGdF$_4$ was used for UCL imaging. The only Gd-doped ions in

Scheme 13.7 Schematic illustration of NIR light activation of platinum(IV) prodrug and intracellular apoptosis imaging through upconversion-luminescent nanoparticles. Reproduced from Ref. [44] by permission of John Wiley & Sons Ltd

the UCNPs were used for MRI while Yb- and Gd-based/doped UCNPs were used for computed tomography imaging.

In another study, Xing and his group demonstrated the use of NIR-to-visible application of UCNPs for triggering the photo-induced reduction of Pt(IV) prodrug and also sensing of apoptosis in living cells [44]. An apoptosis sensing peptide (KKKKKC), which consists of FRET pair (Cy5 and its quencher Qsy21) for reporting caspase-3 (a key enzyme responsible for apoptosis) activity, was conjugated with the light-activated prodrug DPP (*trans,trans,trans*-[Pt(N$_3$)$_2$(NH$_3$)(py) (O$_2$CCH$_2$CH$_2$COOH)$_2$]), functionalized UCNPs@SiO$_2$ through an oligo(ethyl glycol) (dPEG$_6$) linker to generate Pt(IV) probe UCNPs@SiO$_2$ (Scheme 13.7). When the probe peptide was positioned very close to caspase, a cleavage of the peptide occurred, which resulted in turning on fluorescence of Cy5. Upconversion-assisted photoactivation (photo-induced reduction) of prodrug Pt(IV) probe UCNPs@SiO$_2$ was tested on the cisplatin-sensitive A2780 and resistant A2780cis tumor cell lines. NIR irradiation (power density = 0–2.6 W/cm^{-2}) enabled the active Pt(II) complex released in the cells over time and induced significant cytotoxicity. In addition, cell imaging and flow cytometry studies confirmed that the caspase-3 activation (Cy5 fluorescence) was due to the apoptosis caused by NIR-induced Pt(IV) UCNPs@SiO$_2$ prodrug activation.

13.3.4 Polymer Degradation and Cargo Release by Upconverted Light

Light-sensitive degradable polymers, which respond to photolysis or photoisomerization, are attractive vesicle material for the remote-control release of drugs [45]. Several approaches have been adopted to synthesize polymer containing light-responsive groups, such as azobenzene, spiropyran, o-nitrobenzyl, and coumarin, and are applied in polymeric drug release systems. However, their applications are suppressed by the usage of the short penetration depth and high energy UV light. Researchers started focusing on utilizing the upconverted UV emission of UCNPs for photoactivation of these polymeric systems to overcome the problems associated with UV light photoactivation, as their long wavelength allow them to penetrate deep into tissues and their low energy is not harmful to healthy cells.

Branda and Zhao's group demonstrated the use of UCNPs to disrupt block copolymer (BCP) micelles and to trigger the release of their payloads under NIR irradiation [46]. Core–shell NaYF$_4$:TmYb UCNPs were loaded into micelles, which was obtained from a photosensitive diblock copolymer composed of hydrophilic poly-(ethylene oxide) (PEO) and a hydrophobic polymethacrylate bearing photolabile o-nitrobenzyl groups (PNBMA). Irradiation at 980 nm NIR laser caused the photocleavage of o-nitrobenzyl groups in the micelle and led to dissociation of the micelle followed by the release of payloads (Scheme 13.8). Dissociation kinetics study was conducted upon the encapsulation of hydrophobic dye Nile Red into the micelles. The effects of the NIR laser power and concentration of UCNPs on NIR-induced micellar dissociation and dye release as a function of NIR light exposure time were investigated.

The use of the upconversion emission of UCNPs to trigger the photolysis-induced structural changes in photosensitive hydrogels, which contain a cross-linked hybrid polyacrylamide–poly(ethylene glycol) (PEG) in association with photoresponsive o-nitrobenzyl groups, has been demonstrated by Branda, Zhao, and their collaborators [47]. Core–shell UCNPs (NaYF$_4$:Yb,Tm@NaYF$_4$) along with the biomacromolecules were loaded into the photosensitive hydrogel by polymerizing an aqueous mixture of the acrylamide monomer and the photocleavable PEG cross-linker by a redox mediated radical polymerization process (Scheme 13.9). In order to demonstrate the NIR light-triggered release of biomolecules from the hydrogel containing UCNPs, bovine serum albumin (BSA) conjugated with fluorescein isothiocyanate (first demonstration) and trypsin (second demonstration) was selected as a model protein and enzyme, respectively. Upon the exposure of NIR laser (3–5 W), the amount of proteins and enzymes released from the hybrid system increased significantly, clearly demonstrating their activity as a result of hydrogel degradation. Under dark condition, there was no release of biomolecules, confirming its potential applications where a temporally controllable, stepwise release is desired.

Almutairi and his co-workers have demonstrated the ability of UCNP upconversion emission to induce degradation of light-sensitive polymer backbone and
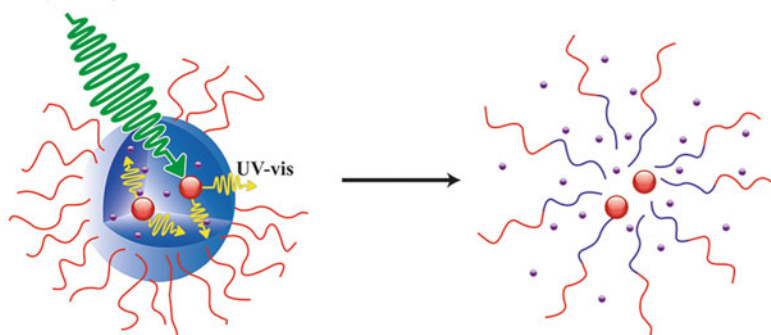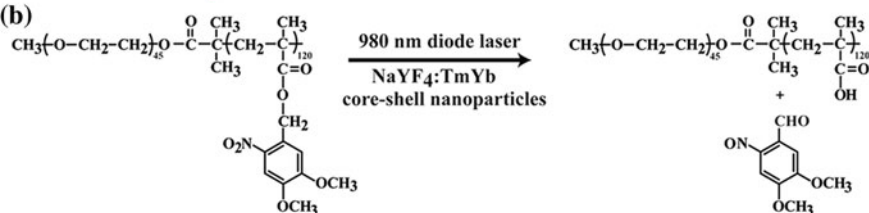
Scheme 13.8 **a** Schematic illustration of using NIR light excitation of UCNPs to trigger dissociation of BCP micelles. **b** NIR light-triggered photoreaction with the used BCP of PEO-*b*-PNBMA and UCNPs of NaYF$_4$:TmYb. Reprinted with the permission from Ref. [46]. Copyright 2011 American Chemical Society
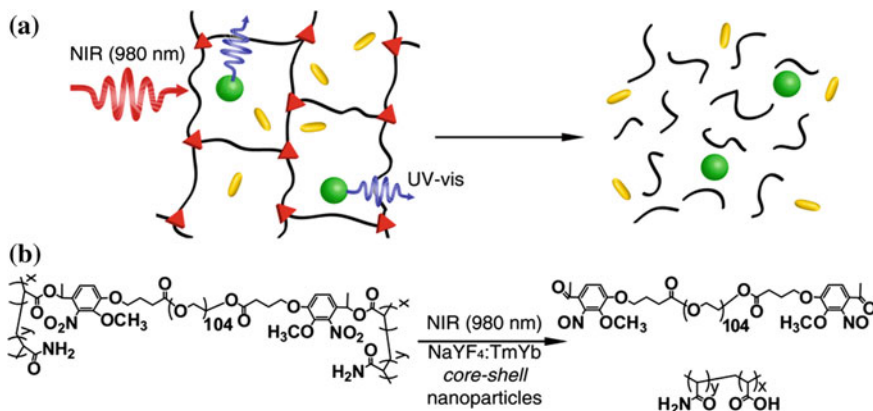
Scheme 13.9 **a** Schematic illustration of the NIR light-triggered degradation of a photosensitive hydrogel using the UV light generated by encapsulated UCNPs. The polymeric components are depicted as *black lines*, the photocleavable crosslinkers as *red triangles*, the UCNPs as *green spheres*, and the trapped biomacromolecules as *yellow rods*. **b** Chemical structure of the hydrogel containing photocleavable *o*-nitrobenzyl moieties in the cross-linker and the NIR light-induced photoreaction of the hydrogel via UV light emitted by loaded NaYF$_4$:TmYb core–shell UCNPs. Reprinted with the permission from Ref. [47]. Copyright 2012 American Chemical Society
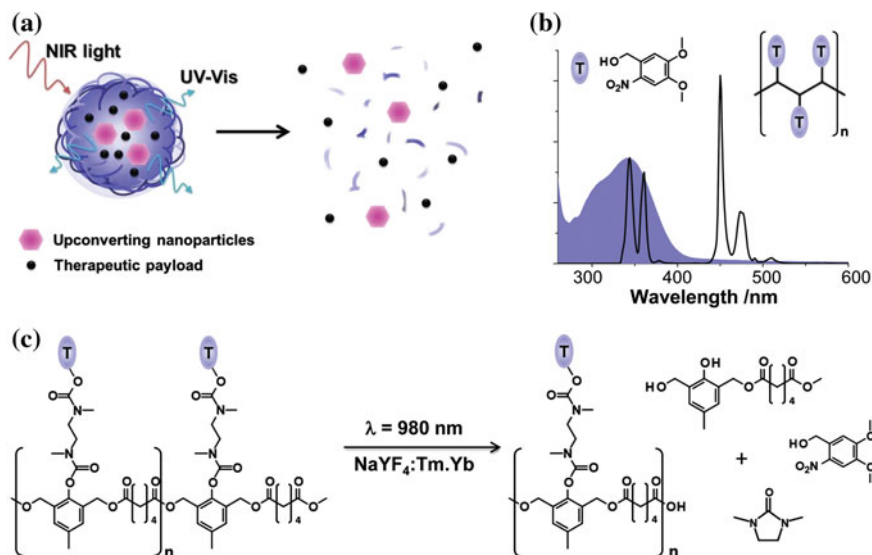
Fig. 13.7 Schematic representation: **a** upconverted luminescence triggers degradation and release from light-sensitive nanoparticles; **b** spectral overlap between the UV emission profile of NaYF$_4$: YbTm core–shell UCNPs (*black trace*) and the absorption spectrum (*shaded blue*) of ONB triggering groups; **c** photochemical mechanism of light-triggered degradation. Reproduced from Ref. [48] by permission of John Wiley & Sons Ltd

subsequent cargo release [48]. Core–shell NaYF$_4$:Yb.Tm@NaFY$_4$ along with a hydrophobic model cargo, coumarin 153 (C153) was loaded into the light-sensitive polymer capsules using an electrospray technique, which allows highly efficient in encapsulating of both hydrophilic and hydrophobic molecules. After irradiated by NIR light, the upconverted UV emission cleaved the *o*-nitrobenzyl protecting groups and initiated the cascade degradation of the polymer carriers (Fig. 13.7), as evidenced by gel permeation chromatography (GPC). When irradiated by NIR laser at 0.5 W power, the molecule weight of polymer started decreasing, confirming the polymer fragmentation, and significant molecule weight degrease was observed upon NIR irradiation at 1 W power. The dye release was also strongly correlated with the irradiation power density. Control experiment showed that there was only minimal increase in heat-induced release due to temperature increased by 10 °C upon exposure to NIR laser irradiation at 1 W.

The first demonstration of photoregulated chemotherapeutical drug release in living animal level using UCNPs is reported by Li and co-workers [49]. A yolk–shell NaYF$_4$:Yb,Tm@NaLuF$_4$ upconversion nanoparticle (YSUCNPs) was coated with silica and then encapsulated with an anticancer drug chlorambucil caged by a hydrophobic 7-amino-coumarin derivative. Upon the exposure of 980 nm NIR laser, the upconverted emission from YSUCNP-ACCh (amino-coumarin and chlorambucil, denoted as ACCh) photolyzed the chemical bond of the aminocoumarin site to release (and restored the active form of chlorambucil) while the

hydrophobic amino-coumarin phototrigger was totally retained within the YSUCNP (Fig. 13.8). Moreover, the release of drug was clearly dependent on the on–off pattern of the excitation source. The antitumor activity of YSUCNP-ACCh UCNPs was examined in KB cells (in vitro) and malignant murine tumor cell line S180 bearing mice (in vivo) upon irradiated with NIR light. The UCNPs was intratumorally administrated, and NIR-induced release delivered the drug at the tumor sites so that significant decrease in the viability of cells and tumor size was observed. The absence of NIR irradiation or control experiments showed no significant responses. In this study, the power density of NIR laser used was moderate, but gave good response for the release of drug when the power density was used at 570 mW cm^{-2} in vitro and 50 mW cm^{-2} in vivo studies. The significant response caused by weak power NIR irradiation, although not discussed in this paper, could be due to the aminocoumarin caging derivative. Unlike *o*-nitrobenzyl derivatives which only response to 360 nm band, aminocourmarin derivatives response to both 360 nm and 450 nm, and hence the generation of 450 nm upconverted light require much less power density due to the nonlinear optical properties of UCNPs.

In another study, Liu's group used mesoporous silica-coated core–shell UCNPs $NaYF_4$:Yb/Tm@$NaYF_4$ to functionalize with hydrocarbon octadecyltrimethoxysilane C18 long alkyl chain to form hydrophobic MUCNP, which were further coated
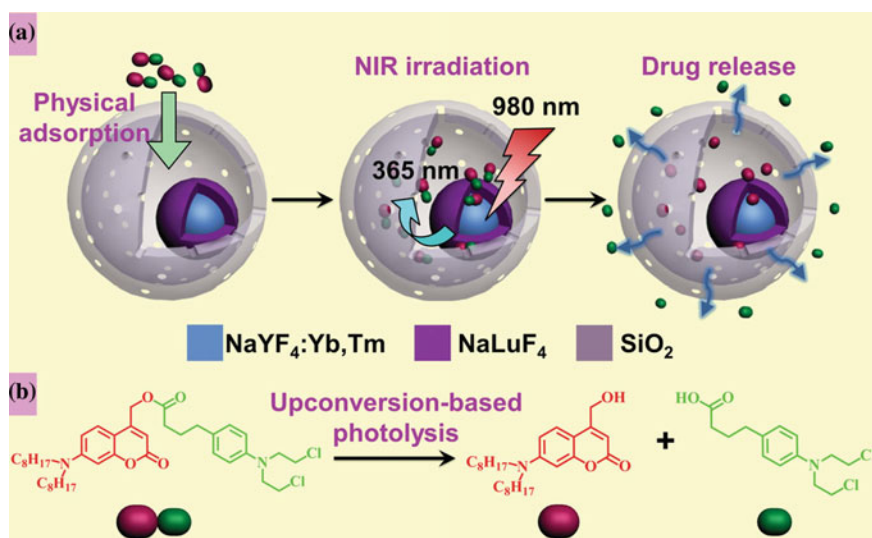

Fig. 13.8 Schematic illustration of the NIR-regulated upconversion-based phototrigger-controlled drug release devices (PDD) and the photolysis of the prodrug under upconversion emission from the YSUCNPs. Reproduced from Ref. [49] by permission of John Wiley & Sons Ltd
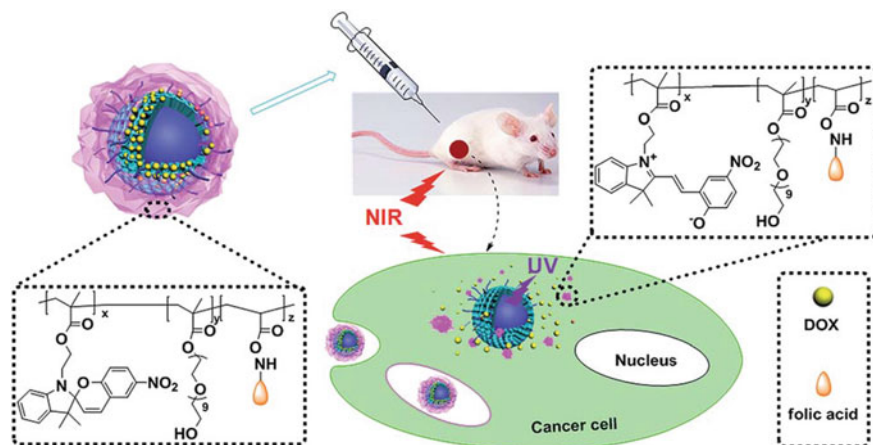
Fig. 13.9 Schematic illustration of upconversion nanoparticles/polymer multifunctional nanocomposite and the NIR light-triggered drug release process. Reproduced from Ref. [50] by permission of The Royal Society of Chemistry

with folic acid containing, light-responsive copolymer to generate MUCNP@C18@ PSMN-FA via self-assembly through hydrophobic van der Waals interactions (Fig. 13.9) [50]. The light-responsive amphiphilic copolymer poly (SPMA-MAPEG-NSA) was synthesized by free radical copolymerization reaction of hydrophobic monomer 1′-(2-Methacryloxyethyl)-3′,3′-dimethyl-6-nitro-spiro(2H-1-benzopyran-2′,2′-in-doline) (SPMA), NAS and poly(ethylene glycol) methacrylate (MAPEG) using AIBN initiator and then conjugated with FA-NHS to obtain PSMN-FA. SPMA unit in the copolymer, upon the upconverted UV irradiation, isomerized into an open-ring confirmation, resulted in less "gating" effect and caused content payload release. Anticancer drug DOX was loaded into the mesopores of the silica layer prior to polymer coating. Drug release was observed when the MUCNP@C18@PSMN-FA was irradiated with a NIR laser. Remote controlling drug release was done efficiently using a NIR laser for several on–off cycles. A significant decrease of KB cell viability was observed when the DOX-loaded MUCNP@C18@PSMN-FA carrier was treated with NIR light, indicating the effective delivery of DOX into the tumor cells, as evidenced by the confocal laser scanning microscopy (CLSM). When the DOX-loaded DOX-MUCNP@ C18@PSMN-FA nanocarrier was intratumorally injected into tumor-bearing mice followed by exposure of 980 nm irradiation, DOX-loaded drug carrier inhibited tumor growth more efficiently with NIR laser treatment. Both in vitro and in vivo studies proved that the targeting moiety offered by folic acid is efficient at enhancing tumor cell targeting with a biocompatibility of the nanocarrier.

13.3.5 Drug Release from Porous Materials by Upconverted Light

In a unique selection of targeting moieties, Tan et al. synthesized a $N–TiO_2/NaYF_4$: Yb,Tm UCNPs to photocatalytically generate short-lived reactive hydroxyl radical to scissor the C–H bond between model drugs on the TiO_2 surface to generate drug release using a safe (lower power density) NIR laser [51]. The surface of $NaYF_4$:Yb, Tm UCNPs was decorated with thioglycolic acid modified $N–TiO_2$ ($TGA–N–TiO_2$) through covalent bonding and then heating at 160 °C to generate $N–TiO_2/NaYF_4$: Yb,Tm nanocomposite. Upon the exposure of NIR laser irradiation, the UCNPs ($NaYF_4$:Yb,Tm) emitted visible light at $\lambda = 470$ nm (Fig. 13.10), which could excite N-doped TiO_2 to generate electron–hole pairs for redox reaction. A fluorescence dye, 7-methoxycoumarin-3-carboxylic acid (as a model drug) was used to investigate NIR-induced release, by measuring the fluorescence at 405 nm. The nanocomposite was also conjugated with antibody cAngptl4 Ab to form anti-cAngptl4Ab NCs and then subjected to NIR irradiation after being uptake by A-5RT3 human squamous cell carcinoma cells. They exerted good cytotoxic effects toward the targeted A-5RT3 cells compared with HaCat non-tumorigenic cell.

In another study, Xing's group has demonstrated the use of cross-linked photocleavable oligo (ethylene) glycol polymer coated mesoporous silica-coated UCNP nanoconjugates as folate-targeted cancer therapeutics [52]. Mesoporous silica-coated core–shell UCNPs $NaYF_4$:Yb/Tm@$NaYF_4$ was designed as a platform, which was surface-functionalized with 1-(2-nitrophenyl) ethyl caged oligo (ethylene) glycol linker, to encapsulate DOX into the photocaged mesoporous nanostructures (Scheme 13.10). The photo-controlled drug release from the mesoporous silica-UCNPs was investigated by analysis of fluorescence of Dox. In vitro study, Dox-encapsulated mesoporous silica-UCNPs conjugate was incubated with A-498

Fig. 13.10 Upconversion emission spectra of: *A* N–TiO_2; *B* N–$TiO_2/NaYF_4$:Yb, Tm; *C* $NaYF_4$:Yb,Tm; *blue line* shows the light absorption spectra of N–TiO_2; *Inset* photographs show the light emission of the particle solutions. Reproduced from Ref. [51] by permission of John Wiley & Sons Ltd
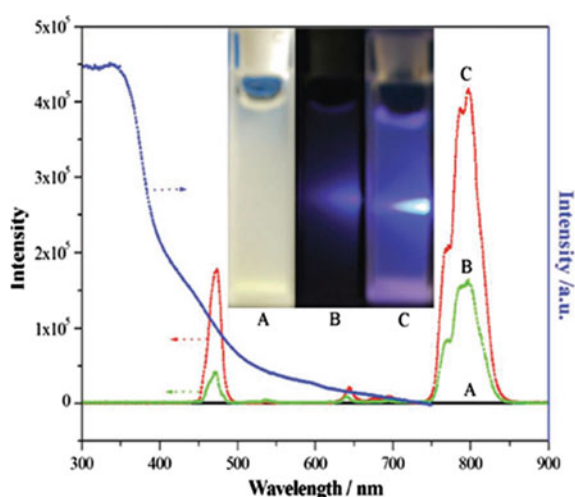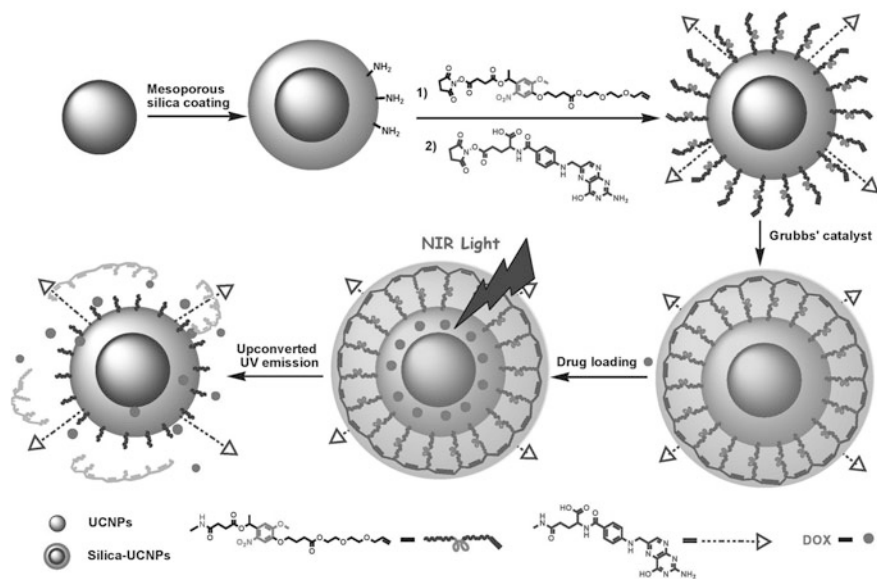
Scheme 13.10 Experimental design for photo-controlled Dox delivery through photocaged mesoporous silica-coated UCNPs with folic acid. Reproduced from Ref. [52] by permission of John Wiley & Sons Ltd

tumor cells for 2 h. After the exposure of 980 nm NIR light, there was an excessive fluorescence signal detected in cells, owing to the release of DOX molecules caused by the cleavage of the photocaged 1-(2-nitrophenyl)ethyl group linker groups and consequent fragmentation of polymer grafting on the surface of nanocarriers.

13.3.6   Gene Expression Regulated by Upconverted Light

Gene expression regulates many important cell functions, including cell proliferation and differentiation, which are naturally organized with high spatial and temporal resolution. In order to investigate and to reengineer these processes, stimuli-responsive chemicals or genetic materials, which are a careful design, offer alternative ways for elucidating complex biological processes at the molecular level. For example, addition of inducers such as Isopropyl β-D-1-thiogalactopyranoside (IPTG) or ecdysone in the expression system having corresponding promoters or siRNA to block the expression without spatial resolution. To achieve gene expression regulation with spatiotemporal resolution, photoactivation design can be applied on gene expression inducer or siRNA so that light can be used as a trigger to control the gene expression with easily controlled timing, location, and amplitude to

enable the precisely activate. In practical, spatiotemporal regulation of genetic functions can be obtained through the attachment of photoactive moieties onto the phosphate backbone or the nucleotide base in DNA or RNA fragments. In this section, we mainly focus on the NIR photoactivatable nanoparticle platforms with a payload of caged plasmid or siRNA moieties to successfully control gene expression in cells and living animals upon photolysis.

NIR-to-UV UCNPs platform has been shown an enormous potential in the fields of photo-controlled gene therapy and specific gene delivery/knockdown [53]. In this study, Zhang and his group synthesized photocaged plasmid DNA and siRNA using [1-(4,5-dimethoxy-2-nitrophenyl)diazoethane] (DMNPE) to make them unrecognizable by transcription and translation machinery. These photocaged nucleic acids (DNA and siRNA) were efficiently loaded onto the surface of mesoporous silica-coated NaYF$_4$:Yb,Tm UCNPs by physical adsorption as it protected from the surrounding harsh biological conditions (Fig. 13.11). These
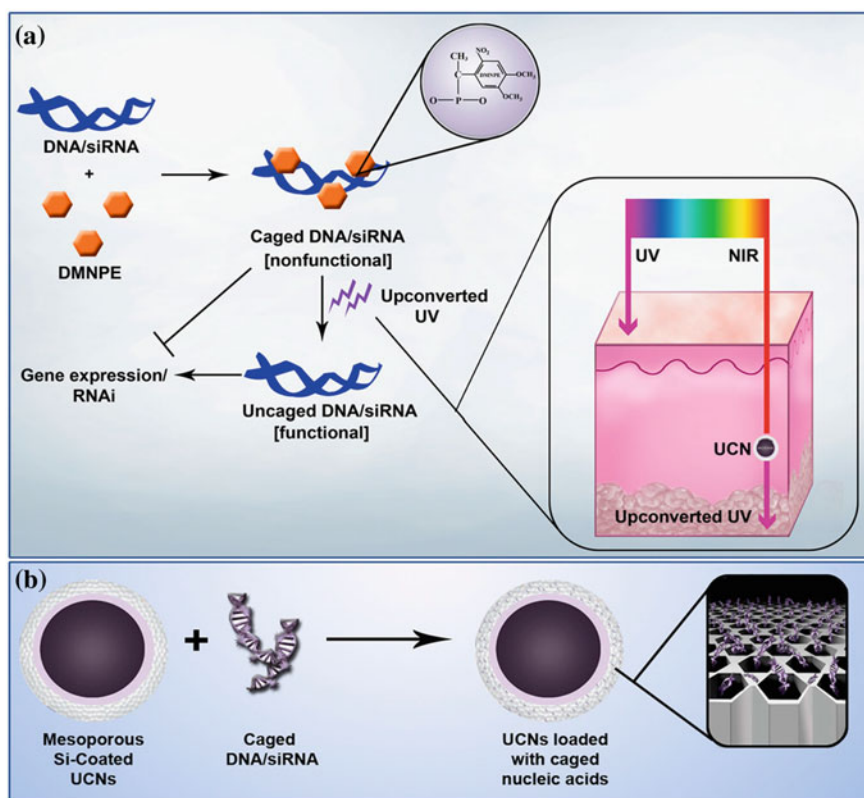

Fig. 13.11 Schematic illustration. Plasmid DNA and siRNA are caged with DMNPE and then uncaged by upconverted UV light from NIR-to-UV UCNs. *Inset* shows the penetration depth of UV and NIR light in the skin (**a**). Loading of caged plasmid DNA/siRNA into the mesopores of UCNs (**b**). Reprinted with permission from Ref. [53]

UCNPs were then irradiated by NIR light with deep tissue penetration and low phototoxicity, and the caged nucleic acids were present in both test tubes and cells. The upconverted UV produced by the irradiated nanoparticles was also used to track the nanoparticle uptake by cells during their delivery and activation process. Experimental results suggested that UCNPs can photoactivate the gene expression of the nucleic acids in the cellular environment. In addition, gene expression and knockdown of green fluorescent protein (GFP) were accomplished in cells by using caged EGFP (enhanced green fluorescence protein) plasmids and caged GFP siRNA, thereby the amount of protein expressed was controlled. This result highlighted not only the activation of photocaged nucleic acids but also proved the activation with very high spatial and temporal resolution, which is achieved by UCNP platform. Moreover, this technique was accomplished to activate the photocaged nucleic acids in tissue of different thickness as well as tissue in mice model.

Since "naked" siRNA possesses a highly negative charges, it cannot cross cellular membranes freely, which limits its utility for gene therapy [54]. However, a limited number of nanomaterials have been explored as delivery carriers for transporting siRNA into living cells [55, 56]. In 2013, Xing and his group reported the loading and light-induced release of siRNA from the photocaged UCNPs platform [57]. By this method, the Si-coated UCNPs were first functionalized with maleimide-terminated oligo(ethylene glycol) linker, which also facilitates the dispersion stability of nanoparticles in aqueous solutions. Then a photolabile, positively charged choline-containing linker was further installed to particle surface to electrostatically immobilize siRNA. After the loading of anionic Alexa Fluor@546 labeled siRNA to photocaged silica-coated UCNPs surface, the particle complex was delivered to HeLa cells (Scheme 13.11). Upon 980 nm light exposure, the photolabile linker on Si-UCNPs surface was fragmented, and the Alexa-siRNA was released effectively from UCNPs platform complex in HeLa cell due to *o*-nitrobenzyl linker photolysis caused by the upconverted UV light, as evidenced by cellular studies. The effective siRNA delivery to silence EGFP gene expression in HeLa cells was achieved using Si-UCNPs–EGFP and siRNA (Si-UCNPs–siRNA) complex under the exposure of NIR light. The NIR irradiation released the positively charged choline group, and hence, free the siRNA to cytoplasm to interfere the EGFP translation and achieve the knockdown. The above results presented the evidence that Si-UCNPs conjugate with photolinker could be employed as a safe and reliable nanoplatform for the NIR light controllable gene and siRNA delivery.

13.3.7 Targeting Ligands Activation by Upconverted Light

Most of the drug delivery systems are found to distribute the payloads throughout the entire body without selectivity, rather than at the desired site needs treatment, and hence reduce their efficacy and increase toxicity to off-target cells [58]. Specific ligands can guide drug or nanoparticle to a particular cell type, hence active targeting ligands are a potential solution to this long existing problem in drug delivery
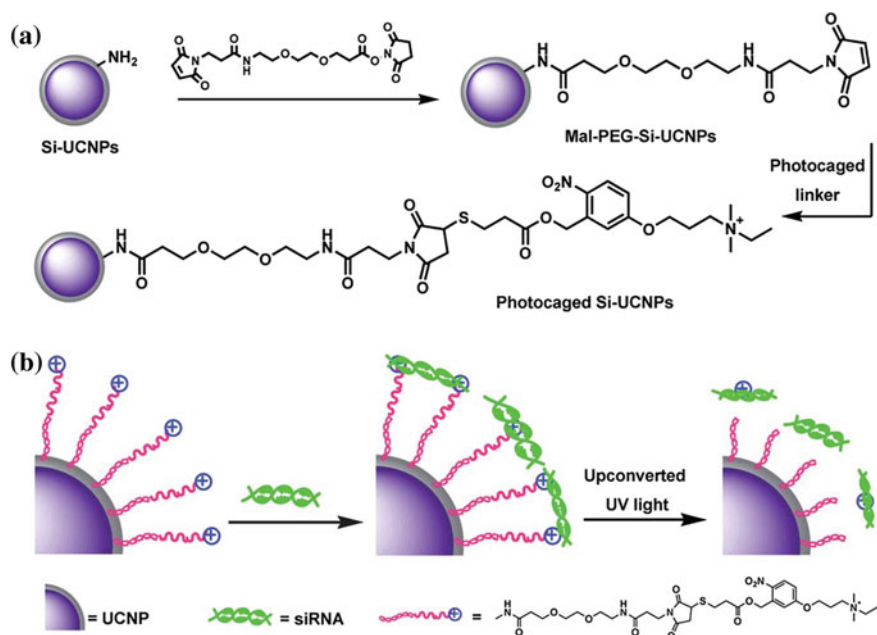
Scheme 13.11 Schematic illustration of **a** the synthesis processes of cationic photocaged Si-UCNPs; **b** siRNA adsorption on the particles surface and then photorelease by upconverted UV light from UCNPs. Reproduced from Ref. [57] by permission of The Royal Society of Chemistry

[59]. The ligands include antibodies, peptides, aptamers, or small molecules agonist/antagonist/nutrient, which can bind tightly with specific receptors, channels, etc., on the specific cell membrane.

One of the most widely used targeting moieties in the nanoparticle-based drug delivery system is folic acid, as it benefits including smaller size vitamin, non-immunogenicity, stability, and high affinity to folate receptors (FR) that are selectively overexpressed on the surface of many human cancers [60]. In order to improve targeting delivery of drugs to their desired site of action in a controlled manner, Yeh and co-workers have masked FA using a caging molecule (*o*-nitrobenzyl derivatives) and then conjugated on UCNPs [61]. First, core NaYF$_4$: Yb, Tm UCNPs were coated with a layer of silica for making them hydrophilic as well as for ease of surface modification. The surface of UCNPs@SiO$_2$ was then modified with PEG followed by DOX loading to yield PEGylated UCNPs@SiO$_2$-DOX. The caged folate was then decorated on the surface of PEGylated UCNPs@SiO$_2$-DOX to generate caged folate-PEGylated UCNPs@SiO$_2$-DOX (Fig. 13.12). Upon irradiation of a 980 nm diode laser, the emitted converting UV light uncaged a photolabile protecting group and allowed folate-conjugated UNCPs to target HeLa cancer cells. The low FR expression of lung A549 cells exhibited much less particle uptake compared with HeLa cells, supporting the susceptibility of phototargeting design to improve selective uptake for tumor-homing agents. The photolabile nature
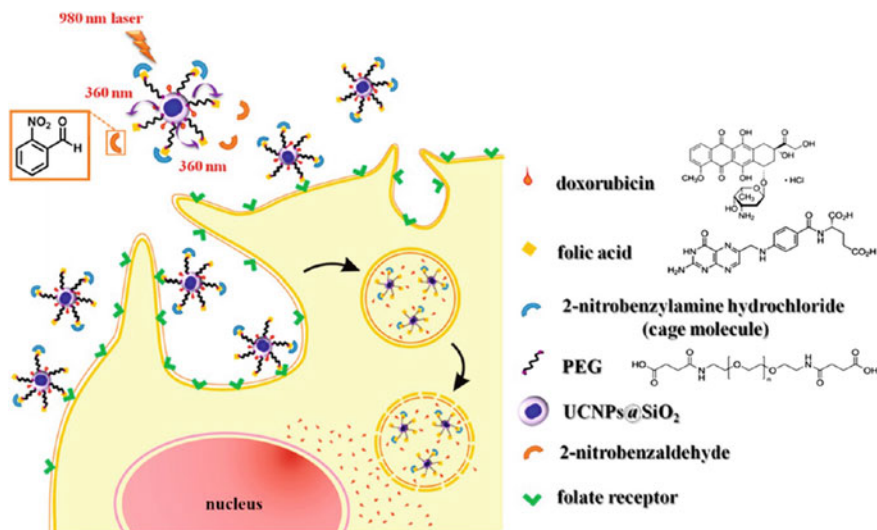
Fig. 13.12 Illustration of photocaged UCNPs following NIR laser activation to remove cage molecules and subsequent targeting of cancer cells. Reprinted with the permission from Ref. [61]. Copyright 2013 American Chemical Society

of the cage NBA was followed by the change in absorbance at 285 nm due to the formation of the photocleavage product 2-nitroso-benzaldehyde. Detailed intracellular drug delivery studies revealed that under the irradiation of NIR light, the uncaged folate-PEGylated UCNPs@SiO$_2$-DOX was distributed across the cytoplasm of HeLa cells, from which the DOX was released from the cytoplasm and entered into the nuclei, resulting in cell shrinkage due to the cytotoxicity of DOX. In addition, therapeutic efficacy of tumor shrinkage and ex vivo organ dissection photoluminescence imaging was evaluated by the injection of UNCPs complex through tail vein into mice bearing HeLa tumors upon the exposure of NIR light.

13.4 Concluding Remarks

This chapter has described the latest developments in the field of UCNPs-based photocaging technology with an emphasis on their potential applications. Photoactivation strategies, which mostly rely on photolabile protecting groups that can be cleaved after UV light absorption with a high spatiotemporal resolution, have especially found a widespread use in the control of dynamics of biological processes remotely. The use of UV light or two-photon excitation has limitations in the biological application of caged systems mainly due to the low level of tissue penetration along with phototoxic effects (UV) and the availability of low NIR

absorption cross section of multiphoton caging groups associated with the use of high-peak power pulsed laser (two-photon process), respectively. However, UCNPs have opened intriguing platforms in photocaging systems, offering the possibility to cleave photolabile compounds by irradiation with highly tissue-penetrating NIR light, without expensive light source or redeveloping the photoprotecting groups. In addition, the emission tunability, high photostability along with higher efficiency of upconversion process have made UCNPs the nanocarriers of choice for photocaging applications. The use of these upconversion nanoparticles has been comprehensively reviewed in photo-triggered release (including encapsulating polymer fragmentation and linker cleavage), photoactivation of targeting ligands, photoactivation of bioluminescence, and photo-triggered prodrug activation. At present, the advances of this UCNP-assisted photouncaging technique are still recognized at its infancy stage. There is considerable scope for further development of stimulus-responsive nanocarriers designed to enhance the localization and efficacy of drug payloads, and new strategies for controlled drug release are continuously being proposed. On the other hand, despite their superior advantages, the community of UCNPs still exist some limitations including low quantum yields, high water absorption (leading to heating effects) at 980 nm NIR excitation wavelength, high batch to batch variability, and uncertain systematic toxicity and clearance. Hence, researchers start focusing on making efforts to overcome the issues on reducing heating effects [62], friendlier excitation wavelength, enhancing upconverted emission, reducing surface quenching effects by coating with inactive/active shells, in-depth toxicity, drug delivery studies, etc. Based on the potential advantages offered by UCNPs with all the innovations in chemistry and biology, photoactive technique will continue to improve and provide more exciting fruitful inspirations in both preclinical studies and clinic use.

References

1. Mayer G, Heckel A (2006) Biologically active molecules with a "light switch". Angew Chem Int Ed 45: 4900−4921.
2. Lee HM, Larson DR, Lawrence DS (2009) Illuminating the chemistry of life: design, synthesis, and applications of "caged" and related photoresponsive compounds. ACS Chem Biol 4: 409−427.
3. Idris NM, Jayakumar MKG, Bansala A, Zhang Y (2015) Upconversion nanoparticles as versatile light nanotransducers for photoactivation applications. Chem Soc Rev 44: 1449−1478.
4. Klan P, Solomek T, Bochet CG, Blanc A, Givens R, Rubina M, Popik V, Kostikov A, Wirz J (2013) Photoremovable protecting groups in chemistry and biology: reaction mechanisms and efficacy. Chem Rev 113: 119−191.
5. Kaplan JH, Forbush B, Hoffman JF (1978) Rapid photolytic release of adenosine 5'-triphosphate from a protected analog: utilization by the sodium:potassium pump of human red blood cell ghosts. Biochemistry 17: 1929–1935.
6. Deiters A (2010) Principles and applications of the photochemical control of cellular processes. ChemBioChem 11: 47–53.

7. Rothman DM, Shults MD, Imperiali B (2005) Chemical approaches for investigating phosphorylation in signal transduction networks. Trends Cell Biol 15: 502–510.

8. Lee HM, Xu WC, Lawrence DS (2011) Construction of a photoactivatable profluorescent enzyme via propinquity labeling. J Am Chem Soc 133: 2331−2333.

9. Brieke C, Rohrbach F, Gottschalk A, Mayer G, Heckel A (2012) Light-controlled tools. Angew Chem Int Ed 51: 8446−8476.

10. Shao Q, Xing B (2010) Photoactive molecules for applications in molecular imaging and cell biology. Chem Soc Rev 39: 2835−2846.

11. Zhang YG, Ma WY, Kaji A, Bode AM, Dong ZG (2002) Requirement of ATM in UVA-induced Signaling and Apoptosis. J Biol Chem 277: 3124−3131.

12. He YY, Huang JL, Chignell CF (2004) Delayed and sustained activation of extracellular signal-regulated kinase in human keratinocytes by UVA: IMPLICATIONS IN CARCINOGENESIS. J Biol Chem 279: 53867−53874.

13. Olson JP, Banghart MR, Sabatini BL, Ellis-Davis GCR (2013) Spectral evolution of a photochemical protecting group for orthogonal two-color uncaging with visible light. J Am Chem Soc 135: 15948–15954.

14. Fournier L, Gauron C, Xu L, Aujard I, Saux TL, Gagey-Eilstein N, Maurin S, Dubruille S, Baudin JB, Bensimon D, Volovitch M, Vriz S, Jullien LA (2013) Blue-absorbing photolabile protecting group for *in vivo* chromatically orthogonal photoactivation. ACS Chem Biol 8: 1528−1536.

15. Priestman MA, Lawrence, DS (2010) Light-mediated remote control of signaling pathways. Biochim Biophys Acta 1804: 547–558.

16. Furuta T, Wang SS, Dantzker JL, Dore TM, Bybee WJ, Callaway EM, Denk, W, Tsien RY (1999) Brominated 7-hydroxycoumarin-4-ylmethyls: photolabile protecting groups with biologically useful cross-sections for two photon photolysis, Proc Natl Acad Sci USA 96: 1193–1200.

17. Shell TA, Shell JR, Rodgers ZL, Lawrence DS (2014) Tunable visible and near-IR photoactivation of light-responsive compounds by using fluorophores as light-capturing antennas. Angew Chem Int Ed 53: 875−878.

18. Dakin K, Li W (2006) Infrared-LAMP: two-photon uncaging and imaging of gap junctional communication in three dimensions. Nat Methods 3: 959−959.

19. Szacitowski K, Macyk W, Drzewiecka-Matuszek A, Brindell M, Stochel G (2005) Bioinorganic photochemistry: frontiers and mechanisms. Chem Rev 105: 2647−2694.

20. Denk W (1994) Two-photon scanning photochemical microscopy: mapping ligand-gated ion channel distributions. Proc Natl Acad Sci USA 91: 6629−6633.

21. Wang P, Ahmadov TO, Lee C, Zhang P (2013) Ligase-assisted signal-amplifiable DNA detection using upconversion nanoparticles. RSC Adv 3: 16326−16329.

22. Liu J, Liu Y, Liu Q, Li C, Sun L, Li F (2011) Iridium(III) complex-coated nanosystem for ratiometric upconversion luminescence bioimaging of cyanide anions. J Am Chem Soc 133: 15276−15279.

23. Zhou J, Liu Z, Li F (2012) Upconversion nanophosphors for small-animal imaging. Chem Soc Rev 41: 1323–1349.

24. Li C, Yang D, Ma P, Chen Y, Wu Y, Hou Z, Dai Y, Zhao J, Sui C, Lin J (2013) Multifunctional upconversion mesoporous silica nanostructures for dual modal imaging and in vivo drug delivery. Small 9: 4150–4159.

25. Zhou J, Liu Q, Feng W, Sun Y, Li F (2015) Upconversion luminescent materials: advances and applications. Chem Rev 115: 395−465.

26. Chen G, Agren H, Ohulchanskyya TY, Prasad PN (2015) Light upconverting core–shell nanostructures: nanophotonic control for emerging applications. Chem Soc Rev 44: 1680−1713.

27. Gao HD, Thanasekaran P, Chiang CW, Hong JL, Liu YC, Chang YH, Lee HM (2015) Construction of a near-infrared-activatable enzyme platform To remotely trigger intracellular signal transduction using an upconversion nanoparticle. ACS Nano 9: 7041–7051.

28. Chen X, Peng D, Ju Q, Wang F (2015) Photon upconversion in core–shell nanoparticles. Chem Soc Rev 44: 1318−1330.

29. Jalil RA, Zhang Y (2008) Biocompatibility of silica coated NaYF$_4$ upconversion fluorescent nanocrystals. Biomaterials 29: 4122–4128.
30. Wu SW, Han G, Milliron DJ, Aloni S, Altoe V, Talapin DV, Cohen BE, Schuck PJ (2009) Non-blinking and photostable upconverted luminescence from single lanthanide-doped nanocrystals. Proc Natl Acad Sci USA 106: 10917–10921.
31. Cheng L, Yang K, Shao M, Lu X, Liu Z (2011) *In vivo* pharmacokinetics, long-term biodistribution and toxicology study of functionalized upconversion nanoparticles in mice. Nanomedicine 6: 1327–1340.
32. Cheng L, Wang C, Liu Z (2013) Upconversion nanoparticles and their composite nanostructures for biomedical imaging and cancer therapy. Nanoscale 5: 23−37.
33. Hilderbrand SA, Weissleder R (2010) Near-infrared fluorescence: application to *in vivo* molecular imaging. Curr Opin Chem Biol 14: 71−79.
34. Yu H, Li J, Wu D, Qiu Z, Zhang Y (2010) Chemistry and biological applications of photo-labile organic molecules. Chem Soc Rev 39: 464−473.
35. Zhu C, Ninh C, Bettinger CJ (2014) Photoreconfigurable polymers for biomedical applications: chemistry and macromolecular engineering. Biomacromolecules 15: 3474−3494.
36. Carling CJ, Nourmohammadian F, Boyer JC, Branda NR (2010) Remote-control photorelease of caged compounds using near-infrared light and upconverting nanoparticles. Angew Chem Int Ed 49: 3782–3785.
37. Garcia JV, Yang J, Shen D, Yao C, Li X, Wang R, Stucky GD, Zhao D, Ford PC, Zhang F (2012) NIR-triggered release of caged nitric oxide using upconverting nanostructured materials. Small 8: 3800–3805.
38. Burks PT, Garcia JV, GonzalezIrias R, Tillman JT, Niu M, Mikhailovsky AA, Zhang J, Zhang F, Ford PC (2013) Nitric oxide releasing materials triggered by near-infrared excitation through tissue filters. J Am Chem Soc 135: 18145−18152.
39. Fedoryshin LL, Tavares AJ, Petryayeva E, Doughan S, Krull U (2014) Near-infrared-triggered anticancer drug release from upconverting nanoparticles. ACS Appl Mater Interfaces 6: 13600 −13606.
40. Carling CJ, Boyer JC, Branda N (2009) Remote-control photoswitching using NIR light. J Am Chem Soc 131: 10838–10839.
41. Yang Y, Shao Q, Deng R, Wang C, Teng X, Cheng K, Cheng Z, Huang L, Liu Z, Liu X, Xing B (2012) *In vitro* and *in vivo* uncaging and bioluminescence imaging by using photocaged upconversion nanoparticles. Angew Chem Int Ed 51: 3125–3129.
42. Shen J, Chen G, Ohulchanskyy TY, Kesseli SJ, Buchholz S, Li Z, Prasad PN, Han G (2013) Tunable near infrared to ultraviolet upconversion luminescence enhancement in (α-NaYF$_4$:Yb, Tm)/CaF$_2$ core/shell nanoparticles for in situ real-time recorded biocompatible photoactivation. Small 9: 3213–3217.
43. Dai Y, Xiao H, Liu J, Yuan Q, Ma P, Yang D, Li C, Cheng Z, Hou Z, Yang P, Lin J (2013) *In vivo* multimodality imaging and cancer therapy by near-infrared light-triggered *trans*-platinum pro-drug-conjugated upconverison nanoparticles. J Am Chem Soc 135: 18920−18929.
44. Min Y, Li J, Liu F, Yeow EKL, Xing BG (2014) Near-infrared light-mediated photoactivation of a platinum antitumor prodrug and simultaneous cellular apoptosis imaging by upconversion-luminescent nanoparticles. Angew Chem Int Ed 53: 1012−1016.
45. Fomina N, McFearin C, Sermsakdi M, Edigin O, Almutairi A (2010) UV and near-IR triggered release from polymeric nanoparticles. J Am Chem Soc 132: 9540−9542.
46. Yan B, Boyer JC, Branda NR, Zhao YJ (2011) Near-infrared light-triggered dissociation of block copolymer micelles using upconverting nanoparticles. J Am Chem Soc 133: 19714–19717.
47. Yan B, Boyer JC, Habault D, Branda NR, Zhao Y (2012) Near infrared light triggered release of biomacromolecules from hydrogels loaded with upconversion nanoparticles. J Am Chem Soc 134: 16558–16561.
48. Viger ML, Grossman M, Fomina N, Almutairi A (2013) Low power upconverted near-IR light for efficient polymeric nanoparticle degradation and cargo release. Adv Mater 25: 3733–3738.

49. Zhao L, Peng J, Huang Q, Li C, Chen M, Sun Y, Lin Q, Zhu L, Li F (2014) Near-infrared photoregulated drug release in living tumor tissue via yolk-shell upconversion nanocages. Adv Funct Mater 24: 363–371.

50. Xing Q, Li N, Jiao Y, Chen D, Xu J, Xu Q, Lu J (2015) Near-infrared light-controlled drug release and cancer therapy with polymer-caged upconversion nanoparticles. RSC Adv 5; 5269–5276.

51. Xu QC, Zhang Y, Tan MJ, Liu Y, Yuan S, Choong C, Tan NS, Tan TTY (2012) Anti-cAngptl4 Ab-conjugated N-TiO$_2$/NaYF$_4$:Yb,Tm nanocomposite for near infrared-triggered drug release and enhanced targeted cancer cell ablation. Adv Healthcare Mater 1: 470–474.

52. Yang Y, Velmurugan B, Liu X, Xing B (2013) NIR photoresponsive crosslinked upconverting nanocarriers toward selective intracellular drug release. Small 9: 2937–2944.

53. Jayakumar MKG, Idris NM, Zhang Y (2012) Remote activation of biomolecules in deep tissues using near-infrared-to-UV upconversion nanotransducers. Proc Natl Acad Sci USA 109: 8483–8488.

54. Dykxhoorn DM, Lieberman J (2006) Knocking down disease with siRNAs. Cell 126: 231–235.

55. Liu G, Choi KY, Bhirde A, Swierczewska M, Yin J, Lee SW, Park JH, Hong JI, Xie J, Niu G, Kiesewetter DO, Lee S, Chen X (2012) Sticky nanoparticles: A platform for siRNA delivery by a bis(zinc(II)dipicolylamine)-functionalized, self-assembled nanoconjugate. Angew Chem Int Ed 51: 445–449.

56. Dunn SS, Tian S, Blake S, Wang J, Galloway AL, Murphy A, Pohlhaus PD, Rolland JP, Napier ME, DeSimone JM (2012) Reductively responsive siRNA-conjugated hydrogel nanoparticles for gene silencing. J Am Chem Soc 134: 7423–7430.

57. Yang Y, Liu F, Liu X, Xing B (2013) NIR light controlled photorelease of siRNA and its targeted intracellular delivery based on upconversion nanoparticles. Nanoscale 5: 231–238.

58. Kadam RS, Bourne DWA, Kompella UB (2012) Nano-advantage in enhanced drug delivery with biodegradable nanoparticles: contribution of reduced clearance. Drug Metab Dispos 40: 1380−1388.

59. Dvir T, Banghart MR, Timko B, Langer R, Kohane D (2010) Photo-targeted nanoparticles. Nano Lett 10: 250−254.

60. Xia L, Kong X, Liu X, Tu L, Zhang Y, Chang Y, Liu K, Shen D, Zhao H, Zhang B H (2014) An upconversion nanoparticle-zinc phthalocyanine based nanophotosensitizer for photodynamic therapy. Biomaterials 35: 4146–4156.

61. Chien YH, Chou YL, Wang SW, Hung ST, Liau MC, Chao YJ, Su CH, Yeh CS (2013) Near-infrared light photocontrolled targeting, bioimaging, and chemotherapy with caged upconversion nanoparticles *in vitro* and *in vivo*. ACS Nano 7: 8516–8528.

62. Wang YF, Liu GY, Sun LD, Xiao JW, Zhou, JC, Yan CH (2013) Nd^{3+}-sensitized upconversion nanophosphors: efficient *in vivo* bioimaging probes with minimized heating effect. ACS Nano 7: 7200−7206.

Chapter 14
Foundations of White Light Quantum Dots

Shu-Ru Chung

Abstract White light by the combination of blue light-emitting diode (LED) and yellow phosphors is a relatively simple manufacturing process. However, it cannot be avoided the problem of reduced efficiency caused by scattering due to the large size of phosphors. In order to improve the color rendering index (CRI) of device, mixing various phosphors to meet the requirement is the main trends. However, the mixing ratio and decay rates between different phosphors will affect the device performance. Even using semiconductor nanocrystals (NCs, also called quantum dots, QDs) as nanophosphor, the same problems still exist, especially when they are applicated in lighting. If we can prepare white light quantum dot (W-QD) with high quantum yield (QY), the above problem can be overcome. Therefore, how to design synthesis process to obtain high quality of W-QDs with both band-edge and surface-state emission is the key issue. In this chapter, I describe the fundamental mechanism and preparation method of W-QDs. Some challenges for the application of W-QDs, especially in solid-state lighting and backlight, are also discussed.

14.1 Introduction

Because of the energy demands, the white light-emitting diodes (WLEDs) are booming development. Those WLED can be used in solid-state lighting and backlight in liquid crystal displays (LCD). As we know that in order to get white light, mixing two kinds of wavelength is necessary. Therefore, white light by the combination of blue LED and yellow phosphors is a relatively simple manufacturing process. However, it cannot be avoided the problem of reduced efficiency caused by scattering due to the large size of phosphors. In order to improve the color rendering index (CRI) of device, mixing various phosphors to meet the requirement is the main trends. However, the mixing ratio and decay rates between

S.-R. Chung (✉)

Energy Materials and Devices Laboratory, Materials Science and Engineering, National Formosa University, Yunlin 63201, Taiwan, ROC
e-mail: srchung@nfu.edu.tw

different phosphors will affect the device performance. Even using semiconductor nanocrystals (NCs, also called quantum dots, QDs) as nanophosphor, the same problems still exist, especially when they are applicated in lighting. For lighting application, monochromatic semiconductors QDs have the additional issues, which are the thermal stability and the package form. For backlight application, the unique advantage of monochromatic semiconductor QD relative to the phosphor is the wavelength tunability, and such monochromatic semiconductor QDs such as Cd-based binary or ternary QDs have been extensively studied. The present chapter reviews the principle and process for white light-emitting semiconductor QD such as CdSe, CdS, $Zn_{0.93}Cd_{0.07}Se$, and $Zn_xCd_{1-x}S$, expected to contribute to the future of the white nanocrystalline materials in lighting and backlight applications.

14.2 Fundamental Mechanism of White Light Quantum Dots

A large number of colloidal routes that operate in the range of 90–320 °C were developed for the synthesis of luminescence binary (CdSe, CdTe) and ternary QDs ($Zn_xCd_{1-x}Se$, $Zn_xCd_{1-x}Te$). These colloidal routes provide monodispersed QDs that exhibit narrow and symmetrical photoluminescence spectra. Figures 14.1 and 14.2 shows the photograph of those QDs excited by 365-nm UV lamp. An obvious blue shift can be observed due to quantum confinement and compositional effect. On the other hand, the white light-emitting CdSe, $Zn_xCd_{1-x}Se$, CdS, and $Zn_xCd_{1-x}S$ QDs
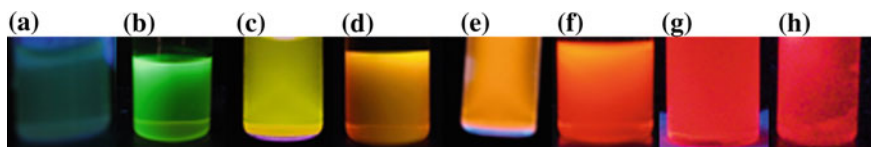
Fig. 14.1 Photographs of CdSe QDs. **a** 480–510 nm, **b** 510–540 nm, **c** 540–560 nm, **d** 560–570 nm, **e** 570–590 nm, **f** 590–610 nm, **g** 610–630 nm, and **h** 630–650 nm (provided by National Formosa University, Energy Materials and Devices Lab)
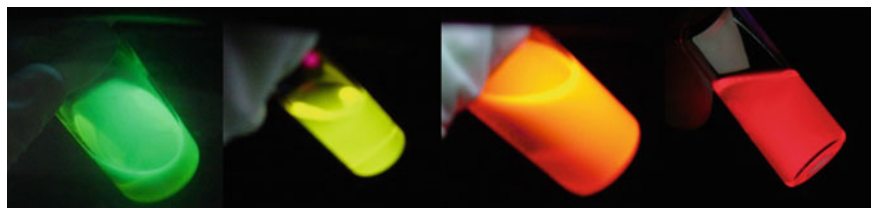

Fig. 14.2 Photographs of $Zn_xCd_{1-x}Se$ QDs (provided by National Formosa University, Energy Materials and Devices Lab)

have broad photoluminescence spectrum [1–6]. Using these QDs can achieve pure white light with high CRI without suffering from self-absorption. Above literatures mentioned that the white light from CdSe, CdS, and $Zn_xCd_{1-x}Se$ QDs is a result of contributions by emission from surface midgap states that arise from the presence of non-coordinated surface Se or S sites [1, 7], while for $Zn_xCd_{1-x}S$ QDs, Zn content and Zn oxide state play an important role [5, 6]. Moreover, those white light-emitting QDs (W-QDs) are unusual, and they are not popular in organometallic pyrolysis route [1, 4–6] or aqueous decomposition–precipitation method [2, 3]. Sapra et al. [8] pointed out that the W-QDs can be prepared by chance or by design (core/shell/shell) of the fabrication process. They think that white light emission CdSe and CdS QDs are prepared by chance. Moreover, multi-injection of Se-trioctylphosphine (TOP) precursor into coordinating solvent can produce nonuniform particle size distribution of QDs, resulting in the combination of two or three emission peaks to produce white light. However, the peaks position and the intensity of those peaks are not easy to control during process. Can we get W-QDs with single composition, one-pot, and single injection process, not only by chance? Is it possible to get those W-QDs by designing surfactants or other parameters? If we can find the formation mechanism of W-QD, we can synthesize the W-QD by design, and it is also possible to improve the quantum yield (QY) by design. High QY of W-QD is the first criteria to make WLED with high efficacy. Those single composition and uniform size distribution of W-QDs have the common features. First, they have two emission peaks: One is narrow and sharp and the other one is broad. Secondary, narrow, and sharp peak locates on high energy site, while broad one in low energy site. Third, the QY of those W-QDs is lower. Four, all of them only can be excited by UV-LED (i.e., the excitation wavelength is less than 410 nm). In terms of W-QDs, for the CdSe QDs, the very broad emission spectrum can be observed when the particle size is down to less than 2 nm. It is caused by the combination of band-edge and surface-state emission [1], as shown in Fig. 14.3. In CdSe QDs, Puzder et al. [9] conclude that the emission is from a

Fig. 14.3 Absorption and emission spectra of magic-size CdSe NC. Reprinted with the permission from Ref. [1]. Copyright 2005 American Chemical Society
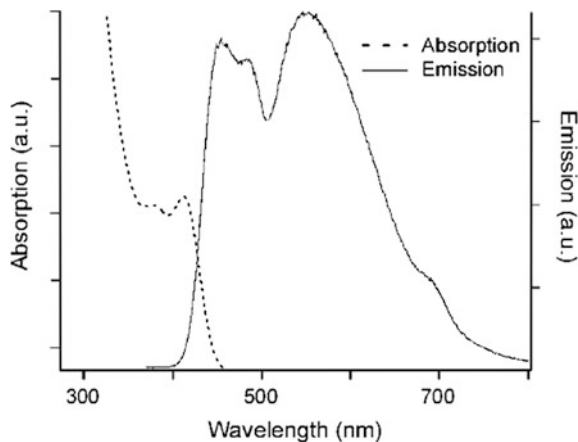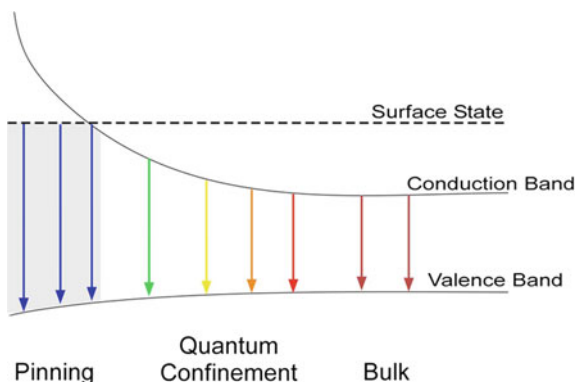
surface state, while work by Lee et al. [10] suggests that the emission arises from a
state in the upper conduction band that is unaffected by quantum confinement. At
bulk sizes, CdSe has fixed band gap energy. As CdSe enters the quantum con-
finement regime, the band gap becomes size dependent. However, at ultrasmall
sizes, the emission spectrum becomes pinned when the conduction band becomes
higher in energy than a size-independent surface state, as shown in Fig. 14.4 [11].

The fluorescent spectrum of the $Zn_{0.93}Cd_{0.07}Se$ QDs also consists of a band-edge
emission at 431 nm and a trap-state emission at 499 nm [2], as shown in Fig. 14.5.
This result is also consistent with ultrasmall CdSe QDs [1].

Khanna and Singh [12] pointed out that the stable orange light emission from
CdS NCs in dimethylformamide (DMF) was believed to be due to trap state created
because of the presence of metal-rich surfaces, and Chen et al. [3] explain that an
effect of band broadening is that the surface of CdS NCs and the particle size of
CdS change when CdS NCs are embedded in polymethylmethacrylate (PMMA)
matrix as shown in Fig. 14.6. Nizamoglu et al. [4] also pointed out that the CdS
surface-state-emitting (SSE) NCs (as shown in Fig. 14.7) with a typical dot
diameter of 2–3 nm were found to exhibit a relatively higher QY of 17 %. Based on
these literatures, the white light of CdS QDs is also radiative combination of
band-edge and surface-state (midgap states) emission.

For white $Zn_xCd_{1-x}S$ QD, it also combines band-edge and surface-state
emission peaks to produce white light [5]. The difference between CdSe (CdS) and
$Zn_xCd_{1-x}S$ W-QD is the peak ratio and position between band edge and surface
state, which can be tuned by adjusting the Zn concentration [5, 6]. Chung's group
pointed that the Zn shell of QDs may enhance the surface-state emission, thereby
promoting the white light emission and increasing the QY to 56 %. Moreover, the
stability of NCs is also excellent. The surface oxide-rich structure could be the
reason that influences the surface-state emission and stability of the $Zn_xCd_{1-x}S$ NCs
[6], as shown in Fig. 14.8.

According to those literatures, we can summarize that the emission mechanism
of W-QD is due to the combination of band-edge and surface-state emission, which
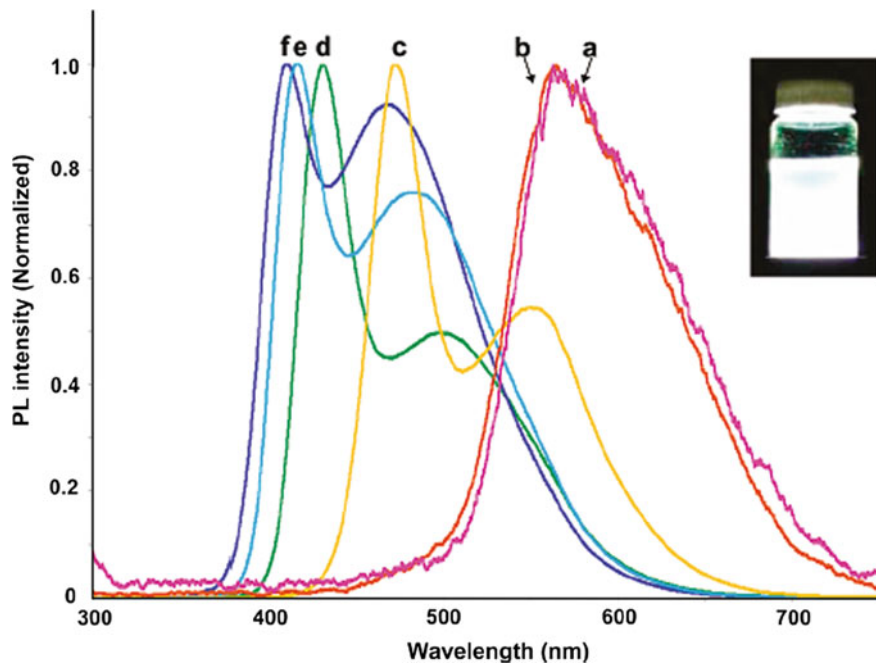can exist during the synthesis process. Therefore, to eliminate non-band-to-band

Fig. 14.5 PL spectra for the $Zn_xCd_{1-x}Se$ QDs with Zn mole fractions of **a** 0.00, **b** 0.02, **c** 0.30, **d** 0.93, **e** 0.97, and **f** 1.00. The excitation wavelength was set at 340 nm. *Inset* Fluorescent photoimage of the $Zn_{0.93}Cd_{0.07}Se$ QDs excited by a 365-nm UV lamp. Reprinted with the permission from Ref. [2]. Copyright 2009 American Chemical Society
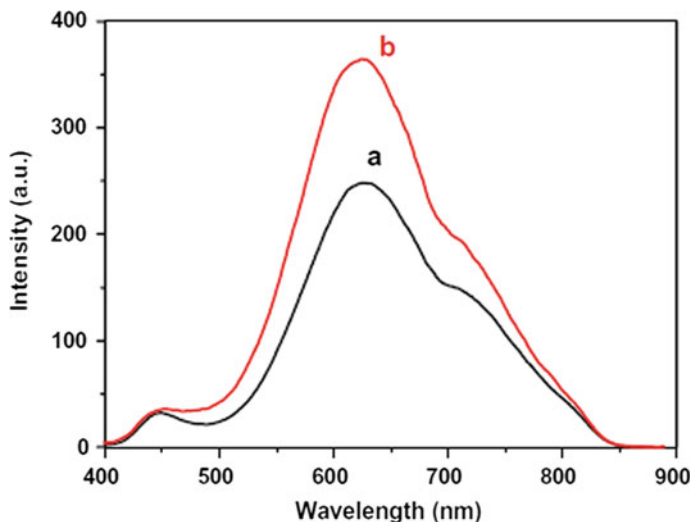

Fig. 14.6 Fluorescence emission spectra of **a** hydroxyl-coated CdS NCs suspension; **b** CdS-PMMA hybrid, CdS wt% = 6.0 wt%, dispersed in DMF with excitation at 302 nm. Reproduced from Ref. [3] by permission of The Royal Society of Chemistry
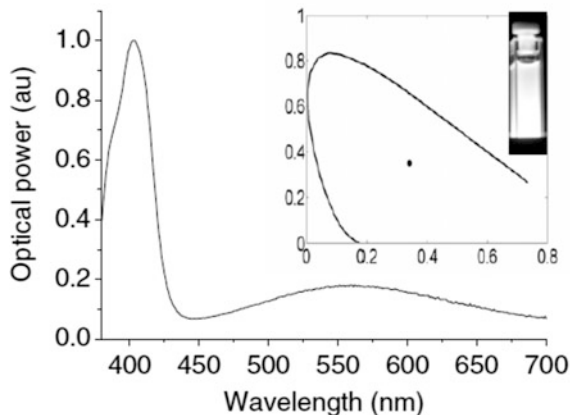
Fig. 14.7 The PL spectrum of CdS NCs in toluene solution. The corresponding (x, y) chromaticity coordinates and a photograph of the white light generated by these CdS NCs in toluene under UV excitation are also provided in the *inset*. Reprinted from Ref. [4], with kind permission from IOP Publishing
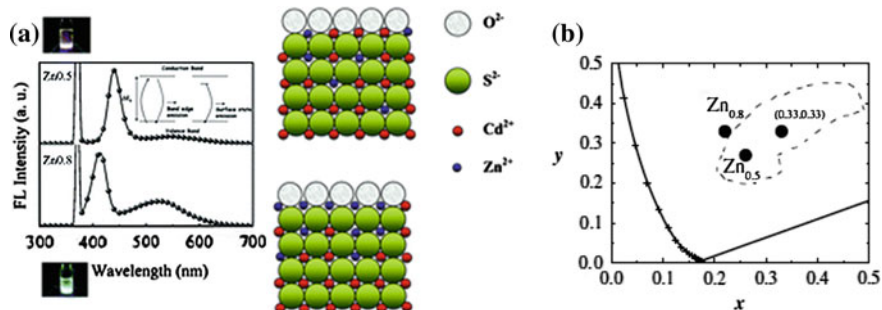

Fig. 14.8 Emission spectra, CIE coordinates, and schematic of $Zn_{0.5}Cd_{0.5}S$ and $Zn_{0.8}Cd_{0.2}S$ QDs reactions for 60 min. **a** Reproduced from Ref. [6] by permission of The Royal Society of Chemistry. **b** Reprinted from Ref. [5], with kind permission from Optical Society of America

emission upon the synthesis process, such as trap states and surface states, can get high-quality monochromic light. However, if we want to obtain W-QDs by one-pot synthesis process, we need to create or keep surface state and midgap state. Multiple injection of Se-TOP precursor into hot coordinating solvent, such as tri-octylphosphine oxide (TOPO) and TOPO/hexadecylamine (HDA), to produce different particle size distributions can also get white light. A midgap state can be easily created by doping skill, while it is difficult to create surface state or let the surface-state emission obvious by synthesis process. In CdSe W-QD, the energy state of band-to-band emission is higher than that of surface-state emission as the particle size is quite small. However, in other W-QDs, the particle size seems not so important, and the white light from those QDs is not due to small particle size.

However, until now, the emission mechanism of W-QDs is unclear especially for CdS and $Zn_xCd_{1-x}S$ W-QDs. We only know that the white light comes from the combination of band-edge emission and surface-state emission, but how to control the surface-state emission has not been clear yet.

14.3 Synthesis and Design of White Light Quantum Dots

W-QDs have a large stokes shift separating the absorption and emission peaks. Consequently, devices based on these QDs will not suffer from self-absorption, potentially resulting in higher device efficiency. Another advantage is that W-QD-based WLEDs would not require a mixture of phosphors or a complex feedback system to generate white light, resulting in much simpler devices. Furthermore, the addition of emission in the red portion of the spectrum gives higher color rendering than in devices emitting mostly blue and yellow light. The emission wavelengths of W-QDs are frequency down-converter to produce white light from 400 to 700 nm [1–6]. How to get white light through synthesis conditions and design procedures is a critical issue. The W-QDs might be prepared by design procedures instead of by chance. This section will summarize some procedures for W-QD synthesis, and introduces about the way to obtain W-QDs with simple and single composition by design.

14.3.1 Synthesis

As we know, QDs are nanometer-sized semiconductor particles with unique optical and electrical properties dictated by their size, shape, and the quantum physics that arise at the nano-scale. In the 1970s, physicists explored QDs as they were related to quantum wells and quantum wires, while in the 1980s, physical chemists explored the chemical methods to realize freestanding colloidal particles of such materials [13, 14], rather than relying on top-down methodologies. The 1990s saw major expansion of the chemical synthetic method toolkit [15–17], leading to colloidal QDs with relatively high monodispersity, efficient emission, and compositional control. These synthetic advances in combination with the exploration of early applications taking place in academia [18] led to a strong commercialization effort in the 2000s, including companies such as Quantum Dot Corp, Nanosys, Evident Technologies, Nanoco, QD Vision, and many others. Following decades of pioneering academic and industrial work [19, 20], the 2010s seems beyond doubt to be the decade of widespread product introduction, potentially penetrating into diverse markets such as solid-state lighting, displays, imaging, solar cells. Color tunable characteristic feature is the main advantage for QDs. However, those commercialized QD products are monochromatic light with core/shell structure.

Organometallic synthesis method is a more popular method to prepare high crystalline, monodisperse, and highly luminescent QDs with desirable surface functionalities. In 1993, Bawendi et al. used this method to prepare CdE (E = S, Se, and Te) QD [15]. The precursor of group II is dimethyl cadmium [(CH$_3$)$_2$Cd] and that of group VI is Se powder dissolved in TOP solution. They are injected into hot coordination solvent TOPO together. This procedure can be considered as a co-precipitation method. Temporally discrete nucleation is followed by slow growth on the existing nuclei [21]. The colloidal system can also undergo so-called Ostwald ripening; when the high surface energy of the small particles promotes their dissolution, re-deposition of the material onto the larger particles enables their further growth. Thus, the nucleation and growth processes dictate the final particle size and morphology. Peng et al. [22] used CdO as precursor and stearic acid (SA)/TOPO as capping reagent. Typical emission spectra of QD solutions show a full width at half maximum (FWHM) of less than 30 nm, depending on the degree of monodispersity achieved during the colloidal synthesis. TOPO and HDA are the most popular solvents to prepare high QY QDs due to the good passivation of QD surface [23, 24]. However, those QD products are monochromatic light with core/shell structure or alloyed composition. After organic or inorganic passivation, high QYs and uniform size distribution of QDs are obtained. But, how to prepare W-QDs?

Traditional NCs, with diameters >2 nm, exhibit near-monochromatic band-edge photoluminescence with high QYs approaching unity for core/shell structures [25–27]. A broad emission red-shifted from the band-edge emission is also well known in larger NCs and has been attributed to trap-state emission [28, 29]. However, as the diameter of the NC is reduced, this deep-trap emission becomes more prevalent and can eventually dominate the NC emission.

Rosenthal's group used an organometallic approach to achieve direct white light by integrating the broad surface-state emissions and band-edge emission from ~ 1.5-nm magic-sized CdSe NCs with an emission efficiency of 2–3 % [1]. This relatively low efficiency at the early and exploratory stage may not be considered as an intrinsic disadvantage, because the utility of directly W-QDs as the emitter eliminates the need for complex color mixing or conversion techniques. The modified approaches have the potential to enhance the lighting efficiency. One proposed modification was to increase the chain length of surface ligands, phosphonic acid, to enhance the NC QY to ~ 10 % [30]. Also, utilizing the modulation of the phosphonic acid ligand could control the NC surface-state emission, indicating that the surface ligand plays the dominant role in tuning the emission properties of these NCs.

Li et al. pointed out that high-quality colloidal photoluminescent CdS QDs were synthesized in non-coordinating solvent octadecene (ODE) using oleic acid (OA) as capping molecule. They found that the surface-state emission could be easily controlled by tuning the growth time and the molar ratio of Cd to S [31]. The synthesis procedure provided by Li et al. is similar to Nizamoglu et al. [4] publication in 2008.

CdS NCs can also be prepared by a simple one-step aqueous synthesis method using thioglycolic acid (TGA, C$_2$H$_4$O$_2$S) as the capping molecule. It was found that all of the as-prepared CdS NCs showed a strong broad emission in the range of 450–700 nm centered at 560 nm, which was attributed to the recombination of an

electron trapped in a sulfur vacancy with a hole in the valance band of CdS. The surface-defect-states emission intensity of CdS NCs significantly increased with the increase in Cd/S molar ratio and was maximum when Cd/S molar ratio was 2.0. If Cd/S molar ratio continued to increase, the surface-defect-states emission intensity would decrease. It was found that the surface-defect-states emission intensity increased with the increase in the TGA/Cd molar ratio and was maximum when the TGA/Cd molar ratio was equal to 1.8, and a further increase in the TGA/Cd molar ratio would lead to the decrease in the surface-defect-states emission intensity [31, 32]. Raevskaya et al. synthesized stable water-soluble ultrasmall 1.8-nm CdS NCs co-stabilized with Cd(II) complexes with NH_3 and mercaptoacetate ions. $CdCl_2$, mercaptoacetic acid, and NH_4OH were mixed together, and then, Na_2S solution was rapidly injected to form CdS NCs. The CdS NCs emit broad-band photoluminescence with a peak at 2.3 eV and a quantum yield of up to 15 % [33]. CdS NCs were prepared using a thermochemical approach. Here, TGA is used as the capping agent. TGA proved better in capping NCs, as the photoluminescence quantum efficiency is nearly 4 times increased. Briefly, 50 ml mixed solution of $CdSO_4$, $Na_2S_2O_3$, and TGA was prepared in the first step. In the second step, the solution pH was adjusted to 8.5 and heated at 80 °C for 1 h. The sample was permanently stirred during the heating process under ambient atmosphere. The synthesized CdS NCs were finally centrifuged and re-dispersed in DI water. The emission curve of CdS NC contains a peak located at 490 nm and a full width at half maximum (FWHM) of 140 nm with QY of 12 %. The emission is due to the surface trap states located in a broad energy spectrum inside the band gap [34].

Protière and Reiss prepared 4-nm CdS NC by organometallic decomposition route. Cadmium stearate, stearic acid (SA), oleylamine, and ODE were mixed in a three-neck flask equipped with a condenser and heated under argon to 300 °C. Then, a solution of sulfur in ODE was swiftly injected. The temperature was allowed to decrease to 250 °C and kept at this value for 20 min. A broad emission spectrum combined with band-edge and surface-state peaks can be obtained. However, the surface-state emission is restrained by capping with ZnS shell, and the band-edge emission increases with increasing the ZnS shell thickness. Finally, surface-state emission totally disappeared, and only the emission peaks ranging from 440 to 480 nm can be observed, depending on the thickness of ZnS shell [35].

$Zn_xCd_{1-x}S$ NCs are also prepared by organometallic route [5, 6]. CdO and ZnO were mixed with SA and then heated at 230 °C under Ar flow. TOPO and HDA were added, and then, the sample was reheated up to 320 °C. At this temperature, the S-ODE precursor, which was sulfur powder dissolved in ODE, was swiftly injected into a three-neck flask. After the reaction for 60 min, the mixed solution was swiftly cooled down to 150 °C. The $Zn_{0.5}$ and $Zn_{0.8}$ QDs after growth for 60 min have a broad excitation range. Moreover, the emission spectrum of two samples is created by two different emission peaks, including band-to-band (narrow peak) and surface defect emission (broad peak), resulting in white light emission. The QY of $Zn_{0.5}$ and $Zn_{0.8}$ is 35 and 52 %, respectively.

14.3.2   *Design*

There are two additional routes to generate white light [8]. The first one is to fabricate
the multishell structures on a NC core (e.g., core/shell/shell/shell, onion structure).
Different wavelengths can be obtained from the emission and thus can be mixed to
generate white light. This route is somewhat similar to the one based on color mixing.
The other route resembles the one reported by Rosenthal's group [1] combining
surface-state emissions with the band-edge emission in plain NCs to emit white light.
This strategy was also employed by Ozel et al. [36] who carefully integrated the silver
nano-island film with CdS NCs in a poly(methyl methacrylate) (PMMA) matrix. Such
careful integration could enhance the broad surface-state emission and simultaneously
suppress the band-edge transition of CdS NCs through matching their surface-state
emissions with the localized plasmon resonance of silver films. This resonance
engineering approach provided an alternative for the W-QD-based solid-state light-
ing. Also, broad and white emission from CdS NCs was realized by Nizamoglu et al.
and Shea-Rohwer et al. [4, 37, 38] via the surface modification and ligand displace-
ment. The fluorescence quantum yield for these CdS nanocrystals could be increased
to 37 %. Dai and his coworkers reported that the combination of the emissions from
magic- and regular-sized NC colloids could also achieve the goal of white light
generation [39].

The preparation methods of W-QDs are summarized in Table 14.1. According to
Table 14.1, we can find that low temperature or non-coordinating solvent seems to
be the critical condition to prepare W-QDs. Chung's group use this concept to
design a process to prepare CdSe W-QDs at 180 °C, and those CdSe W-QDs blend
with polymer, deposit into UV-LED, and cure by UV light [40]. They found that
the emission band of white CdSe QDs is quite broad (as shown in Fig. 14.9). The
white light of these CdSe QDs is a result of contributions by emissions from surface
midgap states that arise from the presence of non-coordinated surface selenium sites

Table 14.1 Preparation conditions of various W-QDs

| Compound	Precursor	Precursor	Complex	Surfactant	Temperature (°C)
CdSe [1]	CdO	Se:TBP: ODE	–	TOPO/HDA/DPA	330/270
CdSe [40]	CdO	Se:TOP	OA	ODE/HDA	180
$Zn_xCd_{1-x}Se$ [2]	$Zn(ClO_4)_2$ + $Cd(ClO_4)_2$	NaHSe	–	3-Mercaptopropionic acid	80
CdS [4]	CdO	S:ODE	–	ODE/oleic acid	250
CdS [34]	$C_{36}H_{70}CdO_4$	S:ODE	SA	Oleylamine/ODE	250
CdS [12]	$Cd(CH_3CO_2)_2$	H_2S	–	DMF	120–130
CdS [3]	$CdCl_2$	Na_2S	–	2-Mercaptoethanol/DMF	RT
CdS [33]	$CdSO_4$	$Na_2S_2O_4$	–	$C_2H_4O_2S$	80
$Zn_xCd_{1-x}S$ [5]	CdO + ZnO	S:ODE	SA	TOPO/HDA	320/290
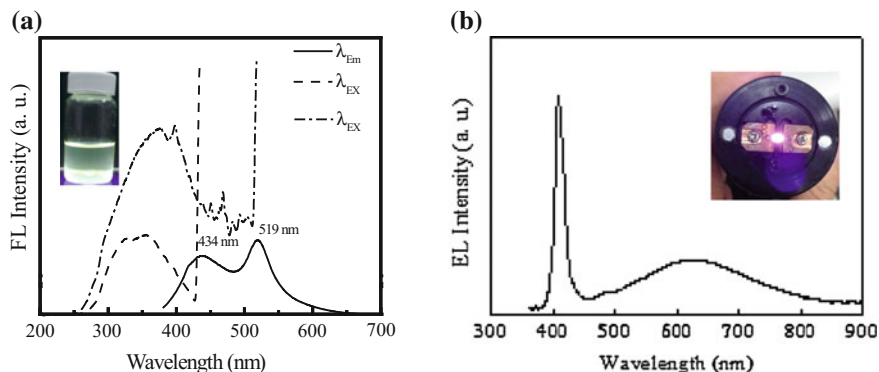
Fig. 14.9 **a** Excitation and emission spectra of white CdSe QDs and **b** EL spectrum of W-QD CdSe-based WLED (provided by National Formosa University, Energy Materials and Devices Lab)

[40]. This white LED is pumped by 405-nm UV chip, and the emission peak is also quite broad. This experimental result demonstrates that W-QDs can be obtained by the design of process parameters.

14.4 Applications and Challenges of White Light Quantum Dots

Solid-state lighting and display are the two main potential applications for W-QDs. However, both of them are faced with thermal stability problems and low quantum efficiency. In this section, I want to discuss the applications and challenges of W-QDs.

14.4.1 Applications

The electronic structure of colloidal QDs with diameter less than 10 nm is dominated by quantum size effects. This gives colloidal QDs with a narrowband emission that can be spectrally positioned by controlling the NC size during synthesis. Typical emission spectra of QD in hexane or toluene solutions show a FWHM of less than 30 nm, depending on the degree of monodispersity achieved during the colloidal synthesis. This is the feature of monochromatic light QDs and makes them quite suitable to applicate in backlight in liquid crystal display (LCD). The first demonstration of optical down-conversion with QDs used blue LEDs (GaN) to excite QDs in polylaurylmethacrylate (PLMA) and generate point sources of saturated color light [41]. The colorful QDs (i.e. we can tune the particle size and compositions of QDs to emit light very efficiently at precise red, green, and blue wavelengths, thus

creating an ideal light spectrum for LCDs) with pure color (i.e. QDs have very narrow spectral distribution of only 20-40 nm at full width at half-maximum (FWHM)) make them have the potential to application in blue LED-based backlight. A full color and flexible electroluminescent display was achieved using inkjet-printed thin films of QDs in polyisobutylene, optically excited by the blue EL from a commercial phosphor powder [42]. For the backlight of a LCD, temperatures can be around 100 °C. "At this temperature, the QDs lose efficiency and up to half of their brightness," said by QD Vision cofounder and chief technology officer Seth Coe-Sullivan. QD Vision spent a long time tuning the chemistry of its QDs to make them stable at higher temperatures [43]. Organic passivation of QD surface by capping reagent such as TOPO and HDA is used to improve QY. However, the melting point of TOPO and HDA is lower than 60 °C. Therefore, the main challenge of monochromatic QD application in display is the thermal stability, and quantum dot-enhanced films (QDEF) is the main design to prevent the thermal problem

Colloidal QD light-emitting devices (QD-LEDs) have generated considerable interest for applications such as thin film displays with improved color saturation (use the QD with monochromatic light) and white lighting with a high color rendering index (CRI) (add orange or red light QDs). If scientists and researchers can design a structure to maintain the QY of QDs, it is possible to use QDs in solid-state lighting. QD Vision Inc., in partnership with Nexxus Lighting, is currently commercializing a solid-state lighting solution based on optical excitation of QDs [44]. In their technology, QDs in a transparent matrix are dispersed onto a substrate to form a QD optic with recorded solid-state QD photoluminescence efficiency of 95 % ± 5, and are excited by an array of efficient blue LEDs to provide mixed color emission across the visible spectrum. This Nexxus/QD Vision Quantum Light™ platform demonstrated chromatic light quality with a CRI of 90 at a color temperature of 2700 K (soft white), a quality similar to that of an incandescent luminaire but with power to light conversion efficiency about 60 lm/W, which is four times higher than incandescent [44]. This noncontact design solves the heat problem coming from LED chip, resulting in the improvement in the CRI of LED by the combination of commercial WLED and QD plate. This noncontact concept is also used in Rosenthal's group to increase the loading level of these white light nanocrystals into the encapsulating polymer [45–47], such as biphenylperfluorocyclobutyl polymer. In this polymer, the NC loading level could reach up to 18 %, where the encapsulated ultrasmall CdSe NCs created white light with CIE coordinates of (0.324, 0.322) and a high CRI of 93. It should be noted that the loading level of NCs could not be unlimitedly increased, because the overload would lead to the aggregation of NCs.

Although recent progress shows that the strategies associated with ultrasmall NCs are able to tailor the white light shades through surface chemistry and synthetic modulation [47, 48], the related WLEDs have very low luminous efficiency (∼ 1.0 lm/W), and the stability of optical properties needs further to be improved [46].

W-QD with broad emission spectrum has a FWHM of larger than 50 nm, depending on the ratio between band-edge emission and surface-state emission achieved during the colloidal synthesis. They can produce WLED with more simple process without mixing several kinds of phosphors, and achieve the WLED with

high CRI. The device performances of W-QD-based WLED are summarized in Table 14.2. Chung's group reports the highest efficacy of 4.1 lm/W of WLED, due to the higher QY of ZnCdS QDs [5, 6]. For solid-state light application, W-QD is quite suitable with high CRI, while for backlight application, it seems not a good choice because the emission spectrum may not match with color filter and the efficacy is also low.

14.4.2 Challenges

In this section, I will talk about the challenges of white light-emitting QDs in synthesis and applications in white light-emitting devices. As mentioned above, those W-QDs can be prepared upon special process. However, the examples are not enough. Moreover, the thermal stability of W-QDs is quite poor, and surface-mounted device may not be a suitable package method. Unfortunately until now, W-QD only can be excited by UV-LED and the emission intensity ranging from 600 to 630 nm is low, although W-QD can be used as light emitter in backlight. Above two reasons are the main challenges of W-QDs applicated in LCD. The following section will discuss the challenges of W-QDs synthesis process and application in solid-state lighting.

14.4.2.1 Development of White Light Quantum Dots

The synthesis of monochromatic light emission NCs of controlled size and shape plays a crucial role in nanotechnology. Microscale and larger semiconducting crystals have electronic and optical properties that depend on their bulk band structure. When the size of NCs is reduced to the nano-scale, they essentially become molecule-like and this gives rise to unique properties which result in the NCs differing greatly from their bulk counterparts. Most importantly in NCs, certain properties are no longer influenced by their band structure, but by size and shape. However, in W-QDs, we need to control not only particle size and shape but also band structure. Table 14.1 shows the preparation method of W-QDs. In this table, we can find that low temperature or non-coordinating solvent seems to be a critical parameter to produce W-QDs, and high QY of W-QDs is a more important criteria factor to produce high performance of WLED. Until now, it seems not to have a rule to predict the W-QD products through the chemical process. This is the main challenge in W-QDs synthesis.

14.4.2.2 Development of White Light-Emitting Quantum Dot-Based White Light-Emitting Devices (W-QD-WLED)

Wood et al. pointed that QD-LEDs based on optical down-conversion have made it possible to begin the commercialization of QD-containing products. Electrically

Table 14.2 Device performance of white QD-based WLED

Samples	Resin	CIE (x, y)	CCT (K)	CRI	Efficacy (lm/W)	Photographs
CdSe [1] QY: 2–3 %	Polyurethane	(0.32, 0.37)	–	–	–	
CdSe [40] QY: 25 %	UV gel	(0.36, 0.30)	3900	85	2.7	
CdSe [46] QY: 2–3 %	BP-PFCB	(0.32, 0.32)	–	93	0.19	
CdS [4] QY: 17 %	PMMA	(0.35, 0.40)	4718	75	–	
$Zn_{0.8}Cd_{0.2}S$ [5] QY: 30–50 %	Silicone	(0.36, 0.33)	4200	86	4.1	
$Zn_{0.5}Cd_{0.5}S$ [5] QY: 20–30 %	Silicone	(0.43, 0.37)	2800	90	0.9	
$Zn_{0.93}Cd_{0.07}Se$ [2] QY: 12 %	Poly (dimethylsiloxane)	–	–	–	–	

excited QD films would eliminate the need for multicomponent integration of a QD optic with point-source standard III–V semiconductor LEDs. Demonstrations of such electrically excited planar-format QD-LED technologies could be utilized in novel-format lighting applications at high brightness, or alternatively could be the foundation of a new technology for high color quality, paper-thin flat panel-emissive display that would be structurally simpler than the present LCD display technologies [44].

The complications associated with the design and fabrication of W-QD-based WLED devices have generated great interest in developing white light phosphors that do not depend on complex doping schemes or combinations of materials. One proposed solution is to use a mixture of semiconductor NCs as the intrinsic emitting layer for an LED device. Semiconductor NCs exhibit high fluorescence quantum efficiencies and large molar absorptivities. However, they still suffer from the problem that simply mixing the traditional red, green, and blue colors to achieve white light results in a loss of total device efficiency due to self-absorption for a device of more than a few monolayers.

There are four key challenges facing the optical excitation of colloidal QDs: low quantum efficiency of W-QD, compatibility between W-QD and encapsulated polymer, W-QD only can be excited by UV-LED, and the last one is the thermal stability of W-QDs. In our laboratory, although high quantum efficiency of $Zn_{0.8}Cd_{0.2}S$ QDs can be prepared, it is also not high enough when compared to

commercial phosphor. Now, the highest efficacy of W-QD-based WLED in our laboratory is about 12 lm/W. If W-QDs suspended in solution routinely have photoluminescence quantum yields ranging from 2 to 56 %, then the QDs deposited in a close-packed thin film have the luminescence efficiency decreased by approximately an order of magnitude (to 5 or 10 %). Embedding QDs in an insulating polymer matrix decreases the amount of QD luminescence quenching observed in close-packed QD structures; however, dc electrical conductivity through these QD polymer composites is impeded by the low conductance of the wide band gap polymers.

14.5   Summary

This chapter focused on talking about the preparations and applications of W-QD. Although there is no clear way to control surface radiation energy state, from the literatures we can find some clues to help scientists and researcher to design and fabricate direction for the W-QD. Low temperature and non-coordinating solvents may be a good condition to prepare W-QDs. Those W-QDs can applicate in WLED with high CRI. However, the thermal stability and low QY of W-QDs are the critical problems, and it will limit their application in solid-state light. A good understanding of the fundamentals of W-QDs is not only important for the fabrication and processing of W-QDs, it is equally important to the application of W-QDs.

References

1. Bowers II, MJ, McBride, JR, Rosenthal, SJ (2005) White-Light Emission from Magic-Sized Cadmium Selenide Nanocrystals. J Am Chem Soc 127: 15378.
2. Shen CC, Tseng, WL (2009) One-Step Synthesis of White-Light-Emitting Quantum Dots at Low Temperature. Inorg Chem 48: 8689.
3. Chen L, Zhu J. Li Q, Chen S, Wang Y (2007) Controllable synthesis of functionalized CdS nanocrystals and CdS/PMMA nanocomposite hybrids. European Polymer Journal 43: 4593.
4. Nizamoglu S, Mutlugun E, Akyuz O, Perkgoz NK, Demir HV, Liebscher L, Sapra S, Gaponik N, Eychmüller A (2008) White emitting CdS quantum dot nanoluminophores hybridized on near-ultraviolet LEDs for high-quality white light generation and tuning. New J Physics 10: 023026.
5. Chen HS, Wang KW, Chen SS, Chung SR (2013) $Zn_xCd_{1-x}S$ quantum dots-based white light-emitting diodes. Optics Lett 38: 2080.
6. Chen HS, Chung SR, Chen TY, Wang KW (2014) Correlation between surface state and band edge emission of white light $Zn_xCd_{1-x}S$ nanocrystals. J Mater Chem C 2: 2664.
7. Schreuder MA, Xiao K, Ivanov IN, Weiss SM, Rosenthal SJ (2010) White Light-Emitting Diodes Based on Ultrasmall CdSe Nanocrystal Electroluminescence. Nano Lett 10: 573.
8. Sapra S, Mayilo S, Klar TA, Rogach AL, Feldmann J (2007) Bright White-Light Emission from Semiconductor Nanocrystals: by Chance and by Design. Adv Mater 19: 569.

9. Puzder A, Williamson A, Gygi F, Galli G (2004) Self-Healing of CdSe Nanocrystals: First-Principles Calculations. Phys Rev Lett 92: 217401.

10. Lee JRI, Meulenberg RW, Hanif KM, Mattoussi H, Klepeis JE, Terminello LJ, Buuren T van (2007) Experimental Observation of Quantum Confinement in the Conduction Band of CdSe Quantum Dots. Phys Rev Lett 98: 146803.

11. Dukes AD, Schreuder MA, Sammons JA, McBride JR, Smith NJ, Rosenthal SJ (2008) Pinned emission from ultrasmall cadmium selenide nanocrystals. J Chem Phys 129: 121102.

12. Khanna PK, Singh N (2007) J. Luminescence 127: 474.

13. Goldstein L, Glas F, Marzin JY, Charasse MN, Le Roux G (1985) Growth by molecular beam epitaxy and characterization of InAs/GaAs strained-layer superlattices. Appl Phys Lett **47**: 1099.

14. Steigerwald ML, Alivisatos AP, Gibson JM, Harris TD, Kortan R, Muller AJ, Thayer AM, Duncan TM, Douglass DC, Brus LE (1988) Surface derivatization and isolation of semiconductor cluster molecules. J Am Chem Soc 110: 3046.

15. Murray CB, Norris DJ, Bawendi MG (1993) Synthesis and characterization of nearly monodisperse CdE (E = sulfur, selenium, tellurium) semiconductor nanocrystallites. *J Am Chm Soc* **115**: 8706.

16. Hines MA, Guyot-Sionnest P (1996) Synthesis and Characterization of Strongly Luminescing ZnS-Capped CdSe Nanocrystals. *J Phys Chem* **100**: 468.

17. Dabbousi BO, Rodriguez-Viejo J, Mikulec FV, Heine JR, Mattoussi H, Ober R, Jensen KF, Bawendi MG (1997) (CdSe)ZnS Core-Shell Quantum Dots: Synthesis and Characterization of a Size Series of Highly Luminescent Nanocrystallites. *J Phys Chem B* **101**: 9463.

18. Bruchez M, Moronne M, Gin P, Weiss S, Alivisatos AP (1998) Semiconductor Nanocrystals as Fluorescent Biological Labels. *Science* **281**: 2013.

19. Kazlas P, Zhaoqun Z, Stevenson M, Niu Y, Breen C, Perkins J, Kim S, Mahan G, Steckel JS, Coe-Sullivan S, Ritter J (2010) Quantum Dot Light Emitting Diodes for Full-color Active-matrix Displays. *SID Symposium Digest of Technical Papers 41: 473.*

20. Dang C, Lee J, Breen C, Steckel JS, Coe-Sullivan S, Nurmikko A (2012) Red, green and blue lasing enabled by single-exciton gain in colloidal quantum dot films. *Nature Nanotechnol* **7:** 335.

21. Murray CB, Kagan CR, Bawendi MG (2000) Synthesis and Characterization of Monodisperse Nanocrystals and Close-Packed Nanocrystal Assemblies. Annu Rev Mater Sci 30: 545.

22. Peng ZA, Peng X (2001) Formation of High-Quality CdTe, CdSe, and CdS Nanocrystals Using CdO as Precursor. J Am Chem Soc 123: 183.

23. Chung SR, Wang KW, Chen HS (2013) Green Light Emission of $Zn_xCd_{1-x}Se$ Nanocrystals Synthesized by One-Pot Method. J Nanomaterials 2013: Article ID 526862.

24. Chung SR, Wang KW, Chen HS, Chen HH (2015) Novel red-emission of ternary ZnCdSe semiconductor nanocrystals. J Nanoparticle Research 17: 101.

25. Alivisatos AP (1996) Perspectives on the Physical Chemistry of Semiconductor Nanocrystals. *J Phys Chem 100:* 13226.

26. Bawendi MG, Wilson WL, Rotheberg L, Carroll PJ, Jedju TM, Steigerwald ML, Brus LE (1990) Electronic structure and photoexcited-carrier dynamics in nanometer-size CdSe clusters. Phys Rev Lett 65: 1623.

27. Manna L, Scher E, Li L, Alivisatos AP (2002) Epitaxial Growth and Photochemical Annealing of Graded CdS/ZnS Shells on Colloidal CdSe Nanorods. J Am Chem Soc *124*: 7136.

28. Bawendi MG, Carroll PJ, Wilson WL, Brus LE (1992) Luminescence properties of CdSe quantum crystallites: Resonance between interior and surface localized states. *J Chem Phys 96:* 946.

29. Underwood DF, Kippeny T, Rosenthal SJ (2001) Charge carrier dynamics in CdSe nanocrystals: implications for the use of quantum dots in novel photovoltaics. *Eur Phys J D 16:* 241.

30. Schreuder MA, McBride JR, Dukes AD, Sammons JA, Rosenthal SJ (2009) Control of Surface State Emission via Phosphonic Acid Modulation in Ultrasmall CdSe Nanocrystals: The Role of Ligand Electronegativity. J Phys Chem C 113: 8169.

31. Li Q, Guo S, Xu P, Wu L (2013) Controllable surface-state emission from colloidal CdS quantum dots under different growth conditions. Cryst Res Technol 48: 977.
32. Xiao Q, Xiao C (2009) Surface-defect-states photoluminescence in CdS nanocrystals prepared by one-step aqueous synthesis method. Appl Surf Sci 255: 7111.
33. Raevskaya AE, Stroyuk OL, Solonenko DI, Dzhagan VM, Lehmann D, Kuchmiy SY, Plyusnin VF, Zahn DRT (2014) Synthesis and luminescent properties of ultrasmall colloidal CdS nanoparticles stabilized by Cd(II) complexes with ammonia and mercaptoacetate. J Nanoparticle Research 16: 2650.
34. Molaei M, Marandi M, Saievar-Iranizad E, Taghavinia N, Liu B, Sun HD, Sun XW (2012) Near-white emitting QD-LED based on hydrophilic CdS nanocrystals. J. Luminescence 132: 467.
35. Protière M, Reiss P (2006) Facile synthesis of monodisperse ZnS capped CdS nanocrystals exhibiting efficient blue emission. Nanoscale Res Lett 1: 62.
36. Ozel T, Soganci IM, Nizamoglu S, Huyal IO, Mutlugun E, Sapra S, Gaponik N, Eychmüller A, Demir HV (2008) Selective enhancement of surface-state emission and simultaneous quenching of interband transition in white-luminophor CdS nanocrystals using localized plasmon coupling. New J Phys 10: 083035.
37. Shea-Rohwer LE, Martin JE (2007) Luminescence decay of broadband emission from CdS quantum dots. J Lumin 127: 499.
38. Shea-Rohwer LE, Martin JE, Kelley DF (2010) Increasing the Luminescent Quantum Yield of CdS Nanoparticles Having Broadband Emission. J Electrochem Soc 157: J1.
39. Dai Q, Li D, Chang J, Song Y, Kan S, Chen H, Zou B, Xu W, Xu S, Liu B, Zou G (2007) Facile synthesis of magic-sized CdSe and CdTe nanocrystals with tunable existence periods. Nanotechnology 18: 405603.
40. Chung SR, Yu YH, Wang KW (2014) Application of Quantum Dots in Solid State Lighting. Proc. SPIE 9200: 92000K1.
41. Lee J, Sundar VC, Heine JR, Bawendi MG, Jensen KF (2000) Full color emission from II-VI semiconductor quantum dot polymer composites. Adv Mater 12: 1102.
42. Wood V, Panzer ML, Long J, Bradley MS, Halpert JE, Bawendi MG (2009) Inkjet printing of polymer-quantum dot composites for full color AC electroluminescent displays. Adv Mater 21: 2151.
43. Bourzac K (2013) Quantum dots go on display. Nature 493: 283.
44. Wood V, Bulović V (2010) Colloidal quantum dot light-emitting devices. Nano Reviews 1: 5202.
45. Gosnell JD, Schreuder MA, Bowers MJ, Rosenthal SJ, Weiss SM (2006) Cadmium selenide nanocrystals as white-light phosphors. Proc SPIEsInt Soc Opt Eng 6337: 63370A.
46. Schreuder MA, Gosnell JD, Smith NJ, Warnement MR, Weiss SM, Rosenthal SJ (2008) Encapsulated white-light CdSe nanocrystals as nanophosphors for solid-state lighting. J Mater Chem 18: 970.
47. Gosnell JD, Rosenthal SJ, Weiss SM (2010) White Light Emission Characteristics of Polymer-encapsulated CdSe Nanocrystal Films. IEEE Photon Technol Lett 22: 541.
48. Yu K, Hu MZ, Wang R, Piolet ML, Frotey M, Zaman MB, Wu X, Leek DM, Tao Y, Wilkinson D, Li C (2010) Thermodynamic Equilibrium-Driven Formation of Single-Sized Nanocrystals: Reaction Media Tuning CdSe Magic-Sized versus Regular Quantum Dots. J Phys Chem C 114: 3329.

Chapter 15
Cadmium Free Quantum Dots: Principal Attractions, Properties, and Applications

Anush Mnoyan, Yonghee Lee, Hankyeol Jung, Somang Kim and Duk Young Jeon

Abstract For the past thirty years, interest on semiconductor nanocrystals from versatile systems of II–VI Quantum Dots (QDs) has been actively grown depending upon their application to light-emitting diodes (Gaponik in Mater Chem 10: 2163–2166, 2000 [1]), lasers (Artemyev et al. in Nano Lett 1:309–314, 2001 [2]), and biomedical research (Bruchez et al. in Science 281:2013–2016, 1998 [3]; Chan and Nie in Science 281:2016–2018, 1998 [4]; Michalet et al. in Science 307:538–544, 2005 [5]). However, the presence of highly toxic cadmium limits the application range particularly in the lighting and biological fields. To lessen the toxicity issue, various approaches were developed, such as overcoating the toxic core by non-toxic ZnS shell preventing the leakage of cadmium ions (Chou and Chan in Nat Nanotechnol 7(7):416–417, 2012 [6]; Ghaderi et al. in J Drug Targeting 19:475–486, 2011 [7]; Winnik and Maysinger in Acc Chem Res 46:672–680, 2012 [8]). Despite this action, II–VI QDs still remain unsafe due to initiated response to UV irradiation- or oxidation-resulted cadmium release through oxidized surface sites (Derfus et al. in Nano Lett 4:11–18, 2004 [9]). Therefore, the research focus was shifted to so-called cadmium free QDs, such as ZnSe, InP, and CuInS$_2$.

15.1 II–VI Compounds: ZnSe-Based Semiconductor Nanocrystals

15.1.1 Introduction

Among non-cadmium-based II-VI groups, zinc chalcogenides have been attracting much scientific interest due to the demand for replacing heavy metal-based toxic semiconductor materials including Cd, Pb, and Hg [10].

A. Mnoyan · Y. Lee · H. Jung · S. Kim · D.Y. Jeon (✉)
Department of Materials Science and Engineering, Korea Advanced Institute of Science and Technology (KAIST), 291, Daehak-ro, Yuseong-gu, Daejeon 305-338, South Korea
e-mail: dyj@kaist.ac.kr

The most developed zinc chalcogenides nanocrystals (NCs) via solution-based synthetic approach are zinc selenide (ZnSe) and zinc sulfide (ZnS) NCs which have remarkable versatility and long been subjects of study in science and engineering. Since photoluminescence (PL) of ZnS under irradiation was first discovered in 1930, [11] ZnS has been utilized to the diverse applications including light-emitting diodes (LEDs), electroluminescence (EL) devices, sensors, and solar cells. Due to its intrinsic low PL quantum yield (less than 5 %) and largest bandgap 3.72 eV (for cubic zinc-blende) among semiconductor materials, ZnS NC has been explored as a transition metal-doped NC, or shell material passivating core resulting in the type-I core/shell structured nanocrystals [12].

More recently, colloidal ZnSe-based nanocrystals have been spotlighted by many researchers as promising alternatives to Cd-based quantum dots in the near-UV and blue spectral region, owing to their high brightness and thermal stability, since they were first produced by Margaret A. Hines in University of Chicago via organometallic synthetic route [13].

ZnSe NC has also attracted the research community with its fascinating physical, chemical, and optoelectronic properties. Its optical bandgap is 2.7 eV which has potential applicability for blue-emitting light source ($\sim$470 nm), and ZnSe has exciton Bohr radius of 3.8 nm with large binding energy at room temperature [14, 15]. Compared to ZnS NCs, ZnSe NCs have much higher PL QY up to 50 % when doped with a transition metal [16–18].

Since studies of the doped ZnSe NCs with various dopants are relatively new and actively published in the prominent journals over recent years, compared to those of undoped ZnSe NCs, we will focus on introducing some intriguing researches dealing with the synthesis and the application of the doped ZnSe-based nanocrystals, and the several hypotheses explaining the doping mechanism and some unique luminescence properties of doped ZnSe will be discussed.

15.1.2 Doped ZnSe Nanocrystals

Doping makes semiconductor nanocrystals more useful and practical in their applicability by tuning their photo-physical, electrical, chemical, and magnetic properties. In an optical aspect, large Stokes shift which means the difference between maximum of the absorption and that of the emission spectrum minimizes self-reabsorption among the nanocrystals [19]. It was also reported that a lasing threshold could be efficiently reduced by incorporating dopants that provide extra carriers [20]. A nanocrystal doped with an intentional impurity resulting in more electrons or holes which can exhibit an improved electrical behavior. An impurity with one more valence electron compared with its counterpart in a semiconductor

nanocrystal donates its extra electron to the host resulting in the *n*-type doped nanocrystal, and an impurity with one less electron creates the *p*-type doped nanocrystal by taking electrons from a semiconductor nanocrystal. Dopant can also alter physical and magnetic properties of the mother host. For example, doping can turn a non-magnetic host material into a magnetic material [21]. Besides, an exchange from zinc-blende phase to wurtzite phase can occur by introducing dopant ions into the ZnS host material [22]. It is reported that the doping also brings about enhanced thermal and environmental stability and minimized toxicity of doped semiconductor nanocrystals [23–27].

Much effort to develop high-quality doped ZnSe semiconductor nanocrystals is being conducted as viable alternatives to the Cd-based nanocrystals. Various dopants have been attempted in the ZnSe system such as Mn^{2+}, Cu^{2+}, Fe^{2+}, Ni^{2+}, and Tb^{3+} [27–31].

In a Cu^{2+} ion doped ZnSe system, the insertion of Cu^{2+} ions into the ZnSe host reduces the sharp blue emission from the host and generates a broad emission at a longer wavelength up to green region. A strong blue to green emission from the ZnSe: Cu is unique and required the property, provided that most of the dopants can only tune the wavelength in the range of yellow to red. Unlike a Mn-doped system, a serious problem occurs in the Cu-doped ZnSe system. A poor photochemical stability caused by the photo-oxidation in the presence of air and light is still a challenging issue [24]. Santanu Jana et al. reported that the photo-oxidation of the Cu-doped ZnSe is facilitated by the hindered exciton relaxation process by Se atoms on the surface, and the stability of the nanocrystals can be improved by introducing a delicate amount of S anions at the end of the growth stage of ZnSe:Cu NCs (PL QY > 40 %) [27].

Luminescent water-soluble ZnSe:Fe NCs were prepared by aqueous synthesis approaches showing the strong PL in the range of 426–442 nm with PL QY up to 39 % [29]. More recently, some efforts have been devoted to the synthesis of rare-earth (RE) doped ZnSe NCs such as La^{3+}, Tb^{3+} [32], because, RE elements act as effective luminescent sites when doped, due to their longer lifetimes, sharp, and thermally stable luminescence attributing to the 4f shells which are less affected by the crystalline field [21, 33]. Among various dopants, manganese is the most developed and studied element. Though luminescence from the band edge of ZnSe nanocrystals is in the range of 360–440 nm [13], photonic energy is shifted to 580–600 nm when they are doped with Mn^{2+} ions. Since the lattice constants of the zinc-blende ZnSe and MnSe are almost identical [24], the amount of Mn^{2+} ions inside the host can be up to 1 % and maximum PL QY of Mn-doped NCs can reach over 50 % [18]. Besides, the luminescence is based on excellent thermal, chemical, and photochemical stabilities of the emitters, which are attributed to the atomic-like emission states of that. Fluorescence of the ZnSe nano-emitters doped with various dopants is shown in Fig. 15.1. Intrinsic fluorescence located around the near-UV region which comes from the band edge of ZnSe can be tuned in the visible range from sky blue (Cu-doped) to red (Mn-doped).
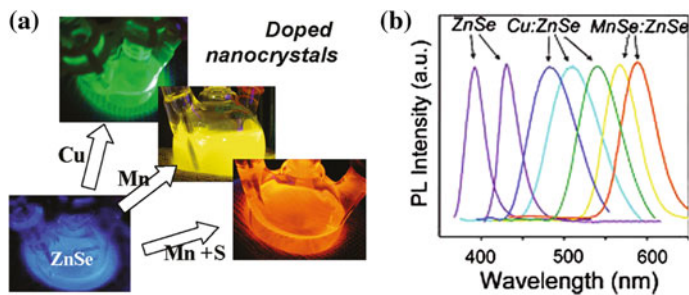
Fig. 15.1 **a** Fluorescence of Cu- and Mn-doped ZnSe nanocrystals. Reprinted with the permission from Ref. [34]. Copyright 2011 American Chemical Society, **b** PL spectra of doped ZnSe NCs with various dopants. Reprinted with the permission from Ref. [23]. Copyright 2005 American Chemical Society

15.1.3 Synthesis and Application of Doped ZnSe Nanocrystals

15.1.3.1 Synthesis of Doped ZnSe

Doped ZnSe nanocrystals are synthesized by combining various precursors that contain the constituent elements. We discuss three major doping strategies of the ZnSe NCs, and the manganese ion is chosen as a dopant in all cases. (1) The introduction of the dopant to the reaction system along with the host precursors, (2) the introduction of the dopant before nucleation of the host (nucleation doping), and (3) the introduction of the dopant in the shell of a core/shell.

Norris et al. [26] injected Se source into the reaction flask where Zn and Mn precursors were loaded and heated the flask to the elevated temperatures to obtain ZnSe:Mn NCs. As shown in Fig. 15.2a, an excitonic emission ($\sim$420 nm) from the host still remains and shifts to a lower energy, as the size of the host become larger with time. Fluorescence from the Mn^{2+} site stays in the orange region ($\sim$600 nm), regardless of the growth of the host. The improved PL emission was observed with a 22 % of PL QY which is explained by suppression of competing decay channels as the Mn dopants are well-passivated by the host lattices.

To overcome the problem that is the coexistence of the excitonic emission from the hosts and the dopants, Narayan Pradhan et al. introduced nucleation doping techniques where MnSe nanoclusters are first formed and subsequently followed by ZnSe host semiconductors growth. This technique gives rise to the pure PL from the dopants with PL QY up to 50 %, as shown in Fig. 15.2b, the techniques given above are based on the way that keeps dopants in the host lattice. Yang et al. [17], in the University of Florida reported a doped nanocrystal with PL QY of 56 % synthesized by radial-position-controlled doping. This approach starts with a formation of the host nanoparticles followed by Mn growth on top of the host, and finally host/dopants are covered with ZnS outer shell for a further increase in the
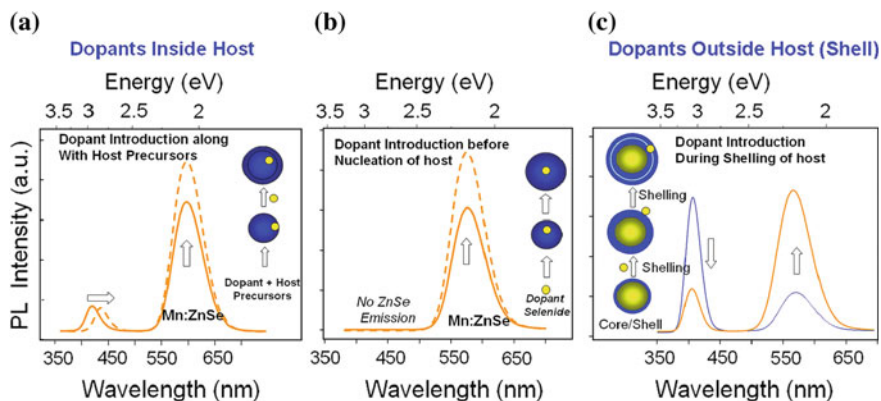
(a) Dopants Inside Host

Energy (eV)

(b)

Energy (eV)

(c) Dopants Outside Host (Shell)

Energy (eV)

Fig. 15.2 Successive PL spectra obtained during different doping processes. **a** Representation of the introduction of the dopant to the reaction system along with the host precursors, **b** representation of the introduction of the dopant before nucleation of the host, and **c** representation of the introduction of the dopant in the shell of a core/shell structured nanocrystal. All PL spectra are recorded with an excitation wavelength of 350 nm. Reprinted with the permission from Ref. [34]. Copyright 2011 American Chemical Society

PL QY (Fig. 15.2c). The PL QY of the nanocrystals increases as Mn-doping level becomes higher, while the excitonic blue emission decreases. Blue-emission arising from the host is completely disappeared as the doping level reaches 0.44 %. This technique allows us to have the precise control of the doping level and radial position of Mn dopant. In this Mn-doping approach, CdS was utilized as a host material covered with a thin layer of ZnS shell, as expected ZnSe:Mn synthesized by the same approach would bring a similar result.

15.1.3.2 Application of Doped ZnSe

Traditional II–VI luminescent nanocrystals such as CdSe, CdS, and CdTe have narrow emission, excellent PL QY with a broad absorption range, however, a strong toxicity arising from the cadmium component has hindered their application to bio-medical field. Doped ZnSe NCs having mitigated toxicity are promising candidates for various applicable field such as photovoltaic cells, light-emitting diodes, and bio-medical application as well [35]. Biocompatibility of QDs is a challenging issue, since the synthesized nanocrystals would be exogenous and hazardous substances to the living creatures.

Zhou et al. [36] introduced the hydroxyapatite-based nanomaterials which are the ingredient of bones and teeth in the organism to accord biocompatibility of ZnSe:Mn/ZnS nanocrystals (Fig. 15.3a). Due to the improved biocompatibility, most of the cells can be alive after being incubated with 200 μg mL^{-1} nano-FAp-QD conjugates up to 48 h (Fig. 15.3b).
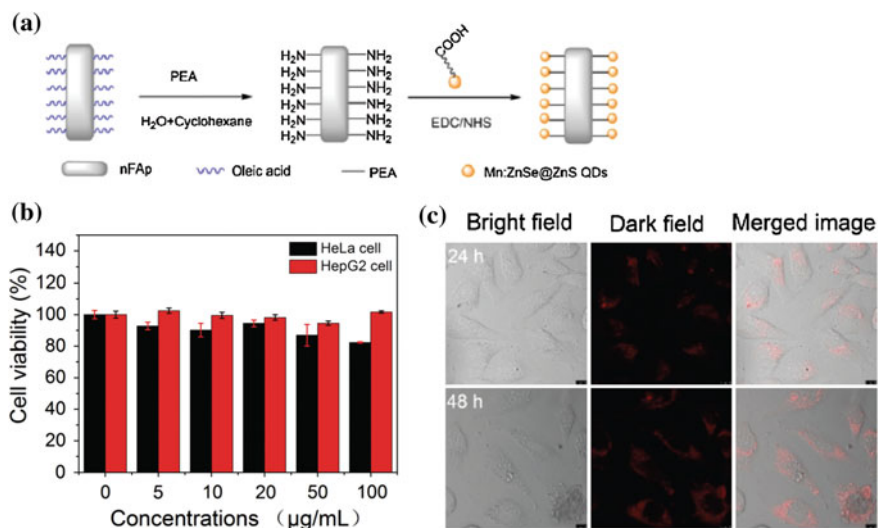
Fig. 15.3 **a** Schematic illustration of the conjugation of MPA-capped ZnSe:Mn/ZnS NCs with the nano-FAp. **b** Cell viability in HeLa cell and HepG2 cell. **c** Cell images of the nano-FAp-QD conjugates performed by confocal laser scanning microscopy in HeLa cell with time (24, 48 h). Bright field (*left*), fluorescent images (*middle*) and merged images (*right*). Reproduced from Ref. [36] by permission of The Royal Society of Chemistry

Fluorescence from the doped ZnSe nanocrystals makes possible for the nanocrystalline emitters applied in the photo-detection. Fluorescence lifetime of Cd-based NCs such as CdS, CdSe, and CdTe is so short (<100 nm) that their fluorescence is interrupted by the background autofluorescence, which restricts their application to the time-resolved fluorometry. On the contrary, the ZnSe:Mn NCs have a long fluorescence lifetime (up to 400 μs), which is 10,000 times longer than that of the Cd-based NCs. Zhu et al. [37] reported the ZnSe:Mn NCs capped with mercaptopropionic acid (MPA) emitting strong PL with a long lifetime which can be successfully utilized as an alternative to lathanide-based probe for the time-resolved fluorescence detection of 5-fluorouracil (5-FU) (Fig. 15.4).

15.1.4 Doping Mechanism and Luminescence Properties of Doped ZnSe

15.1.4.1 Doping Mechanism

A considerable body of ZnSe quantum dot has been utilized in the form of the doped nanocrystal; thus, it is required to understand the background knowledge of the general doping process in the semiconductor nanocrystals.
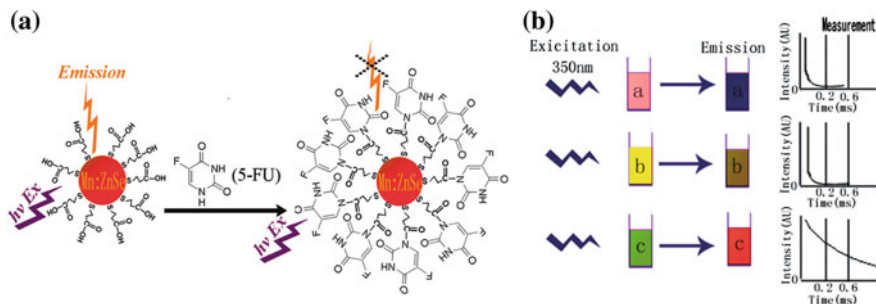
Fig. 15.4 a Schematic illustrations of MPA-capped Mn QDs for detection of 5-FU. **b** Fluorescence temporal selection of **a** 5-FU, **b** human serum, and **c** the Mn QDs. Reprinted with the permission from Ref. [37]. Copyright 2011 American Chemical Society

There are three main theoretical models to describe doping mechanism in the semiconductor nanocrystals. Doping model by Turnbull is based on the statistics that the number of impurities per nanocrystal statistically decreases with a crystallite size [38]. In this argument, dopant solubility is the same as in the bulk. However, this argument cannot properly explain the case of Mn-doped II–IV system. Self-purification model [39] has aroused as an alternative, assuming that the nanocrystals are in the thermodynamically equilibrium with their surroundings, and atomic exchanges between the doped nanocrystals and the environment are possible. To minimize their Gibbs free energy, the nanocrystals expel the impurities to the environment. This model explains the low solubility of the impurities in the nano-sized crystal, compared to that in the bulk counterpart. However, assuming thermal equilibrium may not be an appropriate starting point to describe how intentional impurities are incorporated into the nanocrystals. Another doping model based on kinetics is presented by Erwin et al. [40].

There have been several reports that Mn impurities are successfully doped into ZnSe, ZnS, and CdS in the Zinc-blende structures. [41–45] On the contrary, wurtzite CdSe or Pb chalcogenide nanocrystals with rock-salt structure are not well-doped by general doping procedures. Steven C. Erwin ascribes that to the binding energies of a dopant adsorbed on a given facet. Figure 15.5 describes the binding energies of Mn adsorbates calculated by density-functional theory [46]. The binding energies on the (100) plane of zinc-blende nanocrystals are considerably larger than those of other planes, which is originated from the arrangement of anion dimers providing stable binding site on the (001) surface. The resulting strong binding energy of Mn impurity on the (001) plane in Zinc-blende structures corresponds to the earlier findings that described the difference in the Mn-doping characteristics with the materials mentioned above. This model strongly suggests new concept that Mn impurities are individually incorporated into the nanocrystals by adsorbing on their (001) planes.

Achieving the doping level to a desired extent has been a difficulty, so the most of the earlier works conducted by many groups reported low-level of Mn-doping into the ZnSe nanocrystals. Although the solubility of Mn^{2+} ions in the bulk ZnSe is
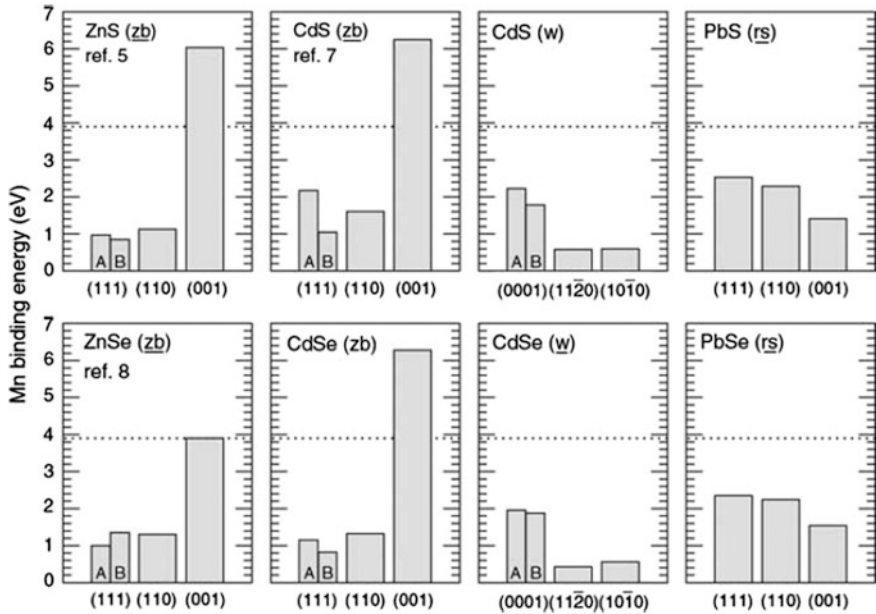
Fig. 15.5 Theoretically calculated binding energies for Mn impurities on the given planes of the several semiconductor nanocrystals. The most favorable structure in the formation of nanocrystal is *underlined*. The crystal structure is indicated as wurtzite (w) zinc-blende (zb), and rock salt (rs). Reprinted by permission from Macmillan Publishers Ltd. Ref. [40]. Copyright 2005

fairly high (tens of percent), the doping level of Mn^{2+} ions in the ZnSe nanocrystals is much smaller (1–2 %) [39].

There are some interpretations to explain the low-level limit of Mn-doping in the nanocrystalline structures. As discussed above, a doped nanocrystal has the tendency to eject the dopant to the outer side to reach its lowest energy configuration by self-purification process [25, 47]. However, an outstanding thermal stability over 300 °C of the Mn-doped ZnSe nanocrystal implies that the meta-stability of doped nanocrystals may not be the only origin of the low-doping level in the nanocrystal. In an alternative argumentation [40], low-level of doping is attributed to a low diffusion coefficient of Mn^{2+} ions. It is not a facile case that Mn^{2+} ions diffuse deeply into a formed nanocrystal to make it doped. Nanocrystals are doped as Mn^{2+} ions are adsorbed to the semiconductor nanocrystals and sequentially buried by host materials. Accordingly, the extent of doping level is determined by a capability of Mn^{2+} ions to adsorb on the facets of the nanocrystals. Nag et al. [48] demonstrated that the wurtzite $Zn_xCd_{1-x}S$ nanocrystal system can be doped up to 7.5 % of Mn^{2+} ions. Figure 15.6a shows a compositional ratio of Mn in the $Zn_xCd_{1-x}S$ nanocrystals with various x values, and differences in the lattice mismatch between MnS and $Zn_xCd_{1-x}S$ with various Zn compositions are shown in Fig. 15.6b. In this argument, it is shown that lattice mismatch between dopant-anion and the host can
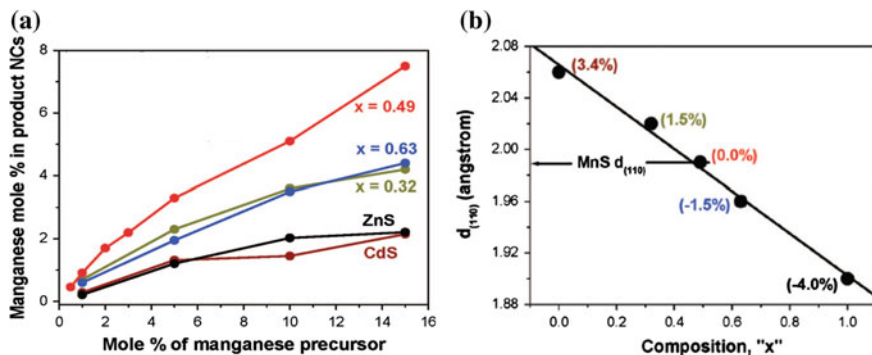
Fig. 15.6 **a** Mole percent of Mn for various compositions of $Zn_xCd_{1-x}S$ nanocrystal as a function of manganese precursors in the reaction mixture. The amount of Manganese in the nanocrystals was measured by ICP-AES. **b** Inter planar distance for (100) plane of $Zn_xCd_{1-x}S$ nanocrystal as a function of x. The difference in the lattice mismatch of MnS with $Zn_xCd_{1-x}S$ for different x values is shown in parentheses. Adapted with the permission from Ref. [48]. Copyright 2008 American Chemical Society

be another consideration for the maximized capacity of incorporation of dopant into the host.

It is known that ionic size of Mn^{2+} (0.85 Å) is an average value of Zn^{2+} (0.75 Å) and Cd^{2+} (0.95 Å). By tuning lattice parameters of the $Zn_xCd_{1-x}S$ nanocrystals close to MnS ($x \approx 0.5$), the extent for host to accommodate the Mn ions can be extended to a much larger one than that was achieved in earlier reports. This work implies that the adsorption of Mn^{2+} to the surface of the host may not be the determining step in the doping process.

15.1.4.2 Luminescence Properties of Doped ZnSe

A doped ZnSe has several advantages over an undoped ZnSe. As stated above, a large difference between absorption edge of the nanocrystals and the peak of the dopant emission can minimize self-absorption of the emitted light. Intrinsic emission from near-UV to violet of undoped ZnSe can be tuned at a desired visible region by doping a transition metal into them (Fig. 15.1). Transition metal-doped ZnSe is more eco-friendly compared to toxic Cd or Pb-based nanocrystals, thereby extending its applications to optoelectronics and the bio-medical field. In addition, thermal stability of the dopant emission makes the system more attractive, since undoped ZnSe requires a high-energy level of shell material to cover them to reach a certain level of stability.

It is noted that Mn emission arising from 580 to 590 nm is independent of the size and the nature of the host while the emission from band edge of the nanocrystals is strongly affected by the host condition (Fig. 15.2). On the contrary, fluorescence from other transition metal like Cu^{2+} ions is strongly dependent on the
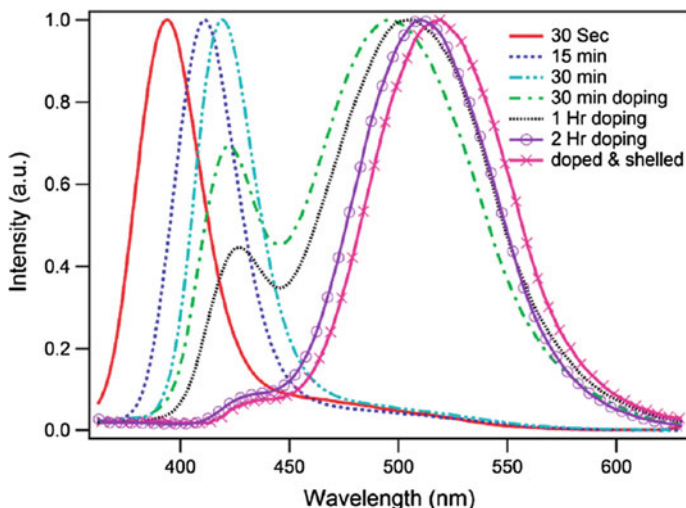
Fig. 15.7 Normalized PL spectra of ZnSe:Cu. Cu precursor was added after 30 min of the ZnSe growth. Reprinted with the permission from Ref. [49]. Copyright 2011 American Chemical Society

size of the host. Figure 15.7 shows a normalized spectral evolution of PL of the Cu-doped ZnSe nanocrystals. The Cu dopant precursor was added at the time when host ZnSe NCs had grown for 30 min. The PL of the host is decreased while the emission from the Cu dopant has increased. Unlike the case of Mn-doped ZnSe synthesized through the general synthetic procedures, where the PL peak of the dopant emission is less varied according to the size of the host, the dopant emission steadily shifted to the lower energy [49]. Such a different dopant emission property among the doped nanocrystals is originated from the different luminescence transition site. For Mn-doped ZnSe NCs, an electronic energy is affected by the strength of the crystal field and the exchange interaction within the Mn d multiplets. Atomic-like Mn d-states are less influenced by quantum confinement effect which means that the emission from the d–d transition of Mn is not dependent on the size of the host. For Cu-doped ZnSe NCs, however, both d-state of Cu and the host state are involved in the luminescence process, thus they exhibit sensitive PL characteristics with respect to the size of the host [50].

A lifetime of band edge emission of a quantum dot is affected by the dipolar overlap of the wave functions between the conduction band and the valence band, and typical lifetime is in the range of 1–30 ns [34].

On the contrary, as mentioned above, dopant emission from ZnSe:Mn NC has a long lifetime around hundreds of microseconds. Such a long lifetime of the Mn-doped nanocrystal is because of Mn emission corresponding to a forbidden d-d transition within the Mn 3d multiplet. Since the energy transfer from the host to the Mn d-state takes place in a very short time (a few picoseconds) [51], radiative decay

process in the d-d transition dominates over the other non-radiative channels leading to the high PL QY of the doped nanocrystals.

Recently, there have been a few attempts to generate white emission by combining ZnSe NCs with various dopants [52, 53]. Typical white-light emission generated by the mixture of phosphors and quantum dots has been afflicted by the deteriorated efficiencies due to the re-absorption of light among them and the subsequent undesired energy transfer. It was realized to generate the efficient white-light emission by introducing both manganese and copper into the ZnSe NCs, since yellow and blue emission is resulted from the $^4T_1$–$^6A_1$ transition of Mn^{2+} ions and the Cu d-states, respectively. Tunable white-light emission generated by co-doping of Mn and Cu into ZnSe NCs facilitates the minimized self-absorption due to the large Stokes shift of the nanocrystals, leading to exhibiting the high efficiency [52]. With its various excellent optical characteristics and versatility as well as the mitigated toxicity, the ZnSe-based nanocrystal has been actively studied and utilized throughout various applicable fields, and we hope that it will steadily exhibit remarkable progress as one of the strong candidate that can replace Cd-based quantum dots.

15.2 III–V Compounds: InP-Based Semiconductor Nanocrystals

15.2.1 Introduction

For the last two decades, III–V QDs have a big interest in fabrication of "green" or non-toxic semiconductor nanocrystals. In this group, arsenides are deemed unsuitable due to the toxicity of arsenic; therefore, research has focused on group III phosphide QDs. In particular, InP QDs, with a direct bandgap of 1.27 eV at 300 K, are considered as the most promising representative of the group. The cytotoxicity of InP QDs was found to be reduced upon in vivo decomposition, which characterizes this material as safe one for consumer using [54]. Principle attraction of these semiconductors comes from the robustness of the covalent bond in III–V group compared with the ionic bond found to be in II–VI group semiconductors. This characteristic covalent bond has a significant effect on two important properties such as improved optical stability of QDs and reduction of toxicity due to its non-erosion ability in biological environment [55, 56]. Additionally, the other interest in III–V system relies on the fact of larger excitonic Bohr radius compared to II–VI system (Table 15.1). Correspondingly, the effect of size quantization here exhibits stronger in comparison with the representative counterparts of II–VI group [57]. PL properties of InP QDs are easily tunable from the green to the near-infrared (NIR) region of the electromagnetic spectrum making it suitable as a color-converting material for ultraviolet (UV) or blue solid-state LEDs. However, the blue region of the visible spectrum remains a challenge requiring a fabrication

Table 15.1 Band gap (E_g) and excitonic Bohr radius (r_B) in some semiconductors

Compound	Bandgap (eV)	r_B (nm)
InP	1.35	15
InAs	0.354	34
InSb	0.17	65.6
CdS	2.43	5.8
CdSe	2.87	5.3
CdTe	1.5	7.3
ZnSe	2.67	4.5

Adapted from Ref. [59]. Copyright © 2012 Paul Mushonga et al.

of extremely small particles to attain a sufficiently large bandgap. Some progress in this area has been achieved using alloy structures [58].

15.2.2 General Approaches of InP QD Synthesis

The all properties of QDs are in strong dependence on particle quality controlled by size distribution and crystal defects. Thus, the general synthesis of high-quality nanocrystals is directly interconnected to their fulfillment. Two general synthesis techniques have been established, named hot-injection and heating-up methods, which are applicable also to the majority of reported QDs [60, 61].

The hot-injection technique involves the rapid injection of a precursor solution in a room temperature into a reaction media with chosen surfactant molecules, stabilized in a corresponding high temperature condition. The rapid injection of precursor solution causes a sudden supersaturation condition of monomers in a reaction media initiating the nucleation process. As a result, the reaction temperature drops down due to injected solution. This fact, in combination with low concentration of the remaining precursor molecules, prevents the further nucleation. Thus, the growth process of nanocrystals follows at a relatively lower temperature than that of the nucleation. Here, surfactant may have several roles, such as (a) acting as a coordinating solvent for stabilizing nanocrystal core, (b) controlling growth process by making a barrier on the surface of nanocrystal, (c) preventing the aggregation and improving colloidal stability, and (d) passivating the surface defects of nanocrystals. The strength of this method relies on the precise control of particle size and shape of semiconductor nanocrystals.

In the case of heating-up technique, all precursors are mixed at room temperature followed to its rapid heating to the appropriate growth temperature of the nanocrystals. Here, the solution temperature increases as well supersaturation level, and both determine the nucleation rate. The typical high-resolution TEM micrograph of InP QDs is shown in Fig. 15.8.

A variety of methods to synthesize colloidal InP QDs have been also reported including gas phase precursor methods [62], and microfluidic approaches [63]. Gas

3.4nm
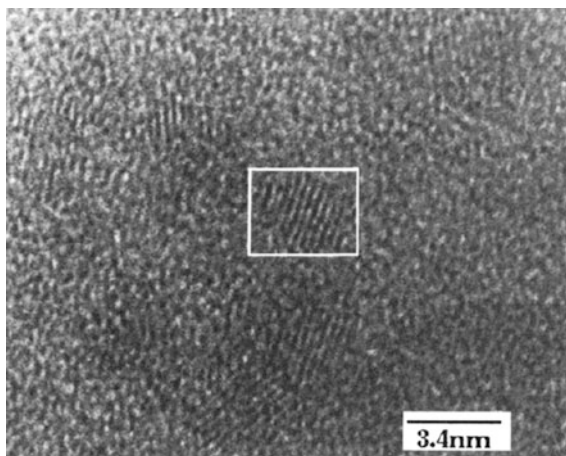
phase precursor method is a stepwise approach for the synthesis of highly lumi-
nescent InP/ZnS QDs. Here, PH_3 gas, which is generated by the reaction of HCl and
Zn_3P_2, is used as the phosphorous precursor. The relatively low reactivity of Zn_3P_2
led to a slow generation of PH_3 gas, which makes the reaction more controllable.
Microfluidic approach provides the relatively large-scale synthesis of thermally
grown core and core/shell QDs. Here, a hybrid flow reactor is used which is formed
by serial connections of batch and continuous processes. This synthetic method
enabled to use the solid state of chemicals. The quality of QDs is managed by
controlling the flow rate and furnace temperature of the reactor. To date, it is
reported that the reaction yields are beyond a few grams [64].

The commercial viability of InP QDs requires scalable synthesis methods
involving reproducible and increased batch yields. The reported impressively large
kilogram scale synthesis method is considered also called "molecular seeding
method" [66, 67]. The synthesis employs identical molecules of a cluster compound
to nucleate nanoparticle growth, eliminating the need for a high-temperature
nucleation step. Further precursors are periodically added to the reaction media to
maintain the particle growth under the control of incremental temperature changes,
providing highly confined and monodisperse particles over the emission
wavelength.

15.2.3 Issues in InP QDs and Approaches to Overcome

In order to extend and succeed in application fields of InP-based QDs, most
important improvements are required in the following areas: homogeneity of the
particle size distributions, surface state treatments, bandgap tuning for full spectral
range emission, QD stability, and synthesis scalability.

For InP QDs, the relatively broader particle size distribution compared to CdSe QDs leads to broader FWHM. The fact of large Bohr radius and, correspondingly, the strong quantum confinement effect has direct impact on PL properties. Therefore, even a small variation in particle size has strongly effect on large change in the emission wavelength in contrast to CdSe QDs, for which the particle diameter is in the range of the Bohr radius, and the quantum confinement is less distinct.

The known two main approaches affecting on reduction of the FWHM for the InP nanoparticles are greater synthetic control and size-selective precipitation techniques. Commercially, the second option is uneconomical, so improved synthetic technique will be the preferred route. The separation of nucleation step from growth phase of the nanoparticle synthesis reaction determines the main control on shape and size distribution. The well-known hot-injection method allows such a control. In particular, the narrow FWHM of $\sim$46 nm was reported for InP/ZnS QDs synthesis by hot-injection of precursors in highly polar polyethylene glycol solvents [68]. Here, the higher solvent polarity provides a better dissolution of precursors, resulting in more controlled reactions. The synthesis of InP/ZnS QDs with FWHM as narrow as 38 nm via a solvothermal method at 300 °C was reported also by Yang et al. [69]. Since the scalability of hot-injection and high-temperature reactions is challenging, alternative routes of nanoparticle growth control are needed to overcome both the optical and yield requirements of the production.

The high surface area to volume ratio of nanocrystals generates a large number of surface atoms which tend to coordinate, resulting in high reactivity and particle agglomeration. QD surface passivation with organic capping agents may mitigate the problem. The capping agents are also able to protect QD surface from the surrounding chemical environment and improve solubility in specific solvents providing a solution processible QD deposition by conventional printing or coating techniques.

The interaction of charge carriers and surrounding environment through the surface defects and dangling bonds has a significant effect on QD stability and QE. The direct way to enhance QD stability and to improve QE is the modification of structural and electronic architecture by one or more shell layers formation with different bandgap semiconductor on the QD core surface (Fig. 15.9). For example, in the case of InP/ZnS core–shell structure, the ZnS wider bandgap material is grown on InP core surface.

QD stability improvement can be progressed more by formation of additional shell layer resulting in multishell structure on core. However, with increasing the thickness of shells the lattice mismatch with core becomes significant causing interfacial strain and creating defects and traps that can act as non-radiative recombination centers to lower the QE. The alternative architecture of core/multishell is the quantum dot/quantum well structure (QD/QW), where the core and outer shell have wider bandgap than the intermediate thin inner shell (1–5 monolayers), in which the exciton wave functions are confined. Such an architecture is observed for ZnS/InP/ZnS [71]. Correspondingly, depending on the thickness of inner shell, the shift of PL emission wavelength can be recorded.
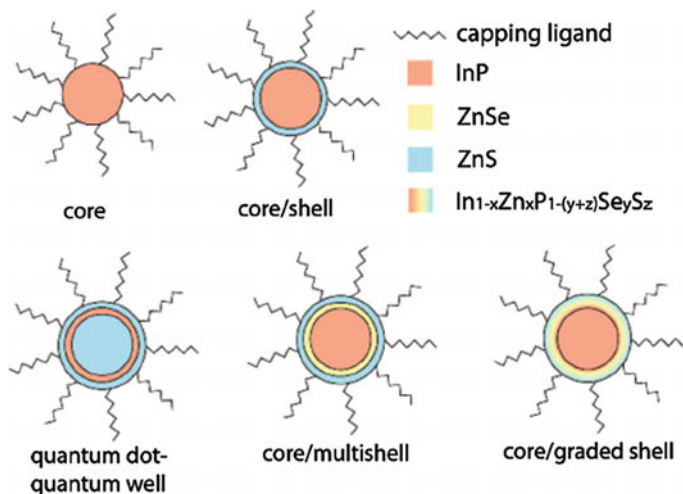
Fig. 15.9 Sketch of different architectures for non-cadmium quantum dots. Reproduced with permission from Ref. [70]. Copyright 2013, The Electrochemical Society

The poor PL properties of as-prepared InP nanocrystals can be drastically improved by subsequent photochemical etching of the nanocrystal surface by UV-assisted HF treatment. By using this method, the PL efficiencies are obtained comparable to those of the best core–shell samples [72]. The first example of all inorganic ligand passivated InP nanocrystals in polar solvent reported to show up to 5 % of PL efficiency [73, 74]. In particular, absorption profile of S^{2-}-capped InP NCs in formamide (FA) is observed to be similar to those of organically capped NCs dispersed in toluene (Fig. 15.10).

In general, the difficulties in PL emission tuning for pure InP QDs have been detected mostly in blue range, in which the InP QD stability and particle size are competing vice versa. Xu et al. [75] reported InP/ZnS QDs with the range of 480–750 nm spectral emission, and the fluorescence QE was obtained in a range of 20 % for blue and 60 % for red emitters. Yang et al. [69] reported InP/ZnS QDs synthesized by solvothermal method emitting from blue to NIR. Authors reported that zinc carboxylate used for two general reasons such as shelling precursor and stabilizing agent of InP QD surface during growth process, aiming to reduce the critical nuclear diameter.

For alloyed III–V nanostructures the fine-tuning of emission profiles can be also realized by composition change, allowing them to have emission even in the near-infrared region. As an example, $InAs_xP_{1-x}$/InP/ZnSe system, with a PL QY of about 3.5 %, has been reported by Kim et al. [76]. Alloyed InGaP QD system was synthesized using a microwave-enhanced method [77] showing 15 % of QY prior to etching and then improved to 68 % after etching due to the passivation of surface defect states. For alloyed structure InPZnS/ZnS blue emission was reported by

Fig. 15.10 Absorption
spectra of InP NCs capped
with organic ligands and S^{2-}
ligands dispersed in toluene
and FA, respectively. *Inset*
shows the optical photograph
of colloidal dispersion of InP
NCs in FA. Reprinted with
the permission from Ref. [73].
Copyright 2011 American
Chemical Society
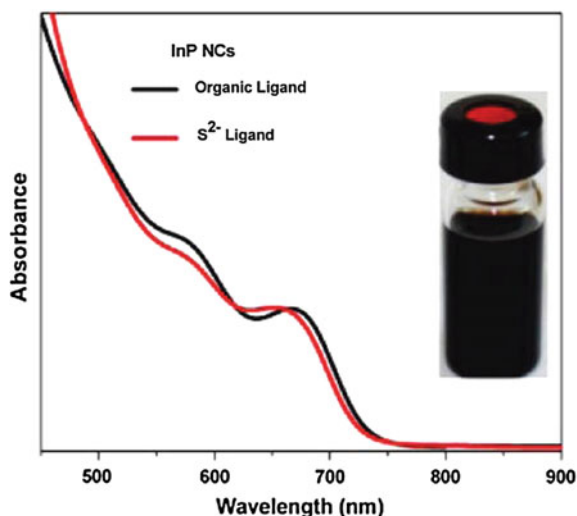
Kim et al. [64]. Here, the increased physical dimensions of QD enhance the colloidal stability while maintaining a sufficiently wide bandgap for blue emission.

The low solubility of the dopants in common organic solvents significantly reduces the number of reports on the doped In-based QDs [78, 79]. For instance, manganese-doped InP QDs were obtained by using the high-temperature dehalodesilylation and injection methods in a coordinating solvent revealing only small differences between the doped and undoped samples. In another report, InP: Mn QDs showed a PL spectrum with a peak at 570 nm and a FWHM of 110 nm [80]. However, it is hard to estimate the contribution of the dopant to the overall PL property of this system. The emission profiles for copper-doped InP/ZnSe (InP/ZnSe:Cu) QDs have reported to be tuned from 630 to 1100 nm, thus covering the critical near-infrared (NIR) window for biomedical applications [81]. Here, the band edge emission from InP is eliminated as shown in Fig. 15.11, and pure dopant emission, with PL QYs of up to 40 %, is achieved.

15.2.4 Application of InP Nanocrystals in Bioimaging

The recent and most major application field of QDs implies bio-imaging area. For this, the critical requirement is to use high-quality and water-soluble QD probes [82–86]. However, the large hydrodynamic sizes, a susceptibility for nonspecific bindings to proteins and cellular membranes, controlled conjugation chemistry, and decreased brightness with reducing the crystalline core size make challenging the application of these QDs. Three general modes of conjugation between biomolecules and QDs are known to be realized such as (a) covalent attachment, (b) direct attachment, and (c) non-covalent electrostatic interaction [87]. There are several
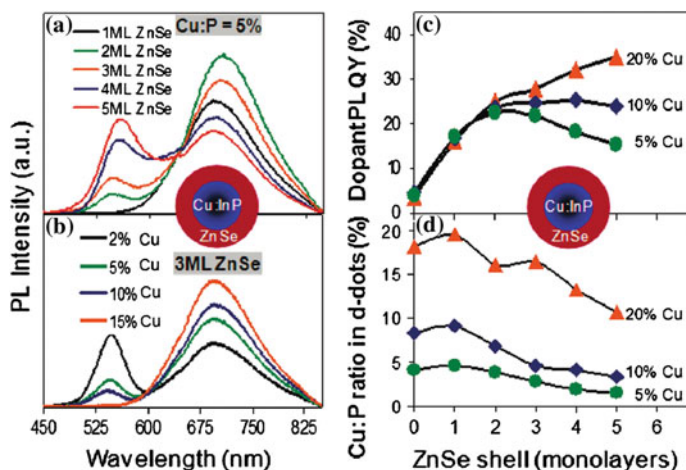
Fig. 15.11 a PL spectra of Cu:InP d-dots (formed with 5 % of Cu:P precursor ratio) with different thicknesses of ZnSe shells. **b** PL spectra of Cu:InP/ZnSe core/shell d-dots (three monolayers for ZnSe) formed with different Cu:P precursor ratios for the Cu:InP cores. **c** Dopant PL QY of d-dots versus the ZnSe shell thickness with a different initial Cu:P precursor concentration. **d** The Cu concentration in the Cu:InP/ZnSe core/shell d-dots versus the ZnSe shell thickness with a different initial Cu:P precursor concentration. Reprinted with the permission from Ref. [81]. Copyright 2009 American Chemical Society

approaches have been applied to reduce the effect of nonspecific bindings between QD and cellular species, and to avoid further increase in the particle size. Particularly, the coating of QDs by neutral hydrophilic polymer like polyethylene glycol (PEG) is able to reduce the nonspecific binding, but meanwhile the hydrodynamic size can be increased [88]. The other approach is using zwitterionic ligands such as cysteine resulting in particles that are both small and resistant to nonspecific binding [89–92]. However, the low colloidal stability, photobleaching effect, or low quantum yield of these QDs are considered as the big challenges.

The application of In-based QDs in bio-imaging was reported by Bharali et al. to investigate a folate-receptor-mediated delivery using mercaptoacetic acid-capped InP-ZnS [55]. Generally, in human cancerous cells of the kidney, ovary, or prostate the folate receptors are mostly dominant. The capture of the QD-FA conjugates in the KB cells was confirmed by their rapid uptake which was immediately followed by the formation of multivesicular bodies (MVBs). The series of experiments in which the KB cells were first saturated with excess of folic acid and then subsequently incubated with the QD conjugates confirmed the receptor-mediated delivery of the QDs (Fig. 15.12).

The demonstration of possibility to use the bio-functionalized InP/ZnS QDs raised interest in the development of future nanoprobes for biomedical applications. These nanoprobes would be a more favorable replacement of the highly toxic cadmium-based QD systems that have dominated current bio-imaging studies.
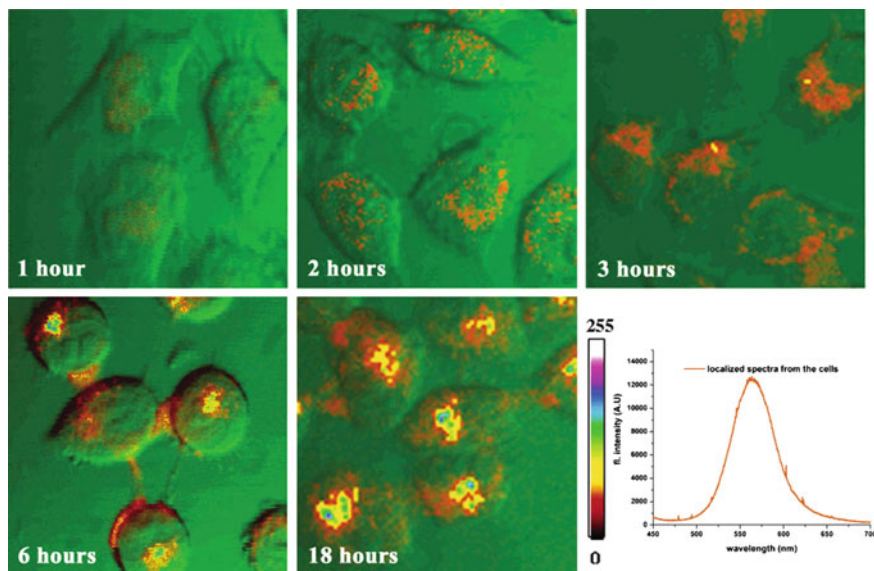
Fig. 15.12 Confocal images showing fluorescence of QD-FA in KB cells and a localized PL emission spectrum. Here, *green* channel shows the transmission images, while the intensity-coded (*red* to *white*) channel shows the fluorescence. Reprinted with the permission from Ref. [55]. Copyright 2005 American Chemical Society

The imaging of human pancreatic cancer cells (MiaPaCa or Panc-1) by using mercaptosuccinic acid-capped InP/ZnS QDs has also been reported by Yong et al. [56]. In this system, on the first step, QDs were bioconjugated to pancreatic cancer targeting monoclonal antibodies anticlaudin 4 and antiprostate stem cell antigen (anti-PSCA). The corresponding antigens of those are well known to be over expressed in primary and metastatic pancreatic cancer. Next, the cellular uptake of the QD bioconjugates was observed from the optical signal of the MiaPaCa cells as shown in Fig. 15.13.

As reported, no any sign of morphological damage to the cells was observed, proofing the low cytotoxicity of the InP QDs and making their usage highly favorable for biological applications.

15.3 I–III–VI Compounds: CuInS$_2$ Semiconductor Nanocrystals

15.3.1 Introduction

Multinary chalcogenide nanocrystals are highly promising to replace heavy metal semiconductor nanocrystals which contain cadmium or lead. CuInS$_2$ (CIS) is one of the most popular compositions among ternary nanocrystals due to its relatively high
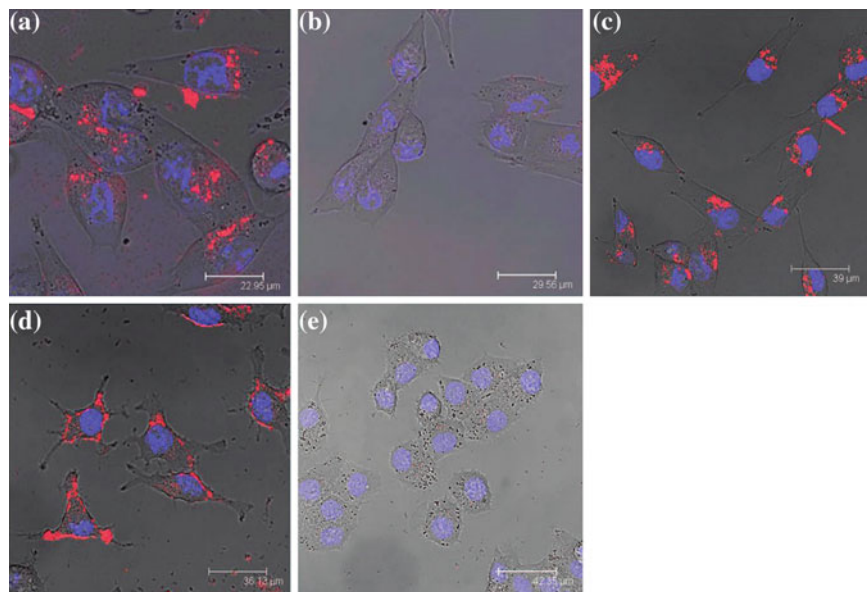
Fig. 15.13 Confocal microscopic images of **a** MiaPaCa cells treated with anticlaudin 4-conjugated InP/ZnS QDs; **b** MiaPaCa cells treated with unconjugated InP/ZnS QDs; **c** MiaPaCa cells treated with anti-PSCA-conjugated InP/ZnS QDs; **d** XPA3 cells treated with anticlaudin4-conjugated InP/ZnS QDs; and **e** KB (human nasopharyngeal epidermal carcinoma cell line) cells treated with anticlaudin4-conjugated InP/ZnS QDs. In all cases, *blue* represents emission from Hoechst 33342 and *red* represents emission from InP/ZnS QDs. Reprinted with the permission from Ref. [56]. Copyright 2009 American Chemical Society

PL quantum yield over 50 % after shell coating [93–95]. CIS nanocrystals also have direct bandgap (1.5 eV) in bulk state and high absorption coefficient of the order of 10^5 cm^{-1}, which make them suitable for solar energy conversion. Their absorption and emission are controllable from entire visible to even near-infrared (NIR) range. The Bohr exciton radius of CIS is 4.1 nm so they go through quantum confinement effect when they are smaller than about 8 nm. However, it is challenging to adjust the reactivity of two different cationic precursors (Cu and In) in the synthesis process of CIS nanocrystals. Due to the stoichiometric effect caused by two cations, not only their size but also composition highly influences the bandgap of CIS nanocrystals. Unique optical properties originated from their peculiar structure and non-toxicity of CIS nanocrystals lead to active studies on their application to solar cells, LEDs, bio-imaging, etc.

Fig. 15.14 Crystal structures of chalcopyrite, zinc blende and wurtzite CuInS$_2$. Adapted from Ref. [96] by permission of The Royal Society of Chemistry
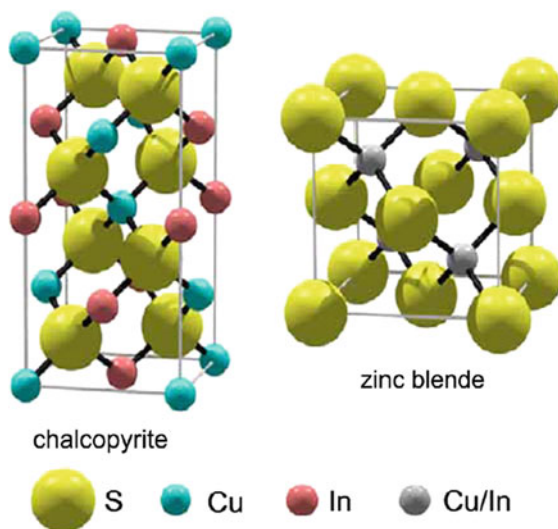
15.3.2 Unique Optical Properties of CuInS$_2$ Nanocrystals

As CIS nanocrystals are composed of three elements, they have unique trends in their optical properties compared to other nanocrystals that consist of two elements.

15.3.2.1 Off-Stoichiometry

CIS nanocrystals frequently do not have an exact proportion of 1:1:2 among copper, indium and sulfur but their composition is governed by so-called "off-stoichiometry effect". As a result, their crystal structures and optical properties are changed depending upon the ratio of Cu to In. The chalcopyrite structure of CuInS$_2$ QDs is commonly based on zinc-blende cubic structure. By randomly replacing zinc cations in zinc-blende structure with indium or copper cations, chalcopyrite structure of CIS QDs is formed (Fig. 15.14). When the ratio of copper and indium is changed, crystal distortion occurs due to difference of bonding length of [Cu–S] and [In–S], resulting in the change of the PL spectral shape of CuInS$_2$ QDs [97]. Chen et al. revealed that crystal distortions in chalcopyrite crystal structure of CIS occurred in accordance with the variation of [Cu]/[In] ratio [98]. They also reported that off-stoichiometry effect impacted on the PL and absorption (Fig. 15.15). The PL and absorption spectra showed blueshift with decreasing [Cu]/[In] ratio. In copper deficient CIS nanoparticles, the valence band comprised of Cu 3d and S 3p orbitals is lowered, and PL quantum yield (QY) was significantly improved up to 11 % with the ratio of 0.7. This means that the off-stoichiometry effect can influence the donor-acceptor level and the defect state concentration of CIS.
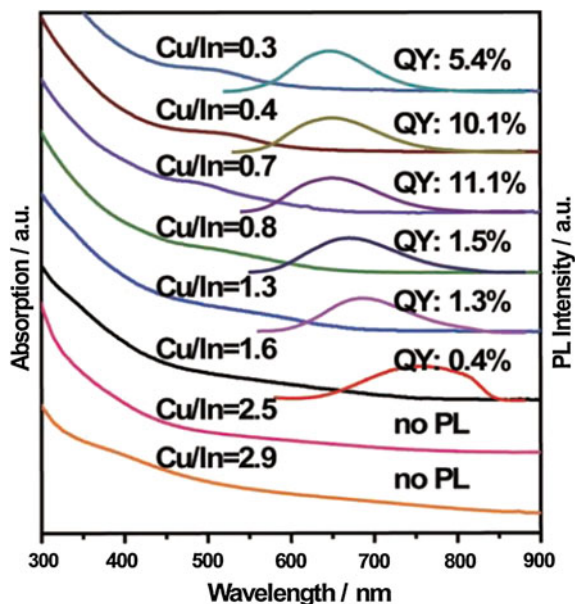
Fig. 15.15 Absorption and PL spectra of as-prepared CuInS$_2$ NCs with different [Cu]/[In] molar ratios. Reproduced from Ref. [99] by permission of John Wiley & Sons Ltd.

15.3.2.2 Broad and Long Tail Absorption Spectrum

CIS QDs have different trends in absorption spectrum compared to conventional binary QDs: they have no distinct excitonic peaks but several shoulder peaks as represented in Fig. 15.16 [100]. This unusual shape of absorption spectrum might originate from the intrinsic property of CIS, the broad size distribution of the
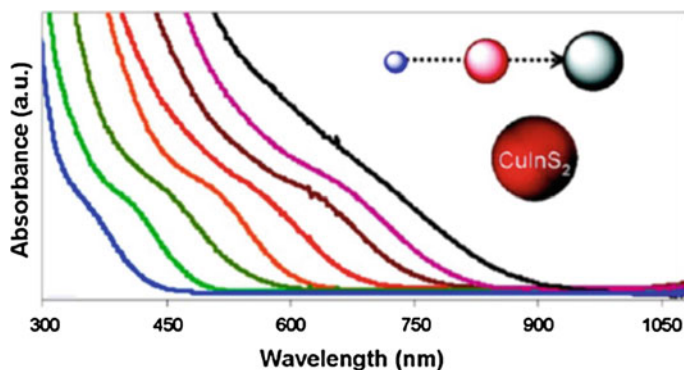
Fig. 15.16 Absorption spectra of CIS nanocrystals of different sizes between 2 and 16 nm. Reprinted with the permission from Ref. [100]. Copyright 2009 American Chemical Society

prepared CIS QDs sample, inhomogeneity in shape and composition, or combination of aforementioned origins [101].

In addition to indistinct excitonic peaks, the absorption spectrum of CIS QDs has a tail in the low-energy range. Two hypotheses were suggested to explain the tail at the long wavelength side of the absorption spectrum. One is related to the electronic states of the ligands on CIS surface and the other is the intraband states of CIS. It was revealed by Castro et al. that the species of surface ligands did not influence the shape of absorption spectrum [102]. Therefore, the latter one, intraband states of CIS is more reliable explanation for this phenomenon.

15.3.2.3 Defect Emission

I–III–VI compounds such as $CuInS_2$ have structural peculiarity that originates from the three different component atoms and the bond alternation (bond lengths: $R_{Cu–S} < R_{In–S}$) [99]. Crystal distortions are generated from the structural peculiarity, resulting in vacancies, interstitial sites, and substitutional sites. They affect the crystal structure and optical properties of nanocrystals by trapping excited photo-carriers. The origins of the defect levels were analyzed by comparing defect formation energies, ionization energies, and PL peak energies of defect states.

Liu et al. proposed energy band diagram represented in Fig. 15.17 that shows PL from surface-related state (PL2), and shallow or deep defect-related donor-acceptor transitions (PL3). In the case of CIS nanocrystals, band edge emission (PL1) is not generally observed because of the fast relaxation of excited carriers [103, 104]. They reported that donor states of CIS nanocrystals may originate from sulfur vacancies, interstitial Cu, or In ions replaced at Cu sites. On the other hand, the acceptor states may originate from Cu vacancies, interstitial In, and Cu ions substituted at In sites [105]. Consequently, $CuInS_2$ nanocrystals show defect emission that originated from intrinsic defects and surface defects which are formed by crystal distortions, rather than band edge emission. Thus, the concentration of defects of CIS can determine fluorescence quantum yield. These defects as trapping sites result in the longer PL lifetime, large Stokes shift as well as broad PL spectrum.

15.3.2.4 Long Decay Time, Large Stokes Shift

It was revealed that the lifetime of $CuInS_2$ nanocrystals is longer than that of binary QDs by the time-resolved photoluminescence. In binary semiconductor nanocrystals, most photo-generated electron–hole pairs (excitons) go through radiative recombination at their band edge with tens of nanoseconds. On the other hand, CIS nanocrystals have a long lifetime with hundreds of nanoseconds, which originated from surface defects and donor-acceptor transitions [107, 108]. Therefore, CIS nanocrystals show unique optical properties; a broad emission peak (FWHM: 100–150 nm) and a significant Stokes shift (0.5–0.6 eV) are observed in PL spectra, and
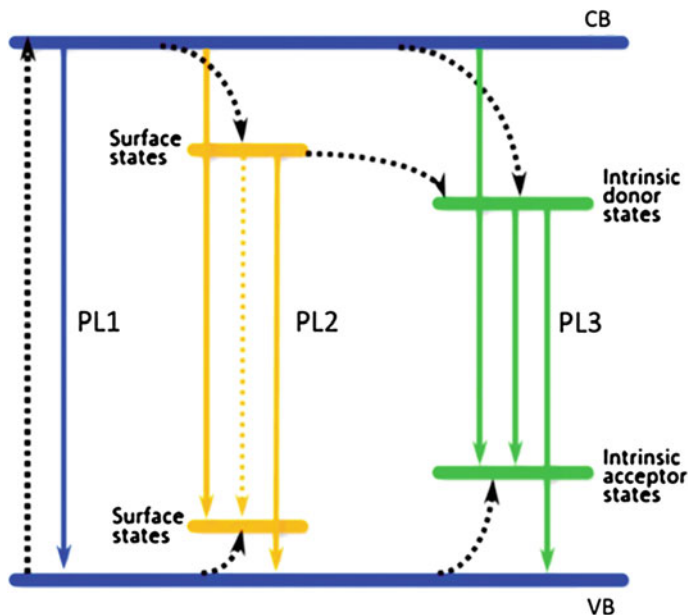
Fig. 15.17 Scheme of the possible relaxation pathways in ternary and quaternary nanocrystals. Band edge emission (PL1) is generally not observed due to the rapid relaxation of excited carriers to surface or internal defects, from which different de-excitation paths are possible (PL2, PL3), including DAP recombination. Reproduced from Ref. [106] by permission of The Royal Society of Chemistry

a comparably long lifetime (hundreds of ns) is exhibited [109] (Fig 15.18). The large Stokes shift is advantageous for bio-imaging or LED because it reduces the self-reabsorption which prevents exact signaling in bio-imaging or decreases the device efficiency in LED.

15.3.3 CIS/ZnS Core/Shell Structure and Blueshift of Photoluminescence

The recombination of excited charge carriers after absorption of light is relatively inefficient in CIS nanocrystals. The PL QY of core-only CIS nanocrystals was reported usually below 4 %. To improve the stability and quantum yield of CIS nanocrystals, ZnS is often introduced to form CIS/ZnS core/shell structure. After covering CIS nanocrystals with ZnS shells, the PL QY was remarkably enhanced compared to core-only CIS nanocrystals, achieving over 50 %. This phenomenon is well explained by the passivation of the dangling bonds at the QD surfaces with the binary zinc sulfide layer, which recovers surface defects and the non-radiative intra-gap trap states. Furthermore, CIS/ZnS is type 1 core/shell structure in which
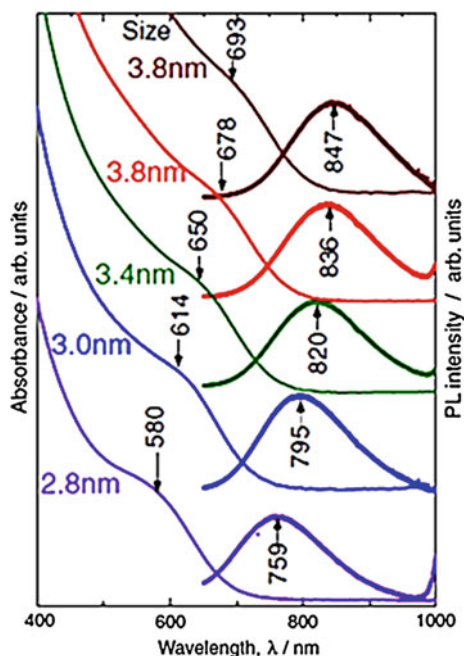
the bandgap of core material is smaller than that of shell materials. Therefore, the excitons generated in CIS core in CIS/ZnS structure are governed by quantum confinement effect more intensively than those in only CIS QDs.

After shelling CIS core with ZnS, the decay time also elongated significantly. The emission band of ternary nanocrystals is comprised of the shorter PL lifetime component originated from surface defect states, and the longer PL lifetime component originated from trap states. Komarala et al. explained that radiative recombination process of surface defect states was attributed to fast decay lifetime component, because surface-related trap states are generally placed at shallow energy level, and slow decay time component was found to represent the radiative recombination of the excitons [109]. Figure 15.19 exhibits CIS QDs decay lifetime

with ZnS shell and without ZnS shell layer. Time-resolved PL decay lifetime of core is remarkably faster (~ 68 ns) than that of the ZnS shell layer (~ 200 ns). When CIS QDs are coated by ZnS shell layer, the contributions of decay channels are changed. Fast decay time component is reduced from 61 to 36 % by reducing surface defects, which act as trap site of the electrons and holes. Meanwhile, slow decay time component increased from 39 to 64 %. It can be explained that the introduction of ZnS layer can prevent carrier losses related non-radiative recombination process.

In CIS/ZnS core/shell nanocrystals, PL spectrum is also different from only CIS nanocrystals. Unlike other core/shell structures, the PL spectrum of CIS/ZnS nanocrystals goes through blueshift without significant change in their size. There are several mechanisms that explain this unusual blueshift in photoluminescence: surface reconstruction, inter-diffusion, Cu etching, and cation exchange. The most reliable theory at this moment is the cation exchange shown in Fig. 15.20. Cation exchange is supported by the crystalline similarity between chalcopyrite and zinc blend of CIS with similar lattice parameters of 5.40 and 5.52 Å, respectively, similar ionic radius of Zn^{2+}, Cu^{2+}, and In^{3+} ions of 60–62 pm in four coordinate structure and similar Gibbs formation enthalpy of $CuInS_2$ and ZnS, −221 and −206 kJ/mol, respectively [111]. As a result, Cu^{2+} and In^{3+} can be replaced by Zn^{2+} at high temperatures by thermodynamic driving force. Furthermore, exchange reactions can happen in nanoparticles because of the effective reaction barrier of a diffusion-controlled mechanism.

This blueshift, however, is unfavorable when CIS/ZnS nanocrystals are used for in vivo bio-imaging which requires NIR region emission. To inhibit the blueshift in bio-application, Guo et al. added zinc ion into CIS core initially to form ZCIS alloy and then coated shallow ZnS shell on the ZCIS core [112]. This method succeeded to suppress the blueshift in PL effectively.
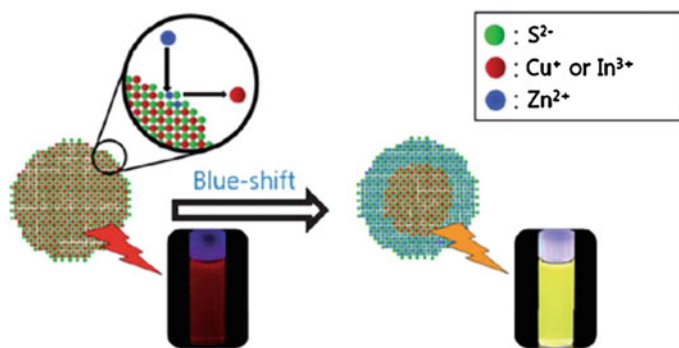

Fig. 15.20 A schematic illustration of cation exchange by Zn^{2+} ions in the CIS core. Reproduced from Ref. [111] by permission of The Royal Society of Chemistry

15.3.4   Surface Tailoring of CIS Nanocrystals and Their Application

15.3.4.1   Ligand Exchange

Ligand exchange is the process of manipulating surface properties of nanocrystals by changing the ligands. There have been many trials to replace hydrophobic ligands of CIS nanocrystals with hydrophilic ligands for their application in water-based environment, for example, in vivo bio-imaging [113, 114] or photo-catalysis [115]. Ligand exchange of CIS nanocrystals from long ligands to short ligands also have been reported for effective charge transfer [116].

However, PL QY of QDs decreases in most cases of ligand exchange due to damages on the surface of the nanocrystals and local agglomeration. Kim et al. suggested in situ ligand exchange of CIS/ZnS core/shell nanocrystals without significant decrease in luminescent efficiencies [117]. They injected extra amount of appropriate hydrophilic ligands to replace hydrophobic ligands during the growth stage as shown in Fig. 15.21. Their strategy was designated to utilize the "on–off" state of the ligands during growth period of nanocrystals proposed by Pradhan et al. [118]. This theory suggests that ligands are not permanently attached to QDs but in the "on–off state" so that QDs can grow during the "off" state of ligand. Therefore, injecting enormous hydrophilic ligands can replace the hydrophobic ligands during the "on–off" states by increasing the possibility of hydrophilic ligands being attached to QD surface. They succeeded in replacing hydrophobic 1-dodecanethiol (DDT) to hydrophilic 11-mercapto-1-undecanol (MUD), which was possible because both have thiol functional group and the same chain length. By putting excessive MUD ligands during the growth stage of QDs, hydrophobic ligands were successfully exchanged without significant loss in luminescence efficiency (Fig. 15.22).

On the other hand, Lefrancois et al. reported the replacement of long bulky DDT surface ligands to relatively short 1,2-ethylhexanethiol (EHT) ligands to induce effective charge transfer in hybrid solar cells structure [116]. They transformed the
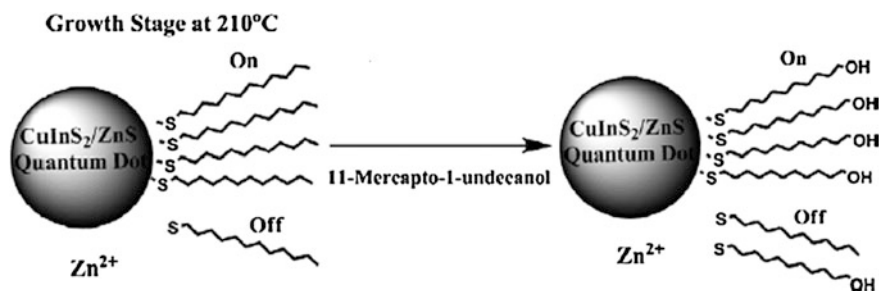

Fig. 15.21 Schematic description of in situ ligand exchange during "on–off" states of ligands. Adapted from Ref. [117]. Copyright 2011, with permission from Elsevier
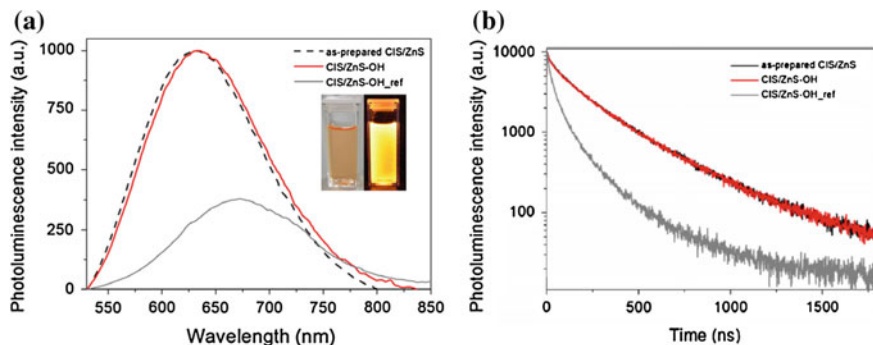
Fig. 15.22 **a** PL spectra (510 nm excitation) and **b** luminescence decay curve (375 nm excitation and 650 nm emission) of as-prepared CIS/ZnS QDs, CIS/ZnS-OH QDs, and CIS/ZNS-OH_ref QDs (*gray*) Adapted from Ref. [117]. Copyright 2011, with permission from Elsevier

Table 15.2 Solar cell characteristics measured under AM1.5 one sun conditions after annealing for 14 min at 120 °C in argon atmosphere; values in brackets: before annealing [116]

	FF	V_{oc}(V)	J_{sc}(mA/cm^2)	Efficiency (%)
P3HT:PCBM 1:1	0.40 (0.43)	0.58 (0.33)	−3.47 (2.00)	0.81 (0.29)
P3HT:PCBM:NCs-DDT 1:1:0.5	0.23 (0.27)	0.40 (0.23)	−2.70 (0.07)	0.24 (0.06)
P3HT:PCBM:NCs-EHT 1:1:0.5	0.48 (0.39)	0.52 (0.30)	−6.34 (4.05)	1.60 (0.47)
P3HT:PCBM:NCs-EHT 1:1:1	0.37 (0.36)	0.44 (0.32)	2.19 (1.79)	0.35 (0.20)

DDT-coated 7.4 nm sized CIS QDs into 70 % EHT and 30 % DDT-covered ones by simply mixing EHT in room temperature and keeping it overnight. Introducing the modified CIS QDs as an intermediate layer in hybrid solar cell improved the performance compared to DDT-covered CIS QDs-based cell, due to the reduction of the insulating layer thickness (Table 15.2).

15.3.4.2 Encapsulation

To avoid the damages caused by ligand exchange process, there is another way to tailor the surface of nanocrystals for bio-imaging application: encapsulation of QDs with amphiphilic molecules such as polymers or lipids (Fig. 15.23).

For biomedical application, QDs should be small after surface coating, biocompatible, available to conjugate them with biomolecules and targeting ligands and specific to targeted interaction within corresponding biological environment. However, there is no method reported that covers all the requirements. Ligand exchange enables compact probes but results in degraded stability and fluorescence
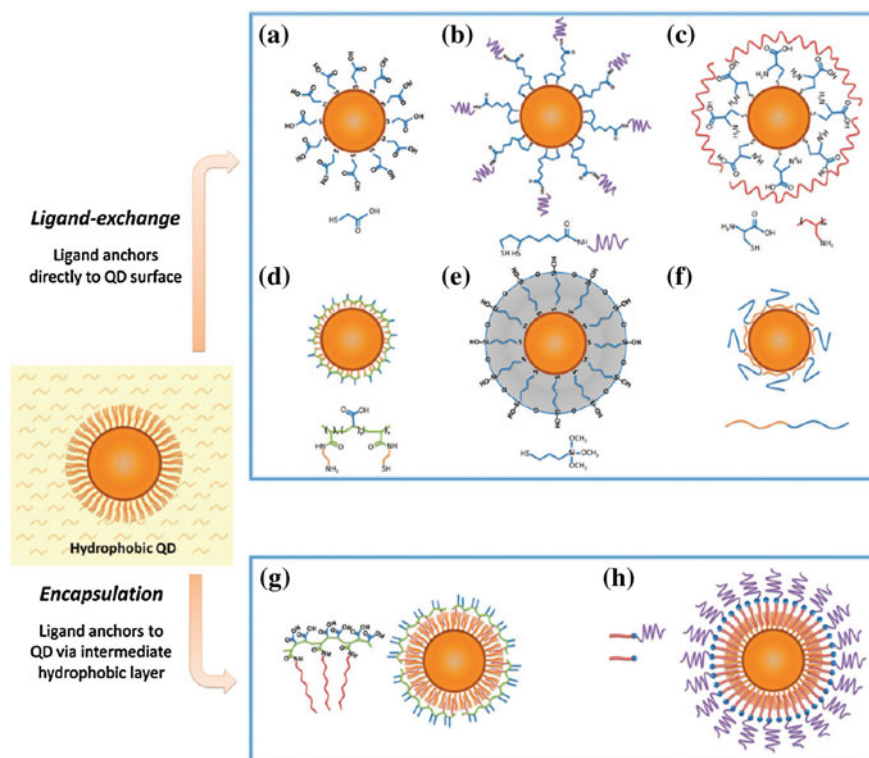
Fig. 15.23 Routes for water-solubilization of hydrophobic QDs. Ligand exchange procedures **a–f** involve replacing the native hydrophobic surface ligands (e.g., TOPO) with hydrophilic ones by direct anchoring of ligands to the QD surface. **g, h** Encapsulation procedures preserve the native QD surface structure and overcoat QDs with amphiphilic molecules (such as polymers or lipids) via hydrophobic interactions. Reproduced from Ref. [119] by permission of The Royal Society of Chemistry

efficiency, while polymer-encapsulation enables highly stable and bright particles but results in increased size. So, finding novel coating methods which satisfy both protective features of encapsulation procedures and compactness of small ligands is an active research area.

CIS QDs for cancer diagnostics grow as an emerging field recently. Lee et al. [120] introduced a new shell cross-linked CIS QD-protein hybrid nanostructure as a serum-stable nano-carrier for tumor-targeting in vivo imaging application (Fig. 15.24). In that research, the synthesized CIS/ZnS-human serum albumin-poly (ethylene glycol) nanocrystals showed a high PL intensity in hydrophilic environment, which is comparable to that of a hydrophobic organic solvent, with excellent dispersion stability. Although the size of the nano-capsule is around 20–40 nm in diameter, which is rather big, it has much potential to be a nano-carrier
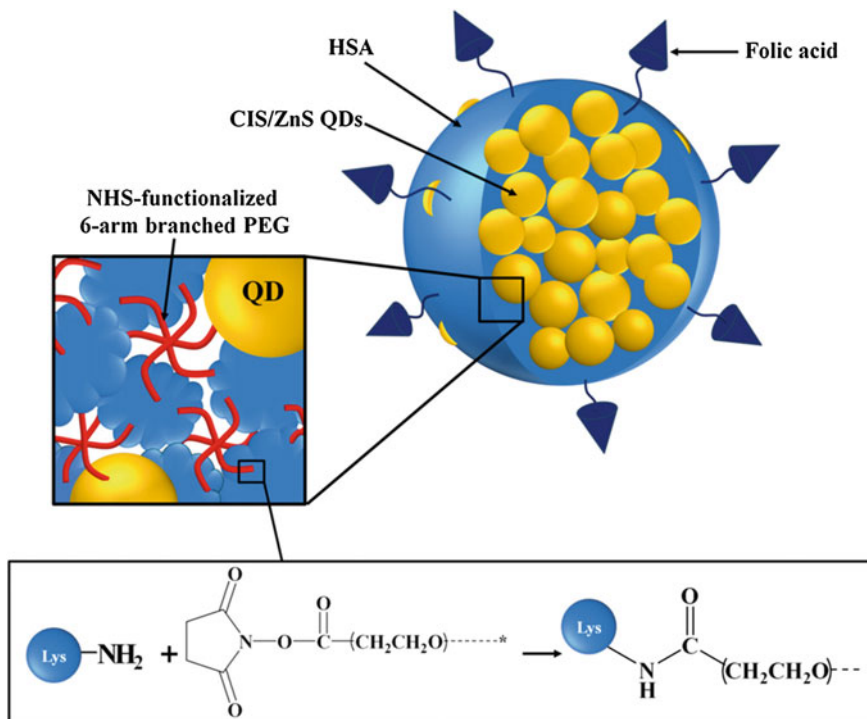
Fig. 15.24 Schematic illustration of the formation of the CIS/ZnS QDs-loaded shell crosslinked HAS-PEG NCs decorated with folic acid. Reprinted with permission from Ref. [120], © 2014 IOP Publishing Ltd.

platform for the stable systemic circulation of semiconductor nanocrystals. They do not contain heavy metals which induce cytotoxicity but show PL intensity strong enough for tumor-targeted imaging.

15.4 Summary

This chapter focused on the characterization and application aspects of the several representative compounds (ZnSe, InP and CIS) among Cd-free quantum dots. A brief review of the general photo-physical properties, various synthetic approaches, and the attempts to solve the issues faced in each composition was presented. Inherent toxicity of Cd-based quantum dots has been an obstacle for applications in advanced technologies. Studies on the syntheses of eco-friendly Cd-free QDs have extended the effective application field such as bio-sensor, in vivo imaging as well as solid-state lighting, and solar energy conversion. We believe that the steady and persistent research on Cd-free QDs that has been performed and will be conducted is a cornerstone to open a new prospect in the field of the advanced future industry.

References

1. Gaponik N. P., Talapin D. V., Rogach A. L., Eychmuller A. (2000) Electrochemical synthesis of CdTe nanocrystal/polypyrrole composites for optoelectronic applications. Materials Chemistry 10: 2163–2166

2. Artemyev M.V., Woggon U., Wannemacher R., Jaschinski H., Langbein W. (2001) Light trapped in a photonic dot: microspheres act as a cavity for quantum dot emission. Nano Letters 1: 309–314

3. Bruchez Jr.M., Moronne M., Gin P., Weiss S., Alivisatos A.P. (1998) Semiconductor nanocrystals as fluorescent biological labels. Science 281: 2013–2016

4. Chan W.C.W., Nie S. (1998) Quantum dot bioconjugates for ultrasensitive nonisotopic detection. Science 281: 2016–2018

5. Michalet X., Pinaud F. F., Bentolila L. A., Tsay J.M., Doose S., Li J.j., Sundaresan G., Wu A.M., Gambhir S.S., Weiss S. (2005) Quantum dots for live cells, in vivo imaging, and diagnostics. Science 307: 538–544

6. Chou L.Y.T., Chan W.C.W. (2012) Nanotoxicology No Signs of Illness. Nat. Nanotechnol 7 (7): 416-417

7. Ghaderi S., Ramesh B., Seifalian A.M. (2011) Fluorescence Nanoparticles Quatnum Dots as Drug Delivery System and Their Toxicity: A Review. J. Drug Targeting 19: 475-486

8. Winnik F.M., Maysinger D. (2012) Quantum Dot Cytotoxicity and Ways To Reduce It. Acc. Chem. Res. 46: 672-680

9. Derfus M., Chan W.C.W., Bhatia S. N. (2004) Probing the cytotoxicity of semiconductor quantum dots. Nano Letters 4: 11–18

10. Lesnyak V, Gaponik N, Eychmüller A (2013) Colloidal semiconductor nanocrystals: the aqueous approach. Chem Soc Rev 42: 2905-2929

11. Gessner GS (1930) The Luminescence of Zinc Sulphide Under the Action of Alpha, Beta and Gamma-Rays. Phys Rev 36: 207-213

12. Fang X, Zhai T, Gautam UK, Lib L, Wu L, Bando Y, Golberg D (2011) ZnS nanostructures: From synthesis to applications. Progress in Materials Science 56: 175-287

13. Hines MA, Guyot-Sionnest P (1998) Bright UV-Blue Luminescent Colloidal ZnSe Nanocrystals. J Phys Chem B 102: 19

14. Cozzoli PD, Manna L, Curri ML, Kudera S, Giannini C, Striccoli M, Agostiano A (2005) Shape and phase control of colloidal ZnSe nanocrystals. Chem Mater 17: 1296–1306

15. Liu XD, Ma JM, Peng P, Meng WJ (2010) One-Pot Hydrothermal Synthesis of ZnSe Hollow Nanospheres from an Ionic Liquid Precursor. Langmuir 26: 9963-9973

16. Chin PTK, Stouwdam JW, Janssen RAJ (2009) Highly Luminescent Ultra narrow Mn Doped ZnSe Nanowires. Nano Lett 9: 745-750

17. Yang Y, Chen O, Angerhofer A, Cao YC (2006) Radial-Position-Controlled Doping in CdS/ZnS Core/Shell Nanocrystals. J Am Chem Soc 128: 12428-12429

18. Zeng R, Zhang T, Dai G, Zou B (2011) Highly Emissive, Color-Tunable, Phosphine-Free ZnSe:Mn/ZnS Core/Shell and ZnSe:MnS Shell-Alloyed Doped Nanocrystals. J Phys Chem C 115: 3005-3010

19. Srivastava BB, Jana S, Karan N S, Paria S, Jana NR, Sarma DD, Pradhan N (2010) Highly Luminescent Mn-Doped ZnS Nanocrystals: Gram-Scale Synthesis. J Phys Chem Lett 1: 1454-1458

20. Wang C, Wehrenberg BL, Woo CY, Guyot-Sionnest P (2004) Light Emission and Amplification in Charged CdSe Quantum Dots. J Phys Chem B 108: 9027

21. Wang G, Peng Q, LI Y (2011) Lanthanide-Doped Nanocrystals : Synthesis Optical-Magnetic Properties, and Applications. Acc Chem Res 44: 322-332

22. Karan NS, Sarkar S, Sarma DD, Kundu P, Ravishankar N, Pradhan N (2011) Thermally Controlled Cyclic Insertion/Ejection of Dopant Ions and Reversible Zinc blende/Wurtzite Phase Changes in ZnS Nanostructures. J Am Chem Soc 133: 1666-1669

23. Pradhan N, Goorskey D, Thessing J, Peng X (2005) An Alternative of CdSe Nanocrystal Emitters: Pure and Tunable Impurity Emissions in ZnSe Nanocrystals. J Am Chem Soc 127: 17586-17587

24. Pradhan N, Peng X (2007) Efficient and Color-Tunable Mn-Doped ZnSe Nanocrystal Emitters: Control of Optical Performance via Greener Synthetic Chemistry. J Am Chem Soc 129: 3339-3347

25. Norris DJ, Efros AL, Erwin SC (2008) Doped Nanocrystals. Science 319: 1776-1779

26. Norris DJ, Yao N, Charnock FT, Kennedy TA (2001) High-Quality Manganese-Doped ZnSe Nanocrystals. Nano Lett 1: 3-7

27. Jana S, Srivastava BB, Acharya S, Santra PK, Jana NR, Sarma DD, Pradhan N (2010) Prevention of Photooxidation in Blue-Green Emitting Cu Doped ZnSe Nanocrystals. Chem Commun 46: 2853-2855

28. Brovelli S, Galland C, Viswanatha R, Klimov VI (2012) Tuning Radiative Recombination in Cu-Doped Nanocrystals via Electrochemical Control of Surface Trapping. Nano Lett 12: 4372-4379

29. Xie R, Li Y, Jiang L, Zhang X (2014) A facile and green strategy to fabricate luminescent ZnSe:Fe nanocrystals and their structural and optical properties. Journal of Alloys and Compounds 613: 213-218

30. Yadav K, Dwivedi Y, Jaggi N (2015) Structural and optical properties of Ni doped ZnSe nanoparticles. Journal of Luminescence 158: 181-187

31. Xie R, Li L, Li Y, Liu L, Xiao D, Zhu J (2011) ZnSe:Fe Semiconductor Nanocrystals: Synthesis, Surface Capping, and Optical Properties. Journal of Alloys and Compounds 509: 3314-3318

32. Das S, Mandal KC (2013) Optical down-conversion in doped ZnSe:Tb^{3+} nanocrystals. Nanoscale 5: 913

33. Bhargava R, Gallagher R (1994) Optical properties of manganese-doped nanocrystals of ZnS. Phys Rev Lett 72: 416-419

34. Pradhan N, Sarma DD (2011) Advances in Light-Emitting Doped Semiconductor Nanocrystals. J Phys Chem Lett 2: 2818-2826

35. Liu S, Su X (2013) The synthesis and application of doped semiconductor nanocrystals. Anal Methods 5: 4541-4548

36. Zhou R, Li M, Wang S, Wu P, Wu L, X Hou (2014) Low-toxic Mn-doped ZnSe@ZnS quantum dots conjugated with nano-hydroxyapatite for cell imaging. Nanoscale 6: 14319

37. Zhu D, Chen Y, Jiang L, Geng J, Zhang J, Zhu JJ (2011) Manganese-Doped ZnSe Quantum Dots as a Probe for Time-Resolved Fluorescence Detection of 5-Fluorouracil. Anal Chem 83: 9076-9081

38. Turnbull D (1950) Formation of crystal nuclei in liquid metals. J Appl Phys 21: 1022-1028

39. Dalpian GM, Chelikowsky JR (2006) Self-Purification in Semiconductor Nanocrystals. Phys Rev Lett 96: 226802

40. Erwin SC, Zu L, Haftel MI, Efros AL, Kennedy TA, Norris DJ (2005) Doping semiconductor nanocrystals. Nature 436: 91

41. Wang Y, Herron N, Moller K, Bein T (1991) 3-dimensionally confined diluted magnetic semiconductor clusters: $Zn_{1-x}Mn_xS$. Solid State Commun 77: 33-38

42. Bhargava RN, Gallagher D, Hong X, Nurmikko A (1994) Optical properties of manganese-doped nanocrystals of ZnS. Phys Rev Lett 72: 416-419

43. Levy L, Hochepied JF, Pileni MP (1996) Control of the size and composition of three dimensionally diluted magnetic semiconductor clusters. J Phys Chem 100: 18322-18326

44. Gonzalez ES, Roces L, Garcia-Granda S, Fernandez-Arguelles MT, Costa-Fernandez JM, Sanz-Medel A (2013) Influence of Mn2 + concentration on Mn2 + -doped ZnS quantum dot synthesis: evaluation of the structural and photoluminescent properties. Nanoscale 5, 9156-9161

45. Suyver JF, Wuister SF, Kelly JJ, Meijerink A (2000) Luminescence of nanocrystalline ZnSe: Mn2 + . Phys. Chem Chem Phys 2: 5445-5448

46. Kresse G, Furthmuller J (1996) Efficient iterative schemes for ab initio total-energy calculations using a plane-wave basis set. Phys Rev B 54: 11169-11186

47. Chelikowsky JR (2006) The Role of Self-Purification and the Electronic Structure of Magnetically Doped Semiconductor Nanocrystals. Phase Transitions 79: 739-753

48. Nag A, Chakraborty S, Sarma DD (2008) To Dope Mn^{2+} in a Semiconducting Nanocrystal. J Am Chem Soc 130: 10605-10611

49. Gul S, Cooper JK, Corrado C, Vollbrecht B, Bridges F, Guo J, Zhang JZ (2011) Synthesis, Optical and Structural Properties, and Charge Carrier Dynamics of Cu-Doped ZnSe Nanocrystals. J Phys Chem C 115: 20864-20875

50. Srivastava BB, Jana S, Pradhan N (2011) Doping Cu in Semiconductor Nanocrystals: Some Old and Some New Physical Insights. J Am Chem Soc 133: 1007-1015

51. Sapra S, Prakash A, Ghangrekar A, Periasamy N, Sarma DD (2005) Emission Properties of Manganese-Doped ZnS Nanocrystals. J Phys Chem B 109: 1663-1668

52. Panda SK, Hickey SG, Demir HV, Eychmller A (2011) Bright White-Light Emitting Manganese and Copper Co-Doped ZnSe Quantum Dots. Angew Chem 123: 4524-4528

53. Sharma, VK, Guzelturk B, Erdem T, Kelestemur Y, Demir HV (2014) Tunable White-Light-Emitting Mn-Doped ZnSe Nanocrystals. ACS Appl Mater Interfaces 6: 3654−3660

54. Chibli H, Carlina L, Park S, Dimitrijevic NM, Nadeau JL (2011) Cytotoxicity of InP/ZnS quantum dots related to reactive oxygen species generation. Nanoscale 3: 2552-2559

55. Bharali DJ, Lucey DW, Jayakumar HH, Pudavar E, Prasad PN (2005) Folate-receptor-mediated delivery of InP quantum dots for bioimaging using confocal and two-photon microscopy. Journal of the American Chemical Society 127: 11364–11371

56. Yong KT, Ding HI, Roy I, Law WC, Bergey EJ, Maitra A, Prasad PN (2009) Imaging pancreatic cancer using bioconjugated InP quantum dots. ACS Nano 3: 502-510

57. Langof L, Ehrenfreund E, Lifshitz E, Micic OI, Nozik AJ (2002) Continuous-wave and time-resolved optically detected magnetic resonance studies of nonetched/etched InP nanocrystals. Journal of Physical Chemistry B 106: 1606–1612

58. Thuy UTD, Reiss P, Liem NQ (2010) Luminescence properties of In(Zn)P alloy core/ZnS shell quantum dots. Appl Phys Lett 97: 193104

59. Mushonga P, Onani MO, Madiehe AM, Meyer M (2012) Indium Phosphide-Based Semiconductor Nanocrystals and Their Applications. Journal of Nanomaterials 2012: 869284

60. Reiss P (2007) ZnSe based colloidal nanocrystals: synthesis, shape control, core/shell, alloy and doped systems. New Journal of Chemistry 31: 1843–1852

61. Kwon BH, Jang DS, Kim HK, Jeon DY (2013) Controlled Growth of Quantum Dots and Their Application as Wavelength Converters for LEDs. Controlled Nanofabrication: Advances and Applications, Edited by Ru-Shi Liu Copyright © Pan Stanford Publishing Pte. Ltd. ISBN 978-981-4316-87-3 (Hardcover), 978-981-4364-51-5 (eBook)

62. Fan F, Ren J (2012) Gas-liquid phase synthesis of highly luminescent InP/ZnS core/shell quantum dots using zinc phosphide as a new phosphorus source. J Mater Chem 22: 1794-1799

63. Kim K, Jeong S, Woo JY, Han C-S (2012) Successive and large-scale synthesis of InP/ZnS quantum dots in a hybrid reactor and their application to white LEDs. Nanotechnology 23: 065602

64. Kim T, Kim SW, Kang M, Kim S-W (2012) Large-Scale Synthesis of InP/ZnS Alloy Quantum Dots with Dodecanethiol as a Composition Controller. J Phys Chem Lett 3: 214-218

65. Micic OI, Curtis JC, Jones KM, Sprague JR, Nozik AJ (1994) Synthesis and Characterization of InP Quantum Dots. J Phys Chem 98: 4966-4969

66. Mushtaq, Daniels S, Pickett N: Preparation of Nanoparticle Material. US Patent 7,588,828 B2, September 10, (2007)

67. www.nanocotechnologies.com

68. Hussain S, Won N, Nam J, Bang J, Chung H, Kim S (2009) One-pot fabrication of high-quality InP/ZnS (core/shell) quantum dots and their application to cellular imaging. Chem Phys Chem 10: 1466-1470

69. Yang X, Zhao D, Leck KS, Tan ST, Tang YX, Zhao J, Demir HV, Sun XW (2012) Full Visible Range Covering InP/ZnS Nanocrystals with High Photometric Performance and Their Application to White Quantum Dot Light-Emitting Diodes. Adv Mater 24: 4180-4185

70. Anc MJ, Pickett NL, Gresty NC, Harris JA, Mishra KC (2013) Progress in Non-Cd Quantum Dot Development for Lighting Applications. ECS Journal of Solid State Science and Technology 2: R3071-R3082

71. Pickett N, Daniels S, O'Brien P: Nanoparticles. US Patent 7,867,557 B2, January 11, (2006)

72. Talapin DV, Gaponik N, Borchert H, Rogach AL, Haase M, Weller H (2002) Etching of Colloidal InP Nanocrystals with Fluorides: Photochemical Nature of the Process Resulting in High Photoluminescence Efficiency. J Phys Chem B 106: 12659-12663

73. Nag A, Kovalenko MV, Lee J-S, Liu W, Spokoyny B, Talapin DV (2011) Metal-free Inorganic Ligands for Colloidal Nanocrystals: S^{2-}, HS^-, Se^{2-}, HSe^-, Te^{2-}, HTe^-, TeS_3^{2-}, OH^-, and NH_2^{2-} as Surface Ligands. J Am Chem Soc 133: 10612–10620

74. Liu W, Lee J-S, Talapin DV (2013) III-V Nanocrystals Capped with Molecular Metal Chalcogenide Ligands: High Electron Mobility and Ambipolar Photoresponse. J Am Chem Soc 135: 1349-1357

75. Xu S, Ziegler J, Nann T (2008) Rapid synthesis of highly luminescent InP and InP/ZnS nanocrystals. J Mater Chem 18: 2653-2656

76. Kim SW, Zimmer JP, Ohnishi S, Tracy JB, Frangioni JV, Bawendi MG (2005) Engineering InAsxP1-x/InP/ZnSe III-V alloyed core/shell quantum dots for the near-infrared. Journal of the American Chemical Society 127: 10526–10532

77. Gerbec JA, Magana D, Washington A, Strouse GF (2005) Microwave-enhanced reaction rates for nanoparticle synthesis. Journal of the American Chemical Society 127: 15791–15800

78. Somaskandan K, Tsoi GM, Wenger LE, Brock SL (2005) Isovalent doping strategy for manganese introduction into III-V diluted magnetic semiconductor nanoparticles: InP:Mn. Chemistry of Materials 17: 1190–1198

79. Mocatta D, Cohen G, Schattner J, Millo O, Rabani E, Banin U (2011) Heavily doped semiconductor nanocrystal quantum dots. Science 332: 77–81

80. Sahoo Y, Poddar P, Srikanth H, Lucey DW, Prasad PN (2005) Chemically fabricated magnetic quantum dots of InP:Mn. Journal of Physical Chemistry B 109: 15221–15225

81. Xie R, Peng X (2009) Synthesis of Cu-doped InP nanocrystals (d-dots) with ZnSe diffusion barrier as efficient and colortunable NIR emitters. J Am Chem Soc 131: 10645–10651

82. Chan WCW, Nie S (1998) Quantum dot bioconjugates for ultrasensitive nonisotopic detection. Science 281: 2016–2018

83. Alivisatos P (2004) The use of nanocrystals in biological detection. Nat Biotechnol 22: 47–52

84. Medintz IL, Uyeda HT, Goldman ER, Mattoussi H (2005) Quantum dot bioconjugates for imaging, labelling and sensing. Nat Mater 4: 435–446

85. Gao X, Yang L, Petros JA, Marshall FF, Simons JW, Nie S (2005) In vivo molecular and cellular imaging with quantum dots. Curr Opin Biotechnol 16: 63–72

86. Smith AM, Wen MM, Nie S (2010) Imaging dynamic cellular events with quantum dots - the bright future. Biochemist 32:12–17

87. Sapsford KE, Pons T, Medintz IL, Mattoussi H (2006) Biosensing with luminescent semiconductor quantum dots. Sensors 6: 925–953

88. Ballou B, Lagerholm BC, Ernst LA, Bruchez MP, Waggoner AS (2004) Noninvasive imaging of quantum dots in mice. Bioconjug Chem 15: 79–86

89. Liu WH, Choi HS, Zimmer JP, Tanaka E, Frangioni JV, Bawendi MG (2007) Compact cysteine-coated CdSe (ZnCdS) quantum dots for in vivo applications. J Am Chem Soc 129: 14530–14531

90. Liang GX, Gu MM, Zhang JR, Zhu JJ (2009) Preparation and bioapplication of high-quality, water soluble, biocompatible, and near-infrared-emitting CdSeTe alloyed quantum dots. Nanotechnology 20: 415103

91. Choi HS, Liu W, Misra P, Tanaka E, Zimmer JP, Ipe BI, Bawendi MG, Frangioni JV (2007) Renal clearance of quantum dots. Nat Biotechnology 25: 1165-1170

92. Liu XF, Gao Y, Wang XM, Wu SJ, Tang ZY (2011) Preparation of stable, water-soluble, highly luminescence quantum dots with small hydrodynamic sizes. J Nanoscience Nanotechnology 11: 1941–1949

93. Kim HK, Han JY, Kang DS, Kim SW, Jang DS, Suh MW, Kirakosyan A, Jeon DY (2011) Characteristics of CuInS$_2$/ZnS Quantum Dots and Its Application on LED. J Cryst Growth 236: 90-93

94. Nam D, Song W, Yang H (2011) Facile, air-insensitive solvothermal synthesis of emission-tunable CuInS$_2$/ZnS quantum dots with high quantum yields. J Mater Chem 21: 18220-18226

95. Deng D, Chen Y, Cao J, Tian J, Qian Z, Achilefu S, Gu Y (2012) High-quality CuInS$_2$/ZnS quantum dots for in vitro and in vivo bioimaging. Chem Mater 24: 3029–3037

96. Lu X, Zhuang Z, Peng Q, Li Y (2011) Controlled synthesis of wurtzite CuInS$_2$ nanocrystals and their side-by-side nanorod assemblies. Cryst Eng Comm 13: 4039-4045

97. Zhong H, Zhou Y, Ye M, He Y, Ye J, He C, Yang C, Li Y (2008) Controlled synthesis and optical properties of colloidal ternary chalcogenide CuInS$_2$ nanocrystals. Chem Mater 20: 6434–6443

98. Crooker SA, Barrick T, Hollingsworth JA, Klimov VI (2003) Multiple temperature regimes of radiative decay in CdSe nanocrystal quantum dots: intrinsic limits to the dark-exciton lifetime. Appl Phys Lett 82: 2793

99. Chen B, Zhong H, Zhang W, Tan Z, Li Y, Yu C, Zhai T, Bando Y, Yang S, Zou B (2012) Highly emissive and color-tunable CuInS$_2$-based colloidal semiconductor nanocrystals: off-stoichiometry effects and improved electroluminescence performance. Adv Funct Mater 22: 2081-2088

100. Xie R, Rutherford M, Peng X (2009) Formation of high-quality I-III-VI semiconductor nanocrystals by tuning relative reactivity of cationic precursors. J Am Chem Soc 131: 5691–5697

101. Kolny-Olesiak J, Weller H (2013) Synthesis and application of colloidal CuInS$_2$ semiconductor nanocrystals. ACS Appl Mater Interfaces 5: 12221-12237

102. Castro SL, Bailey SG, Raffaelle RP, Banger KK, Hepp AF (2004) Synthesis and characterization of colloidal CuInS$_2$ nanoparticles from a molecular single-source precursor. J Phys Chem B 108: 12429-12435

103. Seo JT, Raut S, Abdel-Fattah M, Rice Q, Tabibi B, Rich R, Fudala R, Gryczynski I, Gryczynski Z, Kim WJ, Jung SS, Hyun R (2013) Time-resolved and temperature-dependent photoluminescence of ternary and quaternary nanocrystals of CuInS$_2$ with ZnS capping and cation exchange. J Appl Phys 114: 094310

104. Komarala VK, Xie C, Wang Y, Xu J, Xiao M (2012) Time-resolved photoluminescence properties of CuInS$_2$/ZnS nanocrystals: Influence of intrinsic defects and external impurities. J Appl Phys 111: 124314

105. Ueng HY, Hwang HL (1989) The defect structure of CuInS$_2$. part I: Intrinsic defects. J Phys Chem Solids 50: 1297–1305

106. Aldakov D, Lefrançois A, Reiss P (2013) Ternary and quaternary metal chalcogenide nanocrystals: synthesis, properties and applications. J Mater Chem C 1: 3756–3776

107. Uehara M, Watanabe K, Tajiri Y, Nakamura H, Maeda H (2008) Synthesis of CuInS$_2$ fluorescent nanocrystals and enhancement of fluorescence by controlling crystal defect. J Chem Phys 129: 134709

108. Li L, Pandey A, Werder DJ, Khanal BP, Pietryga JM, Klimov VI (2011) Efficient Synthesis of Highly Luminescent Copper Indium Sulfide-Based Core/Shell Nanocrystals with Surprisingly Long-Lived Emission. J Am Chem Soc 133: 1176–1179

109. Zhong H, Lo SS, Mirkovic T, Li Y, Ding Y, Li Y, Scholes GD (2010) Noninjection Gram-Scale Synthesis of Monodisperse Pyramidal CuInS$_2$ Nanocrystals and Their Size-Dependent Properties. ACS Nano 4: 5253–5262

110. Omata T, Tani Y, Kobayashi S, Otsuka-Yao-Matsuo S (2012) Quantum dot phosphors and their application to inorganic electroluminescence device. Thin Solid Films 520: 3829–3834

111. Park J, Kim S (2011) CuInS$_2$/ZnS core/shell quantum dots by cation exchange and their blue-shifted photoluminescence. J Mater Chem 21: 3745-3750

112. Guo W, Chen N, Tu Y, Dong C, Zhnag B (2013) Synthesis of Zn-Cu-In-S/ZnS core/shell quantum dots with inhibited blue-shift photoluminescence and applications for tumor targeted bioimaging. Theranostics 3: 99-108

113. Li L, Daou TJ, Texier I, Chi TTK, Liem NQ, Reiss P (2009) Highly luminescent CuInS$_2$/ZnS core/shell nanocrystals: cadmium-free quantum dots for in vivo imaging. Chem. Mater 21: 2422–2429

114. Pons T, Pic E, Lequeux N, Cassette E, Bezdetnaya L, Guillemin F, Marchal F, Dubertret B (2010) Cadmium-free CuInS$_2$/ZnS quantum dots for sentinel lymph node imaging with reduced toxicity. ACS Nano 4: 2531–2538

115. Li T, Teng H (2010) Solution synthesis of high-quality CuInS$_2$ quantum dots as sensitizers for TiO$_2$ photoelectrodes. J Mater Chem 20: 3656-3664

116. Lefrançois A, Luszczynska B, Pepin-Donat B, Lombard C, Bouthinon B, Verilhac M, Gromova M, Faure-Vincent J, Pouget P. Chandezon F, Sadki S, Reiss P (2015) Enhanced charge separation in ternary P3HT/PCBM/CuInS$_2$ nanocrystals hybrid solar cells. Sci Rep 5: 7768

117. Kim HK, Suh MW, Kwon BH, Jang DS, Kim SW, Jeon DY (2011) In situ ligand exchange of thiol-capped CuInS$_2$/ZnS quantum dots at growth stage without affecting luminescent characteristics. Journal of Colloid and Interface Science 363: 703–706

118. Pradhan N, Reifsnyder D, Xie R, Aldana J, Peng X (2007) J Am Chem Soc 129: 9500

119. Zrazhevskiy P, Sena M, Gao X (2010) Designing multifunctional quantum dots for bioimaging, detection, and drug delivery. Chem Soc Rev 39: 4326-4354

120. Lee JY, Nam DH, Oh MH, Kim YS, Choi HS, Jeon DY, Park CB, Nam YS (2014) Serum-stable quantum dot-protein hybrid nanocapsules for optical bio-imaging. Nanotechnology 25: 175702

Chapter 16
Synthesis of InP Quantum Dots and Their Application

Hung-Chia Wang and Ru-Shi Liu

Abstract For more than two decades, research interest has been focused on groups II–VI of quantum dots (QDs) because of their potential applications in lasers, light-emitting diodes, and biological imaging. Given the highly intrinsic toxicity of cadmium, the biological applications of Cd-QDs have been limited. The European Union prohibits the use of Cd-QDs in electronic devices by 2017 (Anc et al. in ECS J Solid State Sci and Technol 2:R3071, 2013 [1]. This problem is addressed by developing Cd-free QDs. Groups III–V QDs exhibit narrow full width at half maximum compared with other Cd-free QDs, such as $CuInS_2$, and are suitable for backlight units. With increasing number of related publications, the main attraction to these semiconductors focuses on the robustness of the covalent bond in groups III–V semiconductor materials rather than the ionic bond in groups II–VI semiconductors. Moreover, the covalent bond can enhance the stability of Cd-free QDs. Indium phosphide (InP) core easily facilitates non-radiative decay because of the surface environment. Thus, other semiconductors with larger bandgap should be preferred over InP to prevent solvent quenching. The recombination of hole and electrons decreases with increasing shell thickness, and the photoluminescence intensity consequently increases. Many synthesis strategies are available for InP QDs, including one-pot, hydrothermal, and continuous heating-up methods. In this chapter, we introduce these three techniques, and an example is given for each method to achieve further understanding.

H.C. Wang · R.S. Liu (✉)
Department of Chemistry, National Taiwan University, Taipei 106, Taiwan
e-mail: rsliu@ntu.edu.tw

R.S. Liu
Department of Mechanical Engineering and Graduate Institute of Manufacturing Technology,
National Taipei University of Technology, Taipei 106, Taiwan

16.1 Comparison of Three General Synthesis Method of InP/ZnS

16.1.1 One-Pot Method for InP

We introduce high-quality InP/ZnS QDs by using a simple one-pot synthesis method [2]. The precursors of indium and phosphorous are initially mixed in a glove box and then transferred to a three-neck bottle. In this method, the precursors are mixed under low-temperature condition, which can easily tune the color of the QDs compared with the common hot-injection method, in which the precursor is injected into the reaction solution under high temperature. The novel method accelerates nucleation and then rapidly cools to avoid overreaction. Moreover, the hot-injection method is difficult to control. Another advantage of the new method is the small size distribution. By contrast, traditional hydrothermal methods require long-term reaction under high pressure and temperature. The size distribution is very wide, and the yield of particular wavelength is low. The following schematic illustrates an example of one-pot synthesis. In 2012, Yang et al. [2] used indium myristate $(In(MA)_3)$ and tris(trimethylsilyl)phosphine $P(TMS)_3$ as precursors to synthesize InP QDs. Figure 16.1 shows the synthesis of this method. The precursors are mixed in a glove box. The first step presents a nuclear reaction, and then, zinc stearate is added as a stabilizer. In the nuclear reaction, the proportion of Zn and In can control the specific wavelength. A higher proportion of zinc precursor indicates a stronger blueshift. In the present case, we use a single precursor for another zinc sulfide shell, which is expected to improve its stability and quantum efficiency. This method can tune the wavelength from 450 to 750 nm with high yield.
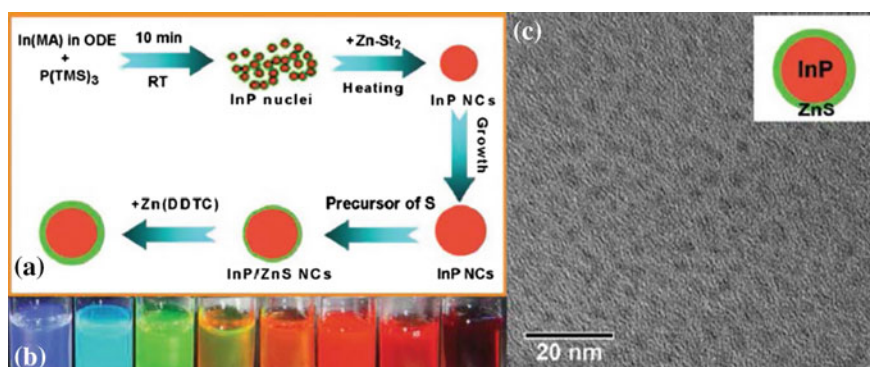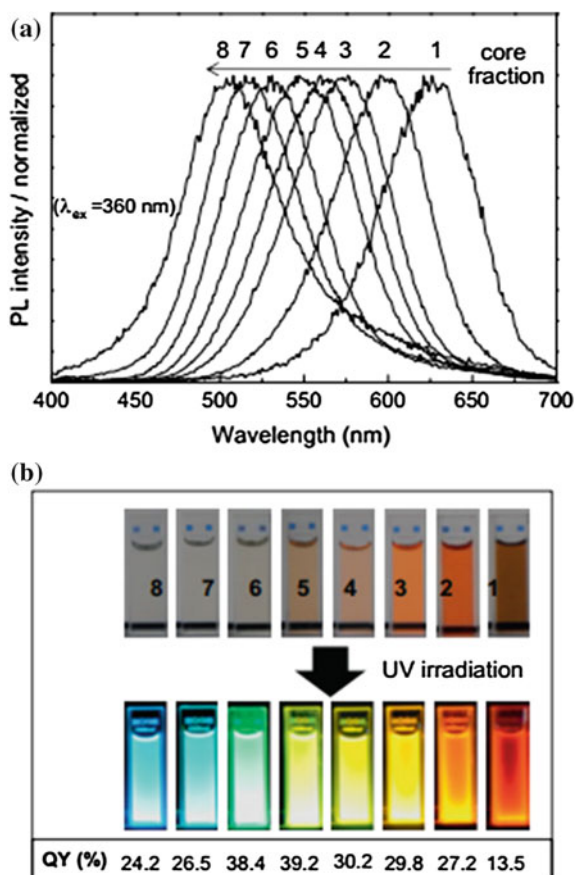

Fig. 16.1 a Synthesis of InP/ZnS quantum dots. **b** Image of different wavelengths of InP/ZnS quantum dots excited by UV light. **c** TEM image of resulting InP/ZnS quantum dots. *Inset* in **c** illustrates core–shell structure of InP/ZnS quantum dots. Reproduced from Ref. [2] by permission of John Wiley & Sons Ltd

16.1.2   Hydrothermal Method for InP

In hydrothermal method, the precursor is placed in an autoclave and heated in a high-temperature oven for a long period. This method requires size-selective precipitation to acquire the different wavelengths of QDs. In 2012, Byun et al. [3] proposed a low-toxicity phosphorus compound tris(dimethylamino)phosphine P(N(CH3)$_2$)$_3$ to replace the highly toxic P(TMS)$_3$; however, the yield is low, and the synthesis is long; thus, mass production of this application is not easy. The photoluminescence spectra and different wavelengths of QDs under UV-light irradiation are presented in Fig. 16.2.

Fig. 16.2 a Photoluminescence spectra of InP/ZnS quantum dots. **b** Image of different wavelengths of InP/ZnS quantum dots excited by UV light. Reprinted from Ref. [3]. Copyright 2010, with permission from Elsevier
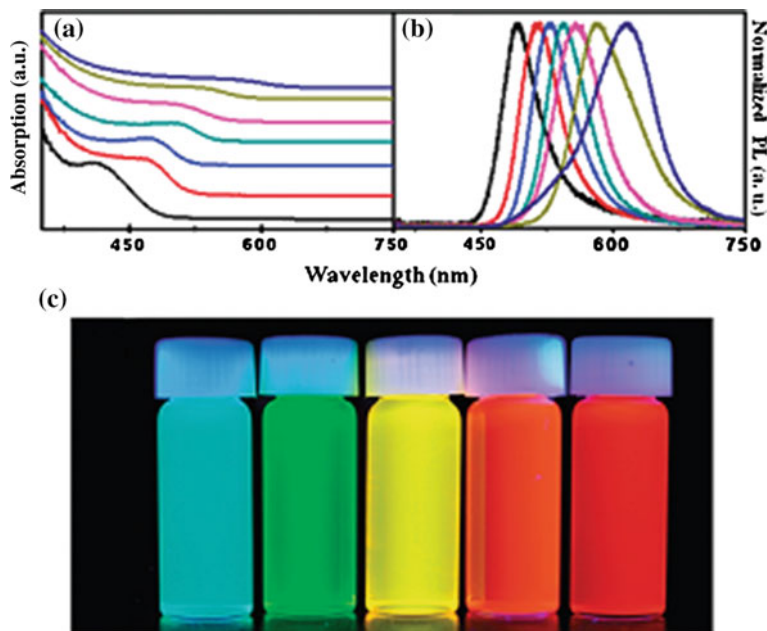
Fig. 16.3 **a** Photoluminescence spectra of InP/ZnS quantum dots. **b** UV spectra of InP/ZnS NCs. **c** Image of different wavelengths of InP/ZnS quantum dots excited by UV light. Reprinted with the permission from Ref. [4]. Copyright 2012 American Chemical Society

16.1.3 Continuous Heating-up Method for InP

Numerous researchers focus on fitting the commercial model to produce QDs, but it is difficult for mass production. In this section, we introduce continuous heating-up method, in which the precursor is slowly injected under stable condition. In 2011, Kim et al. [4] proposed a QD mass production method. In this production method, the precursors are mixed together in a three-neck flask, and then, phosphorous precursor tris(trimethylsilyl) phosphine P(TMS)$_3$ is slowly injected inside the solution with a high-pressure pump. This method can make the QD nucleation uniform and reduce unreacted precursors, thereby significantly increasing the yield. This method can also improve future optimization for mass production of Cd-free QDs (Fig. 16.3; Table 16.1).

16.2 InP Application in Electroluminescence and Photoluminescence

Colloidal semiconductor QDs have shown great potential as light emitters in solar cells and biological imaging. Therefore, we will focus on this type of QDs for its application in light-emitting diodes (LEDs).

Table 16.1 Comparison of the three methods

Synthetic method	Advantages	Drawback
One pot method	✓ High production ✓ Good size distribution ✓ Good quantum efficiency ✓ Short reaction time (core: 60 min) shell: 20 min)	• Vaccum system • Multiple step
Hydrothermal Method	• Easy • Non-toxic precusor	• Long time (24 h) • Low prodiction • Wide size distribution
Continuous heating-up method	• Mass production	• Long time (10 h) • Multiple step

16.2.1   Introduction of QD-LEDs

QDs have shown great promise as visible emitters for both fabrication of electro-luminescent QD-based LEDs and photoluminescence. In this section, we introduce the general model of QD-LEDs and the development of Cd-free QDs in QD-LEDs. The basic principle of QD-LEDs indicates that the emitting layer materials are placed between two electrodes in the form of thin layers. When holes (or electrons) are injected into the emission layer through the hole-transport layer (HTL) from an anode with high-work function or through the electron-transport layer (ETL) from a cathode with low-work function, the electron–hole pairs are injected into the emitting layer and radiated photons by recombination process. For the injection of electrons to conduction band/LUMO levels, low-work function cathodes, such as magnesium, calcium, and lithium fluoride/aluminum, are often used, whereas O_2 plasma-treated indium tin oxide is often employed for high-work function trans-parent anodes. The schematic is shown in Fig. 16.4. Several advantages of using QDs as emitting layers in these electrically pumped LEDs include tunable emission, saturated color, stability, and processable solution.

In the QD-LED system, we are confronted with four great challenges, which we will introduce and discuss with their corresponding solutions.

1. The mismatch of the QDs between HTL and ETL shows that the well match of QDs is the inorganic ETL and organic HTL (Fig. 16.5) [5].
2. Fluorescence resonance energy transfer (FRET) [6]. FRET phenomenon occurs when the distance between the two QDs is approximately <10 nm. However,
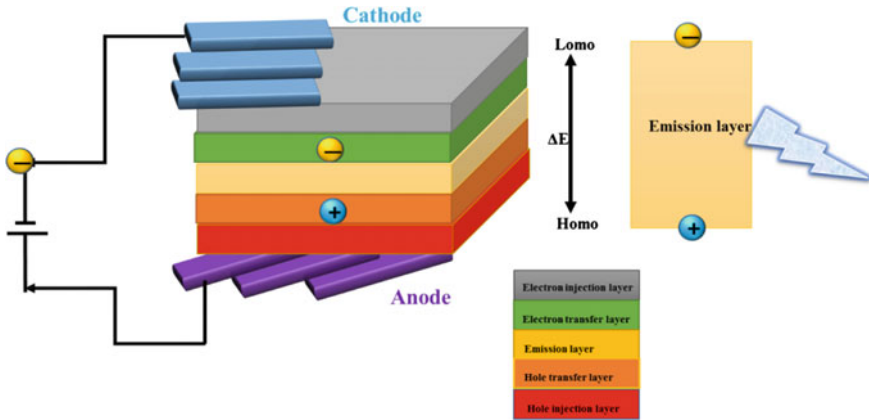
Fig. 16.4 QD-LED structure, QD emitting layer was sandwiched between an organic hole-transport layer (HTL) and an organic electron-transport layer (ETL)
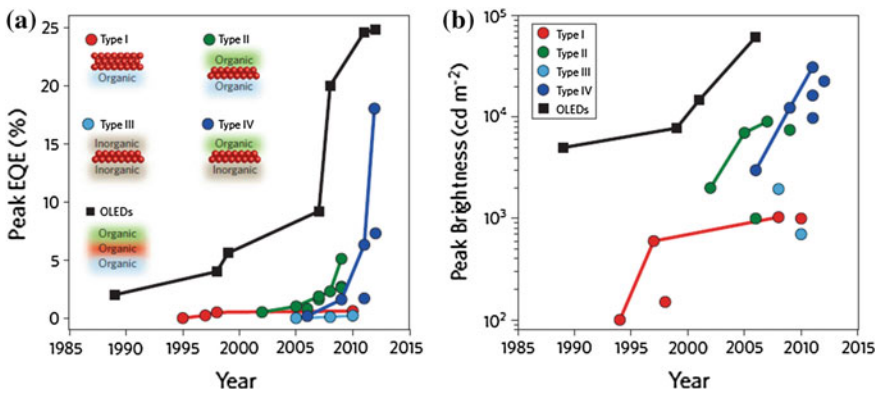

Fig. 16.5 QD-LED structure, with emitting layer sandwiched between an organic hole-transport layer (HTL) and an organic electron-transport layer (ETL). Reprinted by permission from Macmillan Publishers Ltd: Ref. [5]. Copyright 2012

given that the QY of QDs is not 100 %, this process will cause QY decline. When the pieces are coated with QDs into a film structure, these QDs are mostly close-packed and tightly stacked because their quantum yield may decrease from 100 to 10 % compared with solution.

3. Endurance to water, oxygen, and temperature [7]. Little surface oxidation or structural changes result in decreased QY because the shell is very thin. Moreover, when the carrier injection in the electron–hole complex exhibits a similar p-n junction, the QLED device temperature increases, resulting in more excitons. Large thermal kinetic energy can be provided over the limitations of the shell to reach the surface defects, and the electron–hole recombination rate decreases.
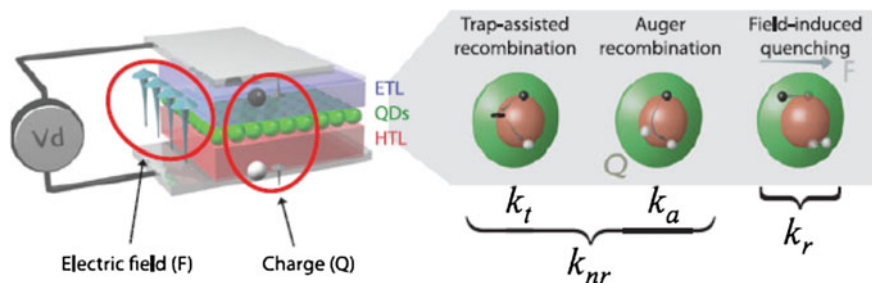
Fig. 16.6 Schematic of QD-LED structure. The QD-emitter layer is located between *ETL* and *HTL*. Non-radiative emission involves trap-assisted recombination (k_t) and Auger recombination (k_t). Radiative emission results from the electric field, which is caused by the LED operation process. Reprinted with permission from Ref. [8]. Copyright © Materials Research Society 2013

4. Non-radiative emissions between different layers. In a QD-LED device, the major contributions to non-radiative emissions are the electronic trap states and free-charge carriers. If the QD layer exhibits a surface defect, trap-assisted recombination occurs, in which the hole and electron recombine on the surface defect. Free-charge carriers may cause an imbalance between electron and hole injections. This phenomenon is known as Auger non-radiative recombination, which is clearly illustrated in Fig. 16.6 [8].

Overcoating of QDs is a good solution for high-efficiency QD-LEDs. To date, the optimum EQE device uses red [9], green [10], and blue [11] colors for the overcoating method. Subsequently, the QDs are enlarged by more than 10 nm. Hence, these QDs are called "giant quantum dots."

16.2.2 InP QD Application in QD-LEDs

QD-LEDs present two types of devices: normal and inverted. The example in this paper [12] is an inverted-type device. Figure 16.7 shows that the ETL is composed of zinc oxide, which is made by the sol–gel method. The HTL is composed of an organic material Tris(4-carbazoyl-9-ylphenyl) amine. This Cd-free device is bright, efficient, and environmentally friendly. The InP/ZnSeS heterostructure of QDs is passivated by ZnSeS shell. This shell can increase the efficient recombination of electron and hole in the emission layer. Thus, the quantum yield is higher than those in previous reports. The resulting QLEDs record 3.46 % of external quantum efficiency and 3900 cd m^{-2} of maximum brightness. We speculate that such comprehensive scheme in designing device architecture and structural formulation of QDs provides a reasonable guideline for practical realization of environmentally benign, high-performance QLEDs in the future.
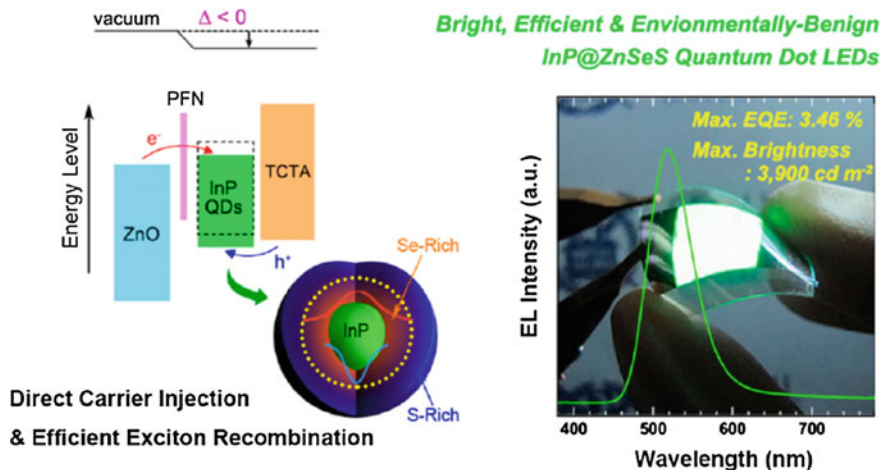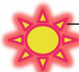
Fig. 16.7 Schematic of Cd-free QD-LED structure, with QDs sandwiched between an organic hole-transport layer (HTL) and an organic electron-transport layer (ETL). Reprinted with the permission from Ref. [12]. Copyright 2013 American Chemical Society

16.2.3 InP QD Application in White-Light LED

In this section, we focus on the application of QDs as LED wavelength converters to decrease the consumption of electrical energy. Studies showed that most lighting devices, such as incandescent and fluorescent lamps, consume high energy. Therefore, many people focus on low-power consumption devices. QD-LEDs present a good alternative. Such LEDs do not only decrease the consumption of energy but also exhibit high color quality. LED purchase provides a potential alternative to other types of lighting devices with higher efficacy, lower power

Table 16.2 Comparison of different types of light source in color temperature, CRI, luminescence, and lifetime

	Light source	Color temperature	CRI	Lum. efficacy (lm W^{-1})	Lifetime (h)
	Sunlight	5600	100	93	Billions
	Tungsten light bulb	2790	100	<18	1000
	Fluorescent lamp	3000–5000	50–80	50–100	10000
	Commercial white-light LED	3200–6500	70(90)	30–70	50000

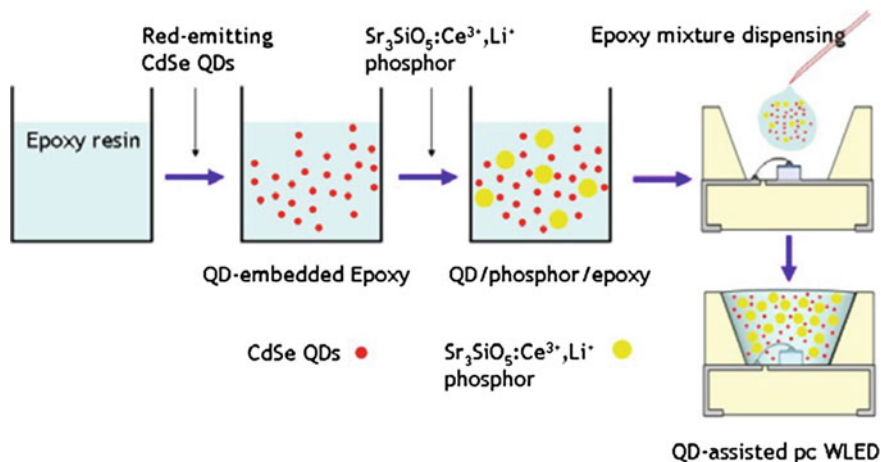Reproduced from Ref. [13] by permission of John Wiley & Sons Ltd

Fig. 16.8 Schematic of fabrication process of QD-assisted phosphor-based white-light LEDs. Reproduced from Ref. [13] by permission of John Wiley & Sons Ltd

consumption, longer lifetime, and a rapid response time. White-light LEDs are recently introduced with blue LED chip and yellow light-emitting $Y_3Al_5O_{12}:Ce^{3+}$ (YAG:Ce) phosphors [13]. Although this type of white-light LEDs has shown simple fabrication, high efficacy, and good stability, such LEDs also exhibit a poor color rendering index (CRI), which is a quantitative measure of the ability of a light source to reproduce the colors of various objects faithfully in comparison with an ideal or natural light source (Table 16.2).

To fabricate LEDs with QDs and phosphors, we can follow the method in Fig. 16.8. We initially need to mix the epoxy resin with our QDs and then dry at
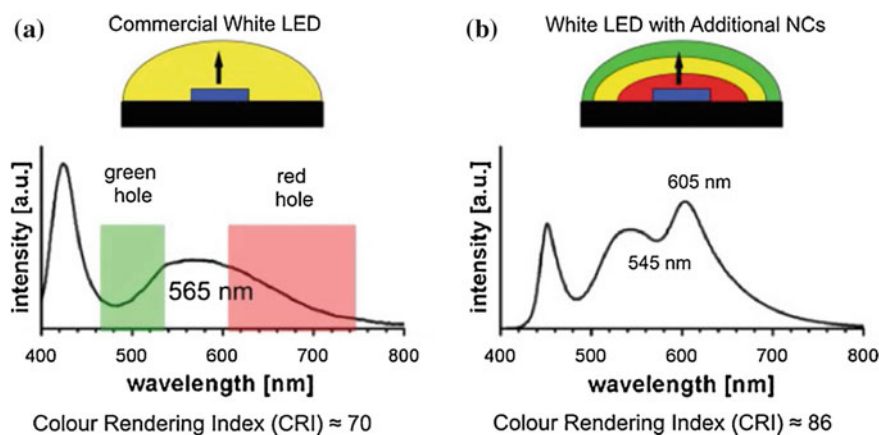

Fig. 16.9 a Photoluminescence of commercial white-light LED. **b** Photoluminescence of QD-based white-light LED. Reproduced from Ref. [14] by permission of John Wiley & Sons Ltd
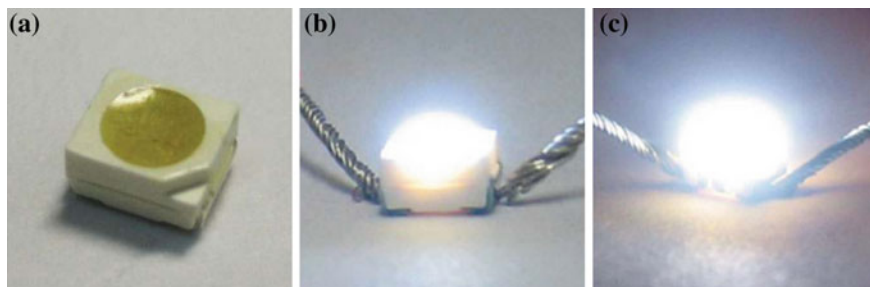
Fig. 16.10 **a** Image of CdSe QDs and $Sr_3SiO_5:Ce^{3+}$, Li^{3+} phosphor-based white light LED, **b** LED device operated at 5 mA, **c** LED device operated at 20 mA. Reproduced from Ref. [13] by permission of John Wiley & Sons Ltd

60 °C. After the cooling step, we add the yellow YAG phosphor to the mixture and dry at 150 °C for 2 h. Epoxy mixture dispenses on the blue chip, and the device emits white light. In contrast to phosphors, QDs can obviously enhance the CRI value and color saturation of the device. Ziegler et al. [14] used red InP/ZnS QDs to increase the CRI value and make the light more colorful (Fig. 16.9). We can see the result of the QDs-based white-light LED operated at different current (Fig. 16.10).

16.3 Conclusions

Colloidal QDs exhibit unique optical properties depend on the particle size, which can be changed by tuning their particle sizes. Given their unique size-dependent photoluminescence spectra, these QDs have attracted great interest for their application in LEDs. QDs demonstrate good luminescence efficiency and photo-stability. These unique properties make QD-LEDs promising candidates for the application in backlight display. Cd-free InP QDs are non-toxic and environmentally friendly; thus, many people prefer this devices. The Cd-free-based display is the optimal choice for the next generation display.

References

1. Anc MJ, Pickett NL, Gresty NC, Harris JA, Mishra KC (2013) Progress in non-Cd quantum dot development for lighting applications. ECS J Solid State Sci and Technol 2:R3071
2. Yang X, Zhou D, Leck KS, Tan ST, Tang YX, Zhao J, Demir HV, Sun XW (2012) Full visible range covering InP/ZnS nanocrystals with high photometric performance and their application to white quantum dot light-emitting diodes. Adv Mater 24:4180
3. Byun HJ, Lee JC, Yang H (2010) Solvothermal Synthesis of InP Quantum Dots and Their Enhanced Luminescent Efficiency by Post-synthetic Treatments. J. Colloid Interf. 355:35

4. Kim T, Kim S, Woo KM., Kim S-W (2012) Large-scale synthesis of InP/ZnS alloy quantum dots with dodecanethiol as a composition controller. J Phys Chem Lett 3:214

5. Shirasaki Y, Supran GJ, Bawendi MG, Bulovic V (2012) Emergence of colloidal quantum-dot light-emitting technologies. Nat photonics 7: 13

6. Chen CJ, Lin CC, Lien JY, Wang SL, Chiang RK, (2015) Preparation of quantum dot/polymer light conversion films with alleviated Förster resonance energy transfer redshift. J Mater Chem C 3:196

7. Boldt K, Kirkwood N, Beane GA, Mulvaney P (2013) Synthesis of highly luminescent and photo-stable, graded shell CdSe/CdxZn$_{1-x}$S nanoparticles by in situ alloying Chem. Mater 25:4731

8. Bozyigit D, Wood V (2013) Challenges and solutions for high-efficiency quantum dot-based LEDs. MRS Bulletin 38:731.

9. Dai X, Zhang Z, Jin Y, Niu Y, Cao H, Liang X, Chen L, Wang J, Peng X (2014) Solution-processed, high-performance light-emitting diodes based on quantum dots Nature 515:96

10. Lee KH, Lee JH, Kang HD, Park B, Kwon Y, Ko H, Lee C, Lee J, Yang H (2014) Over 40 cd/A Efficient Green Quantum Dot Electroluminescent Device Comprising Uniquely Large-Sized Quantum Dots ACS Nano 8:4893

11. Lee KH, Lee JH, Song WS, Ko H, Lee C, Lee JH, Yang H (2013) Highly efficient, color-pure, color-stable blue quantum dot light-emitting devices ACS Nano 7:7295

12. Lim J, Park M, Bae WK, Lee D, Lee SH, Lee CH, Char K (2013) Highly efficient cadmium-free quantum dot light-emitting diodes enabled by the direct formation of excitons within InP@ZnSeS quantum dots ACS Nano 10:9019

13. Jang, HS, Yang H, Kim SW, Han JY, Lee S, Jeon DY (2008) White light-emitting diodes with excellent color rendering based on organically capped CdSe quantum dots and $Sr_3SiO_5:Ce^{3+}$, Li^+ phosphors Adv Mater 20:2696.

14. Ziegler J, Xu S, Kucur E, Meister F, Batentschuk M, Gindele F, Nann T(2008) Silica-coated InP/ZnS nanocrystals as converter material in white-light LED Adv Mater 20:4068.

Chapter 17
Carbon Nitride Quantum Dots and Their Applications

Ming-Hsien Chan and Ru-Shi Liu

Abstract This chapter discusses graphitic carbon nitride (g-C$_3$N$_4$) quantum dot (CNQD), which is a novel carbon-containing material. The synthetic resource of g-C$_3$N$_4$ comes from bulk carbon material, such as melamine or urea powder. Further quantized synthesis of g-C$_3$N$_4$ is often performed by thermal etching and hydrothermal method. After the preliminary steps during synthesis, bulk g-C$_3$N$_4$ lumps into a sheet and then splits into a spot-shaped material. CNQDs equipped with multiple electronic properties can be modified as a photocatalytic material that can be extensively used in electrochemistry. Moreover, g-C$_3$N$_4$ is a candidate for biological applications, e.g., the blue fluorescence of g-C$_3$N$_4$ may be used for biological imaging. This chapter explores the synthesis and properties of CNQDs. The unique advantageous properties from CNQDs will be applied in current science and technology.

17.1 Introduction

Graphitic carbon nitride (g-C$_3$N$_4$) quantum dots (CNQDs) are polymeric materials consisting of C, N, and some H impurities, which are connected via tri-s-triazine-based patterns. Compared with the majority of carbon materials, CNQDs have diverse electron-rich properties and basic surface functionalities (Fig. 17.1). The application of g-C$_3$N$_4$ has increased in recent years. g-C$_3$N$_4$ was first primarily used as a solid lubricant and other purposes. In 2008, g-C$_3$N$_4$ was used as a photocatalyst because it does not contain metal and can be applied to decompose
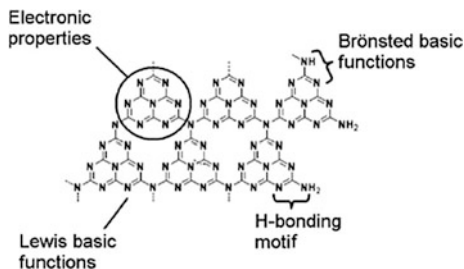
M.H. Chan · R.S. Liu (✉)
Department of Chemistry, National Taiwan University, Taipei 106, Taiwan
e-mail: rsliu@ntu.edu.tw

R.S. Liu
Department of Mechanical Engineering and Graduate Institute of Manufacturing Technology, National Taipei University of Technology, Taipei 106, Taiwan

water, so g-C$_3$N$_4$ became a new member of the family of photocatalysts [1]. The current work can be a milestone in the study of g-C$_3$N$_4$. The unique advantage of g-C$_3$N$_4$ is its metal-free characteristic. This feature is very impressive, because most of the available photocatalysts are metals, which produce unnecessary resource damage and are toxic to the environment [2]. The absence of metal in g-C$_3$N$_4$ renders it a good candidate for biological application. Pure carbon and nitrogen compounds are undoubtedly very favorable because of their biocompatibility. Thermal stripping or hydrothermal method can be used to fabricate CNQDs as fluorescent probes for cell labeling, which are fitted into cells, similar to light bulb tracking cells, to locate cells, most especially for tumor cell imaging [3]. However, the excitation wavelength of g-C$_3$N$_4$ is located in the UV region, which facilitates the penetration of g-C$_3$N$_4$ fluorescent light into the skin layer, which may also harm the human body. This characteristic limits the biological applications of g-C$_3$N$_4$. In this section, we will first discuss the physical and chemical properties of raw synthetic g-C$_3$N$_4$. Second, we will discuss the application of g-C$_3$N$_4$ technology. Finally, we will propose an application with integrated g-C$_3$N$_4$ for future studies.

17.2 Basis of CNQDs

This section will focus on CNQDs and introduce its basic concepts. First, we will discuss carbon as a basic quantum dot. The synthesis of g-C$_3$N$_4$ will be introduced. Finally, the characteristics and future applications of g-C$_3$N$_4$ will be discussed to elucidate the current popularity of this material as another nanomaterial. The limitations of g-C$_3$N$_4$ will be presented.

17.2.1 Carbon Quantum Dot Materials

Carbon quantum dots are similar to various metal quantum dots, and they emit bright fluorescence under irradiation. Thus, carbon quantum dots can be potentially applied to improve biological sensors, medical imaging devices, tiny light-emitting

diodes, and other related areas. Many studies have investigated these materials, and these papers were published in the *Journal of the American Chemical Society* [4].

The most important feature of carbon quantum dots is their non-toxicity, which indicates that they are less harmful to the environment compared with metal quantum dots. Carbon quantum dots may be used to produce sensors for detecting explosives, anthrax, or other biochemical reagents. Sun stated that "Carbon is not a semiconductor, but a light-emitting nanomaterial. Nanosized carbon material is very interesting both theoretically and practically." This statement defines "carbon" as a new luminescent platform of nanoparticle research [5]. Quantum dots have recently been extensively investigated, especially in biological research and medicine. Quantum dots are typically extracted from lead, cadmium, and a mixture of silicon. However, these materials generally have acute toxicity and may harm the environment. Thus, scientists have attempted to extract quantum dots from benign compounds. Given that a carbon nanoparticle has a large surface area, this nanoparticle is believed to have very peculiar chemical and physical properties that are comparable with those of macroscopic carbon material.

Similar to a tiny flash ball, carbon nanoparticles emit bright fluorescence under irradiation. Incidentally, the mechanism of light-emitting carbon quantum dots slightly differs from that of metal quantum dots (Fig. 17.2) [6]. The light-emitting mechanism of metal quantum dot is presented by internal electronics. The upward movement of particles is limited, resulting in quantum confinement effects. Scientists believe that the photoluminescence of carbon quantum dots is probably due to the fact that hollow surface can store energy under strong illumination, and carbon quantum dots can facilitate surface electron transfer, resulting in the release of energy and fluorescence. Carbon quantum dots have become popular in recent years. They are non-toxic, environmentally friendly, and inexpensive. Thus, these quantum dots are considered in studies on light-emitting nanoparticles. Preparing carbon quantum dots involves a three-step process, namely the removal of graph it
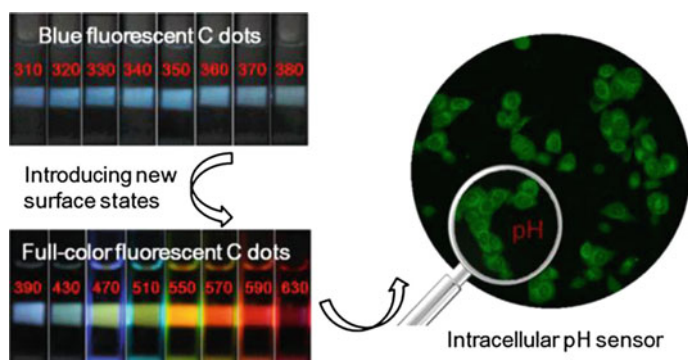

Fig. 17.2 Images of *blue* fluorescent C dots (*upper row*) and full-color fluorescent C dots (*lower row*) in ethanol excited with the indicated wavelengths. These unique fluorescent C dots could be used as cell tracking nanomaterials. Reprinted with the permission from Ref. [6]. Copyright 2014 American Chemical Society

eat high temperature and pressure, hydrothermal synthesis, and electrochemical scanning.

17.2.2   Nitrogen-Doped Carbon Quantum Dots

In 1989, Liu and Cohen examined the crystal structure of β-Si_3N_4 and replaced C with Si. The local density of states, which were determined via first pseudo-potential approximation method, was used to predict β-C_3N_4 theoretically. β-C_3N_4, which has a hardness comparable with that of diamond, can be considered a new synthetic compound. In 1996, Teter and Hemley determined through calculation that C_3N_4 may display five structures, namely α-, β-, cubic, quasi-cubic, and graphitic-like phases. Except for the graphitic-like phase, the other four kind materials exhibit hardness comparable with that of diamond. Although g-C_3N_4 does not possess high hardness, it is equipped with a unique electronic structure and excellent chemical stability. g-C_3N_4 has been applied as a catalyst and nonmetal component catalyst carrier in recent years. Additionally, this material is also widely used in the selective conversion of organic functional groups, photocatalytic decomposition of water, oxygen reduction, and precious metal loading with Au, Pd, Ag, and Pt. g-C_3N_4 can also be utilized as a green energy storage material for H_2 and CO_2. Thus, g-C_3N_4 has gradually attracted attention in related studies on energy and materials. Thus, the preparation and application of g-C_3N_4 materials will be discussed to summarize domestic and foreign counterparts. Important developments in the field for future trends will also be reviewed. Finally, the energy and environmental applications will be provided (Fig. 17.3) [7].
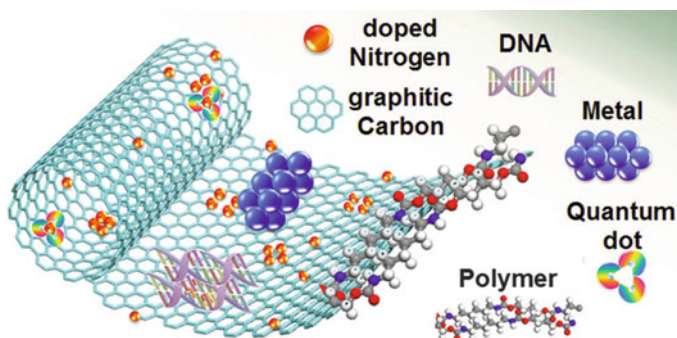

Fig. 17.3 Schematic illustration of N-doped carbon nitride and graphene-based composites with various functional materials. Reproduced from Ref. [7] by permission of the Royal Society of Chemistry
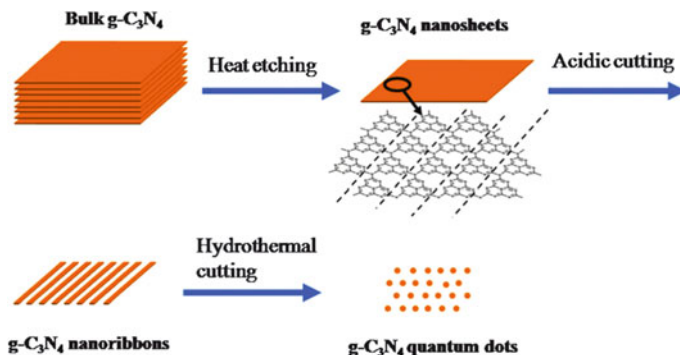
Fig. 17.4 Schematic illustration of the controllable synthesis of g-C_3N_4 nanosheets, nanoribbons, and quantum dots. Reproduced from Ref. [8] by permission of the Royal Society of Chemistry

17.2.3 Synthesis Methods of CNQDs

17.2.3.1 Thermal Split Etching Method

Thermal split etching is the most common technique for synthesizing nanoscale g-C_3N_4. This process breaks down bulk g-C_3N_4 into small g-C_3N_4 molecules (Fig. 17.4). This method produces highly uniform g-C_3N_4 particles and generates g-C_3N_4 particles with varied morphologies, such as sheets, lines, or dots. The "top-to-down" synthesis is performed at high temperatures (825–950 °C), at which material corrosion occurs [8]. At temperatures higher than 884 °C, the surface of g-C_3N_4 will become a molten state, inducing the transformation of the uneven surface of g-C_3N_4 into CO_2 and other gas emissions. Moreover, given the relatively weak force between each layer of g-C_3N_4, bulk g-C_3N_4 gradually transforms into g-C_3N_4 sheets.

Other low-temperature (650–750 °C) thermal etching techniques may be used. Although the temperature does not reach the melting point, catalyst addition may generate lower melting point and accelerate corrosion. After heating, nanosheet g-C_3N_4 can be obtained by acid and hydrothermal cutting. Smaller nanoparticles will form CNQDs.

17.2.3.2 Solid-Phase Hydrothermal Synthesis

In 2013, Zhang et al. proposed a new g-C_3N_4 synthesis method (Fig. 17.5). This "bottom-to-top" method is performed by combining the small molecules of carbon carriers (e.g., sodium citric acid) and nitrogen carriers (e.g., urea) and then allowing them to react in a hydrothermal environment to fabricate g-C_3N_4 at high temperature. In the current paper, regulating the ratio of these two compounds will result in g-C_3N_4 with different fluorescence, extending the application of g-C_3N_4 [9].
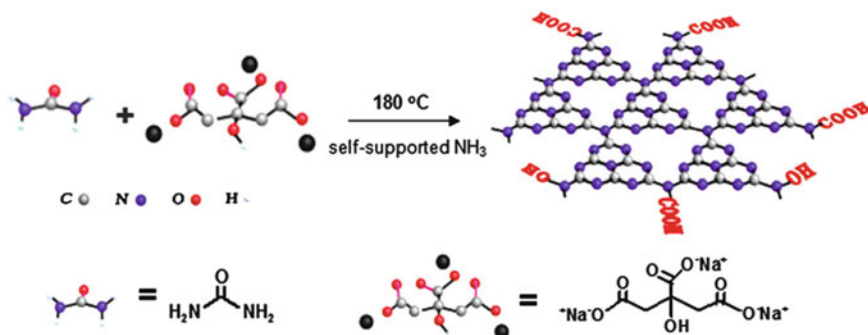
Fig. 17.5 Mechanism for the formation of highly fluorescent g-CNQDs. Reproduced from Ref. [9] by permission of the Royal Society of Chemistry

## 17.3   Applications of CNQDs

The carbon quantum dots, which are novel carbon nanomaterials, emit a stable fluorescent signal, have other unique optical properties, and present no light flashes. Their excitation and emission wavelengths can be regulated. These materials have low biological toxicity and high biocompatibility. This section will discuss the reaction mechanism of $g\text{-}C_3N_4$ fluorescence [10].

17.3.1   CNQDs for Photocatalytic Hydrogen Production

Living standards have improved because of global industrialization, but this development is accompanied with environmental pollution and energy crisis [11]. Photocatalyst technology can effectively process contaminants in liquid organic chlorobenzene, chlorophenol contaminant compounds, cyanides, and metal ions. To solve air pollution, photocatalysis can also effectively treat nitrogen oxides (NO_x), sulfur oxides (SO_x), and other pollutants. Given that photocatalytic reactions only play the role of catalysts, the material itself will not be decomposed, so no side effects would be produced. Furthermore, photocatalysts can be used to prevent and control the quality of air and water. If the semiconductor photocatalyst [e.g., titanium dioxide (TiO_2)] is soaked in water and UV-irradiated, water can be decomposed into oxygen and hydrogen. This reaction, which converts light energy to chemical energy, is similar to photosynthesis. Thus, this process was used to produce clean and environmentally friendly energy, namely hydrogen, during the oil crisis. However, the efficiency of this technique is not high enough, so this process is still being explored.

The photocatalytic reaction is shown in Fig. 17.6 [12]. Through UV or sunlight irradiation, the surface electrons of the catalyst absorb sufficient energy to

Fig. 17.6 Catalytic reaction mechanism of photocatalytic activation. Reprinted with the permission from Ref. [13]. Copyright 2005 American Chemical Society
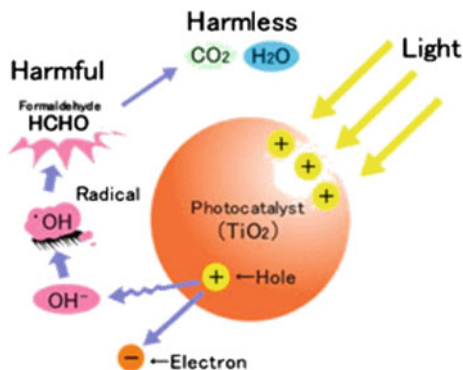
disengage from their position. This phenomenon generates a positive electron hole. The charged hole will remove electrons from water molecules and create a free hydroxyl group (OH^-) in the vicinity of oxidation, which enhances the activity of OH^- radical. For an environment with organic molecules, OH^- radicals will not only recapture electrons, but also collapse the organic molecular bond. Most pollutants or pathogens are carbohydrates, and these compounds will transform into harmless water and carbon dioxide after decomposition. Therefore, decontamination and sterilization are achieved.

Polymeric g-C_3N_4 semiconductors are widely used in solar photocatalytic conversion because of their excellent chemical stability and unique electronic band structure [14]. g-C_3N_4 is a cheap, stable, and nonmetal component, so it is considered a green and environmental protection catalyst [15]. The composition and chemical properties of g-C_3N_4, metal/nonmetal doping regulation of g-C_3N_4, and soft/hard template optimized method of g-C_3N_4 have been explored [16].

g-C_3N_4 is a typical polymer semiconductor that is composed of C and N atoms via highly sp^2 hybrid to generate a π-conjugated system. In the formation of g-C_3N_4, Np_z orbital composes the highest occupied molecular orbital (HOMO), and Cp_z composes the orbital lowest unoccupied molecular orbital (LUMO), with a 2.7 eV band gap between these two orbitals [17]. This suitable band gap can absorb the solar spectrum of UV light, which is less than 475 nm. Theoretical and experimental studies have shown that g-C_3N_4 has a very suitable semiconductor band edge position. Its HOMO and LUMO are located at +1.4 and −1.3 eV (vs. NHE, pH 7), respectively, which satisfy the thermodynamic requirements of hydrogen and oxygen production. In addition, compared with conventional TiO_2 photocatalyst, g-C_3N_4 can activate oxygen effectively to produce superoxide radicals for photocatalysis or inhibit the formation of OH^- radicals for excessive oxidation [18]. Theoretically, g-C_3N_4 can convert solar energy as a catalyst for visible light photocatalysis (Fig. 17.7).

Sun et al. (Chemistry and Chemical Engineering, Southeast University) recently collaborated with Zeng et al. (University of Science and Technology of China National Laboratory for Physical Sciences at Microscale) and Zeng et al.
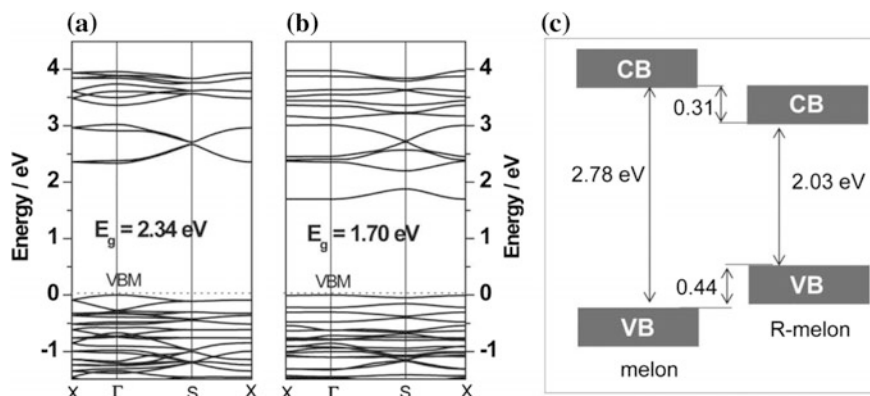
Fig. 17.7 Calculated band structures of **a** melon (original g-C$_3$N$_4$) and **b** R-melon (nitrogen-vacant g-C$_3$N$_4$), and **c** band structure alignments of melon and R-melon. Reproduced from Ref. [17] by permission of John Wiley & Sons Ltd

(Massachusetts Institute of Technology). They showed that excess N heteroatoms actually cause electrons to transfer into the ground state through non-radiative transition, which results in fluorescence quenching. In addition, unexpectedly, when they loaded g-C$_3$N$_4$ on the surface of the TiO$_2$ nanofiber, photogenerated electrons from g-C$_3$N$_4$ were rapidly injected into the conduction band of TiO$_2$. The special one-dimensional fiber structure of TiO$_2$ resulted in efficient transport of electrons, and it reduced the pairing of the electron–hole recombination rate under visible or UV light. This phenomenon indicated that TiO$_2$ at g-C$_3$N$_4$ could produce a stable output photocurrent, which is very promising in optoelectronic materials. This work was not only published in the latest issue of *Particle and Particle Systems Characterization*, but also selected as its cover paper (Fig. 17.8) [19].

17.3.2 CNQDs for Solar Cells

Photocatalytic semiconductor technology is a sunlight-driven series of important chemical reactions. The high density of solar energy can be transformed from chemical energy or degraded from organic pollutants [20], which is an important application prospect for solving energy shortage and environmental pollution problems. The modification of g-C$_3$N$_4$ photocatalyst and important development in g-C$_3$N$_4$ photocatalysis, such as theoretical studies on g-C$_3$N$_4$ composition structure and chemical properties of metal/nonmetal dopants to regulate the semiconductor band of g-C$_3$N$_4$, are discussed [21]. The soft/hard template method is one of the most common synthesis techniques. This approach is based on surface chemical modification to improve the surface reaction kinetics and semiconductor composite on g-C$_3$N$_4$. This process enhances the separation efficiency of light carriers.
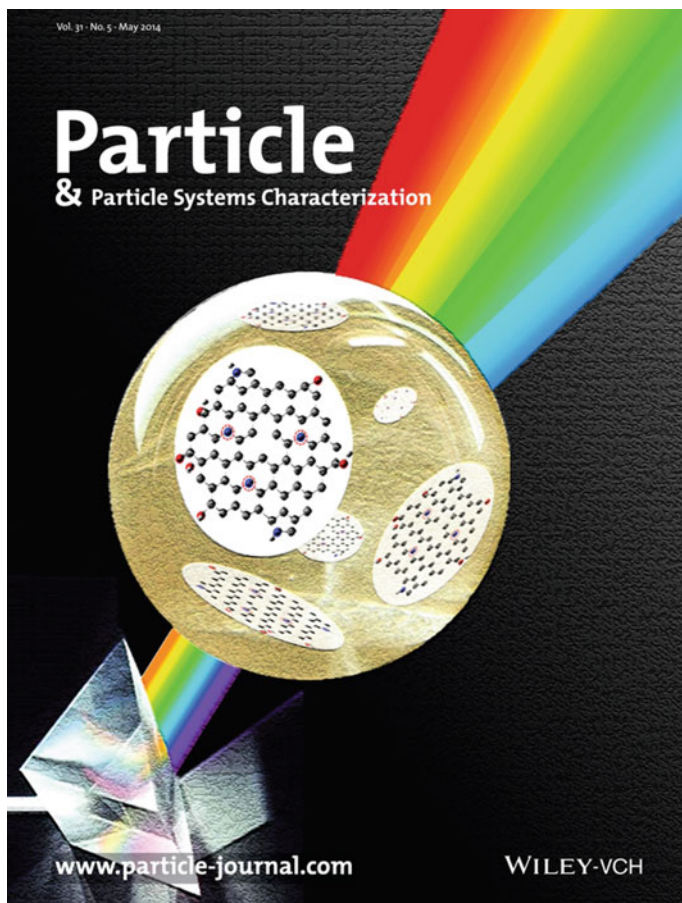
Fig. 17.8 Report of Sun et al. on how N dopants were tailored as substitutional and pyrrolic N in graphene quantum dots with controllable chemical properties. Reproduced from Ref. [19] by permission of John Wiley & Sons Ltd

Dye-sensitized solar cells (DSSCs) have been developed in recent years. Contrary to commercial expensive siliceous solid-state semiconductor/thin-film solar cells, DSSCs are considered potential solar storage materials (Fig. 17.9). This new solar cell technology, which integrates theory and nanotitanium dioxide (TiO_2), can be applied to multiple cross-cutting fields of optoelectronic semiconductor technology, science, and photocatalyst dye. Although the photoelectric conversion efficiency of solar cells can reach 8–10 %, the power generation efficiency is still not sufficiently high.

In addition, given that a battery element needs liquid electrolyte, the DSSC presents several drawbacks, such as electrolyte leak, high cost, and difficulty in obtaining dye material under long-term use. These characteristics seriously affect
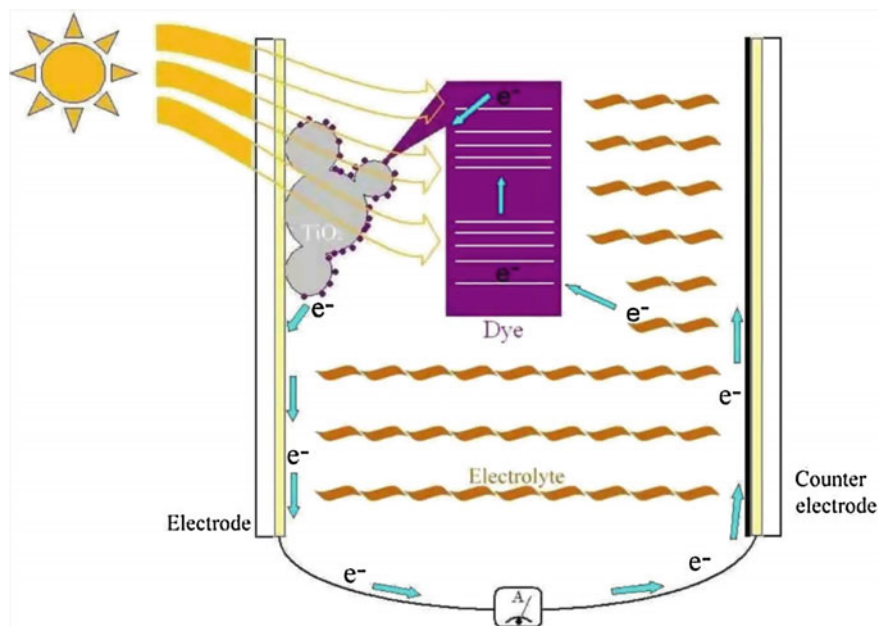
Fig. 17.9 Working principle of the dye-sensitized solar cell (DSSC), a schematic view of the photoelectric conversion and chemical reaction processes. C.E. represents the electrolyte. Reproduced from Ref. [21] by permission of John Wiley & Sons Ltd

Fig. 17.10 Schematic illustration of the photocatalytic process of sunlight-driven semiconductor TiO_2 at g-C_3N_4 nanosheets. g-C_3N_4 contributes additional electrons to enhance the performance of DSSCs. Reprinted from Ref. [22], Copyright 2014, with permission from Elsevier
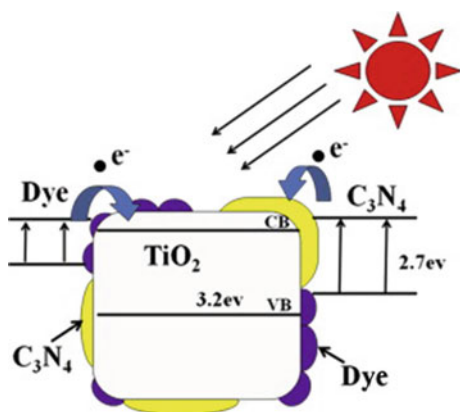
the development and production costs of this energy device. g-C_3N_4 is highly suitable for TiO_2 because its band edge energy is located at the right position [22]. It can effectively improve electron conduction, so the photoelectric conversion efficiency of DSSCs will be improved. Moreover, g-C_3N_4 is inexpensive and involves a very simple production process. Theoretically, g-C_3N_4 can be used as a catalyst for visible light photocatalytic conversion of solar energy (Fig. 17.10).

17.3.3 CNQDs for Biosensing and Bioimaging In Vivo

CNQD is a new class of carbon quantum dot. Considering the limitation of all internal electronic motion directions in g-C_3N_4, this material shows significant quantum confinement and edge effects. When the particle size of g-C_3N_4 is less than 10 nm, these two effects will lead to numerous new physical and chemical properties [23]. g-C_3N_4 is advantageous over traditional GQDs because of its low price, adjustable band gap, and stable photoluminescence activity. Nitrogen and carbon heteroatoms bring novel electrocatalytic activity, photoluminescence properties, low cytotoxicity, and good biocompatibility. Therefore, CNQDs have huge potential in optoelectronic devices, cell imaging, biomedicine, and other applications.

The fluorescence quantum efficiency of g-C_3N_4 can reach 34.5 % [24], which is an order of magnitude higher than that of traditional GQDs. Obviously, the quantum efficiency of g-C_3N_4 is sufficiently high for cell imaging to produce contrasting images (Fig. 17.11) [25].

g-C_3N_4 can be applied for detecting biological molecules with unique optical property. This application has been reported in a number of publications [26]. g-C_3N_4 exhibits strong blue fluorescence and enhances the fluorescence quantum yields by up to 29 %, whereas the highest quantum yield compared with graphene is 11.4 %. These results implied that g-C_3N_4 for biomolecular detection is a good choice. In recent years, g-C_3N_4 studies in the field of energy are gradually extended to biological studies [27]. As biosensors, g-C_3N_4 should combine biological, physical, and chemical factors to precisely detect analytes. Biosensors should include the following parts:

1. Sensitive biological elements (biological material, such as tissue, cell receptors, enzymes, antibodies, and nucleic acids).
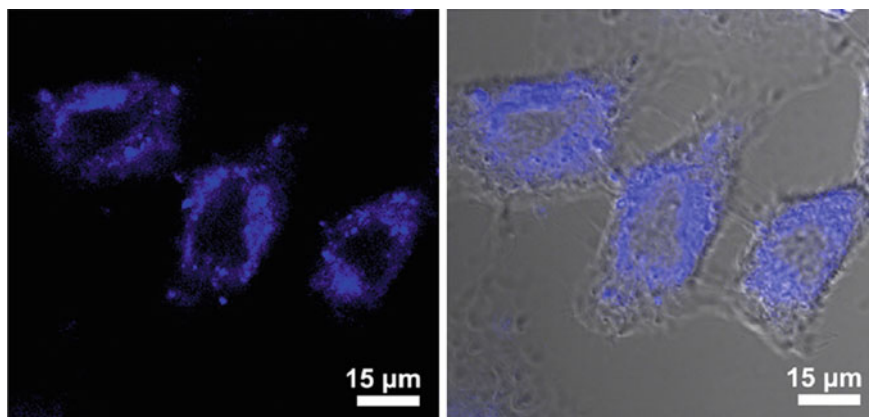

Fig. 17.11 Confocal fluorescence image and overlay image of bright field and confocal fluorescence image of HeLa cells incubated with g-C_3N_4 nanosheets for approximately 1 h. Reprinted with the permission from Ref. [25]. Copyright 2013 American Chemical Society
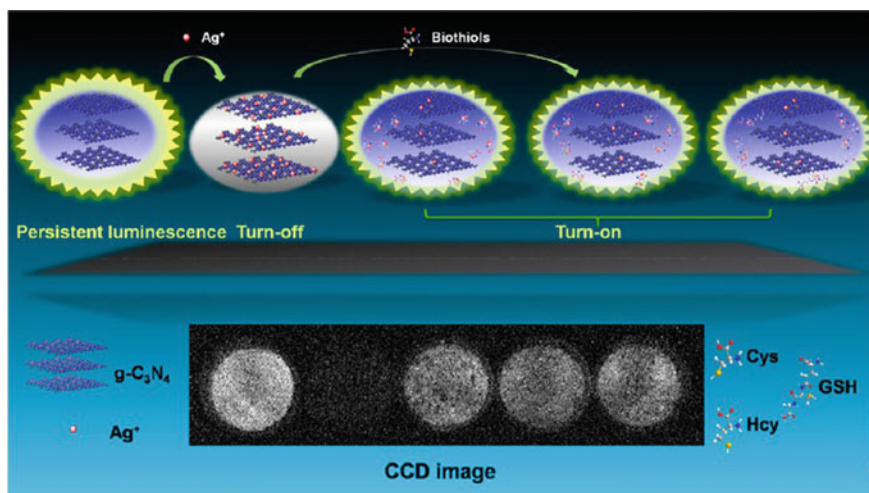
Fig. 17.12 Prepared g-C$_3$N$_4$ nanosheets intensively emit long-term luminescence that can avoid interference from biological media, such as tissue automatic fluorescence and scattering light. Reprinted with the permission from Ref. [28]. Copyright 2013 American Chemical Society

2. Connection of material platforms (a good platform, e.g., g-C$_3$N$_4$, can combine biological, physical, and chemical factors).
3. Detection element (with optical, electrochemical, temperature, and other physical and chemical means or magnetic work).

Recent developments in this field have also been achieved. Tian et al. used g-C$_3$N$_4$ to detect the content of biological sulfur (Figs. 17.12 and 17.13) [28]. This phenomenon was possible not only because g-C$_3$N$_4$ has sufficiently sensitive fluorescent properties, but also it is equipped with easily modifiable surface, facilitating its high potential as a biosensor.

17.3.4 CNQDs for Cancer Therapy

Reactive oxygen species (ROS) is a by-product of biological aerobic metabolism. ROS includes oxygen ions, peroxide, and oxygen free radicals [29]. These particles are quite small and very active because of their unpaired free electrons. High levels of ROS will result in cell and gene structural damage (Table 17.1) [30]. Active oxygen includes oxygen ions and hydrogen peroxide. ROS adversely affects cell signaling and homeostasis (Fig. 17.14) [31]. Nevertheless, cells have enzymes that can efficiently metabolize active oxygen. However, an extreme external environment that is unsuitable for survival (exposure to strong UV or strong heat) will remarkably enhance the amount of ROS. This process will block the electron transport chain of mitochondria and considerably damage the cellular structure.
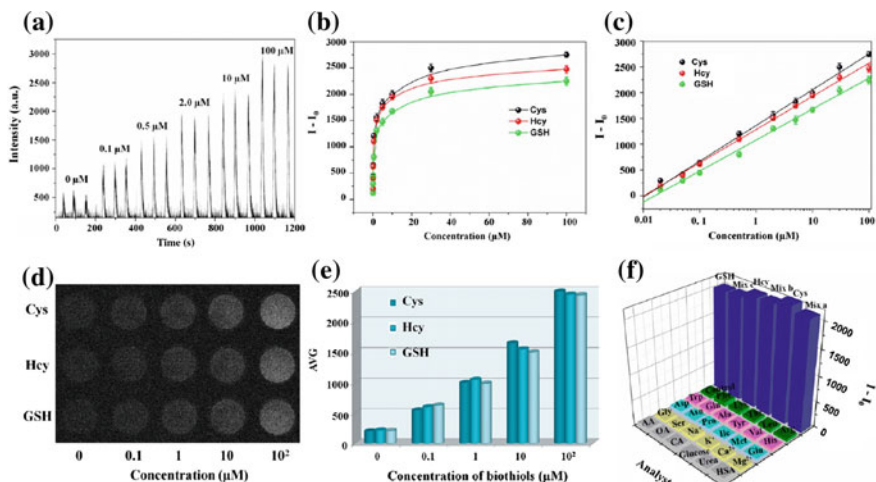
Fig. 17.13 Effect of the concentrations of Cys, Hcy, and GSH on the recovery of persistent luminescence intensity and after glow imaging of g-C_3N_4. Reprinted with the permission from Ref. [28]. Copyright 2013 American Chemical Society

Table 17.1 ROS reaction transfer the activity of protein for signaling [30]

Protein	Activity	Oxidation effect
Tyrosine phosphatase	Suppression	The kinase cascade is usually stopped, and phosphate on the target protein is hydrolyzed After oxidation, this protein is suppressed, resulting in rapid cell proliferation
Mitogen-activated protein kinase	Promotion	After oxidation of proteins, the activity will increase and enhance cell division messaging
Nuclear factor κB	Promotion	After oxidation of proteins, the activity will increase and promote the rapid transcription of cell division efficiency
For jun/fos gene AP1 feel transcription complex	Promotion	The protein complex is oxidized, and activity will increase. Thus, Ref-1 transcription factor will reduce cysteines and increase the efficiency of transcription

Summary ROS may change the activity of proteins to affect cells through messaging and promote rapid cell division in the human body, thereby causing damage

This phenomenon is also known as oxidative stress. ROS might also be generated by the body under ionizing radiation. In the current study, many scientists used oxidative stress, such as ROS damage, to treat diseases [32].

Typically, graphene and its derivatives (e.g., graphene oxide) have shown significant potential for biomedical applications, especially in DNA detection, bioimaging, drug delivery, and photodynamic therapy. Moreover, other 2D inorganic nanomaterials, such as MoS_2 nanosheet, have been developed for cancer
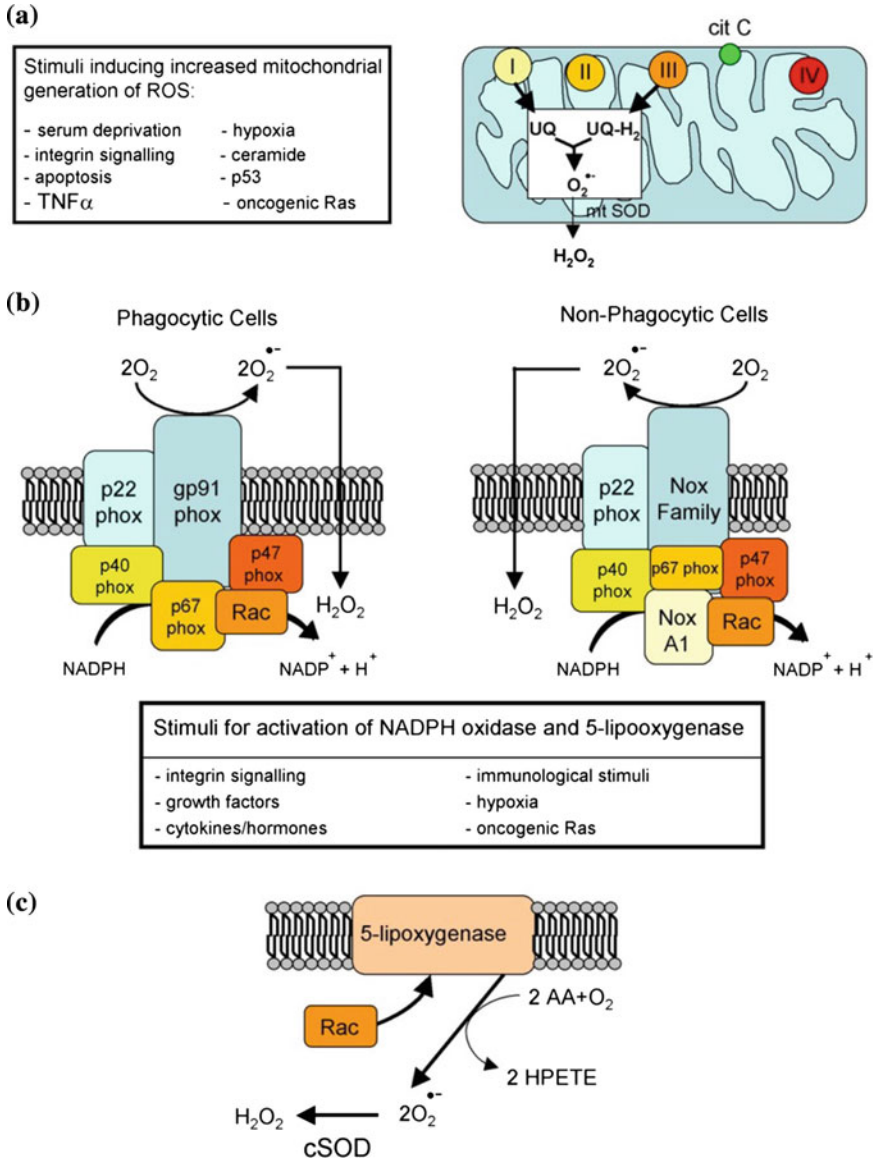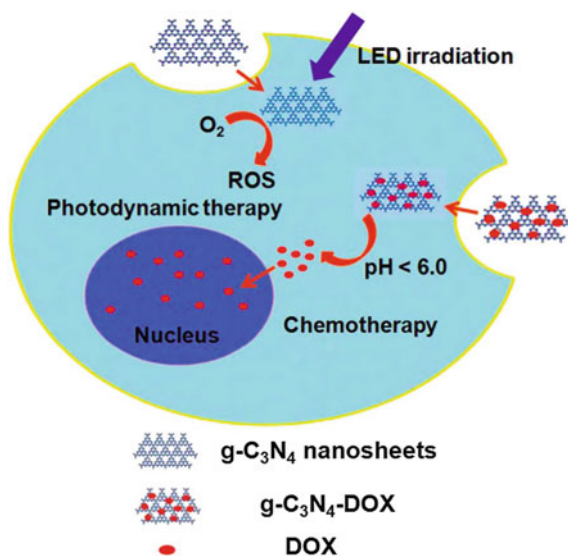
Fig. 17.14 ROS changes the chemical mechanism in organelles or enzymes. Reprinted from Ref. [31] **a** Mitochondria. **b** NADPH oxidase. **c** 5-lipoxygenase

therapy and biological analysis. However, many topics on g-C$_3$N$_4$ studies need to be developed. Similar to other carbon nanomaterials, g-C$_3$N$_4$ also exhibits significant photodynamic activity, which can induce the energy of UV light to generate oxygen radicals into the environment. Thus, Li and Yang et al. reported that g-C$_3$N$_4$ can be applied to cancer imaging and therapy as a potential photosensitizer and pH-responsive drug carrier (Fig. 17.15). In photodynamic therapy, g-C$_3$N$_4$ functions as a photosensitizer to produce ROS by irradiation at the appropriate wavelength [33]. When the environment has higher oxidative stress, it will be able to kill cancer cells (Fig. 17.16).

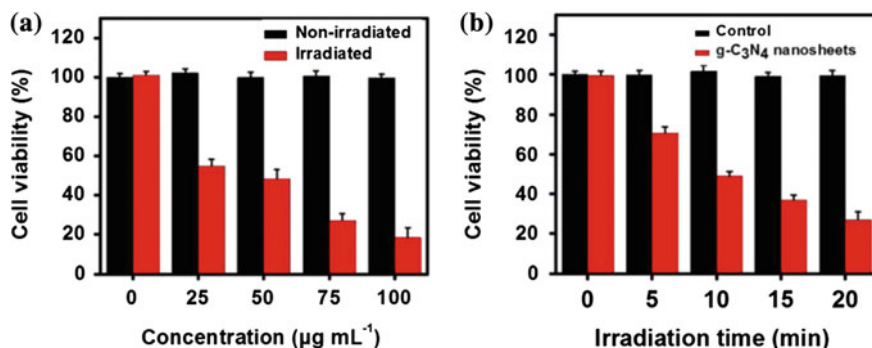**Fig. 17.16** In vitro photodynamic therapy. **a** Concentration-dependent cell viability of HeLa cells incubated with g-C$_3$N$_4$ nanosheets (power density: 20 mW cm^2; irradiation time: 10 min). **b** Viability of HeLa cells incubated with 50 mg mL^{-1} g-C$_3$N$_4$ nanosheets under different irradiation time intervals (power density: 20 mW cm^2) Reproduced from Ref. [33] by permission of the Royal Society of Chemistry
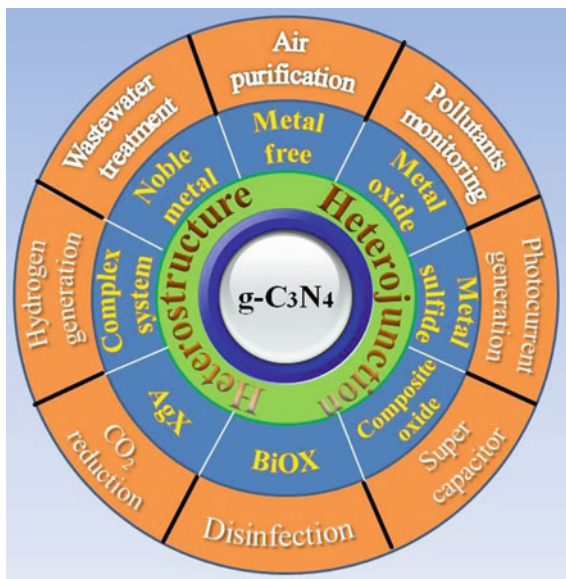
Compared with g-C$_3$N$_4$, most conventional photosensitizers have several limitations, such as poor water solubility, photobleaching, and high toxicity. Thus, g-C$_3$N$_4$ can be effectively used as a novel type of drug nanocarrier. However, the absorption spectra of g-C$_3$N$_4$ are located in the UV region, and human biological tissues have strong absorptive capacity to UV light. The high energy of UV light will increase damage to human tissue, which indicates that g-C$_3$N$_4$ is unsuitable for biological treatment. Therefore, although g-C$_3$N$_4$ has great potential, its application in biomedicine should still be subject to considerable restrictions.

17.4 Summary

This chapter focused on the application of graphitic CNQDs (Fig. 17.17). We summarized published reports, but also complemented them with several other synthetic experiments.

In summary, various types of g-C$_3$N$_4$ nanocomposite systems have been designed and configured. g-C$_3$N$_4$ can function with other nanocomposite syntheses, provide unique properties in photocatalysis, and induce other nanocomposites to further enhance performance. Moreover, for green energy storage, the photocatalytic activity of g-C$_3$N$_4$ has widely been applied for pollutant photocatalytic degradation, disinfection, and solar cell fabrication [34]. g-C$_3$N$_4$ nanocomposites can be applied for biological organisms, but its use as a sensor or biomedical nanoplatform is currently being determined. g-C$_3$N$_4$ nanocomposites will continue to attract much interest in the future.

References

1. Arne T, Frederic G, Markus A, Jens M, Schlogl R, Carlsson JM (2008) Graphitic carbon nitride materials: variation of structure and morphology and their use as metal-free catalysts. J Mater Chem 18: 4893.
2. She Y, Lu Z, Ni M, Li L, Leung MK (2015) Facile synthesis of nitrogen and sulfur codoped carbon from ionic liquid as metal-free catalyst for oxygen reduction reaction. ACS Appl Mater Interfaces 7: 7214.
3. Ding H, Zhang P, Wang TY, Kong JL, Xiong HM (2014) Nitrogen-doped carbon dots derived from polyvinyl pyrrolidone and their multicolor cell imaging. Nanotech 25: 205604.
4. Li Y, Zhao Y, Cheng H, Hu Y, Shi G, Dai L, Qu L (2012) Nitrogen-doped graphene quantum dots with oxygen-rich functional groups. J Am Chem Soc 134: 15.
5. Khanam A, Tripathi SK, Roy D, Nasim M (2013) A facile and novel synthetic method for the preparation of hydroxyl capped fluorescent carbon nanoparticles. Colloid Surf B Biointerfaces 102: 63.
6. Nie H, Li Q, Liang S, Tan Y, Sheng L, Shi W, Zhang SX-A (2014) Carbon Dots with Continuously Tunable Full-Color Emission and Their Application in Ratiometric pH Sensing. Chem Mater 26: 3104.
7. Lee WJ, Maiti UN, Lee JM, Lim J, Han TH, Kim SO (2014) Nitrogen-doped carbon nanotubes and graphene composite structures for energy and catalytic applications. Chem Commun 50: 6818.
8. Wang W, Yu JC, Shen Z, Chan DK, Gu T (2014) g-C3N4 quantum dots: direct synthesis, upconversion properties and photocatalytic application. Chem Commun 50: 10148.
9. Zhou J, Yang Y, Zhang CY (2013) A low-temperature solid-phase method to synthesize highly fluorescent carbon nitride dots with tunable emission Chem Commun 49: 8605.
10. Zhao Z, Sun Y, Dong F (2015) Graphitic carbon nitride based nanocomposites: a review. Nanoscale 7: 15.
11. Miller S (1983) Renewable energy. Environ Sci Technol 17: 75A.
12. Maness PC, Smolinski S, Blake DM, Huang Z, Wolfrum EJ, Jacoby WA (1999) Bactericidal activity of photocatalytic TiO(2) reaction: toward an understanding of its killing mechanism. Appl Environ Microbiol 65: 4094.
13. Kim S, Hwang SJ, Choi W (2005) Visible light active platinum-ion-doped TiO2 photocatalyst J Phys Chem B 109: 24260.
14. Chen D, Wang K, Ren T, Ding H, Zhu Y (2014) Synthesis and characterization of the ZnO/mpg-C(3)N(4) heterojunction photocatalyst with enhanced visible light photoactivity. Dalton Trans 43: 13105.
15. Tian J, Liu Q, Ge C, Xing Z, Asiri AM, Al-Youbi AO, Sun X (2013) Ultrathin graphitic carbon nitride nanosheets: a low-cost, green, and highly efficient electrocatalyst toward the reduction of hydrogen peroxide and its glucose biosensing application. Nanoscale 5: 8921.
16. Ong WJ, Tan LL, Chai SP, Yong ST (2015) Graphene oxide as a structure-directing agent for the two-dimensional interface engineering of sandwich-like graphene-g-C3N4 hybrid nanostructures with enhanced visible-light photoreduction of CO2 to methane. Chem Commun 51: 858.
17. Niu P, Yin LC, Yang YQ, Liu G, Cheng HM (2014) Increasing the visible light absorption of graphitic carbon nitride (melon) photocatalysts by homogeneous self-modification with nitrogen vacancies. Adv Mater 26: 8046.
18. Boonprakob N, Wetchakun N, Phanichphant S, Waxler D, Sherrell P, Nattestad A, Chen J, Inceesungvorn B (2014) Enhanced visible-light photocatalytic activity of g-C$_3$N$_4$/TiO$_2$ films. J Colloid Interface Sci 417: 402.
19. Dai Y, Wang X, Wang Y, Gu Q, Jiang W, Wang Y, Li C, Zeng T, Zeng H, Sun Y, Zeng J (2013) Versatile Graphene Quantum Dots with Tunable Nitrogen Doping Part Part Syst Charact 31: 597.
20. Gray HB, (2009) Powering the planet with solar fuel. Nat Chem 1: 7.

21. Algara-Siller G, Severin N, Chong SY, Bjorkman T, Palgrave RG, Laybourn A, Antonietti M, Khimyak YZ, Krasheninnikov AV, Rabe JP, Kaiser U, Cooper AI, Thomas A, Bojdys MJ (2014) Triazine-based graphitic carbon nitride: a two-dimensional semiconductor. Angew Chem Int Ed Engl 53: 7450.

22. Jian X, Jiajie F, Baoshun L, Shaowen C, Jiaguo Y (2015) g-C_3N_4 modified TiO2 nanosheets with enhanced photoelectric conversion efficiency in dye-sensitized solar cell. J Power Sources 274: 77.

23. Liu Y, Wang Q, Lei J, Hao Q, Wang W, Ju H (2014) Anodic electrochemiluminescence of graphitic-phase C(3)N(4) nanosheets for sensitive biosensing. Talanta 122: 130.

24. Zhang X, Wang H, Zhang Q, Xie J, Tian Y, Wang J, Xie Y (2014) Single-layered graphitic-C_3N_4 quantum dots for two-photon fluorescence imaging of cellular nucleus Adv Mater 26: 4438.

25. Zhang X, Xie X, Wang H, Zhang J, Pan B, Xie Y (2013) Enhanced photoresponsive ultrathin graphitic-phase C_3N_4 nanosheets for bioimaging. J Am Chem Soc 135: 18.

26. Rong M, Lin L, Song X, Wang Y, Zhong Y, Yan J, Feng Y, Zeng X, Chen X (2015) Fluorescence sensing of chromium (VI) and ascorbic acid using graphitic carbon nitride nanosheets as a fluorescent "switch". Biosens Bioelectron 68: 210.

27. Tian J, Liu Q, Asiri AM, Qusti AH, Al-Youbi AO, Sun X (2013) Ultrathin graphitic carbon nitride nanosheets: a novel peroxidase mimetic, Fe doping-mediated catalytic performance enhancement and application to rapid, highly sensitive optical detection of glucose. Nanoscale 5: 11604.

28. Tian J, Liu Q, Asiri AM, Al-Youbi AO, Sun X (2013) Ultrathin graphitic carbon nitride nanosheet: a highly efficient fluorosensor for rapid, ultrasensitive detection of Cu^{2+}. Anal Chem 85: 5595.

29. Hideg E (2004) Detection of free radicals and reactive oxygen species Methods. Mol Biol 274: 249.

30. Novo E, Parola M (2012) The role of redox mechanisms in hepatic chronic wound healing and fibrogenesis. Fibrogenesis tissue repair 5: S4.

31. Novo E, Parola, M (2008) Redox mechanisms in hepatic chronic wound healing and fibrogenesis. Fibrogenesis & tissue repair 1: 5.

32. Idris NM, Gnanasammandhan MK, Zhang J, Ho PC, Mahendran R, Zhang Y (2012) In vivo photodynamic therapy using upconversion nanoparticles as remote-controlled nanotransducers. Nat Med 18: 1580.

33. Lin LS, Li J, Ke KM, Guo SS, Yang HH, Chen GN (2014) Graphitic-phase C3N4 nanosheets as efficient photosensitizers and pH-responsive drug nanocarriers for cancer imaging and therapy. J Mater Chem B 2: 1031.

34. Niu P, Yang Y, Yu JC, Liu G, Cheng HM (2014) Switching the selectivity of the photoreduction reaction of carbon dioxide by controlling the band structure of a g-C_3N_4 photocatalyst. Chem Commun 50: 10837.

Chapter 18
Luminescent Materials for 3D Display Technology

Haizheng Zhong, Ziwei Wang, Wengao Lu, Juan Liu and Yongtian Wang

Abstract As an interesting fashioned and useful technology, three-dimensional (3D) display provides enhanced information for understanding and exhibition. Among the principles or concepts to realize 3D visualization, upconversion volumetric display and computer-generated holographic display are attractive and promising technologies without using eyewears. In these display systems, luminescent materials have been widely explored as display mediums, which are the key components in determining the quality of reconstructed images. This chapter deals with the luminescent materials for 3D display technology. We first explain the principles of upconversion 3D volumetric display and computer-generated holographic display, then describe the progress of luminescence materials as well as the criteria and concepts of materials design, and finally offer a summary with our perspective. Compared with the well-established applications of luminescence materials in lighting and display technologies, the use of luminescence materials in 3D display is in their infancy, yet has not been fully explored. We hope the chapter could evoke the research interest to design and develop luminescent materials toward real naked-eyes 3D display technology.

H. Zhong (✉) · Z. Wang
Beijing Key Laboratory of Nanophotonics and Ultrafine Optoelectronic Systems,
School of Materials Science and Engineering, Beijing Institute of Technology,
5 Zhongguancun South Street, Haidian District, 100081 Beijing, People's Republic of China
e-mail: hzzhong@bit.edu.cn

W. Lu · J. Liu · Y. Wang
Beijing Engineering Research Center of Mixed Reality and Advanced Display,
School of Optoelectronics, Beijing Institute of Technology, 5 Zhongguancun South Street,
Haidian District, 100081 Beijing, People's Republic of China

18.1 Introduction

Because the world is physically three dimensional (3D), human beings already get used to viewing and processing parallax information with relative depth of objects, which accurately creates a mental image. The breakthrough of computer and optical technology provides various display products to reconstruct visual world, which are changing our daily life. Unfortunately, current commercialized display products mainly rely on the panel display technology, only providing two-dimensional (2D) images. Due to the significant advantages of stereoscopic imaging in understanding and illustrating visual information, there is an increased need to develop 3D display technologies, especially in the field of military command-and-control, industrial design, flight simulators, medical imaging, advertisements, movies and exhibitions [1].

Historically, 3D stereoscopy rendering imaging requires the viewers to use special eyewears [2]. The drawbacks of this technique are user fatigue and the inability to reproduce all of the information from the original objects [3]. Alternatively, naked-eyes 3D technologies provide better ways to make viewing easier. Based on different principles, many and various naked-eyes 3D technologies were proposed and demonstrated [4, 5]. Similar to the flat panel display technology, display medium also plays a key role in determining the quality of reconstructed images in 3D display systems [6]. Table 18.1 summarized the techniques and corresponding display mediums of current ongoing 3D technologies. To deal with these various materials that are chosen as 3D display medium, materials design and process engineering is an urgent task to achieve enhanced performance. Among these technologies, upconversion volumetric display and holographic display technologies are interesting 3D display technology and have been the focus in the field of 3D display research [7]. In these display systems, display mediums are required to represent true 3D images and their performance strongly depends on the properties of luminescent materials. Meanwhile, the revolution of luminescent materials provides upconversion nanocrystals [8], novel rare earth-doped glass [9], colloidal quantum dots (QDs) [10] and fluorescent polymers [11] that exhibit

Table 18.1 Summary of the ongoing 3D display techniques and their corresponding display mediums

Technology		Display mediums
Stereoscopic displays	Glasses-based stereoscopic displays	Plastic resin materials [1]
	Autostereoscopic displays	Liquid crystal [12]
Volumetric displays	Swept volume displays	Plastic materials [13]
	Static volume displays	Rare earth-doped crystal [14] Gaseous materials [15] Dye-based composites [16] Upconversion materials [17] Multiplanar LCD [7]
Holographic displays		Quantum dots [18]

unique properties for numerous applications. Advances in chemistry and material science have led to the precise tuning and control of their luminescence properties, opening up the possibility to enhance the performance of 3D display technology.

To the best of our knowledge, there is less literature that concerns the materials engineering for 3D display technologies. In this chapter, we would like to introduce the progress of luminescent materials for 3D applications and the current challenge, especially for volumetric and holographic display. The chapter is organized as follows. Section 18.2 explains the principles of upconversion 3D volumetric display and computer-generated holographic display; Sect. 18.3 describes the progress of luminescence materials as well as the criteria and concepts of materials design for upconversion 3D volumetric display and computer-generated holographic display; and finally Sect. 18.4 offers a conclusion and perspective. We hope the chapter could evoke the research interest of materials scientists to design and develop materials for 3D display technology.

18.2   Principle

18.2.1   *Upconversion 3D Volumetric Display*

Among the many and varied methods for 3D displays, volumetric display technology based on upconversion materials is a static system that can provide most of the depth cues automatically without employing mechanical motion. The pioneering concept using upconversion materials was firstly proposed by Lewis et al. in Battelle Laboratories in 1971 [19]. In 1996, this concept was greatly developed by Downing et al. with utilizing rare earth-doped heavy metal fluoride glasses [17]. Figure 18.1 schematically illustrates the principle of upconversion volumetric display technique. In this system, upconversion materials were used as display medium under near-infrared light excitation (laser or light emitting diodes). The excitation process mainly contain three steps: (i) The absorption of first near-infrared photon populates the intermediate energy level of ions in the medium, (ii) subsequently the absorption of another photon with a different wavelength at the intersection point of the two beams excites the ions in the intermediate level to the upper level, and (iii) ions in the upper level then decay to the ground state while radiating visible light. This process is called two-step, two-frequency upconversion (TSTF-UC).

Later on, Honda et al. from Stanford University proposed an alternative pumping scheme using a one-color, one-beam pumping method in which Er^{3+}-doped heavy metal fluoride glasses were used [20]. By selecting the display mediums that can be excited by two photons at the same wavelength, it is possible to use single-frequency laser source to excite the materials by focusing one laser beam at a near-IR wavelength into a transparent medium.
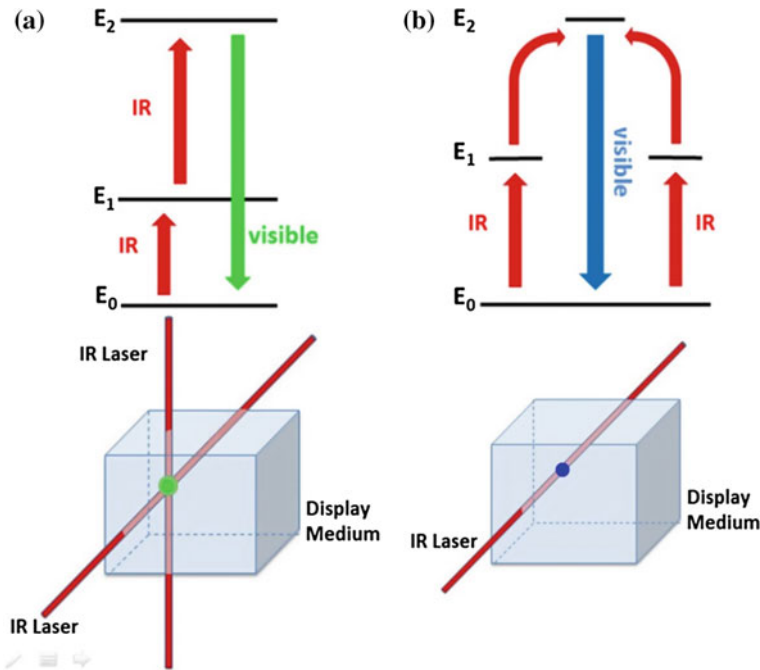
Fig. 18.1 Schematic diagram of the upconversion volumetric display. **a** Diagram of two-step upconversion process. **b** One-color, one-beam pumping method

18.2.2 Computer-Generated Holographic 3D Display

The point of holography was first presented by Dennis Gabor in 1948 [21]. After the development of laser technology, holography received a great attention in information recording and display. Holographic display technology record the 3D object's information on a hologram through light interference, and the 3D image can be reconstructed from the hologram by light diffraction [22]. Because of the feasibility in reconstructing signal waves with amplitude and phase, holographic display became an ideal 3D display technology to fill all the visual features for 3D imaging.

Computer-generated holography (CGH) [23], as one branch of holography, has attracted extensive attention because of the development of the computer technology. CGH technique is a procedure to generated holograms through computer reconstruction. As illustrated in Fig. 18.2, computer programs are used to create virtual objects and then simulate the interference of the object light and reference light. After this step, one can obtain the mathematical expression of the complex amplitude of the light field in the hologram plane. Next, the complex amplitude distribution will be encoded as positive real number distribution for recording the holograms. The fourth step is using masks or films to record the encoded
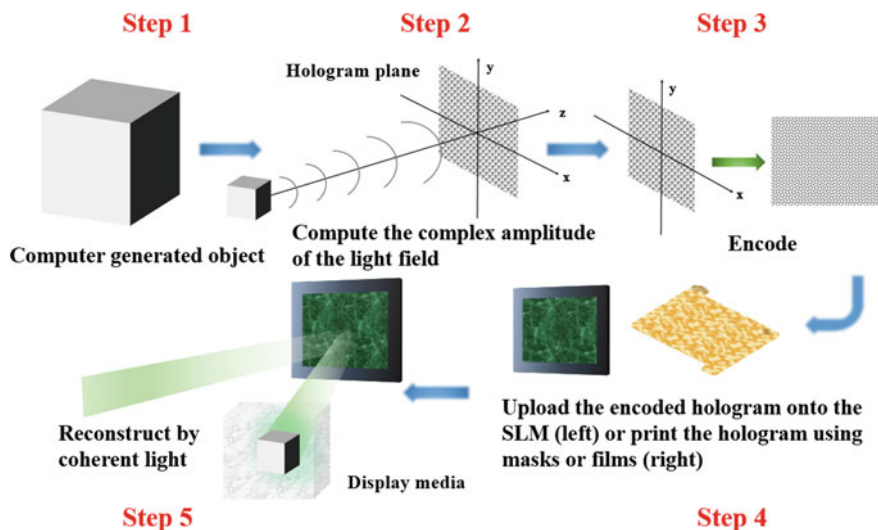
Fig. 18.2 Illustration of the system for CGH technique. The whole process includes virtual object generation, computing and encoding, information uploading and reconstruction of the original object [59]

holograms. More prevalent, in order to display dynamic 3D images, the encoded holograms can be uploaded onto optoelectronic devices such as spatial light modulators (SLMs) for the last step: using coherent light to reconstruct the original virtual objects.

CGH technique possesses the advantage of displaying objects that are not real, easier data storage and transmission, promoting the quality of the image using digital method and so forth. However, the viewing angle was limited by the space bandwidth of the SLM. Generally, the images can be only visualized among several degrees to around 10° [24]. This has been an obstacle toward the applications. In this technique, the display medium plays a key role to determine the quality of the final holograms. To meet the requirements of ideal 3D displays, the display medium must be block materials at least in centimeter level and homogeneous materials. It provides an approach of obtaining wide viewing angle as large as 30°, and it is very suitable for 3D displays [18].

18.3 Progress Luminescent Display Mediums

Since display medium generates visible emission by the conversion of signal light, the quality of reconstructed image is mainly determined by their luminescence properties. As illustrated in Fig. 18.3, the display mediums at least fulfill the following requirements: (i) high transparency to visible wavelengths and to the
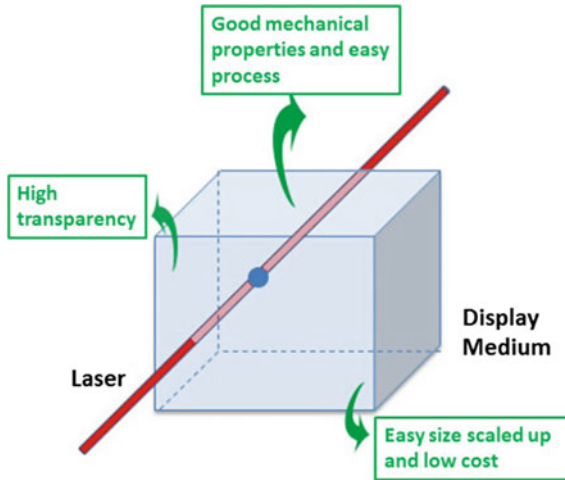
Fig. 18.3 Illustration of the three main requirements of materials for display mediums

wavelengths used to excite visible emission from a voxel; (ii) good mechanical properties and easy process; (iii) easy size scaled up (volumes at least 30 cm on a side) and low cost. With the development of display technology, different types of materials were explored as a display medium. For example, gaseous materials, organic dyes, upconversion phosphors and QDs were explored as possible display media for upconversion volumetric and computer-generated holographic 3D displays. In the following section, we will summarize these display mediums and their features in 3D image visualization.

18.3.1　Gaseous Materials

The use of gaseous materials for 3D display applications has a long history. To the best of our knowledge, gaseous materials like mercury vapor, iodine monochloride vapor and rubidium vapor have been studied as potential candidates for 3D display application [25–27]. In the earlier report, Zito firstly reported the analysis of multiple-step excitation process in mercury vapor for the possible application in 3D display [25]. Later on, Verber et al. investigated the two-photon excitation properties of iodine monochloride vapor [26]. However, only after twenty years, Kim et al. demonstrated the first 3D volumetric display based on atomic vapor using a pair of laser diodes with optical powers of 12.7 mW (633 nm) and 41.5 mW (780 nm) [27]. Figure 18.4 presents the schematic diagram of 3D volumetric display based on atomic vapor and the corresponding image test. They realized three-dimensional viewing in the real time using Rb gas cell as the medium under the intersection of two power diode laser beams. However, gaseous materials suffer
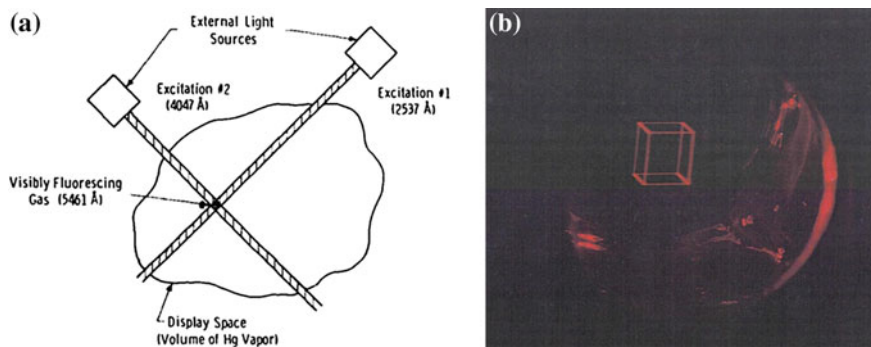
Fig. 18.4 **a** Schematic diagram of 3D volumetric display based on atomic vapor. Reprinted with permission from Ref. [25]. Copyright 2004, American Institute of Physics. **b** The view of 3D display. Reprinted from Ref. [27], copyright 1996 society of photo optical instrumentation engineers

much less distortion of images than does a solid medium, owing to the refractive index difference between the medium and air. The operation needs precise frequency tuning of the laser and requires high-pressure container in the display. In the case of Rb vapor, heating of the medium is also required. Due to the limitations in operation, the use of gaseous materials as display mediums for 3D display is not a practical technology.

18.3.2 Organic Dyes

Organic dyes include a broad range of materials such as organic molecules, conjugated polymers and organic–inorganic hybrids, which have the advantages of structure-tunable properties [16, 28–30]. They are common luminescent materials that find wide applications in many fields. The exploration of organic dyes in 3D display has been discussed in a recent review paper [31]. In 1999, Rapaport et al. discussed the two-photon absorption of a single infrared pump wavelength in several of the dye-doped liquids and polymeric matrix [32]. Although some dyes in liquid and polymeric solutions can be excited to emit visible light by simultaneous absorption of two infrared light sources of different wavelengths, it is not easy to confine the dyes and solvents due to their hazardous properties [31]. Instead of that, dye-doped polymers are advantageous to serve as display medium. It should be noted that regular dyes have small Stokes shifts, and the overlap between the absorption and emission causes the color of the observed visible emission to depend on the location of the emitting site within the sample. To reduce the self-absorption effect, multiple dyes system with large Stokes shift became more attractive candidate for 3D display applications. As a recently investigated promising upconversion technology, multiple organic dyes-based triplet–triplet annihilation
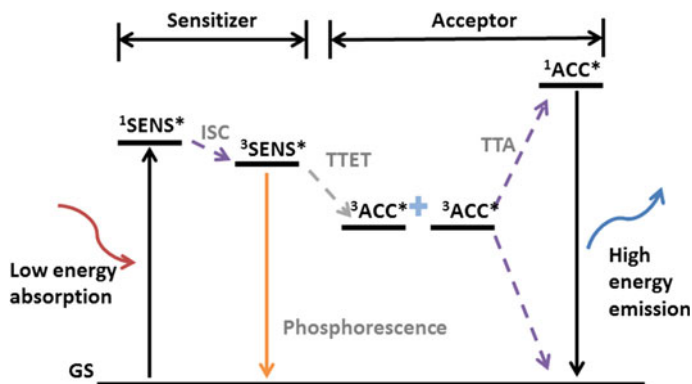
Fig. 18.5 Mechanism of TTA. TTA is triplet–triplet annihilation. ISC is intersystem crossing. TTET is triplet–triplet energy transfer. GS is ground state. SEN is sensitizer. ACC is acceptor

upconversion (TTA-UC) system shows high upconversion quantum yield up to 32 % at low excitation intensity, which is much higher than that of other upconversion processes [33]. From this viewpoint, triplet–triplet annihilation-assisted upconversion systems can be promising as display mediums for 3D applications.

Triplet–triplet annihilation (TTA) [33] was firstly demonstrated by Parker and Hatchard in 1962 [34]. The mechanism of TTA is illustrated in Fig. 18.5 The TTA-UC process is a sequence of events: a sensitizer becomes excited and reaches a triplet state through intersystem crossing (ISC); triplet–triplet energy transfer occurs (TTET) between sensitizer and emitters; triplet–triplet annihilation (TTA) between two emitters leads to a singlet excitation state with higher energy; and the finally upconverted emission comes from the emitter at singlet excitation states. The first requirement of sensitizers is based on the ability to absorb light in visible-to-near-IR region of the spectrum, which allows for low energy excitation. Another select requirement of sensitizers is that they must possess a relatively long lifetime of triplet excited state, which is significant to facilitate conditions for efficient diffusion-based quenching. As to the energy state, the sensitizer molecule should have singlet excited state which lies below that of the acceptor's singlet manifold while the triplet state of sensitizer lies above the acceptor's. In other words, the sensitizer's singlet and triplet excited states should be strategically nested between the singlet and triplet excited states of the acceptor. In addition, the combined energy of two triplets of acceptor molecules should be equal to or higher than the energy of singlet of the acceptor. If the system fits the above energy criteria, upconverted fluorescence is generated under appropriate excitation [35].

Due to their perfect optical characteristics, they could be the possible and hopeful candidate for luminescent materials in the field of 3D display. Even though the upconversion efficiency of TTA-based systems is much higher than other upconversion processes, there are still critical challenges to be solved before pushing them into 3D display applications (Table 18.2).

(i) Improve the upconversion efficiency at moderate excitation intensity. Methods to increase the upconversion efficiency have been intensively studied in recent years. Among these methods, Cao et al. observed TTA-UC with very high upconversion efficiency in singlet sensitizer/multi-acceptor system [36]. The synergistic effect of a hetero-TTA process between triplet acceptors leads to the high upconversion efficiency. They used Platinum(II) octaethylporphyrin (PtOEP) as the single sensitizer and 1,3-diphenylisobenzofuran (DPBF)/9,10-diphenylanthracene (DPA) as dual acceptor. This TTA-UC system can obtain a very high upconversion of 32 % at a excitation energy of 115 mW/cm^2, which is the highest quantum yield of presented numerous TTA-UC systems. However, another problem to be solved is the quantum efficiency of the high power density. Only when the power density exceeds to a certain standard, the quantum efficiency and fluorescence intensity approach to the maximum value.

(ii) Look for solid matrix. Recently, most TTA processes were observed in solution, which can be hardly applied in various devices. TTA system in solid state is significant for their applications. In 2012, Kim et al. used commercially available polyurethane precursors, combined with the benchmark green-to-blue UC pair, which is palladium(II) octaethylporphyrin (PdOEP) and 9,10-diphenylanthracene (DPA), dissolved in tetrahydrofuran (THF), resulting in upconverting transparent solid-state materials with quantum efficiency of 20 % at a excitation energy of 115 mW/cm^2 [37]. Figure 18.6 shows that the materials are shape persistent when removed from the molds and display.

However, the bottleneck of the strategy using polymeric matrix is their limited mobility of chromophores (sensitizers and/or emitters), as well as the limited solubility and aggregation of chromophores in the polymer. Upconverting organogels obtain the characteristics from both upconverting solutions and solid including transparency, high quantum efficiency, shape persistence, low dye content and considerable oxygen tolerance. These features lead them to the possibility to obtain stable matrix for high-efficiency upconversion. Vadrucci et al. presented the first sample of very efficient upconverting gels which are on account of TTA-UC chromophores pair Pd(II) mesoporphyrin IX and 9,10-diphenylanthracene in 2015 [38]. This new gels are shape persistent, highly transparent and display efficient green-to-blue upconversion with upconversion quantum yields of >0.6 and 14 % under ambient and oxygen-free conditions, respectively.

(iii) Solve the oxygen oxidation problem. Because the presence of molecular oxygen can effectively depopulate the triplet states of the sensitizer, various methods, including microcapsules and protect layers [39, 40], are under investigation to further avoid the influences of oxygen, besides the use of various polymers.
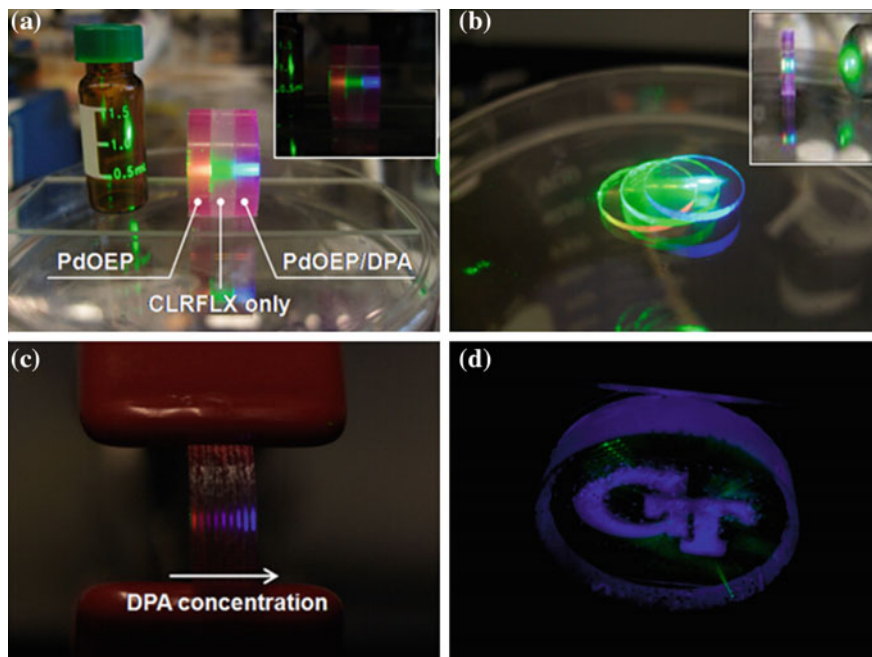
Fig. 18.6 Photographs of the prepared polymer samples which are irradiated by a *green* laser pointer. Light emission from **a** polymer disk and **b** the polymer film. **c** Shows the gradual change in light emission from *blue* to *purple* to *red* in the stacked polymer films containing different concentrations of DPA. **d** Shows *blue* light emission of the PdOEP/DPA blend polymer. Reprinted with the permission from Ref. [37]. Copyright 2012 American Chemical Society

Table 18.2 A comparison of the features of gases, upconversion materials (rare earth-doped crystals, glasses, nanocomposites), organic dyes and QDs for 3D display applications

Properties	Gaseous materials	Rare earth-doped phosphors	Dyes	QDs in hydrogel
Transparency	Good	Good	Moderate	Good
Efficiency	<5 %	Bulk materials <5 % Nanocrystals <1 %	Upconversion <32 % Downconversion 40–90 %	>30 %
Stability	Poor	Good	Poor	Moderate
Excitation source	Two-step	>10 W cm^{-2}	~	<10 mW cm^{-2}
Response time	~0.1 ms	~μs	~ns	~ns
Color	Multicolor	Multicolor	Multicolor	Multicolor
Other features	Sensitive	Expensive	Photo-bleaching	Scalable healable
Refs.	[25–27]	[8, 17, 42, 50, 57]	[58]	[18]

18.3.3 Rare Earth-Doped Phosphors

The use of crystalline rare earth materials in display technology has been extensively studied over the past 20 years. Considering the requirements for high upconversion efficiency in volumetric 3D display, rare earth-doped crystals are the interesting candidates to be explored. However, the direct use of single crystals as the 3D display medium presents practical difficulties due to the limited size and expensive cost.

In contrast to the single crystals, rare earth-doped glasses are less expensive materials. The use of rare earth-doped glasses as display mediums in upconversion volumetric displays was firstly studied by Elizabeth Downing in 1996 [17]. They used several different rare earth ions, for example Pr^{3+}, Er^{3+} and Tm^{3+}, to obtain rare earth-doped heavy metal fluoride glass as bulk medium. Infrared laser beams were used to intersect inside a transparent volume of active optical materials to address green, red and blue voxels. By scanning the point of intersection of the lasers around inside the materials, 3D wire-frame images, surface areas and solids are drawn and the 3D image could be seen through naked eyes. However, the imaging quality was limited by the scanning speed of laser beams; there is urgent need to implement more fully integrated system architecture as well as enhance upconversion efficiencies with novel material systems. To obtain three basic colors, Yang et al. used a multi-rare-earth-doped glass in full-color display in 2005 [41]. They used two luminescence ions, Er^{3+} and Tm^{3+}, as blue, green and red emitters to control the color of the emitted light. Yb^{3+}, as sensitizer ions, was applied to increase the emission intensity of upconversion. The co-doped method is easy to control, but interference during the display process might occur.

Although rare earth-doped glass are less expensive, it is still a great challenge to obtain rare earth-doped glass large enough to fulfill the requirement of upconversion volumetric 3D display. To obtain scalable display medium, in 2007, Jenssen and coworkers proposed to disperse rare earth-doped crystal powder into a refractive index-matched polymer [31]. They tried to disperse micrometer-sized crystals into transparent polymer or sol–gel matrix. However, the strategy was limited by the inherent scattering effects due to the mismatch of refractive index. Later on, Laine et al. reported the fabrication of polycrystalline RE: $Yb^{3+}:Y_2O_3$ ceramics with photonic transparency quality by using preformed nanocrystals with average diameter <50 nm [42]. The samples can emit red and blue light, showing great potential for 3D volumetric display applications. To overcome the inherent scattering effects, it is essential to reduce the size of particles (Fig. 18.7).

Recent developments in nanoscience and nanotechnology make colloidal upconversion nanocrystals as a new generation of luminescent materials [43, 44]. Owing to their characteristics such as small size and high content dispersion, colloidal upconversion nanocrystals can be readily incorporated into polymer matrices to construct functional composites that exhibit advantageous electrical, optical or magnetic properties [45]. Compared with rare earth-doped crystals, hybrid composites have many advantages such as reduced weight and cost as well as scalable
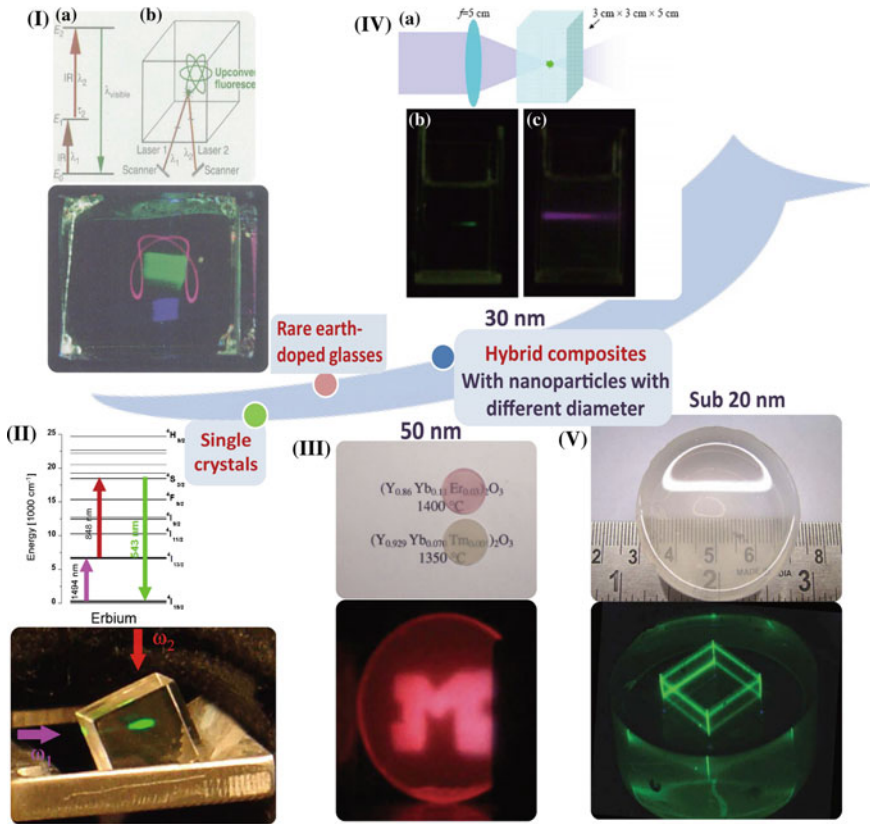
Fig. 18.7 Developments and luminescent images of various kinds of rare earth-doped materials including *I* single crystals (From Ref. [17], Reprinted with permission from AAAS); *II* rare earth-doped glasses (Reproduced from Ref. [31] by permission of John Wiley & Sons Ltd) and (II)–(IV) hybrid composites (*III* Reproduced from Ref. [42] by permission of John Wiley & Sons Ltd; *IV* Reproduced from Ref. [46], © 2008 Optical Society of America; *V* Reprinted by permission from Macmillan Publishers Ltd: Ref. [50], copyright 2010)

size. The feasibility of using upconversion nanocrystals in volumetric display was firstly explored by Liu et al. in 2008 [46]. They synthesized lanthanide-doped $NaYF_4$ nanocrystals with diameter of ~ 30 nm using a solvothermal route using ethylene glycol (EG) as the solvent and demonstrated their possibility as display medium.

Motivated by their promising application in many fields including biological technology and optical devices, upconversion nanocrystals have been intensively explored in the past few years [47, 48]. As the optical properties of upconversion nanocrystals can be finely tuned by varying their crystallographic phase, size as well as doping concentration, much effort has been paid to the synthetic chemistry.

Along with the application exploration in display and photovoltaic cells, the incorporation of upconversion nanocrystals into polymer matrix is also an interesting topic [49]. Despite the progress in the synthetic chemistry, it has been a great challenge to prepare small-sized nanocrystals (sub-20 nm) with high upconversion luminescence under low-power infrared light excitation. A milestone of upconversion nanocrystals was achieved by Wang et al. in 2010 [50]. In their work, the influence of ion doping on the crystal growth and the optical properties in $NaYF_4$ upconversion nanocrystals was demonstrated, proving very high quality materials with tunable emissions from blue to green color. These nanocrystals can be readily incorporated into polydimethylsiloxane (PDMS) monoliths to construct volumetric 3D displays, presenting unique interface applications for 3D image visualization. The left photograph in Fig. 18.8 shows physical dimension and transparency of a PDMS sample composed of 0.1 wt% of $NaYF_4$: Yb/Er/Gd(18/2/5 mol%) nanocrystals. The right photograph shows luminescent image of a 3D structure generated in the PDMS sample through computer-controlled near-infrared laser scanning. Even up to date, the most efficient upconversion materials are Yb^{3+}/Er^{3+}-doped $NaYF_4$ nanocrystals, these materials are still not ideal for the display demands of daily life because the low absorption cross section of rare earth ions leads to low upconversion efficiency of materials [51].

To dynamically tune the emission of material in full-color range, Liu's group designed and fabricated multiple-shelled $NaYF_4$-based core–shell nanocrystals, containing five sets of lanthanide ions (Yb^{3+}, Nd^{3+}, Tm^{3+}, Ho^{3+} and Ce^{3+}) into specific layers at precisely defined concentrations [52]. Then, they fabricated nanocrystals/PDMS composite monoliths. As shown in Fig. 18.8, the composites are available to dynamically fine-tune the emission in the full-color range from a new class of core–shell upconversion nanocrystals by adjusting the pulse width of two infrared laser beams of 808 and 980 nm.

18.3.4   Quantum Dots

Quantum dots (QDs) are emerging as novel functional materials for lighting and display technologies because of their colorful saturated emissions as well the solution process fabrications [53, 54]. Typical full-width at half-maximum (FWHM) values are around 30 nm, which is less than half of the spectral distribution found in conventional organic emitters (60–120 nm FWHM) [55]. Hydrogels are "half-liquid like" and "half-solid like" materials with attractive abilities to change shape and respond to many different stimuli. The combination of narrow colorful emissions from QDs and scalable and healable characteristics from hydrogels provides an intelligent system to display 3D images generated by the spatial light modulator (SLM). Recently, Zhong and Wang et al. from Beijing Institute of Technology demonstrated the concept that use polyvinyl alcohol
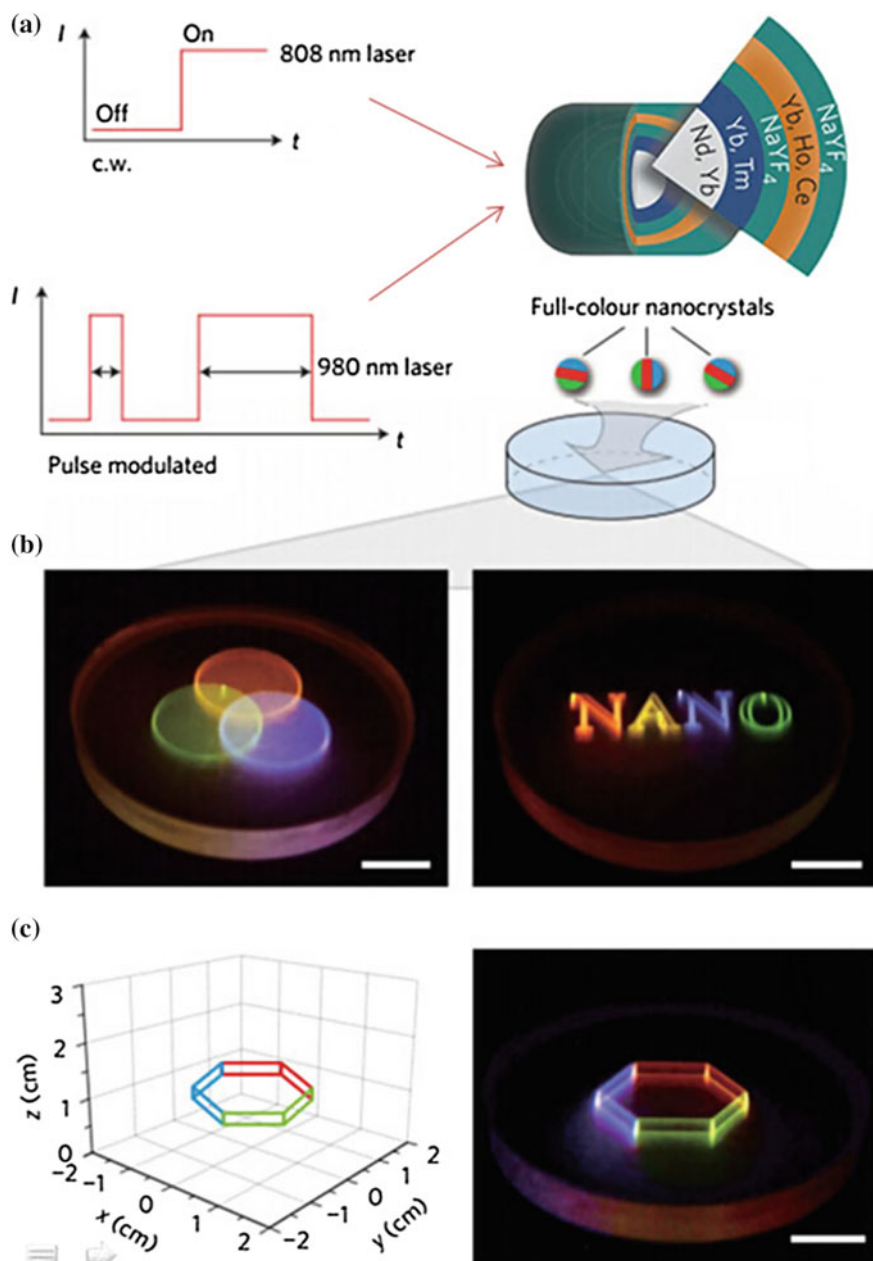
◄ **Fig. 18.8** Demonstration of full-color volumetric three-dimensional display in nanocrystals/
PDMS composite materials. **a** Schematic of the experimental setup for volumetric three-
dimensional full-color display. **b** Luminescence color images generated in the nanocrystal/PDMS
composite monolith show the ability to display additive colors (*left*) and three-dimensional objects
with wide color gamuts (*right*) using the as-developed display system. **c** Schematic representation
of the computational design of a volumetric full-color three-dimensional display (*left*) and the true
image (*right*) generated through use of the multilayer upconversion nanocrystals. Reprinted by
permission from Macmillan Publishers Ltd: Ref. [52], copyright 2015

(PVA) hydrogel embedded with QDs as display medium for holographic display
applications [18]. Figure 18.9 shows the PVA hydrogel embedded with different
QDs. As shown in Figs. 18.10 and 18.11, the PVA hydrogel with QDs can display
the computer-generated holograms efficiently and reconstruct 3D visual effects
almost instantaneously on laser irradiation. Along with the viewing angle change,
the image presents different profile similar to real object, indicating that the
reconstructed image is three dimensional.

However, the use of physical cross-linked PVA hydrogel leads to shape insta-
bility. Glass container was needed to keep the shape of bulk hydrogel which hinders
audience watching the image in a wide viewing angle range. Moreover, the
mechanical strength restricts its application in holographic display. In our following
work, double-network (DN) hydrogels were introduced as polymeric matrix to
improve the mechanical properties [59] (Fig. 18.12). High mechanical strength and
transparent DN hydrogel made from 2-acrylamido-2-methylpropane-sulfonic acid
(AMPS) and acrylamide (AAm) replaces the PVA as matrices for QDs. The per-
formance of QDs-embedded PAMPS/PAAm hydrogel in computer-generated
holographic display system was determined. A simple kaleidoscope hologram was
applied for the reconstruction test which consists of 200 independent light spots. As
shown in Fig. 18.13, a kaleidoscope 3D image was successfully reconstructed by
hybrid DN hydrogel as display medium via 533-nm laser excitation source. As long
as the hybrid hydrogel was irradiated by the modulated laser, independent spots of
kaleidoscope were displayed clearly with high luminescence, allowing audience to
watch without using any auxiliary equipment.

QDs-embedded hydrogels were demonstrated to be suitable polymeric matrix for
the preparation of highly luminescent bulk composites with enhanced transparency.
The composites have good mechanical strength like resistance to shear force or
pressure and provide the free-standing characteristics. The combination of QDs and
transparent hydrogel could be potential display mediums for holographic 3D dis-
play. However, to reduce the self-absorption effects, these QDs need to be further
designed and developed through band engineering. For example, the concept of
doped semiconductor nanocrystals (NCs) was demonstrated to show small lumi-
nescent solar concentrators (LSC) reabsorption losses [56]. However, the idea
should be further developed to balance the excitation and emission color for 3D
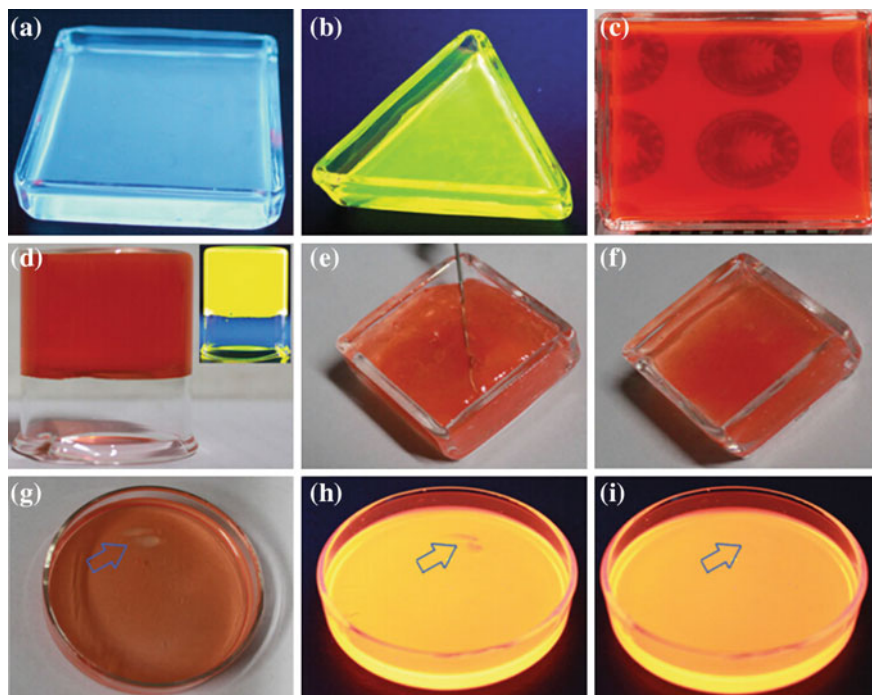display applications.

Fig. 18.9 Fluorescent image of PVA hydrogel incorporated with different QDs. Reproduced from Ref. [18] by permission of John Wiley & Sons Ltd

18.4 Summary and Perspectives

This chapter of the book summarizes the progress on the use of luminescent materials as display mediums for 3D display applications, mainly focus on the materials for upconversion volumetric display and computer-generated holographic display. Despite the recent progress in various luminescent materials, there is still no available material that can fulfill all the requirements of display medium for 3D display applications.

Upconversion materials are ideal systems for the integration into volumetric display technology; however, the high upconversion quantum yield at appropriate power density is imperative. It is unlikely that a solution will be provided by one single organic or inorganic material at this point in time; integration of the positive characteristics of each into a hybrid material or device could be necessary. Especially, the use of TTA-UC system seems to be promising in the future. The future work will focus on the solid-state systems. Improvement in its stability and efficiency may open up the possibility to design and develop novel 3D display mediums.
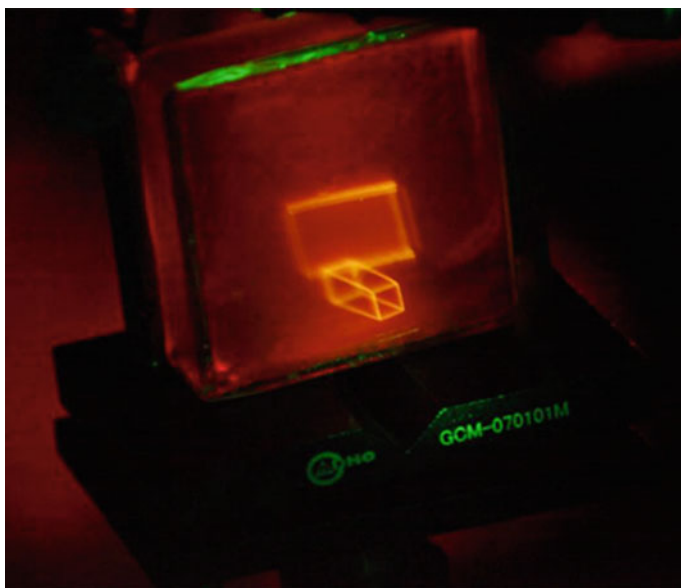
Fig. 18.10 Digital camera images for holographic reconstruction of cuboid under room light. Reproduced from Ref. [18] by permission of John Wiley & Sons Ltd
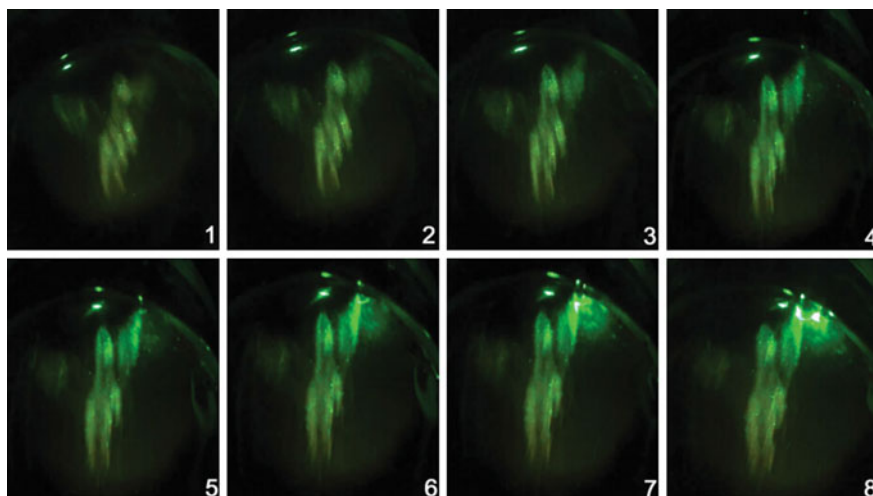

Fig. 18.11 Pegasus images of diverse viewing angle (±15°) under room light. Reproduced from Ref. [18] by permission of John Wiley & Sons Ltd
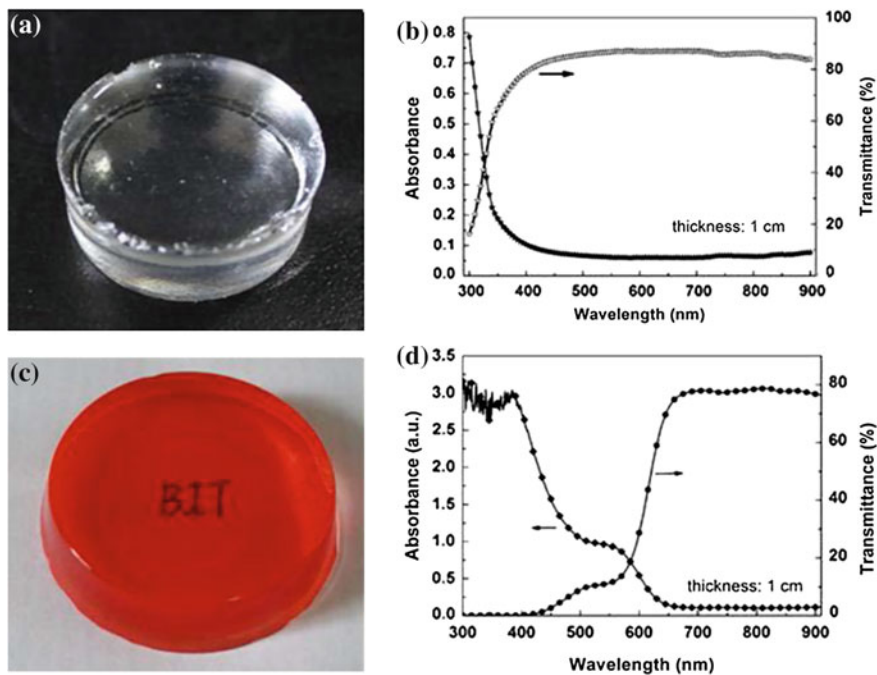
Fig. 18.12 **a** A picture of pure DN hydrogel; **b** absorption and transmittance spectra of pure DN hydrogel; **c** a picture of QDs–DN hybrid hydrogel; **d** absorption and transmittance spectra of QDs–DN hybrid hydrogel [59]
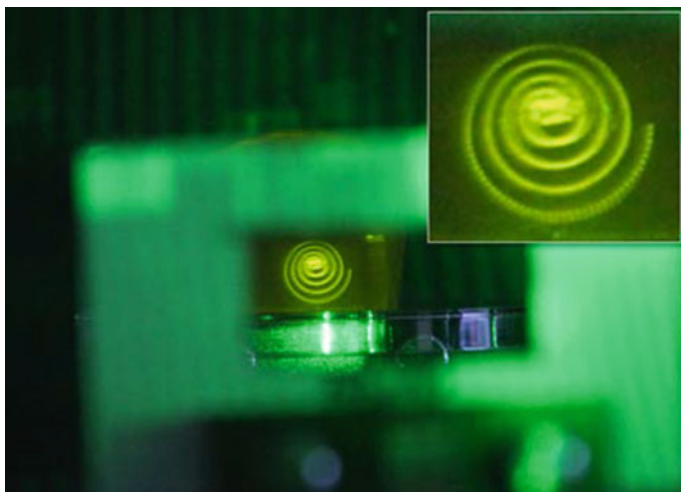

Fig. 18.13 Digital camera images for holographic reconstruction of kaleidoscope by QDs-doped PAMPS/PAAm hydrogel under room light. *Inlet*: amplified reconstruction image of kaleidoscope [59]

QDs present the advantages when their optical properties are tuned through band engineering. There is also chance to enhance their two-photon upconversion properties by designing new materials, which may open up a new door for upconversion materials. In another aspect, the incorporation of QDs into polymeric matrix is always a topic for their applications in lighting and display field. Due to the high stability and numerous ways to tune the surface, there is no problem to obtain large volume display medium. However, the colorful display in QDs-based medium is still a great challenge for holographic 3D display.

Although impressive progress has been made to obtain high-quality and large 3D images with upconversion volumetric display and computer-generated holographic display, these display systems are based on the laser source, which is difficult to be integrated into a product. In the future, the design and development of luminescent materials as display mediums also need to consider the integration into display systems. Moreover, the comparison between different materials is also an urgent work, and there is also need to build standard performance evaluations.

References

1. Hong J, Kim Y, Choi HJ, Hahn J, Park JH, Kim H, Min SW, Chen N, Lee B (2011) Three-dimensional display technologies of recent interest: principles, status, and issues. Appl Optics 50: H87.
2. Dodgson NA (2005) Autostereoscopic 3D displays. Computer 38: 31.
3. Hecht J (2011) 3-D TV and movies: exploring the hangover effect. Optics and Photonics News 22: 20.
4. Li X, Ren H, Chen X, Liu J, Li Q, Li C, Xue G, Jia J, Cao L, Sahu A, Hu B, Wang Y, Jin G, Gu M (2015) Athermally photoreduced graphene oxides for three-dimensional holographic images. Nat Commun 6.
5. Sun B, Edgar MP, Bowman R, Vittert LE, Welsh S, Bowman A, Padgett MJ (2013) 3D computational imaging with single-pixel detectors. Science 340: 844.
6. Tay S, Blanche PA, Voorakaranam R, Tunc AV, Lin W, Rokutanda S, Gu T, Flores D, Wang P, Li G, St Hilaire P, Thomas J, Norwood RA, Yamamoto M, Peyghambarian N (2008) An updatable holographic three-dimensional display. Nature 451: 694.
7. Favalora GE (2005) Volumetric 3D displays and application infrastructure. Computer 38: 37.
8. Cheng L, Wang C, Liu Z (2013) Upconversion nanoparticles and their composite nanostructures for biomedical imaging and cancer therapy. Nanoscale 5: 23.
9. Auzel F (2004) Upconversion and anti-stokes processes with f and d ions in solids. Chem Rev 104: 139.
10. Zhang F, Zhong H, Chen C, Wu XG., Hu X, Huang H, Han J, Zou B, Dong Y (2015) Brightly luminescent and color-tunable colloidal $CH_3NH_3PbX_3$ (X = Br, I, Cl) quantum dots: potential alternatives for display technology. ACS Nano 9: 4533.
11. Zhu CL, Liu LB, Yang Q, Lv FT, Wang S (2012) Water-soluble conjugated polymers for imaging, diagnosis, and therapy. Chem Rev 112: 4687.
12. Eichenlaub JB (1991) Progress in autostereoscopic display technology at Dimension Technologies Inc. Proc SPIE 1457: 290.
13. Favalora GE, Napoli J, Hall DM, Dorval RK, Giovinco M, Richmond MJ, Chun WS (2002) 100-million-voxel volumetric display. Proc SPIE 4712: 300.

14. Langhans K, Bahr D, Bezecny D, Homann D, Oltmann K, Oltmann K, Guill C, Rieper E, Ardey G (2002) FELIX 3D display: an interactive tool for volumetric imaging. Proc SPIE 4660: 176.
15. Cho YW, Oh JE, Kim YH (2012) Storage and retrieval of ghost images in hot atomic vapor. Opt Express 20: 5809.
16. Iwanaga H (2009) Development of highly soluble anthraquinone dichroic dyes and their application to three-layer guest-host liquid crystal displays. Materials 2: 1636.
17. Downing E, Hesselink L, Ralston J, Macfarlane R (1996) A three-color, solid-state, three-dimensional display. Science 273: 1185.
18. Zhu M, Zhong HZ, Jia J, Fu WP, Liu J, Zou BS, Wang YT (2014) PVA hydrogel embedded with quantum dots: a potential scalable and healable display medium for holographic 3D applications. Adv Opt Mater 2: 338.
19. Lewis JD, Verber CM, McGhee RB (1971) A true three-dimensional display. Electron Devices, IEEE Transactions on 18: 724.
20. Honda T, Doumuki T, Akella A, Galambos L, Hesselink L (1998) One-color one-beam pumping of Er^{3+}-doped ZBLAN glasses for a three-dimensional two-step excitation display. Optics Letters 23: 1108.
21. Gabor D (1948) A new microscopic principle. Nature 161: 777.
22. Blanche PA, Bablumian A, Voorakaranam R, Christenson C, Lin W, Gu T, Flores D, Wang P, Hsieh WY, Kathaperumal M, Rachwal B, Siddiqui O, Thomas J, Norwood RA, Yamamoto M, Peyghambarian N (2010) Holographic three-dimensional telepresence using large-area photorefractive polymer. Nature 468: 80.
23. Teng DD, Pang ZY, Liu LL, Wang B (2014) Displaying three-dimensional medical objects by holographical technique. Opt Eng 53: 6.
24. Takaki Y, Nakamura J (2011) Zone plate method for electronic holographic display using resolution redistribution technique. Opt Express 19: 14707.
25. Zito R (1963) Rate analysis of multiple-step excitation in mercury vapor. J Appl Phys 34: 1535.
26. Barnes RH, Moeller CE, KircherJF, Verber CM (1974) Two-step excitation of fluorescence in iodine monochloride vapor. Appl Phys Lett 24: 610.
27. Kim II, KorevaarEJ, Hakakha H (1996) Three-dimensional volumetric display in rubidium vapor. Proc SPIE 2650: 274.
28. Zhao YS, Fu HB, Peng AD, Ma Y, Xiao DB, Yao JN (2008) Low-dimensional nanomaterials based on small organic molecules: preparation and optoelectronic properties. Adv Mater 20: 2859.
29. Kraft A, Grimsdale AC, Holmes AB (1998) Electroluminescent conjugated polymers-seeing polymers in a new light. Angew Chem Int Ed 37: 402.
30. Carlos LD, Ferreira RAS, Bermudez VZ, Ribeiro SJL (2009) Lanthanide-containing light-emitting organic–inorganic hybrids: abet on the future. Adv Mater 21: 509.
31. Cho JH, Bass M, Jenssen HP (2007) Volumetric three-dimensional up-conversion display medium. J Soc Inf Display 15: 1029.
32. Rapaport A, Ayrault K, St Matthew-Daniel E, Bass M (1999) Visible light emission from dyes excited by simultaneous absorption of two different frequency beams of light. Appl Phys Lett 74: 329.
33. Singh-Rachford TN, Castellano FN (2010) Photon upconversion based on sensitized triplet–triplet annihilation. Coordin Chem Rev 254: 2560.
34. Parker CA, Hatchard CG (1962) Sensitised anti-stokes delayed fluorescence. Proc Chem Soc Lond 386.
35. Singh-Rachford TN, Haefele A, Ziessel R, Castellano FN (2008) Boron dipyrromethene chromophores: next generation triplet acceptors/annihilators for low power upconversion schemes. J Am Chem Soc 130: 16164.
36. Cao X, Hu B, Zhang P (2013) High upconversion efficiency from hetero triplet–triplet annihilation in multiacceptor systems. J Phys Chem Lett 4: 2334.
37. Kim JH, Deng F, Castellano FN, Kim JH (2012) High efficiency low-power upconverting soft materials. Chem Mater 24: 2250. http://pubs.acs.org/doi/pdf/10.1021/cm3012414

38. Vadrucci R, Weder C, Simon YC (2015) Organogels for low-power light upconversion. Mater Horizons 2: 120.
39. Kim JH, Deng F, Castellano FN, Kim JH (2014) Red-to-blue/cyan/green upconverting microcapsules for aqueous- and dry-phase color tuning and magnetic sorting. ACS Photonics 1: 382.
40. Svagan AJ, Busko D, Avlasevich Y, Glasser, G, Baluschev S, Landfester K (2014) Photon energy upconverting nanopaper: a bioinspired oxygen protection strategy. ACS Nano 8: 8198.
41. Yang Z, Feng Z, Jiang Z (2005) Upconversion emission in multi-doped glasses for full colour display. J Phys D Appl Phys 38: 1629.
42. Hinklin TR, Rand SC, Laine RM (2008) Transparent, polycrystalline upconverting nanoceramics: towards 3-D displays. Adv Mater 20: 1270.
43. Wang GF, Peng Q, Li YD (2011) Lanthanide-doped nanocrystals: synthesis, optical-magnetic properties, and applications. Accounts Chem Res 44:322.
44. Stouwdam JW, Hebbink GA, Huskens J, Van Veggel FCJM (2003) Lanthanide-doped nanoparticles with excellent luminescent properties in organic media. Chem Mater 15: 4604.
45. Boyer JC, Johnson NJJ, Van Veggel FCJM (2009) Upconverting lanthanide-doped NaYF$_4$-PMMA polymer composites prepared by in situ polymerization. Chem Mater 21: 2010.
46. Liu XF, Dong GP, Qiao YB, Qiu JR (2008) Transparent colloid containing upconverting nanocrystals: an alternative medium for three-dimensional volumetric display. Appl Optics 47: 6416.
47. Wang F, Liu XG (2009) Recent advances in the chemistry of lanthanide-doped upconversion nanocrystals. Chem Soc Rev 38: 976.
48. Liu XG, Yan CH, Capobianco JA (2015) Photon upconversion nanomaterials. Chem Soc Rev 44: 1299.
49. Lin C, Berry MT, Anderson R, Smith S, May PS (2009) Highly luminescent NIR-to-visible upconversion thin films and monoliths requiring no high-temperature treatment. Chem Mater 21: 3406.
50. Wang F, Han Y, Lim CS, Lu Y, Wang J, Xu J, Chen H, Zhang C, Hong M, Liu X (2010) Simultaneous phase and size control of upconversion nanocrystals through lanthanide doping. Nat 463: 1061.
51. Zhu HM, Lin CC, Luo WQ, Shu ST, Liu ZG, Liu YS, Kong JT, Ma E, Cao YG, Liu RS, Chen XY (2014) Highly efficient non-rare-earth red emitting phosphor for warm white light-emitting diodes. Nat Commun 5: 4312.
52. Deng R, Qin F, Chen R, Huang W, Hong M, Liu X (2015) Temporal full-colour tuning through non-steady-state upconversion. Nat Nanotechnology 10: 237.
53. Shirasaki Y, Supran GJ, Bawendi MG, Bulovic V (2013) Emergence of colloidal quantum-dot light-emitting technologies. Nat Photonics 7: 13.
54. Zhong H, Bai Z, Zou B (2012) Tuning the luminescence properties of colloidal I–III–VI semiconductor nanocrystals for optoelectronics and biotechnology applications. The Journal of Physical Chemistry Letters 3: 3167.
55. Turro NJ, Ramamurthy V, Scaiano JC (2012) Modern molecular photochemistry of organic molecules. Photochem Photobiol 88: 1033.
56. Bradshaw LR, Knowles KE, McDowall S, Gamelin DR (2015) Nanocrystals for luminescent solar concentrators. Nano Lett 15: 1315.
57. Wang M, Chen Z, Zheng W, Zhu H, Lu S, Ma E, Tu D, Zhou S, Huang M, Chen (2014) Lanthanide-doped upconversion nanoparticles electrostatically coupled with photosensitizers for near-infrared-triggered photodynamic therapy. Nanoscale 6: 8274.
58. Liu WT, Huang WY (2012) Enhancing the color gamut of white displays using novel deep-blue organic fluorescent dyes to form color-changed thin films with improved efficiency. Opt Eng 51: 104001.
59. Wang ZW, Zhu M, Bai ZL, Chen BK, Wang YT, Zhong HZ (*Unpublished*) Double-network hydrogel embedded with quantum dots: enhanced visual performance for holographic 3D display.